Transactions of the ASME®

Journal of Applied Mechanics

Published Bimonthly by The American Society of Mechanical Engineers

VOLUME 70 • NUMBER 6 • NOVEMBER 2003

Transactions of the ASME, Journal of Applied Mechanics (ISSN 0021-8936) is published bimonthly (Jan., Mar., May, July, Sept., Nov.) The American Society of Mechanical Engineers, Three Park Avenue, New York, NY 10016. Periodicals postage paid at New York, NY and additional mailing office. POSTMASTER: Send address changes to Transactions of the ASME, Journal of Applied Mechanics, c/o THE AMERICAN SOCIETY OF MECHANICAL ENGINEERS, 22 Law Drive, Box 2300, Fairfield, NJ 07007-2300.
CHANGES OF ADDRESS must be received at Society headquarters seven weeks before they are to be effective. Please send old label and new address.
STATEMENT from By-Laws. The Society shall not be responsible for statements or opinions advanced in papers or . . . printed in its publications (B7.1, Para. 3).
 INDEXED by Applied Mechanics Reviews and Engineering Information, Inc. Canadian Goods & Services Tax Registration #126148048.
Reduced-Order Models for Nonlinear Dynamical

TECHNICAL PAPERS

BRIEF NOTES

(Contents continued on inside back cover)

This journal is printed on acid-free paper, which exceeds the ANSI Z39.48-1992 specification for permanence of paper and library materials. ∞™
♲ 85% recycled content, including 10% post-consumer fibers.

(**Contents continued**)

Journal of Applied Mechanics **Volume 70, Number 6** **NOVEMBER 2003**

DISCUSSION

ANNOUNCEMENTS

The Interaction of Two Spherical Gas Bubbles in an Infinite Elastic Solid

F. Chalon

F. Montheillet

Division for Materials and Structures Sciences,
URA CNRS 1884,
Ecole Nationale Supérieure des Mines de Saint-Etienne,
158 cours Fauriel,
42000 Saint-Etienne, France

The elastic strain and stress fields between two bubbles of different sizes and different pressures were estimated by using the fundamental result of Eshelby. The equivalent inclusion method was extended to the case of two inclusions in an infinite elastic solid. This approach, which remains totally analytical, was compared successfully to finite element calculations. The mean stress provides information about gas diffusion between the bubbles: according to the results, the bubbles are likely to progressively equalize their sizes. Moreover, the derivation of the von Mises equivalent stress showed that its value, in the vicinity of the bubbles, is larger than the elasticity limit. Therefore, for a complete mechanical description of the problem, plasticity should be taken into account. In spite of its simplicity, this method nevertheless leads to results, which are very close to the prediction of numerical calculations. [DOI: 10.1115/1.1629110]

1 Introduction

The elastic interaction of two spherical cavities with internal pressure (bubbles) is important from the standpoint of materials engineering and has already been investigated by several authors. One of the common applications is the aging of nuclear fuels: nuclear fission produces helium atoms, which form bubbles that eventually damage the material (Lässer [1]). The knowledge of the stress field between two bubbles gives information about their further evolutions. More specifically, the von Mises equivalent stress level is related to the possible occurrence of local damage associated with plastic strain, while the mean stress (hydrostatic pressure) is associated with bubble growth. An analytical or/and numerical approach on this kind of material is necessary, since it is very difficult to carry out direct measurements of the material evolution with time. It is also relevant to derive analytical expressions of the mechanical interaction between two bubbles, that could be simply implemented into more complex numerical models. Sternberg and Sadowsky [2] were the first to be interested in the problem of interaction of two spherical cavities of the same size. They solved it for a uniform field of tension at infinity using the Boussinesq [3] stress-function approach to obtain a series expansion solution. Other authors then extended this method to more than two cavities and for cavities of different sizes under uniaxial loading along the common axis of the cavities, Miyamoto [4], and uniaxial tension in the direction perpendicular to the axis of the cavities, Tsuchida, Nakahara, and Kodama [5]. Shelley and Yu [6], still following Sternberg and Sadowsky [2], developed this method for inclusions. Chen and Acrivos [7] extended it to an arbitrary strain field applied at infinity. Willis and Bullough [8] proposed a slightly different approach: They considered the total energy of the bubbles, i.e., the elastic energy, the energy of the gas, and the surface energy. Their approach was therefore not only mechanical but also thermodynamical. They gave a solution for the energy interaction between two excess pressure bubbles but they did not derive precisely the stress field from their results.

All the above authors, except Willis and Bullough, started their analysis with Boussinesq [3], Papkovitch [9], or Neuber [10] functions and gave series expansion solutions. In this work, a different approach is proposed, based on the fundamental result of Eshelby [11] extended to two inhomogeneities. The determination of the eigenstrain of each inclusion from the equivalent inclusion method is used to derive the stress and strain fields between the inclusions. The present approach involving cavities with an internal pressure is the same as for cavities in a material submitted to external loading, but it seems important to explain the transposition from one problem to the other. This method is quite general since it allows the interaction between two gas bubbles of different sizes and different pressures to be investigated. Three configurations are analyzed, i.e., two identical bubbles with the same pressure, two bubbles of different sizes with identical pressures, and two identical bubbles with different pressures. For each case, the mean stress and von Mises equivalent stress are displayed along the symmetry axis of the bubbles and in the form of isovalue maps. These results are then discussed by comparison with finite element calculations that are described later. It should be noted that, although finite element calculations generally give accurate results for linear problems, they may nevertheless sometimes depart from the exact solution. In particular, finite element solutions around voids are very mesh sensitive. Numerical results need therefore be considered carefully when compared with the analytical derivations.

2 The Equivalent Inclusion Method of Eshelby

Eshelby has established the following fundamental result. Let D be an elastic and isotropic infinite body. Consider Ω as a part of D, small in comparison with D. We can isolate fictitiously Ω which is supposed to represent an ellipsoidal inclusion. Now remove this inclusion from D and impose to it an eigenstrain $\underset{\sim}{\beta}$, that has no relation with any stress: for example, a thermal deformation or a phase transformation. If the inclusion is replaced into D, which has not been transformed yet, its deformation is no longer free due to the influence of the surrounding matrix. Thus, a stress field appears in Ω and D. The inclusion deformation, $\underset{\sim}{\xi}$, due to the presence of the matrix D, is related to the eigenstrain by $\underset{\sim}{\xi} = \underset{\approx}{S}:\underset{\sim}{\beta}$, where $\underset{\approx}{S}$ is the fourth-order Eshelby tensor. Through this derivation, Eshelby showed that the deformation of an ellipsoidal inclusion embedded in an infinite homogeneous medium, submitted to uniform remote loading, is homogeneous. This result allows the inhomogeneity problem to be dealt with. Consider now

Contributed by the Applied Mechanics Division of THE AMERICAN SOCIETY OF MECHANICAL ENGINEERS for publication in the ASME JOURNAL OF APPLIED MECHANICS. Manuscript received by the ASME Applied Mechanics Division, February 26, 2002; final revision received, June 10, 2003. Associate Editor: A. Needleman. Discussion on the paper should be addressed to the Editor, Prof. Robert M. McMeeking, Department of Mechanical and Environmental Engineering, University of California—Santa Barbara, Santa Barbara, CA 93106-5070, and will be accepted until four months after final publication of the paper itself in the ASME JOURNAL OF APPLIED MECHANICS.

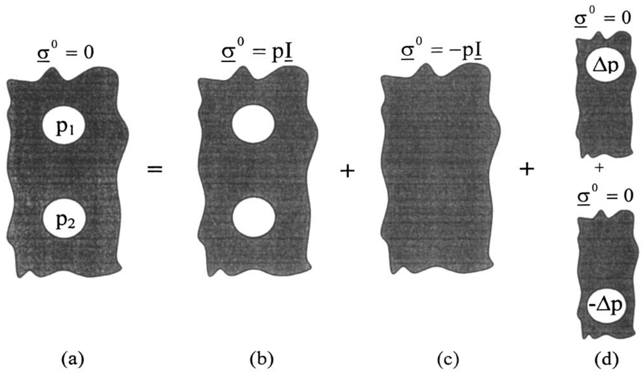

Fig. 1 Decomposition of the problem

an ellipsoidal region, referred to as an inhomogeneity, in an infinite medium, with elastic constants different from the rest of the material.

The Eshelby result is applied to the inhomogeneity. Consider the infinite elastic body of Hooke tensor $\underline{\underline{C}}$, submitted to $\underline{\sigma}^0$ and the corresponding strain $\underline{\varepsilon}^0$ at infinity. The ellipsoidal inhomogeneity Ω with Hooke tensor $\underline{\underline{C}}^i$ disturbs locally the stress field. The aim of the analysis is to determine the perturbations caused by this inhomogeneity. The basic idea of Eshelby is to substitute to the inhomogeneity an homogeneous inclusion with the same properties as the matrix, but submitted to an eigenstrain. The eigenstrain must be determined such as to produce the same stresses and strains as the former inhomogeneity. In the inhomogeneity, the elastic strain is $\underline{\varepsilon}^0+\underline{\xi}$, whereas in the equivalent inclusion it is given by $\underline{\varepsilon}^0+\underline{\xi}-\underline{\beta}$. The equivalence condition for the stresses in the inhomogeneity and the inclusion is therefore

$$\underline{\underline{C}}^i:(\underline{\varepsilon}^0+\underline{\xi})=\underline{\underline{C}}:(\underline{\varepsilon}^0+\underline{\xi}-\underline{\beta}) \tag{1}$$

which, combined with $\underline{\xi}=\underline{\underline{S}}:\underline{\beta}$ allows the eigenstrain tensor $\underline{\beta}$ to be determined.

3 Extension of the Equivalent Inclusion Method of Eshelby

While the problem of interacting inhomogeneities cannot be solved in closed form (the "exact" solution involves infinite series expansions, [12]), an approximate analytical derivation is proposed below. In a first step, the interaction of two bubbles with equal internal pressures will be dealt with. Using the superposition principle illustrated in Fig. 1(*a*), 1(*b*), and 1(*c*), it is sufficient to consider merely cavities. Application of the equivalent inclusion method extended to two inclusions then leads accordingly to introduce two eigenstrains, $\underline{\beta}^{\mathrm{I}}$ and $\underline{\beta}^{\mathrm{II}}$, that depend on the space coordinates. For the sake of simplicity, they will be approximated by their values at the centers of the respective bubbles. In a second step, the effect of a pressure difference Δp between the two bubbles will be addressed in the form of a small perturbation to the above solution. It is worth to note that the boundary conditions at the bubble surfaces, i.e., $\sigma_{rr}=-p$ and $\sigma_{r\theta}=0$, are not strictly fulfilled by such an estimation of the exact solution.

Solid inhomogeneities will first be considered, but in further derivations their elastic constants will be set equal to zero in order to deal with cavities. The problem, which is axisymmetric, will be solved in a plane containing the center of the two inhomogeneities. In Fig. 1, the transition from gas bubbles to cavities without internal pressure is shown, with p_1 greater than p_2, $p=(p_1+p_2)/2$ and $\Delta p=p_1-p$. The case illustrated in Fig. 1(*b*) is more difficult to solve than the other ones that are quite obvious. It seems important to remind that the applied stress at infinity is hydrostatic, so that $\underline{\sigma}^0$ is a diagonal tensor.

Problem (*b*) of Fig. 1 will first be solved for inhomogeneities. Consider two ellipsoidal inhomogeneities Ω_1 and Ω_2 with Hooke tensors $\underline{\underline{C}}^{\mathrm{I}}$ and $\underline{\underline{C}}^{\mathrm{II}}$ in a matrix with Hooke tensor $\underline{\underline{C}}$ under remote stress $\underline{\sigma}^0$. Deformation in inhomogeneity I is influenced by inhomogeneity II such that

$$\underline{\varepsilon}^{\mathrm{I}}=\underline{\varepsilon}^0+\underline{\xi}^{\mathrm{I}}+\underline{\eta}^{\mathrm{II}} \tag{2}$$

with

$$\underline{\xi}^{\mathrm{I}}=\underline{\underline{S}}:\underline{\beta}^{\mathrm{I}} \tag{3}$$

where $\underline{\underline{S}}$ is constant and the same for the two inclusions since its expression depends only on the shape of the inclusions, which are both spherical here, and

$$\underline{\eta}^{\mathrm{II}}=\underline{\underline{D}}^{\mathrm{II}}:\underline{\beta}^{\mathrm{II}} \tag{4}$$

where $\underline{\underline{D}}^{\mathrm{II}}$ is the influence tensor associated with inclusion II. Thus, the strain $\underline{\eta}^{\mathrm{II}}$ represents the influence of inclusion II on inclusion I. In the same way, the influence of inclusion I on inclusion II is $\underline{\eta}^{\mathrm{I}}$.

Note that the eigenstrains could be expanded in polynomial series, e.g.,

$$\beta_{ij}^{\mathrm{II}}(\mathbf{x})=B_{ij}^{\mathrm{II}}+B_{ijk}^{\mathrm{II}}x_k+B_{ijkl}^{\mathrm{II}}x_kx_l+\ \ldots\ . \tag{5}$$

As $\underline{\xi}=\underline{\underline{S}}:\underline{\beta}$ and $\underline{\eta}=\underline{\underline{D}}:\underline{\beta}$, they could be expanded in polynomial series in the same way.

However, to a first approximation, the eigenstrains β^{I} and β^{II} will be assumed uniform, whence

$$\underline{\xi}^{\mathrm{I}}=\underline{\underline{S}}:\underline{\beta}^{\mathrm{I}} \tag{6}$$

is constant while

$$\eta_{ij}^{\mathrm{II}}(\mathbf{x})=D_{ijkl}^{\mathrm{II}}(\mathbf{x})B_{kl}^{\mathrm{II}} \tag{7}$$

remains a function of the space variables through the influence tensor.

The equivalence conditions for the stresses in the two inhomogeneities and the two inclusions can now be written:

$$\begin{cases}\underline{\underline{C}}^{\mathrm{I}}:(\underline{\varepsilon}^0+\underline{\xi}^{\mathrm{I}}+\underline{\eta}^{\mathrm{II}})=\underline{\underline{C}}:(\underline{\varepsilon}^0+\underline{\xi}^{\mathrm{I}}+\underline{\eta}^{\mathrm{II}}-\underline{\beta}^{\mathrm{I}}) & \text{in } \Omega_1\\ \underline{\underline{C}}^{\mathrm{II}}:(\underline{\varepsilon}^0+\underline{\xi}^{\mathrm{II}}+\underline{\eta}^{\mathrm{I}})=\underline{\underline{C}}:(\underline{\varepsilon}^0+\underline{\xi}^{\mathrm{II}}+\underline{\eta}^{\mathrm{I}}-\underline{\beta}^{\mathrm{II}}) & \text{in } \Omega_2.\end{cases} \tag{8}$$

Since the material is isotropic, the constitutive equation can be written in the following form:

$$\sigma_{ij}=2\mu\varepsilon_{ij}+(\kappa-2\mu/3)\varepsilon_{kk}\delta_{ij} \tag{9}$$

where κ and μ are the bulk and shear moduli, respectively.

Equation (8) then becomes

$$\begin{aligned}
&2\mu^{\mathrm{I}}(\varepsilon_{ij}^0+S_{ijkl}\beta_{kl}^{\mathrm{I}}+D_{ijkl}^{\mathrm{II}}\beta_{kl}^{\mathrm{II}})\\
&\qquad+(\kappa^{\mathrm{I}}-2\mu^{\mathrm{I}}/3)(\varepsilon_{kk}^0+S_{kkmn}\beta_{mn}^{\mathrm{I}}+D_{kkmn}^{\mathrm{II}}\beta_{mn}^{\mathrm{II}})\delta_{ij}\\
&\quad=2\mu(\varepsilon_{ij}^0+S_{ijkl}\beta_{kl}^{\mathrm{I}}+D_{ijkl}^{\mathrm{II}}\beta_{kl}^{\mathrm{II}}-\beta_{ij}^{\mathrm{I}})\\
&\qquad+(\kappa-2\mu/3)(\varepsilon_{kk}^0+S_{kkmn}\beta_{mn}^{\mathrm{I}}+D_{kkmn}^{\mathrm{II}}\beta_{mn}^{\mathrm{II}}-\beta_{kk}^{\mathrm{I}})\delta_{ij}\quad \text{in } \Omega_1\\
&2\mu^{\mathrm{II}}(\varepsilon_{ij}^0+S_{ijkl}\beta_{kl}^{\mathrm{II}}+D_{ijkl}^{\mathrm{I}}\beta_{kl}^{\mathrm{I}})\\
&\qquad+(\kappa^{\mathrm{II}}-2\mu^{\mathrm{II}}/3)(\varepsilon_{kk}^0+S_{kkmn}\beta_{mn}^{\mathrm{II}}+D_{kkmn}^{\mathrm{I}}\beta_{mn}^{\mathrm{I}})\delta_{ij}\\
&\quad=2\mu(\varepsilon_{ij}^0+S_{ijkl}\beta_{kl}^{\mathrm{II}}+D_{ijkl}^{\mathrm{I}}\beta_{kl}^{\mathrm{I}}-\beta_{ij}^{\mathrm{II}})+(\kappa-2\mu/3)\\
&\qquad\times(\varepsilon_{kk}^0+S_{kkmn}\beta_{mn}^{\mathrm{II}}+D_{kkmn}^{\mathrm{I}}\beta_{mn}^{\mathrm{I}}-\beta_{kk}^{\mathrm{II}})\delta_{ij}\quad \text{in } \Omega_2.
\end{aligned} \tag{10}$$

As seen above, the Eshelby tensors are the same for Ω_1 and Ω_2. The above system must now be solved in order to determine the eigenstrains for each inclusion.

4 Analytical Resolution

4.1 Derivation of the Influence Tensors D_{ijkl}. The expression of D_{ijkl} for a spherical inclusion of radius a is given by Mura [12]:

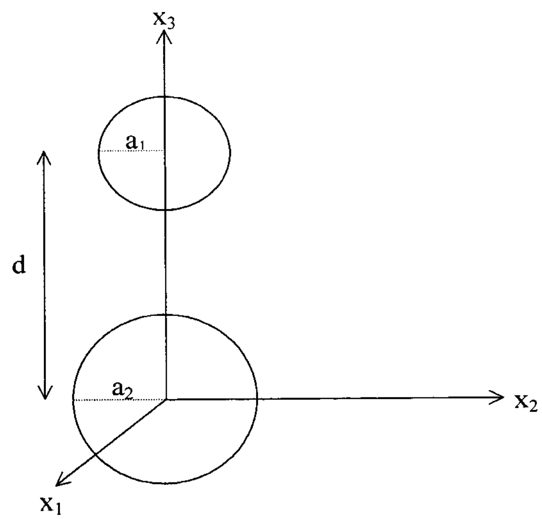

Fig. 2 The two cavities and the set of Cartesian coordinates

$$8\pi(1-\nu)D_{ijkl}(\mathbf{x})=\Psi,_{klij}-2\nu\delta_{kl}\Phi,_{ij}-(1-\nu)[\Phi,_{kl}\delta_{il}+\Phi,_{ki}\delta_{jl}+\Phi,_{lj}\delta_{ik}+\Phi,_{li}\delta_{jk}] \tag{11}$$

with

$$\Phi=\frac{1}{2}[I(\lambda)-x_kx_kI_K(\lambda)] \quad \text{and}$$

$$\Psi,_i=\frac{x_i}{2}[I(\lambda)-x_kx_kI_K(\lambda)-a^2(I_I(\lambda)-x_kx_kI_{IK}(\lambda))] \tag{12}$$

and

$$\lambda=x_1^2+x_2^2+x_3^2-a^2, \quad \text{and} \quad \underbrace{I_{IK}}_{n}(\lambda)=\frac{4\pi a^3}{(2n+1)(a^2+\lambda)^{n+1/2}}. \tag{13}$$

Here, the following convention is used: summation from 1 to 3 is extended over repeated lower case indices; capital indices take the same values as the corresponding lower case ones but without summation. Note that, in Eq. (13), the number of indices $n=0$, 1, or 2.

As seen before, the unknown eigenstrain tensors $\underset{\sim}{\beta}^{\mathrm{I}}$ and $\underset{\sim}{\beta}^{\mathrm{II}}$ are assumed to be uniform in each inclusion. Owing to axisymmetry, the expressions of the eigenstrains can be simplified (Fig. 2).

Since $\beta_{11}=\beta_{22}$, $\beta_{13}=\beta_{23}$, and $\beta_{12}=0$, only three eigenstrain components are to be determined, namely β_{11}, β_{33}, and β_{13}. The linear system (10) then decomposes into one set of four equations for the "diagonal" unknowns β_{11}^{I}, β_{33}^{I}, β_{11}^{II}, and β_{33}^{II} on the one hand, and a set of two equations for the "nondiagonal" unknowns β_{13}^{I} and β_{13}^{II}. This system will be solved for two inclusions centered at (0,0,0) and (0,0,d). The (constant) values of the two eigenstrain tensors are those derived at the center of the associated inclusion, although such a choice is somewhat arbitrary since they could be calculated anywhere in the inclusions. The derivation is detailed below for one inclusion, Ω_1. Thus, owing to axisymmetry, $\underset{\sim}{\eta}$ can be written in the following form:

$$\underset{\sim}{\eta}=\begin{pmatrix}\eta_{11} & 0 & \eta_{13}\\ 0 & \eta_{11} & \eta_{13}\\ \eta_{13} & \eta_{13} & \eta_{33}\end{pmatrix} \tag{14}$$

Therefore only $3\times 6=18\ D_{ijkl}$ components are needed:

$$D_{1111}=D_{2222}=\frac{9\alpha_2^5+5\alpha_2^3(1-2\nu)}{30(1-\nu)}$$

$$D_{3333}=\frac{15\alpha_2^5-10\alpha_2^3(2-\nu)}{15(1-\nu)}$$

$$D_{1122}=D_{2211}=\frac{3\alpha_2^5-5\alpha_2^3(1-2\nu)}{30(1-\nu)}$$

$$D_{3311}=D_{3322}=\frac{-6\alpha_2^5+5\alpha_2^3(1-2\nu)}{15(1-\nu)}$$

$$D_{1133}=D_{2233}=\frac{-6\alpha_2^5+5\alpha_2^3(1+\nu)}{15(1-\nu)}$$

$$D_{1313}=D_{2323}=\frac{-12\alpha_2^5+5\alpha_2^3(1+\nu)}{30(1-\nu)}$$

and all the other $D_{ijkl}=0$.

In the above equations, $\alpha_2=a_2/d$, and for the second inclusion the corresponding components are the same with $\alpha_1=a_1/d$.

4.2 Derivation of the Eigenstrains and the Stress Field

As seen above, $\underset{\sim}{\xi}$ can be written in the following form:

$$\underset{\sim}{\xi}=\begin{pmatrix}\xi_{11} & 0 & \xi_{13}\\ 0 & \xi_{11} & \xi_{13}\\ \xi_{13} & \xi_{13} & \xi_{33}\end{pmatrix} \tag{15}$$

with the 18 associated S_{ijkl}:

$$S_{1111}=S_{2222}=S_{3333}=\frac{7-5\nu}{15(1-\nu)} \qquad S_{1212}=S_{2323}=S_{3131}\ \frac{4-5\nu}{15(1-\nu)}$$

$$S_{1122}=S_{2233}=S_{3311}=S_{1133}=S_{2211}=S_{3322}=\frac{5\nu-1}{15(1-\nu)}$$

and all the other $\mathrm{S}_{ijkl}=0$.

The system (10) can now be solved. For i and $j=1,3$, it leads very easily to

$$\beta_{13}^{\mathrm{I}}=\beta_{13}^{\mathrm{II}}=0 \tag{16}$$

so that the system reduces to four equations for only four unknowns. The elastic moduli μ^{I}, μ^{II}, κ^{I}, and κ^{II} are now set equal to zero, since cavities are considered, and the hydrostatic loading is accounted for by specifying $\varepsilon_{ij}^0=(p/3\kappa)\delta_{ij}$. The following system is obtained:

$$\begin{cases} A_{11}\beta_{11}^{\mathrm{I}}+A_{12}\beta_{33}^{\mathrm{I}}+A_{13}\beta_{11}^{\mathrm{II}}+A_{14}\beta_{33}^{\mathrm{II}}=-p\\ A_{21}\beta_{11}^{\mathrm{I}}+A_{22}\beta_{33}^{\mathrm{I}}+A_{23}\beta_{11}^{\mathrm{II}}+A_{24}\beta_{33}^{\mathrm{II}}=-p\\ A_{31}\beta_{11}^{\mathrm{I}}+A_{32}\beta_{33}^{\mathrm{I}}+A_{33}\beta_{11}^{\mathrm{II}}+A_{34}\beta_{33}^{\mathrm{II}}=-p\\ A_{41}\beta_{11}^{\mathrm{I}}+A_{42}\beta_{33}^{\mathrm{I}}+A_{43}\beta_{11}^{\mathrm{II}}+A_{44}\beta_{33}^{\mathrm{II}}=-p \end{cases} \tag{17}$$

where the coefficients A_{ij}, given in the Appendix, depend on the components of the Eshelby and influence tensors. Once the eigenstrains are determined (see Appendix), the interaction fields between the inclusions can be calculated with the help of the influence tensors $\underset{\approx}{D}^{\mathrm{I}}$ and $\underset{\approx}{D}^{\mathrm{II}}$.

The strain field in the matrix associated with the case of Fig. 1(b) can now been written in the form

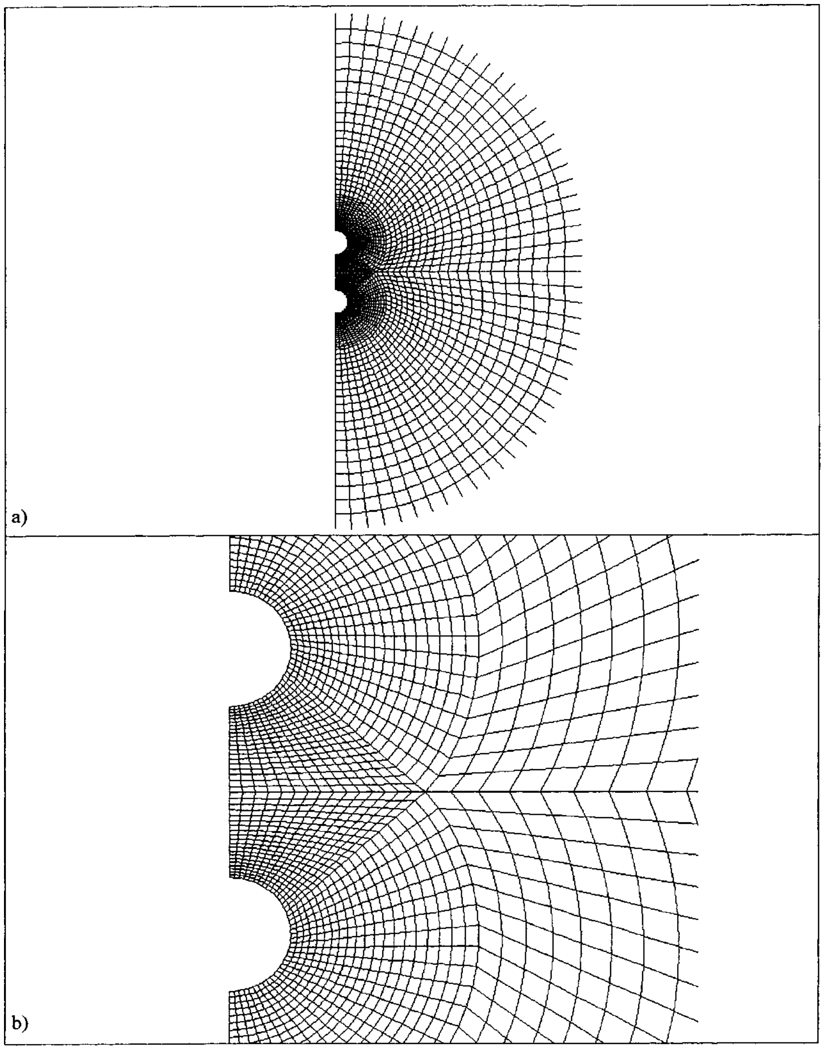

Fig. 3 The finite element mesh: (*a*) general view; (*b*) the area close to the cavities

$$\underset{=}{\varepsilon}=\underset{=}{\varepsilon}^{0}+\underset{\equiv}{D}^{\mathrm{I}}(x_1,x_2,x_3):\underset{=}{\beta}^{\mathrm{I}}+\underset{\equiv}{D}^{\mathrm{II}}(x_1,x_2,x_3):\underset{=}{\beta}^{\mathrm{II}}. \tag{18}$$

Owing to the axisymmetric configuration, the interactions are analyzed in the plane (x_1,x_3). Since the eigenstrain tensor has the following diagonal form:

$$\begin{pmatrix} \beta_{11} & 0 & 0 \\ 0 & \beta_{11} & 0 \\ 0 & 0 & \beta_{33} \end{pmatrix}, \tag{19}$$

the only required components of the influence tensor are D_{ij11} and D_{ij33}. The interaction strains for the case of Fig. $1(b)$ are given by

$$\begin{aligned}\eta_{11}=&(D^{\mathrm{I}}_{1111}+D^{\mathrm{I}}_{1122})\beta^{\mathrm{I}}_{11}+D^{\mathrm{I}}_{1133}\beta^{\mathrm{I}}_{33}+(D^{\mathrm{II}}_{1111}+D^{\mathrm{II}}_{1122})\beta^{\mathrm{II}}_{11}\\&+D^{\mathrm{II}}_{1133}\beta^{\mathrm{II}}_{33}\\ \eta_{22}=&\ \eta_{11}\\ \eta_{33}=&(D^{\mathrm{I}}_{3311}+D^{\mathrm{I}}_{3322})\beta^{\mathrm{I}}_{11}+D^{\mathrm{I}}_{3333}\beta^{\mathrm{I}}_{33}+(D^{\mathrm{II}}_{3311}+D^{\mathrm{II}}_{3322})\beta^{\mathrm{II}}_{11}\\&+D^{\mathrm{II}}_{3333}\beta^{\mathrm{II}}_{33}.\end{aligned} \tag{20}$$

Therefore, only 12 components of the influence tensor need be calculated. The stresses for the case of two cavities with the same pressure p are then obtained from the constitutive Eq. (9). Furthermore, the effect of a pressure difference between the two bubbles may be estimated to a first approximation by adding the stresses determined in (25) below.

It is worth to note that the general solution of the problem proposed here is only an estimation. Indeed we first assumed the eigenstrains uniform. The second approximation is related to the boundary conditions. In order to apply the principle of linear superposition, the tangential components due to the pressure difference between the bubbles are neglected. Under such approximation, the equality between the boundary conditions illustrated in Fig. 1 remains correct.

For two cavities with the same internal pressure p, the solution of the case depicted in Fig. $1(c)$ is

$$\varepsilon^{c0}_{ij}=(-p/3\kappa)\,\delta_{ij}. \tag{21}$$

Since $\varepsilon^{c0}_{ij}+\varepsilon^{0}_{ij}=0$, the strain field for two interacting cavities with the same pressure is the linear superposition of solutions for the problems illustrated in Fig. $1(b)$ and $1(c)$:

$$\underset{=}{\varepsilon}=\underset{\equiv}{D}^{\mathrm{I}}(x_1,x_2,x_3):\underset{=}{\beta}^{\mathrm{I}}+\underset{\equiv}{D}^{\mathrm{II}}(x_1,x_2,x_3):\underset{=}{\beta}^{\mathrm{II}} \tag{22}$$

The case depicted in Fig. $1(d)$ is easy to analyze since the stress field of an isolated bubble in an infinite elastic solid has an ana-

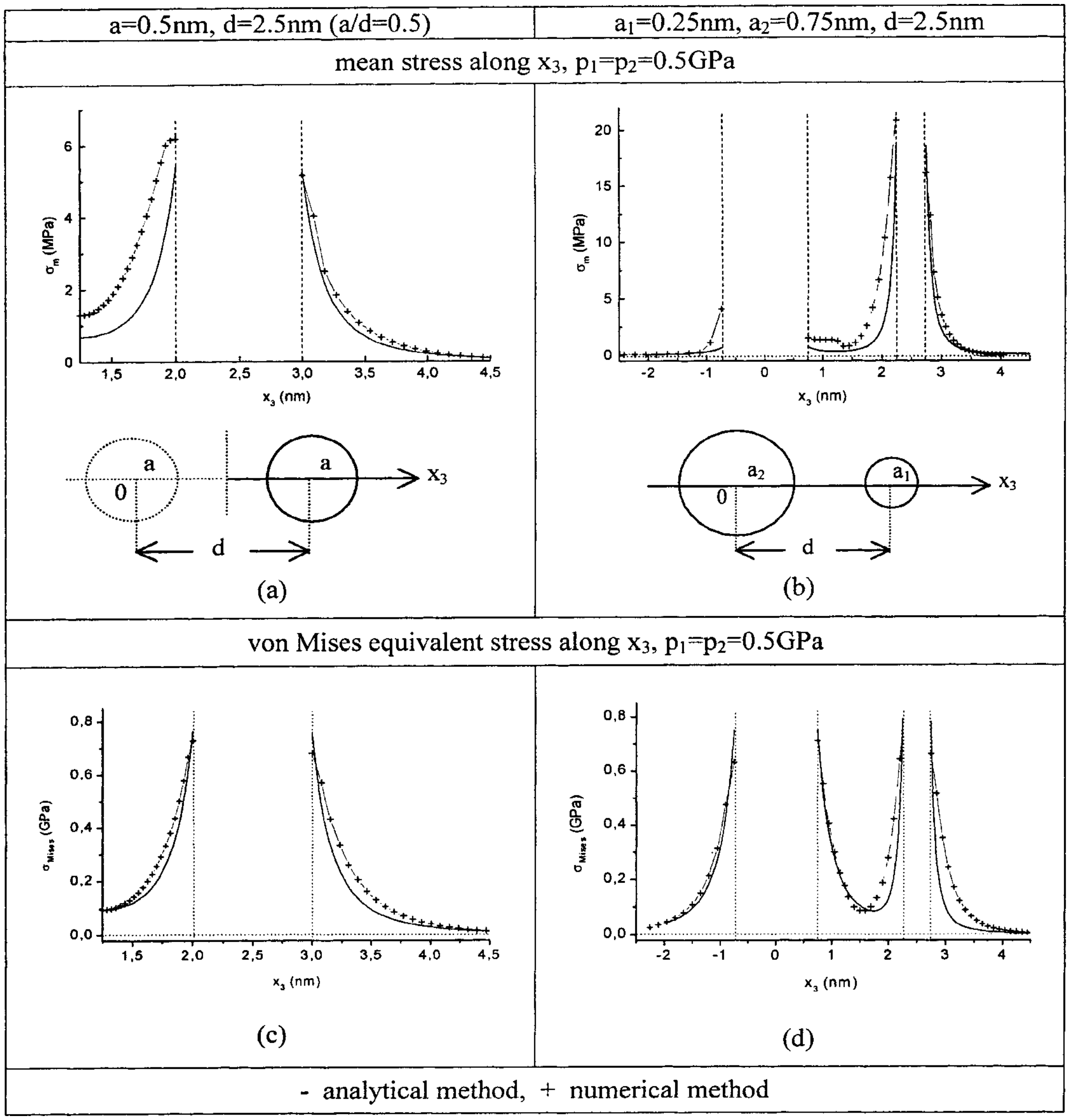

Fig. 4 (*a*) Mean stress along axis x_3 for two bubbles of same size with same pressure; (*b*) mean stress along axis x_3 for two bubbles of different sizes with same pressure; (*c*) von Mises equivalent stress along axis x_3 for two bubbles of same size with same pressure, and (*d*) von Mises equivalent stress along axis x_3 for two bubbles of different sizes with same pressure

lytical expression. If an internal pressure Δp is applied in the absence of remote loading, the displacement field exhibits spherical symmetry:

$$\mathbf{u}=u_r(r)\mathbf{e}_r \tag{23}$$

where $\mathbf{e}_r$ denotes the radial unit vector.

Resolution of the equilibrium equations then yields

$$u(r)=\frac{\Delta p}{4\mu}\frac{a^3}{r^2}, \quad \varepsilon_{rr}=-\frac{\Delta p}{2\mu}\frac{a^3}{r^3}, \quad \varepsilon_{\theta\theta}=\varepsilon_{\varphi\varphi}=\frac{\Delta p}{4\mu}\frac{a^3}{r^3}, \tag{24}$$

$$\sigma_{rr}=-\Delta p\frac{a^3}{r^3}, \quad \sigma_{\theta\theta}=\sigma_{\varphi\varphi}=\frac{\Delta p}{2}\frac{a^3}{r^3}. \tag{25}$$

Finally the mean stress and the von Mises equivalent stress are derived:

$$\sigma_m=\frac{1}{3}(\sigma_{11}+\sigma_{22}+\sigma_{33}) \tag{26}$$

$$\overline{\sigma}_{VM}=\sqrt{\frac{1}{2}[(\sigma_{11}-\sigma_{22})^2+(\sigma_{22}-\sigma_{33})^2+(\sigma_{33}-\sigma_{11})^2]+3(\sigma_{12}^2+\sigma_{23}^2+\sigma_{31}^2)}. \tag{27}$$

Hence the distribution of the two above quantities for two cavities of different sizes with different pressures can be analyzed.

For the spherical coordinates, we change $1\rightarrow r$, $2\rightarrow\theta$, and $3\rightarrow\varphi$.

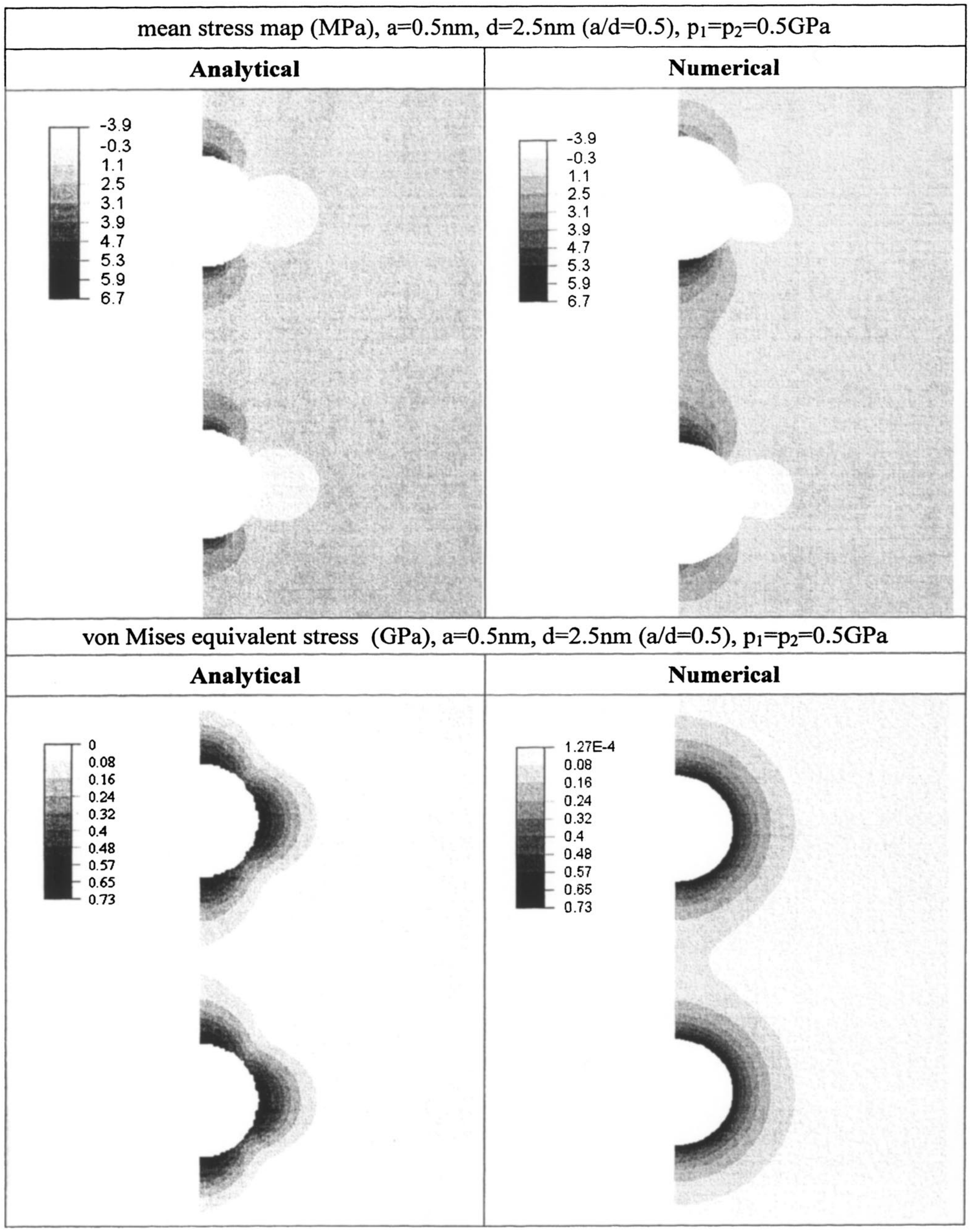

Fig. 5 Mean stress and von Mises equivalent stress maps for two bubbles of same size with same pressure

5 Results and Discussion

It is important to note that for an isolated bubble, the mean stress vanishes at any point:

$$\sigma_{rr} = -\Delta p \frac{a^3}{r^3}, \quad \sigma_{\theta\theta} = \sigma_{\varphi\varphi} = \frac{\Delta p}{2} \frac{a^3}{r^3} \Rightarrow \sigma_m = 0. \tag{28}$$

It is therefore not possible to determine the influence of Δp on the mean stress around the two bubbles because the contribution of the configuration illustrated in Fig. 1(d) is zero. The above approach is expected, however, to give a good estimation of the von Mises equivalent stress.

The present method allows various configurations to be easily investigated. Three parameters can be changed: the size and pressure of each bubble, and the distance between the bubble centers. In the following, three different cases are considered. The first case (i) consists of two bubbles of same size with same internal pressure, the second one (ii) of two different bubbles of different sizes with same pressure, and the third one (iii) of two bubbles of same size with different pressures. In the two first cases the mean stress and the von Mises equivalent stress are analyzed, while for the third case only the von Mises equivalent stress can be discussed (see above). Two representations of the results are used for each case: the stresses are displayed both along the symmetry axis and on a map in the half-plane (x_1, x_3). To discuss the analytical approach, the results are compared with numerical calculations carried out with the Abaqus® software. An example of the mesh used for two bubbles of equal size is given in Fig. 3. It is divided into two different regions: in the first one, close to the cavities,

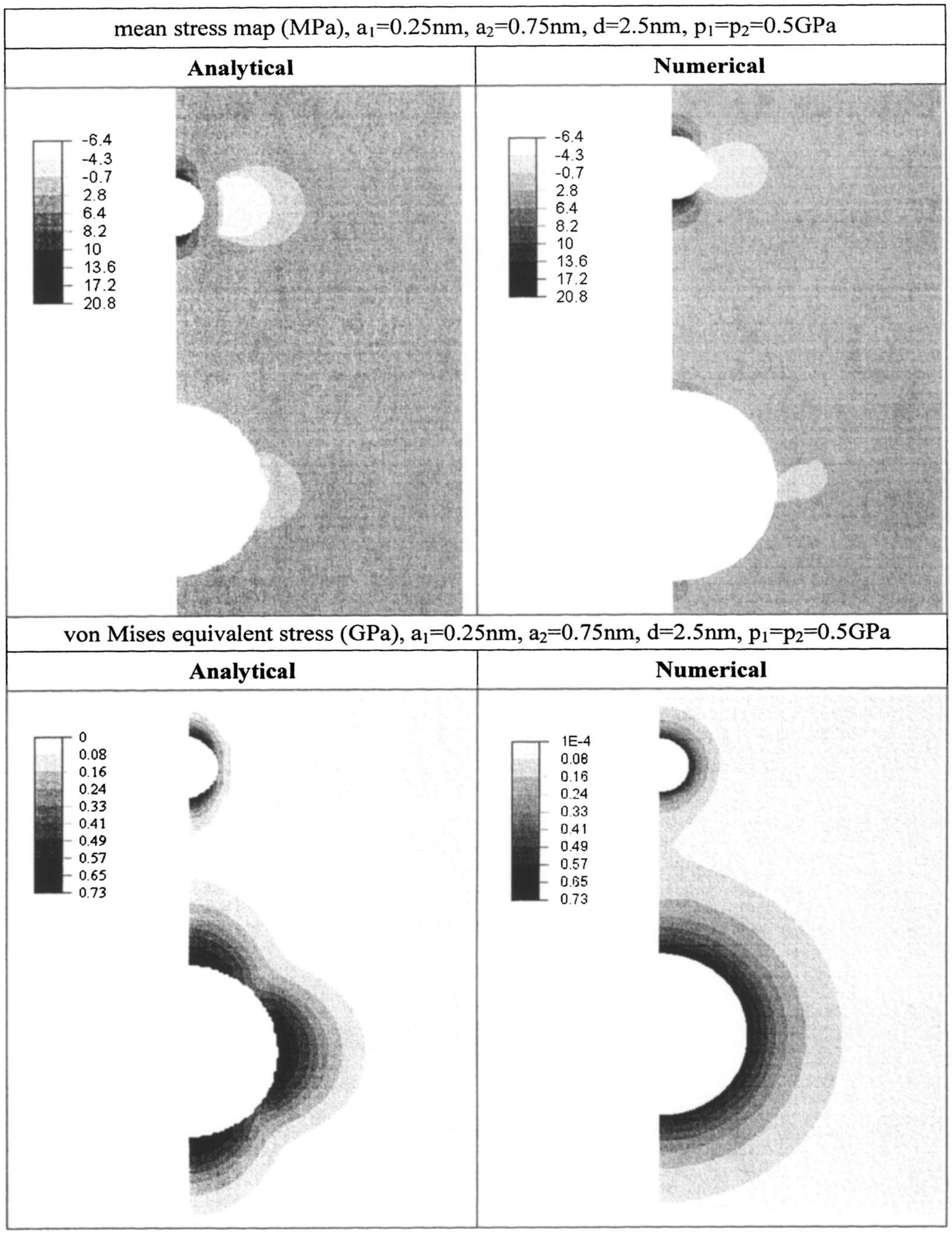

Fig. 6 Mean stress and von Mises equivalent stress maps for two bubbles of different sizes with same pressure

where the stress fields are to be determined precisely, the elements are small. The second one, far away from the cavities, is made of larger elements. To obtain the best results, the mesh must be very fine and the elements must be close to squares. Moreover, for ensuring a good representation of an infinite solid, the mesh is very large compared to the bubble sizes and infinite elements are used far away from the bubbles. These requirements are fulfilled in the mesh. In Fig. 4, the stress distributions along the symmetry axis are displayed for the two first cases. The corresponding maps are given in Fig. 5 and 6. The last case is shown in Fig. 7. All calculations were carried out using the elastic constants of palladium, which is usually employed to store nuclear fuels, i.e., $\kappa = 171.3$ GPa, $\mu = 42.7$ GPa, and $\nu = 0.385$.

As shown on the curves and the maps, there are slight differences between the analytical and numerical values of the mean stress, which are very small with respect to the von Mises equivalent stress. This is because the nonzero mean stress is induced by the interaction of the bubbles (it vanishes for an isolated bubble), whereas this interaction only introduces a perturbation of the von Mises equivalent stress.

The errors brought to the exact solution by the above-mentioned approximations can be estimated by considering the values of the normal stresses at the bubble surfaces, in particular along the symmetry axis x_3. The discrepancies between the exact values (i.e., $\sigma_{rr} = -p$) and that predicted by the analytical approach are less than 1% for the three investigated configurations.

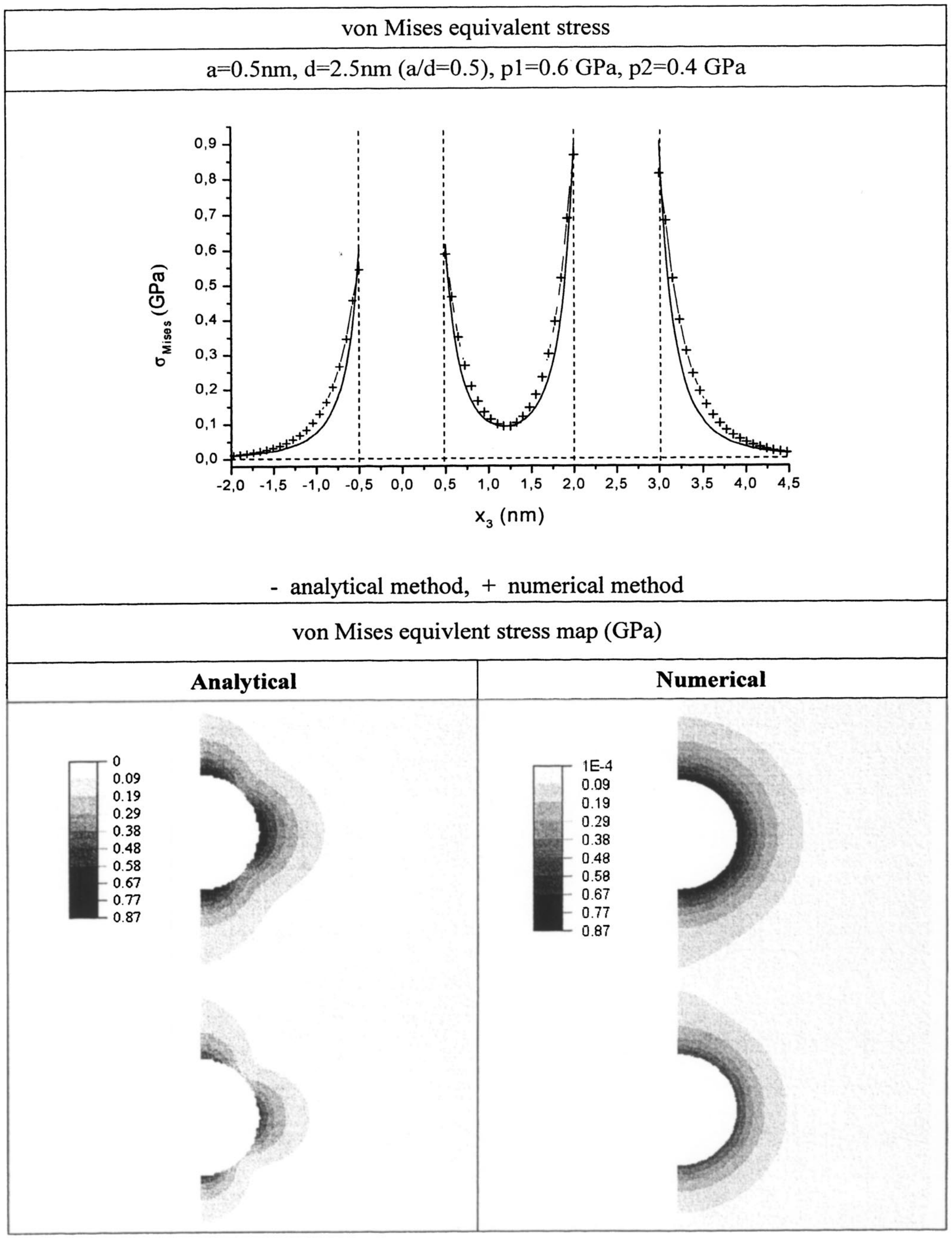

Fig. 7 Von Mises equivalent stress along axis x_3 and von Mises equivalent stress maps for two bubbles of same size with different pressures

The largest errors (overestimations) occur of course at points where the two bubbles are facing. Moreover, the gap is significantly smaller along the equators of the bubbles.

In Fig. 4, it is apparent that the analytical curves are very close to the numerical results except for a few points where the latter are slightly larger than the analytical predictions. The assumption of uniform eigenstrains is likely to be responsible for this discrepancy. Similarly, the von Mises equivalent stresses derived analytically (see Fig. 5 and 6), exhibit local maxima along the x_1 and x_3 axes, that can be related to the Taylor first-order expansions. This first analysis therefore shows that, despite its simplifying assumptions, the present approach leads to analytical results which are quite similar to the finite element predictions.

The mean stress maps allow the material regions undergoing tensile or compressive loading to be easily localized. Such results can be taken into account in a diffusion model. Helium atoms, after being created by tritium decay, diffuse in the material towards the bubbles. From the point of view of mechanics, the evolution of a pair of bubbles of different sizes can be predicted from the mean stress map in Fig. 6. The tension mean stress is larger near the smaller bubble than near the larger one. Helium atoms will therefore diffuse preferentially towards the small bubble, until the latter reaches the same size as the larger one. It is thus likely that the bubbles will tend to progressively equalize their sizes. This is a part of the mechanism of diffusion, which should be added to a thermodynamical analysis to obtain a complete description of the evolution of the system.

The above results can also be used to predict the occurrence of cracks in the vicinity of the bubbles. The levels of the von Mises equivalent stresses also give quite an important information about the areas where plasticity occurs, i.e., at each point where the von Mises equivalent stress is larger than the yield stress (0.23 GPa) of the material. Therefore, a complete mechanical description of the material evolution will require to take plasticity into account.

6 Conclusions

A new approach for the estimation of the elastic fields between two bubbles loaded by an internal pressure was proposed. In spite of its simplicity, it leads to analytical results, which are in good agreement with finite element calculations. The diameters and pressures of the two bubbles can be easily varied, such that various configurations can be investigated straightforwardly. The two main results are the following:

i. According to the mean stress distributions, the mechanical contribution to the diffusion process is likely to progressively equalize the sizes of the neighboring bubbles.
ii. The levels of the von Mises equivalent stresses indicate the areas where plasticity must be taken into account for a complete mechanical description of the system.

Appendix

(a) Analytical Expressions of the A_{ij} Coefficients of the Linear System (17)

$$A_{11}=H(69\tau+8)$$
$$A_{12}=H(21\tau-8)$$
$$A_{13}=H\{-2\alpha_2^3[6\alpha_2^2(3\tau+1)+5(3\tau-1)]\}$$
$$A_{14}=H\{\alpha_2^3[12\alpha_2^2(3\tau+1)-5(3\tau+4)]\}$$
$$A_{21}=H\{-2\alpha_1^3[6\alpha_1^2(3\tau+1)+5(3\tau-1)]\}$$
$$A_{22}=H\{\alpha_1^3[12\alpha_1^2(3\tau+1)-5(3\tau+4)]\}$$
$$A_{23}=A_{11}$$
$$A_{24}=A_{12}$$
$$A_{31}=2H(21\tau-8)$$
$$A_{32}=16H(3\tau+1)$$
$$A_{33}=2A_{14}$$
$$A_{34}=H\{-8\alpha_2^3[(3\alpha_2^2-5)(3\tau+1)]\}$$
$$A_{41}=2A_{22}$$
$$A_{42}=H\{-8\alpha_1^3[(3\alpha_1^2-5)(3\tau+1)]\}$$
$$A_{43}=A_{31}$$
$$A_{44}=A_{32}$$

where $H=2\mu/15(3\tau+4)$ with $\tau=\kappa/\mu$.

(b) Analytical Expressions of the Eigenstrains β_{ij}

$$\beta_{11}^{\mathrm{I}}=-\frac{1}{12}\frac{A_{11}^{\mathrm{I}}}{B_{11}^{\mathrm{I}}}\frac{p}{\kappa}$$

with

$$\begin{aligned}A_{11}^{\mathrm{I}}=&20(81\tau^3+135\tau^2+36\tau)\alpha_1^5\alpha_2^6\\&-8(486\tau^3+972\tau^2+486\tau+72)\alpha_1^5\alpha_2^5\\&+120(27\tau^3+63\tau^2+42\tau+8)\alpha_1^5\alpha_2^3\\&-75(25\tau^3+48\tau^2+16\tau)\alpha_1^3\alpha_2^6\\&+60(81\tau^3+171\tau^2+96\tau+16)\alpha_1^3\alpha_2^5\\&-5(891\tau^3+2160\tau^2+1536\tau+320)\alpha_1^3\alpha_2^3\\&+30(15\tau^3+30\tau^2+16\tau)\alpha_2^3+(243\tau^3+756\tau^2+768\tau+256)\end{aligned}$$

$$\begin{aligned}B_{11}^{\mathrm{I}}=&(225\tau^2)\alpha_1^6\alpha_2^6-144(9\tau^2+6\tau+1)\alpha_1^5\alpha_2^5\\&+120(9\tau^2+9\tau+2)\alpha_1^5\alpha_2^3+120(9\tau^2+9\tau+2)\alpha_1^3\alpha_2^5\\&-10(117\tau^2+144\tau+40)\alpha_1^3\alpha_2^3+(81\tau^2+144\tau+64).\end{aligned}$$

Similarly, $\beta_{11}^{\mathrm{II}}=-1/12A_{11}^{\mathrm{II}}/B_{11}^{\mathrm{II}}p/\kappa$ where A_{11}^{II} and B_{11}^{II} are obtained from A_{11}^{I} and B_{11}^{I} by permutation of α_1 and α_2.

$$\beta_{33}^{\mathrm{I}}=-\frac{1}{12}\frac{A_{33}^{\mathrm{I}}}{B_{33}^{\mathrm{I}}}\frac{p}{\kappa}$$

with

$$\begin{aligned}A_{33}^{\mathrm{I}}=&20(81\tau^3+135\tau^2+36\tau)\alpha_1^5\alpha_2^6\\&-8(486\tau^3+972\tau^2+486\tau+72)\alpha_1^5\alpha_2^5\\&+120(27\tau^3+63\tau^2+42\tau+8)\alpha_1^5\alpha_2^3\\&-300(3\tau^2+4\tau)\alpha_1^3\alpha_2^6+240(9\tau^2+15\tau+4)\alpha_1^3\alpha_2^5\\&-5(81\tau^3+540\tau^2+816\tau+320)\alpha_1^3\alpha_2^3\\&-30(27\tau^3+60\tau^2+32\tau)\alpha_2^3+(243\tau^3+756\tau^2+768\tau+256)\end{aligned}$$

$$\begin{aligned}B_{33}^{\mathrm{I}}=&(225\tau^2)\alpha_1^6\alpha_2^6-144(9\tau^2+6\tau+1)\alpha_1^5\alpha_2^5\\&+120(9\tau^2+9\tau+2)\alpha_1^5\alpha_2^3+120(9\tau^2+9\tau+2)\alpha_1^3\alpha_2^5\\&-10(117\tau^2+144\tau+40)\alpha_1^3\alpha_2^3+(81\tau^2+144\tau+64)\end{aligned}$$

Similarly, $\beta_{33}^{\mathrm{II}}=-1/12A_{33}^{\mathrm{II}}/B_{33}^{\mathrm{II}}p/\kappa$ where A_{33}^{II} and B_{33}^{II} are obtained from A_{33}^{I} and B_{33}^{I} by permutation of α_1 and α_2.

References

[1] Lasser, R., 1989, *Tritium and Helium-3 in Metals*, Springer-Verlag, Berlin.
[2] Sternberg, E., and Sadowsky, M. A., 1952, ''On the Axisymmetric Problem of the Theory of Elasticity for an Infinite Region Containing Two Spherical Cavities,'' ASME J. Appl. Mech., **19**, pp. 19–27.
[3] Boussinesq, J., 1885, *Applications des Potentiels*, Gauthier-Villars, Paris.
[4] Miyamoto, H., 1958, ''On the Problem of Theory of Elasticity for a Region Containing More Than Two Spherical Cavities,'' Bull. JSME, **1**(2), pp. 103–108.
[5] Tsuchida, E., Nakahara, I., and Kodama, M., 1976, ''On the Asymmetric Problem of Elasticity Theory for Infinite Elastic Solid Containing Some Spherical Cavities,'' Bull. JSME, **19**(135), pp. 993–1000.
[6] Shelley, J. F., and Yu, Y. Y., 1966, ''The Effect of Two Rigid Spherical Inclusions on the Stresses in an Infinite Elastic Solid,'' ASME J. Appl. Mech., **33**, pp. 68–74.
[7] Chen, H. S., and Acrivos, A., 1978, ''The Solution of the Equations of Linear Elasticity for an Infinite Region Containing Spherical Inclusions,'' Int. J. Solids Struct., **14**, pp. 331–348.

[8] Willis, J. R., and Bullough, R., 1969, "The Interaction of Finite Gas Bubbles in a Solid," J. Nucl. Mater., **32**, pp. 76–87.
[9] Papkovitch, P. F., 1932, "Solution générale des équations différentielles fondamentales d'élasticité, exprimées par trois fonctions harmoniques," C. R. Acad. Sci. Paris, **195**, pp. 513–515.
[10] Neuber, H., 1944, *Kerbspannungslehre*, J. W. Edwards, Ann Arbor, MI.
[11] Eshelby, J. D., 1957, "The Determination of the Elastic Field of an Ellipsoidal Inclusion and Related Problems," Proc. R. Soc. London, Ser. A, **A241**, pp. 376–396.
[12] Mura, T., 1982, *Micromechanics of Defects in Solids*, Martinus Nijhoff, Dordrecht, The Netherlands.

Crushing of an Elastic-Plastic Ring Between Rigid Plates With and Without Unloading

T. J. McDevitt
Naval Surface Warfare Center,
Dahlgren Division,
Dahlgren, VA 22448-5100
Mem. ASME

J. G. Simmonds
Department of Civil Engineering,
University of Virginia,
P.O. Box 400742
Charlottesville, VA 22904–4742
Fellow ASME

Load-deflection curves are computed for an elastic-plastic ring that is slowly crushed between frictionless, rigid plates (platens). The ring is assumed to be inextensional with plane sections remaining plane and to obey a bi-linear stress-strain law with isotropic hardening. These assumptions lead to a local nonlinear moment-curvature relation identical to that developed by Liu et al. When inserted into the exact equation for moment equilibrium, this constitutive relation yields a second-order, nonlinear ordinary differential equation for the angle α between the deformed centerline of the ring and the horizontal. The numerical solution of this equation, which uses a combined penalty-continuation method, along with an auxiliary equation relating the vertical deflection to α, leads to overall load-deflection curves that depend on two dimensionless parameters, λ and μ. The first is the ratio of the plastic modulus to the elastic modulus; the second measures the ratio of plastic to elastic effects. As $\mu \rightarrow 0$, the overall load-deflection curve of Frish-Fay for the elastica is recovered; as $\mu \rightarrow \infty$, that of DeRuntz and Hodge for a rigid-perfectly plastic ring is recovered. Three scenarios are considered: I_0, in which an initially straight, stress-free beam is bent elastically into a ring and then crushed; II_0, in which an initially stress-free ring is crushed; and III_0, in which an initially straight beam is bent first elastically and then elastically-plastically into a ring and then crushed. Results for scenario II_0 are shown to agree well with experiments of Reddy and Reid if $\lambda = 0.01$ and $\mu = 10$ and 20 and with experiments of Avalle and Goglio if $\lambda = 0.02$ and $\mu = 11$. In scenarios I_0 and II_0, the effects of unloading prove to be small, reinforcing a similar conclusion of Liu et al., who considered the large-deflection of an elastic-plastic cantilever under a tip load. If no unloading is assumed, a more analytical treatment is possible, as shown in the second part of the present paper. The model predicts that the ring always remains in full contact with the platens, in agreement with recent experiments by Avalle and Goglio on annealed aluminum tubes. Pull-away from the platens also observed in experiments is ascribed to end effects which cannot be modeled by a one-dimensional beam theory. However, it is argued that, even if there is pull-away, the effect on the overall force-deflection relation must be small because in both cases the forces exerted by the platens are concentrated at the ends of the contact region. Moving pictures of successive stages of deformation of the ring showing the formation of plastic loading and unloading zones in all three scenarios may be found on the web site www.people.virginia.edu/~jgs/ring.html. [DOI: 10.1115/1.1630814]

1 Introduction

The determination of the load-deflection curve of an elastic-plastic ring of initial mean radius R and thickness $2H$, slowly crushed between two frictionless rigid plates (platens), is a fundamental problem in mechanics because a knowledge of the energy absorbed is essential to the design of crash-worthy vehicles. Moreover, the experimental determination of the load-deflection curve for a ring affords perhaps the easiest verification of the accuracy of various approximations used in modeling more elaborate structures.

In computing such a theoretical load-deflection curve, three scenarios of ever increasing complexity come to mind. (I) An initially straight, stress-free beam is bent slowly by end couples into a ring and the ends then butt welded. The beam remains *elastic* during this process. In this scenario, a portion of the ring is always elastic, both before and after the ring has flattened against the platens, because flattening tends to reduce the strain. (II) The ring is initially stress-free. Here, the ring may or may not become plastic before it starts to flatten against the platens, depending on whether the half-thickness-to-radius ratio, H/R, exceeds the yield strain. (III) The ring is formed as in (I) except the beam becomes plastic (beginning at the outer fibers and moving inward towards the centerline) before a complete ring has been formed. A complicating factor in all three scenarios is that, due to changes in geometry during crushing, portions of the ring may begin to *unload* as the external load increases.

Finally, we note that our one-dimensional ring model may accommodate a tangential extensional strain, *e*, or it may be *inextensional*, as in the classical theory of curved beams. Thus, there are at least *six* plausible scenarios we might consider: I_0, I_e, $\cdots$, III_e. The present paper focuses on I_0, II_0, and III_0, i.e., on inextensional scenarios.

A major difficulty in applying numerical methods to elastic-plastic structures is that the plastic strains are often much larger than the elastic ones. To bypass the potential difficulties associated with such a disparity, DeRuntz and Hodge [1] assumed rigid, perfect plasticity and derived a formula for the load-deflection curve that occurs after four plastic hinges have formed, two at the points of contact with the rigid plates and two at the ends of a

Contributed by the Applied Mechanics Division of THE AMERICAN SOCIETY OF MECHANICAL ENGINEERS for publication in the ASME JOURNAL OF APPLIED MECHANICS. Manuscript received by the ASME Applied Mechanics Division, July 20, 2001; final revision, April 22, 2003. Associate Editor: N. Triantafyllidis. Discussion on the paper should be addressed to the Editor, Prof. Robert M. McMeeking, Department of Mechanical and Environmental Engineering, University of California—Santa Barbara, Santa Barbara, CA 93106-5070, and will be accepted until four months after final publication of the paper itself in the ASME JOURNAL OF APPLIED MECHANICS.

horizontal diameter. Redwood [2] refined the model of DeRuntz and Hodge by adding linear strain-hardening. Reid and Reddy [3] and Reddy and Reid [4] refined these models by assuming a rigid, linearly hardening moment-curvature relation within a small region near horizontal, diametrically opposed points where the bending moment is the greatest and where the deformed curvature is relatively high. They ignored unloading and assumed that the ring moved as a rigid body in the portions of the ring between these plastic zones and the points of contact with the platens. However, as we shall show, elastic effects may contribute significantly to the deflections of the ring, depending of the load, the relative thickness, and the material properties. In a subsection following Eq. (12), we discuss pull-away from the platens, after we have introduced certain assumptions and notation.

The first aim of the present paper is to quantify the relative roles of elasticity and plasticity in the crushing of a ring and to account for the possible effects of unloading. In particular, we show by numerical calculation that unloading is not a major effect in the overall load-deflection behavior of a ring in scenarios I_0 and II_0, but is in scenario III_0. To this end, we assume that the dominant hoop stress σ in the ring can be represented by a bilinear stress-strain relation which, if there is no unloading, is given by the following *odd* function of the engineering strain ε:

$$\sigma=\hat{\sigma}(\varepsilon)\equiv E\begin{cases}\varepsilon \ \text{ if } \ |\varepsilon|<\varepsilon_Y \\ (1-\lambda)\varepsilon_Y \operatorname{sgn}\varepsilon+\lambda\varepsilon \ \text{ if } \ \varepsilon_Y\leqslant|\varepsilon|\end{cases}, \tag{1}$$

where E is Young's modulus, $\varepsilon_Y>0$ is the yield strain, λ is the (constant) ratio of the plastic to elastic modulus, E_P/E, and $\operatorname{sgn} x=|x|/x$, $x\neq 0$. See Fig. 1(*a*) of Liu et al. [5] (where their α is our λ).

If unloading first begins at some strain ε_1 at some point in the ring, then isotropic hardening (Lubliner [6], p. 137) implies that we have a new stress-strain relation of the form (1) but shifted to the right by $\varepsilon_1^*=(1-\lambda)(\varepsilon_1-\varepsilon_Y \operatorname{sgn}\varepsilon_1)$. That is,

$$\sigma=\hat{\sigma}_1(\varepsilon-\varepsilon_1^*), \tag{2}$$

where $\hat{\sigma}_1$ means $\hat{\sigma}$ with ε_Y replaced by $|\varepsilon_1|$. If there is a second unloading at a strain $\varepsilon_2>\varepsilon_1$, then in (2) we replace the subscript 1 by a 2, etc.

As will be seen, the governing dimensionless equations contain, beside λ, the two additional dimensionless parameters

$$\mu=\frac{H}{R\varepsilon_Y} \quad \text{and} \quad \nu=\frac{3P}{bEH\varepsilon_Y^2}, \tag{3}$$

where $2P$ is the net vertical load on the ring produced by the platens and b is the width of the ring. Clearly, $0\leqslant\lambda\leqslant 1$, but $0<\mu<\infty$; if $\lambda=0$, we have elastic-perfectly plastic behavior. The parameter μ is a measure of the relative balance between elastic and plastic effects. As $\mu\rightarrow 0$, the effects of plasticity diminish and our analysis reduces to that of Frish-Fay [7] for an elastica compressed between platens, providing we first re-scale the dimensionless load by setting $\nu/\mu^2=3PR^2/bEH^3$. As $\mu\rightarrow\infty$, we obtain rigid-plastic behavior. However, as we shall see, in scenario I_0 (where the ring is formed by bending a straight beam elastically and inextensionally) we must assume that $0\leqslant\mu\leqslant 1$; in scenario III_0, which is the complement of scenario I_0, $1<\mu<\infty$. In scenario II_0, $0\leqslant\mu<\infty$.

The second aim of the present paper is to show that in scenario II_0 appropriate choices of λ (which measures relative strain-hardening) and μ (which measures the relative ratio of plastic to elastic effects) give an excellent fit to the experimental data presented by Reddy and Reid [4] and Avalle and Goglio [8].

Because of the possibility of unloading, we must solve the governing ordinary differential equation numerically. A penalty-continuation method proves to be particularly effective. However, as we show numerically, the effect of unloading on the overall force-deflection curves for scenarios I_0 and II_0 is small. This justifies the analysis in the second part of this paper that ignores unloading, thus permitting a more extensive analytical treatment.

In scenario III_0, where a relatively thick beam ($\mu>1$) is first bent into a ring, there is plastic deformation before crushing begins and more than half of the ring begins to unload as the platens start to move together.

2 The Equilibrium Equations and Kinematic Relations

Elementary equilibrium considerations show that, at any point on the deformed centerline of the ring, the horizontal component of the stress resultant is zero and the downward vertical component is equal to P. The remaining *exact* equation of moment equilibrium is, from equation (O.5) of Chap. IV of Libai and Simmonds [9].

$$dM/ds=(1+e)P\cos\alpha, \tag{4}$$

where M is the bending moment (positive in a counterclockwise sense and with dimensions of [FORCE]×[LENGTH]), s is distance to the right along the undeformed centerline of the beam, measured from the fixed lowest point on the bent ring, and α is the angle the tangent to the deformed centerline makes with the horizontal. The vertical distance moved by the platens is

$$\delta=2\left[R-\int_0^{\pi/2}(1+e)\sin\alpha ds\right]. \tag{5}$$

Once constitutive relations are in hand that express M and e in terms of κ, the bending strain, and $N=-P\sin\alpha$, the tangential component of the stress resultant, (4) reduces to a second-order ordinary differential equation for the unknown α. The boundary conditions are

$$\alpha(s_B)=0, \quad \alpha(R\pi/2)=\alpha_H. \tag{6}$$

Here, s_B is the location of the (generally) unknown point B where the lower right quarter of the ring loses contact with the lower platen. See Fig. 1. The value of s_B depends on the dimensionless load ν, the combined geometric-yield strain parameter μ, and the specific form of the constitutive relations. If $\lambda\neq 0$, the *hinge angle* $\alpha_H=\pi/2$, whereas if $\lambda=0$, α_H may be less than $\pi/2$, depending on μ, ν, and the scenario (I_0, II_0, or III_0). Herein, we approach perfect plasticity ($\lambda=0$) by letting $\lambda\rightarrow 0$ ($\lambda=10^{-6}$, numerically). Later in this paper, where we assume no unloading, we treat perfect plasticity exactly by taking $\lambda=0$ and solving for the hinge angle α_H.

3 Constitutive Relations for Scenarios I_0, II_0, and III_0

At the outset, we make a major (but conventional) assumption: The deformed reference curve is inextensional, i.e., $e=0$ in (4) and (5). This assumption, which simplifies the analysis considerably, may be justified heuristically by noting that the maximum tangential compressive force in each vertical half of the ring is P and occurs at the extreme horizontal points C and C' in Fig. 1 (that shows the successive stages of deformation in scenario I_0, but that is typical of the general trend in scenarios II_0 and III_0). The maximum bending moment also occurs at these points and, from elementary equilibrium considerations, is equal to PL, where L is the unknown horizontal distance from point B where the ring separates from the platen to point C. We estimate the direct stresses in the deformed reference curve at C to be $O(P/bH)$ and the outer fiber (bending) stresses to be $O(PL/bH^2)$. Thus, the ratio of the direct stresses to the bending stresses is $O(H/L)$, which is quite small except near the final stages of crushing when most of the net vertical displacement has already taken place. A somewhat different argument for ignoring the effects of extensional strain is given by DeRuntz and Hodge [1]; experimental evidence for near inextensionality is offered by Avalle and Goglio

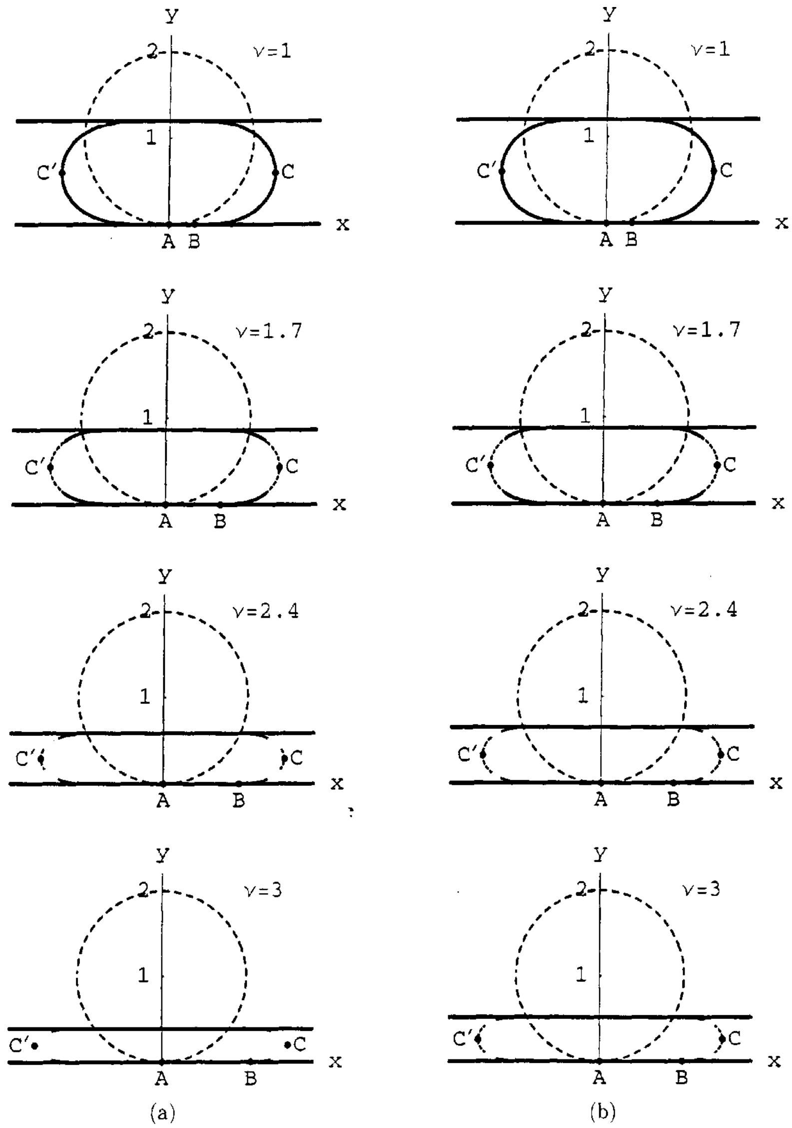

Fig. 1 Two crushing sequences for an initially straight beam bent elastically into a ring (scenario I_0) with $\mu=0.5$. The parts of the rings shown in solid black are elastic; dashed (loading) and solid gray (unloading) parts are plastic. In (*a*), $\lambda=10^{-6}$; in (*b*), $\lambda=0.1$.

in the second column on p. 232 of [10]. However, we remind the reader that the analysis to be presented already represents a generalization of the two extreme cases, $\mu=0$ and $\mu\rightarrow\infty$, examined, respectively, by Frish-Fay [7] and DeRuntz and Hodge [1]. To introduce yet another dimensionless parameter to measure extensional strain effects would distract from the main focus of the present investigation which is to determine the load-deflection curve predicted by the more representative elastic-plastic stress-strain relations (1) or (2) in which $0\leqslant\mu<\infty$.

Scenarios I_0 and III_0. The procedure for obtaining a moment-curvature relation is standard: we consider a finite piece of the ring under a uniform bending moment M. (This would be the setup were this relation to be determined experimentally.) By symmetry, plane sections remain plane and a straight unstretched fiber at a distance y from the undeformed centerline of the straight beam deforms into a stretched circular fiber a distance $y[1+\varepsilon_N(y)]$ from the deformed centerline, where ε_N is the normal engineering strain—a Poisson ratio effect that will be neglected.

For an initially straight beam, we take the bending strain to be the curvature of the bent but unstretched centerline,

$$\kappa=d\alpha/ds \quad \text{so that} \quad \varepsilon=-y\kappa. \tag{7}$$

Since $M=-2b\int_0^H y\sigma dy$, it follows from (1) and $(7)_2$ that

$$m=f(\eta)\equiv\begin{cases}\eta \ \text{ if } \ |\eta|\leqslant 1\\ \left(\dfrac{1-\lambda}{2}\right)\left[3-\dfrac{1}{\eta^2}\right]\operatorname{sgn}\eta+\lambda\eta \ \text{ if } \ |\eta|>1,\end{cases} \tag{8}$$

where

$$m=\frac{3M}{2bEH^2\varepsilon_Y} \quad \text{and} \quad \eta=\frac{H\kappa}{\varepsilon_Y} \tag{9}$$

are a dimensionless moment and a dimensionless curvature. Figure 2 is a graph of m versus η for $\lambda=0$, 0.01, 0.1. This is essentially Fig. 3 of Liu et al. [5], with their α equal to our λ.

Whether points in the ring are loading or unloading, to solve the governing equations we need only the slope of the moment-curvature relation, namely

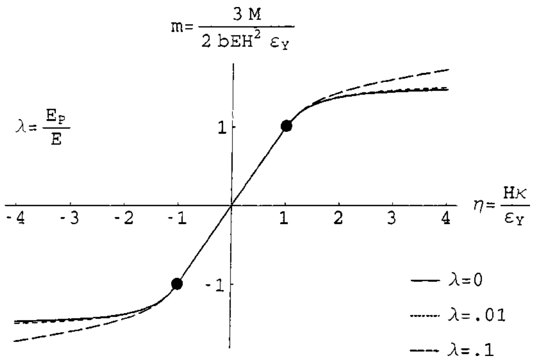

Fig. 2 Dimensionless moment-curvature relation for an elastic-plastic ring

$$\frac{dm}{d\eta}=f'(\eta)=\begin{cases}1 & \text{if elastic}\\ (1-\lambda)|\eta|^{-3}+\lambda & \text{if loading plastically}\end{cases}. \tag{10}$$

Scenario II_0. The major difference from scenarios I_0 and III_0 just analyzed is that, in place of $(7)_1$, the bending strain is now defined as

$$\kappa=\bar{R}^{-1}-R^{-1}, \quad \text{where } \bar{R}=ds/d\alpha \tag{11}$$

is the radius of the deformed centerline. To relate κ to the bending moment M, we consider again a segment of the ring under a pure bending moment, except now we have an initially circular fiber of length $(1-y/R)ds$ lying a normal distance y from the centerline of the undeformed ring. Under the action of a uniform moment M and the assumption that the centerline is inextensional, this fiber deforms into another circular arc of length $[1-(y/\bar{R})(1+\varepsilon_N)]ds$, where, as before, ε_N is the normal strain. Thus, the engineering hoop strain is

$$\varepsilon=-\frac{y\left(\dfrac{1+\varepsilon_N}{\bar{R}}-\dfrac{1}{R}\right)}{1-y/R}=-y\kappa[1+\mathrm{O}(\varepsilon_N,H/R)]. \tag{12}$$

Henceforth, we shall neglect the effects of normal strain (Poisson ratio effect) and relative thickness. That is, we shall take $\varepsilon=-\kappa y$, as in Eq. $(7)_2$ for scenarios I_0 and III_0. This means that the dimensionless moment-curvature relation (8) and its derivative (10) remain unchanged.

Contact With the Platens. Both referees of the original version of this paper have insisted that we discuss why our model fails to predict the partial separation (pull-away) of the ring from the platens observed in some experiments. However, recent experimental work on tubes by Avalle and Goglio [8,10] and finite element calculations on infinite tubes in a state of plane strain by Leu [11] have shown that, away from their ends, annealed aluminum tubes flatten against the platens and *never* separate. That is, end effects must be the essential cause of pull-away. Indeed, to quote from p. 231 of [10],

> It can also be noted that at the front [and rear] end of the tube . . . where a plane stress condition prevails, the upper and lower walls lose contact with the plates and assume curvatures opposite to those of the undeformed state. Conversely, in the central portion (and most) of the tube, the material remains in contact with the compressing plates.

Because we model a one-dimensional beam and not a two-dimensional circular cylindrical shell, we cannot account for end effects. Moreover, because contact between the platens and the ring is assumed to be frictionless, there is no way this contact could generate a compressive hoop stress that might cause local buckling, i.e., pull-away. Finally, we note that once the beam begins to flatten against the platens, *the only contact forces are four identical concentrated vertical loads at the ends of the contact regions*. This conclusion follows immediately from (4) and the moment-curvature relation of Fig. 2; since P vanishes inside the contact region, the moment M and hence the curvature κ is constant there. Thus, whether there is pull-away or not, the contact forces are always concentrated at the ends of the contact region, so any differences in the overall force-displacement curve must be small.

These remarks are still at odds with the finite element analysis of Leu [11] who considers an infinite tube in plane strain and whose results show that, although an annealed, strain-hardening aluminum tube indeed remains in contact with the platens, a non-annealed nearly perfectly-plastic aluminum tube may *not*. However, Leu shows that, according to his analysis, if there is sufficient friction between the platens and the tube (Fig. 6(*a*) of [11]) or if the elastic modulus is sufficiently high (Fig. 7(*a*) of [11]) or if the tube is sufficiently thin (Fig. 8(*a*) of [11]), there is no pull-away. Because Leu does not present dimensionless graphs and because he only takes three elements in the thickness direction (as opposed to 10 in [8]), it is difficult to assess whether his results for the nonannealed aluminum tubes are a numerical artifact or a result of some dimensionless parameter exceeding a critical value. We note that, although Leu refers to pull-away as "buckling," he never attempts to give a physical explanation of this phenomenon.

Finally, we mention a paper by Wang [12] which analyzes a tube with an elastic-perfectly plastic moment curvature relation that is crushed between frictionless platens. He finds no pull-away from the platens but states in his introduction that his analysis "applies to very *thin* [original emphasis] flexible rings or tubes." He then states that "For thick inelastic rings the crushed shape consists of plastic hinges and segments of rigid arcs. In such a case a rigid-perfectly plastic constitutive equation is more appropriate (DeRuntz and Hodge [1] and Reid and Reddy [3])." We find this statement most curious because Wang's moment-curvature relation *includes rigid-perfect plastic behavior as a limiting case*. (Let Young's modulus $E\to\infty$ and the yield curvature $\kappa_0\to 0$, keeping $E\kappa_0$ a constant.) Thus, were there a combination of parameters where pull-away occurs, Wang's analysis fails to reveal it.

4 The Governing Differential Equation and Boundary Conditions

Because the centerline of the ring is a circle of radius R before crushing, we henceforth set $s=R\theta$. With this change of variable and with the introduction of (7), (10), and (11) along with the dimensionless quantities defined by (3) and (9) into the basic differential Eq. (4), we have, because $e=0$,

$$f'(\eta)\frac{d^2\alpha}{d\theta^2}=\frac{\nu}{2\mu^2}\cos\alpha. \tag{13}$$

If $\lambda>0$, as we now assume (and regard perfect plasticity as the limit as $\lambda\to 0$), there are no plastic hinges and the boundary condition $(6)_2$ can be replaced by

$$\alpha(\pi/2;\nu)=\pi/2. \tag{14}$$

Here, in anticipation of the continuation method that we introduce presently, we have included the dimensionless load as the second argument of the deformed angle. Furthermore, because our model, that assumes frictionless contact, has no mechanism that permits the ring to separate from the platens (as is sometimes observed in practice—see Fig. 4 of [1] and Fig. 3(*b*) of [4]), we may replace $(6)_1$ by the boundary condition and constraint,

$$\alpha(0;\nu)=0, \quad \alpha(\theta;\nu)\geqslant 0, \quad 0\leqslant\theta\leqslant\pi/2. \tag{15}$$

5 The Penalty Method

An effective way of handling the constraint in (15) numerically is with a so-called *penalty method*. In the present case, this entails replacing (13)–(15) by the *unconstrained* two-point boundary value problem,

$$f'(\eta)\frac{d^2\alpha}{d\theta^2}=\frac{\nu}{2\mu^2}\cos\alpha+pT(\alpha),\quad T\equiv\begin{cases}0 & \text{if } \alpha\geqslant 0\\ \alpha^2 & \text{if } \alpha<0\end{cases},\quad p\to\infty, \tag{16}$$

subject to the boundary conditions

$$\alpha(0;\nu)=0,\quad \alpha(\pi/2;\nu)=\pi/2. \tag{17}$$

In practice, we take p to be large, say 10^5. Physically, the penalty term pT imposes a very large vertical force at any point along the centerline corresponding to a point on the outer face of the ring that penetrates the platens.

6 The Continuation Method

Any solution of the nonlinear boundary value problem (16), (17) is of the form $\alpha=\alpha(\theta;\nu)$. To use the continuation method of solution, we differentiate the ordinary differential Eq. (16) and the boundary conditions (17) with respect to ν. Noting from $(3)_1$, $(7)_1$, $(9)_2$, and (11) that

$$\eta_\nu=\mu\alpha_{\theta\nu}\quad\text{and}\quad f'_\theta=\mu f''(\eta)\alpha_{\theta\theta}, \tag{18}$$

where partial derivatives are denoted by subscripts, we obtain the *linear boundary value problem*,

$$[f'(\eta)A_\theta]_\theta+\left[\frac{\nu}{2\mu^2}\sin\alpha-pT'(\alpha)\right]A=\frac{\cos\alpha}{2\mu^2},\quad 0<\theta<\pi/2, \tag{19}$$

$$A(0;\nu)=0,\quad A(\pi/2;\nu)=0, \tag{20}$$

coupled with the two *nonlinear initial value problems*

$$\alpha_\nu=A(\theta;\nu),\quad \alpha(\theta;0)=\theta,\quad 0<\nu<\infty \tag{21}$$

and

$$\eta_\nu=\mu A_\theta(\theta;\nu),\quad 0<\nu<\infty,$$
$$\eta(\theta;0)=\begin{cases}\mu \text{ in scenario } I_0 \text{ or } III_0\\ 0 \text{ in scenario } II_0\end{cases}. \tag{22}$$

In (19) α and η are regarded as known and in (21) and (22) the dimensionless load ν plays the role of a timelike variable.

One advantage of the continuation method is that the solution of (19)–(22) at any intermediate value of ν represents the state of the ring when it is *partially* crushed. Another advantage of the continuation method is that there is loading {unloading} if $\eta\eta_\nu$ is positive {negative}, an easily monitored variable. At any value of θ where $|\eta|>1$ and $\eta_\nu=\mu A_\theta=0$, the expression for $f'(\eta)$ may switch from the first line of (10) to the second.

7 Determining $A(\theta;0)$

The simplest numerical procedure for solving the coupled system (19)–(22) is to (i) compute $A(\theta;0)$ and $A_\theta(\theta;0)$ from (19) with $\alpha=\theta$ and $p=0$; (ii) compute $\alpha(\theta;\Delta\nu)$ from (21) and $\eta(\theta;\Delta\nu)$ from (22), where $\Delta\nu$ is some small increment of ν; (iii) substitute these value into (19) and set p to some suitably large value; (iv) solve for $A(\theta;\Delta\nu)$ and $A_\theta(\theta;\Delta\nu)$; and (v) repeat to obtain $\alpha(\theta;2\Delta\nu)$ and $\eta(\theta;2\Delta\nu)$. Although $A(\theta;0)$ can be determined numerically, the following simple closed-form expressions are easily obtained. Because $\alpha=\theta$ if $\nu=0$, we can drop the penalty term in (19) in this initial step.

Scenario $I_0(0<\mu\leqslant 1)$. Here, the beam remains elastic as it is bent into a ring with $\eta=\mu\leqslant 1$. Thus, $f'(\eta)=1$ and hence

$$A(\theta;0)=\frac{1}{2\mu^2}\left(1-\frac{2\theta}{\pi}-\cos\theta\right)\equiv\frac{g(\theta)}{2\mu^2}. \tag{23}$$

Scenario $II_0(0<\mu<\infty)$. Here, the ring is initially unstressed so that $\eta=0$ and $f'(\eta)=1$. Hence,

$$A(\theta;0)=\frac{g(\theta)}{2\mu^2}, \tag{24}$$

the same as for scenario I_0.

Scenario $III_0(\mu>1)$. Here, as the beam is bent by end couples, it first deforms elastically into an open circular arc and then, once its dimensionless curvature η exceeds 1, undergoes plastic loading as it is bent further into the final shape of a ring with dimensionless curvature $\eta=\mu>1$. Next, when the dimensionless load ν is first applied, the ring begins to ovalize, i.e., near point A (see Fig. 1) η begins to decrease from μ (unloading) whereas near point C, η begins to increase from μ (loading). Thus, as $\nu\to 0+$, there is some value of $\theta=\theta^*$ where $f'(\eta)$ switches from 1 to $(1-\lambda)\mu^{-3}+\lambda$. With $A(\theta;0)\equiv\overset{0}{A}(\theta)$, (19) and (20) may be replaced by

$$\overset{0}{A}{}''=\frac{\cos\theta}{2\mu^2},\quad 0<\theta<\theta^* \tag{25}$$

and

$$\overset{0}{A}{}''=\frac{\cos\theta}{2\mu^2 f'(\mu)},\quad \theta^*<\theta<\pi/2, \tag{26}$$

subject to the boundary conditions

$$\overset{0}{A}(0)=\overset{0}{A}(\pi/2)=0, \tag{27}$$

the continuity condition

$$\overset{0}{A}(\theta^*+)=\overset{0}{A}(\theta^*-), \tag{28}$$

and the condition that θ^* marks the boundary between loading and unloading,

$$\overset{0}{A}{}'(\theta^*\pm)=0. \tag{29}$$

Thus,

$$\overset{0}{A}=\frac{1}{2\mu^2}\begin{cases}1-\theta\sin\theta^*-\cos\theta, & 0<\theta<\theta^*\\ \dfrac{(\pi/2-\theta)\sin\theta^*-\cos\theta}{f'(\mu)}, & \theta^*<\theta<\pi/2\end{cases}, \tag{30}$$

where θ^* satisfies the transcendental equation

$$\theta^*\sin\theta^*+\cos\theta^*=\frac{(\pi/2)\sin\theta^*-f'(\mu)}{1-f'(\mu)},$$
$$\sin^{-1}(2/\pi)<\theta^*<\pi/2. \tag{31}$$

From (10), $\lambda<f'(\mu)<1$ if $1<\mu<\infty$, so it is easily seen that (31) always has exactly one solution on the given interval.

8 The Shape of the Ring During Crushing

The shape of the ring at successive loads is given by solving the differential equations with initial conditions

$$d\bar{x}/d\theta=\cos\alpha(\theta;\nu),\quad \bar{x}(0;\nu)=0\quad\text{and}\quad d\bar{y}/d\theta=\sin\alpha(\theta,\nu),$$
$$\bar{y}=(0;\nu)=0, \tag{32}$$

where $(R\bar{x},R\bar{y})$ are the Cartesian coordinates of a point on the deformed centerline of the ring.

Figure 1 shows the ring at several stages of loading for $\lambda=10^{-6}$ and $\lambda=0.1$ for scenario I_0 with $\mu=0.5$. Note the near

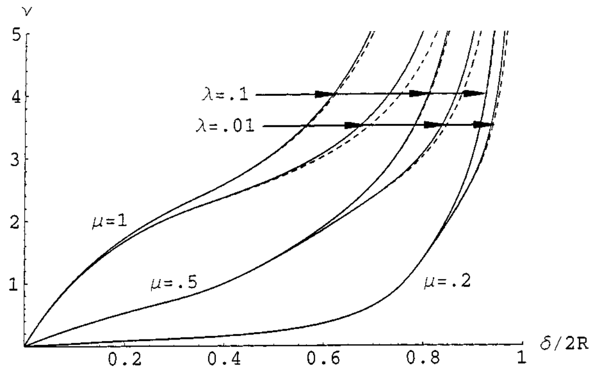

Fig. 3 Dimensionless load-deflection curves for an initially straight beam bent elastically and inextensionally into a ring (scenario I_0) for various values of dimensionless material (λ) and geometric-material (μ) parameters. Solid curves include unloading effects; dashed curves do not.

formation of a plastic hinge at points C and C' if $\lambda \approx 0$ and ν sufficiently large. Similar figures (not shown) are obtained for scenarios II_0 and III_0. Overall load-deflection curves for an inextensional centerline ($e=0$) follow from (5) and $(32)_2$ as

$$\delta/2R = 1 - \overline{y}(\pi/2;\nu). \tag{33}$$

Figures 3, 4, and 5 plot these curves for several values of λ and μ. The dashed lines are produced if we assume no unloading; the solid lines correspond to unloading. In scenarios I_0 and II_0 the effect of unloading is small, but not so in scenario III_0. As we

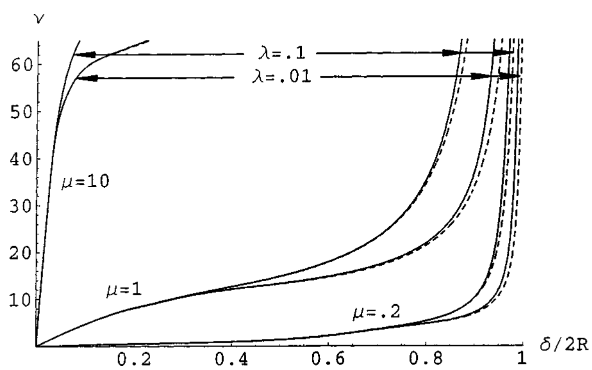

Fig. 4 Dimensionless load-deflection curves of an initially stress-free ring (scenario II_0). Solid curves include unloading effects; dashed curves do not.

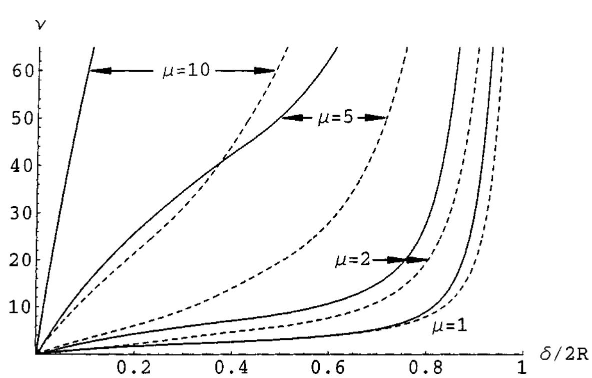

Fig. 5 Dimensionless load-deflection curves of an initially straight beam bent elastically-plastically into a ring (scenario III_0) with $\lambda=0.1$. Note that unloading effects (dashed curves) become increasingly important as μ increases.

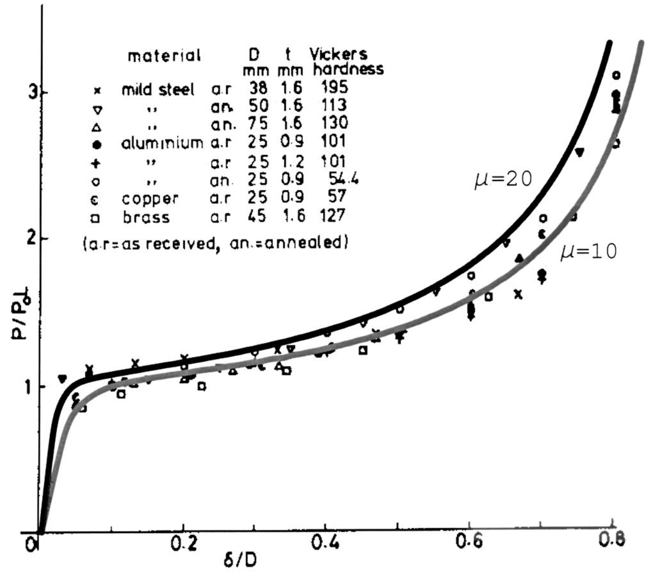

Fig. 6 Comparison of rescaled dimensionless predicted load-deflection curves for scenario II_0 with $\lambda=0.01$ and $\mu=10,20$ with experimental data from Reddy and Reid [4]

show later in this paper, the assumption of no unloading permits a more detailed—but not total—analytic treatment of scenarios I_0 and II_0.

In Fig. 6, we have re-scaled the ordinate in Fig. 4 (for scenario II_0) to read $\nu/6\mu$ and superimposed the resulting graphs for $\lambda=0.01$ and $\mu=10$, 20 on Fig. 3(a) of Reddy and Reid [4] that gives experimental data for P/P_0 versus $\delta/2R$ for a variety of metal tubes—not rings—both "as-received" and annealed. Agreement is quite reasonable for the given metals for μ between 10 and 20. Here, P_0 is what DeRuntz and Hodge [1] call the *yield point load* of the tube. If we regard each cross section of the tube as a ring (and thus neglect the end effects discussed in [4]), then the dimensionless yield point load is $\nu_0=6\mu$. See the Appendix for a derivation. In Fig. 7, we have compared the predicted load-deflection curve of our model for $\lambda=0.02$ and $\mu=11$ against the

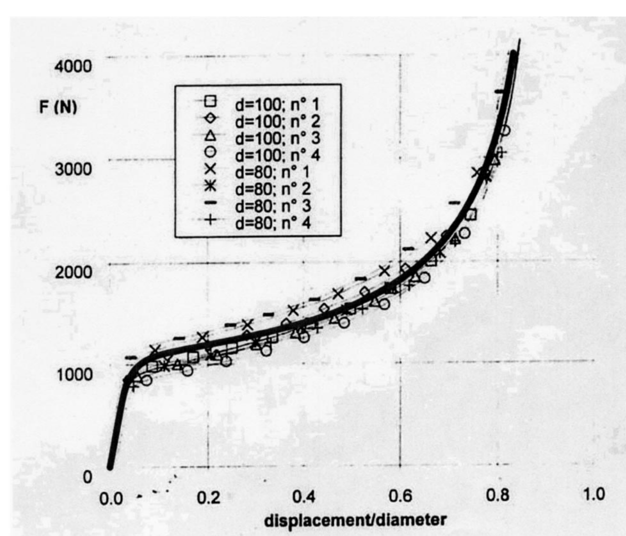

Fig. 7 Comparison of predicted load-deflection curve for Scenario II_0 with $\lambda=0.02$ and $\mu=11$ with experimental data from Avalle and Goglio [8]

experimental results presented in Fig. 6 of [8]. The agreement is quite good. Note, especially, how the model captures the rather rapid increase in slope near complete crushing.

Because unloading does not have a major effect on the overall load-deflection curves in scenarios I_0 and II_0, we now show that the neglect of this phenomenon in these two cases permits a more detailed analytic treatment of crushing.

9 Elastic and Plastic Regions in Scenario I_0 (No Unloading)

Recall that in this scenario, we assume that, when the initially straight beam is bent into a ring, the resulting deformation is elastic. That is, $\mu \leqslant 1$. Thus, when the load is first applied through the platens, the ring is elastic. From Eqs. (4.52), (4.57), and (4.66) of Frish-Fay [7], the maximum dimensionless elastic bending moment occurs at points C and C' in Fig. 1 and is given by

$$m_C = \sqrt{m_A^2 + \nu}, \tag{34}$$

where the subscripts A or C denote values of the unknowns at points A or C. As ν increases, m_A *decreases* and vanishes, according to Frish-Fay, when the dimensionless load $\nu = (1/\pi) \times [\Gamma(1/4)/\Gamma(3/4)]^2 \mu^2 = (2.78\cdots)\mu^2$, where Γ is the gamma function. *For higher loads, the portion AB of the ring in Fig. 1 lies flat against the lower platen and suffers no bending moment. Moreover, because the bending moment (unlike the vertical shear force) is continuous at B, there is always some part of the ring to the right of B that remains elastic.*

The inextensionality of the centerline of the ring may be expressed with the aid of $(3)_1$, $(7)_1$, and $(9)_2$ as

$$\begin{aligned} \pi/2 &= \int_0^{\pi/2} d\theta = \theta_B + \int_0^{\alpha_H} (d\theta/d\alpha)\, d\alpha \\ &= \theta_B + \mu\left[\int_0^{\alpha_P} (d\alpha/\eta) + \int_{\alpha_P}^{\alpha_H} (d\alpha/\eta)\right]. \end{aligned} \tag{35}$$

Here, $\alpha_P \in (0, \alpha_H]$ is the angle (if any) at which plastic deformation begins whereas, as explained following (6), $\alpha_H = \pi/2$, except possibly if $\lambda = 0$. As we shall see, a *plastic hinge* forms if the dimensionless load ν exceeds $3 - \eta^2(0)$. We note that the change in variable from θ to α in (35) is permissible because α is a strictly increasing function of θ for $\theta_B < \theta < \alpha_H$. Once η as a function of α has been determined, the first integral on the right side of (35) can be evaluated in terms of elliptic integrals; the second, if needed, can be evaluated numerically with the aid of a symbol manipulating program such as *Mathematica*.

10 Solution of the Differential Equation of Moment Equilibrium and Determination of the Load-Deflection Curve for Scenario I_0

Taking α rather than $s = R\theta$ as the independent variable in (4), applying the chain rule, using $(7)_1$ and (8), introducing the dimensionless load ν and curvature η from $(3)_2$ and $(9)_2$, and ignoring the extensional strain e, we obtain

$$\eta f'(\eta) \frac{d\eta}{d\alpha} = \frac{\nu \cos\alpha}{2}, \quad 0 < \alpha < \alpha_H. \tag{36}$$

Solution in the Elastic Region $0 < \alpha < \alpha_P$ Where $\eta \leqslant 1$. From (10), $f'(\eta) = 1$ and (36) can be integrated immediately to yield

$$\eta(\alpha) = \sqrt{\eta^2(0) + \nu \sin\alpha}. \tag{37}$$

If the ring has flattened, then $\eta(0) = 0$. The dimensionless curvature η increases with α until either $\alpha = \pi/2$, in which case the entire ring remains elastic and Frish-Fay's analysis applies, or else, from (37), there is a value

$$\alpha_P = \sin^{-1}\left[\frac{1 - \eta^2(0)}{\nu}\right] < \frac{\pi}{2} \tag{38}$$

at which $\eta = 1$.

The deflection of the inextensional ring due to pure elastic deformation, δ_E, is computed from (5). Using $(7)_1$ to switch from s to α as the variable of integration and noting $(3)_1$, $(9)_2$, and (37), we find that

$$\frac{\delta_E}{2R} = 1 - \mu \int_0^{\alpha_P} \frac{\sin\alpha\, d\alpha}{\sqrt{\eta^2(0) + \nu \sin\alpha}}. \tag{39}$$

The integral is elliptic. To bring it to standard form, make the change of variable

$$\sin\alpha = 1 - 2\sin^2\phi, \quad \phi_P \leqslant \phi \leqslant \pi/4, \tag{40}$$

and let

$$p^2 = \frac{2\nu}{\eta^2(0) + \nu} \quad \text{and} \quad \phi_P = \sin^{-1}\left(\sqrt{\frac{1 - \sin\alpha_P}{2}}\right). \tag{41}$$

Thus,

$$\begin{aligned} \int_0^{\alpha_P} \frac{\sin\alpha\, d\alpha}{\sqrt{\eta^2(0) + \nu \sin\alpha}} &= \sqrt{2/\nu}\, p \int_{\phi_P}^{\pi/4} \frac{(1 - 2\sin^2\phi)\, d\phi}{\sqrt{1 - p^2 \sin^2\phi}} \\ &= \sqrt{2/\nu}\,(2/p) \int_{\phi_P}^{\pi/4} \left(\sqrt{1 - p^2\sin^2\phi} \right. \\ &\quad \left. + \frac{1/2p^2 - 1}{\sqrt{1 - p^2\sin^2\phi}}\right) d\phi \end{aligned} \tag{42}$$

so that, from (39),

$$\begin{aligned} \delta_E/2R = 1 &- (2\sqrt{2/\nu})(\mu/p)\{E(p,\pi/4) - E(p,\phi_P) + (1/2p^2 - 1) \\ &\times [F(p,\pi/4) - F(p,\phi_P)]\}, \end{aligned} \tag{43}$$

where $F(p,\phi)$ and $E(p,\phi)$ are, respectively, Legendre's elliptic integrals of the first and second kind.

Solution in the Plastic Region $\alpha_P < \alpha \leqslant \alpha_H$ Where $\eta > 1$. Substitution of (10) into (36) and integration from 1 to η yields

$$\begin{aligned} \nu(\sin\alpha - \sin\alpha_P) &= (\eta - 1)[2(1-\lambda)\eta^{-1} + \lambda(\eta + 1)] \\ &\sim \begin{cases} 2, & \lambda = 0 \\ \lambda\eta^2, & \lambda \neq 0 \end{cases} \quad \text{as} \quad \eta \to \infty. \end{aligned} \tag{44}$$

Since the left side of (44) is bounded, the last line on the right shows that a plastic hinge can occur, i.e., η can approach infinity, only if $\lambda = 0$.

The deflection due to any purely elastic deformation of the ring is given by (39) or, equivalently, by (43). The additional elastic-plastic contribution is given by

$$\delta_P = -2R\mu \int_{\alpha_P}^{\alpha_H} \frac{\sin\alpha\, d\alpha}{g(\alpha; \alpha_P, \lambda, \nu)} \equiv -2R\mu\Delta, \tag{45}$$

where $\eta = g(\alpha; \alpha_P, \lambda, \nu)$ is that root of (44) which equals 1 when $\alpha = \alpha_P$. (This involves finding the root of a cubic polynomial.)

For the special case of elastic-perfect plasticity, $\lambda = 0$ and (44) has the explicit solution

$$\eta = g(\alpha; \alpha_P, 0, \nu) = \frac{2}{2 + \nu(\sin\nu_P - \sin\alpha)} = \frac{2}{3 - \eta^2(0) - \nu\sin\alpha}. \tag{46}$$

Clearly, if $\nu \geqslant 3 - \eta^2(0)$, there is a value $\alpha = \alpha_H \leqslant \pi/2$ where η becomes infinite. Substitution of (46) into (45) yields

$$\begin{aligned} \Delta = \cos\alpha_P - \cos\alpha_H &+ (\nu/4)[\alpha_P - \alpha_H + (\cos\alpha_P - \cos\alpha_H)\sin\alpha_P \\ &+ (\sin\alpha_H - \sin\alpha_P)\cos\alpha_H]. \end{aligned} \tag{47}$$

For $\lambda \neq 0$, we used *Mathematica* to first determine $g(\alpha;\alpha_P,\lambda,\nu)$ analytically and then to evaluate the integral in (45) numerically. There are two cases to be considered.

(i) Unflattened ring: $0<\eta(0)<1$, $\theta_B=0$.

As can be seen from (38), if $\nu \leqslant 1-\eta^2(0)$, the ring remains elastic. By $(41)_2$, $\phi_P=0$ and from (43) the deflection reduces to

$$\delta/2R = 1-(2\sqrt{2/\nu})(\mu/p)[E(p,\pi/4)+(p^2/2-1)F(p,\pi/4)]. \tag{48}$$

Except for a slightly different notation, this is Eq. (4.67) of Frish-Fay [7].

To relate the dimensionless load ν to $\delta/2R$, we follow Frish-Fay and impose the inextensionality condition (35). With the change of variable (40), we have, since $\theta_B=0$ and $\alpha_P=\pi/2$,

$$\frac{\pi}{2\mu}=\sqrt{2/\nu}p\int_0^{\pi/4}\frac{d\phi}{\sqrt{1-p^2\sin^2\phi}}=\sqrt{2/\nu}pF(p,\pi/4). \tag{49}$$

Thus,

$$\frac{\nu}{\mu^2}=\frac{3PR^2}{bEH^3}=\frac{8p^2F^2(p,\pi/4)}{\pi^2}. \tag{50}$$

Substitution of this result into (48) yields

$$\frac{\delta}{2R}=1-\frac{\pi[E(p,\pi/4)+(1/2p^2-1)F(p,\pi/4)]}{p^2F(p,\pi/4)}. \tag{51}$$

The load-deflection curve for the unflattened ring in the elastic range is thus given in parametric form by (50) and (51) with p as the parameter.

If $\nu>1-\eta^2(0)$, the ring becomes plastic when $\alpha=\alpha_P \leqslant \pi/2$, where α_P is given by (38). In this subcase, the analytical/numerical procedure is as follows: Fix λ and μ (both less than one). For each value of ν, solve for $\eta(0)$ by requiring that

$$\sqrt{2/\nu}\mu p[F(p,\pi/4)-F(p,\phi_P)]+\int_{\alpha_P}^{\pi/2}g^{-1}(\alpha;\alpha_P,\lambda,\nu)d\sigma=\pi/2. \tag{52}$$

This was done using the secant method in *Mathematica*. Once $\eta(0)$ was found, we computed the total deflection from (43) and (45) as $\delta=\delta_E-2R\mu\Delta(\pi/2)$, where Δ was determined by integrating (45) numerically.

(ii) Flattened ring: $\eta(0)=0$, $\theta_B>0$.

Numerically, this case is simpler than the first subcase because the inextensionality constraint (35) may be regarded as an equation for determining θ_B (which is *not* needed in determining the load-deflection curve—the goal of the present paper). Again there are two subcases.

If $\nu \leqslant 1$, the ring remains elastic and the analysis in Section 4.9 of Frish-Fay [7] applies. In this subcase, (39) reduces to $\delta/2R = 1-(\mu/\sqrt{\nu})\int_0^{\pi/2}\sqrt{\sin\alpha}d\alpha$ which leads to the load-deflection curve

$$\frac{\nu}{\mu^2}=\frac{3PR^2}{bEH^3}=\frac{\pi}{4}\left[\frac{\Gamma(3/4)}{(1-\delta/2R)\Gamma(5/4)}\right]^2. \tag{53}$$

If $\nu>1$, then, by (38), the ring is elastic if $0\leqslant\alpha\leqslant\sin^{-1}(1/\nu)$ and plastic otherwise. The total deflection is $\delta=\delta_E+\delta_P$, where, from (41) and (43), $p=\sqrt{2}$, $2\nu\sin^2\phi_P=\nu-1$,

$$\delta_E/2R=1-(2\mu/\sqrt{\nu})[E(\sqrt{2},\pi/4)-E(\sqrt{2},\phi_P)], \tag{54}$$

and δ_P comes from integrating (45) numerically (with the aid of *Mathematica*).

Our final results agree with the dashed curves presented in Fig. 3 that were computed using the numerical methods discussed in Sections 5–7.

11 Elastic and Plastic Regions in Scenario II_0 (No Unloading)

In this scenario, the parameter μ that measures the ratio of plastic to elastic effects has the full range $0<\mu<\infty$. Moreover, the bending strain at point A in Fig. 1 (which is drawn for scenario I_0, but whose general features are the same as for scenario II_0) *decreases from zero* as the load is applied. If the ring flattens, then $R=\infty$; i.e., from $(9)_2$ and (11), $\eta=-\mu$. As $\eta=-1$ marks the transition from elastic to plastic behavior, the ring will not go plastic before it flattens if $\mu\leqslant 1$.

At point C in Fig. 1 the bending strain *increases from zero*. Because M (and hence κ) is a continuous function of θ, there is always some point between A and C (which depends on the load) where $\kappa=0$. Thus, in scenario II_0, *some segment of the ring always remains elastic* so that there are two values, α_- and α_+, depending on λ, μ, and ν, such that the ring is elastic for $0\leqslant\alpha_-\leqslant\alpha\leqslant\alpha_+\leqslant\alpha_H\leqslant\pi/2$. This in turn implies that there may be two separate plastic zones, $0\leqslant\alpha\leqslant\alpha_-$ where $\eta<-1$, and $\alpha_+\leqslant\alpha\leqslant\alpha_H\leqslant\pi/2$ where $\eta>1$.

12 Solution of the Differential Equation of Moment Equilibrium for Scenario II_0

Taking, as before, α rather than θ as the independent variable in (4), applying the chain rule, using (10) and (11), introducing the dimensionless load ν and curvature η from $(3)_2$ and $(9)_2$, and ignoring the extensional strain e, we have

$$(\eta+\mu)f'(\eta)\frac{d\eta}{d\alpha}=\frac{\nu\cos\alpha}{2}. \tag{55}$$

Solution in the Elastic Region $0\leqslant\alpha_-\leqslant\alpha\leqslant\alpha_+$. From (10), $f'(\eta)=1$. Integrating (55) from α_- to α, we have

$$\eta=-\mu+\sqrt{[\eta(\alpha_-)+\mu]^2+\nu(\sin\alpha-\sin\alpha_-)}. \tag{56}$$

If $\mu\leqslant 1$, the ring is relatively thin; as the load increases from zero, the ring first flattens at $\nu=(1/\pi)[\Gamma(1/4)/\Gamma(3/4)]^2\mu^2=(2.78\ldots)\mu^2$ and becomes plastic at C when $\nu=(1+\mu)^2$. As the load increases further, a *single* plastic zone spreads from C inward to some point where $\alpha=\alpha_+$.

If $\mu>1$, the ring is relatively thick and—if we look ahead to (70)—first becomes plastic at A when the dimensionless load ν is such that $\pi/2=\sqrt{2/\nu}\mu pF(p,\pi/4)$, where p is given by $(67)_1$ with $\alpha_-=0$ and $\eta(0)=-1$. (The ring need not to have begun to flatten at this load). As the load increases further, this zone spreads from A, extending to some point where $\alpha=\alpha_-$. (It makes no difference in the analysis to follow whether the ring has flattened or not because we work with the deformed angle α which is always zero at the point of contact of the ring with the lower platen, whether that point be at A or B.) At some load level, which must be determined numerically, a second plastic zone begins to spread from C. We now analyze both cases simultaneously with the understanding that if $\mu<1$, a plastic zone near the platens does not exist.

Solution in the Plastic Region $0\leqslant\alpha\leqslant\alpha_-(-\mu\leqslant\eta<-1)$. If $\eta<-1$, then from (10), $f'(\eta)=-(1-\lambda)\eta^{-3}+\lambda$. Substituting this expression into (55), integrating, and choosing the constant of integration so that $\eta\to-1$ as $\alpha\to\alpha_-$, we obtain

$$(1+\eta)\left[\frac{\mu(1-\lambda)(1-\eta)}{\eta^2}+\frac{2(1-\lambda)}{\eta}+2\lambda\mu-\lambda(1-\eta)\right]$$
$$=\nu(\sin\alpha-\sin\alpha_-). \tag{57}$$

Upon multiplying by η^2 we obtain a quartic polynomial in η. Let

$$\eta=g_-(\alpha;\alpha_-,\lambda,\mu) \tag{58}$$

denote that root which reduces to -1 when $\alpha=\alpha_-$.

Solution in the Plastic Region $\alpha_+ \leqslant \alpha \leqslant \alpha_H \leqslant \pi/2$. Because $\eta > 1$, (10) yields $f'(\eta) = (1-\lambda)\eta^{-3} + \lambda$. Substituting this expression into (55), integrating, and choosing the constant of integration so that $\eta \to 1$ as $\alpha \to \alpha_+$, we obtain

$$\nu(\sin\alpha - \sin\alpha_+) = (\eta - 1)\left[\frac{\mu(1-\lambda)(\eta+1)}{\eta^2} + \frac{2(1-\lambda)}{\eta} + 2\lambda\mu + \lambda(\eta+1)\right] = \begin{cases} 2+\mu, & \lambda = 0 \\ \lambda\eta^2, & \lambda \neq 0 \end{cases} \quad \text{as} \quad \eta \to \infty. \tag{59}$$

As in scenario I_0, the last line on the right of this equation shows that a plastic hinge is possible only if $\lambda = 0$. Upon multiplying the first line of (59) by η^2 we obtain a quartic polynomial in η. Let

$$\eta = g_+(\alpha; \alpha_+, \lambda, \mu) \tag{60}$$

denote that root which reduces to 1 when $\alpha = \alpha_+$.

13 Determination of $\alpha_\pm$ if $\mu > 1$ and the Ring has Flattened

To find α_-, set $\eta = -\mu$ at $\alpha = 0$ in (57). It follows that

$$\alpha_- = \sin^{-1}\left\{\frac{(\mu-1)^2[1+\lambda(\mu-1)]}{\mu\nu}\right\}. \tag{61}$$

To find α_+, impose (56) at $\alpha = \alpha_+$ where $\eta = 1$. It follows with the aid of (61) that

$$\alpha_+ = \sin^{-1}\left\{\frac{4\mu^2 + (\mu-1)^2[1+\lambda(\mu-1)]}{\mu\nu}\right\}. \tag{62}$$

14 Computation of the Load-Deflection Curve for Scenario II_0

If $0 < \mu \leqslant 1$ (i.e., if the ring is relatively thin), there are three distinct stages of deformation as the load slowly increases: (i) the entire ring is elastic and there is no flattening; (ii) the ring begins to flatten, but remains elastic; (iii) a plastic zone begins to spread from *C*. Qualitatively, the stages of deformation are similar to those for scenario I_0 shown in Fig. 1. If $\lambda = 0$ (elastic-perfect plasticity), a plastic hinge can form at *C*.

If $\mu > 1$, but not too large (say $\mu = 2$), there are four distinct stages of deformation as the load slowly increases. To describe these, let *D* denote the point where $\alpha = \alpha_-$ and *E* the point where $\alpha = \alpha_+$. (i) the entire ring is elastic and there is no flattening; (ii) the segment *AD* is plastic whereas *DC* remains elastic and there is no flattening; (iii) *AB* is flattened and plastic, *BD* is plastic, and *DC* elastic; (iv) *AB* is flattened and plastic, *BD* is plastic, *DE* is elastic, and *EC* is plastic. Although λ and μ are given, the load at which any point switches from elastic to plastic is usually unknown and must be determined numerically. For larger values of μ (say, $\mu = 10$), stage (ii) above is modified: *AD* is plastic, *DE* is elastic, and *EC* is plastic *before* flattening occurs.

If $\lambda = 0$, a plastic hinge can form at *C* under a sufficiently high load. To find the associated hinge angle, α_H, we set $\lambda = 0$ and let $\eta \to \infty$ in (59). Using (62), we obtain

$$\alpha_H = \sin^{-1}\left(\frac{\mu^{-1} + 6\mu}{\nu}\right). \tag{63}$$

Clearly, the denominator must exceed the numerator for the hinge angle to be less than $\pi/2$.

The deflection in scenario II_0, from $(3)_1$, (5) (with $e = 0$), $(9)_2$, and (11), is

$$\frac{\delta}{2R} = 1 - \mu\int_0^{\alpha_H}\frac{\sin\alpha\, d\alpha}{\mu + \eta}. \tag{64}$$

Breaking the integral into the sum of three integrals and using (56), (58), and (60), we have

$$\begin{aligned}\frac{\delta}{2R} = 1 - \mu\Bigg[&\int_0^{\alpha_-}\frac{\sin\alpha\, d\alpha}{\mu + g_-(\alpha;\alpha_-,\lambda,\mu)} \\ &+ \int_{\alpha_-}^{\alpha_+}\frac{\sin\alpha\, d\alpha}{\sqrt{[\eta(\alpha_-)+\mu]^2 + \nu(\sin\alpha - \sin\alpha_-)}} \\ &+ \int_{\alpha_+}^{\alpha_H}\frac{\sin\alpha\, d\alpha}{\mu + g_+(\alpha;\alpha_+,\lambda,\mu)}\Bigg] \\ \equiv 1 - \mu[&\Delta_-(\alpha_-,\lambda,\mu) + \Delta(\alpha_-,\alpha_+,\lambda,\mu) \\ &+ \Delta_+(\alpha_+,\alpha_H,\lambda,\mu)].\end{aligned} \tag{65}$$

Unless the ring has flattened, that would allow us to use (61)–(63), the angles α_-, α_+, and α_H must be determined (numerically) as part of the solution.

The middle integral is elliptic and may be brought to standard form with the change of variable

$$\sin\alpha = 1 - 2\sin^2\phi, \qquad \phi_+ \leqslant \phi \leqslant \phi_-, \tag{66}$$

and by setting

$$p^2 = \frac{2\nu}{[\eta(\alpha_-)+\mu]^2 + \nu(1-\sin\alpha_-)} \quad \text{and} \quad \phi_\pm = \sin^{-1}\sqrt{\frac{1-\sin\alpha_\pm}{2}}. \tag{67}$$

Thus—see (42) and (43)—,

$$\begin{aligned}\Delta &= \sqrt{2/\nu}\,p\int_{\phi_+}^{\phi_-}\frac{(1-2\sin^2\phi)\,d\phi}{\sqrt{1-p^2\sin^2\phi}} \\ &= \sqrt{2/\nu}(2/p)\{E(p,\phi_-) - E(p,\phi_+) \\ &\quad + (p^2/2 - 1)[F(p,\phi_-) - F(p,\phi_+)]\}.\end{aligned} \tag{68}$$

As in scenario I_0, the dimensionless deflections in the elastic-plastic portions of the deformed ring, $\Delta_\pm$, were computed numerically with the aid of *Mathematica*.

In case (i) for $0 < \mu \leqslant 1$ and cases (i) and (ii) for $\mu > 1$, where the ring has not yet flattened, the inextensionality constraint must be satisfied, which produces a relation between the dimensionless load ν and the dimensionless deflection $\delta/2R$. (In the other cases, inextensionality merely serves to determine the extent of the flattened portion of the ring, if needed.) Thus, in analogy to (35), we have

$$\begin{aligned}\pi/2\mu &= \int_0^{\pi/2} d\alpha/(\mu+\eta) \\ &= \int_0^{\alpha_-}\frac{d\alpha}{\mu + g_-(\alpha;\alpha_-,\lambda,\mu)} \\ &\quad + \int_{\alpha_-}^{\alpha_+}\frac{d\alpha}{\sqrt{[\eta(\alpha_-)+\mu]^2 + \nu(\sin\alpha - \sin\alpha_-)}} \\ &\quad + \int_{\alpha_+}^{\pi/2}\frac{d\alpha}{\mu + g_+(\alpha;\alpha_+,\lambda,\mu)} \\ &\equiv \psi_-(\alpha_-,\lambda,\mu) + \psi(\alpha_+,\alpha_-,\lambda,\mu) + \psi_+(\alpha_+,\lambda,\mu).\end{aligned} \tag{69}$$

With the change of variable (66) and the definitions (67), the middle integral reduces to

$$\psi = \sqrt{2/\nu}\,p[F(p,\phi_-) - F(p,\phi_+)]. \tag{70}$$

The integrals $\psi_\pm$ were computed numerically using *Mathematica*.

Load-deflection curves for scenario II_0 without unloading agree with the dashed curves in Fig. 4 that were computed by the numerical methods described in Sections 5–7.

In the Appendix, we show that as the material approaches rigid-perfect plasticity $(\lambda=0,\mu\to\infty)$, we recover from (65) what DeRuntz and Hodge [1] call the *yield point load* of the tube, P_0, which, in dimensionless form, is given by $\nu_0/\mu=6$.

15 Conclusions

We have produced numerical solutions for three simple benchmark problems for circular rings made of a bi-linear elastic-plastic material that may undergo isotropic hardening. In scenario I_0, an initially straight beam is bent elastically into a ring and then slowly crushed; in scenario II_0, and initially stress-free circular ring is slowly crushed; in scenario III_0, the complement of scenario I_0, a straight beam is bent first elastically and then plastically into a ring before being slowly crushed. For simplicity, the centerline of the rings has been assumed to be inextensional, as indicated by the subscript 0.

The analysis confirms, in a more quantitative way than before, what workers in the field have long known, namely, that when both strains and deflections are large, the amount of strain hardening has a significant influence on the deformed configuration of a structure. This is quite evident in Figs. 3 and 4, where the influence of λ, the ratio of the plastic to elastic modulus, is extremely pronounced in the final stages of crushing. On the other hand, the effect of unloading in scenarios I_0 and II_0 is not large. This observation motivated the more analytical treatment of these two cases given in Sections 9–14.

Although it may be justly claimed that a bi-linear stress-strain relation is an idealization, we remind the reader that our purpose was to analyze precisely, a simple mechanical model that not only may used to check elaborate structural codes, but also may be compared against experiments, as Figs. 6 and 7 demonstrate.

Appendix

Determining the Limit Load $(\lambda=0,\ \mu\to\infty)$ in Scenario II_0. Herein, we show that if $\lambda=0$ (perfect plasticity), then the dimensionless deflection for scenario II_0 given by (65) yields

$$\frac{\nu}{\mu}\sim\frac{6}{\sqrt{1-(\delta/2R)^2}}\quad\text{as}\quad\mu\to\infty. \tag{A1}$$

This expression corresponds to Eq. (14) of DeRuntz and Hodge [1] and also, according to Redwood [2], to a similar formula in an unpublished report by Burton and Craig [13]. Redwood [2] refined the analysis of DeRuntz and Hodge by assuming a rigid, linear strain-hardening stress-strain relation and generalized their load-deflection relation with his Eq. (1).

From (57)–(60) we have

$$g_{\pm}(\alpha;\alpha_{\pm},0,\mu)=\mathrm{O}(1)\quad\text{as}\quad\mu\to\infty. \tag{A2}$$

Moreover, if we assume that the ring has flattened so that $\eta(0)=-\mu$ and $\eta(\alpha_-)=-1$, then, setting $\nu=k\mu$ in the denominator of the second integral in (65), we have

$$\sqrt{(\mu-1)^2+k\mu(\sin\alpha-\sin\alpha_-)}=\mu+\mathrm{O}(1)\quad\text{as}\quad\mu\to\infty. \tag{A3}$$

Thus, (65) yields

$$\delta/2R=1-\int_0^{\alpha_H}\sin\alpha d\alpha+\mathrm{O}(\mu^{-1})=\cos\alpha_H+\mathrm{O}(\mu^{-1}). \tag{A4}$$

But from (63),

$$\cos\alpha_H=\sqrt{1-(6/k)^2}+\mathrm{O}(\mu^{-2}). \tag{A5}$$

Solving for $k=\nu/\mu$, we obtain the asymptotic dimensionless force-deflection relation (A1).

The dimensionless *yield point load*

$$\nu_0/\mu=6, \tag{A6}$$

corresponding to $\delta/2R\to 0$ in (A1), may be derived from simple mechanical considerations. At the load $2P_0$ when the ring first flattens at point A—see Fig. 1—, the dimensionless bending strain there, $\eta(0)$, is equal to $-\mu$. Thus, as $\mu\to\infty$, we have a plastic hinge *both* at A and C, with moments of magnitude $E\varepsilon_Y H^2$ but of opposite sign. Because the ring is essentially rigid before these hinges come into play, equilibrium of a quarter of the ring requires that $P_0R=2E\varepsilon_Y bH^2$. By (3), this is just the dimensional form of (A6). According to DeRuntz and Hodge [1], the yield point load P_0 was first computed by Drybye and Hansen [14].

References

[1] DeRuntz, J. A., and Hodge, P. G., 1963, "Crushing of a Tube Between Plates," ASME J. Appl. Mech., **30**, pp. 391–395.
[2] Redwood, R. G., 1964, "Crushing of a Tube Between Rigid Plates," ASME J. Appl. Mech., **31**, pp. 357–358.
[3] Reid, S. R., and Reddy, T. Y., 1978, "Effect of Strain Hardening on the Lateral Compression of Tubes Between Rigid Plates," Int. J. Solids Struct., **14**, pp. 213–225.
[4] Reddy, T. Y., and Reid, S. R., 1980, "Phenomena Associated With the Crushing of Metal Tubes Between Rigid Plates," Int. J. Solids Struct., **16**, pp. 545–562.
[5] Liu, J. H., Stonge, W. J., and Yu, T. X., 1989, "Large Deflections of an Elastoplastic Strain-Hardening Cantilever," ASME J. Appl. Mech., **56**, pp. 737–743.
[6] Lubliner, J., 1990, *Plasticity Theory*, Macmillan, New York.
[7] Frish-Fay, R., 1962, *Flexible Bars*, Butterworths and Co., London.
[8] Avalle, M., and Goglio, L., 1997, "Static Lateral Compression of Aluminum Tubes: Strain Gauge Measurements and Discussion of Theoretical Models," J. Strain Anal., **32**, pp. 335–343.
[9] Libai, A., and Simmonds, J. G., 1998, *The Nonlinear Theory of Elastic Shells*, 2nd Ed., Cambridge University Press, New York.
[10] Avalle, M., and Goglio, L., 1999, "Lateral Compression of Thin-Walled Tubes: Strain Measurements by Image Analysis," Exp. Mech., **39**, pp. 231–235.
[11] Leu, D.-K., 1999, "Finite-Element Simulation of the Lateral Compression of Aluminum Tube Between Rigid Plates," Int. J. Mech. Sci., **41**, pp. 621–638.
[12] Wang, C. Y., 1987, "Crushing of an Elastic-Perfectly Plastic Ring or Tube Between Two Planes," ASME J. Appl. Mech., **54**, pp. 159–164.
[13] Burton, R. H., and Craig, J. M., 1963, "An Investigation into the Energy Absorbing Properties of Metal Tubes Loaded in the Transverse Direction," *B. Sc. (Engr.) Rept.* University of Bristol, Bristol, UK.
[14] Dyrbye, C., and Hansen, P. L., 1954, "Studies on the Load Carrying Capacities of Steel Structures," Research Laboratory of Building Technique, Technical University of Denmark, Bulletin No. 3.

Effective Constitutive Equations for Porous Elastic Materials at Finite Strains and Superimposed Finite Strains

V. A. Levin
Department of Mechanics and Mathematics,
Moscow State University,
Moscow 119899, Russia

K. M. Zingermann
Department of Applied Mathematics and
Computer Science,
Tver State University,
Tver 170000, Russia

A method is developed for derivation of effective constitutive equations for porous nonlinear-elastic materials undergoing finite strains. It is shown that the effective constitutive equations that are derived using the proposed approach do not change if a rigid motion is superimposed on the deformation. An approach is proposed for the computation of effective characteristics for nonlinear-elastic materials in which pores are originated after a preliminary loading. This approach is based on the theory of superimposed finite deformations. The results of computations are presented for plane strain, when pores are distributed uniformly. [DOI: 10.1115/1.1630811]

1 Introduction

Effective constitutive equations are constructed using well-known general principles that are considered, in particular, by Hashin and Rozen [1], Christensen [2], Kachanov et al. [3], and Mauge and Kachanov [4]. A representative volume (area for the two-dimensional case) which mechanical behavior represents the properties of material as a whole is extracted in a body. The static problem of nonlinear elasticity is solved for this volume at given loads applied to its boundary. Then the strains and stresses are averaged over the representative volume (area), and the effective constitutive equations are constructed as a relation between the average strains and the average stresses.

It should be noted that there is a rigorous approach for homogenization, when the limit is taken for the homogenized constitutive equations as the characteristic size of a representative region tends to infinity (at the fixed characteristic size of structural elements). In particular, this approach is described by Zhikov et al. [5]. For nonlinear inhomogeneous periodic media (without voids) this approach has been developed by A. Braides [6] and by S. Müller [7]. This problem goes beyond the scope of this paper. Note also that the approach of [6] is extended to nonlinear inhomogeneous materials with initiated cracks by Braides et al. [8].

Analyzing the effective properties of inhomogeneous materials one should answer the question, how to define a ''comparison'' material so that the physical sense of this definition will be clear (for the use in experiments), and the mathematical representation of this definition will be simple enough? In addition, it is not clear how to define the average strains for porous medium correctly because the strains within the pores are undefined (this is the difference between porous materials and composites with elastic inclusions). For infinitesimal strains these problems are solved simply enough, [2,3,9]. In particular, the strain tensor of the comparison material is taken as

$$\mathbf{E}^e = \frac{1}{V}\int_V \mathbf{E}\, dV = \frac{1}{2V}\int_V (\nabla\mathbf{u} + \mathbf{u}\nabla)\, dV,$$

where V is a representative volume. Then, using the divergence theorem, one can write

$$\mathbf{E}^e = \frac{1}{2V}\oint_\Gamma (\mathbf{nu} + \mathbf{un})\, d\Gamma,$$

where Γ is the boundary of the representative volume. By this, one can formally find the average strains within pores using the assumption that the pores are filled by a special elastic material so that the displacements of boundary points of the special material are the same as the displacements of the correspondent points of the matrix material at the boundaries of the pores, and the stresses within the special material are equal to zero (provided that there is no pressure in pores). This approach permits one to determine the average strains over the volume of a pore by the displacements of its boundary; these displacements are obtained from the solution of the elasticity problem. So, there is no need to determine strains at each point of a pore.

This approach can't be applied directly for finite strains because each strain tensor (for example, the Green or the Almansi strain tensor) nonlinearly depends on the displacement gradient in the coordinate basis of the initial or the deformed state, [10], and, therefore, it is impossible to replace the volume integral by the surface integral using the divergence theorem. By this, the following difficulty takes place: the averaging of each strain tensor over a representative volume gives different results if we define the displacements within pores by different ways, even if the continuity of displacements over the boundaries of pores is assumed.

Therefore, if the strains are finite, it is necessary to modify the approach that is used by Kachanov et al. [3] and Vavakin and Salganik [9] for infinitesimal strains. We use the following way: the deformation gradient (but not the strain tensor) is averaged over a representative volume in the undeformed state, and then the strain tensor of the comparison material is expressed in terms of the averaged deformation gradient.

2 Definitions in the Case When the Shapes of Pores are Given in the Undeformed State

Let the shape of pores be determined in the undeformed state. Let V_0 be a representative volume extracted in this state, Γ_0 the boundary of V_0, $\overset{0}{\mathbf{N}}$ the normal to the boundary Γ_0. Let V be the correspondent representative volume in the deformed state, Γ its boundary, $\mathbf{N}$ the normal to the boundary Γ. (We assume that the boundary of the representative volume does not intersect the pore

Contributed by the Applied Mechanics Division of THE AMERICAN SOCIETY OF MECHANICAL ENGINEERS for publication in the ASME JOURNAL OF APPLIED MECHANICS. Manuscript received by the ASME Applied Mechanics Division, August 9, 2001; final revision, June 2, 2003. Associate Editor: E. Arruda. Discussion on the paper should be addressed to the Editor, Prof. Robert M. McMeeking, Department of Mechanical and Environmental Engineering, University of California–Santa Barbara, Santa Barbara, CA 93106-5070, and will be accepted until four months after final publication of the paper itself in the ASME JOURNAL OF APPLIED MECHANICS.

space). By $\overset{0}{\nabla}$ and ∇ denote the gradient operators referring to the base of the initial and the deformed states, respectively. Let $\boldsymbol{\Psi} = \mathbf{I} + \overset{0}{\nabla}\mathbf{u} = (\mathbf{I} - \nabla\mathbf{u})^{-1}$ denote the deformation gradient, $\mathbf{u}$ the displacement vector, $\mathbf{R}$ position vector of a point in the deformed state.

Let the boundary condition

$$\mathbf{N}\cdot\sigma|_{\Gamma} = \mathbf{N}\cdot\tilde{\sigma}|_{\Gamma} \tag{1}$$

be given at the boundary Γ of the deformed volume. Here σ is the true (Cauchy) stress tensor, and $\tilde{\sigma}$ is an arbitrary constant (independent on coordinates), symmetric tensor.

Following Hashin and Rozen [1], it may be shown that if the condition (1) is satisfied and the body forces are equal to zero, then the averaged true stresses over the deformed volume are equal to $\tilde{\sigma}$. Indeed, the equilibrium equation in this case has a form

$$\nabla\cdot\sigma = 0. \tag{2}$$

Consider the identity

$$\nabla\cdot(\sigma\mathbf{R}) = (\nabla\cdot\sigma)\mathbf{R} + \sigma\cdot(\nabla\mathbf{R})^* = (\nabla\cdot\sigma)\mathbf{R} + \sigma\cdot\mathbf{I} = (\nabla\cdot\sigma)\mathbf{R} + \sigma.$$

Taking into account (2), we obtain from this identity

$$\sigma = \nabla\cdot(\sigma\mathbf{R}).$$

Integrating the last equation over the deformed volume and using the divergence theorem, we have

$$\int_V \sigma dV = \int_V \nabla\cdot(\sigma\mathbf{R})dV = \oint_{\Gamma}\mathbf{N}\cdot\sigma\mathbf{R}d\Gamma.$$

Using (1) and taking into account that the tensor $\tilde{\sigma}$ is symmetric and constant, we get

$$\oint_{\Gamma}\mathbf{N}\cdot\sigma\mathbf{R}d\Gamma \equiv \oint_{\Gamma}\mathbf{N}\cdot\tilde{\sigma}\mathbf{R}d\Gamma \equiv \oint_{\Gamma}\tilde{\sigma}\cdot\mathbf{N}\mathbf{R}d\Gamma = \tilde{\sigma}\cdot\oint_{\Gamma}\mathbf{N}\mathbf{R}d\Gamma.$$

And finally, applying the divergence theorem to the last integral, we obtain

$$\tilde{\sigma}\cdot\oint_{\Gamma}\mathbf{N}\mathbf{R}d\Gamma = \tilde{\sigma}\cdot\int_V \nabla\mathbf{R}dV = \tilde{\sigma}\cdot\int_V \mathbf{I}dV = V\tilde{\sigma}.$$

Thus,

$$\frac{1}{V}\int_V \sigma dV = \tilde{\sigma}.$$

Note that the boundary condition (1) may be written in the coordinates of the undeformed state in the form

$$\overset{0}{\mathbf{N}}\cdot\overset{0}{\boldsymbol{\Sigma}}|_{\Gamma_0} = (\det\boldsymbol{\Psi})\overset{0}{\mathbf{N}}\cdot\boldsymbol{\Psi}^{*-1}\cdot\tilde{\sigma}\cdot\boldsymbol{\Psi}^{-1}|_{\Gamma_0}. \tag{3}$$

Here $\overset{0}{\boldsymbol{\Sigma}}$ is the second Piola-Kirchhoff stress tensor, [10]:

$$\overset{0}{\boldsymbol{\Sigma}} = (\det\boldsymbol{\Psi})\boldsymbol{\Psi}^{*-1}\cdot\sigma\cdot\boldsymbol{\Psi}^{-1}. \tag{4}$$

Now we shall give the definition of a comparison material. Let a representative volume V_0 be extracted in an undeformed porous material, and let the loads be applied to the boundary Γ_0 of this volume in accord with (3). Let the true stresses in the porous material be averaged over the deformed volume (the average true stresses in this case are equal to $\tilde{\sigma}$, as shown above), and the deformation gradient of the porous material be averaged over the undeformed volume. Then a uniform material is called a comparison material if the following condition holds: if the true stresses in this material are equal to $\tilde{\sigma}$, then the deformation gradient of this material is equal to the averaged deformation gradient of the porous material.

In accord with this definition we can write

$$\sigma^e = \tilde{\sigma} = \frac{1}{V}\int_V \sigma dV, \quad \boldsymbol{\Psi}^e = \frac{1}{V_0}\int_{V_0}\boldsymbol{\Psi}dV_0. \tag{5}$$

Here and further in this paper the superscript "e" over a quantity indicates that this quantity is a property of a comparison material.

Using the divergence theorem, we can write the second Eq. (5) in the form

$$\boldsymbol{\Psi}^e = \frac{1}{V_0}\int_{V_0}\boldsymbol{\Psi}dV_0 = \frac{1}{V_0}\int_{V_0}(\mathbf{I} + \overset{0}{\nabla}\mathbf{u})dV_0 = \mathbf{I} + \frac{1}{V_0}\oint_{\Gamma_0}\overset{0}{\mathbf{N}}\mathbf{u}d\Gamma_0. \tag{6}$$

Consider now an approach to the construction of effective constitutive equations for porous materials on the basis of the proposed concept. A representative volume V_0 is extracted in a porous medium (in the undeformed state). The solution of the nonlinear elasticity problem is obtained subject to the boundary condition (3) at the external boundary Γ_0 of this volume (it will be recalled that $\tilde{\sigma}$ in (3) is a constant, symmetric tensor), and the boundary conditions at the boundaries of pores. In particular, the displacement vector $\mathbf{u}$ is obtained. Next, the deformation gradient $\boldsymbol{\Psi}^e$ of the comparison material is obtained from (6). Then the Green strain tensor $\overset{0}{\mathbf{E}}{}^e$ and the second Piola-Kirchhoff stress tensor $\overset{0}{\boldsymbol{\Sigma}}{}^e$ of the comparison material are determined using the relations

$$\overset{0}{\mathbf{E}}{}^e = \frac{1}{2}(\boldsymbol{\Psi}^e\cdot\boldsymbol{\Psi}^{e*} - \mathbf{I}), \tag{7}$$

$$\begin{aligned}\overset{0}{\boldsymbol{\Sigma}}{}^e &= (\det\boldsymbol{\Psi}^e)(\boldsymbol{\Psi}^e)^{*-1}\cdot\sigma^e\cdot(\boldsymbol{\Psi}^e)^{-1}\\ &= (\det\boldsymbol{\Psi}^e)(\boldsymbol{\Psi}^e)^{*-1}\cdot\tilde{\sigma}\cdot(\boldsymbol{\Psi}^e)^{-1},\end{aligned} \tag{8}$$

and the effective constitutive equations are constructed as a relation between $\overset{0}{\boldsymbol{\Sigma}}{}^e$ and $\overset{0}{\mathbf{E}}{}^e$. For example, these equations may be written in the form $\overset{0}{\boldsymbol{\Sigma}}{}^e = \mathcal{F}(\overset{0}{\mathbf{E}}{}^e)$.

There is a limitation of our method, because of the assumption that the boundary of the representative volume does not intersect the pore space. This assumption is not valid for the case when the pore space has a connected component which spans all space (for example, for open-cell foamed plastics). In our opinion, the possible approach in this case is to impose affine boundary conditions on the displacements at the boundary of the representative region and to calculate the resulting average stress through its integral over the representative volume. For gridwork materials this approach is developed by Brovko and Ilyushin [11].

Note also that our approach to the homogenization is primarily similar to the one developed by R. Hill [12], although Hill did not consider porous materials as a special case of inhomogeneous materials.

3 Analysis of Superimposed Rigid-Body Motions

Now we claim that the effective constitutive equations that are constructed using the method which is described above are not changed if a body, including a representative volume extracted in it, carries out a rigid motion after the deformation. Let the body be passed to a certain state after the rigid motion. Following Lurie [10], we shall prime the quantities relating to this state. Let $\mathbf{O}$ be the orthogonal tensor that describes this rigid motion; by definition of a rigid motion this tensor is independent on coordinates. It is known, [10], that the deformation gradient $\boldsymbol{\Psi}$ and the true stress tensor σ are transformed by the rules

$$\boldsymbol{\Psi}' = \boldsymbol{\Psi}\cdot\mathbf{O}, \quad \sigma' = \mathbf{O}^*\cdot\sigma\cdot\mathbf{O}, \tag{9}$$

when the rigid motion is superimposed on the deformation.

Using (5) and (9) and taking into account that the tensor $\mathbf{O}$ is constant and orthogonal, we have

$$\mathbf{\Psi}'^{e}=\frac{1}{V_0}\int_{V_0}\mathbf{\Psi}'dV_0=\frac{1}{V_0}\int_{V_0}\mathbf{\Psi}\cdot\mathbf{O}dV_0=\frac{1}{V_0}\left(\int_{V_0}\mathbf{\Psi}dV_0\right)\cdot\mathbf{O}$$
$$=\mathbf{\Psi}'^{e}\cdot\mathbf{O},$$
$$\sigma'^{e}=\frac{1}{V'}\int_{V'}\sigma'dV'=\frac{1}{V}\int_{V}\mathbf{O}^{*}\cdot\sigma\cdot\mathbf{O}\det\mathbf{O}dV$$
$$=\frac{1}{V}\mathbf{O}^{*}\cdot\left(\int_{V}\sigma dV\right)\cdot\mathbf{O}=\mathbf{O}^{*}\cdot\sigma^{e}\cdot\mathbf{O}.$$

Thus,

$$\mathbf{\Psi}'^{e}=\mathbf{\Psi}^{e}\cdot\mathbf{O},\qquad \sigma'^{e}=\mathbf{O}^{*}\cdot\sigma^{e}\cdot\mathbf{O}. \tag{10}$$

Taking into account Eq. (10) we obtain, from (7), (8),

$$\overset{0}{\mathbf{E}}{}'^{e}=\frac{1}{2}(\mathbf{\Psi}'^{e}\cdot\mathbf{\Psi}'^{e*}-\mathbf{I})=\frac{1}{2}(\mathbf{\Psi}^{e}\cdot\mathbf{O}\cdot\mathbf{O}^{*}\cdot\mathbf{\Psi}^{e*}-\mathbf{I})$$
$$=\frac{1}{2}(\mathbf{\Psi}^{e}\cdot\mathbf{\Psi}^{e*}-\mathbf{I})=\overset{0}{\mathbf{E}}{}^{e},$$

$$\overset{0}{\mathbf{\Sigma}}{}'^{e}=(\det\mathbf{\Psi}'^{e})(\mathbf{\Psi}'^{e})^{*-1}\cdot\sigma'^{e}\cdot(\mathbf{\Psi}'^{e})^{-1}$$
$$=(\det\mathbf{\Psi}^{e}\det\mathbf{O})(\mathbf{\Psi}^{e})^{*-1}\cdot\mathbf{O}\cdot\mathbf{O}^{*}\cdot\sigma^{e}\cdot\mathbf{O}\cdot\mathbf{O}^{-1}\cdot(\mathbf{\Psi}^{e})^{-1}$$
$$=(\det\mathbf{\Psi}^{e})(\mathbf{\Psi}^{e})^{*-1}\cdot\sigma^{e}\cdot(\mathbf{\Psi}^{e})^{-1}=\overset{0}{\mathbf{\Sigma}}{}^{e}.$$

Thus, the tensors $\overset{0}{\mathbf{E}}{}^{e}$ and $\overset{0}{\mathbf{\Sigma}}{}^{e}$ that are determined by the approach which is described above do not change when the rigid motion is superimposed on the deformation. Therefore, the relation between these tensors (that is, the effective constitutive equation) doesn't change, too.

4 Some Particular Cases

At infinitesimal strains the proposed approach to averaging coincides with the conventional approach, which is presented, for example, by Kachanov et al. [3] and Vavakin and Salganik [9]. Indeed, if we substitute (7) into (6), we have

$$\overset{0}{\mathbf{E}}{}^{e}=\frac{1}{2V_0}\oint_{\Gamma_0}(\overset{0}{\mathbf{N}}\mathbf{u}+\mathbf{u}\overset{0}{\mathbf{N}})d\Gamma_0+\frac{1}{2V_0^2}\left(\oint_{\Gamma_0}\overset{0}{\mathbf{N}}\mathbf{u}d\Gamma_0\right)$$
$$\cdot\left(\oint_{\Gamma_0}\mathbf{u}\overset{0}{\mathbf{N}}d\Gamma_0\right).$$

If strains are infinitesimal, we can write this equation up to the first order of smallness as

$$\overset{0}{\mathbf{E}}{}^{e}=\frac{1}{2V_0}\oint_{\Gamma_0}(\overset{0}{\mathbf{N}}\mathbf{u}+\mathbf{u}\overset{0}{\mathbf{N}})d\Gamma_0. \tag{11}$$

This equation is similar to the well-known relations presented in [3,9].

In our previous papers, [13,14], another definition of a comparison material was given. Let us outline the approach that was used in those papers. Let a representative volume (area), which assumes the shape of a parallelepiped (parallelogram in the two-dimensional case), be extracted in a porous body. Then a uniform material is called a comparison material if the following condition holds. If the representative volume (area) is filled by the comparison material, then the average displacements over each side of this volume (area) are equal to the ones for the given porous material at the same loads.

The definition that is given in this paper is more general than the definitions proposed in [13,14], because it doesn't impose restrictions to the shape of the representative volume. If the representative volume assumes the shape of a parallelepiped (parallelogram), then our new definition gives the same equations for $\mathbf{\Psi}^{e}$ as the definitions that are given in [13,14].

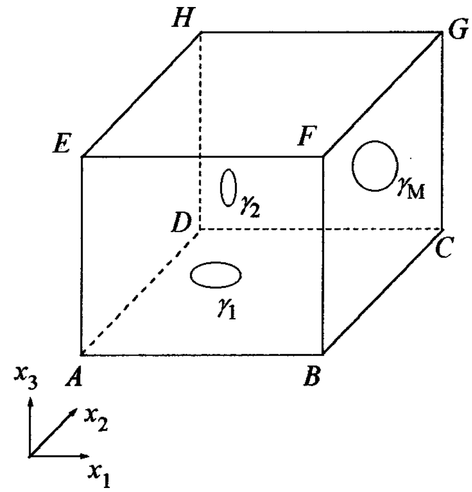

Fig. 1 Three-dimensional case: the representative volume is a rectangular prism

Consider now the equations which follow from (6) in some special cases.

If the representative volume assumes the shape of a rectangular prism such that its edges are parallel to the coordinate axes ($AB\|x_1$, $AD\|x_2$, $AE\|x_3$, Fig. 1), then the components of the deformation gradient for the comparison material may be determined as

$$\Psi^{e}_{1i}=\delta_{1i}+\frac{1}{|AB|}[\langle u_i\rangle|_{BCGF}-\langle u_i\rangle|_{ADHE}],$$
$$\Psi^{e}_{2i}=\delta_{2i}+\frac{1}{|AD|}[\langle u_i\rangle|_{DCGH}-\langle u_i\rangle|_{ABFE}], \tag{12}$$
$$\Psi^{e}_{3i}=\delta_{3i}+\frac{1}{|AE|}[\langle u_i\rangle|_{EFGH}-\langle u_i\rangle|_{ABCD}],$$
$$(i=1,2,3).$$

Here we use the notation $\langle u\rangle|_{PQRS}=1/s\int_{PQRS}udl$, where $PQRS$ is an arbitrary side of the parallelepiped, and s is the area of this side.

In (12) and further, where equations are written in suffix notation, it is assumed that the Cartesian coordinates are chosen in the basis of the state, in which the problem is solved.

In the two-dimensional case (in plane strain) a representative area is considered instead of a representative volume. Suppose that the representative area S_0 is a parallelogram of sides a and b that make angles of α and β with the x_1-axis, respectively (Fig. 2). Let A, B, C, D be the vertices of S_0, then the components of the deformation gradient of the comparison material may be found from the equations

$$\Psi_{1i}=\delta_{1i}+\frac{1}{S_0}\left(\int_{AB}u_i\sin\alpha dl+\int_{BC}u_i\sin\beta dl-\int_{CD}u_i\sin\alpha dl\right.$$
$$\left.-\int_{DA}u_i\sin\beta dl\right),$$

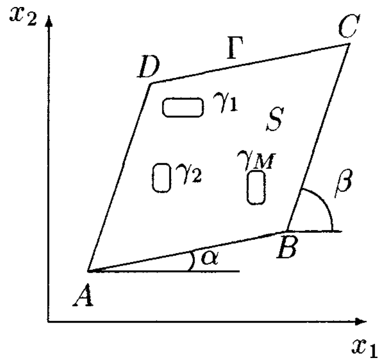

Fig. 2 Two-dimensional case: the representative area is a parallelogram

$$\Psi_{2i}=\delta_{2i}-\frac{1}{S_0}\left(\int_{AB}u_i\cos\alpha dl+\int_{BC}u_i\cos\beta dl\right.$$
$$\left.-\int_{CD}u_i\cos\alpha dl-\int_{DA}u_i\cos\beta dl\right),$$

where $S_0=ab\sin(\beta-\alpha)$.

These equations are equivalent to the correspondent equations given by Levin et al. [14]. In the particular case, when the representative area is a rectangle of sides a and b that are parallel to the axes x_1 and x_2, respectively (i.e., at $\alpha=0$, $\beta=\pi/2$), we have

$$\Psi_{1i}=\delta_{1i}+\frac{1}{ab}\left(\int_{BC}u_i dl-\int_{DA}u_i dl\right),$$
$$\Psi_{2i}=\delta_{2i}+\frac{1}{ab}\left(\int_{CD}u_i dl-\int_{AB}u_i dl\right). \tag{13}$$

Equations (13) coincide with the correspondent equations that are presented by Levin et al. [13], within a notation.

5 Approximate Method for the Construction of Effective Constitutive Equations

In general, the considered approach to the construction of effective constitutive equations is not restricted by the value of the deformation. This approach may be used whenever the boundary value problem of nonlinear elasticity with the boundary conditions (1) or (3), where $\tilde{\sigma}$ is an arbitrary constant, symmetric tensor, may be solved for a representative region with holes. However, it is not clear whether this model adequately reflects the overall mechanical behavior of a porous material when the strains are infinitely increased. In addition, as is known, [10], even in the two-dimensional case the exact solutions of nonlinear problems of elasticity at large strains are found only for some special potentials. By these reasons we consider the approximate method for the construction of the effective constitutive equations. This method is based on the solution of nonlinear problems of elasticity using the perturbation technique. Naturally, this approach may be used at a limited range of strains. Note that even when the average strain is small, the local strain in some regions could be large, depending on the microstructure. In particular, this effect takes place for a body with closely situated circular holes, especially when one hole is considerably larger than another in its size (Levin and Zingerman [15]), or for a body with narrow slots (for example, elliptical).

Let the nonlinear problem of elasticity with the boundary condition (3) at the external boundary of the representative volume be solved by the perturbation technique up to the second order. Then we can represent the components of the displacement vector $\mathbf{u}$ as

$$u_m=\overset{(0)}{u}_{mij}\tilde{\sigma}_{ij}+\overset{(1)}{u}_{mijkl}\tilde{\sigma}_{ij}\tilde{\sigma}_{kl}=\overset{(0)}{u}_{mij}\sigma^e_{ij}+\overset{(1)}{u}_{mijkl}\sigma^e_{ij}\sigma^e_{kl}. \tag{14}$$

Substituting (14) in (6), we get

$$\Psi^e_{mn}=\delta_{mn}+\overset{(0)}{S}_{mnij}\sigma^e_{ij}+\overset{(1)}{S}_{mnijkl}\sigma^e_{ij}\sigma^e_{kl}. \tag{15}$$

If we substitute (15) into the expression (7) for the Green strain tensor of the comparison material and retain in the obtained expression only linear and quadratic terms, we have

$$\overset{0}{E}{}^e_{mn}=\overset{(0)}{T}_{mnij}\sigma^e_{ij}+\overset{(1)}{T}_{mnijkl}\sigma^e_{ij}\sigma^e_{kl}, \tag{16}$$

where

$$\overset{(0)}{T}_{mnij}=\overset{(0)}{S}_{mnij}+\overset{(0)}{S}_{nmij},$$
$$\overset{(1)}{T}_{mnijkl}=\overset{(1)}{S}_{mnijkl}+\overset{(1)}{S}_{nmijkl}+\overset{(0)}{S}_{mpij}\overset{(0)}{S}_{npkl}.$$

$\overset{(0)}{T}_{mnij}$ and $\overset{(1)}{T}_{mnijkl}$ are the first-order and the second-order compliance moduli, respectively.

Solving system (16) with respect to σ^e_{ij} by the perturbation technique up to the second order, we have

$$\sigma^e_{mn}=\overset{(0)}{\tilde{C}}_{mnij}\overset{0}{E}{}^e_{ij}+\overset{(1)}{\tilde{C}}_{mnijkl}\overset{0}{E}{}^e_{ij}\overset{0}{E}{}^e_{kl}.$$

And finally, if we substitute the last expression together with expression (15) into formula (8) for the second Piola-Kirchhoff stress tensor and retain in the obtained expression only linear and quadratic terms, we can write the effective constitutive equations in the form

$$\overset{0}{\Sigma}{}^e_{mn}=\overset{(0)}{C}_{mnij}\overset{0}{E}{}^e_{ij}+\overset{(1)}{C}_{mnijkl}\overset{0}{E}{}^e_{ij}\overset{0}{E}{}^e_{kl}. \tag{17}$$

Here $\overset{(0)}{C}_{mnij}$ and $\overset{(1)}{C}_{mnijkl}$ are the first-order and the second-order elastic moduli, respectively.

Note that the described method may be used for isotropic matrix materials as well as for anisotropic ones. The comparison material is generally anisotropic.

6 Definitions in the Case When the Shapes of Pores are Given in the Final State

If pores assume a given shape in the deformed (final) state, it is appropriate to use another definition of a comparison material. In this case we average the inverse of the deformation gradient $\mathbf{\Phi}=\mathbf{\Psi}^{-1}=\mathbf{I}-\nabla\mathbf{u}$ over a representative volume in the deformed state. Let the representative volume V be extracted in the deformed porous material, and the loads be applied to the boundary Γ of this volume in accord with (1). Let the true stresses and the inverse of the deformation gradient be averaged over the volume V in the deformed state (the averaged true stresses in this case are equal to $\tilde{\sigma}$). Then the uniform material is called a comparison material if the following condition holds: If the true stresses in this material are equal to $\tilde{\sigma}$, then the inverse of the deformation gradient for the comparison material is equal to the averaged inverse of the deformation gradient for the porous material.

According to this definition, we get

$$\mathbf{\Psi}^{e-1}=\frac{1}{V}\int_V\mathbf{\Phi}dV=\frac{1}{V}\int_V(\mathbf{I}-\nabla\mathbf{u})dV=\mathbf{I}-\frac{1}{V}\oint_\Gamma\mathbf{Nu}d\Gamma.$$

7 Load-Induced Pores

Now we construct effective constitutive equations for the case when pores are originated in materials after loading. Such equations may be used to simulate the mechanical behavior of materials in which microdefects (submicrocracks) are originated at loading, [16,17]. There may be diverse approaches to this problem. In this paper we consider an accumulation of microdefects as a discrete process such that each stage of this process is associated with the application of a load. This approach may be verified experimentally by the fact that the concentration of submicrocracks in polymeric materials at first increases after the application of a load, but then reaches a steady-state value within some time of loading if the load is time-independent, and this steady-state value of concentration depends on the value of the applied load, as shown by Zhurkov and Kuksenko [16] and Zhurkov et al. [17]. Tamuzh and Kuksenko [18] note that submicrocracks may be considered as holes in a homogeneous medium. In other words, the approaches that were developed for the analysis of macroscopic holes may be extended to submicrocracks, and one can analyze the submicrocracks within the scope of continuum mechanics neglecting the structural inhomogeneity of polymeric materials.

Assuming that the accumulation of microdefects is a discrete process, we can analyze this process using the theory of superimposed finite deformations that was developed by Levin [19,20]. The basic concepts of this theory are as follows. Let us distinguish N states of a body: initial (undeformed) state; $(N-2)$ intermediate states, for which body goes step by step by successively applied external effects; final state, to which body goes after the application of all external loads to it in the predetermined order. By ‘‘application of load’’ we mean application of body forces and application or removal of load over both the pre-existing boundaries of regions and the newly formed ones.

Within the scope of this theory, the origination of holes in the body may be simulated using the scheme, which is proposed by Levin [19,20]. Assume large plane static strains and stresses are brought about by external forces in a nonlinear elastic body that was in the initial (unstressed) state. The body passes to the first intermediate state. Then a closed surface is imagined in the body, and its contents, bounded by this surface, is removed, and the effect of the removed part of the body on the remainder is replaced by forces, distributed over this closed surface (on the principle of releasing from constraints). It is clear that this transformation doesn't change the stress and strain states in the body. Then these forces, changed to the category of external forces, are reduced to zero quasistatically. It raises large (at the vicinity of the originated surface) strains and stresses that are superimposed on the large initial strains and stresses already existing in the body. The body passes to the next state. The shape of the introduced boundary surface is changed. Then this procedure is repeated for the origination of the second hole, etc.

Below, three states of a body are considered: initial, intermediate, and final. The indices 0, 1, and 2 correspond to these states, respectively.

Consider now two schemes of construction of effective constitutive equations for previously loaded porous materials.

1 A continuous (undamaged) body is loaded. Finite initial strains are brought about in it. The body passes to the intermediate state. Then pores (microdefects) are originated in the body by the scheme which is proposed by Levin [19,20]. It is assumed that the pores are uniformly distributed over the body. The origination of pores raises additional finite strains that are superimposed on the finite initial strains.

By this, the average stresses do not change. The additional external loads are not applied to the body. The effective constitutive equations are constructed as a relation between the average total deformation gradient and average stresses caused by loading.

2 A continuous body is subjected to initial loading. Then pores are originated in the body. Then additional external loads are applied to the body. Additional finite strains are brought about in the body due to the origination of pores and the additional loading. These additional strains are superimposed on the initial ones. The effective constitutive equations are constructed either as a relation between the average additional strains and the average additional stresses or as a relation between the average total deformation gradient and the average total stresses.

This scheme may be used for simulation of a partial unloading of polymeric materials in which pores are originated after loading. It is experimentally shown by Tamuzh and Kuksenko [18] that the concentration of micropores do not decrease significantly after partial unloading, that is the originated micropores do not close. This scheme may be also used for examination of cavitation phenomena (sudden opening of cavities at loading) in rubber-like materials, [21,22].

The general approach to the construction of effective constitutive equations is the same for the both cases. Consider this approach now using the notation of Levin [19,20] and Levin and Zingerman [23]. Let the initial deformation be affine. Let $\mathbf{\Psi}^e$ be the deformation gradient of the comparison material, $\mathbf{\Psi}_{0,1}$, $\mathbf{\Psi}_{1,2}$, and $\mathbf{\Psi}_{0,2}$ the initial, additional and total deformation gradients of porous material, respectively, $\mathbf{u}_2$ the additional displacement vector, $\sigma_{0,1}$ and $\sigma_{0,2}$ the initial and the total true stress tensors respectively. Let V_0 be a representative volume in the initial state, and let this volume be transformed to the volumes V_1 and V_2 after the initial and the total deformation respectively. By Γ_0, Γ_1, and Γ_2 denote the boundaries of volumes V_0, V_1, and V_2 respectively. Let $\overset{i}{\mathbf{N}}$ $(i=0,1,2)$ be the normal to Γ_i.

Let the boundary condition

$$\overset{2}{\mathbf{N}}\cdot \sigma_{0,2}|_{\Gamma_2}=\overset{2}{\mathbf{N}}\cdot \tilde{\sigma}|_{\Gamma_2} \tag{18}$$

be given at the boundary Γ_2 in the deformed state. Here $\tilde{\sigma}$ is a constant, symmetric tensor, as before.

As in the case, when deformations are not superimposed, it may be shown that if condition (18) holds and the body forces are equal to zero, then the averaged true total stresses over the volume V_2 are equal to $\tilde{\sigma}$, i.e.,

$$\tilde{\sigma}=\frac{1}{V_2}\int_{V_2}\sigma_{0,2}dV_2 .$$

Boundary condition (18) may be written in the coordinates of the intermediate state as

$$\overset{1}{\mathbf{N}}\cdot \overset{1}{\mathbf{\Sigma}}_{0,2}|_{\Gamma_1}=(\det \mathbf{\Psi}_{1,2})\overset{1}{\mathbf{N}}\cdot \mathbf{\Psi}_{1,2}^{*-1}\cdot \tilde{\sigma}\cdot \mathbf{\Psi}_{1,2}^{-1}|_{\Gamma_1}. \tag{19}$$

Here $\overset{1}{\mathbf{\Sigma}}_{0,2}$ is the total (for the final state) stress tensor referring to the base of the intermediate state, [19].

Now we shall give the definition of a comparison material for the case of superimposed deformations. Let the loads be applied to the boundary Γ_1 in the intermediate state in accord with (19). Let the true stresses in the porous material be averaged over the volume V_2 in the final state (the averaged true stresses in this case are equal to $\tilde{\sigma}$, as noted above), and the additional deformation gradient be averaged over the volume V_1 in the intermediate state. Then a uniform material is called a comparison material if the following condition holds: If the true stresses in this material are equal to $\tilde{\sigma}$, then the deformation gradient of the comparison material is equal to the initial deformation gradient multiplied on the averaged additional deformation gradient of the porous material.

In accord with this definition we can write

$$\sigma^e=\tilde{\sigma}=\frac{1}{V_2}\int_{V_2}\sigma_{0,2}dV_2 , \qquad \mathbf{\Psi}^e=\mathbf{\Psi}_{0,1}\cdot \frac{1}{V_1}\int_{V_1}\mathbf{\Psi}_{1,2}dV_1 . \tag{20}$$

Taking into account that $\mathbf{\Psi}_{1,2}=\mathbf{I}+\nabla^{1}\mathbf{u}_2$ and using the divergence theorem, we can write the second Eq. (20) in the form

$$\mathbf{\Psi}^e=\mathbf{\Psi}_{0,1}\cdot\frac{1}{V_1}\int_{V_1}\left(\mathbf{I}+\nabla\overset{1}{\mathbf{u}}_2\right)dV_1=\mathbf{\Psi}_{0,1}\cdot\left(\mathbf{I}+\frac{1}{V_1}\oint_{\Gamma_1}\overset{1}{\mathbf{N}}\mathbf{u}_2 d\Gamma_1\right). \tag{21}$$

This equation may be written as

$$\mathbf{\Psi}^e=\mathbf{\Psi}_{0,1}\cdot\mathbf{\Psi}^e_{1,2}, \tag{22}$$

where

$$\mathbf{\Psi}^e_{1,2}=\mathbf{I}+\frac{1}{V_1}\oint_{\Gamma_1}\overset{1}{\mathbf{N}}\mathbf{u}_2 d\Gamma_1. \tag{23}$$

Thus, we formally consider the deformation of a comparison material as a sequence of two stages of deformation assuming that the first stage of deformation coincides with the initial deformation of the original material.

Now, using the last definition, we shall consider an approach to the construction of effective constitutive equations for materials in which pores are originated after loading. This approach basically coincides with the approach that is stated above for materials in which pores exist initially. Let the shape of pores be prescribed in the intermediate state. At first, the gradient of initial deformations $\mathbf{\Psi}_{0,1}$ is determined from the given initial stresses $\sigma_{0,1}$. Then a representative volume V_1 is extracted in a body in the intermediate state. The solution of the nonlinear problem of elasticity is obtained subject to the boundary condition defined by (19) at the external boundary Γ_1 of this volume, and the boundary conditions at the boundaries of pores. In particular, the additional displacements $\mathbf{u}_2$ are found. Then the deformation gradient $\mathbf{\Psi}^e$ of the comparison material is received from (21). The Green strain tensor $\overset{0}{\mathbf{E}}{}^e$ and the second Piola-Kirchhoff stress tensor $\overset{0}{\mathbf{\Sigma}}{}^e$ of the comparison material are obtained from the equations

$$\overset{0}{\mathbf{E}}{}^e=\frac{1}{2}(\mathbf{\Psi}^e\cdot\mathbf{\Psi}^{e*}-\mathbf{I}),\quad \overset{0}{\mathbf{\Sigma}}{}^e=(\det\mathbf{\Psi}^e)(\mathbf{\Psi}^e)^{*-1}\cdot\sigma^e\cdot(\mathbf{\Psi}^e)^{-1}. \tag{24}$$

Then the effective constitutive equations are constructed as a relation between the tensors $\overset{0}{\mathbf{\Sigma}}{}^e$ and $\overset{0}{\mathbf{E}}{}^e$.

If the nonlinear problem of elasticity is solved approximately, then the effective constitutive equations are constructed approximately, too. Consider this approximate method in detail for the first scheme (when additional external loads are not applied to a body after the origination of pores). In this case we can write

$$\sigma_{0,1}=\sigma^e=\tilde{\sigma}.$$

Let the nonlinear problem of elasticity be solved for the representative volume with pores using the perturbation technique up to the second order. Then the solution can be represented in the form

$$u_{2_m}=\overset{(0)}{u}_{mij}\sigma_{ij}+\overset{(1)}{u}_{mijkl}\sigma^e_{ij}\sigma^e_{kl}. \tag{25}$$

Substituting the last expression into (23), we have the expansion for $\mathbf{\Psi}^e_{1,2}$

$$\Psi^e_{1,2_{mn}}=\delta_{mn}+\overset{(0)}{Q}_{mnij}\sigma^e_{ij}+\overset{(1)}{Q}_{mnijkl}\sigma^e_{ij}\sigma^e_{kl}. \tag{26}$$

The similar expansion may be received for $\mathbf{\Psi}_{0,1}$:

$$\Psi^e_{0,1_{mn}}=\delta_{mn}+\overset{(0)}{P}_{mnij}\sigma^e_{ij}+\overset{(1)}{P}_{mnijkl}\sigma_{ij}\sigma^e_{kl}. \tag{27}$$

If we substitute (26) and (27) into (22) and retain in the obtained expression only linear and quadratic terms, we have

$$\Psi^e_{mn}=\delta_{mn}+\overset{(0)}{S}_{mnij}\sigma^e_{ij}+\overset{(1)}{S}_{mnijkl}\sigma^e_{ij}\sigma^e_{kl}, \tag{28}$$

where

$$\overset{(0)}{S}_{mnij}=\overset{(0)}{P}_{mnij}+\overset{(0)}{Q}_{mnij},$$

$$\overset{(1)}{S}_{mnijkl}=\overset{(1)}{P}_{mnijkl}+\overset{(1)}{Q}_{mnijkl}+\overset{(0)}{P}_{mpij}\overset{(0)}{Q}_{pnkl}.$$

Note that Eq. (28) has the same structure as Eq. (15).

Further computations are similar to the ones that are presented above for materials in which pores exist initially, beginning with Eq. (16).

8 Numerical Results

Consider now some numerical results. The effective moduli are computed for the two-dimensional case (for plane strain) when the mechanical properties of the matrix are described by Murnaghan's potential, [10,24],

$$\overset{0}{\mathbf{\Sigma}}=\lambda(\overset{0}{\mathbf{E}}:\mathbf{I})\mathbf{I}+2G\overset{0}{\mathbf{E}}+3C_3(\overset{0}{\mathbf{E}}:\mathbf{I})^2\mathbf{I}$$

$$+C_4(\overset{0}{\mathbf{E}}{}^2:\mathbf{I})\mathbf{I}+2C_4(\overset{0}{\mathbf{E}}:\mathbf{I})\overset{0}{\mathbf{E}}+3C_5\overset{0}{\mathbf{E}}{}^2. \tag{29}$$

The nonlinear problem of elasticity is solved by the perturbation technique, [14,23], up to the second order. By this, the assumption of Mori-Tanaka's scheme, [25], is used: Instead of specification of loads at the boundary of the representative area, far-field true stresses σ^∞_{ij} are given. These far-field stresses are assumed to be equal to the average stresses in the matrix and are determined as

$$\sigma^\infty_{ij}=(1-p)^{-1}\sigma^e_{ij},$$

where σ^e_{ij} are the average stresses in the porous medium, and p is the porosity of the material in the final state. Note that the last equation takes place whenever the boundaries of pores are traction-free.

It is known that Mori-Tanaka's scheme may be used at relative small porosities. Levin et al. [14] attempted to analyze the applicability of this scheme considering representative regions with some interacting pores. The interactions between pores within the representative region was taken into account during the solution of the problem of nonlinear elasticity. The computations was performed for the isotropic elastic material with uniformly distributed equal circular holes and showed that the correction for the effects of interaction between pores within the representative area does not exceed 3% for the first-order effective moduli and 20% for the second-order effective moduli for $p\leqslant 0.4$. Mauge and Kachanov [4] discovered the same effect analyzing the effective properties of linear-elastic solids with arbitrarily located microcracks.

In accord with Mori-Tanaka's scheme, the boundary condition (1) or its equivalent (3) may be replaced by the condition

$$\sigma_{ij}|_\infty=\sigma^\infty_{ij}.$$

The computations are performed for the case when pores are equal in size and assume a circular shape either in the undeformed state or in the intermediate state (after a preliminary loading). The ensemble averaging technique which is developed by Levin et al. [14] is used in order to approximately simulate the uniform distribution of pores. This averaging permits one to represent the effective constitutive equations in the form

$$\overset{0}{\mathbf{\Sigma}}{}^e=\lambda^e(\overset{0}{\mathbf{E}}{}^e:\mathbf{I})\mathbf{I}+2G^e\overset{0}{\mathbf{E}}{}^e+3C^e_3(\overset{0}{\mathbf{E}}{}^e:\mathbf{I})^2\mathbf{I}+C^e_4[(\overset{0}{\mathbf{E}}{}^e)^2:\mathbf{I}]\mathbf{I}$$

$$+2C^e_6(\overset{0}{\mathbf{E}}{}^e:\mathbf{I})\overset{0}{\mathbf{E}}{}^e+3C^e_5(\overset{0}{\mathbf{E}}{}^e)^2, \tag{30}$$

where λ^e and G^e are the first-order effective elastic moduli, and $C^e_i(i=3,\ldots,6)$ the second-order effective elastic moduli.

The isotropy of the comparison material takes place due to a special ensemble averaging procedure, which is developed by Levin et al. [14]. This procedure includes the averaging of the

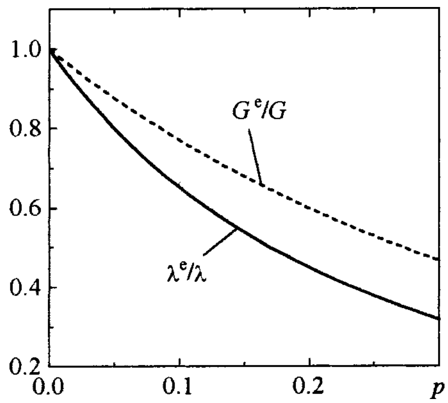

Fig. 3 Effective linear elastic moduli λ^e, G^e referred to the correspondent matrix moduli versus porosity. $\lambda/G=2$.

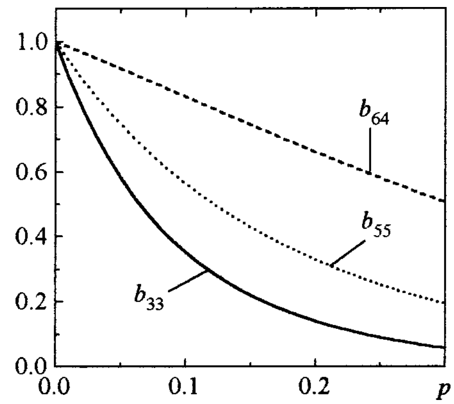

Fig. 5 Coefficients b_{33}, b_{55}, and b_{64} versus porosity for $\lambda/G=2$

effective moduli $\overset{(0)}{C}_{mnij}$, $\overset{(1)}{C}_{mnijkl}$ in (17) by all possible orientations of coordinate axes. If we do not do this additional averaging, the comparison material will be generally anisotropic.

It is noted by Levin et al. [13] that one of the moduli C_3^e, C_4^e, C_5^e, C_6^e may be given arbitrarily in the case of plane strain. In the present paper the computations are performed under the assumption $C_4^e=C_4(1-p)^2$.

Because the solution of the nonlinear problem of elasticity, obtained by the perturbation technique up to the second order, depends linearly on the material constants C_3, C_4, and C_5, the effective moduli C_i^e, computed by the scheme considered, also depend linearly on these constants:

$$C_i^e=a_i+\sum_{j=3}^{5} b_{ij}C_j \quad (i=3,5,6). \tag{31}$$

Note that if the nonlinear problem of elasticity will be solved with regard for higher-order effects, the dependence between the effective moduli C_i^e and the matrix moduli C_i will not be linear.

The computations are performed as for the case when pores exist in an undeformed (unloaded) material as for the case when pores are originated in a previously loaded material. In the last case, it is assumed that the material isn't loaded additionally after the origination of pores, i.e., the first scheme of construction of effective constitutive equations for previously loaded porous materials is used. The computations show that the moduli λ^e, G^e, a_3, and all the coefficients b_{ij} are the same for these both cases, and the coefficients a_5 and a_6 are different.

The plots of the effective moduli λ^e, G^e, and the coefficients a_i and b_{ij} in (31) versus porosity p are presented for matrix materials with $\lambda/G=2$. The ratios λ^e/λ, G^e/G are plotted in Fig. 3. The coefficients a_i are plotted in Fig. 4 (in this figure a_5^* and a_6^* denote the coefficients a_5 and a_6, respectively, for the case when

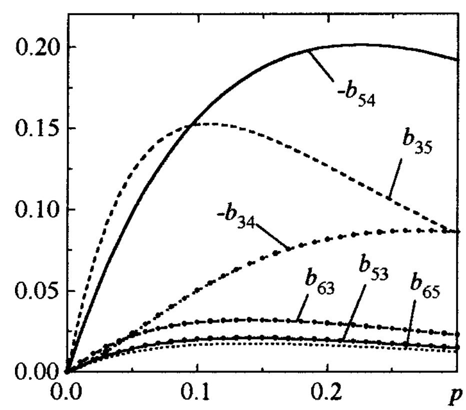

Fig. 6 Coefficients b_{34}, b_{35}, b_{53}, b_{54}, b_{63}, and b_{65} versus porosity for $\lambda/G=2$

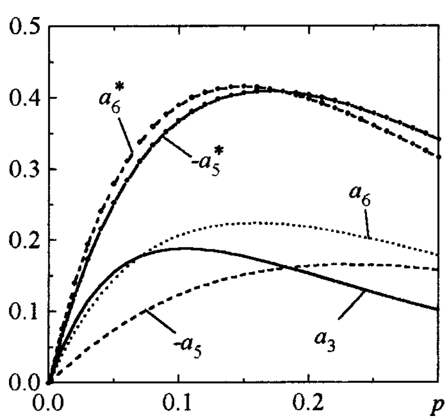

Fig. 4 Coefficients a_i versus porosity for $\lambda/G=2$. The plots for the case when pores are originated in previously loaded materials are marked by circles.

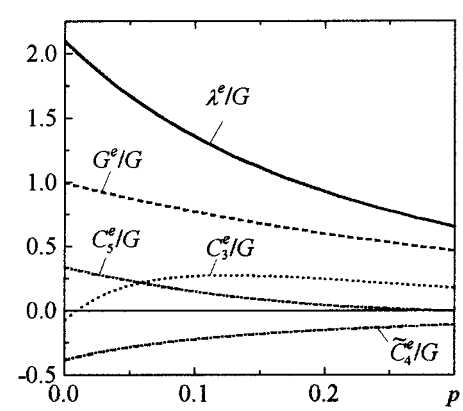

Fig. 7 Effective elastic moduli versus porosity for the porous organic glass

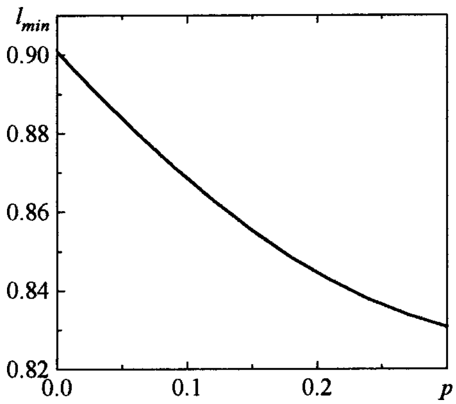

Fig. 8 Relation between porosity and the critical stretch ratio $l_{\min}$ at which the loss of ellipticity takes place in compression

pores are originated in previously loaded materials, and the plots for this case are marked by circles). The coefficients b_{ij} are plotted in Figs. 5 and 6.

Consider now some results for a specific material. Figure 7 shows the effective moduli as a function of porosity for the organic glass. The material constants are determined by Guz et al. [26] and presented in [10]. With the preceding notation, $\lambda/G=2.1$, $C_3/G=-0.07$, $C_4/G=-0.38$, $C_5/G=0.34$, where $G=1.86\times 10^{10}$ Pa. In Figure 7, the modulus $\tilde{C}_4^e$ is the result of an additional averaging: $\tilde{C}_4^e=(C_4^e+C_6^e)/2$. This additional averaging is performed in order to obtain the effective constitutive equations in the same form as the Eqs. (29) for Murnaghan's potential:

$$\overset{0}{\mathbf{\Sigma}}{}^e=\lambda^e(\overset{0}{\mathbf{E}}{}^e:\mathbf{I})\mathbf{I}+2G^e\overset{0}{\mathbf{E}}{}^e+3C_3^e(\overset{0}{\mathbf{E}}{}^e:\mathbf{I})^2\mathbf{I}+\tilde{C}_4^e[(\overset{0}{\mathbf{E}}{}^e)^2:\mathbf{I}]\mathbf{I}$$

$$+2\tilde{C}_4^e(\overset{0}{\mathbf{E}}{}^e:\mathbf{I})\overset{0}{\mathbf{E}}{}^e+3C_5^e(\overset{0}{\mathbf{E}}{}^e)^2. \quad (32)$$

Finally, let us analyze the ellipticity of the equilibrium equations for the porous organic glass using the results presented in Fig. 7. The verification of Hadamard's condition is performed for the case of volumetric deformation. By this, we use the approach that is developed by Zubov and Rudev [27]. The computations show that the loss of ellipticity takes place in compression at some value $l_{\min}$ of a stretch ratio, and this value depends on porosity. This dependence is shown in Fig. 8. In addition, the loss of ellipticity takes place for the undamaged material in tension at the value $l_{\max}\approx 2.04$ and for the porous material at very small porosities. When $p>0.003$, Hadamard's condition is satisfied in tension for the unrestricted stretch ratio.

Acknowledgments

This research was supported by the Russian Foundation of Basic Research (Project No. 98-01-00458), the Russian Ministry of Education (grant from the Grants Center for Natural Sciences), and the "Russian Universities" program (Project No. 990858).

References

[1] Hashin, Z., and Rozen, B. W., 1964, "The Elastic Moduli of Fiber Reinforced Materials," ASME J. Appl. Mech., **31**, pp. 223–232.
[2] Christensen, R. M., 1979, *Mechanics of Composite Materials*, John Wiley and Sons, New York.
[3] Kachanov, M., Tsukrov, I., and Shafiro, B., 1994, "Effective Moduli of a Solid With Holes and Cavities of Various Shapes," Appl. Mech. Rev., **47**, pp. S151–S174.
[4] Mauge, C., and Kachanov, M., 1994, "Effective Elastic Properties of an Anisotropic Material With Arbitrary Oriented Interacting Cracks," J. Mech. Phys. Solids, **42**, pp. 561–584.
[5] Zhikov, V. V., Kozlov, S. M., and Olejnik, O. A., 1994, *Homogenization of Differential Operators and Integral Functionals*, Springer-Verlag, Berlin.
[6] Braides, A., 1985, "Homogenization of some almost periodic functional," Rendiconti. Accademia Nazionale delle Scienze, **XL**(103), pp. 313–322.
[7] Müller, S., 1987, "Homogenization of Nonconvex Integral Functionals and Cellular Elastic Material," Arch. Ration. Mech. Anal., **99**, pp. 189–212.
[8] Braides, A., Defranceschi, A., and Vitali, E., 1996, "Homogenization of Free Discontinuity Problems," Arch. Ration. Mech. Anal., **135**(4), pp. 297–356.
[9] Vavakin, A. S., and Salganik, R. L., 1975, "Effective Characteristics of Nonhomogeneous Media With Isolated Inhomogeneities," Izvestia AN SSSR, Mekhanika Tverdogo Tela, (**3**), pp. 65–75 (in Russian).
[10] Lurie, A. I., 1990, *Nonlinear Theory of Elasticity*, North-Holland, Amsterdam.
[11] Brovko, G. L., and Ilyushin, A. A., 1993, "On a Plane Model of Perforated Plates," Moscow Univ. Mech. Bull., (**2**), pp. 83–91.
[12] Hill, R., 1972, "On Constitutive Macrovariables for Heterogeneous Solids at Finite Strain," Proc. R. Soc. London, Ser. A, **326**(1565), pp. 131–147.
[13] Levin, V. A., Lokhin, V. V., and Zingerman, K. M., 1997, "A Method of Estimation of Effective Characteristics of Porous Bodies Under Finite Deformations," Mekhanika Tverdogo Tela, (**4**), pp. 45–50 (in Russian).
[14] Levin, V. A., Lokhin, V. V., and Zingerman, K. M., 2000, "Effective Elastic Properties of Porous Materials With Randomly Dispersed Pores: Finite Deformation," ASME J. Appl. Mech., **67**, pp. 667–670.
[15] Levin, V. A., and Zingerman, K. M., "The Influence of Small Defects on the Stress Concentration Near a Hole," Phys. Dokl., **47**(10), pp. 738–741.
[16] Zhurkov, S. N., and Kuksenko, V. S., 1975, "The Micromechanics of Polymer Fracture," Int. J. Fract., **11**, pp. 629–639.
[17] Zhurkov, S. N., Kuksenko, V. S., and Slutsker, A. I., 1969, "Submicrocrack Formation Under Stress," *Proc. Second International Conference on Fracture*, Chapman and Hall, London, pp. 531–549.
[18] Tamuzh, V. P., and Kuksenko, V. S., 1978, *Micromechanics of Fracture of Polymeric Materials*, Zinatne, Riga (in Russian).
[19] Levin, V. A., 1998, "Theory of Repeated Superposition of Large Deformations. Elastic and Viscoelastic Bodies," Int. J. Solids Struct., **35**, pp. 2585–2600.
[20] Levin, V. A., 1999, *Repeated Superposition of Large Deformations in Elastic and Viscoelastic Solids*, Nauka (Science), Moscow (in Russian).
[21] Gent, A. N., 1990, "Cavitation in Rubber: A Cautionary Tale," Rubber Chem. Technol., **63**, pp. G49–G53.
[22] Horgan, C. O., and Poligone, D. A., 1995, "Cavitation in Nonlinearly Elastic Solids: A Review" Appl. Mech. Rev., **48**, pp. 471–485.
[23] Levin, V. A., and Zingerman, K. M., 1998, "Interaction and Microfracturing Pattern for Succesive Origination (Introduction) of Pores in Elastic Bodies: Finite Deformation," ASME J. Appl. Mech., **65**, pp. 431–435.
[24] Murnaghan, F. D., 1951, *Finite Deformation of an Elastic Solid*, John Wiley and Sons, New York.
[25] Mori, T., and Tanaka, K., 1973, "Average Stress in Matrix and Average Elastic Energy of Materials With Misfitting Inclusions," Acta Metall., **21**, pp. 571–574.
[26] Guz, A. N., Makhort, F. G., Gushcha, O. I., and Lebedev, V. K., 1970, "On the Theory of Wave Distribution in Elastic Isotropic Medium Subjected to Initial Strains," Prikl. Mekh., **6**(12), pp. 42–49.
[27] Zubov, L. M., and Rudev, A. N., 1992, "The Effective Method for the Verification of Hadamard's Condition in a Nonlinear Elastic Compressible Medium," Prikl. Mat. Mekh., **56**(2), pp. 296–305.

V. Mantič
e-mail: mantic@esi.us.es

F. J. Calzado

F. París

Group Elasticity and Strength of Materials,
School of Engineering,
University of Seville,
Camino de los Descubrimientos s/n,
Seville, E-41092 Spain

Novel Boundary Integral Equations for Two-Dimensional Isotropic Elasticity: An Application to Evaluation of the In-Boundary Stress

A new nonsingular system of boundary integral equations (BIEs) of the second kind for two-dimensional isotropic elasticity is deduced following a recently introduced procedure by Wu (J. Appl. Mech., **67***, pp. 618–621, 2000) originally applied for anisotropic elasticity. The physical interpretation of the new integral kernels appearing in these BIEs is studied. An advantageous application of one of these BIEs as a boundary integral representation (BIR) of tangential derivative of boundary displacements on smooth parts of the boundary, and subsequently as a BIR of the in-boundary stress, is presented and analyzed in numerical examples. An equivalent BIR obtained by an integration by parts of the integral including tangential derivative of displacements in the former BIR is presented and analyzed as well. The resulting integral is only apparently hypersingular, being in fact a regular integral on smooth parts of the boundary.*
[DOI: 10.1115/1.1630813]

1 Introduction

The strongly singular character of the integral involving displacements, u_i, in the fundamental boundary integral equation (BIE) of linear elasticity, i.e., Somigliana displacement identity, is well known, Rizzo [1]. This integral, evaluated in a Cauchy principal value sense, makes analysis and numerical solution of this BIE more difficult than, for example, analysis and numerical solution of an analogous BIE in the potential theory, París and Cañas [2]. This strongly singular integral may be regularized by the subtraction of rigid-body displacements (a usual approach in the boundary element method (BEM)) or by integration by parts, Ghosh et al. [3].

A very novel approach to obtain a BIE system of the second kind with nonsingular integrals involving unknown elastic variables defined on the boundary has been recently introduced by Wu [4] for the two-dimensional case. Wu's BIE system, in its original form, involves a nonsingular integral with tractions, t_i, and a strongly singular integral with tangential derivative of displacements, $\partial_s u_i$, in the first BIE and a nonsingular integral with $\partial_s u_i$ and a strongly singular integral with t_i in the second BIE. Thus, considering the first BIE on the boundary part where displacements are prescribed and the second BIE on the boundary part where tractions are prescribed, the final form of the nonsingular BIE system of the second kind is obtained. This system can be applied to solve boundary value problems (BVPs) of linear elasticity.

The derivation of the nonsingular BIE system of the second kind by Wu [4] is based on some basic results of the Stroh formalism of two-dimensional anisotropic elasticity (Ting [5]), in particular on Stroh orthogonality relations for complex matrices of eigenvectors, **A** and **B**, of the fundamental elasticity matrix **N**, and on relations of these matrices with the Barnett-Lothe tensors, **H**, **L**, and **S**. Taking into account the fact that these relations hold in the basic form used by Wu [4] only for the so-called mathematically nondegenerate anisotropic materials (with simple or semisimple matrix **N**, Ting [5]), explicit expressions of the integral kernels presented by Wu [4] hold only for these nondegenerate materials. Consequently, results by Wu [4] cover the case of mathematically degenerate materials only as a limit case (considering a variation of elastic stiffnesses) and not in an explicit way.

The first objective of the present study is to complete Wu's [4] work by deducing explicit expressions of the integral kernels which are involved in the nonsingular BIE system of the second kind for isotropic materials. Note that isotropic materials represent the most important case of the so-called mathematically degenerate materials in the framework of the Stroh formalism. Explicit expressions of these integral kernels will be presented in both complex and real variable formulations.

The second objective of the present work is to study an application of the advantageous nonsingular character of Wu's [4] BIE system, which was not discussed in his original work. This application is an accurate evaluation of the in-boundary stress σ_{ss} in a post-processing procedure applied after a numerical solution of a BIE formulation which directly involves as variables boundary displacements u_i and tractions t_i, but not σ_{ss}. An accurate evaluation of the complete stress tensor at the boundary is of crucial importance for engineering decisions in view of the fact that stress critical locations in elastic BVPs typically appear at or near the boundary, where maximum values of different failure criteria are usually achieved. The present study is concerned with boundary points situated at locally smooth boundary parts (i.e., excluding boundary corners) and where the stress tensor is continuous.

The standard procedure to evaluate σ_{ss} in boundary element method (BEM) codes, proposed in the very early stages of BEM by Rizzo and Shippy [6] and Cruse and Van Buren [7] and used to date, starts with the evaluation of the tangential derivative of tangential displacement, $\partial_s u_s$, by differentiation of a boundary element approximation of u_s, giving the in-boundary strain tensor component, ε_{ss}. Then, σ_{ss} is computed from ε_{ss} and from the boundary normal stress component, $t_n = \sigma_{nn}$, applying Hooke's

Contributed by the Applied Mechanics Division of THE AMERICAN SOCIETY OF MECHANICAL ENGINEERS for publication in the ASME JOURNAL OF APPLIED MECHANICS. Manuscript received by the ASME Applied Mechanics Division, September 18, 2002; final revision, July 28, 2003. Associate Editor: R. C. Benson. Discussion on the paper should be addressed to the Editor, Prof. Robert M. McMeeking, Department of Mechanical and Environmental Engineering, University of California–Santa Barbara, Santa Barbara, CA 93106-5070, and will be accepted until four months after final publication of the paper itself in the ASME JOURNAL OF APPLIED MECHANICS.

constitutive law. A possible loss of accuracy due to the numerical differentiation applied and the discontinuities of the in-boundary stress evaluated in this way at boundary element junctions are the main disadvantages of this simple procedure. Several averaging or smoothing techniques have been proposed recently in order to avoid the above-mentioned discontinuities and also to obtain results of a higher accuracy, e.g., Zhao [8] and Mantič et al. [9], respectively, for quadratic and linear boundary elements.

Starting from pioneering work of Cruse and Van Buren [7] a great deal of research has been devoted to boundary integral representations (BIRs), and in particular to the hypersingular BIRs (Guiggiani et al. [10]), as another way to obtain the in-boundary stress with a high accuracy. Following the study by Graciani et al. [11], there are situations (e.g., straight boundaries with some particular boundary conditions) where the hypersingular BIRs can provide highly accurate results because in these situations they are only apparently hypersingular, and are actually regular BIRs. Nevertheless, in general, a really hypersingular character of the corresponding integral kernel implies too restrictive continuity requirements on displacement approximations (Krishnasamy et al. [12]), which are violated at element junctions in conventional BEM based on Lagrangian shape functions. As a consequence, the convergence of results by the hypersingular BIRs can be slower than the convergence of displacements and tractions evaluated directly in BEM analysis, see Graciani et al. [11] for examples of such a slow convergence at element junctions and element centers in potential theory, and Avila et al. [13] for values at element centers in elasticity.

It can be expected that a BIR whose integral kernels do not imply too restrictive continuity requirements, like the hypersingular BIRs traditionally used, could provide results of a high accuracy. In particular, considering the continuity of usual approximations of u_i and discontinuity of $\partial_s u_i$ in BEM, it is required that the kernel multiplying u_i is strongly (or less) singular, or equivalently the kernel multiplying $\partial_s u_i$ is weakly singular (or regular). Obviously the best results are expected if these kernels are either bounded, continuous or even smooth at smooth boundary parts. Thus, new BIRs with special Green's functions are required. Niu and Shepard [14] derived such a BIR of σ_{ss} using the Green's function defined by an application of a force dipole at the traction-free boundary of a semiplane. Taking the semiplane boundary tangent to the actual solid boundary at the point of σ_{ss} evaluation, the integral kernel representing tractions vanishes along the tangent line to the actual boundary. For an evaluation point placed at a smooth curved boundary (with nonzero curvature), this traction kernel is in fact strongly singular.

In the present work two BIRs of $\partial_s u_i$ are analyzed. The first one is defined by the second BIE from the BIE system introduced by Wu [4], with integral densities $\partial_s u_i$ and t_i. The second one, with integral densities u_i and t_i, is obtained from the first one by integration by parts in the integral involving $\partial_s u_i$. In both BIRs studied the integral kernels multiplying $\partial_s u_i$ or u_i vanish along the line tangent to the boundary at the evaluation point, and are bounded and smooth along smooth boundary parts. The in-boundary stress σ_{ss} is obtained using $\partial_s u_s$, evaluated by means of these BIRs, and t_n. The numerical examples studied show a high accuracy of the in-boundary stress obtained in this way with a quadratic $O(h^2)$ pointwise convergence for linear boundary elements.

2 A Nonsingular Boundary Integral Equation (BIE) System for Isotropic Elasticity

2.1 Integral Kernels. Consider an isotropic infinite body subjected to a plane-strain state caused by a line force $\mathbf{F}=(F_1,F_2)$ and a straight dislocation of Burgers vector $\mathbf{b}=(b_1,b_2)$ acting along the line parallel to the x_3-axis and intersecting the plane $x_3=0$ at the source point $\mathbf{y}=(y_1,y_2)$. Displacement and stress function vectors originated by this force and dislocation at the field point $\mathbf{x}=(x_1,x_2)$ were given by Wu et al. [15][1] as

$$\mathbf{u}(\mathbf{x})=\mathbf{U}(\mathbf{x},\mathbf{y})\mathbf{F}+\mathbf{W}(\mathbf{x},\mathbf{y})\mathbf{b},$$
$$\boldsymbol{\varphi}(\mathbf{x})=\mathbf{W}^T(\mathbf{x},\mathbf{y})\mathbf{F}+\mathbf{V}(\mathbf{x},\mathbf{y})\mathbf{b}, \tag{1}$$

with $\mathbf{U}$, $\mathbf{V}$, and $\mathbf{W}$ being the imaginary parts of the following complex matrix functions representing fundamental singular elastic solutions:

$$\tilde{\mathbf{U}}(\mathbf{x},\mathbf{y})=\mathbf{U}^*+i\mathbf{U}=-\frac{1}{2\pi G(\kappa+1)}\left[i\kappa\log z\mathbf{I}+i\frac{z-\bar{z}}{2z}\begin{pmatrix}1 & i\\ i & -1\end{pmatrix}\right],$$
$$\tilde{\mathbf{V}}(\mathbf{x},\mathbf{y})=\mathbf{V}^*+i\mathbf{V}=\frac{2G}{\pi(\kappa+1)}\left[i\log z\mathbf{I}+i\frac{z-\bar{z}}{2z}\begin{pmatrix}1 & i\\ i & -1\end{pmatrix}\right],$$
$$\tilde{\mathbf{W}}(\mathbf{x},\mathbf{y})=\mathbf{W}^*+i\mathbf{W}=\frac{1}{2\pi(\kappa+1)}\left[\log z\begin{pmatrix}(\kappa+1) & i(\kappa-1)\\ -i(\kappa-1) & (\kappa+1)\end{pmatrix}+\frac{z-\bar{z}}{z}\begin{pmatrix}1 & i\\ i & -1\end{pmatrix}\right], \tag{2}$$

where $z=(x_1-y_1)+i(x_2-y_2)$, i is the imaginary unit, G is the shear modulus, $\kappa=3-4\nu$ is Kolosoff constant with ν as Poisson ratio, and $\mathbf{I}$ is the identity matrix. Note that $\mathbf{U}^*$, $\mathbf{V}^*$ are bounded functions, and $\mathbf{W}^*$, $\mathbf{U}$, $\mathbf{V}$, and $\mathbf{W}$ are weakly singular when $\mathbf{y}$ approaches $\mathbf{x}$. Observe also that $\tilde{\mathbf{U}}$ and $\tilde{\mathbf{V}}$ are symmetric matrices, their real and imaginary parts thus being symmetric as well. General complex variable expressions of $\tilde{\mathbf{U}}$, $\tilde{\mathbf{V}}$, and $\tilde{\mathbf{W}}$ for degenerate anisotropic materials can be found in Ting [16].

The real and imaginary parts of $\tilde{\mathbf{U}}$, $\tilde{\mathbf{V}}$, and $\tilde{\mathbf{W}}$ can be written in real variable formulation using index notation in the following way:

$$\tilde{U}_{ij}(\mathbf{x},\mathbf{y})=U^*_{ij}(\mathbf{x},\mathbf{y})+iU_{ij}(\mathbf{x},\mathbf{y})=\frac{1}{2\pi G(\kappa+1)}[(\kappa\theta\delta_{ij}+\varepsilon_{ik}r_{,k}r_{,j})+i(-\kappa\log r\,\delta_{ij}+r_{,i}r_{,j})],$$
$$\tilde{V}_{ij}(\mathbf{x},\mathbf{y})=V^*_{ij}(\mathbf{x},\mathbf{y})+iV_{ij}(\mathbf{x},\mathbf{y})=\frac{2G}{\pi(\kappa+1)}[(-\theta\delta_{ij}-\varepsilon_{ik}r_{,k}r_{,j})+i(\log r\,\delta_{ij}-r_{,i}r_{,j})],$$
$$\tilde{W}_{ij}(\mathbf{x},\mathbf{y})=W^*_{ij}(\mathbf{x},\mathbf{y})+iW_{ij}(\mathbf{x},\mathbf{y})=\frac{1}{2\pi(\kappa+1)}\times\begin{bmatrix}((\kappa+1)\log r\,\delta_{ij}-(\kappa-1)\,\theta\varepsilon_{ij}-2r_{,i}r_{,j})+\\ i((\kappa+1)\,\theta\delta_{ij}+(\kappa-1)\log r\,\varepsilon_{ij}+2\varepsilon_{ik}r_{,k}r_{,j})\end{bmatrix}, \tag{3}$$

where $\mathbf{r}=(r_1,r_2)=(x_1-y_1,x_2-y_2)$, $r=|\mathbf{r}|$, $r_{,i}=r_i/r$, $\theta=\arg z$ is the angle of the radius vector $\mathbf{r}$ with the x_1-axis, δ_{ij} is the Kronecker delta symbol, and ε_{ij} is the permutation symbol $(\varepsilon_{12}=-\varepsilon_{21}=1, \varepsilon_{11}=\varepsilon_{22}=0)$. Note that expressions of $\tilde{\mathbf{U}}$, $\tilde{\mathbf{V}}$, and $\tilde{\mathbf{W}}$ in (2) and (3) differ by some physically non-significant constant terms, corresponding, for example, in the case of displacements to rigid-body movements. It can also be verified that the real variable expression of W_{ij} in Eq. (3) coincides, except for a physically nonsignificant constant term, with the expression of W_{ij} in Ghosh et al. [3], as could be expected.

A relation between singular elastic solutions given by the real and imaginary parts of $\tilde{\mathbf{U}}$, $\tilde{\mathbf{V}}$, and $\tilde{\mathbf{W}}$, and in particular a physical interpretation of their real parts, can be easily identified for aniso-

[1] There is a misprint in Eq. (17) by Wu et al. [15]: the correct expression of $\mathbf{V}$ does not include the first minus sign on the right-hand side therein.

tropic (nondegenerate) materials using a basic relation of Stroh formalism between the Barnett-Lothe tensors, **H**, **L**, and **S**, and the matrices of the eigenvectors **A** and **B**, [4,5]. This relation implies that

$$\begin{bmatrix} \mathbf{U}^*(\mathbf{x},\mathbf{y}) & \mathbf{W}^*(\mathbf{x},\mathbf{y}) \\ \mathbf{W}^*(\mathbf{x},\mathbf{y})^T & \mathbf{V}^*(\mathbf{x},\mathbf{y}) \end{bmatrix} = \tilde{\mathbf{N}} \begin{bmatrix} \mathbf{U}(\mathbf{x},\mathbf{y}) & \mathbf{W}(\mathbf{x},\mathbf{y}) \\ \mathbf{W}(\mathbf{x},\mathbf{y})^T & \mathbf{V}(\mathbf{x},\mathbf{y}) \end{bmatrix} = \begin{bmatrix} \mathbf{U}(\mathbf{x},\mathbf{y}) & \mathbf{W}(\mathbf{x},\mathbf{y}) \\ \mathbf{W}(\mathbf{x},\mathbf{y})^T & \mathbf{V}(\mathbf{x},\mathbf{y}) \end{bmatrix} \tilde{\mathbf{N}}^T, \quad (4)$$

where

$$\tilde{\mathbf{N}} = \begin{bmatrix} \mathbf{S} & \mathbf{H} \\ -\mathbf{L} & \mathbf{S}^T \end{bmatrix} \quad \text{and} \quad \tilde{\mathbf{N}}\tilde{\mathbf{N}} = \tilde{\mathbf{N}}^T\tilde{\mathbf{N}}^T = -\mathbf{I}. \quad (5)$$

Note that the second equality in Eq. (4) is a simple consequence of the first identity and symmetry of 6×6 matrices of real and imaginary parts of $\tilde{\mathbf{U}}$, $\tilde{\mathbf{V}}$, and $\tilde{\mathbf{W}}$ on the left and right-hand side of the first equality in (4). Using the argument of the continuity of elastic solutions with respect to a material limit it is obvious that Eq. (4) holds for isotropic materials as well. The Barnett-Lothe tensors are defined for isotropic materials, [5], as

$$H_{ij} = \frac{3-4\nu}{4G(1-\nu)}\delta_{ij}, \quad L_{ij} = \frac{G}{1-\nu}\delta_{ij}, \quad S_{ij} = -\frac{1-2\nu}{2(1-\nu)}\varepsilon_{ij}. \quad (6)$$

Sources of singularities in $\mathbf{U}^*$, $\mathbf{V}^*$, and $\mathbf{W}^*$ can be determined, in view of Eq. (1), directly from the second equality in Eq. (4). Let $\mathbf{q}$ be a real vector. Then, for example, $\mathbf{U}^*(\mathbf{x},\mathbf{y})\mathbf{q}$ represents a displacement vector at $\mathbf{x}$ originated by a line force $\mathbf{F}=\mathbf{S}^T\mathbf{q}$ and a line dislocation of Burgers vector $\mathbf{b}=\mathbf{Hq}$, and $\mathbf{V}^*(\mathbf{x},\mathbf{y})\mathbf{q}$ represents a stress function vector at $\mathbf{x}$ originated by a line force $\mathbf{F}=-\mathbf{Lq}$ and a line dislocation of Burgers vector $\mathbf{b}=\mathbf{Sq}$.

Consider now a smooth non self-intersecting curve $\Gamma_S\subset R^2$. Let $\mathbf{s}(\mathbf{x})=(s_1,s_2)$ and $\mathbf{n}(\mathbf{x})=(n_1,n_2)$ respectively denote the unit vectors tangent and normal to Γ_S at a point $\mathbf{x}\in\Gamma_S$ related by $n_i=\varepsilon_{ij}s_j$. The corresponding definitions in complex variable are $s_x=s_1+is_2$, $n_x=n_1+in_2$, $s_x=in_x$. Then, tangential derivative at $\mathbf{x}\in\Gamma_S$ of a function $f(r_1,r_2)=f(z,\bar{z})$ (where $\bar{z}$ is complex conjugate of z) defined on Γ_S, considering $\mathbf{y}$ fixed, is evaluated as follows: $\partial_{s_x}f=s_1\partial_{x_1}f+s_2\partial_{x_2}f=s_x\partial_z f+\bar{s}_x\partial_{\bar{z}}f$.

Tangential derivatives of singular solutions **U**, **V**, **W** and $\mathbf{U}^*$, $\mathbf{V}^*$ and $\mathbf{W}^*$ will appear in BIEs considered in the next section. Explicit expressions of these derivatives in complex variable are

$$\partial_{s_x}\tilde{\mathbf{U}}(\mathbf{x},\mathbf{y}) = \hat{\mathbf{U}}^* + i\hat{\mathbf{U}} = \frac{1}{2\pi G(\kappa+1)} \times \left[\kappa\frac{n_x}{z}\mathbf{I} + \frac{n_x\bar{z}+\bar{n}_x z}{2z^2}\begin{pmatrix} 1 & i \\ i & -1 \end{pmatrix}\right],$$

$$\partial_{s_x}\tilde{\mathbf{V}}(\mathbf{x},\mathbf{y}) = \hat{\mathbf{V}}^* + i\hat{\mathbf{V}} = -\frac{2G}{\pi(\kappa+1)}\left[\frac{n_x}{z}\mathbf{I} + \frac{n_x\bar{z}+\bar{n}_x z}{2z^2}\begin{pmatrix} 1 & i \\ i & -1 \end{pmatrix}\right],$$

$$\partial_{s_x}\tilde{\mathbf{W}}(\mathbf{x},\mathbf{y}) = \hat{\mathbf{W}}^* + i\hat{\mathbf{W}} = \frac{1}{2\pi(\kappa+1)}\left[i\frac{n_x}{z}\begin{pmatrix} (\kappa+1) & i(\kappa-1) \\ -i(\kappa-1) & (\kappa+1) \end{pmatrix} + i\frac{n_x\bar{z}+\bar{n}_x z}{z^2}\begin{pmatrix} 1 & i \\ i & -1 \end{pmatrix}\right], \quad (7)$$

where $\hat{\mathbf{U}}^*(\mathbf{x},\mathbf{y})=\partial_{s_x}\mathbf{U}^*(\mathbf{x},\mathbf{y})$, $\hat{\mathbf{U}}(\mathbf{x},\mathbf{y})=\partial_{s_x}\mathbf{U}(\mathbf{x},\mathbf{y})$ and analogously for other singular solutions. Simple expressions of these singular solutions in real variable formulation can be obtained either by differentiation of Eq. (3) or directly from Eq. (7) (for details of algebraic manipulations see Calzado [17]):

$$\hat{U}^*_{ij}(\mathbf{x},\mathbf{y}) = \frac{1}{2\pi G(\kappa+1)r}((\kappa-1)r_{,m}\delta_{ij}+2r_{,i}r_{,j}r_{,m})n_m(x),$$

$$\hat{V}^*_{ij}(\mathbf{x},\mathbf{y}) = -\frac{2G}{\pi(\kappa+1)r}2r_{,i}r_{,j}r_{,m}n_m(x),$$

$$\hat{W}^*_{ij}(\mathbf{x},\mathbf{y}) = \frac{1}{2\pi(\kappa+1)r}(-(\kappa+1)r_{,l}\delta_{ij}\varepsilon_{lm}-(\kappa-1)r_{,m}\varepsilon_{ij} + 2r_{,j}\varepsilon_{im}+2r_{,i}\varepsilon_{jm}-4r_{,i}r_{,j}r_{,l}\varepsilon_{lm})n_m(x), \quad (8)$$

$$\hat{U}_{ij}(\mathbf{x},\mathbf{y}) = \frac{1}{2\pi G(\kappa+1)r}(\kappa r_{,l}\delta_{ij}\varepsilon_{lm}-r_{,j}\varepsilon_{im}-r_{,i}\varepsilon_{jm} + 2r_{,i}r_{,j}r_{,l}\varepsilon_{lm})n_m(x),$$

$$\hat{V}_{ij}(\mathbf{x},\mathbf{y}) = \frac{2G}{\pi(\kappa+1)r}(-r_{,l}\delta_{ij}\varepsilon_{lm}+r_{,j}\varepsilon_{im}+r_{,i}\varepsilon_{jm} - 2r_{,i}r_{,j}r_{,l}\varepsilon_{lm})n_m(x),$$

$$\hat{W}_{ij}(\mathbf{x},\mathbf{y}) = \frac{1}{2\pi(\kappa+1)r}((\kappa-1)(r_{,m}\delta_{ij}-r_{,i}\delta_{jm}+r_{,j}\delta_{im}) + 4r_{,i}r_{,j}r_{,m})n_m(x). \quad (9)$$

Note that Eq. (4) is valid for tangential derivatives of **U**, **V**, **W** and $\mathbf{U}^*$, $\mathbf{V}^*$ and $\mathbf{W}^*$ as well, which has been checked by Calzado [17] explicitly for isotropic materials. Recall that tangential derivatives of $\tilde{\mathbf{U}}$ and $\tilde{\mathbf{V}}$ are symmetric matrices. Considering a Taylor series of a parametrization of Γ_S about a fixed $\mathbf{x}\in\Gamma_S$, it can be shown that $\mathrm{Re}\{n_x/z\}$ and $\bar{z}/z$ and also equivalently $r_{,m}n_m/r$ and $r_{,k}r_{,j}$ are smooth and bounded functions of $\mathbf{y}\in\Gamma_S$. This implies that $\hat{\mathbf{U}}^*(\mathbf{x},\mathbf{y})$ and $\hat{\mathbf{V}}^*(\mathbf{x},\mathbf{y})$, apparently singular functions, are in fact smooth and bounded functions of $\mathbf{y}\in\Gamma_S$. With reference to the other matrix functions defined in Eqs. (7)–(9), off-diagonal elements of $\hat{\mathbf{U}}(\mathbf{x},\mathbf{y})$, $\hat{\mathbf{V}}(\mathbf{x},\mathbf{y})$, $\hat{\mathbf{W}}^*(\mathbf{x},\mathbf{y})$ and diagonal elements of $\hat{\mathbf{W}}(\mathbf{x},\mathbf{y})$ are smooth functions of $\mathbf{y}\in\Gamma_S$, the rest of their elements being strongly singular functions of $\mathbf{y}\in\Gamma_S$.

2.2 Nonsingular Boundary Integral Equations (BIEs). Consider an elastic body whose section domain $\Omega\subset R^2$ has a piecewise smooth Lipschitz boundary Γ. Let $\Gamma_S\subset\Gamma$ denote the smooth part of Γ, i.e., excluding corners, points where a jump of boundary curvature takes place, etc. Following Wu [4] the procedure of deduction of the nonsingular BIE system starts with a pair of strongly singular BIEs introduced by Wu et al. [15], which can be written in the following compact matrix form for $\mathbf{x}\in\Gamma_S$:

$$\frac{1}{2}\begin{pmatrix} \partial_s\mathbf{u}(\mathbf{x}) \\ -\mathbf{t}(\mathbf{x}) \end{pmatrix} = \text{p.v.}\int_\Gamma \begin{pmatrix} \hat{\mathbf{U}}(\mathbf{x},\mathbf{y}) & \hat{\mathbf{W}}(\mathbf{x},\mathbf{y}) \\ \hat{\mathbf{W}}(\mathbf{x},\mathbf{y})^T & \hat{\mathbf{V}}(\mathbf{x},\mathbf{y}) \end{pmatrix}\begin{pmatrix} \mathbf{t}(\mathbf{y}) \\ -\partial_s\mathbf{u}(\mathbf{y}) \end{pmatrix} d\Gamma_y, \quad (10)$$

all the integrals being evaluated in a Cauchy principal value (p.v.) sense. Multiplying Eq. (10) by $\tilde{\mathbf{N}}$ from the left, another pair of BIEs is obtained, whose form is, in view of Eq. (4), as follows (Wu [4][2]):

$$\frac{1}{2}\tilde{\mathbf{N}}\begin{pmatrix} \partial_s\mathbf{u}(\mathbf{x}) \\ -\mathbf{t}(\mathbf{x}) \end{pmatrix} = \text{p.v.}\int_\Gamma \begin{pmatrix} \hat{\mathbf{U}}^*(\mathbf{x},\mathbf{y}) & \hat{\mathbf{W}}^*(\mathbf{x},\mathbf{y}) \\ \hat{\mathbf{W}}^*(\mathbf{x},\mathbf{y})^T & \hat{\mathbf{V}}^*(\mathbf{x},\mathbf{y}) \end{pmatrix}\begin{pmatrix} \mathbf{t}(\mathbf{y}) \\ -\partial_s\mathbf{u}(\mathbf{y}) \end{pmatrix} d\Gamma_y. \quad (11)$$

Due to the smoothness of integral kernels $\hat{\mathbf{U}}^*$, $\hat{\mathbf{V}}^*$ and off-diagonal elements of $\hat{\mathbf{W}}^*$, only the integrals including diagonal elements of $\hat{\mathbf{W}}^*$ are in fact evaluated in a Cauchy principal value sense.

As has already been discussed, taking advantage of the fact that $\hat{\mathbf{U}}^*$ and $\hat{\mathbf{V}}^*$ are smooth kernels, these BIEs can be organized in

[2]There is a misprint in Eq. (12) in Wu [4]: The correct form does not include the first minus sign on the right-hand side there.

such a way that regular integrals involve unknown elastic variables and that strongly singular integrals involve variables defined by the boundary conditions of an elastic BVP. Let Γ be partitioned in two parts Γ_u and Γ_t (both open in Γ), $\Gamma=\overline{\Gamma}_u\cup\overline{\Gamma}_t$ (an overline denotes the closure of a set), $\Gamma_u\cap\Gamma_t=\emptyset$, displacements being prescribed on Γ_u and tractions on Γ_t. Then, when the first equation from (11) is applied at points placed on the smooth part of Γ_u, i.e., $\mathbf{x}\in\Gamma_u\cap\Gamma_S$,

$$\frac{1}{2}\mathbf{H}\mathbf{t}(\mathbf{x})+\int_\Gamma\hat{\mathbf{U}}^*(\mathbf{x},\mathbf{y})\mathbf{t}(\mathbf{y})d\Gamma_y =\frac{1}{2}\mathbf{S}\partial_s\mathbf{u}(\mathbf{x})+\text{p.v.}\int_\Gamma\hat{\mathbf{W}}^*(\mathbf{x},\mathbf{y})\partial_s\mathbf{u}(\mathbf{y})d\Gamma_y, \tag{12}$$

and the second equation from (11) is applied at points placed on the smooth part of Γ_t, i.e., $\mathbf{x}\in\Gamma_t\cap\Gamma_S$,

$$-\frac{1}{2}\mathbf{L}\partial_s\mathbf{u}(\mathbf{x})+\int_\Gamma\hat{\mathbf{V}}^*(\mathbf{x},\mathbf{y})\partial_s\mathbf{u}(\mathbf{y})d\Gamma_y =\frac{1}{2}\mathbf{S}^T\mathbf{t}(\mathbf{x})+\text{p.v.}\int_\Gamma\hat{\mathbf{W}}^*(\mathbf{x},\mathbf{y})^T\mathbf{t}(\mathbf{y})d\Gamma_y, \tag{13}$$

a nonsingular BIE system of the second kind is obtained, which can be used to solve the BVP posed.

After a rearrangement of Eq. (13) and considering that $\mathbf{L}$ is a diagonal matrix, see Eq. (6), a BIR of $\partial_s\mathbf{u}$ can be obtained as follows:

$$\frac{1}{2}\mathbf{L}\partial_s\mathbf{u}(\mathbf{x})=-\frac{1}{2}\mathbf{S}^T\mathbf{t}(\mathbf{x})-\text{p.v.}\int_\Gamma\hat{\mathbf{W}}^*(\mathbf{x},\mathbf{y})^T\mathbf{t}(\mathbf{y})d\Gamma_y +\int_\Gamma\hat{\mathbf{V}}^*(\mathbf{x},\mathbf{y})\partial_s\mathbf{u}(\mathbf{y})d\Gamma_y. \tag{14}$$

A principal advantage of this BIR is that errors produced in the differentiation of an approximation of $\mathbf{u}$ substituted into the last integral on the right-hand side are expected to be smoothened by the smooth and bounded integral kernel $\hat{\mathbf{V}}^*$. Actually, tangential derivative of an approximation of $\mathbf{u}$ is not required to be continuous along Γ any more.

3 An (Apparently) Hypersingular Boundary Integral Equation for Isotropic Elasticity

Thinking of evaluating σ_{ss} on Γ_S as an objective of the present work, another BIE will be deduced in this section starting from Eq. (14). Consider a fixed point $\mathbf{x}\in\Gamma_S$. The regular integral on the right-hand side of Eq. (14) can be evaluated using an integration by parts as

$$\int_\Gamma\frac{\partial\mathbf{V}^*(\mathbf{x},\mathbf{y})}{\partial s_x}\partial_{s_y}\mathbf{u}(\mathbf{y})d\Gamma_y=-\int_\Gamma\frac{\partial^2\mathbf{V}^*(\mathbf{x},\mathbf{y})}{\partial s_y\partial s_x}\mathbf{u}(\mathbf{y})d\Gamma_y. \tag{15}$$

Note that the above integration by parts is permitted because $\hat{\mathbf{V}}^*(\mathbf{x},\mathbf{y})$ and $\mathbf{u}(\mathbf{y})$ are continuous functions of $\mathbf{y}\in\Gamma$ and also smooth functions except for a finite number of points on Γ. Explicit expressions of the integral kernel in complex and real variable formulations on the right-hand side of Eq. (15) can be written as

$$\frac{\partial^2\mathbf{V}^*(\mathbf{x},\mathbf{y})}{\partial s_y\partial s_x}=\hat{\hat{\mathbf{V}}}^*(\mathbf{x},\mathbf{y})=\frac{2G}{\pi(\kappa+1)}\text{Im}\left\{\frac{n_xn_y}{z^2}\mathbf{I} +\frac{(n_x\overline{n}_y+\overline{n}_xn_y)z+2n_xn_y\overline{z}}{2z^3}\begin{pmatrix}1 & i\\ i & -1\end{pmatrix}\right\}$$

$$\hat{\hat{V}}^*_{ij}(\mathbf{x},\mathbf{y})=\frac{4G}{\pi(\kappa+1)r^2}\{(\delta_{ik}r_{,j}r_{,m}+\delta_{jk}r_{,i}r_{,m}+\delta_{mk}r_{,i}r_{,j}) -4r_{,i}r_{,j}r_{,k}r_{,m}\}\varepsilon_{lk}n_l(\mathbf{y})n_m(\mathbf{x}). \tag{16}$$

Recall that this kernel is hypersingular, i.e., proportional to r^{-2} for $\mathbf{y}\in\Gamma$, $\mathbf{y}\to\mathbf{x}\in\Gamma_S$, only apparently because it has been obtained as a tangential derivative of a smooth function $\hat{\mathbf{V}}^*(\mathbf{x},\mathbf{y})$. Thus, $\hat{\hat{\mathbf{V}}}^*(\mathbf{x},\mathbf{y})$ is in fact a smooth function of $\mathbf{y}\in\Gamma_S$ for a fixed $\mathbf{x}\in\Gamma_S$ and it is bounded for all $\mathbf{y}\in\Gamma$. Observe also that the following symmetry relations hold $\hat{\hat{V}}^*_{ij}(\mathbf{x},\mathbf{y})=\hat{\hat{V}}^*_{ji}(\mathbf{x},\mathbf{y})=\hat{\hat{V}}^*_{ij}(\mathbf{y},\mathbf{x})$.

Substituting Eq. (15) into Eq. (14) the following BIE is obtained for $\mathbf{x}\in\Gamma_S$:

$$\frac{1}{2}\mathbf{L}\partial_s\mathbf{u}(\mathbf{x})=-\frac{1}{2}\mathbf{S}^T\mathbf{t}(\mathbf{x})-\text{p.v.}\int_\Gamma\hat{\mathbf{W}}^*(\mathbf{x},\mathbf{y})^T\mathbf{t}(\mathbf{y})d\Gamma_y -\int_\Gamma\hat{\hat{\mathbf{V}}}^*(\mathbf{x},\mathbf{y})\mathbf{u}(\mathbf{y})d\Gamma_y. \tag{17}$$

An additional advantage of BIE in Eq. (17) when applied as a BIR in a BEM post-processing, in comparison with that in Eq. (14), is that a boundary displacement approximation appears directly as an integral density on the right-hand side of the BIR, no differentiation of this approximation then being required here. Note that there is no restrictive continuity requirement on a displacement approximation used on the right-hand side of BIR (17) in order to obtain a continuous approximation of ∂_su_s over Γ_S on the left-hand side.

4 Application for the In-Boundary Stress Evaluation

Starting from Hooke's law an expression of the in-boundary stress σ_{ss} in terms of the normal stress to the boundary $\sigma_{nn}=t_n$ and in-boundary strain $\varepsilon_{ss}=\partial_su_s$ is obtained in the following form for a plane-strain state

$$\sigma_{ss}=\frac{\nu}{1-\nu}t_n+\frac{E}{1-\nu^2}\partial_su_s, \tag{18}$$

where E is Young's modulus.

Although an application of BIRs in Eqs. (14) and (17) to evaluate ∂_su_s and subsequently σ_{ss} through Eq. (18) is the most advantageous approach on smooth boundary parts where tractions $\mathbf{t}$ are prescribed, these BIRs can successfully be applied on other smooth boundary parts as well. The accuracy of σ_{ss} evaluated in this way can be expected to be similar to that of direct results of a BEM analysis, tractions $\mathbf{t}$ and displacements $\mathbf{u}$.

Two examples are presented to illustrate the performance of the above BIRs. Note that BIRs given in Eqs. (14) and (17) are in fact equivalent, except for rounding-off errors and errors in integrations, if the same approximations of the solution of a BVP on Γ are applied on their right-hand sides as integral densities and integrations (and also differentiation of the displacement approximation in the case of Eq. (14)) are performed over the actual boundary Γ. Thus only results obtained by the BIR given in Eq. (14) are presented here for the sake of simplicity.

Material properties in both examples are given by $E=200$ GPa and $\nu=0.25$. Uniform meshes of continuous linear boundary elements (París and Cañas [2]) are used for discretization of both problems. All integrations in the BEM solution are carried out analytically. Recall that approximations of ∂_su_s, obtained by a differentiation of piecewise linear interpolations of displacement nodal values and used in BIR (14), are piecewise constant over Γ.

4.1 Example 1: Simply Supported Beam Under a Constant Load. Consider a simply supported beam of dimensions $L\times H$, $L=2H$, subjected to a constant load of value p applied at its top surface, see Fig. 1. An analytic elastic solution of an approximation of this problem given in Timoshenko and Goodier [18] is

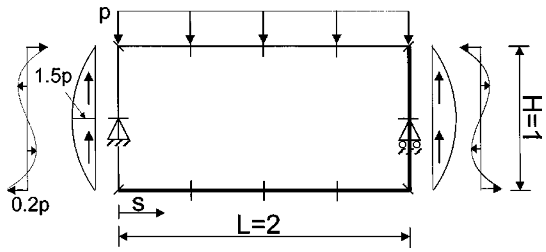

Fig. 1 Simply supported beam subjected to a uniform load. Basic boundary element mesh.

adopted here for this test problem. All boundary conditions are prescribed in tractions. Rigid-body movements are removed by a procedure developed by Blázquez et al. [19] applying supports as shown in Fig. 1. Basic mesh of 12 elements is also shown in Fig. 1. A sequence of uniform refinements of this mesh with 36, 108, and 324 elements is used for a convergence analysis.

Nodal values of σ_{ss} (normalized by p) obtained for the first two meshes on the bottom and right-hand side are compared with the analytic solution in Fig. 2. Analyzing distributions of normalized errors in σ_{ss} at nodes for finer meshes shown in Fig. 3, it is possible to observe, first a high convergence rate at each particular node, and second an increase in errors at nodes approaching a corner for each particular mesh. This characteristic increase in errors near corners is possibly related to the observed increase in errors in displacements obtained by the direct BEM solution (Calzado [17]). A stable quadratic convergence of normalized errors of σ_{ss} evaluated at the center of the bottom side, where a maximum value of σ_{ss} is achieved, can be observed in Fig. 4.

4.2 Example 2: Uniaxial Tension of an Infinite Plate With a Circular Hole. An infinite plate with a circular hole of a radius R subjected to a uniaxial tension of value p, see Fig. 5, is analyzed using a superposition approach (París and Cañas [2]). Boundary conditions are prescribed in tractions. Basic mesh of eight elements is also shown in Fig. 5. A sequence of uniform refinements of this mesh with 24, 72, and 216 elements is used for a convergence analysis.

Nodal values of the hoop stress $\sigma_{ss}=\sigma_\theta$ (normalized by p) obtained for the first two meshes on a quarter circle part are compared with the analytic solution in Fig. 6. From distributions of normalized errors in σ_θ at nodes for finer meshes shown in Fig. 7, it is possible to observe, as in the previous example, first a high

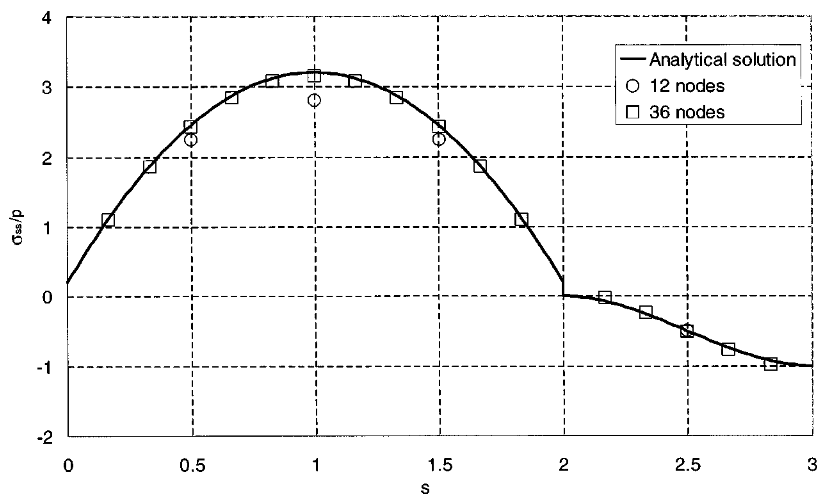

Fig. 2 In-plane stress evaluated using boundary integral representation (14). Beam discretization by meshes of 12 and 36 linear elements.

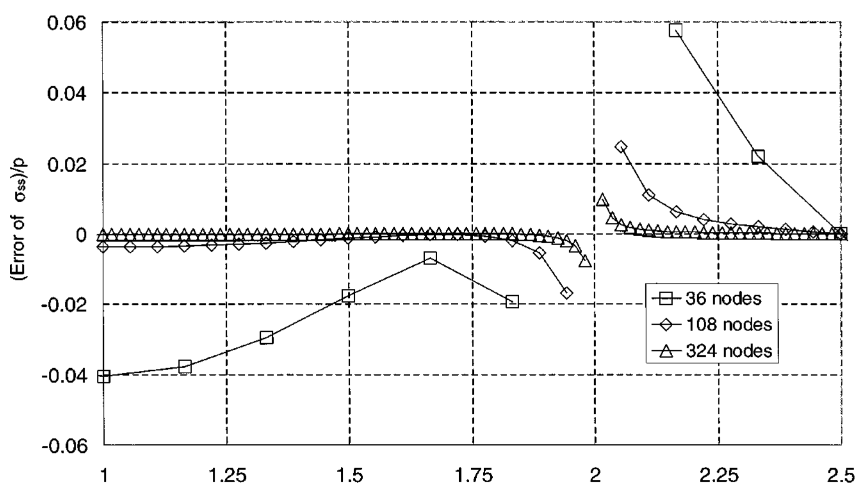

Fig. 3 Normalized errors of the in-plane stress evaluated using boundary integral representation (14). Beam discretization by meshes of 36, 108, and 324 linear elements.

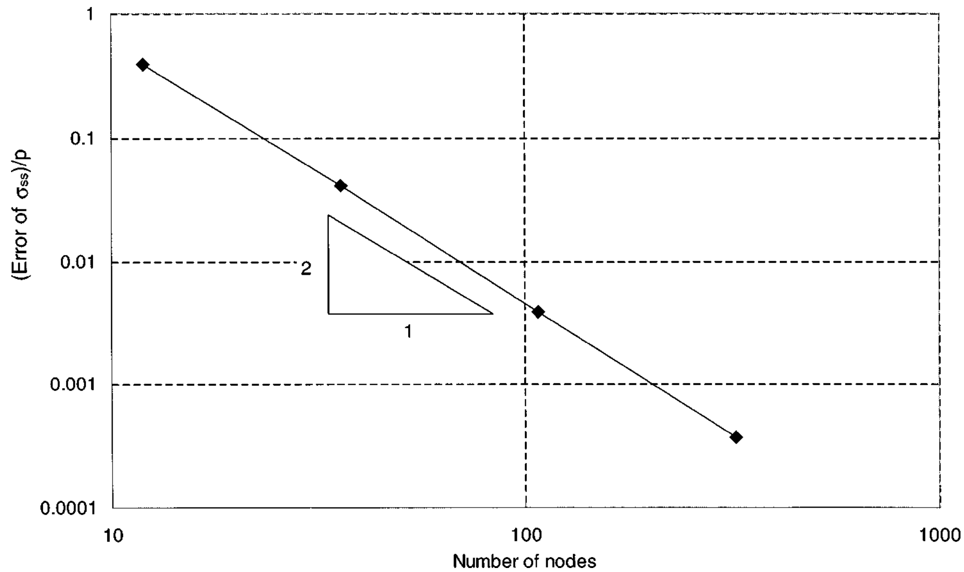

Fig. 4 Convergence of the normalized error of the in-plane stress evaluated using boundary integral representation (14). Beam discretization by meshes of 12, 36, 108, and 324 linear elements.

convergence rate at each particular node, and second a moderate increase in errors at nodes approaching stress concentration point for each particular mesh. Nevertheless, when comparing with results by other authors for similar discretizations of this problem, e.g., those by París and Cañas [2] using the standard BEM procedure with linear elements and also those obtained by Wu et al. [15] using special BIEs given by Eq. (10) with constant elements, the accuracy obtained by the present approach can be considered excellent. Recall, however, that integration in BIR (14) is performed over the real circular boundary Γ in the present work. A stable quadratic convergence of normalized errors of σ_θ evaluated at points of polar angle $\theta=0$ deg, 90 deg, can be observed in Fig. 8.

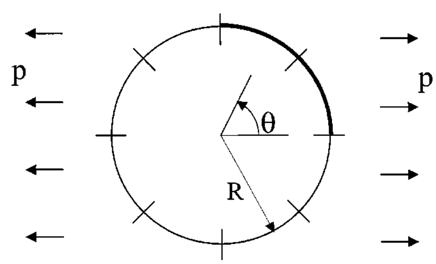

Fig. 5 An infinite plate with a circular hole subjected to uniaxial tension. Basic boundary element mesh.

5 Concluding Remarks

Following Wu's [4] procedure a novel nonsingular BIE system of the second kind for isotropic materials has been developed presenting explicit expressions of its integral kernels in complex and real variable formulation. The physical interpretation of the singularity sources of these integral kernels has been elucidated. Whereas a complex variable formulation is advantageously applied in developing analytic integrations over straight boundary elements (Calzado [17]), real variable formulation is usually adopted by BEM programmers in numerical integration procedures. Note that an important advantageous feature of this BIE

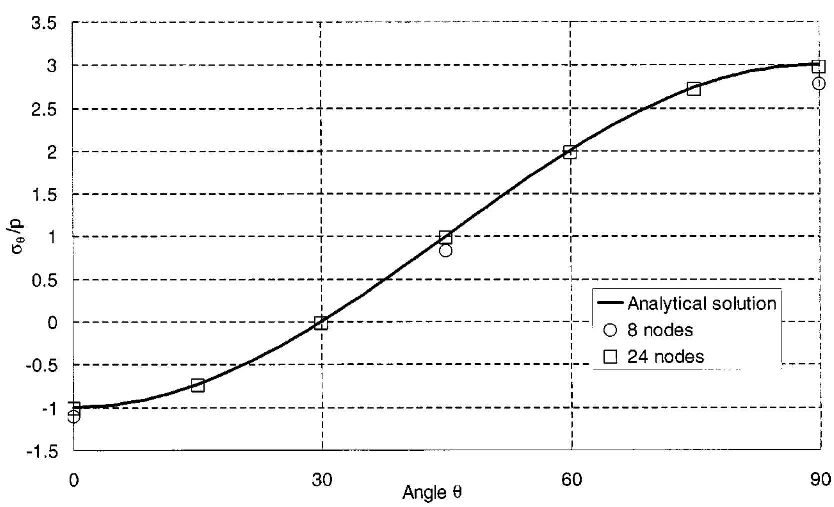

Fig. 6 Hoop stress evaluated using boundary integral representation (14). Circumference discretization by meshes of 8 and 24 linear elements.

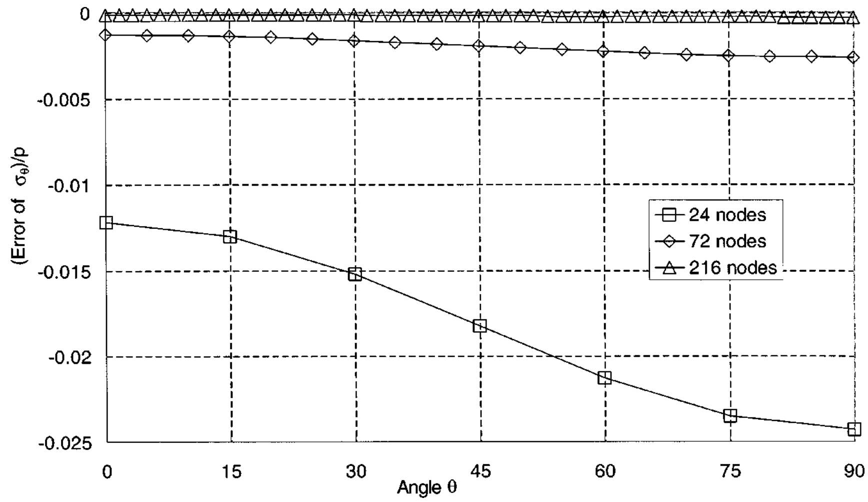

Fig. 7 Normalized errors of the hoop stress evaluated using boundary integral representation (14). Circumference discretization by meshes of 24, 72, and 216 linear elements.

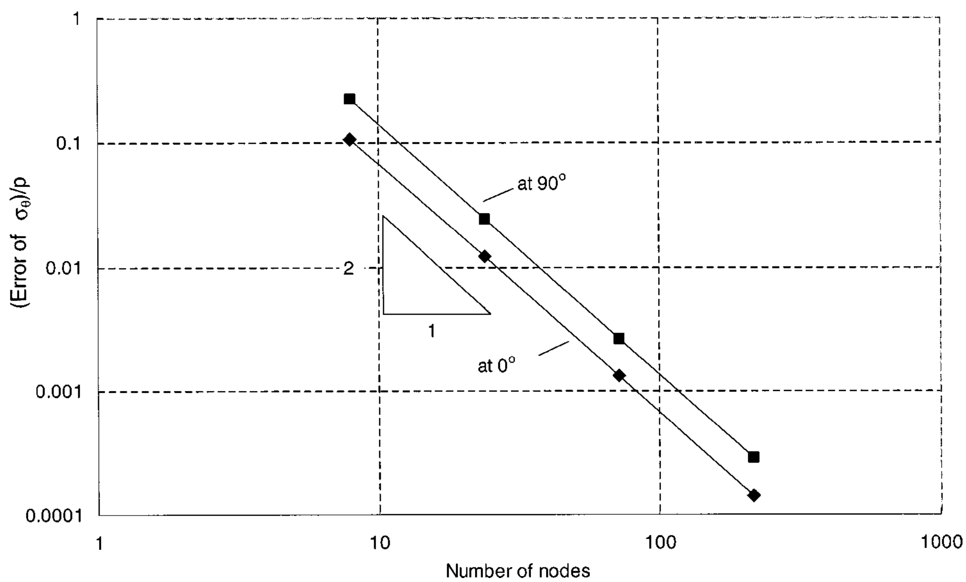

Fig. 8 Convergence of the normalized error of the hoop stress evaluated using boundary integral representation (14). Circumference discretization by meshes of 8, 24, 72, and 216 linear elements.

system, namely a low conditioning number (associated to its second-kind character) of the resulting linear system when discretized by a BEM approach, has not been studied here and will require further study.

Two closely related BIRs of tangential derivative of boundary displacements have been deduced, both with smoothing integral kernels operating on displacements and their tangential derivatives as integral densities. Thus, no restrictive continuity requirements have to be fulfilled by boundary element approximations of these integral densities at element junctions, and consequently no smoothing procedure applied to these densities is required in these BIRs. Excellent accuracy of the in-boundary stress evaluated at smooth boundary parts, including stress concentration points, has been obtained using these BIRs in test problems.

Acknowledgments

The work was supported by the Spanish Ministry of Education and Culture under grant No. PB98-1118 and Spanish Ministry of Science and Technology under grant No. MAT2000-1115. The authors thank E. Graciani and R. Avila for their BEM code used to solve elasticity problems in this study.

References

[1] Rizzo, F. J., 1967, "An Integral Equation Approach to Boundary Value Problems of Classical Elastostatics," Q. Appl. Math., **25**, pp. 83–95.

[2] París, F., and Cañas, J., 1997, *Boundary Element Method, Fundamentals and Applications*, Oxford University Press, Oxford, UK.

[3] Ghosh, N., Rajiyah, H., Ghosh, S., and Mukherjee, S., 1986, "A New Boundary Element Method Formulation for Linear Elasticity," ASME J. Appl. Mech., **53**, pp. 69–76.

[4] Wu, K.-C., 2000, "Non-singular Boundary Integral Equations for Two-Dimensional Anisotropic Elasticity," ASME J. Appl. Mech., **67**, pp. 618–621.

[5] Ting, T. C. T., 1996, *Anisotropic Elasticity—Theory and Applications*, Oxford University Press, New York.

[6] Rizzo, F. J., and Shippy, D. J., 1968, "A Formulation and Solution Procedure for the General Non-Homogeneous Elastic Inclusion Problem," Int. J. Solids Struct., **4**, pp. 1161–1179.

[7] Cruse, T., and Van Buren, W., 1971, "Three-Dimensional Elastic Stress Analy-

sis of a Fracture Specimen with an Edge Crack,'' Int. J. Fract. Mech., **7**, pp. 1–15.
[8] Zhao, Z. Y., 1996, ''Interelement Stress Evaluation by Boundary Elements,'' Int. J. Numer. Methods Eng., **39**, pp. 2399–2415.
[9] Mantič, V., Graciani, E., and París, F., 1999, ''A Simple Local Smoothing Scheme in Strongly Singular Boundary Integral Representation of Potential Gradient,'' Comput. Methods Appl. Mech. Eng., **178**, pp. 267–289.
[10] Guiggiani, M., Krishnasamy, G., Rudolphi, T. J., and Rizzo, F. J., 1992, ''A General Algorithm for the Numerical Solution of Hypersingular Boundary Integral Equations,'' ASME J. Appl. Mech., **59**, pp. 604–614.
[11] Graciani, E., Mantič, V., París, F., and Cañas, J., 2000, ''A Critical Study of Hypersingular and Strongly Singular Boundary Integral Representations of Potential Gradient,'' Comput. Mech., **26**, pp. 542–559.
[12] Krishnasamy, G., Rizzo, F. J., and Rudolphi, T. J., 1992, ''Continuity Requirements for Density Functions in the Boundary Integral Equation Method,'' Comput. Mech., **9**, pp. 267–284.
[13] Avila, R., Mantič, V., and París, F., 1997, ''Application of the Boundary Element Method to Elastic Orthotropic Materials in 2D: Numerical Aspects,'' *Proceedings, Boundary Elements XIX*, M. Marchetti, C. A. Brebbia, and M. H. Aliabadi, eds., Computational Mechanics Publications, Southampton, pp. 55–64.
[14] Niu, Q., and Shepard, M. S., 1993, ''Superconvergent Extraction Techniques for Finite Element Analysis,'' Int. J. Numer. Methods Eng., **36**, pp. 811–836.
[15] Wu, K.-C., Chiu, Y.-T., and Hwu, Z.-H., 1992, ''A New Boundary Integral Equation Formulation for Linear Elastic Solids,'' ASME J. Appl. Mech., **59**, pp. 344–348.
[16] Ting, T. C. T., 1992, ''Anatomy of Green's Functions for Line Forces and Dislocations in Anisotropic Media and in Degenerate Materials,'' Phys. Scr., **T44**, pp. 137–144.
[17] Calzado, F. J., 2001, ''Evaluation of Stress Tensor at the Boundary by BEM in Plane Elasticity (in Spanish),'' Final Project, School of Engineering, University of Seville.
[18] Timoshenko, S. P., and Goodier, J. N., 1970, *Theory of Elasticity*, 3rd Ed., McGraw-Hill, New York.
[19] Blázquez, A., Mantič, V., París, F., and Cañas, J., 1996, ''On the Removal of Rigid Body Motions in the Solution of Elastostatic Problems by Direct BEM,'' Int. J. Numer. Methods Eng., **39**, pp. 4021–4038.

The Stress Field Caused by a Circular Cylindrical Inclusion in a Transversely Isotropic Elastic Solid

H. Hasegawa
Professor

M. Kisaki
Graduate Student

Department of Mechanical Engineering,
Meiji University,
Tama-ku, Kawasaki 214-8571, Japan

Exact solutions are presented in closed form for the axisymmetric stress and displacement fields caused by a circular solid cylindrical inclusion with uniform eigenstrain in a transversely isotropic elastic solid. This is an extension of a previous paper for an isotropic elastic solid to a transversely isotropic solid. The strain energy is also shown. The method of Green's functions is used. The numerical results for stress distributions are compared with those for an isotropic elastic solid. [DOI: 10.1115/1.1629755]

1 Introduction

The theory of inclusions has been successfully applied to composite materials including fiber, precipitate, and martensite problems. A review of inclusion problems has been given by Mura [1,2]. A number of results were shown for the stress fields caused by an ellipsoidal inclusion. A circular cylindrical inclusion problem has recently been solved by Takao et al. [3] and Hasegawa et al. [4,5] who investigated the circular cylindrical inclusion with uniform axial eigenstrain and they obtained a closed-form solution for stress and displacement fields caused by the inclusion in an infinite elastic solid or in an elastic half-space. Wu and Du [6–8] gave a solution for the cylindrical inclusion with arbitrary uniform eigenstrain in an infinite elastic solid or in an elastic half-space. In these papers mentioned above, the elastic moduli of the inclusion are assumed to be the same as the matrix. Hasegawa and Yoshiie [9] have studied an infinite elastic solid with a circular cylindrical inhomogeneity under tension.

This paper shows closed-form solutions for the elastic field caused by a circular cylindrical inclusion with uniform axial eigenstrain in a transversely isotropic infinite solid. The strain energy of the system is also shown.

It is well known, [1] that the stress fields caused by an inclusion can be obtained by using Green's functions for body force problems. In a previous paper, [10], the fundamental solutions for axisymmetric problems of a transversely isotropic elastic solid have been shown by applying Leknitsky's stress functions, [11,12]. Therefore, we apply the fundamental solutions for axisymmetric problems as Green's functions for obtaining the displacement and stress fields caused by a circular cylindrical inclusion in a transversely isotropic solid.

2 Definition of the Problem and Stress Functions

We consider a circular cylindrical inclusion with length $2b$ and radius c in a transversely isotropic infinite solid as shown in Fig. 1. Cylindrical coordinates (r,θ,z) or $(i=1,2,3)$ are used, and the axial eigenstrain ε_z^* is given by

$$\varepsilon_z^* = \varepsilon_0\{S(z+b)-S(z-b)\}\{1-S(r-c)\} \tag{1}$$

and other components of ε_{ij}^* equal zeroes. Here $S(\ )$ is a Heviside step function and ε_0 is the magnitude of the eigenstrain. The present problem is to determine displacement and stress fields caused by the eigenstrain of Eq. (1). We express the elastic moduli of a transversely isotropic solid by C_{mn} and assume that the axis of elastic symmetry of the solid is coincident with the z-axis of the cylindrical inclusion.

It is well known, [10–12] that the axisymmetric displacements $u_i(r,z)$, $(i=1,2,3)$, due to the axisymmetric body forces $F_i(r,z)$, $(i=1,2,3)$, are expressed by

$$u_1 = c_{33}\frac{\partial^2\phi_1}{\partial z^2} + c_{44}\frac{\partial}{\partial r}\left\{\frac{1}{r}\frac{\partial}{\partial r}(r\phi_1)\right\} - (c_{13}+c_{44})\frac{\partial^2\phi_3}{\partial r\partial z},$$

$$u_2 = \phi_2, \tag{2}$$

$$u_3 = -(c_{13}+c_{44})\frac{\partial}{\partial z}\left\{\frac{1}{r}\frac{\partial}{\partial r}(r\phi_1)\right\} + c_{11}\frac{1}{r}\frac{\partial}{\partial r}\left(r\frac{\partial\phi_3}{\partial r}\right) + c_{44}\frac{\partial^2\phi_3}{\partial z^2}$$

where ϕ_i, $(i=1,2,3)$, are stress functions satisfying the equations

$$\left(\nabla_1^2 - \frac{1}{r^2}\right)\left(\nabla_2^2 - \frac{1}{r^2}\right)\phi_1 = -\frac{F_1}{c_{11}c_{44}},$$

$$\left(\nabla_3^2 - \frac{1}{r^2}\right)\phi_2 = -\frac{F_2}{c_{66}}, \tag{3}$$

$$\nabla_1^2\nabla_2^2\phi_3 = -\frac{F_3}{c_{11}c_{44}}$$

where

$$\nabla_i^2 = \frac{\partial^2}{\partial r^2} + \frac{1}{r}\frac{\partial}{\partial r} + c_i^2\frac{\partial^2}{\partial z^2}, \quad (i=1,2,3) \tag{4}$$

and $c_3^2 = c_{44}/c_{66}$, and c_i^2, $(i=1,2)$, are roots X for the following algebraic equation:

$$c_{11}c_{44}X^4 + (c_{13}^2 + 2c_{13}c_{44} - c_{11}c_{33})X^2 + c_{33}c_{44} = 0. \tag{5}$$

3 Method of Solution

3.1 Green's Functions. For problems of inclusion with eigenstrain, the Kelvin's solution for a point force has been widely used, [1]. However, for the present problem, it is convenient to use Green's functions for axisymmetric body force problems of

Contributed by the Applied Mechanics Division of THE AMERICAN SOCIETY OF MECHANICAL ENGINEERS for publication in the ASME JOURNAL OF APPLIED MECHANICS. Manuscript received by the ASME Applied Mechanics Division, October 29, 2002; final revision, April 25, 2003. Associate Editor: D. A. Kouris. Discussion on the paper should be addressed to the Editor, Prof. Robert M. McMeeking, Department of Mechanical and Environmental Engineering, University of California–Santa Barbara, Santa Barbara, CA 93106-5070, and will be accepted until four months after final publication of the paper itself in the ASME JOURNAL OF APPLIED MECHANICS.

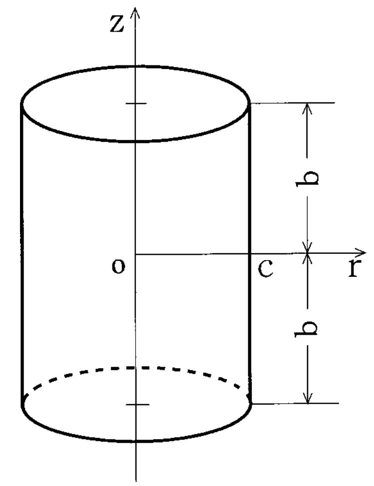

Fig. 1 A circular cylindrical inclusion in a transversely isotropic elastic solid

elasticity. The Green's functions used here are defined as the solutions for the problem of a transversely isotropic infinite elastic solid subjected to the axisymmetric body forces

$$F_k = \frac{1}{2\pi r}\delta(r-a)\delta(z-h) \tag{6}$$

distributed along the circle $(r=a,\ z=h)$ as shown in Fig. 2. In Eq. (6), $\delta(\ )$ is the Dirac delta function and F_k, $(k=1,2,3)$, are a radial, a torsional, and an axial force, respectively. We represent the Green's functions by $u_i^k(r,z,a,h)$ for displacements and $\sigma_{ij}^k(r,z,a,h)$ for stresses. Here u_i^k denotes the displacement component in the i-direction at a point (r,z) when a unit ring force in the k-direction acts along a circle (a,h) located at $z=h$ with radius a.

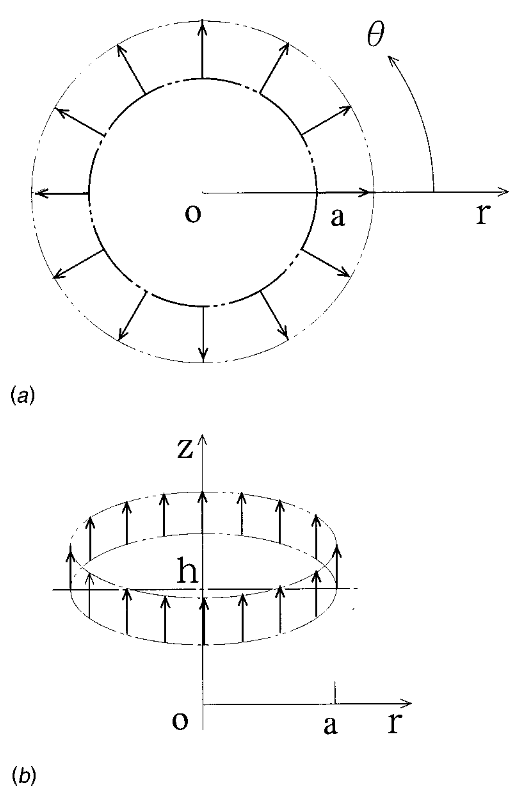

Fig. 2 The body force acting along a circle; (a) a radial force, (b) an axial force

It was shown in the previous paper, [10] that the stress functions ϕ_1 and ϕ_3 for the axisymmetric body forces F_1 and F_3 are expressed by

$$\phi_i = \phi_{is} + \phi_{ic}, \quad (i=1,3) \tag{7}$$

where

$$\begin{Bmatrix} \phi_{ic} \\ \phi_{is} \end{Bmatrix} = -\frac{1}{\pi c_{11}c_{44}}\int_0^\infty\int_0^\infty \frac{\alpha J_n(\alpha r)}{(\alpha^2+c_1^2\beta^2)(\alpha^2+c_2^2\beta^2)} \times \begin{Bmatrix} F_{ic}\cos\beta z \\ F_{is}\sin\beta z \end{Bmatrix} d\alpha d\beta \tag{8}$$

with

$$\begin{Bmatrix} F_{ic} \\ F_{is} \end{Bmatrix} = \int_{-\infty}^\infty\int_0^\infty rF_i(r,z)J_n(\alpha r)\begin{Bmatrix} \cos\beta z \\ \sin\beta z \end{Bmatrix} drdz. \tag{9}$$

In these expressions, $J_n(\alpha r)$ is a Bessel function of the first kind of the order n. Here we take $n=1$ for F_1 and $n=0$ for F_3. Note that $F_2=0$ and $u_2=0$ for the present problem.

By Eqs. (6) and (9), we have

$$\begin{Bmatrix} F_{ic} \\ F_{is} \end{Bmatrix} = \frac{1}{2\pi}J_n(\alpha a)\begin{Bmatrix} \cos\beta h \\ \sin\beta h \end{Bmatrix}, \quad (i=1,3). \tag{10}$$

Substituting Eq. (7) into Eq. (2) yields

$$u_i^k = u_{ic}^k + u_{is}^k, \quad (i,k=1,3) \tag{11}$$

with

$$\begin{aligned}
\begin{Bmatrix} u_{1c}^1 \\ u_{1s}^1 \end{Bmatrix} &= \frac{1}{\pi D}\int_0^\infty\int_0^\infty \alpha J_1(\alpha r)A_1\begin{Bmatrix} F_{1c}\cos\beta z \\ F_{1s}\sin\beta z \end{Bmatrix} d\alpha d\beta, \\
\begin{Bmatrix} u_{3c}^1 \\ u_{3s}^1 \end{Bmatrix} &= \frac{c_{13}+c_{44}}{\pi D}\int_0^\infty\int_0^\infty \frac{\alpha^2}{\beta}J_0(\alpha r)A_3\begin{Bmatrix} -F_{1c}\sin\beta z \\ F_{1s}\cos\beta z \end{Bmatrix} d\alpha d\beta, \\
\begin{Bmatrix} u_{1c}^3 \\ u_{1s}^3 \end{Bmatrix} &= \frac{c_{13}+c_{44}}{\pi D}\int_0^\infty\int_0^\infty \frac{\alpha^2}{\beta}J_1(\alpha r)A_3\begin{Bmatrix} F_{3c}\sin\beta z \\ -F_{3s}\cos\beta z \end{Bmatrix} d\alpha d\beta, \\
\begin{Bmatrix} u_{3c}^3 \\ u_{3s}^3 \end{Bmatrix} &= \frac{1}{\pi D}\int_0^\infty\int_0^\infty \alpha J_0(\alpha r)A_2\begin{Bmatrix} F_{3c}\cos\beta z \\ F_{3s}\sin\beta z \end{Bmatrix} d\alpha d\beta
\end{aligned} \tag{12}$$

where A_1, A_2, and A_3 are shown in Eq. (24) and

$$D = c_{11}c_{44}(c_2^2 - c_1^2). \tag{13}$$

The superscript k in Eq. (11) implies the displacement component produced by the body force F_k. Expressions for the stresses σ_{ij}^k can be obtained from (11) and the following Hooke's law:

$$\begin{aligned}
\sigma_r &= c_{11}\varepsilon_r + c_{12}\varepsilon_\theta + c_{13}\varepsilon_z, \\
\sigma_\theta &= c_{12}\varepsilon_r + c_{11}\varepsilon_\theta + c_{13}\varepsilon_z, \\
\sigma_z &= c_{13}\varepsilon_r + c_{13}\varepsilon_\theta + c_{33}\varepsilon_z,
\end{aligned} \tag{14}$$

$$\tau_{rz} = c_{44}\gamma_{rz}, \quad \tau_{z\theta} = c_{44}\gamma_{z\theta}, \quad \tau_{r\theta} = c_{66}\gamma_{r\theta}.$$

3.2 Stresses and Displacements due to Eigenstrains. Using the Green's functions $u_i^k(r,z,a,h)$ and $\sigma_{ij}^k(r,z,a,h)$ shown above for transversely isotropic solids, the displacement and stress fields caused by an inclusion can be expressed as

$$\begin{Bmatrix} u_i \\ \sigma_{ij} \end{Bmatrix} = -\int_\Omega \begin{Bmatrix} u_i^k(r,z,a,h) \\ \sigma_{ij}^k(r,z,a,h) \end{Bmatrix} f_k(a,h)d\Omega - \begin{Bmatrix} 0 \\ \sigma_{ij}^* \end{Bmatrix} \tag{15}$$

with

$$f_1=\frac{\partial}{\partial r}(c_{11}\varepsilon_r^*+c_{12}\varepsilon_\theta^*+c_{13}\varepsilon_z^*)+c_{44}\frac{\partial}{\partial z}\gamma_{rz}^*+(c_{11}-c_{12})\frac{\varepsilon_r^*-\varepsilon_\theta^*}{r},$$

$$f_2=c_{66}\frac{\partial}{\partial r}\gamma_{r\theta}^*+c_{44}\frac{\partial}{\partial z}\gamma_{z\theta}^*+\frac{2}{r}c_{66}\gamma_{r\theta}^*, \tag{16}$$

$$f_3=c_{44}\left(\frac{\partial}{\partial r}\gamma_{rz}^*+\frac{1}{r}\gamma_{rz}^*\right)+\frac{\partial}{\partial z}\{c_{13}(\varepsilon_r^*+\varepsilon_\theta^*)+c_{33}\varepsilon_z^*\}.$$

In Eq. (15), Ω is the region of inclusion, $d\Omega$ is a volume element, σ_{ij}^* are stresses in Ω obtained by Eqs. (1) and (14), and $\sigma_{ij}^*=0$ outside of Ω. We must take the summation for $k=1,3$ in Eq. (15).

From Eqs. (1) and (16), Eq. (15) becomes

$$\begin{Bmatrix} u_i \\ \sigma_{ij}\end{Bmatrix}=-\int_\Omega\left(c_{13}\begin{Bmatrix} u_i^1 \\ \sigma_{ij}^1\end{Bmatrix}\frac{\partial\varepsilon_z^*}{\partial a}+c_{33}\begin{Bmatrix} u_i^3 \\ \sigma_{ij}^3\end{Bmatrix}\frac{\partial\varepsilon_z^*}{\partial h}\right)d\Omega-\begin{Bmatrix} 0 \\ \sigma_{ij}^*\end{Bmatrix}. \tag{17}$$

4 A Circular Cylindrical Inclusion

4.1 Displacements. Here we show the displacements u_i caused by a circular cylindrical inclusion in a transversely isotropic solid. Substituting Eq. (1) into Eq. (17) yields

$$u_i=2\pi c\varepsilon_0 c_{13}\int_{-b}^{b}u_i^1(r,z,c,h)dh+2\pi\varepsilon_0 c_{33}\int_0^c a\{u_i^3(r,z,a,b)-u_i^3(r,z,a,-b)\}da. \tag{18}$$

Integrating Eq. (18) with respect to h and a, we get

$$u_1=\frac{2c\varepsilon_0}{\pi D}\int_0^\infty\int_0^\infty\frac{\alpha}{\beta}J_1(\alpha c)J_1(\alpha r)\{c_{13}A_1-c_{33}(c_{13}+c_{44})A_3\}\times\sin\beta b\cos\beta z\,d\alpha\,d\beta,$$

$$u_3=-\frac{2c\varepsilon_0}{\pi D}\int_0^\infty\int_0^\infty J_1(\alpha c)J_0(\alpha r)\left\{(c_{13}+c_{44})A_3\frac{\alpha^2}{\beta^2}-c_{33}A_2\right\}\times\sin\beta b\sin\beta z\,d\alpha\,d\beta, \tag{19}$$

$$u_2=0.$$

Integrating Eq. (19) by using integral formulas [13,14], we can obtain

$$u_1=\frac{c\varepsilon_0c_{13}c_{44}}{4\pi D_1}\sum_{n=1}^{2}(-1)^n\left(c_n^2+\frac{c_{33}}{c_{13}}\right)(q_{81n}-q_{82n}),\quad(b\leqq|z|)$$

$$u_1=\frac{c\varepsilon_0c_{13}}{4D}\left\{\frac{r}{c}+\frac{c}{r}+\left(\frac{r}{c}-\frac{c}{r}\right)\mathrm{SGN}(c-r)\right\}c_{44}(c_2^2-c_1^2)+\frac{c\varepsilon_0c_{13}c_{44}}{4\pi D_1}\sum_{n=1}^{2}(-1)^{n+1}\left(c_n^2+\frac{c_{33}}{c_{13}}\right)(q_{81n}+q_{82n}),\quad(b\geqq|z|) \tag{20}$$

$$u_3=\frac{c\varepsilon_0c_{13}}{4\pi D_1}\sum_{n=1}^{2}(-1)^{n+1}\left\{(c_{13}+c_{44})c_n+\frac{c_{33}}{c_{13}}\frac{c_{44}-c_{11}c_n^2}{c_n}\right\}\times(q_{71n}-q_{72n}),$$

$$u_2=0$$

with

$$q_{7mn}=r\left(2G_2(x_{mn})+\frac{c^2-r^2}{cr}Q_{-1/2}(x_{mn})+\frac{c-r}{c+r}\frac{1}{cr}z_{mn}^2k_{mn}\Pi(p,k_{mn})-\frac{\pi z_{mn}}{\sqrt{cr}}\{1+\mathrm{SGN}(c-r)\}\right),$$

$$q_{8mn}=\frac{\pi}{2\sqrt{cr}}\{r^2+c^2+(r^2-c^2)\mathrm{SGN}(c-r)\}+\frac{z_{mn}}{2cr}\{(c-r)^2k_{mn}\Pi(p,k_{mn})-2crQ_{1/2}(x_{mn})-(c^2+r^2)Q_{-1/2}(x_{mn})\}, \tag{21}$$

$$z_{mn}=|z+(-1)^m b|/c_n,\quad k_{mn}^2=\frac{4cr}{(c+r)^2+z_{mn}^2},$$

$$p=\frac{4cr}{(c+r)^2},\quad x_{mn}=\frac{r^2+c^2+z_{mn}^2/c_n^2}{2cr},$$

$$G_2(x)=xQ_{-1/2}(x)-Q_{1/2}(x),\quad D_1=\sqrt{cr}D$$

where $Q_n(x)$ is the second kind Legendre function of the order n, $\mathrm{SGN}(c-r)$ is $+1$, 0, -1 according to positive, zero, or negative value for $(c-r)$, respectively, and $\Pi(p,k)$ is a complete elliptic integral of the third kind.

4.2 Stresses. Here we show the stresses σ_{ij} caused by a circular cylindrical inclusion in a transversely isotropic solid. Substituting Eq. (1) into Eq. (17) yields

$$\sigma_{ij}=2\pi c\varepsilon_0c_{13}\int_{-b}^{b}\sigma_{ij}^1(r,z,c,h)dh+2\pi\varepsilon_0c_{33}\int_0^c a\{\sigma_{ij}^3(r,z,a,b)-\sigma_{ij}^3(r,z,a,-b)\}da-\sigma_{ij}^*. \tag{22}$$

Integrating Eq. (22) with respect to h and a, we get

$$\sigma_r=\frac{2c\varepsilon_0c_{13}}{\pi D}\int_0^\infty\int_0^\infty J_1(\alpha c)\frac{\alpha}{\beta r}[J_1(\alpha r)(c_{12}-c_{11})A_1+\alpha rJ_0(\alpha r)\{c_{11}A_1-c_{13}(c_{13}+c_{44})A_3\}]\sin\beta b\cos\beta z\,d\alpha\,d\beta+\frac{2c\varepsilon_0c_{33}}{\pi D}\int_0^\infty\int_0^\infty J_1(\alpha c)\left[\frac{\alpha}{\beta r}J_1(\alpha r)(c_{13}+c_{44})(c_{11}-c_{12})A_3-J_0(\alpha r)\left\{c_{11}(c_{13}+c_{44})\frac{\alpha^2}{\beta}A_3-c_{13}\beta A_2\right\}\right]\times\sin\beta b\cos\beta z\,d\alpha\,d\beta,$$

$$\sigma_\theta=\frac{2c\varepsilon_0c_{13}}{\pi D}\int_0^\infty\int_0^\infty J_1(\alpha c)\frac{\alpha}{\beta r}[J_1(\alpha r)(c_{11}-c_{12})A_1+\alpha rJ_0(\alpha r)\{c_{12}A_1-c_{13}(c_{13}+c_{44})A_3\}]\sin\beta b\cos\beta z\,d\alpha\,d\beta+\frac{2c\varepsilon_0c_{33}}{\pi D}\int_0^\infty\int_0^\infty J_1(\alpha c)\left[\frac{\alpha}{\beta r}J_1(\alpha r)(c_{13}+c_{44})(c_{12}-c_{11})A_3-J_0(\alpha r)\left\{c_{12}(c_{13}+c_{44})\frac{\alpha^2}{\beta}A_3-c_{13}\beta A_2\right\}\right]\times\sin\beta b\cos\beta z\,d\alpha\,d\beta, \tag{23}$$

$$\sigma_z=\frac{2c\varepsilon_0c_{13}}{\pi D}\int_0^\infty\int_0^\infty J_1(\alpha c)J_0(\alpha r)\frac{\alpha^2}{\beta}\{c_{13}A_1-c_{33}(c_{13}+c_{44})A_3\}$$
$$\times\sin\beta b\cos\beta zd\alpha d\beta+\frac{2c\varepsilon_0c_{33}}{\pi D}\int_0^\infty\int_0^\infty J_1(\alpha c)J_0(\alpha r)$$
$$\times\left\{c_{33}\beta A_2-c_{13}(c_{13}+c_{44})\frac{\alpha^2}{\beta}A_3\right\}\sin\beta b\cos\beta zd\alpha d\beta,$$

$$\tau_{rz}=\frac{2c\varepsilon_0c_{13}c_{44}}{\pi D}\int_0^\infty\int_0^\infty J_1(\alpha c)J_1(\alpha r)\alpha\left\{(c_{13}+c_{44})\frac{\alpha^2}{\beta^2}A_3-A_1\right\}$$
$$\times\sin\beta b\sin\beta zd\alpha d\beta+\frac{2c\varepsilon_0c_{33}c_{44}}{\pi D}\int_0^\infty\int_0^\infty\alpha J_1(\alpha c)J_1(\alpha r)$$
$$\times\{(c_{13}+c_{44})A_3-A_2\}\sin\beta b\sin\beta zd\alpha d\beta.$$

It holds always that $\tau_{r\theta}=\tau_{z\theta}=0$ in the present problem. In Eq. (23), A_n, $(n=1,2,3)$, represent

$$A_1=\frac{c_{33}-c_{44}c_1^2}{\alpha^2+c_1^2\beta^2}-\frac{c_{33}-c_{44}c_2^2}{\alpha^2+c_2^2\beta^2},$$
$$A_2=\frac{c_{44}-c_{11}c_1^2}{\alpha^2+c_1^2\beta^2}-\frac{c_{44}-c_{11}c_2^2}{\alpha^2+c_2^2\beta^2}, \tag{24}$$
$$A_3=\frac{1}{\alpha^2+c_1^2\beta^2}-\frac{1}{\alpha^2+c_2^2\beta^2}.$$

Integrals in Eq. (23) can be performed by using integral formulas, [13,14], as follows:

(1) Stress σ_r;

(i) for $b\leqslant|z|$;

$$\sigma_r=\frac{c\varepsilon_0c_{13}}{4\pi D_1}\sum_{n=1}^{2}(-1)^{n+1}\Bigg(\frac{c_{12}-c_{11}}{r}(c_{33}-c_{44}c_n^2)(q_{81n}-q_{82n})$$
$$+\{c_{11}(c_{33}-c_{44}c_n^2)-c_{13}(c_{13}+c_{44})\}(q_{31n}-q_{32n})\Bigg)$$
$$+\frac{c\varepsilon_0c_{33}}{4\pi D_1}\sum_{n=1}^{2}(-1)^{n+1}\Bigg[\frac{(c_{13}+c_{44})(c_{11}-c_{12})}{r}(q_{81n}-q_{82n})$$
$$-c_{1113n}(q_{31n}-q_{32n})\Bigg] \tag{25}$$

(ii) for $b\geqslant|z|$;

$$\sigma_r=\frac{2c\varepsilon_0c_{13}}{4\pi D}B+\frac{c\varepsilon_0c_{33}}{4\pi D_1}\sum_{n=1}^{2}(-1)^{n}\Bigg[\frac{(c_{13}+c_{44})(c_{11}-c_{12})}{r}$$
$$\times(q_{81n}+q_{82n})-c_{1113n}(q_{31n}+q_{32n})\Bigg] \tag{26}$$

with

$$B=\frac{c_{12}-c_{11}}{2r}\pi\sum_{n=1}^{2}(-1)^n\Bigg(c_{44}c_n^2\left\{\frac{r}{c}+\frac{c}{r}+\left(\frac{r}{c}-\frac{c}{r}\right)\mathrm{SGN}(c-r)\right\}$$
$$+\frac{1}{\pi\sqrt{cr}}(c_{33}-c_{44}c_n^2)(q_{81n}+q_{82n})\Bigg)$$
$$+\frac{c_{11}\pi}{c}c_{44}(c_2^2-c_1^2)\{1+\mathrm{SGN}(c-r)\}$$
$$+\frac{1}{2\sqrt{cr}}\sum_{n=1}^{2}(-1)^n\{c_{11}(c_{33}-c_{44}c_n^2)-c_{13}(c_{13}+c_{44})\}$$
$$\times(q_{31n}+q_{32n}) \tag{27}$$

(2) Stress σ_θ;

(i) for $b\leqslant|z|$;

$$\sigma_\theta=\frac{c\varepsilon_0c_{13}}{4\pi D_1}\sum_{n=1}^{2}(-1)^{n+1}\Bigg(\frac{c_{11}-c_{12}}{r}(c_{33}-c_{44}c_n^2)(q_{81n}-q_{82n})$$
$$+\{c_{12}(c_{33}-c_{44}c_n^2)-c_{13}(c_{13}+c_{44})\}(q_{31n}-q_{32n})\Bigg)$$
$$+\frac{c\varepsilon_0c_{33}}{4\pi D_1}\sum_{n=1}^{2}(-1)^{n+1}\Bigg[\frac{(c_{13}+c_{44})(c_{12}-c_{11})}{r}(q_{81n}-q_{82n})$$
$$-c_{1213n}(q_{31n}-q_{32n})\Bigg] \tag{28}$$

(ii) for $b\geqslant|z|$;

$$\sigma_\theta=\frac{2c\varepsilon_0c_{13}}{4\pi D}B+\frac{c\varepsilon_0c_{33}}{4\pi D_1}\sum_{n=1}^{2}(-1)^{n}\Bigg[\frac{(c_{13}+c_{44})(c_{12}-c_{11})}{r}$$
$$\times(q_{81n}+q_{82n})-c_{1213n}(q_{31n}+q_{32n})\Bigg] \tag{29}$$

with

$$B=\frac{c_{11}-c_{12}}{2r}\pi\sum_{n=1}^{2}(-1)^n\Bigg(c_{44}c_n^2\left\{\frac{r}{c}+\frac{c}{r}+\left(\frac{r}{c}-\frac{c}{r}\right)\mathrm{SGN}(c-r)\right\}$$
$$+\frac{1}{\pi\sqrt{cr}}(c_{33}-c_{44}c_n^2)(q_{81n}+q_{82n})\Bigg)$$
$$+\frac{c_{12}\pi}{c}c_{44}(c_2^2-c_1^2)\{1+\mathrm{SGN}(c-r)\}$$
$$+\frac{1}{2\sqrt{cr}}\sum_{n=1}^{2}(-1)^n\{c_{12}(c_{33}-c_{44}c_n^2)-c_{13}(c_{13}+c_{44})\}$$
$$\times(q_{31n}+q_{32n}) \tag{30}$$

(3) Stress σ_z;

(i) for $b\leqslant|z|$;

$$\sigma_z=\frac{c\varepsilon_0c_{13}}{4\pi D_1}\sum_{n=1}^{2}(-1)^{n+1}\{c_{13}(c_{33}-c_{44}c_n^2)-c_{33}(c_{13}+c_{44})\}$$
$$\times(q_{31n}-q_{32n})+\frac{c\varepsilon_0c_{33}}{4\pi D_1}\sum_{n=1}^{2}(-1)^{n+1}c_{1333n}(q_{31n}-q_{32n}) \tag{31}$$

(ii) for $b\geqslant|z|$;

$$\sigma_z=\frac{2c\varepsilon_0c_{13}}{4\pi D}B+\frac{c\varepsilon_0c_{33}}{4\pi D_1}\sum_{n=1}^{2}(-1)^{n+1}c_{1333n}(q_{31n}+q_{32n}) \tag{32}$$

with

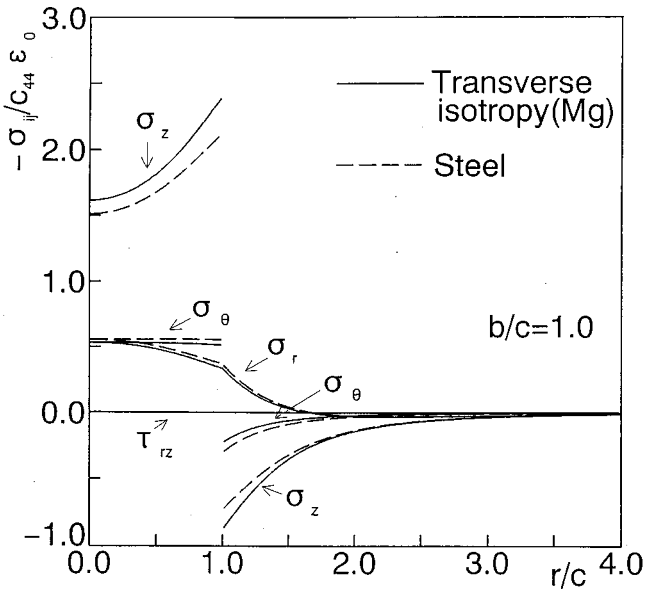

Fig. 3 Distribution of stresses on the plane $z=0$ for magnesium and steel

$$B=\frac{c_{13}\pi}{c}c_{44}(c_2^2-c_1^2)\{1+\mathrm{SGN}(c-r)\}$$

$$-\frac{1}{2\sqrt{cr}}\sum_{n=1}^{2}(-1)^n\{c_{13}(c_{33}-c_{44}c_n^2)-c_{33}(c_{13}+c_{44})\}$$

$$\times(q_{31n}+q_{32n}) \tag{33}$$

(4) Stress τ_{rz};

$$\tau_{rz}=+\frac{c\varepsilon_0c_{33}c_{44}}{2\pi D_1}\sum_{n=1}^{2}(-1)^{n+1}\left\{\frac{c_{33}-c_{44}c_n^2}{c_n}+c_n(c_{13}+c_{44})\right\}$$

$$\times\{Q_{1/2}(x_{1n})-Q_{1/2}(x_{2n})\}, \tag{34}$$

$$+\frac{c\varepsilon_0c_{13}c_{44}}{2\pi D_1}\sum_{n=1}^{2}(-1)^{n+1}\frac{c_{13}+c_{11}c_n^2}{c_n}$$

$$\times\{Q_{1/2}(x_{1n})-Q_{1/2}(x_{2n})\}.$$

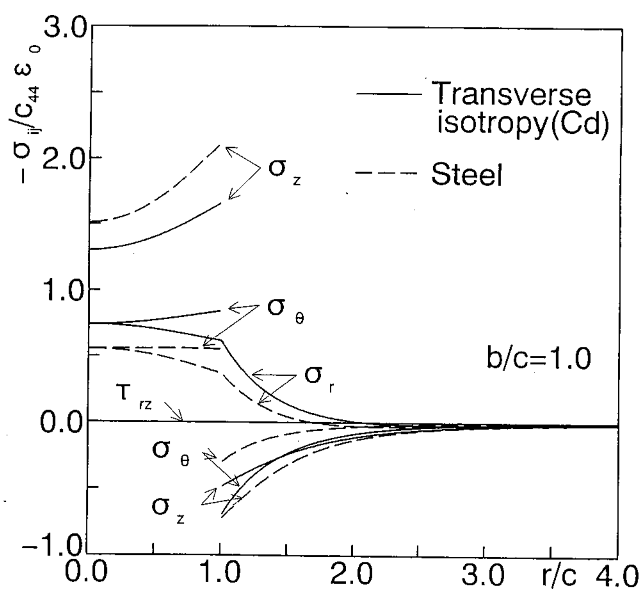

Fig. 4 Distribution of stresses on the plane $z=0$ for cadmium and steel

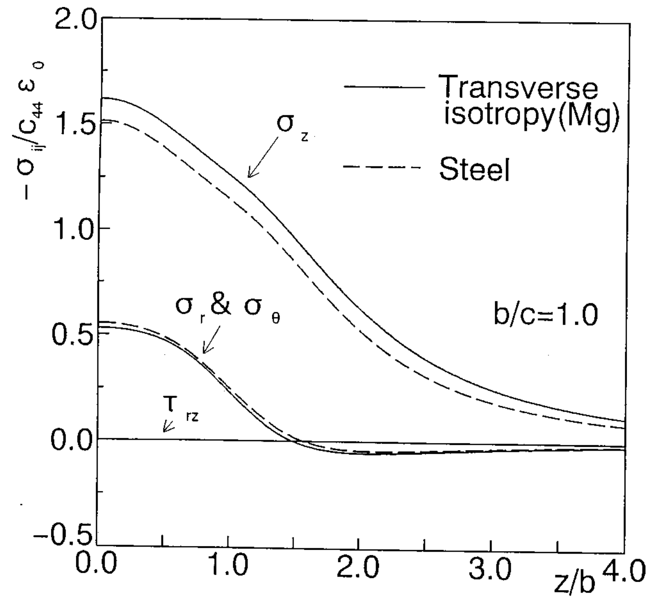

Fig. 5 Variation of stresses along the z-axis for magnesium and steel

In the above expressions, c_{ijkln} and q_{3mn} represent

$$c_{ijkln}=c_{ij}(c_{13}+c_{44})+c_{kl}\frac{c_{44}-c_{11}c_n^2}{c_n^2},$$

$$q_{3mn}=\frac{\pi\sqrt{cr}}{c}\{1+\mathrm{SGN}(c-r)\} \tag{35}$$

$$-\frac{z_{mn}}{c}\left\{Q_{-1/2}(x_{mn})+\frac{c-r}{c+r}k_{mn}\Pi(p,k_{mn})\right\}.$$

5 Strain Energy

The stability of microstructures of materials with inclusions can be discussed in terms of the Gibbes free energy which is the elastic strain energy when the material is traction-free, [1]. Therefore, we show the strain energy in the cylindrical inclusion in a transversely isotropic solid. The strain energy W^* is expressed by

$$W^*=-\frac{1}{2}\int_\Omega\sigma_{ij}\varepsilon_{ij}^*d\Omega \tag{36}$$

where σ_{ij} is the stress caused by the eigenstrain ε_{ij}^*. From Eqs. (1) and (36), we have

$$W^*=-\frac{\varepsilon_0}{2}\int_{-b}^{b}\int_0^c(\sigma_z-c_{33}\varepsilon_0)d\Omega \tag{37}$$

where σ_z is that of Eq. (23). Integrating Eq. (37) by using integral formulas, [13,14], we can obtain

$$W^*=\frac{c^2\varepsilon_0^2}{D}c_{13}\sum_{n=1}^{2}(-1)^n\left(c_{13}(c_{33}-c_{44}c_n^2)\left\{\frac{b}{4}-\frac{c_n}{3\pi}\left(4c-\frac{q_{9n}}{2c}\right)\right\}\right.$$

$$\left.+c_{33}(c_{13}+c_{44})\frac{c_n}{3\pi}\left(4c-\frac{q_{9n}}{2c}\right)\right)$$

$$+\frac{c^2\varepsilon_0^2}{D}c_{13}\sum_{n=1}^{2}(-1)^nc_n\left(\frac{c_{13}(c_{13}+c_{44})}{3}\left(4c-\frac{q_{9n}}{2c}\right)\right.$$

$$\left.+c_{33}(c_{44}-c_{11}c_n^2)\left(\frac{4c}{3}-\frac{q_{9n}}{4c}\right)\right)+\pi bc^2c_{33}\varepsilon_0^2 \tag{38}$$

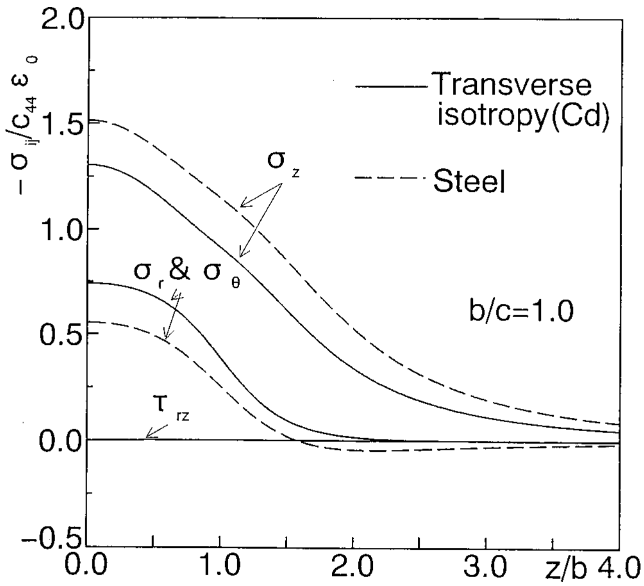

Fig. 6 Variation of stresses along the *z*-axis for cadmium and steel

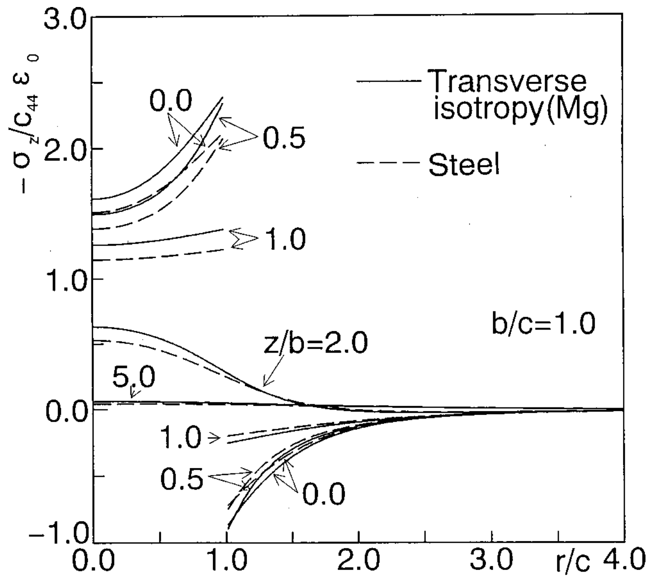

Fig. 8 Variation of stress σ_z for magnesium and steel

with

$$q_{9n}=4c^2G_2(x_n)-\frac{6\pi bc}{c_n}+\frac{4b^2}{c_n^2}\{Q_{1/2}(x_n)+Q_{-1/2}(x_n)\},$$
$$x_n=1+\frac{2b^2}{c^2c_n^2}. \tag{39}$$

6 Discussions and Results

Figures 3–9 show the stress distributions around and in the cylindrical inclusion in the transversely isotropic solids (magnesium and cadmium, as examples) and the isotropic solid (steel, as an example). The figures are sketched in nondimensional form. In these figures, the broken lines show the results for the isotropic solid (steel), which are obtained from the expressions shown above for transversely isotropic solids and the expressions for isotropic solids shown in a previous paper, [4], and both the numerical results agree with each other. From these figures, we see that there are no essential differences between the stress distributions for transversely isotropic solids and those for isotropic solid.

Figures 3, 4 show the stress distributions on the symmetrical plane $(z=0)$ and Figs. 5, 6 show the stress distributions along the z-axis $(r=0)$, under the condition of $b/c=1.0$. In these figures, the stress σ_z has the largest value among the stress components. The largest value for magnesium is larger than that for steel and the value for steel is larger than that of cadmium.

Figures 7, 8 show the distributions of the stress σ_z on the symmetrical plane $(z=0)$ for magnesium. Figure 7 shows the influence of slender ratio b/c of a cylindrical inclusion on the stress distributions. The stress increases as b/c becomes larger and approaches to the upper limit value which appears when $b/c\to\infty$. The stress approaches to uniform distributions according to the increase of b/c. Figure 8 shows the stress variations due to the

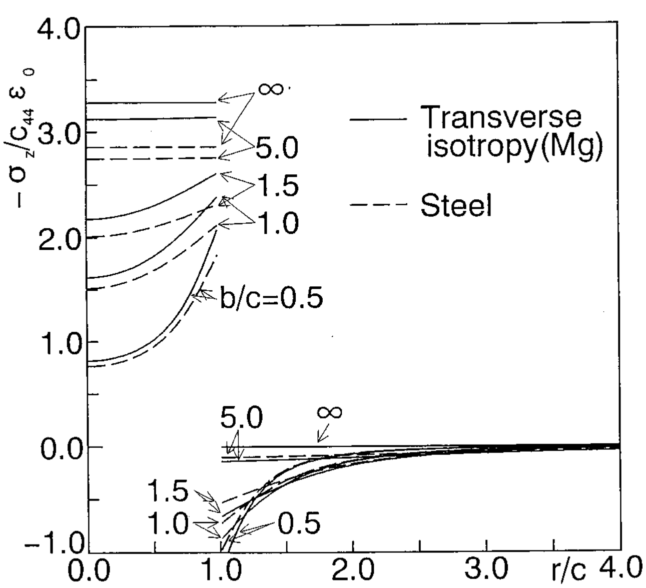

Fig. 7 Effect of the length of inclusion on distributions of stress σ_z on the plane $z=0$ for magnesium and steel

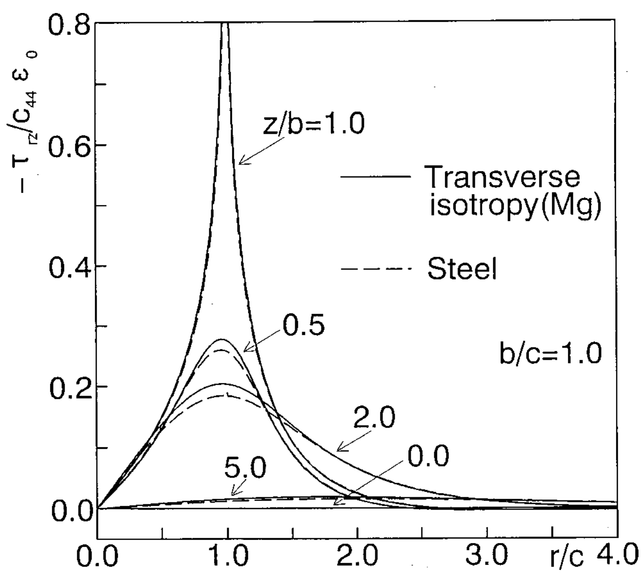

Fig. 9 Variation of shear stress τ_{rz} for magnesium and steel

relative positions z/b under the condition of $b/c=1.0$. The stress has the largest value at $z/b=0$ and decreases as z/b becomes larger.

Figure 9 shows the distributions of the shear stress τ_{rz} for magnesium in the case of $b/c=1.0$. It is observed in the figure that there is a stress singularity in the vicinity of the corner point $(r\to c,\ z\to b)$ of the inclusion. It is easily seen from the relations, [15],

$$\lim_{r\to c,\ |z|\to b} \Pi(p,k_{mn})\to \text{const.}\,\frac{c+r}{c-r},$$
$$\lim_{r\to c,\ |z|\to b} Q_{1/2}(x_{mn})\to \text{const.}\,\log\{(r-c)^2+z_{mn}^2\} \tag{40}$$

that the order of stress singularity is $\log\{(r-c)^2+z_{mn}^2\}$. The result of the logarithmic singularity is the same as that for a cylindrical inclusion, [4], and a cuboidal inclusion, [16], in an isotropic solid.

References

[1] Mura, T., 1982, *Micromechanics of Defects in Solids*, Martinus-Nijhoff, Dordrecht, The Netherlands.
[2] Mura, T., 1988, ''Inclusion Problem,'' Appl. Mech. Rev., **41**(1), pp. 15–20.
[3] Takao, Y., Taya, M., and Chou, T. W., 1981, ''Stress Field Due to a Cylindrical Inclusion With Constant Axial Eigenstrain in an Infinite Elastic Body,'' ASME J. Appl. Mech., **48**, pp. 853–858.
[4] Hasegawa, H., Lee, V. G., and Mura, T., 1992, ''The Stress Fields Caused by a Circular Cylindrical Inclusion,'' ASME J. Appl. Mech., **59**, Part 2, pp. s107–s114.
[5] Hasegawa, H., Lee, V. G., and Mura, T., 1993, ''Hollow Circular Cylindrical Inclusion at the Surface of a Half-Space,'' ASME J. Appl. Mech., **60**, pp. 33–40.
[6] Wu, L. Z., and Du, S. Y., 1995, ''The Elastic Field Caused by a Circular Cylindrical Inclusion—Part I,'' ASME J. Appl. Mech., **62**, pp. 579–584.
[7] Wu, L. Z., and Du, S. Y., 1995, ''The Elastic Field Caused by a Circular Cylindrical Inclusion—Part II,'' ASME J. Appl. Mech., **62**, pp. 585–589.
[8] Wu, L. Z., and Du, S. Y., 1996, ''The Elastic Field in a Half-Space With a Circular Cylindrical Inclusion,'' ASME J. Appl. Mech., **63**, pp. 925–932.
[9] Hasegawa, H., and Yoshiie, K., 1996, ''Tension of Elastic Solid With Elastic Circular-Cylindrical Inclusion,'' JSME Int. J., Ser. A, **39**(2), pp. 186–191.
[10] Hasegawa, H., and Ariyoshi, S., 1996, ''Fundamental Solution for Axisymmetric Problems of Transversely Isotropic Elastic Solid,'' (in Japanese), Trans. Jpn. Soc. Mech. Eng., Ser. A, **62**(596), pp. 1059–1063.
[11] Eubanks, R. A., and Sternberg, E., 1954, ''On the Axisymmetric Problem of Elasticity Theory for Medium With Transverse Isotropy,'' J. Ration. Mech. Anal., **3**(1), pp. 89–101.
[12] Ishida, R., 1987, ''Crack Problem in a Transversely Isotropic Medium With a Penny-Shaped Crack Under Transient Thermal Loading,'' Z. Angew. Math. Mech., **67**(2), pp. 93–99.
[13] Erdelyi, A., 1954, *Tables of Integral Transforms*, Vol. 2, McGraw-Hill, New York.
[14] Eason, G., Noble, B., and Sneddon, I. N., 1955, ''On Certain Integrals of Lipschitz-Hankel Type Involving Products of Bessel Functions,'' Philos. Trans. R. Soc. London, Ser. A, **247**(A935), pp. 529–551.
[15] Byrd, P. F., and Friedman, M. D., 1971, *Handbook of Elliptic Integrals for Engineers and Scientists*, 2nd Ed., Springer-Verlag, New York.
[16] Chiu, Y. P., 1977, ''On the Stress Field Due to Initial Strains in a Cuboid Surrounded by an Infinite Elastic Space,'' ASME J. Appl. Mech., **44**, pp. 587–590.

Tubular Adhesive Joints Under Axial Load

N. Pugno
e-mail: nicola.pugno@polito.it

A. Carpinteri
e-mail: alberto.carpinteri@polito.it

Department of Structural Engineering,
Politecnico di Torino,
Corso Duca Degli Abruzzi 24
10129 Torino, Italy

In this paper a general study on tubular adhesive joint under axial load is presented. We focus our attention on both static and dynamic behavior of the joint, including shear and normal stresses and strains in the adhesive layer, joint optimization, failure load for brittle crack propagation, and crack detection based on free vibrations. First, we have considered the shear and normal stresses and strains in the adhesive layer to propose an optimization to uniform axial strength (UAS) and to reduce the stress peaks in the bond. The stress analysis confirms that the maximum shear stresses are attained at the ends of the adhesive and that the peak of maximum shear stress is reached at the end of the stiffer tube and does not tend to zero as the adhesive length approaches infinity. A fracture energy criterion to predict brittle crack propagation for conventional and optimized joint is presented. The stability of brittle crack propagation and the strength of the joint, as well as the ductile-brittle failure transition, are analyzed. A detection method to predict crack severity, based on joint dynamic behavior, is also proposed. The crack detection is achieved through the determination of the axial natural frequencies of the joint as a function of the crack length, by determining the roots of a determinantal equation.
[DOI: 10.1115/1.1604835]

1 Introduction

Based on modern synthetic adhesives, light, stiff, and economic constructions can be fabricated from a variety of materials without the defects caused by conventional assembly methods, such as welding, soldering, and riveting. Furthermore, together with mechanical strength and stiffness, a number of extra benefits come along free, like sealing action, electrical and thermal insulation, corrosion, and fretting resistance. As a consequence, various kinds of adhesive-bonded joints have been used in the manufacturing of light structures. For example, an analysis was carried out on bonded airframe components from an original Comet aircraft, which was over 30 years old. Redux phenolic adhesives were used extensively to bond stringer/panel assemblies. By careful removal of the bonded areas from the stiffener flange/panel it was possible to obtain lap and wedge cleavage test pieces. The same generic adhesive product continues to be used in current airframe construction. It can be seen that strength and durability of the old Comet test pieces are only about 10% lower than new joints, and some of the differences may be attributable to improvements in the new adhesive rather than degradation of the old joints, [1].

Since the pioneering papers by Goland and Reissner [2], Lubkin and Reissner [3], and more recently by Adams and Peppiatt [4], Renton and Vinson [5], Delale and Erdogan [6], and Chen and Cheng [7], several theoretical, numerical, and experimental analysis on tubular bonded joints have been performed. Only recently nontubular structures have been investigated by Pugno et al. [8–10].

In this paper we propose a special type of tubular joint with tapered adherends, produced by modifying the joint profile and thereby optimizing the tubular joint for uniform axial strength (UAS). As a consequence, the predominant component of the adhesive stress tensor (equivalent to the applied axial load) becomes constant, and the stress peaks of the other components are drastically reduced. This result is of considerable practical utility and makes it possible to produce adhesive bonded joints which are both lighter and stronger under axial load. An analogous optimization for uniform torsional strength (UTS) has been presented in [11].

The brittle failure load for a tubular adhesive joint under axial load, as well as a dynamical approach to crack detection are investigated. A very general formula has been obtained by means of the Griffith [12] energy balance and the application of linear elastic fracture mechanics (see Carpinteri's papers [13–17,18]). It is supposed that crack propagation at the interface between the two adherends takes place in mode I in the adhesive at the point of highest stress concentration, deduced by stress analysis. An energy balance is formulated for a small growth of the debonding: Changes in the strain energy of the joint and in the potential energy of the loading device are equated to the characteristic energy needed for debonding, [19,20]. As a consequence, a general formula to predict the brittle failure load for a tubular adhesive joint with or without UAS tapered adherends can be obtained. This formula generalizes an analogous formula already presented in the literature for tubular joint between a perfectly rigid and an elastic nontapered tubes, [19]. The greater sensitivity to brittle collapse is emphasized for the conventional geometry, if it is compared with the UAS optimized profile one. The stability of brittle crack propagation and the size effects on mechanical collapse behavior, as well as the ductile-brittle transition are emphasized.

A detection method to predict the crack length, influencing the strength of the joint, based on the joint dynamic behavior, is also presented. The study of the joint dynamics provides a system of coupled differential equations with partial derivatives. The crack detection is achieved through the determination of the axial natural frequencies of the damaged joint as a function of the crack length, by determining the roots of the corresponding determinantal equation. This approach has already been successfully applied to the study of undamaged bonded joints under torsion, [21].

Relevant general works on bonded joints and composite materials can be founded in [22–28].

2 Shear Stresses

It is assumed that all three of the materials making up the joint (tubes and adhesive) are governed by isotropic linear elasticity. The tubular bonded joint, consisting of two tubes perfectly circular and co-axial and the interposed adhesive's film (of very small

Contributed by the Applied Mechanics Division of THE AMERICAN SOCIETY OF MECHANICAL ENGINEERS for publication in the ASME JOURNAL OF APPLIED MECHANICS. Manuscript received by the ASME Applied Mechanics Division, June 5, 2002; final revision, Feb. 12, 2003. Associate Editor: M.-J. Pindera. Discussion on the paper should be addressed to the Editor, Prof. Robert M. McMeeking, Department of Mechanical and Environmental Engineering, University of California–Santa Barbara, Santa Barbara, CA 93106-5070, and will be accepted until four months after final publication of the paper itself in the ASME JOURNAL OF APPLIED MECHANICS.

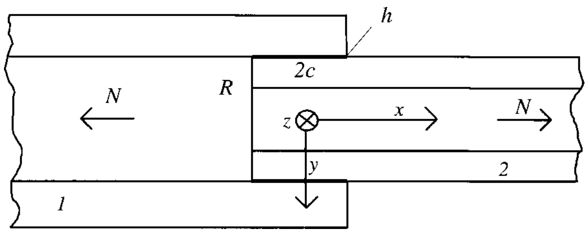

Fig. 1 Tubular adhesive joint subjected to axial load

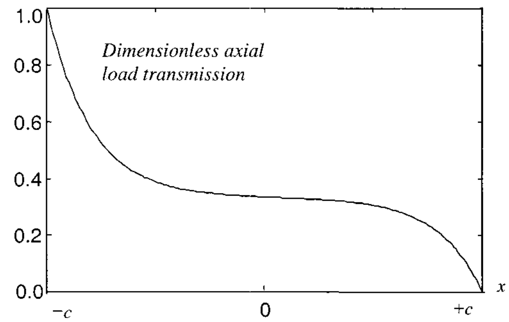

Fig. 2 Qualitative diagram (α=1, β=1/3) for dimensionless axial load transmission $f(x)$

thickness h, axial length $2c$, and radius R), is considered to be subject to axial load (Fig. 1). Under these conditions, the axial equilibrium along the x-axis permits to obtain the predominant component of adhesive stress tensor, equivalent to the applied normal thrust:

$$\tau_{rx}(x) = -\frac{1}{2\pi R}\frac{dN_1(x)}{dx}, \tag{1}$$

where $N_1(x)$ is the axial load of the outer tube in a generic x section. As a consequence of the axial symmetry, the other components of the stress tangential field can be neglected:

$$\tau_{r\vartheta}(x) \approx 0, \quad \tau_{x\vartheta}(x) \approx 0. \tag{2}$$

The strain component γ_{rx} in the adhesive can be obtained as

$$\gamma_{rx}(x) = \frac{\tau_{rx}(x)}{G_a} = -\frac{1}{2\pi R G_a}\frac{dN_1(x)}{dx}, \tag{3}$$

where G_a is the shear elastic modulus of the adhesive. Obviously we have

$$\gamma_{r\vartheta}(x) \approx 0, \quad \gamma_{x\vartheta}(x) \approx 0. \tag{4}$$

The axial load $N_i(x)$ in a generic section x of the tube i can be written as

$$N_1(x) = Nf(x), \quad N_2(x) = N(1 - f(x)), \tag{5}$$

as the sum of the forces absorbed by the two elements must be equivalent to the applied axial load N at each cross section x. Satisfying the load boundary conditions implies

$$f(x=-c) = 1, \quad f(x=+c) = 0. \tag{6}$$

Function $f(x)$, and thus the load absorbed by the two elements at the joint, can be found thanks to the compatibility established for the displacements of the two tubes in a given cross sections. These displacements are expressed as follows:

$$u_1(x) = \int_{-c}^{x} \frac{N_1(t)}{E_1 A_1} dt + u_1^0, \tag{7a}$$

$$u_2(x) = \int_{-c}^{x} \frac{N_2(t)}{E_2 A_2} dt + u_2^0, \tag{7b}$$

where E_i is the Young's modulus, A_i is the cross-section area, and u_i^0 is the displacement of the initial section ($x=-c$), of the tube i. Through an appropriate choice of reference system, we can always have $u_1^0 = 0$ (displacements calculated starting from the strained configuration of the first tube's initial section).

The compatibility equation can be written noting how, after the joint deformation, the relative displacement Δu between two points of interfaces, internal tube-adhesive, and adhesive-external tube, must be the same if we consider the tubes' relative displacement or the shearing adhesive's strain (with a very small thickness h):

$$\Delta u = u_2 - u_1 = h\gamma_{rx}(x). \tag{8}$$

Substituting Eq. (3) into Eq. (8), the compatibility equation can be rewritten as

$$\frac{dN_1(x)}{dx} = -K^*\Delta u(x), \quad K^* = \frac{2\pi R G_a}{h}, \tag{9}$$

where K^* is the adhesive stiffness per unit length.

Inserting the displacement expressions (7) in the compatibility Eq. (9), and recalling Eqs. (5) and (6), gives the following second-order differential equation in $f(x)$:

$$\frac{d^2 f(x)}{dx^2} - \frac{K^*(E_1A_1 + E_2A_2)}{E_1A_1E_2A_2} f(x) = -\frac{K^*}{E_2A_2},$$

$$\text{boundary conditions} \begin{cases} f(x=-c) = 1 \\ f(x=c) = 0 \end{cases}. \tag{10}$$

This differential equation, together with the boundary conditions shown alongside, makes it possible to determine the load section by section at the overlap. The solution of Eq. (10) is

$$f(x) = C_1 e^{\alpha x} + C_2 e^{-\alpha x} + \beta, \quad \alpha = \sqrt{\frac{K^*(E_1A_1 + E_2A_2)}{E_1A_1E_2A_2}},$$

$$\beta = \frac{E_1A_1}{E_1A_1 + E_2A_2}. \tag{11}$$

The constants C_1 and C_2 can be obtained from the boundary conditions as

$$C_1 = \frac{e^{-\alpha c}}{e^{-2\alpha c} - e^{2\alpha c}} + \beta\frac{e^{\alpha c} - e^{-\alpha c}}{e^{-2\alpha c} - e^{2\alpha c}}, \tag{12a}$$

$$C_2 = \frac{e^{\alpha c}}{e^{2\alpha c} - e^{-2\alpha c}} + \beta\frac{e^{-\alpha c} - e^{\alpha c}}{e^{2\alpha c} - e^{-2\alpha c}}. \tag{12b}$$

Comparing the differences between Eqs. (7) with the same obtained by Eq. (9), makes it possible to determine the constant u_2^0, once the reference system has been established with $u_1^0 = 0$:

$$u_2^0 = \frac{N\alpha}{K^*}(C_2 e^{\alpha c} - C_1 e^{-\alpha c}). \tag{13}$$

Function $f(x)$, being known (see Eqs. (11), (12), and Fig. 2), finally we can obtain the predominant shear stress in the adhesive:

$$\tau_{rx}(x) = -\frac{N}{2\pi R}\frac{df(x)}{dx}. \tag{14}$$

The maximum shear stresses are reached at the ends of the adhesive and the higher stress peak appears at the end of the stiffer tube. When the stiffnesses of the two tubes are equal (β=1/2), the stress peaks become lower and symmetric (Fig. 3). The presented stress approach has already been validated numerically for the case of nontubular bonded joints. The discrepancy on stress peak appears lower than 5%, [10].

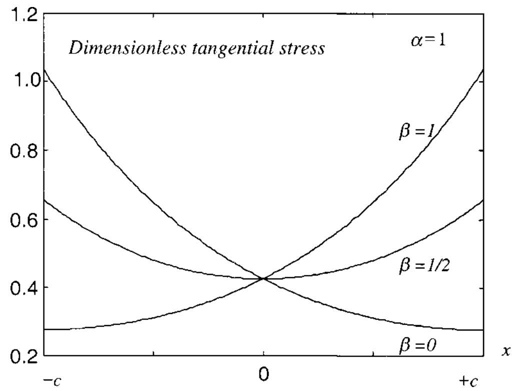

Fig. 3 Qualitative diagram for the dimensionless tangential stress $-df(x)/dx$

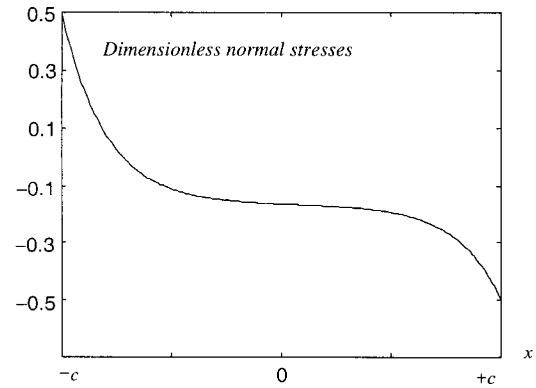

Fig. 4 Qualitative diagram (α=1, β=1/3) for the dimensionless normal stresses ($f(x)-1/2$)

This analysis does not include transverse shear deformation and because of this maximum shear stresses occur very near to but not at the ends of the joints. Obviously, the shearing stresses must be zero at the ends of the joint because there can be no shear stresses on the adhesive free surface, hence no shear stresses in the adhesive at the joint end because of equilibrium. For more details on transverse shear deformation see [22].

3 Normal Stresses

If $v_i(r,x)=-\nu_i N_i/(E_i A_i) r$ is the radial displacement of the tube i (ν_i is its Poisson's ratio), we can obtain the dilations imposed to the adhesive layer ($r\cong R$):

$$\varepsilon_r(x)=\frac{v_1(R,x)-v_2(R,x)}{h}=\frac{NR}{h}\left(\frac{\nu_2(1-f(x))}{E_2A_2}-\frac{\nu_1 f(x)}{E_1A_1}\right), \tag{15a}$$

$$\varepsilon_\theta(x)=\frac{\Delta R}{R}=\frac{v_1(R,x)+v_2(R,x)}{2R}=\frac{N}{2}\left(\frac{\nu_2(f(x)-1)}{E_2A_2}-\frac{\nu_1 f(x)}{E_1A_1}\right), \tag{15b}$$

$$\varepsilon_x(x)=\frac{\partial(u_1(x)+u_2(x))}{2\partial x}=\frac{N}{2}\left(\frac{f(x)}{E_1A_1}+\frac{(1-f(x))}{E_2A_2}\right), \tag{15c}$$

and the normal stresses by the constitutive equations for the adhesive,[18],

$$\sigma_x(x)=\frac{(1-\nu_a)E_a}{(1+\nu_a)(1-2\nu_a)}\varepsilon_x(x)+\frac{\nu_a E_a}{(1+\nu_a)(1-2\nu_a)}(\varepsilon_r(x)+\varepsilon_\theta(x)), \tag{16a}$$

$$\sigma_r(x)=\frac{(1-\nu_a)E_a}{(1+\nu_a)(1-2\nu_a)}\varepsilon_r(x)+\frac{\nu_a E_a}{(1+\nu_a)(1-2\nu_a)}(\varepsilon_x(x)+\varepsilon_\theta(x)), \tag{16b}$$

$$\sigma_\theta(x)=\frac{(1-\nu_a)E_a}{(1+\nu_a)(1-2\nu_a)}\varepsilon_\theta(x)+\frac{\nu_a E_a}{(1+\nu_a)(1-2\nu_a)}(\varepsilon_x(x)+\varepsilon_r(x)), \tag{16c}$$

where E_a, ν_a are the Young modulus and the Poisson's ratio for the adhesive material.

It is interesting to note that if we consider identical material and cross-section areas for the two tubes ($\nu=\nu_1=\nu_2$, $EA=E_1A_1=E_2A_2$) we obtain $\varepsilon_\vartheta=-\nu\varepsilon_x$ with $\varepsilon_x=N/(2EA)$. This physically means that the strain in the adhesive layer along the x-direction is simply imposed by the elongation of the tubes supposed loaded with a constant force equal to its mean value. In these hypothesis the normal stresses (16) assume the form $\sigma_{x,r,\theta}(x)\approx B+D(f(x)-1/2)$ with B, D constants (Fig. 4). Being $R/h\gg 1$ ($B/D\approx 0$) the stress peaks, at the end of the adhesive layer, become $\sigma_{x,\vartheta\,\max}\approx\mp\nu_a\nu/((1+\nu_a)(1-2\nu_a))E_aRN/(EhA)$, $\sigma_{r\,\max}\approx(1-\nu_a)/\nu_a\sigma_{x,\vartheta\,\max}$, i.e., proportional to $E_aRN/(EhA)$.

4 Stress Concentration Factor

The main problem related to the stress peaks is connected to the predominant tangential stress field (14), that in fact cannot be deleted, being equivalent to the applied axial load. On the other hand, the normal stress field (16) has a mean value equal to zero with maximum stresses independent of the function f, that must satisfy the boundary conditions (6). For these reasons we focus our attention on the tangential stress field (14).

Considering Eq. (14) it is possible to define a stress concentration factor which indicates the extent to which maximum shear stress departs from the mean. The higher stress peak appears at the end of the stiffer tube ($x=\bar{c}$):

$$\tau_{rx\,\max}=\tau_{rx}(x=\bar{c})=\frac{N\alpha}{2\pi R}(-C_1e^{\alpha\bar{c}}+C_2e^{-\alpha\bar{c}}),$$

$$\bar{c}=\begin{cases}-c & 0<\beta<\dfrac{1}{2}\\ c & \dfrac{1}{2}\le\beta<1\end{cases}. \tag{17}$$

The mean value of the stress is

$$\tau_{rx\,\text{mean}}=\frac{1}{2c}\int_{-c}^{+c}\tau_{rx}(x)dx=\frac{N}{4\pi Rc}. \tag{18}$$

Consequently, the stress concentration factor is given by

$$\lambda=\frac{\tau_{rx\,\max}}{\tau_{rx\,\text{mean}}}=2\alpha c(-C_1e^{\alpha\bar{c}}+C_2e^{-\alpha\bar{c}}). \tag{19}$$

Of importance is the gain parameter λ^*, i.e., the index of the gain in maximum stress leveling which can be obtained by increasing the bond length. In this context, it should be noted that as the bond length tends to infinity, the maximum stress tends asymptotically to a minimum nonzero value:

$$\tau_{rx\,\max\,\min}=\lim_{c\to\infty}\tau_{rx\,\max}=\frac{N\alpha\beta}{2\pi R}. \tag{20}$$

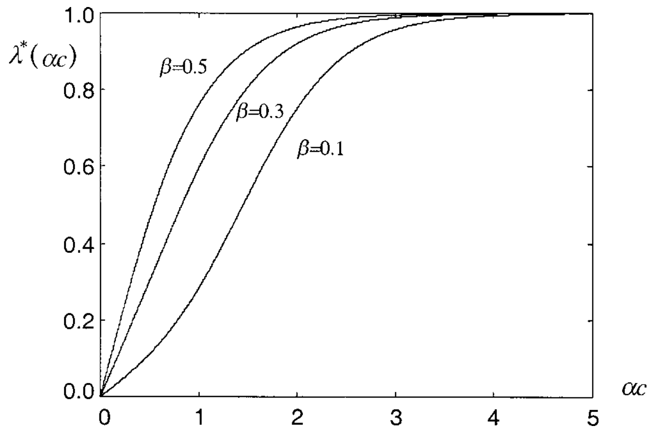

Fig. 5 Gain parameter $\lambda^*(\alpha c)$

For example, if we consider identical material and cross-section areas for the two tubes, we have $\tau_{\substack{rx\\ \max\\ \min}} = \sqrt{G_a/(EARh)}N/(2\sqrt{\pi})$. The gain parameter can thus be defined as

$$\lambda^*(\alpha c) = \frac{\tau_{\substack{rx\\ \max\\ \min}}}{\tau_{\substack{rx\\ \max}}} = \frac{\beta}{(-C_1 e^{\overline{\alpha c}} + C_2 e^{-\overline{\alpha c}})}, \tag{21}$$

and must be as close to unity as it is compatible with the need for a compact joint. Under this assumption the stress concentration factor, prudently overestimated, is detailed as follows:

$$\lambda \cong 2\alpha\beta c \quad \text{for } \lambda^* \cong 1. \tag{22}$$

Figure 5 shows that gain parameter λ^* presents little variation after a certain value of the nondimensional parameter αc ($\sim$3); consequently, further increases in bond length are pointless for the axial strength. Furthermore β must be equal to 1/2 (same stiffness EA for the two tubes) to have a symmetric stress field. Under these assumptions the stress concentration factor appears to be close to 3, an often-used value in elastic problems. This value for the stress concentration factor is very common for the stress peaks in the adhesive layer of tubular and nontubular bonded joints, [10,11].

5 Optimization for Uniform Axial Strength (UAS)

In order to obtain a unit value for the stress concentration factor given by Eq. (19) it is possible to modify the joint profile. This is achieved by chamfering the edges, which are in any case not involved in the tube stress flow induced by the axial load.

The procedure used is a reversal of that employed for a joint of known geometry: rather than starting from the geometry in order to determine the stress field, the procedure starts with the stress field and determines the geometry capable of ensuring it.

In order to make the predominant stress component (1) constant, it must be independent of the *x*-coordinate. In other words, as shown by relation (14), the load must be linear along the joint *x*-axis:

$$f(x) = \left(\frac{1}{2} - \frac{x}{2c}\right). \tag{23}$$

Inserting Eq. (23) in Eq. (10) yields the following relation, which defines the geometry of a uniform axial strength (UAS) adhesive bonded joint:

$$\frac{E_2A_2(x)}{E_1A_1(x)} = \frac{c+x}{c-x}, \tag{24}$$

that represents the equation governing the UAS profile. From Eq. (24) we can seen that the cross-section area of the two optimized tubes must go to zero at the end of the adhesive layer.

Though the number of possible shapes which satisfy the relations indicated above is infinite, the following additional condition must be considered in order to obtain the solution entailing tubes with symmetric stiffness section by section:

$$E_1A_1(x) = E_2A_2(-x), \tag{25}$$

that permits to have an identical stiffness EA for the two tubes out of the bonded area. As a consequence, we obtain the following optimized UAS profiles:

$$E_1A_1(x) = \frac{c-x}{2c}EA, \quad E_2A_2(x) = \frac{c+x}{2c}EA. \tag{26}$$

For example, if we consider identical material and cross-section areas for the two tubes, supposed with thin thickness s_i, we have $s_1(x) \approx (c-x)/(2c)\cdot s$, $s_2(x) \approx (c+x)/(2c)\cdot s$ with $s_1 + s_2 = s$. For this particular case the optimization is corresponding to a perfectly linear tapering of the adherends.

In this context, it should be noted that as the bond length tends to infinity, the stress (equal to the mean value expressed by Eq. (18)) tends asymptotically to a minimum zero value. This is a very important behavior of the UAS joint because theoretically, differently from a nontapered joint, the adhesive can withstand every axial load simply modifying its length surface. This upper bound of force, increasing the adhesive length, for nontapered adherends is (supposing identical material and cross-section areas for the two tubes, and the collapse when $\tau_{\substack{rx\\ \max}} = \tau_f$) $N_f(c \to \infty) = \sqrt{4\pi RhEA/G_a}\tau_f$, and is infinity for the optimized joint.

The optimization permits to have a constant tangential stress and also a large reduction in the normal stresses. Putting Eq. (23) into Eq. (14) we obtain the tangential stress in the UAS joint:

$$\tau_{\substack{rx\\ \mathrm{UAS}}} = \frac{N}{4\pi Rc}. \tag{27}$$

Putting Eqs. (23) and (26) into Eqs. (15), supposing to simplify the equations $\nu = \nu_1 = \nu_2$, we obtain the dilations in the UAS joint: $\varepsilon_r = 0$, $\varepsilon_\theta = -\nu N/(EA)$, $\varepsilon_x = N/A$. Putting them into Eqs. (16) we obtain the normal stresses in the UAS joint that appear constants along the *x*-axis:

$$\sigma_x = \frac{1-\nu_a-\nu\nu_a}{(1+\nu_a)(1-2\nu_a)}\frac{E_aN}{EA}, \tag{28a}$$

$$\sigma_r = \frac{\nu_a-\nu\nu_a}{(1+\nu_a)(1-2\nu_a)}\frac{E_aN}{EA}, \tag{28b}$$

$$\sigma_\vartheta = \frac{\nu_a-\nu+\nu\nu_a}{(1+\nu_a)(1-2\nu_a)}\frac{E_aN}{EA}, \tag{28c}$$

i.e., proportional to $E_aN/(EA)$. For nonoptimized joint the maximum normal stresses are of the order of $E_aRN/(EhA)$, so that the optimization has provided a theoretical reduction by a factor R/h (1,2, or 3 order of magnitude).

However, it is important to note that adhesive bonded joints could be susceptible to brittle collapse. In order to take advantage of the UAS joint geometry it is essential that appropriate technological measures be introduced to ensure that joint collapse cannot involve mechanical fracture phenomena.

6 Energy Balance During Crack Propagation

By virtue of the energy balance, the following relationship between the variation in the total potential energy dW and the fracture energy $\mathcal{G}\,\mathrm{d}S$ must hold:

$$\mathcal{G}\mathrm{d}S + \mathrm{d}W = 0, \tag{29}$$

where dS represents the incremental fracture surface area.

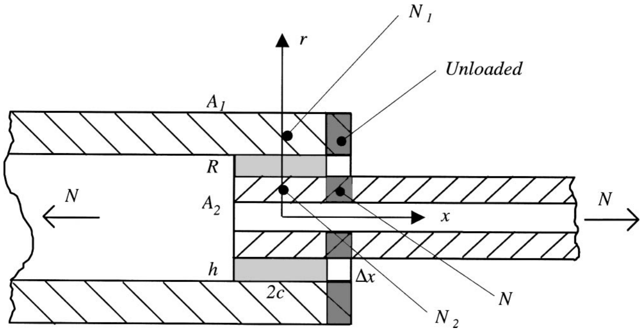

Fig. 6 Adhesive debonding for tubular adhesive joint subjected to axial load

Considering an imposed axial load, the variation in the total potential energy is equal to

$$dW = dL - N du = d\left(\frac{1}{2}Nu\right) - N du = -dL, \tag{30}$$

where dL denotes the variation in the elastic strain energy (evaluated by virtue of Clapeyron's Theorem), N is the external load, and u its dual displacement. The strain energy release rate can be rewritten as

$$\mathcal{G} = -\frac{dW}{dS} = \frac{dL}{dS}. \tag{31}$$

Brittle crack propagation really occurs when $\mathcal{G}$ reaches its critical value $\mathcal{G}_a$, characteristic for the adhesive:

$$\mathcal{G} = \frac{dL}{dS} = \mathcal{G}_a. \tag{32}$$

The propagation will be stable, metastable, or unstable depending on the sign of the second-order derivative of the total potential energy:

$$-\frac{d^2W}{dS^2} = \frac{d\mathcal{G}}{dS} = \frac{d^2L}{dS^2}\begin{cases} <0, & \text{stable} \\ =0, & \text{metastable} \\ >0, & \text{unstable} \end{cases}. \tag{33}$$

7 Joint Elastic Strain Energy

To solve the problem of the crack propagation it is necessary to evaluate the elastic strain energy of the joint as a function of the crack length (in the overlap zone, during crack propagation it being constant out of the overlap). The energy L absorbed by the joint is the sum of three quantities, i.e., the elastic strain energy absorbed by the two tubular bars (pedex 1,2) and by the adhesive (pedex 3):

$$L = L_1 + L_2 + L_3. \tag{34}$$

As previously shown, the predominant shearing stress field in the adhesive (equivalent to the applied normal thrust) has its maximum positive value at the end of the stiffer tubular bar (here indicated by 1). The initial separation at the interface between the two adherends is supposed to take place in this point: the debond is a crown-crack of length Δx (Fig. 6). The elastic strain energy of the cracked joint along the overlap can be calculated, noting how the portions of the joint are loaded. Fixing the origin of the x-axis at the middle of the ligament of length $2c$-Δx of the adhesive (see Fig. 6), we have

$$L_1 = \int_{-c+\Delta x/2}^{c-\Delta x/2} \frac{N_1^2(x)}{2E_1A_1(x)} dx, \tag{35}$$

$$L_2 = \int_{-c+\Delta x/2}^{c-\Delta x/2} \frac{N_2^2(x)}{2E_2A_2(x)} dx + \int_{c-\Delta x/2}^{c+\Delta x/2} \frac{N^2}{2E_2A_2(x)} dx, \tag{36}$$

that are integrals of known functions—see Eqs. (5), (11).

The elastic strain energy absorbed by the adhesive of the cracked joint is equal to

$$L_3 = \int_{-c+\Delta x/2}^{c-\Delta x/2} \left\{ \frac{1}{2E_a}[\sigma_x^2(x) + \sigma_r^2(x) + \sigma_\vartheta^2(x)] - \frac{\nu_a}{E_a}[\sigma_x(x)\sigma_r(x) + \sigma_x(x)\sigma_\vartheta(x) + \sigma_\vartheta(x)\sigma_r(x)] + \frac{\tau_{rx}^2(x)}{2G_a} \right\} 2\pi Rh dx, \tag{37}$$

that is an integral of known functions—see Eqs. (16). Applying Eq. (31), we can obtain the strain energy release rate $\mathcal{G}$, where $dS = 2\pi R d(\Delta x)$. Equation (32) represents the condition of brittle crack propagation. Equation (33) shows whether the fracture propagation is stable, metastable or unstable.

8 Strength and Stability Under Crack Propagation

If we suppose that the height h of the adhesive layer tends to zero (and as a consequence $L_3 \to 0$), the functions f_i will assume the physical meaning of coefficients of distribution:

$$f_i(x) = \frac{E_iA_i(x)}{E_1A_1(x) + E_2A_2(x)}; \quad -c < x < c. \tag{38}$$

In the case of constant high profiles, functions (38) are constant along $x (x \neq \pm c)$ and, putting them into Eqs. (35) and (36), we obtain the joint elastic strain energy $(L = L_1 + L_2)$. From Eq. (32) we obtain the strength of the joint, i.e., the critical value for the axial load corresponding to the crack propagation:

$$N_C = \sqrt{4\pi R\mathcal{G}_a \frac{E_2A_2}{E_1A_1}(E_1A_1 + E_2A_2)}, \quad \frac{E_2A_2}{E_1A_1} < 1. \tag{39}$$

Applying Eq. (33), or observing that N_C is not a function of the crack length, we can deduce that the propagation will be metastable:

$$\frac{dN_C}{d(\Delta x)} = 0 \Rightarrow \text{metastable}. \tag{40}$$

Equation (39) represents an extension of the critical condition presented, and experimentally verified for the particular case of $E_1A_1 \to \infty$, [19]. In addition, the presented approach to study the strength of the joint against brittle crack propagation has already been experimentally validated for the case of nontubular joints, [20].

For uniform axial strength joint, connecting tubular bars with identical stiffness EA, the adherends must be tapered with the profiles of Eq. (26). These profiles are the best from a tensional point of view. In this case, Eqs. (35) and (36) must be rewritten taking into account the symmetrical propagation by the length $\Delta x/2$ of the crack at the end of the two tubular bars:

$$L_1 = \int_{-c+\Delta x/2}^{c-\Delta x/2} \frac{N_1^2(x)}{2E_1A_1(x)} dx + \int_{-c}^{-c+\Delta x/2} \frac{N^2}{2E_1A_1(x)} dx = L_2$$
$$= \int_{-c+\Delta x/2}^{c-\Delta x/2} \frac{N_2^2(x)}{2E_2A_2(x)} dx + \int_{c-\Delta x/2}^{c} \frac{N^2}{2E_2A_2(x)} dx. \tag{41}$$

Equation (39) becomes

$$N_C = \sqrt{4\pi R\mathcal{G}_a \frac{4c - \Delta x}{\Delta x} EA} \quad \text{(UAS joint)}. \tag{42}$$

Applying Eq. (33), or observing that for UAS joint an increase in the crack length causes a reduction in the load of brittle failure, we can deduce that the propagation will be unstable:

$$\frac{\mathrm{d}N_C}{\mathrm{d}(\Delta x)} < 0 \Rightarrow \text{unstable (UAS joint)}. \tag{43}$$

Summarizing, for conventional joints the load of brittle failure is independent of the crack length and the propagation will be metastable, when the load reaches its critical value of Eq. (39). On the other hand, for UAS joints an increasing of the crack length causes a reduction in the load of brittle failure and the propagation will be unstable, when the load reaches its critical value of Eq. (42). In this case, for vanishing pre-existing defects in the adhesive layer ($\Delta x \to 0$), the critical value of Eq. (42) tends to infinity. This simply means that the joint will collapse due to a different mechanism (we will discuss this transition in the following section). As a consequence, the UAS joint, good bonded, is stronger than the conventional one against brittle collapse. In addition, it is interesting to note that tubular joints are "shape-resistant" (the strength is different from zero also without adhesive) with respect to shear and flexure but not with respect to thrust and torque. For these reasons, axial load and torsional moment are more critical than shear and flexure for this kind of joints. Furthermore, for UAS and UTS, [11], (i.e., uniform torsional strength) the optimizations coincide for thin tubes. This means that optimized thin tubes present a global optimization design.

9 Ductile-Brittle Transition

The effective critical load is provided by the lower between the load of brittle crack propagation (39) or (42) and the load of ductile collapse. If we assume that the latter is achieved when the maximum shearing stress in the ligament of the adhesive layer equals its ultimate stress τ_u, and that c is not too short ($\alpha c \geqslant 3$, in the hypothesis of Eq. (22)), we obtain the following ultimate load of ductile collapse for conventional and optimized joint:

$$N_U = \sqrt{\frac{2\pi R h}{G_a}\frac{E_2A_2}{E_1A_1}(E_1A_1 + E_2A_2)}\,\tau_u, \quad \frac{E_2A_2}{E_1A_1} < 1, \tag{44}$$

$$N_U = 2\pi R(2c - \Delta x)\tau_u \quad \text{(UAS joint)}. \tag{45}$$

Comparing the critical values of the loads of brittle—see Eqs. (39), (42)—and ductile collapse—see Eqs. (44), (45)—the brittleness number s of the joint may be defined, [13,14,20]:

$$\frac{N_C}{N_U} = \mu s; \quad \begin{cases} \mu = \sqrt{2}; & s = \dfrac{\sqrt{\mathscr{G}_a G_a}}{\sqrt{h}\,\tau_u}; \\ \mu = \sqrt{\dfrac{1}{\pi}\dfrac{4c/\Delta x - 1}{(2c/\Delta x - 1)^2}\dfrac{A}{\Delta x^2}}; & s = \dfrac{\sqrt{\mathscr{G}_a E}}{\sqrt{R}\,\tau_u} \quad \text{(UAS joint)}. \end{cases} \tag{46}$$

Considering different sizes of self-similar joints the introduced parameter μ is a constant. The brittleness number s shows how the brittle collapse tends to occur with a low fracture energy, a low elastic modulus, a high ultimate stress and/or a large structural size. It is not the individual values of the parameters that are responsible for the nature of the collapse mechanism, but rather only their function s. By Eqs. (39), (42), and (45), (46), we can predict the strength of conventional and UAS joints.

10 Crack Detection by Axial Natural Frequencies

The crack length Δx is a priori unknown. In this section we present a theoretical approach to evaluate this parameter as a function of the axial natural frequencies of the cracked joint. It can be used as a detection method to predict crack severity. The axial natural frequencies can be experimentally obtained from conventional nondestructive tests of axial vibration.

The equation of motion of the overlap in a dynamic regime, [21], can be written introducing the inertia of the tubular bar in the joint equilibrium Eq. (9):

$$\frac{\partial N_1(x,t)}{\partial x} - \rho_1(x)A_1(x)\frac{\partial^2 u_1(x,t)}{\partial t^2} + K^*(x)(u_2(x,t) - u_1(x,t)) = 0, \quad 1 \leftrightarrow 2, \tag{47}$$

where ρ_i is the mass density (and u_i the displacement) of the ith tube. Furthermore,

$$N_1(x,t) = E_1(x)A_1(x)\frac{\partial u_1(x,t)}{\partial x}, \quad 1 \leftrightarrow 2. \tag{48}$$

Putting Eq. (48) into Eq. (47), we obtain the dynamic equations

$$\frac{\partial}{\partial x}\left(E_1(x)A_1(x)\frac{\partial u_1(x,t)}{\partial x}\right) - \rho_1(x)A_1(x)\frac{\partial^2 u_1(x,t)}{\partial t^2} + K^*(x)(u_2(x,t) - u_1(x,t)) = 0, \quad 1 \leftrightarrow 2. \tag{49}$$

To obtain a closed-form solution, we have to consider tubular bars of identical materials and cross-section areas. In these hypothesis, Eq. (49) becomes

$$EA\frac{\partial^2 u_1(x,t)}{\partial^2 x} - \rho A\frac{\partial^2 u_1(x,t)}{\partial t^2} + K^*(x)(u_2(x,t) - u_1(x,t)) = 0, \quad 1 \leftrightarrow 2. \tag{50}$$

If we consider $\rho \to 0$ in Eq. (50), it reduces to the static equilibrium of the joint. On the other hand, if $K^* \to 0$ we obtain the conventional dynamic equilibrium equation for a tubular bar.

In order to derive the equations, and due to the different field equations ruling the axial vibrations in and outside the bonding region, it is necessary to divide both tubular bars in different sections. As a consequence, Sections 1 and 2 of the first tubular bar define the region out of (the corresponding dynamic equilibrium is imposed by Eq. (50) in which we put $K^* = 0$) and inside (Eq. (50) with $K^* \neq 0$) the bonding. For the second tubular bar, Sections 3 and 4 define the region in (Eq. (50) with $K^* \neq 0$ and $1 \to 2$) and outside (Eq. (50) with $K^* = 0$ and $1 \to 2$) the bonding, respectively. Section 5 is the cracked region for the first tubular bar (Eq. (50) with $K^* = 0$). See Fig. 7.

For all these cases, Eq. (50) can be written in the following unified manner (by sum and subtraction of the two equations for which $K^* \neq 0$):

$$\frac{\partial^2 \varphi(x,t)}{\partial t^2} - \xi\frac{\partial^2 \varphi(x,t)}{\partial x^2} + \zeta\varphi(x,t) = 0, \tag{51}$$

where $\xi = E/\rho$ and

$$\varphi(x,t) = u_1(x,t) \quad \zeta = 0, \tag{52}$$

$$\varphi(x,t) = u_2(x,t) - u_3(x,t) \quad \zeta = \frac{2K^*}{\rho A}, \tag{53}$$

$$\varphi(x,t) = u_2(x,t) + u_3(x,t) \quad \zeta = 0, \tag{54}$$

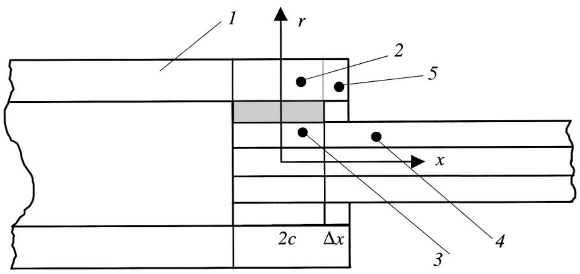

Fig. 7 Regions 1–5 of the cracked tubular bonded joint governed by different axial dynamic equations. Coupled regions (by the adhesive) are 2–3.

$$\varphi(x,t)=u_4(x,t) \quad \zeta=0, \tag{55}$$

$$\varphi(x,t)=u_5(x,t) \quad \zeta=0, \tag{56}$$

where, to simplify the notation, we have indicated with u_i the displacement in the mentioned ith section.

By applying the separation of variables, the solution of Eq. (50) can be written as superposition of solutions of the form

$$\varphi(x,t)=\psi(x)\phi(t), \tag{57}$$

so that Eq. (50) becomes

$$\frac{1}{\phi(t)}\frac{\mathrm{d}^2\phi(t)}{\mathrm{d}t^2}=\frac{\xi}{\psi(x)}\frac{\mathrm{d}^2\psi(x)}{\mathrm{d}x^2}-\zeta=-\omega^2, \tag{58}$$

where the natural circular frequency ω is a constant. We have, therefore,

$$\phi(t)=\sin(\omega t+\vartheta), \tag{59}$$

$$\psi(x)=A\sin(\lambda x)+B\cos(\lambda x), \tag{60}$$

with

$$\lambda^2=\frac{\omega^2-\zeta}{\xi}. \tag{61}$$

By introducing Eqs. (59) and (60) into Eqs. (52)–(56), it is possible to determine the corresponding expression for $u_i(x,t)=u_i(x)\sin(\omega t+\vartheta)$:

$$u_1(x)=A_1\sin(\lambda x)+B_1\cos(\lambda x), \tag{62a}$$

$$u_2(x)=\frac{1}{2}[A_2\sin(\bar{\lambda}x)+B_2\cos(\bar{\lambda}x)+A_3\sin(\lambda x)+B_3\cos(\lambda x)], \tag{62b}$$

$$u_3(x)=\frac{1}{2}[-A_2\sin(\bar{\lambda}x)-B_2\cos(\bar{\lambda}x)+A_3\sin(\lambda x)+B_3\cos(\lambda x)], \tag{62c}$$

$$u_4(x)=A_4\sin(\lambda x)+B_4\cos(\lambda x), \tag{62d}$$

$$u_5(x)=A_5\sin(\lambda x)+B_5\cos(\lambda x), \tag{62e}$$

where

$$\lambda^2=\frac{\rho}{E}\omega^2, \quad \bar{\lambda}^2=\frac{\rho}{E}\omega^2-\frac{2K^*}{EA}. \tag{63}$$

If $\omega\to 0$, we obtain the static solution. If $2L$ is the overall length of the joint, the boundary conditions at the left and right end are $({}'\equiv \mathrm{d}/\mathrm{d}x)$:

$$u_1(-L)=u_1'(-L)=0, \tag{64}$$

for free ends, or

$$u_4(L)=u_4'(L)=0, \tag{65}$$

for clamped ends.

The remaining boundary conditions impose the continuity of the axial displacement and of its derivative, i.e., of the axial load (Fig. 7):

$$u_1(-(c-\Delta x/2))=u_2(-(c-\Delta x/2)), \tag{66a}$$

$$u_1'(-(c-\Delta x/2))=u_2'(-(c-\Delta x/2)), \tag{66b}$$

$$u_2'(c-\Delta x/2)=u_5'(c-\Delta x/2), \tag{66c}$$

$$u_2(c-\Delta x/2)=u_5(c-\Delta x/2), \tag{66d}$$

$$u_5'(c+\Delta x/2)=0, \tag{66e}$$

$$u_3'(-(c-\Delta x/2))=0, \tag{66f}$$

$$u_3(c-\Delta x/2)=u_4(c-\Delta x/2), \tag{66g}$$

$$u_3'(c-\Delta x/2)=u_4'(c-\Delta x/2). \tag{66h}$$

Equations (64) and (65) and (66e) can be rewritten taking into account Eqs. (62) as

$$A_1=-\tan(\lambda L+n_l\pi/2)B_1=C_1B_1, \tag{67a}$$

$$A_4=\tan(\lambda L-n_r\pi/2)B_4=C_4B_4, \tag{67b}$$

$$A_5=\tan(\lambda(c+\Delta x/2))B_5=C_5B_5, \tag{67c}$$

where n_l and n_r refer to the left and right end, respectively, and they are equal to 0 or 1 if the corresponding end is whether free or clamped. The entire system of algebraic boundary conditions can be rewritten taking into account Eqs. (62) as

$$[M(\omega_n(\Delta x))]\{X\}=\{0\}, \tag{68}$$

where

$$[M]=\begin{bmatrix} \bar{S} & S & 2(C+C_1S) & -\bar{C} & -C & 0 & 0 \\ -\bar{C}^* & -C & 2(S-C_1C) & -\bar{S}^* & -S & 0 & 0 \\ \bar{C}^* & C & 0 & -\bar{S}^* & -S & 0 & 2(S-CC_5) \\ -\bar{S} & S & 0 & -\bar{C} & C & -2(C+C_4S) & 0 \\ -\bar{C}^* & C & 0 & \bar{S}^* & -S & 2(S-C_4C) & 0 \\ -\bar{C}^* & C & 0 & -\bar{S}^* & S & 0 & 0 \\ \bar{S} & S & 0 & \bar{C} & C & 0 & -2(C+SC_5) \end{bmatrix}, \tag{69}$$

and

$$\overline{S}=\sin(\overline{\lambda}(c-\Delta x/2)),\quad \overline{S}^{*}=\lambda^{*}\sin(\overline{\lambda}(c-\Delta x/2)),$$
$$\overline{C}=\cos(\overline{\lambda}(c-\Delta x/2)),\quad \overline{C}^{*}=\lambda^{*}\cos(\overline{\lambda}(c-\Delta x/2)),\tag{70}$$
$$S=\sin(\lambda(c-\Delta x/2)),\quad C=\cos(\lambda(c-\Delta x/2)),$$

with $\lambda^{*}=\overline{\lambda}/\lambda$. Furthermore,

$$\{X\}^{T}=[A_2A_3B_1B_2B_3B_4B_5].\tag{71}$$

In order to obtain a nonzero solution, it is necessary to find the eingvalues $\omega_n(\Delta x)$ so that

$$\det[M(\omega_n(\Delta x))]=0.\tag{72}$$

The eigenvalues $\omega_n(\Delta x)$ are the axial natural circular frequencies of the bonded joint with a crack of length Δx, with corresponding eigenvectors (or modeshapes) given by $\{X_n(\Delta x)\}$:

$$[M(\omega_n(\Delta x))]\{X_n(\Delta x)\}=\{0\}.\tag{73}$$

The numerical solution of Eq. (72) provides, in a very simple way, the crack length as a function of the natural frequencies, considering a joint of given material and geometry. Some numerical examples of solution of determinantal equation like Eq. (73)—for undamaged joint under torsion—can be found in [21]. If $\Delta x\rightarrow 0$, we obtain the dynamic behavior of the undamaged bonded joint.

From the displacement (62) we can obtain the predominant stress field in the vibrating adhesive:

$$\tau_{rx}(x,t)=\frac{K^{*}\Delta u(x,t)}{2\pi R}.\tag{74}$$

The remaining components of the stress field can be obtained substituting the static load with the dynamic one of Eq. (48) in the static adhesive stresses of Eqs. (16).

Conclusions

The optimal profile for uniform axial strength, even if purely theoretical, could give useful guidelines to designers of tubular bonded joints under axial load. This optimal shape would permit both reduced weight and increased strength. The constant shearing stress field in the bond would enable the adhesive to withstand large axial loads by simply modifying the adhesive length. Also the normal stresses are strongly reduced by optimization. On the other hand, the developed fracture energy criterion permits to predict the critical load due to brittle crack propagation and the stability of the process. UAS and UTS profiles (uniform axial and uniform torsional strength), optimizing the joint from a stress point of view, coincide for thin tubes. In addition, the proposed approach shows that the optimized profile implies also a decrease in the brittleness of the joint. This is a relevant result for a global optimization design.

The axial natural frequencies of the cracked joint have been evaluated by determining the roots of a determinantal equation. The latter has been written by deriving the equation of motion for the cracked joint in axial vibrations and by imposing the related boundary conditions. This approach permits to evaluate the crack length as a function of the (experimental) axial natural frequencies.

References

[1] Beevers, A., 1999, ''Durability Testing and Life Prediction of Adhesive Joints,'' Int. J. Mat. Prod. Tech., **14**, pp. 373–384.

[2] Goland, M., and Reissner, E., 1944, ''The Stresses in Cemented Joints,'' ASME J. Appl. Mech., **11**, pp. 17–27.

[3] Lubkin, J. L., and Reissner, E., 1956, ''Stress Distribution and Design Data for Adhesive Lap Joints Between Circular Tubes,'' Trans. ASME, **78**, pp. 1213–1221.

[4] Adams, R. D., and Peppiatt, N. A., 1977, ''Stress Analysis of Adhesive Bonded Tubular Lap Joints,'' J. Adhes., **9**, pp. 1–18.

[5] Renton, W. J., and Vinson, J. R., 1977, ''Analysis of Adhesively Bonded Joints Between Panels of Composite Materials,'' ASME J. Appl. Mech., **44**, pp. 101–106.

[6] Delale, F., and Erdogan, F., 1981, ''Viscoelastic Analysis of Adhesively Bonded Joints,'' ASME J. Appl. Mech., **48**, pp. 331–338.

[7] Chen, D., and Cheng, S., 1983, ''An Analysis of Adhesive-Bonded Single-Lap Joints,'' ASME J. Appl. Mech., **50**, pp. 109–115.

[8] Pugno, N., 1999, ''Optimizing a Non-Tubular Adhesive Bonded Joint for Uniform Torsional Strength,'' Int. J. of Materials and Product Technology, **14**, pp. 476–487.

[9] Pugno, N., 2001, ''Closed Form Solution for a Non-Tubular Bonded Joint With Tapered Adherends Under Torsion,'' Int. J. Mech. Control, **2**, pp. 19–27.

[10] Pugno, N., and Surace, G., 2000, ''Non-Tubular Bonded Joint Under Torsion: Theory and Numerical Validation,'' Struct. Eng. Mech., **10**, pp. 125–138.

[11] Pugno, N., and Surace, G., 2001, ''Tubular Bonded Joint Under Torsion: Analysis and Optimization for Uniform Torsional Strength,'' J. Strain Anal. Eng. Des., **1**, pp. 17–24.

[12] Griffith, A. A., 1921, ''The Phenomena of Rupture and Flow in Solids,'' Philos. Trans. R. Soc. London, Ser. A, **221**, pp. 163–198.

[13] Carpinteri, A., 1981, ''Static and Energetic Fracture Parameters for Rocks and Concretes,'' Materials and Structures, **14**, pp. 151–162.

[14] Carpinteri, A., 1989, ''Cusp Catastrophe Interpretation of Fracture Instability,'' J. Mech. Phys. Solids, **37**, pp. 567–582.

[15] Carpinteri, A., 1989, ''Decrease of Apparent Tensile and Bending Strength With Specimen Size: Two Different Explanations Based on Fracture Mechanics,'' Int. J. Solids Struct., **25**, pp. 407–429.

[16] Carpinteri, A., 1989, ''Size Effects on Strength, Toughness and Ductility,'' J. Eng. Mech. Div., **115**, pp. 1375–1392.

[17] Carpinteri, A., 1989, ''Softening and Snap-Back Instability in Choesive Solids,'' Int. J. Numer. Methods Eng., **28**, pp. 1521–1537.

[18] Carpinteri, A., 1997, *Structural Mechanics—A Unified Approach*, E&FN Spon.

[19] Gent, A. N., and Yeoh, O. H., 1982, ''Failure Loads for Model Adhesive Joints Subjected to Tension, Compression or Torsion,'' J. Mater. Sci., **17**, pp. 1713–1722.

[20] Pugno, N., and Carpinteri, A., 2002, ''Strength, Stability and Size Effects in the Brittle Behavior of Bonded Joints Under Torsion: Theory and Experimental Assessment,'' Fatigue Fract. Eng. Mater. Struct., **25**, pp. 55–62.

[21] Pugno, N., and Ruotolo, R., 2002, ''Evaluation of Torsional Natural Frequencies for Non-Tubular Bonded Joints,'' Structural Engineering and Mechanics, **13**, pp. 91–101.

[22] Withney, J. M., and Pagano, N. J., 1970, ''Shear Deformation in Heterogeneous Anisotropic Plates,'' ASME J. Appl. Mech., **37**, pp. 1031–1036.

[23] Newill, J. F., and Vinson, J. R., 1993, ''Some High Strain Rate Effects on Composite Materials,'' *Proceedings of the 9th International Conference on Composite Materials*, Part 5, July 12–16, pp. 269–277.

[24] Bigwood, D. A., and Crocombe, A. D., 1990, ''Non-Linear Adhesive Bonded Joints Design Analysis,'' Int. J. Adhes. Adhes., **10**, pp. 31–41.

[25] Gibson, R. F., 1994, *Principles of Composite Material Mechanics*, McGraw-Hill, New York.

[26] Moloney, A. C., Kausch, H. H., and Stieger, H. R., 1984, ''The Use of the Double Torsion Test Geometry to Study the Fracture of Adhesive Joints,'' J. Mater. Sci. Lett., **3**, pp. 776–778.

[27] Surace, G., and Brusa, E., 1995, ''A Parametric Study of Structural Adhesive Joints for Aerospace Applications,'' *Advanced Technology for Design and Fabrication of Composite Materials and Structures*, G. C. Sih, A Carpinteri, and G. Surace, eds., Kluwer, Dordrecht, The Netherlands.

[28] Tsai, M. Y., and Morton, J., 1994, ''Three-Dimensional Deformations in a Single-Lap Joints,'' J. Strain Anal., **29**, pp. 137–145.

D. V. T. G. Pavan Kumar[1]
Scientist,
National Aerospace Laboratories,
Bangalore 560 017, India
e-mail: pavan@css.cmmacs.ernet.in

B. K. Raghu Prasad[2]
Professor,
Civil Engineering Department,
Indian Institute of Science,
Bangalore 560 012, India
e-mail: bkr@civil.iisc.ernet.in

Higher-Order Beam Theories for Mode II Fracture of Unidirectional Composites

Mathematical models, for the stress analyses of unidirectional end notch flexure and end notch cantilever specimens using classical beam theory, first, second, and third-order shear deformation beam theories, have been developed to determine the interlaminar fracture toughness of unidirectional composites in mode II. In the present study, appropriate matching conditions, in terms of generalized displacements and stress resultants, have been derived and applied at the crack tip by enforcing the displacement continuity at the crack tip in conjunction with the variational equation. Strain energy release rate has been calculated using compliance approach. The compliance and strain energy release rate obtained from present formulations have been compared with the existing experimental, analytical, and finite element results and found that results from third-order shear deformation beam theory are in close agreement with the existing experimental and finite element results. [DOI: 10.1115/1.1607357]

1 Introduction

The most common problem in laminated composite structures is the delamination along the resin rich ply interfaces. In general, a delamination will be subjected to crack driving forces resulting from a combination of mode I (opening or peeling), mode II (sliding or shear), or mode III (antiplane shear). Here, we consider the analysis of the mode II interlaminar fracture specimens namely end notch flexure (ENF) specimen and end notch cantilever (ENC) specimen (also called the end-loaded split (ELS) laminate) shown in Figs. 1(*a*) and 2(*a*), respectively. ENF and ENC specimens are assumed to be made up of unidirectional laminated composites. Laminated composite structures generally contain brittle matrix and thus they have poor resistance to delamination growth. Laminated composites containing delaminations behave in a linear elastic manner and thus they can be treated using linear elastic fracture mechanics to derive the strain energy release rate (SERR), [1]. A critical value of SERR known as interlaminar fracture toughness (IFT) is being widely used to characterize the onset and delamination growth in laminated composite structures, [2].

The state of art in the subject of interlaminar fracture toughness of laminated composites was reviewed by Carlsson and Gillespie [3] and Sela and Ishai [4]. The former covered the detailed technical aspects of analytical, numerical, and experimental methods to analyze ENF specimen for the mode II IFT. Since the present work is related to the analysis of mode II specimens using analytical methods, literature pertinent predominantly to analytical methods has been covered here.

Initially, Barrett and Foschi [5] utilized ENF specimen to characterize the mode II interlaminar fracture of cracked wood beams. Later, Russell and Street [6] used this specimen, by considering Euler-Bernoulli beam theory, to characterize mode II critical strain energy release rates of advanced composites. Carlsson et al. [7] gave compliance and SERR expressions based on Timoshenko beam theory in the uncracked region and an approximate elasticity solution in the cracked region for ENF specimen. Further, Carlsson et al. [8] presented an analysis of ENF specimen for the characterization of mode II IFT using first-order plate theory under cylindrical bending and shear stress singularity at the crack tip.

Whitney et al. [9] and Whitney [10] analyzed the homogeneous orthotropic ENF specimen using first-order beam theory and modified version of Whitney and Sun [11] laminated plate theory under cylindrical bending, respectively. In the former, a singular shear stress function which decays to classical beam theory was also considered in the section ahead of the crack. Whitney [12] analyzed ENF and ENC specimens for mode II interlaminar fracture using a higher order beam theory. The theory is based on second-order displacements in the thickness coordinate and is derived in conjunction with Reissner's [13] variational principle which allows the direct development of constitutive relations without the need for shear correction factors.

Williams [1] gave a general method for calculating the energy release rate G, using conventional beam theory, from the local values of bending moments and loads in a cracked laminate. Further, Williams [14] extended his work to study the shortening of the bending arms due to large displacements during crack growth. Hashemi et al. [15,16] described a detailed study of the methods analysing the experimental data obtained from fracture mechanics tests using DCB, ELS, and ENF. Wang and Williams [17] modified the compliance and SERR expressions, which are based on classical beam theory, by introducing a correction factor to correct the crack length for mode II fracture toughness tests (ENF and ELS).

Analysis of ENF specimen was carried out by Chatterjee [18] using exact stress analysis based on two-dimensional formulation under plane stress or plane strain and approximate analysis based on "beam type" or "plane strain version of laminated plate theory" which appears to be first-order plate theory. Zhou and He [19] derived SERR expression for ENF specimen based on Timoshenko beam theory by taking asymmetric flexure of the specimen into account and further they improved SERR expression by considering the deformation at the crack tip. Corleto and Hogan [20] presented an anlysis based on a new modified beam theory for ENF specimen which considers the solution of a beam on a generalized elastic foundation and Timoshenko beam theory to incorporate the effect of crack-tip deformation and transverse shear deformation, respectively. This approach showed that SERR

[1]Formerly Research Student, Civil Engineering Department, Indian Institute of Science, Bangalore 560 012, India.

[2]To whom correspondence should be addressed.

Contributed by the Applied Mechanics Division of THE AMERICAN SOCIETY OF MECHANICAL ENGINEERS for publication in the ASME JOURNAL OF APPLIED MECHANICS. Manuscript received by the ASME Applied Mechanics Division, Apr. 12, 2002; final revision, Mar. 24, 2003. Associate Editor: R. C. Benson. Discussion on the paper should be addressed to the Editor, Prof. Robert M. McMeeking, Department of Mechanical and Environmental Engineering, University of California–Santa Barbara, Santa Barbara, CA 93106-5070, and will be accepted until four months after final publication of the paper itself in the ASME JOURNAL OF APPLIED MECHANICS.

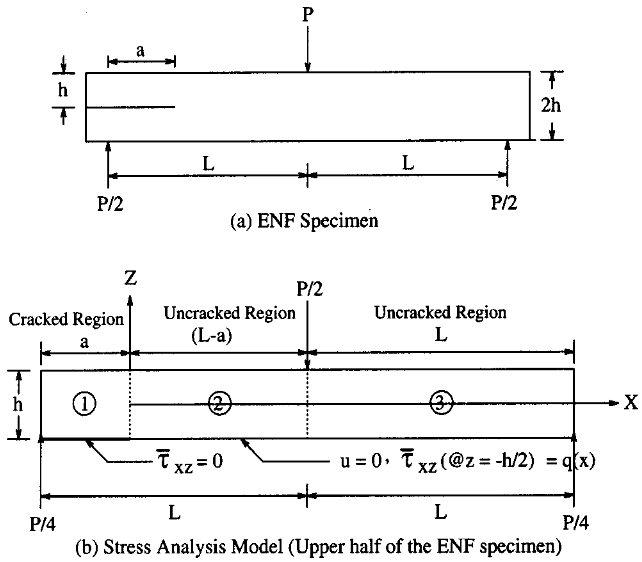

Fig. 1 ENF specimen and its stress analysis model

is only affected by crack-tip deformations and is independent of transverse shear deformations. Davidson et al. [21] presented the deflections and energy release rates of ENF specimens by using one-dimensional models ("generalized plane stress or plane strain") of classical and shear deformable laminated plate theory and three-dimensional finite element analysis. Recently, Ding and Kortschot [22] developed a solution for the ENF specimen using a modified classical beam theory, in which the effect of crack-tip deformation is analyzed by assuming that a region of certain length close to the crack tip rests on an elastic shear spring foundation.

From the above literature review, it can be observed that classical, first, and second-order beam and/or plate theories were used to analyze unidirectional ENF and ENC or ELS specimens. To the authors' knowledge, analysis of unidirectional ENF and ENC specimens, using third-order shear deformation beam theory, has not yet been explored. It will be seen later that as the order of the theory increases, present study results converge towards the experimental and finite element results. However, the problem of matching conditions at the crack tip becomes more involved. In order to apply the third-order beam theory to analyze ENF and ENC specimens, stress analysis models proposed by Whitney [12] (based on second-order beam theory) have been found to be suitable to extend further, but with modifications to the stress analysis models. The modifications are mainly due to the incorporation of the variationally derived matching conditions at the crack tip of ENF and ENC specimens. Hence, in the present study, mathematical models or stress analysis models for the analyses of unidirectional ENF and ENC specimens, using classical beam theory (CBT) and first (FOBT), second (SOBT), and third (TOBT) order shear deformation beam theories, have been developed to determine the mode II interlaminar fracture toughness of composites. In these mathematical models, appropriate matching conditions, in terms of generalized displacements and stress resultants, have been derived and applied at the crack tip by enforcing the displacement continuity at the crack tip in conjunction with the variational equation. This method of applying variationally derived matching conditions at the crack tip becomes the key feature of present stress analysis models of ENF and ENC specimens and makes the present stress analysis models different from the available stress analysis models in the literature. It may be further noted that this may be the first time that the third-order shear deformation beam theory is being used to analyze ENF and ENC specimens.

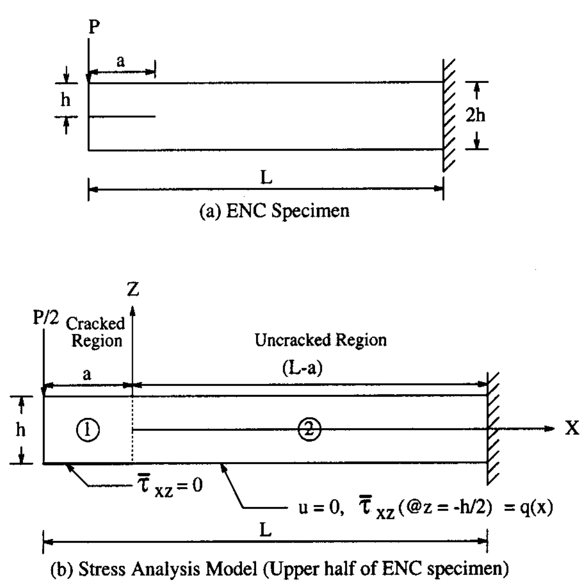

Fig. 2 ENC specimen and its stress analysis model

The compliance and SERR, obtained from the present study, have been compared with the existing experimental, analytical, and finite element results in the literature. The contribution of shear deformation (based on the theories FOBT, SOBT, and in particular TOBT), in compliance, SERR and interlaminar shear stress at the crack tip and its distribution ahead of the crack tip, has been examined and its importance has been highlighted. Further, the significance of variationally derived matching conditions at the crack tip has been clearly brought out. The influence of crack length, ratio of Young's modulus to shear modulus (shear deformation) and span-to-depth (thickness) ratio of the ENF and ENC specimens on the compliance, SERR and interlaminar shear stress distribution ahead of the crack tip have been studied in detail. Certain informative and useful conclusions have been drawn from the comparative and parametric studies.

2 Higher-Order Shear Deformation Beam Theories

The displacement field for unidirectional laminated composite beam, according to third (TOBT), second (SOBT), first (FOBT) order shear deformation, and classical (CBT) beam theories, can be written in an unified form using the tracers "α_1" and "α_2" as

$$u(x,z)=u_0(x)+z\psi_x(x)+\alpha_1 z^2\phi_x(x)+\alpha_2 z^3\xi_x(x);\qquad w(x,z)=w_0(x) \tag{1}$$

The tracer α_1 takes the value "unity" for TOBT and SOBT and "zero" for FOBT and CBT. The tracer α_2 takes the value "unity" for TOBT and "zero" for SOBT, FOBT, and CBT. Further, it should be noted that the terms, equations, and relations, associated with the tracers α_1 and α_2, exist only if the tracer is "unity" and do not exist if the tracer is "zero." For classical beam theory (CBT), $\psi_x = -dw_0/dx$ in Eq. (1) and in subsequent derivations.

Strain displacement relations corresponding to Eq. (1) are

$$\epsilon_{xx}=\frac{du_0}{dx}+z\frac{d\psi_x}{dx}+\alpha_1 z^2\frac{d\phi_x}{dx}+\alpha_2 z^3\frac{d\xi_x}{dx};\qquad \gamma_{xz}=\left(\frac{dw_0}{dx}+\psi_x\right)+\alpha_1 2z\phi_x+\alpha_2 3z^2\xi_x. \tag{2}$$

The stress-strain relations for each orthotropic layer of unidirectional laminated composite beam are

$$\sigma_{xx}=\overline{E}_{11}\epsilon_{xx};\qquad \tau_{xz}=G_{13}\gamma_{xz}. \tag{3}$$

In Eqs. (3), $\overline{E}_{11}=E_{11}$ for plane-stress-type constitutive relation and $\overline{E}_{11}=E_{11}/(1-\nu_{12}\nu_{21})$ for plane-strain-type constitutive relation. E_{11} is the Young's modulus of elasticity in the fiber direction, G_{13} is the shear modulus, and ν_{12} and ν_{21} are the Poisson's ratios.

The strain energy of the unidirectional laminated composite beam, having width "b" and thickness "h," is

$$U=\frac{1}{2}b\int_x\int_{-h/2}^{h/2}(\sigma_{xx}\epsilon_{xx}+\tau_{xz}\gamma_{xz})dzdx. \tag{4}$$

The work done by the external surface forces and edge forces is

$$W=b\int_x\{(\overline{\tau}_{xz}u+\overline{\sigma}_{zz}w)_{\text{at } z=h/2}-(\overline{\tau}_{xz}u+\overline{\sigma}_{zz}w)_{\text{at } z=-h/2}\}dx+\left[b\int_{-h/2}^{h/2}(\overline{\sigma}_{xx}u+\overline{\tau}_{xz}w)dz\right]_{\text{at } x=x_e}. \tag{5}$$

where x_e represents any beam end at which boundary conditions are to be specified.

The total potential energy is

$$\Pi=U-W. \tag{6}$$

According to the principle of minimum potential energy, first variation of total potential energy is zero and can be written as

$$\delta\Pi=\delta U-\delta W=0. \tag{7}$$

By substituting Eq. (4) and Eq. (5) in Eq. (7) along with the displacement field (Eq. (1)), the variation of total potential energy can be written as

$$\begin{aligned}\delta\Pi=b\int_x\int_{-h/2}^{h/2}(\sigma_{xx}\delta\epsilon_{xx}+\tau_{xz}\delta\gamma_{xz})dzdx-b\int_x(q_{0xz}\delta u_0\\+q_{1xz}\delta\psi_x+\alpha_1 q_{2xz}\delta\phi_x+\alpha_2 q_{3xz}\delta\xi_x+p_{zz}\delta w_0)dx\\-\left[b\int_{-h/2}^{h/2}\{\overline{\sigma}_{xx}(\delta u_0+z\,\delta\psi_x+\alpha_1 z^2\delta\phi_x+\alpha_2 z^3\delta\xi_x)\right.\\\left.+\overline{\tau}_{xz}\delta w_0\}dz\right]_{\text{at } x=x_e}=0\end{aligned} \tag{8}$$

in which

$$q_{0xz}=\left\{\overline{\tau}_{xz}\left(\text{at } z=\frac{h}{2}\right)-\overline{\tau}_{xz}\left(\text{at } z=\frac{-h}{2}\right)\right\},$$

$$p_{zz}=\left\{\overline{\sigma}_{zz}\left(\text{at } z=\frac{h}{2}\right)-\overline{\sigma}_{zz}\left(\text{at } z=\frac{-h}{2}\right)\right\},$$

$$q_{1xz}=\left\{\frac{h}{2}\overline{\tau}_{xz}\left(\text{at } z=\frac{h}{2}\right)+\frac{h}{2}\overline{\tau}_{xz}\left(\text{at } z=\frac{-h}{2}\right)\right\},$$

$$q_{2xz}=\left\{\frac{h^2}{4}\overline{\tau}_{xz}\left(\text{at } z=\frac{h}{2}\right)-\frac{h^2}{4}\overline{\tau}_{xz}\left(\text{at } z=\frac{-h}{2}\right)\right\},$$

and

$$q_{3xz}=\left\{\frac{h^3}{8}\overline{\tau}_{xz}\left(\text{at } z=\frac{h}{2}\right)+\frac{h^3}{8}\overline{\tau}_{xz}\left(\text{at } z=\frac{-h}{2}\right)\right\}.$$

Substituting Eqs. (3), (2), and (1) in Eq. (8) and carrying out the integration through the beam thickness results in the following variational equation:

$$\begin{aligned}-\int_x\left\{\left(\frac{dN_{xx}}{dx}+bq_{0xz}\right)\delta u_0+\left(\frac{dM_{xx}}{dx}-Q_{xz}+bq_{1xz}\right)\delta\psi_x\right.\\+\alpha_1\left(\frac{dS_{xx}}{dx}-2R_{xz}+bq_{2xz}\right)\delta\phi_x+\alpha_2\left(\frac{dP_{xx}}{dx}-3T_{xz}\right.\\\left.\left.+bq_{3xz}\right)\delta\xi_x+\left(\frac{dQ_{xz}}{dx}+bq_{zz}\right)\delta w_0\right\}dx+[(N_{xx}-\overline{N}_{xx})\delta u_0\\+(M_{xx}-\overline{M}_{xx})\delta\psi_x+\alpha_1(S_{xx}-\overline{S}_{xx})\delta\phi_x+\alpha_2(P_{xx}-\overline{P}_{xx})\delta\xi_x\\+(Q_{xz}-\overline{Q}_{xz})\delta w_0]_{\text{at } x=x_e}\\=0\end{aligned} \tag{9}$$

in which N_{xx}, M_{xx}, S_{xx}, P_{xx}, Q_{xz}, R_{xz}, T_{xz} are stress resultants and $\overline{N}_{xx}$, $\overline{M}_{xx}$, $\overline{S}_{xx}$, $\overline{P}_{xx}$, $\overline{Q}_{xz}$ are the external edge forces and have the following definitions:

$$[N_{xx},M_{xx},S_{xx},P_{xx}]=b\int_{-h/2}^{h/2}\sigma_{xx}[1,z,z^2,z^3]dz \tag{10}$$

$$[Q_{xz},R_{xz},T_{xz}]=b\int_{-h/2}^{h/2}\tau_{xz}[1,z,z^2]dz \tag{11}$$

$$[\overline{N}_{xx},\overline{M}_{xx},\overline{S}_{xx},\overline{P}_{xx},\overline{Q}_{xz}]=b\int_{-h/2}^{h/2}[\overline{\sigma}_{xx}[1,z,z^2,z^3],\overline{\tau}_{xz}]dz. \tag{12}$$

From Eqs. (10), (11), (3), (2), and (1), the stress resultants are related to displacements as given as follows:

In-plane stress resultants:

$$\begin{aligned}N_{xx}&=\overline{E}_{11}bh\left(\frac{du_0}{dx}+\alpha_1\frac{h^2}{12}\frac{d\phi_x}{dx}\right);\\M_{xx}&=\frac{\overline{E}_{11}bh^3}{12}\left(\frac{d\psi_x}{dx}+\alpha_2\frac{3h^2}{20}\frac{d\xi_x}{dx}\right);\\S_{xx}&=\alpha_1\frac{\overline{E}_{11}bh^3}{12}\left(\frac{du_0}{dx}+\frac{3h^2}{20}\frac{d\phi_x}{dx}\right);\\P_{xx}&=\alpha_2\frac{\overline{E}_{11}bh^5}{80}\left(\frac{d\psi_x}{dx}+\frac{5h^2}{28}\frac{d\xi_x}{dx}\right)\end{aligned} \tag{13}$$

Interlaminar shear stress resultants:

$$\begin{aligned}Q_{xz}&=G_{13}bh\left\{\left(\frac{dw_0}{dx}+\psi_x\right)+\alpha_2\frac{h^2}{4}\xi_x\right\};\\R_{xz}&=\alpha_1 G_{13}b\frac{h^3}{6}\phi_x;\\T_{xz}&=\alpha_2 G_{13}b\frac{h^3}{12}\left\{\left(\frac{dw_0}{dx}+\psi_x\right)+\frac{9h^2}{20}\xi_x\right\}\end{aligned} \tag{14}$$

We now introduce four independent shear correction factors k_1, k_2, k_3, and k_4, which will be determined later, into Eqs. (14) to account for the difference between the shear stress distribution over the thickness from constitutive equations and the exact shear stress distribution over the thickness from equilibrium equations and hence Eqs. (14) are rewritten as

$$\begin{aligned}Q_{xz}&=G_{13}bh\left\{k_1\left(\frac{dw_0}{dx}+\psi_x\right)+\alpha_2 k_4\frac{h^2}{4}\xi_x\right\};\\R_{xz}&=\alpha_1 k_2 G_{13}b\frac{h^3}{6}\phi_x;\\T_{xz}&=\alpha_2 G_{13}b\frac{h^3}{12}\left\{k_4\left(\frac{dw_0}{dx}+\psi_x\right)+k_3\frac{9h^2}{20}\xi_x\right\}.\end{aligned} \tag{15}$$

Present interest is to get the equilibrium equations for the beam subjected to surface traction "q" (shear) at the bottom surface. For this purpose, we need to set $\overline{\tau_{xz}}(\text{at } z=-h/2)=q$, $\overline{\tau_{xz}}(\text{at } z=h/2)=0$ and $\overline{\sigma_{zz}}(\text{at } z=\pm h/2)=0$ in Eqs. (5) and (8). Consequently, we get $q_{0xz}=-q$, $q_{1xz}=qh/2$, $q_{2xz}=-qh^2/4$, $q_{3xz}=qh^3/8$ and $p_{zz}=0$ and these substitutions are to be made in Eq. (9). In the variational Eq. (9), the variations δu_0, $\delta\psi_x$, $\delta\phi_x$, $\delta\xi_x$, and δw_0 are completely arbitrary. Thus Eq. (9) can vanish as required only if the coefficients of the variations of each vanish individually as the generalized displacements are independent of each other. From the vanishing of the coefficients of the variations δu_0, δw_0, $\delta\psi_x$, $\delta\phi_x$, and $\delta\xi_x$ under the integral sign of variational Eq. (9), we can obtain the following five equilibrium equations:

$$\frac{dN_{xx}}{dx}-bq=0;\quad \frac{dQ_{xz}}{dx}=0;\quad \frac{dM_{xx}}{dx}-Q_{xz}+\frac{bh}{2}q=0;$$
$$\alpha_1\left(\frac{dS_{xx}}{dx}-2R_{xz}-\frac{bh^2}{4}q\right)=0;\quad \alpha_2\left(\frac{dP_{xx}}{dx}-3T_{xz}+\frac{bh^3}{8}q\right)=0 \tag{16}$$

along with the boundary conditions N_{xx} (or u_0), M_{xx} (or ψ_x), $\alpha_1 S_{xx}$ (or $\alpha_1\phi_x$), $\alpha_2 P_{xx}$ (or $\alpha_2\xi_x$) and Q_{xz} (or w_0) that are need to be specified at the beam ends.

2.1 Exact Interlaminar Shear Stress Resultant Expressions. For unidirectional laminated composite beam subjected to surface traction "q" (shear) at the bottom surface, Reissner's variational principle, [13], can be written in the following form as given by Whitney [12]

$$\int_x\int_z\left[\left(\frac{\partial u}{\partial x}-\frac{\sigma_{xx}}{E_{11}}\right)\delta\sigma_{xx}+\left(\frac{\partial w}{\partial x}+\frac{\partial u}{\partial z}-\frac{\tau_{xz}}{G_{13}}\right)\delta\tau_{xz}-\left(\frac{\partial\sigma_{xx}}{\partial x}+\frac{\partial\tau_{xz}}{\partial z}\right)\delta u-\frac{\partial\tau_{xz}}{\partial x}\delta w\right]dz\,dx-\int_x(\tau_{xz}(x,-h/2)-q)\,\delta u\,dx$$
$$+\int_z(\sigma_{xx}(\bar{x},z)-\overline{\sigma_{xx}})\,\delta u\,dz+\int_z(\tau_{xz}(\bar{x},z)-\overline{\tau_{xz}})\,\delta w\,dz+\int_z\sigma_{xx}(\hat{x},z)\,\delta u\,dz+\int_z\tau_{xz}(\hat{x},z)\,\delta w\,dz=0. \tag{17}$$

In the above equation, $\bar{x}$ denotes the beam end(s) on which one or both of the stresses $\overline{\sigma_{xx}}$ or $\overline{\tau_{xz}}$ are prescribed and $\hat{x}$ denotes the beam end(s) on which one or both of the displacements u and w are prescribed. Vanishing of terms inside the double integral which are multiplied by stress variations yield the stress resultant expressions, while vanishing of terms multiplied by displacement variations yield the equilibrium equations.

From Eqs. (3), (2), and (13), the distribution of normal stress σ_{xx} over the beam thickness can be written as

TOBT:

$$\sigma_{xx}=\frac{3}{4bh}\left[3-20\left(\frac{z}{h}\right)^2\right]N_{xx}+\frac{15}{bh^2}\frac{z}{h}\left[5-28\left(\frac{z}{h}\right)^2\right]M_{xx}-\frac{15}{bh^3}\left[1-12\left(\frac{z}{h}\right)^2\right]S_{xx}-\frac{140}{bh^4}\frac{z}{h}\left[3-20\left(\frac{z}{h}\right)^2\right]P_{xx} \tag{18}$$

SOBT:

$$\sigma_{xx}=\frac{3}{4bh}\left[3-20\left(\frac{z}{h}\right)^2\right]N_{xx}+\frac{12}{bh^2}\frac{z}{h}M_{xx}-\frac{15}{bh^3}\left[1-12\left(\frac{z}{h}\right)^2\right]S_{xx} \tag{19}$$

FOBT:

$$\sigma_{xx}=\frac{1}{bh}N_{xx}+\frac{12}{bh^2}\frac{z}{h}M_{xx}. \tag{20}$$

From classical theory of two-dimensional elasticity

$$\frac{\partial\sigma_{xx}}{\partial x}+\frac{\partial\tau_{xz}}{\partial z}=0. \tag{21}$$

By substituting Eqs. (18), (19), and (20) in Eq. (21), respectively, for TOBT, SOBT, and FOBT and then integrating w.r.t. z and using the relations given by Eqs. (16), the exact interlaminar shear stress distribution through the beam thickness can be written as

TOBT:

$$\tau_{xz}=\frac{15}{16bh}\left[3-40\left(\frac{z}{h}\right)^2+112\left(\frac{z}{h}\right)^4\right]Q_{xz}+\frac{30}{bh^2}\frac{z}{h}\left[1-4\left(\frac{z}{h}\right)^2\right]R_{xz}-\frac{105}{4bh^3}\left[1-24\left(\frac{z}{h}\right)^2+80\left(\frac{z}{h}\right)^4\right]T_{xz}+\left[3+24\left(\frac{z}{h}\right)-120\left(\frac{z}{h}\right)^2-160\left(\frac{z}{h}\right)^3+560\left(\frac{z}{h}\right)^4\right]\frac{q}{16} \tag{22}$$

SOBT:

$$\tau_{xz}=\frac{3}{2bh}\left[1-4\left(\frac{z}{h}\right)^2\right]Q_{xz}+\frac{30}{bh^2}\frac{z}{h}\left[1-4\left(\frac{z}{h}\right)^2\right]R_{xz}-\left[1-6\left(\frac{z}{h}\right)-12\left(\frac{z}{h}\right)^2+40\left(\frac{z}{h}\right)^3\right]\frac{q}{4} \tag{23}$$

FOBT:

$$\tau_{xz}=\frac{3}{2bh}\left[1-4\left(\frac{z}{h}\right)^2\right]Q_{xz}-\left[1+4\left(\frac{z}{h}\right)-12\left(\frac{z}{h}\right)^2\right]\frac{q}{4}. \tag{24}$$

Interlaminar shear stress distribution expressions given by Eqs. (22), (23), and (24) satisfy the shear-free condition at the top of the beam and applied shear traction "q" condition at the bottom of the beam.

TOBT:

For TOBT, substituting Eqs. (1), (18), and (22) into Eq. (17), and then integrating w.r.t. z, we obtain the required stress resultant expressions, equilibrium equations, and boundary conditions. The in-plane stress resultants and equilibrium equations along with boundary conditions obtained are exactly similar to Eqs. (13) and (16), respectively. Further, the exact interlaminar shear stress resultants obtained from Eq. (17) are as follows:

$$Q_{xz}=G_{13}bh\left\{\frac{14}{15}\left(\frac{dw_0}{dx}+\psi_x\right)+\frac{4}{5}\left(\frac{h^2}{4}\right)\xi_x\right\}+\frac{bhq}{30};$$
$$R_{xz}=\frac{7}{10}G_{13}\frac{bh^3}{6}\phi_x-\frac{bh^2q}{40}; \tag{25}$$
$$T_{xz}=G_{13}\frac{bh^3}{12}\left\{\frac{4}{5}\left(\frac{dw_0}{dx}+\psi_x\right)+\frac{2}{3}\left(\frac{9h^2}{20}\right)\xi_x\right\}+\frac{bh^3q}{120}.$$

It is the usual procedure to satisfy shear-free boundary condition at the top and bottom of the beam to determine the shear correction factors and hence by comparing Eq. (25) (having $q=0$) with Eq. (15), we get the shear correction factors for TOBT as $k_1=14/15$, $k_2=7/10$, $k_3=2/3$ and $k_4=4/5$.

Following similar steps as above, we can get the exact interlaminar shear stress resultant expressions for SOBT and FOBT and the corresponding shear correction factors as given below:

SOBT:

$$Q_{xz}=G_{13}bh\,\frac{5}{6}\left(\frac{dw_0}{dx}+\psi_x\right)+\frac{bhq}{12};$$

$$R_{xz}=\frac{7}{10}G_{13}\frac{bh^3}{6}\,\phi_x-\frac{bh^2q}{40} \tag{26}$$

and $k_1=5/6$, $k_2=7/10$.

FOBT:

$$Q_{xz}=G_{13}bh\,\frac{5}{6}\left(\frac{dw_0}{dx}+\psi_x\right)+\frac{bhq}{12} \tag{27}$$

and $k_1=5/6$.

3 Mathematical Modeling of End Notch Flexure (ENF) and End Notch Cantilever (ENC) Stress Analysis Models

The unidirectional ENF and ENC specimens considered for the analysis have been shown in Figs. 1(*a*) and 2(*a*). The respective stress analysis models have been shown in Figs. 1(*b*) and 2(*b*) and these are similar to the stress analysis models proposed by Whitney [12]. However, present stress analysis models differ from Whitney [12] at the stage of application of variationally derived matching conditions at the crack tip which will be explained later. The stress analysis models consider only upper halves (above delamination plane) of ENF and ENC specimens because of the fact that delamination is at midplane and lamination scheme is symmetric about the midplane of ENF and ENC specimens. Further, ENF stress analysis model has cracked $[-a\leqslant x\leqslant 0]$ and uncracked $[0\leqslant x\leqslant(2L-a)]$ regions. The regions $[-a\leqslant x\leqslant 0]$, $[0\leqslant x\leqslant(L-a)]$ and $[(L-a)\leqslant x\leqslant(2L-a)]$ have been idealised as three different beams 1, 2, and 3, respectively, with imaginary cuts at the crack tip and at the point of load application. Similarly, ENC stress analysis model has cracked $[-a\leqslant x\leqslant 0]$ and uncracked $[0\leqslant x\leqslant(L-a)]$ regions idealized as beams 1 and 2, respectively. In the uncracked region, at the bottom of the stress analysis models (i.e., at the midplane of the actual ENF and ENC specimens), surface traction "q" (shear) exists and axial displacement "u" is zero. Further, it has been assumed that the delaminated faces slide over each other freely which means that the frictional effects between the delaminated faces have been neglected. It may be noted that Carlsson et al. [7] showed that for reasonable values of frictional coefficients and E_{11}/G_{13}, the error in SERR induced by neglecting friction is only 2–5%.

3.1 Governing Differential Equations for Cracked and Uncracked Regions. Equilibrium Eqs. (16) can form a set of governing differential equations for uncracked region, as those equations have been derived for the laminated composite beam with applied surface tration and can simulate the uncracked region. Further, in the case of cracked region, governing differential equations can be obtained again from Eqs. (16) by putting $q=0$ (i.e., delaminated faces slide freely over each other). Next, Eqs. (13) form as corresponding inplane stress resultants for both cracked and uncracked regions. However, in the case of interlaminar shear stress resultants, the following three choices can be considered.

Interlaminar shear stress resultants:

<u>TOBT-Exact, SOBT-Exact, and FOBT-Exact</u>. The interlaminar shear stress resultants based on TOBT, SOBT, and FOBT (Eqs. (25), (26), and (27)) simulate the uncracked region of ENF and ENC specimens (Figs. 1(*b*) and 2(*b*)) exactly as these stress resultants have been obtained from the exact interlaminar shear stress distributions which satisfy shear free condition at the top and applied shear traction condition at the bottom of the beam. This choice has been named as TOBT-E/SOBT-E/FOBT-E based on the beam theory under consideration. The exact shear stress resultants (Eqs. (25), (26), and (27)) for uncracked region based on TOBT-E, SOBT-E, and FOBT-E can be written in an unified form as

$$\begin{aligned}
Q_{xz}&=G_{13}bh\left\{k_1\left(\frac{dw_0}{dx}+\psi_x\right)+\alpha_2k_4\left(\frac{h^2}{4}\right)\xi_x\right\}+f_qbhq;\\
R_{xz}&=\alpha_1\left(k_2G_{13}\frac{bh^3}{6}\,\phi_x-f_rbh^2q\right);\\
T_{xz}&=\alpha_2\left[G_{13}\frac{bh^3}{12}\left\{k_4\left(\frac{dw_0}{dx}+\psi_x\right)+k_3\left(\frac{9h^2}{20}\right)\xi_x\right\}+f_tbh^3q\right].
\end{aligned} \tag{28}$$

In the above Eqs. (28), $k_1=14/15$, $k_2=7/10$, $k_3=2/3$, and $k_4=4/5$ for TOBT-E, $k_1=5/6$ and $k_2=7/10$ for SOBT-E and $k_1=5/6$ for FOBT-E. Further, $f_q=1/30$, $f_r=1/40$, and $f_t=1/120$ for TOBT-E, $f_q=1/12$ and $f_r=1/40$ for SOBT-E and $f_q=1/12$ for FOBT-E. Interlaminar shear stress resultant expressions for cracked region can be obtained by substituting $q=0$ in the Eqs. (28).

Further, it is possible to consider two more choices of interlaminar shear stress resultant expressions for cracked and uncracked regions and they are as follows:

<u>Choice-1 (TOBT-1, SOBT-1, FOBT-1)</u>. For both cracked and uncracked regions, interlaminar shear stress resultants given by Eqs. (14) or Eqs. (15) with $k_1=k_2=k_3=k_4=1$ can be considered. This choice has been named as TOBT-1/SOBT-1/FOBT-1 based on the beam theory under consideration.

<u>Choice-2 (TOBT-2, SOBT-2, FOBT-2)</u>. For both cracked and uncracked regions, interlaminar shear stress resultants given by Eqs. (15) can be considered with $k_1=14/15$, $k_2=7/10$, $k_3=2/3$, and $k_4=4/5$ in the case of TOBT and this choice has been named as TOBT-2. Similarly, for SOBT-2, $k_1=5/6$ and $k_2=7/10$ and for FOBT-2, $k_1=5/6$.

Here, it may appear that TOBT-E and TOBT-2 use same shear correction factors, but they differ with each other w.r.t. shear stress resultant expressions in the uncracked region where $q\neq 0$ and they coincide with each other in the cracked region where $q=0$. Similar explanation is valid for SOBT-E and SOBT-2 and also for FOBT-E and FOBT-2.

3.1.1 Cracked Region $[-a\leqslant x\leqslant 0]$—Beam 1 (Figs. 1(b) and 2(b)). The governing differential equations for cracked region in terms of generalized displacements can be obtained by using the stress resultant expressions (Eqs. (13) and (28) (with $q=0$) or (15)) in the Eqs. (16) (with $q=0$) and they are

$$\begin{aligned}
&\overline{E}_{11}bh\left(\frac{d^2u_0}{dx^2}+\alpha_1\frac{h^2}{12}\,\frac{d^2\phi_x}{dx^2}\right)=0\\
&G_{13}bh\left\{k_1\left(\frac{d^2w_0}{dx^2}+\frac{d\psi_x}{dx}\right)+\alpha_2k_4\frac{h^2}{4}\,\frac{d\xi_x}{dx}\right\}=0\\
&\frac{\overline{E}_{11}bh^3}{12}\left(\frac{d^2\psi_x}{dx^2}+\alpha_2\frac{3h^2}{20}\,\frac{d^2\xi_x}{dx^2}\right)-G_{13}bh\left\{k_1\left(\frac{dw_0}{dx}+\psi_x\right)\right.\\
&\qquad\left.+\alpha_2k_4\frac{h^2}{4}\,\xi_x\right\}=0\\
&\alpha_1\left\{\frac{\overline{E}_{11}bh^3}{12}\left(\frac{d^2u_0}{dx^2}+\frac{3h^2}{20}\,\frac{d^2\phi_x}{dx^2}\right)-k_2G_{13}\frac{bh^3}{3}\,\phi_x\right\}=0\\
&\alpha_2\left[\frac{\overline{E}_{11}bh^5}{80}\left\{\frac{d^2\psi_x}{dx^2}+\frac{5h^2}{28}\,\frac{d^2\xi_x}{dx^2}\right\}-\frac{G_{13}bh^3}{4}\left\{k_4\left(\frac{dw_0}{dx}+\psi_x\right)\right.\right.\\
&\qquad\left.\left.+k_3\frac{9h^2}{20}\,\xi_x\right\}\right]=0.
\end{aligned} \tag{29}$$

3.1.2 Uncracked Regions [$0\leqslant x\leqslant(L-a)$] and [$(L-a)\leqslant x\leqslant(2L-a)$]—Beams 2 and 3 (Figs. 1(b) and 2(b)). In the uncracked regions $[0\leqslant x\leqslant(L-a)]$ and $[(L-a)\leqslant x\leqslant(2L-a)]$, $q\neq 0$. Further, axial displacement along $z=-h/2$ has been assumed to be zero ($z=-h/2$ is the bottom surface of the stress analysis model). This can be written as

$$u(@z=-h/2)=0. \tag{30}$$

By using the first part of Eqs. (1) in Eq. (30), u_0 can be expressed in terms of ψ_x, ϕ_x, and ξ_x as

$$u_0=\frac{h}{2}\psi_x-\alpha_1\frac{h^2}{4}\phi_x+\alpha_2\frac{h^3}{8}\xi_x \tag{31}$$

and now the surface traction "q" is the unknown. Consequently, by using Eq. (31) in Eqs. (13), the in-plane stress resultant expressions of N_{xx} and S_{xx} will be modified as

$$N_{xx}=\frac{\overline{E}_{11}bh^2}{2}\left(\frac{d\psi_x}{dx}-\alpha_1\frac{h}{3}\frac{d\phi_x}{dx}+\alpha_2\frac{h^2}{4}\frac{d\xi_x}{dx}\right);$$

$$S_{xx}=\alpha_1\frac{\overline{E}_{11}bh^4}{24}\left(\frac{d\psi_x}{dx}-\frac{h}{5}\frac{d\phi_x}{dx}+\alpha_2\frac{h^2}{4}\frac{d\xi_x}{dx}\right). \tag{32}$$

By using the two modified in-plane stress resultant expressions of N_{xx}, S_{xx} (Eqs. (32)), stress resultant expressions of M_{xx}, P_{xx} (second and fourth parts of Eqs. (13)) and interlaminar shear stress resultant expressions of Q_{xz}, R_{xz}, T_{xz}, (Eqs. (28)) in Eqs. (16), we get the following governing differential equations in terms of generalized displacements and surface traction "q" for "each" uncracked region separately (beam 2 and beam 3):

$$\frac{\overline{E}_{11}bh^2}{2}\left(\frac{d^2\psi_x}{dx^2}-\alpha_1\frac{h}{3}\frac{d^2\phi_x}{dx^2}+\alpha_2\frac{h^2}{4}\frac{d^2\xi_x}{dx^2}\right)-bq=0$$

$$G_{13}bh\left\{k_1\left(\frac{d^2w_0}{dx^2}+\frac{d\psi_x}{dx}\right)+\alpha_2k_4\frac{h^2}{4}\frac{d\xi_x}{dx}\right\}+f_q\frac{dq}{dx}bh=0$$

$$\frac{\overline{E}_{11}bh^3}{12}\left(\frac{d^2\psi_x}{dx^2}+\alpha_2\frac{3h^2}{20}\frac{d^2\xi_x}{dx^2}\right)-G_{13}bh\left\{k_1\left(\frac{dw_0}{dx}+\psi_x\right)+\alpha_2k_4\frac{h^2}{4}\xi_x\right\}+\left(\frac{1}{2}-f_q\right)qbh=0 \tag{33}$$

$$\alpha_1\left[\frac{\overline{E}_{11}bh^4}{24}\left(\frac{d^2\psi_x}{dx^2}-\frac{h}{5}\frac{d^2\phi_x}{dx^2}+\alpha_2\frac{h^2}{4}\frac{d^2\xi_x}{dx^2}\right)-k_2G_{13}\frac{bh^3}{3}\phi_x+\left(2f_r-\frac{1}{4}\right)qbh^2\right]=0$$

$$\alpha_2\left[\frac{\overline{E}_{11}bh^5}{80}\left(\frac{d^2\psi_x}{dx^2}+\frac{5h^2}{28}\frac{d^2\xi_x}{dx^2}\right)-G_{13}\frac{bh^3}{4}\left\{k_4\left(\frac{dw_0}{dx}+\psi_x\right)+k_3\frac{9h^2}{20}\xi_x\right\}+\left(\frac{1}{8}-3f_t\right)qbh^3\right]=0.$$

The solution of Eqs. (29) and (33), for cracked and uncracked regions, can be easily obtained. The details are omitted here for the sake of brevity and available elsewhere, [23]. However, it may be worth mentioning here that in the process of writing solution to Eqs. (29) and (33), one will come across with second and fourth-order differential equations whose auxiliary equations can have real roots or complex roots or combination of real and complex roots. In the present work, for the material properties considered, roots are found to be real, distinct, and nonzero and hence solution has been written for this case only. In the case of the ENF specimen, there will be 26 (10+8+8) (ten constants for cracked region and eight constants for each uncracked region), 20 (8+6+6), 14 (6+4+4), and 14 (6+4+4) unknown constants for TOBT, SOBT, FOBT, and CBT, respectively. Similarly, in the case of ENC specimen, there will be 18 (10+8), 14 (8+6), 10 (6+4), and 10 (6+4) unknown constants for TOBT, SOBT, FOBT, and CBT, respectively. These unknown constants can be determined from the appropriate boundary and matching conditions which will be derived in the next section. Once the unknown constants are determined, corresponding displacements, strains, stresses, and stress resultants can be easily obtained. It should be noted that the present solutions of ENF and ENC specimen are perfectly compatible with deformations that occur in the lower halves of the ENF and ENC specimens (Whitney [12]). In other words, solutions can be obtained to the lower halves of the ENF and ENC specimens which will produce the same distribution of shear stress in the uncracked region as the present solutions. Since axial displacement "u" is zero along the centerline of the ENF and ENC specimens in uncracked region and the vertical displacement "w" does not vary over the depth, complete compatibility of the upper and lower halves of the ENF and ENC specimens will be assured.

4 Boundary and Matching Conditions

In this section, appropriate boundary and matching conditions will be derived. Special attention is necessary for continuity conditions at the crack tip. In the present study, appropriate matching conditions, in terms of generalized displacements and stress resultants, have been derived that are to be applied at the crack tip and at the point of load application by enforcing displacement continuity conditions at the crack tip and at the point of load application in conjunction with variational equation.

The total potential energy, for the stress analysis models of ENF and ENC specimens, is

$$\Pi=\Pi^{(1)}+\Pi^{(2)}+\Pi^{(3)} \tag{34}$$

where, $\Pi^{(1)}$, $\Pi^{(2)}$, and $\Pi^{(3)}$ are the potential energies of the beams 1, 2, and 3, respectively. Further, it may be noted that $\Pi^{(3)}$ does not exist for ENC specimen in the above and subsequent equations.

For equilibrium, the first variation of total potential energy of ENF and ENC stress analysis models is zero and can be written as

$$\delta\Pi=\delta\Pi^{(1)}+\delta\Pi^{(2)}+\delta\Pi^{(3)}=0. \tag{35}$$

For simplification, Eq. (35) can be split as

$$\delta\Pi=\delta\Pi_{eq}^{(1)}+\delta\Pi_{bt}^{(1)}+\delta\Pi_{eq}^{(2)}+\delta\Pi_{bt}^{(2)}+\delta\Pi_{eq}^{(3)}+\delta\Pi_{bt}^{(3)}=0 \tag{36}$$

where, the subscripts "eq" and "bt" represent equilibrium equations and boundary terms of the potential energy, respectively.

Based on TOBT, SOBT, FOBT, and CBT, variational Eq. (36) can be expressed as

$$\begin{aligned}\delta\Pi_{eq}^{(1)}&+[(N_{xx}^{(1)}-\overline{N}_{xx}^{(1)})\delta u_0^{(1)}+(M_{xx}^{(1)}-\overline{M}_{xx}^{(1)})\delta\psi_x^{(1)}+\alpha_1(S_{xx}^{(1)}-\overline{S}_{xx}^{(1)})\delta\phi_x^{(1)}+\alpha_2(P_{xx}^{(1)}-\overline{P}_{xx}^{(1)})\delta\xi_x^{(1)}+(Q_{xz}^{(1)}-\overline{Q}_{xz}^{(1)})\delta w_0^{(1)}]_{@x=-a}^{@x=0}\\&+\delta\Pi_{eq}^{(2)}+[(N_{xx}^{(2)}-\overline{N}_{xx}^{(2)})\delta u_0^{(2)}+(M_{xx}^{(2)}-\overline{M}_{xx}^{(2)})\delta\psi_x^{(2)}+\alpha_1(S_{xx}^{(2)}-\overline{S}_{xx}^{(2)})\delta\phi_x^{(2)}+\alpha_2(P_{xx}^{(2)}-\overline{P}_{xx}^{(2)})\delta\xi_x^{(2)}+(Q_{xz}^{(2)}-\overline{Q}_{xz}^{(2)})\delta w_0^{(2)}]_{@x=0}^{@x=(L-a)}\\&+\delta\Pi_{eq}^{(3)}+[(N_{xx}^{(3)}-\overline{N}_{xx}^{(3)})\delta u_0^{(3)}+(M_{xx}^{(3)}-\overline{M}_{xx}^{(3)})\delta\psi_x^{(3)}+\alpha_1(S_{xx}^{(3)}-\overline{S}_{xx}^{(3)})\delta\phi_x^{(3)}+\alpha_2(P_{xx}^{(3)}-\overline{P}_{xx}^{(3)})\delta\xi_x^{(3)}+(Q_{xz}^{(3)}-\overline{Q}_{xz}^{(3)})\delta w_0^{(3)}]_{@x=(L-a)}^{@x=(2L-a)}=0.\end{aligned} \tag{37}$$

Since ENF and ENC specimens are loaded only at the center and free end, respectively, externally applied $\overline{Q}_{xz}$ exist only at the point of load application in the variational Eq. (37). Further, it may be noted that $\overline{Q}_{xz}$ (at places other than point of load application), $\overline{N}_{xx}$, $\overline{M}_{xx}$, $\overline{S}_{xx}$ and $\overline{P}_{xx}$ do not exist or zero in the variational Eq. (37). Hence, variational Eq. (37) can be rewritten as

$$\begin{aligned}
&\delta\Pi_{eq}^{(1)}+\delta\Pi_{eq}^{(2)}+\delta\Pi_{eq}^{(3)}+[N_{xx}^{(1)}\delta u_0^{(1)}+M_{xx}^{(1)}\delta\psi_x^{(1)}+\alpha_1 S_{xx}^{(1)}\delta\phi_x^{(1)}\\
&\quad+\alpha_2 P_{xx}^{(1)}\delta\xi_x^{(1)}+Q_{xz}^{(1)}\delta w_0^{(1)}]_{@x=0}-[N_{xx}^{(1)}\delta u_0^{(1)}+M_{xx}^{(1)}\delta\psi_x^{(1)}\\
&\quad+\alpha_1 S_{xx}^{(1)}\delta\phi_x^{(1)}+\alpha_2 P_{xx}^{(1)}\delta\xi_x^{(1)}+(Q_{xz}^{(1)}-\overline{Q}_{xz}^{(1)})\delta w_0^{(1)}]_{@x=-a}\\
&\quad+[N_{xx}^{(2)}\delta u_0^{(2)}+M_{xx}^{(2)}\delta\psi_x^{(2)}+\alpha_1 S_{xx}^{(2)}\delta\phi_x^{(2)}+\alpha_2 P_{xx}^{(2)}\delta\xi_x^{(2)}\\
&\quad+(Q_{xz}^{(2)}-\overline{Q}_{xz}^{(2)})\delta w_0^{(2)}]_{@x=(L-a)}-[N_{xx}^{(2)}\delta u_0^{(2)}+M_{xx}^{(2)}\delta\psi_x^{(2)}\\
&\quad+\alpha_1 S_{xx}^{(2)}\delta\phi_x^{(2)}+\alpha_2 P_{xx}^{(2)}\delta\xi_x^{(2)}+Q_{xz}^{(2)}\delta w_0^{(2)}]_{@x=0}+[N_{xx}^{(3)}\delta u_0^{(3)}\\
&\quad+M_{xx}^{(3)}\delta\psi_x^{(3)}+\alpha_1 S_{xx}^{(3)}\delta\phi_x^{(3)}+\alpha_2 P_{xx}^{(3)}\delta\xi_x^{(3)}\\
&\quad+Q_{xz}^{(3)}\delta w_0^{(3)}]_{@x=(2L-a)}-[N_{xx}^{(3)}\delta u_0^{(3)}+M_{xx}^{(3)}\delta\psi_x^{(3)}\\
&\quad+\alpha_1 S_{xx}^{(3)}\delta\phi_x^{(3)}+\alpha_2 P_{xx}^{(3)}\delta\xi_x^{(3)}+(Q_{xz}^{(3)}\\
&\quad-\overline{Q}_{xz}^{(3)})\delta w_0^{(3)}]_{@x=(L-a)}=0.
\end{aligned}\tag{38}$$

In order to combine beam 1 with beam 2 (at the crack tip) and beam 2 with beam 3 (at the point of load application only for ENF specimen), the following displacement continuity conditions over the depth (thickness) of the ENF and ENC stress analysis models have to be applied at the junctions of the above beams.

Displacement continuity conditions:

At the crack tip $(x=0)$:

$$\begin{aligned}
&u_0^{(1)}+z\psi_x^{(1)}+\alpha_1 z^2\phi_x^{(1)}+\alpha_2 z^3\xi_x^{(1)}=u_0^{(2)}+z\psi_x^{(2)}+\alpha_1 z^2\phi_x^{(2)}\\
&\quad+\alpha_2 z^3\xi_x^{(2)};\quad w_0^{(1)}=w_0^{(2)}.
\end{aligned}\tag{39}$$

At the point of load application $[x=(L-a)]$: (only for ENF specimen):

$$\begin{aligned}
&u_0^{(2)}+z\psi_x^{(2)}+\alpha_1 z^2\phi_x^{(2)}+\alpha_2 z^3\xi_x^{(2)}=u_0^{(3)}+z\psi_x^{(3)}+\alpha_1 z^2\phi_x^{(3)}\\
&\quad+\alpha_2 z^3\xi_x^{(3)};\quad w_0^{(2)}=w_0^{(3)}.
\end{aligned}\tag{40}$$

In Eqs. (39) and (40), $u_0^{(2)}=(h/2\psi_x^{(2)}-\alpha_1 h^2/4\phi_x^{(2)}+\alpha_2 h^3/8\xi_x^{(2)})$ and $u_0^{(3)}=(h/2\psi_x^{(3)}-\alpha_1 h^2/4\phi_x^{(3)}+\alpha_2 h^3/8\xi_x^{(3)})$.

From Eqs. (39) and (40), continuity conditions for generalized displacements can be written by equating the coefficients of like terms. This results in the following continuity conditions in terms of generalized displacements that are required to maintain the displacement continuity over the depth of the stress analysis models at the crack tip and at the point of load application (only for ENF specimen).

At the Crack Tip $(x=0)$:

$$\begin{aligned}
&u_0^{(1)}=u_0^{(2)}=\left(\frac{h}{2}\psi_x^{(2)}-\alpha_1\frac{h^2}{4}\phi_x^{(2)}+\alpha_2\frac{h^3}{8}\xi_x^{(2)}\right);\\
&\psi_x^{(1)}=\psi_x^{(2)};\quad \alpha_1\phi_x^{(1)}=\alpha_1\phi_x^{(2)};\quad \alpha_2\xi_x^{(1)}=\alpha_2\xi_x^{(2)};\\
&w_0^{(1)}=w_0^{(2)}.
\end{aligned}\tag{41}$$

At the Point of Load Application $[x=(L-a)]$: (only for ENF specimen):

$$\begin{aligned}
&\psi_x^{(2)}=\psi_x^{(3)};\quad \alpha_1\phi_x^{(2)}=\alpha_1\phi_x^{(3)};\quad \alpha_2\xi_x^{(2)}=\alpha_2\xi_x^{(3)};\\
&w_0^{(2)}=w_0^{(3)}.
\end{aligned}\tag{42}$$

Substitution of generalized displacement continuity conditions (Eqs. (41) and (42)) in the variational Eq. (38) gives

$$\begin{aligned}
&\delta\Pi_{eq}^{(1)}+\delta\Pi_{eq}^{(2)}+\delta\Pi_{eq}^{(3)}-[N_{xx}^{(1)}\delta u_0^{(1)}+M_{xx}^{(1)}\delta\psi_x^{(1)}+\alpha_1 S_{xx}^{(1)}\delta\phi_x^{(1)}\\
&\quad+\alpha_2 P_{xx}^{(1)}\delta\xi_x^{(1)}+(Q_{xz}^{(1)}-\overline{Q}_{xz}^{(1)})\delta w_0^{(1)}]_{@x=-a}\\
&\quad+\Bigg[\left(\left(M_{xx}^{(1)}+\frac{h}{2}N_{xx}^{(1)}\right)-\left(M_{xx}^{(2)}+\frac{h}{2}N_{xx}^{(2)}\right)\right)\delta\psi_x^{(2)}\\
&\quad+\alpha_1\left(\left(S_{xx}^{(1)}-\frac{h^2}{4}N_{xx}^{(1)}\right)-\left(S_{xx}^{(2)}-\frac{h^2}{4}N_{xx}^{(2)}\right)\right)\delta\phi_x^{(2)}\\
&\quad+\alpha_2\left(\left(P_{xx}^{(1)}+\frac{h^3}{8}N_{xx}^{(1)}\right)-\left(P_{xx}^{(2)}+\frac{h^3}{8}N_{xx}^{(2)}\right)\right)\delta\xi_x^{(2)}\\
&\quad+((Q_{xz}^{(1)}-Q_x^{(2)}))\delta w_0^{(2)}\Bigg]_{@x=0}\\
&\quad+\Bigg[\left(\left(M_{xx}^{(2)}+\frac{h}{2}N_{xx}^{(2)}\right)-\left(M_{xx}^{(3)}+\frac{h}{2}N_{xx}^{(3)}\right)\right)\delta\psi_x^{(2)}\\
&\quad+\alpha_1\left(\left(S_{xx}^{(2)}-\frac{h^2}{4}N_{xx}^{(2)}\right)-\left(S_{xx}^{(3)}-\frac{h^2}{4}N_{xx}^{(3)}\right)\right)\delta\phi_x^{(2)}\\
&\quad+\alpha_2\left(\left(P_{xx}^{(2)}+\frac{h^3}{8}N_{xx}^{(2)}\right)-\left(P_{xx}^{(3)}+\frac{h^3}{8}N_{xx}^{(3)}\right)\right)\delta\xi_x^{(2)}\\
&\quad+((Q_{xz}^{(2)}-Q_{xz}^{(3)})-(\overline{Q}_{xz}^{(2)}-\overline{Q}_{xz}^{(3)}))\delta w_0^{(2)}\Bigg]_{@x=(L-a)}\\
&\quad+\Bigg[\left(\left(M_{xx}^{(3)}+\frac{h}{2}N_{xx}^{(3)}\right)\right)\delta\psi_x^{(3)}+\alpha_1\left(\left(S_{xx}^{(3)}-\frac{h^2}{4}N_{xx}^{(3)}\right)\right)\delta\phi_x^{(3)}\\
&\quad+\alpha_2\left(\left(P_{xx}^{(3)}+\frac{h^3}{8}N_{xx}^{(3)}\right)\right)\delta\xi_x^{(3)}+Q_{xz}^{(3)}\delta w_0^{(3)}\Bigg]_{@x=(2L-a)}=0.
\end{aligned}\tag{43}$$

In the above equation, terms related to beam 3 (terms with superscript (3)) do not exist for ENC specimen.

4.1 Boundary and Matching Conditions for ENF and ENC Specimens. From the variational Eq. (43) and displacement continuity conditions (Eqs. (41) and (42)) at the crack tip and at the point of load application, the following boundary and matching conditions, which are variationally consistent (as they are obtained from the variational equation), can be written for ENF and ENC specimens.

4.1.1 ENF Specimen. Left Simple Support $(x=-a)$:

$$w_0^{(1)}=0;\quad N_{xx}^{(1)}=0;\quad M_{xx}^{(1)}=0;\quad \alpha_1 S_{xx}^{(1)}=0;\quad \alpha_2 P_{xx}^{(1)}=0.\tag{44}$$

At the Crack Tip $(x=0)$:

$$\begin{aligned}
&u_0^{(1)}=u_0^{(2)}=\left(\frac{h}{2}\psi_x^{(2)}-\alpha_1\frac{h^2}{4}\phi_x^{(2)}+\alpha_2\frac{h^3}{8}\xi_x^{(2)}\right);\\
&\psi_x^{(1)}=\psi_x^{(2)};\quad \alpha_1\phi_x^{(1)}=\alpha_1\phi_x^{(2)};\quad \alpha_2\xi_x^{(1)}=\alpha_2\xi_x^{(2)};\\
&w_0^{(1)}=w_0^{(2)};\\
&\left(M_{xx}^{(1)}+\frac{h}{2}N_{xx}^{(1)}\right)=\left(M_{xx}^{(2)}+\frac{h}{2}N_{xx}^{(2)}\right);\quad \alpha_1\left(S_{xx}^{(1)}-\frac{h^2}{4}N_{xx}^{(1)}\right)\\
&\quad=\alpha_1\left(S_{xx}^{(2)}-\frac{h^2}{4}N_{xx}^{(2)}\right);\\
&\alpha_2\left(P_{xx}^{(1)}+\frac{h^3}{8}N_{xx}^{(1)}\right)=\alpha_2\left(P_{xx}^{(2)}+\frac{h^3}{8}N_{xx}^{(2)}\right);\quad Q_{xz}^{(1)}=Q_{xz}^{(2)}.
\end{aligned}\tag{45}$$

At the Point of Load Application $[x=(L-a)]$:

$$\psi_x^{(2)}=\psi_x^{(3)};\quad \alpha_1\phi_x^{(2)}=\alpha_1\phi_x^{(3)};\quad \alpha_2\xi_x^{(2)}=\alpha_2\xi_x^{(3)};$$

$$w_0^{(2)} = w_0^{(3)};$$

$$\left(M_{xx}^{(2)} + \frac{h}{2} N_{xx}^{(2)}\right) = \left(M_{xx}^{(3)} + \frac{h}{2} N_{xx}^{(3)}\right); \quad \alpha_1\left(S_{xx}^{(2)} - \frac{h^2}{4} N_{xx}^{(2)}\right)$$

$$= \alpha_1\left(S_{xx}^{(3)} - \frac{h^2}{4} N_{xx}^{(3)}\right); \tag{46}$$

$$\alpha_2\left(P_{xx}^{(2)} + \frac{h^3}{8} N_{xx}^{(2)}\right) = \alpha_2\left(P_{xx}^{(3)} + \frac{h^3}{8} N_{xx}^{(3)}\right); \quad Q_{xz}^{(2)} - Q_{xz}^{(3)} = \overline{Q}_{xz}^{(2)}$$

$$-\overline{Q}_{xz}^{(3)} = -P/2.$$

Right Simple Support $[x = (2L - a)]$:

$$w_0^{(3)} = 0; \quad \left(M_{xx}^{(3)} + \frac{h}{2} N_{xx}^{(3)}\right) = 0; \quad \alpha_1\left(S_{xx}^{(3)} - \frac{h^2}{4} N_{xx}^{(3)}\right) = 0;$$

$$\alpha_2\left(P_{xx}^{(3)} + \frac{h^3}{8} N_{xx}^{(3)}\right) = 0. \tag{47}$$

4.1.2 ENC Specimen. Free End $(x = -a)$:

$$N_{xx}^{(1)} = 0; \quad M_{xx}^{(1)} = 0; \quad \alpha_1 S_{xx}^{(1)} = 0; \quad \alpha_2 P_{xx}^{(1)} = 0;$$

$$Q_{xz}^{(1)} = \overline{Q}_{xz}^{(1)} = P/2. \tag{48}$$

At the Crack Tip $(x = 0)$:

$$u_0^{(1)} = u_0^{(2)} = \left(\frac{h}{2} \psi_x^{(2)} - \alpha_1 \frac{h^2}{4} \phi_x^{(2)} + \alpha_2 \frac{h^3}{8} \xi_x^{(2)}\right);$$

$$\psi_x^{(1)} = \psi_x^{(2)}; \quad \alpha_1 \phi_x^{(1)} = \alpha_1 \phi_x^{(2)}; \quad \alpha_2 \xi_x^{(1)} = \alpha_2 \xi_x^{(2)};$$

$$w_0^{(1)} = w_0^{(2)}; \tag{49}$$

$$\left(M_{xx}^{(1)} + \frac{h}{2} N_{xx}^{(1)}\right) = \left(M_{xx}^{(2)} + \frac{h}{2} N_{xx}^{(2)}\right);$$

$$\alpha_1\left(S_{xx}^{(1)} - \frac{h^2}{4} N_{xx}^{(1)}\right) = \alpha_1\left(S_{xx}^{(2)} - \frac{h^2}{4} N_{xx}^{(2)}\right);$$

$$\alpha_2\left(P_{xx}^{(1)} + \frac{h^3}{8} N_{xx}^{(1)}\right) = \alpha_2\left(P_{xx}^{(2)} + \frac{h^3}{8} N_{xx}^{(2)}\right); \quad Q_{xz}^{(1)} = Q_{xz}^{(2)}.$$

Clamped Support $[x = (L - a)]$:

$$w_0^{(2)} = 0; \quad \psi_x^{(2)} = 0; \quad \alpha_1 \phi_x^{(2)} = 0; \quad \alpha_2 \xi_x^{(2)} = 0. \tag{50}$$

Boundary and matching conditions for classical beam theory can be obtained by substituting $\psi_x = -dw_0/dx$ in the above equations. From the Eqs. (44)–(50), it can be observed that TOBT, SOBT, FOBT, and CBT have 26, 20, 14, and 14 boundary and matching conditions, respectively, for ENF specimen. Similarly, in the case of ENC specimen, TOBT, SOBT, FOBT, and CBT have 18, 14, 10, and 10 boundary and matching conditions respectively.

5 Determination of Compliance and Strain Energy Release Rate

The compliance "C" can be obtained from the following relation:

$$C = \frac{\delta}{P} \tag{51}$$

in which "δ" is the deflection under the load.

The strain energy release rate (SERR) and the compliance are related by the following formula:

$$G_{\mathrm{II}} = \frac{P^2}{2b} \frac{dC}{da}. \tag{52}$$

In the present study, (dC/da) has not been determined explicitly as it is tedious, particularly in the case of beam theories SOBT and TOBT. And hence, the derivative (dC/da) has been evaluated using the *finite difference method* (by adopting the *central finite difference approximation*). Then the compliance derivative can be written as

$$\left(\frac{dC}{da}\right)_n = \frac{C_{n+1} - C_{n-1}}{2\Delta} \tag{53}$$

in which $(dC/da)_n$ is the compliance derivative at delamination length a_n, C_{n+1} is the compliance when delamination length is a_{n+1}, C_{n-1} is the compliance when delamination length is a_{n-1} and Δ is the spacing between two successive delamination lengths.

Hence, we can obtain SERR from the following expression:

$$G_{\mathrm{II}} = \frac{P^2}{2b}\left(\frac{C_{n+1} - C_{n-1}}{2\Delta}\right). \tag{54}$$

In the case of CBT, the following compliance and SERR expressions can be derived/obtained for ENF and ENC specimens which are similar to those available in the literature, [12]:

$$C^{\mathrm{CBT}} = \frac{c_1 L^3 + 3a^3}{c_2 \overline{E}_{11} b h^3}; \quad G_{\mathrm{II}}^{\mathrm{CBT}} = \frac{9a^2 P^2}{2c_2 \overline{E}_{11} b^2 h^3}; \quad q = \frac{-3P}{4c_3 bh} \tag{55}$$

where $c_1 = 2$ (ENF), 1 (ENC), $c_2 = 8$ (ENF), 2 (ENC), and $c_3 = 2$ (ENF), -1 (ENC).

It may be worth mentioning here that FORTRAN programs have been written for all the required mathematical steps to analyze unidirectional ENF and ENC specimens using the theories TOBT, SOBT, FOBT, and CBT.

6 Results and Discussion

6.1 Comparison With Earlier Research. First, in order to validate present formulation, the compliance and the SERR, obtained from the present stress analysis models of unidirectional ENF and ENC specimens considering various theories CBT, FOBT, SOBT, and TOBT, have been compared with the available results, [7,10,12,17,18,22,24,25], in the literature.

Table 1 Comparison of compliance and SERR values obtained from the present work with the experimental results of Sela et al. [25] for unidirectional ENF specimen

Material Properties: Graphite/Epoxy
$E_{11} = 140$ GPa, $E_{22} = 10$ GPa, $G_{13} = 6$ GPa and $\nu_{13} = 0.34$
Geometrical Properties:
L = half-span = 50.8 mm, b = width = 25.4 mm
h = half-thickness = 1.524 mm, $2h$ = 3.048 mm,
(No. of laminae = 24, lamina thickness = 0.127 mm)
a = crack length = 25.4 mm
Loading: P_c = 67.3 kg = 660.213 N

Model/Theory	Compliance (mm/N)		SERR-$G_{\mathrm{II}c}$ (J/m^2)	
Sela et al. [25]	0.00316		527	
Present Work				
	Pl. ϵ†	Pl. σ‡	Pl. ϵ†	Pl. σ‡
CBT	0.00307	0.003092	490.6896	494.7750
FOBT-E	0.003126	0.003152	491.3822	495.4677
FOBT-1	0.003121	0.003147	490.6896	494.7750
FOBT-2	0.003132	0.003158	490.6896	494.7750
SOBT-E	0.003167	0.003193	512.2981	516.4701
SOBT-1	0.003159	0.003185	509.2989	513.4609
SOBT-2	0.003180	0.003205	512.9724	517.1494
TOBT-E	0.003182	0.003208	524.1528	528.3746
TOBT-1	0.003177	0.003203	520.7998	525.0084
TOBT-2	0.003195	0.003221	527.4948	531.7303

†Pl. ϵ: plane-strain-type analysis.
‡Pl. σ: plane-stress-type analysis.

Table 2 Comparison of normalized SERR values obtained from the present work with the existing results for ENF specimen

Normalized Strain Energy Release Rates G_{II}/G_{II}^{CBT}

Geometry: span $=2L=76.2$ mm (3 in), depth $=2h=3.39979$ mm(0.13385 in), and breadth $=b=25.4$ mm (1 in)
Material: $E_{11}=115.1425$ GPa (16.7×10^3 ksi), $E_{33}=E_{22}=9.6527$ GPa (1.4×10^3 ksi), $G_{13}=4.4816$ GPa (0.65×10^3 ksi), and $\nu_{13}=0.3$
Loading: $P=4.44822$ N (1 lbf)

a/L	Salpekar et al. [24]†	Chatterjee [18]	Ding and Kortschot [22]	Whitney [12]	Whitney [10]	Carlsson et al. [7]
0.2	1.305	1.315	1.298	1.388	1.448	1.256
0.3		1.205		1.247	1.298	1.114
0.4	1.142	1.152	1.16	1.181	1.360	1.064
0.5		1.121		1.143	1.171	1.041
0.6	1.090	1.100	1.108	1.118	1.133	1.028
0.7		1.085		1.101	1.121	1.021
0.8	1.064	1.074	1.082	1.088	1.104	1.016
0.9	1.050	1.066	1.073	1.079	1.071	1.013
	FOBT-2	FOBT-E	SOBT-2	SOBT-E	TOBT-2	TOBT-E
			Present Work—Plane Strain			
0.2	1.0	1.0215	1.1828	1.1894	1.3079	1.2808
0.3	1.0	1.0095	1.1202	1.1210	1.2007	1.1828
0.4	1.0	1.0054	1.0895	1.0888	1.1488	1.1354
0.5	1.0	1.0034	1.0713	1.0701	1.1182	1.1075
0.6	1.0	1.0024	1.0592	1.0578	1.0979	1.0891
0.7	1.0	1.0018	1.0503	1.0491	1.0830	1.0759
0.8	1.0	1.0013	1.0423	1.0419	1.0696	1.0648
0.9	1.0	1.0010	1.0275	1.0310	1.0484	1.0496
			Present Work—Plane Stress			
0.2	1.0	1.0213	1.1821	1.1886	1.3066	1.2797
0.3	1.0	1.0095	1.1197	1.1205	1.1999	1.1821
0.4	1.0	1.0053	1.0891	1.0884	1.1482	1.1349
0.5	1.0	1.0034	1.0710	1.0698	1.1177	1.1071
0.6	1.0	1.0024	1.0589	1.0576	1.0975	1.0888
0.7	1.0	1.0017	1.0501	1.0489	1.0827	1.0756
0.8	1.0	1.0013	1.0421	1.0418	1.0693	1.0646
0.9	1.0	1.0010	1.0275	1.0310	1.0483	1.0495

†SERR values obtained from virtual crack closure technique (VCCT) and two-dimensional plane-strain finite element analysis

Compliance and SERR values, obtained from present work, have been compared with the experimentally obtained compliance and SERR values of Sela et al. [25] for ENF specimen made up of graphite/epoxy material without any tough adhesive layers and presented in Table 1. By closely examining the Table 1, the following observations can be made. In general, as the order of the theory increases compliance and SERR values are converging to the Sela et al. [25] results and hence it can be concluded that the performance of present formulation of the stress analysis models is good. Among all the beam theories considered, SERR values obtained from TOBT are in good agreement with the SERR values of Sela et al. [25]. Hence, it can be said that higher-order shear deformation theories are important to be considered for SERR calculation. Further, it can be observed that there is no difference between the SERR values of CBT and FOBT-1,2. This indicates that transverse shear deformation up to first order (FOBT-1,2) has no influence on SERR values (but not in the case of FOBT-E). A similar observation was pointed out by Corleto and Hogan [20].

In Table 2, normalized SERR values from the shear deformation theories considered (SERR values of shear deformation beam theories have been normalized with SERR values from CBT) have been compared with those from earlier research works. From this table, it can observed that TOBT-2,E theories are in good agreement with those of Salpekar et al. [24], Chatterjee [18], and Ding and Kortschot [22]. Further, the following points can be observed and discussed from Table 2. Whitney [12] presented the results based on second-order beam theory in which it appears, to the authors knowledge, that while applying the matching or continuity conditions at the crack tip, contribution from stress resultant S_{xx} is left out. This approach gives the SERR values which are on the higher side when compared to Salpekar et al. [24]. SOBT-1,2,E of present work are also based on second order beam theories similar to the earlier ones in the literature except that the matching or continuity conditions are applied appropriately which incorporates the contribution of stress resultant S_{xx} into the matching or continuity conditions. Because of this change in the matching conditions, SERR values from SOBT are much lower than those of Salpekar et al. [24]. It can also be seen that SERR values from TOBT (with proper matching conditions at the crack tip) are close to the finite element analysis results of Salpekar et al. [24]. This indicates that as the order of the shear deformation increases SERR values from the shear deformation beam theories (with proper matching conditions at the crack tip) converge towards the SERR values obtained from finite element analysis. This observation highlights the fact that it is equally important to apply proper matching or continuity conditions at the crack tip for more reliable and accurate analysis apart from considering higher-order (second and third) shear deformation effects to obtain compliance and SERR.

Present work results have also been compared with those of Wang and Williams [17] for ENF and ENC specimens in Tables 3 and 4 respectively. Once again it can be observed that, among all the theories, compliance and SERR obtained from third order beam theory (TOBT-E) are in better agreement with those from Wang and Williams [17].

6.2 Comparison Between Plane Stress and Plane Strain Analyses. In order to clarify the point that whether plane stress or plane strain condition (constitutive equation) to be considered for the analysis, a parametric study has been carried out by varying the values E_{11}/E_{22} for fixed a/L, L/h, E_{11}, G_{13}, ν_{13}, and load (P) values and the results have been presented for both compliance and SERR in Table 5. It can be seen clearly from this table that as E_{11}/E_{22} increases the difference between plane stress and

Table 3 Comparison of compliance and SERR values obtained from present work with Wang and Williams [17] results for ENF specimen

Material: $S_{11}=6.8\times10^{-3}\ (\mathrm{GPa})^{-1}$, $S_{22}=128\times10^{-3}\ (\mathrm{GPa})^{-1}$, $S_{66}=362\times10^{-3}\ (\mathrm{GPa})^{-1}$, and $\nu_{12}=0.3$
Geometry: $L=50$ mm, $b=1.0$ mm, and $h=1.5$ mm. Loading: $P=1.0$ N.

a (mm)	Wang and Williams [17]		Present Work—Plane Stress: CBT	FOBT-E	SOBT-E	TOBT-E
	Compliance (mm/N)					
10	0.068876		0.063719	0.066931	0.067663	0.067637
20	0.075197		0.069007	0.072265	0.073545	0.073823
30	0.091374		0.083363	0.086666	0.088856	0.089646
40	0.121900		0.111319	0.114667	0.118123	0.119627
	SERR$\times10^3$ (N/mm)					
	FEM	Semi-Empirical				
10	0.151	0.151	0.113	0.116	0.134	0.144
20	0.551	0.526	0.453	0.456	0.492	0.513
30	1.182	1.128	1.020	1.022	1.077	1.108
40	2.025	1.957	1.813	1.816	1.887	1.927
	Effect of shear deformation (E_{11}/G_{13}) on SERR:					$a=20$ mm
E_{11}/G_{13}						
26.62	0.527	0.508	0.453	0.455	0.480	0.495
53.24	0.551	0.526	0.453	0.456	0.492	0.513
106.47	0.587	0.552	0.453	0.458	0.510	0.538
212.94	0.637	0.592	0.453	0.462	0.536	0.575
735.29	0.783	0.719	0.453	0.485	0.614	0.682

Note: $S_{11}=1/E_{11}$, $S_{22}=1/E_{22}$, $S_{66}=1/G_{12}$, and $G_{13}=G_{12}$

plane strain conditions reduces and becomes less than 5% for $E_{11}/E_{22}\geqslant 2$ and 1% for $E_{11}/E_{22}\geqslant 10$. Hence, one can consider either plane stress or plane strain condition for the analysis when E_{11}/E_{22} is sufficiently large.

6.3 Influence of Crack Length (a/L Ratio). From Tables 3 and 4, it can be observed that compliance and SERR increase as crack length increases.

The material, geometrical properties, and load have been taken from Salpekar et al. [24] to present the results in Figs. 3 to 5. The length $(2L)$, breadth (b), and depth $(2h)$ of the ENF specimen are 76.2 mm (3.0 in), 25.4 mm (1 in), and 3.39979 mm (0.13385 in), respectively. The material properties are $E_{11}=115.1425$ GPa $(16.7\times10^3$ ksi), $E_{22}=E_{33}=9.6527$ GPa $(1.4\times10^3$ ksi), $G_{13}=4.4816$ GPa $(0.65\times10^3$ ksi), and $\nu_{13}=0.3$. Loading is $P=4.44822$ N (1 lbf).

Figure 3 shows the influence of crack length on the normalized SERR values obtained from various shear deformation theories. The SERR values of TOBT-E, SOBT-E, and FOBT-E approach those of CBT as the crack length increases.

Figure 4 shows the normalized shear stress distribution ahead of the crack tip obtained from various beam theories for a given crack length $(a/L=0.5)$. It can be observed that TOBT-E and SOBT-E give high peak shear stress at the crack tip which decays exponentially to that of CBT as distance increases from the crack tip. It can also be observed that shear stress given by FOBT-E is constant ahead of the crack tip and is equal to that of CBT. It implies that first-order shear deformation does not affect the shear stress distribution ahead of the crack tip. Also it can be noted that peak shear stress values of TOBT-E are greater than those of SOBT-E.

Figure 5 gives the influence of crack length "a/L" on the normalized shear stress distribution ahead of the crack tip for TOBT-E. It can be observed from this figure that as crack length increases peak shear stress increases and for all crack lengths the shear stress distribution decays exponentially.

6.4 Influence of Shear Deformation (E_{11}/G_{13} Ratio). Tables 3 and 4 show the performance of FOBT-E, SOBT-E, and TOBT-E for higher E_{11}/G_{13} ratios. TOBT-E shows good agreement with the results of Wang and Williams [17] when compared to SOBT-E and FOBT-E as the E_{11}/G_{13} ratio increases. This proves the fact that third (higher) order shear deformation beam theories are necessary when E_{11}/G_{13} ratios are higher. Further, it can be seen that as E_{11}/G_{13} ratio increases SERR increases for a given crack length.

The material, geometrical properties and load have been taken from Gillespie et al. [26] to present the results shown in Figs. 6 and 7. The material properties are $E_{11}=126.1$ GPa, $E_{33}=9.7$ GPa, and $\nu_{13}=0.3$. The geometrical properties are Length $(2L)=101.6$ mm and breadth $(b)=25.4$ mm. The loading is $P=100$ N.

Figure 6 shows the normalized shear stress distribution ahead of the crack tip based on TOBT-E for various E_{11}/G_{13} ratios and for a given crack length $(a/L=0.5)$. From this figure, it can be seen that test specimens with lower E_{11}/G_{13} ratio will have high peak shear stress where as test specimens with higher E_{11}/G_{13} ratio will have low peak shear stress. Further, it can also be observed that in the case of test specimens with lower E_{11}/G_{13} ratio, TOBT-E decays to CBT more steeply when compared to the test specimens with higher E_{11}/G_{13} ratio. In other words, for higher order shear deformation theories, shear stress decays more steeply in the case of test specimens with lower E_{11}/G_{13} ratios while the decay of shear stress is gradual in the case of test specimens with higher E_{11}/G_{13} ratios.

6.5 Influence of Thickness or Depth of the Specimen (L/h Ratio). Influence of thickness on SERR has been shown in the Table 6. It can be observed from this table that as L/h ratio increases SERR increase for the given crack length. Normalized shear stress distribution ahead of the crack tip, based on TOBT-E, has been shown in the Fig. 7 for various L/h ratios and for a given crack length $(a/L=0.5)$. It can be observed from Fig. 7 that as

Table 4 Comparison of Compliance and SERR values obtained from present work with Wang and Williams [17] results for ENC specimen

Material: $S_{11}=6.8\times10^{-3}$ (GPa)$^{-1}$, $S_{22}=128\times10^{-3}$ (GPa)$^{-1}$, $S_{66}=362\times10^{-3}$ (GPa)$^{-1}$, and $\nu_{12}=0.3$
Geometry: $L=60$ mm, $b=1.0$ mm, and $h=1.0$ mm $P=1.0$ N

a (mm)	Wang and Williams [17]		Present Work—Plane Stress CBT	FOBT-E	SOBT-E	TOBT-E
			Compliance (mm/N)			
2	0.9215		0.7345	0.7459	0.7480	0.7476
5	0.9234		0.7357	0.7472	0.7496	0.7494
10	0.9347		0.7446	0.7563	0.7599	0.7604
20	1.0160		0.8160	0.8280	0.8365	0.8397
30	1.2260		1.0098	1.0220	1.0388	1.0466
40	1.6280		1.3872	1.3997	1.4279	1.4422
50	2.2820		2.0094	2.0222	2.0650	2.0878
55	2.7220		2.4314	2.4443	2.4955	2.5229
			SERR$\times10^2$ (N/mm)			
	FEM J-Integral	Semi-empirical				
2	0.0134	0.014	0.0061	0.0075	0.0107	0.0123
5	0.054	0.056	0.038	0.040	0.048	0.052
10	0.183	0.186	0.153	0.154	0.171	0.180
20	0.672	0.677	0.612	0.613	0.646	0.665
30	1.466	1.474	1.377	1.378	1.427	1.455
40	2.567	2.577	2.448	2.449	2.515	2.552
50	3.972	3.987	3.825	3.826	3.908	3.954
55	4.752	4.806	4.628	4.630	4.708	4.747
	Effect of shear deformation (E_{11}/G_{13}) on SERR:					$a=20$ mm
E_{11}/G_{13}						
2.94	0.647	0.634	0.612	0.612	0.620	0.624
26.62	0.661	0.662	0.612	0.6127	0.636	0.649
53.24	0.672	0.677	0.612	0.6134	0.646	0.665
106.47	0.697	0.700	0.612	0.615	0.661	0.687
212.94	0.727	0.735	0.612	0.617	0.683	0.720
735.29	0.877	0.842	0.612	0.631	0.754	0.820

Note: $S_{11}=1/E_{11}$, $S_{22}=1/E_{22}$, $S_{66}=1/G_{12}$, and $G_{13}=G_{12}$

L/h increases peak shear stress at the crack tip increases. In other words it can be said that shallow (thin) test specimens will have higher peak shear stresses at the crack tip when compared to deeper (thick) test specimens. It can also be observed that the shear stress distribution of TOBT-E converges to CBT more sharply for test specimen with higher (shallow test specimen) L/h ratio when compared to specimen with small (deeper test specimen) L/h ratio.

Table 5 Comparison between plane-stress-type (Pl. σ) and plane-strain (Pl. ϵ)-type analyses for various E_{11}/E_{22} values (ENF specimen)

Theory: TOBT-E
Geometrical properties: $a/L=0.5$, $L/h=22.4$
Material properties: $E_{11}=115.1425$ GPa (16.7×10^3 ksi),
$G_{13}=4.4816$ GPa (0.65×10^3 ksi) and $\nu_{13}=0.3$

	Compliance$\times10^5$ (mm/N)			SERR$\times10^6$ (N/mm)		
E_{11}/E_{22}	Pl. σ	Pl. ϵ	% diff[†]	Pl. σ	Pl. ϵ	−% diff
1	123.1337	112.7151	9.24	12.2529	11.2038	9.36
2	123.1337	117.9256	4.42	12.2529	11.7287	4.47
3	123.1337	119.6614	2.90	12.2529	11.9035	2.94
4	123.1337	120.5299	2.16	12.2529	11.9909	2.19
5	123.1337	121.0501	1.72	12.2529	12.0433	1.74
10	123.1337	122.0916	0.85	12.2529	12.1481	0.86
15	123.1337	122.4388	0.57	12.2529	12.1831	0.57
20	123.1337	122.6124	0.43	12.2529	12.2005	0.43
25	123.1337	122.7169	0.34	12.2529	12.2110	0.34

[†]%diff=(Pl. ϵ−Pl. σ/Pl. ϵ)×100

7 Conclusions

Mathematical models, for the stress analyses of unidirectional ENF and ENC specimens using CBT, FOBT, SOBT, and TOBT, have been developed to determine the interlaminar fracture toughness of unidirectional composites in mode II. In the present study, appropriate matching conditions, in terms of generalized displacements and stress resultants, have been derived and applied at the

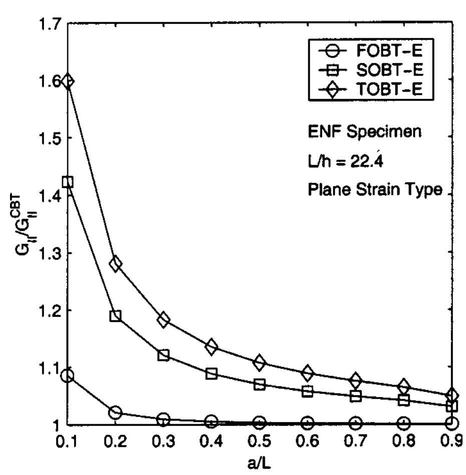

Fig. 3 Influence of crack length on normalized SERR for various shear deformation beam theories

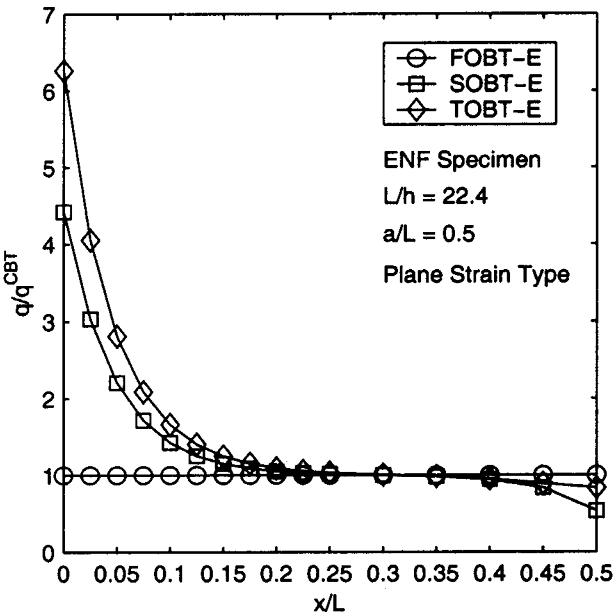

Fig. 4 Normalized interlaminar shear stress distribution ahead of the crack tip based on various shear deformation beam theories

crack tip by enforcing the displacement continuity at the crack tip in conjunction with variational equation. SERR has been calculated using compliance approach. The compliance and SERR obtained from present formulations have been compared with the existing experimental, analytical, and finite element results and found that TOBT is in close agreement with the experimental and finite element results. It has been proved that it is very important to apply proper matching or continuity conditions at the crack tip for more reliable and accurate analysis of ENF and ENC specimens apart from considering higher-order (second and third) shear deformation effects to obtain accurate compliance and SERR.

One can use either plane strain or plane-stress-type condition (constitutive equation) for the analysis of unidirectional ENF and ENC specimens when E_{11}/E_{22} ratio is sufficiently large. Compliance and SERR increase as crack length increases. The SERR values from TOBT-1,2,E, SOBT-1,2,E, and FOBT-E theories approach SERR values from CBT as the crack length increases. In the case of TOBT and SOBT, peak shear stress at the crack tip increases as crack length increases and decays exponentially to CBT as distance increases from the crack tip. For a given crack length, as E_{11}/G_{13} ratio increases SERR increases. E_{11}/G_{13} ratio (shear deformation) will not affect the SERR of FOBT-1,2 theories and the SERR is similar to that of CBT. Test specimens with small E_{11}/G_{13} ratio will have high peak shear stress at the crack tip where as test specimens with larger E_{11}/G_{13} ratio will have low peak shear stress at the crack tip. For a given crack length, as L/h ratio increases SERR increases. Shallow (thin) test specimens will have high peak shear stress at the crack tip when compared to deeper (thick) test specimens.

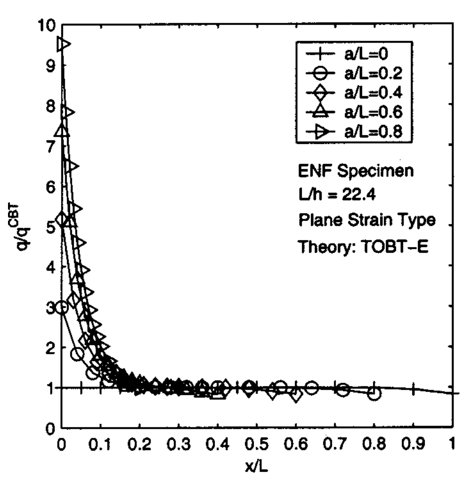

Fig. 5 Influence of various crack lengths on the normalized interlaminar shear stress distribution ahead of the crack tip

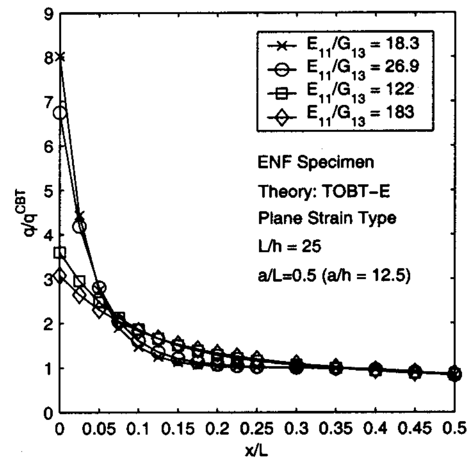

Fig. 6 Normalized interlaminar shear stress distribution ahead of the crack tip for various E_{11}/G_{13} values

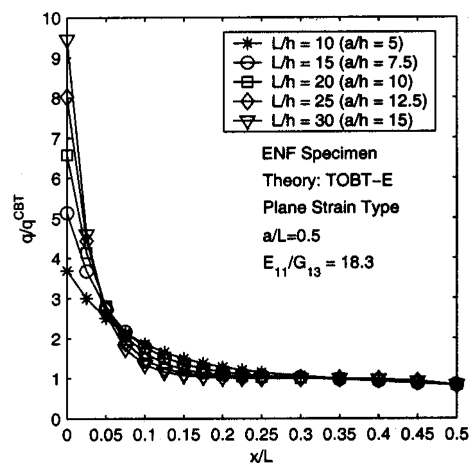

Fig. 7 Normalized interlaminar shear stress distribution ahead of the crack tip for various L/h values

Table 6 Influence of L/h ratio on the SERR based on classical and shear deformation beam theories (ENF specimen)

Present Work—Plane Strain				
$a/L=0.5$, $E_{11}/G_{13}=18.3$				
L/h	CBT	FOBT-E	SOBT-E	TOBT-E
Strain Energy Release Rate $\times 10^4$ (N/mm)				
10	3.3791	3.4206	3.8457	4.0792
15	11.4044	11.4667	12.4256	12.9616
20	27.0327	27.1157	28.8182	29.7767
25	52.7982	52.9020	55.5593	57.0617
30	91.2353	91.3599	95.1838	97.3516

References

[1] Williams, J. G., 1988, ''On the Calculation of Energy Release Rates for Cracked Laminates,'' Int. J. Fract., **36**(2), pp. 101–119.

[2] O'Brien, T. K., 1982, ''Characterization of Delamination Onset and Growth in a Composite Laminate,'' *Damage in Composite Materials*, K. L. Reifsnider, ed., American Society for Testing and Materials, ASTM-STP-775, pp. 140–167.

[3] Carlsson, L. A., and Gillespie, Jr., J. W., 1989, ''Mode II Interlaminar Fracture of Composites,'' *Application of Fracture Mechanics to Composite Materials*, K. Friedrich, ed., Elsevier, Amsterdam, **6**, pp. 113–157.

[4] Sela, N., and Ishai, O., 1989, ''Interlaminar Fracture Toughness and Toughening of Laminated Composite Materials: A Review,'' Composites, **20**(5), pp. 423–435.

[5] Barret, J. D., and Foschi, R. O., 1977, ''Mode II Stress Intensity Factors for Cracked Wood Beams,'' Eng. Fract. Mech., **9**(3), pp. 371–378.

[6] Russell, A. J., and Street, K. N., 1982, ''Factors Affecting the Interlaminar Fracture Energy of Graphite/Epoxy Laminates,'' *Progress in Science and Engineering of Composites*, ICCM-IV, T. Hayashi et al., eds., Japan Society for Composite Materials, Tokyo, **1**, pp. 279–286.

[7] Carlsson, L. A., Gillespie, Jr., J. W., and Pipes, R. B., 1986, ''On the Analysis and Design of End Notch Flexure (ENF) for Mode II Testing,'' J. Compos. Mater., **20**(6), pp. 594–604.

[8] Carlsson, L. A., Gillespie, Jr., J. W., and Whitney, J. M., 1986, ''Interlaminar Fracture Mechanics Analysis of the End Notched Flexure Specimen,'' *Proceedings of the American Society for Composites—First Technical Conference*, Technomic Publishing Company, Lancaster, PA, pp. 421–433.

[9] Whitney, J. M., Gillespie, Jr., J. W., and Carlsson, L. A., 1987, ''Singularity Approach to the Analysis of the End Notch Flexure Specimen,'' *Proceedings of the American Society for Composites—Second Technical Conference*, Technomic Publishing Company, Lancaster, PA, pp. 391–398.

[10] Whitney, J. M., 1987, ''Stress Analysis of the End Notch Flexure Specimen for Mode II Delamination of Composite Materials,'' *AIAA/ASME/ASCE/AHS 28th Structures, Structural Dynamics and Materials Conference*, Part I, ASME, New York, pp. 676–681.

[11] Whitney, J. M., and Sun, C. T., 1973, ''A Higher Order Theory for Extensional Motion of Laminated Composites,'' J. Sound Vib., **30**(1), pp. 85–97.

[12] Whitney, J. M., 1990, ''Analysis of Interlaminar Mode II Bending Specimens Using a Higher Order Beam Theory,'' J. Reinf. Plast. Compos., **9**(6), pp. 522–536.

[13] Reissner, E., 1950, ''Variational Theorem in Elasticity,'' J. Math. Phys., **29**(1), pp. 90–95.

[14] Williams, J. G., 1989, ''The Fracture Mechanics of Delamination Tests,'' J. Strain Anal., **24**(4), pp. 207–214.

[15] Hashemi, S., Kinloch, A. J., and Williams, J. G., 1990, ''The Analysis of Interlaminar Fracture in Uniaxial Fibre-polymer Composites,'' Proc. R. Soc. London, Ser. A, **427**(1872), pp. 173–199.

[16] Hashemi, S., Kinloch, A. J., and Williams, J. G., 1990, ''Mechanics and Mechanisms of Delamination in a Poly(Ether Sulphone)-Fibre Composite,'' Compos. Sci. Technol., **37**(4), pp. 429–462.

[17] Wang, Y., and Williams, J. G., 1992, ''Corrections for Mode II Fracture Toughness Specimens of Composite Materials,'' Compos. Sci. Technol., **43**(3), pp. 251–256.

[18] Chatterjee, S. N., 1991, ''Analysis of Test Specimens for Interlaminar Mode II Fracture Toughness, Part 1: Elastic Laminates,'' J. Compos. Mater., **25**(5), pp. 470–493.

[19] Zhou, J., and He, T., 1994, ''On the Analysis of the End Notched Flexure Specimen for Measuring Mode II Fracture Toughness of Composite Materials,'' Compos. Sci. Technol., **50**(2), pp. 209–213.

[20] Corleto, C. R., and Hogan, H. A., 1995, ''Energy Release Rates for the ENF Specimen Using a Beam on an Elastic Foundation,'' J. Compos. Mater., **29**(11), pp. 1420–1436.

[21] Davidson, B. D., Krüger, R., and König, M., 1995, ''Three Dimensional Analysis and Resulting Design Recommendations for Unidirectional and Multidirectional End Notched Flexure Tests,'' J. Compos. Mater., **29**(16), pp. 2108–2133.

[22] Ding, W., and Kortschot, M. T., 1999, ''A Simplified Beam Analysis of the End Notched Flexure Mode II Delamination Specimen,'' Compos. Struct., **45**(4), pp. 271–278.

[23] Pavan Kumar, D. V. T. G., 1999, ''Interlaminar Fracture Toughness of Composites—Higher Order Shear Deformation Beam Theories,'' Ph.D. thesis, Indian Institute of Science, Bangalore, India.

[24] Salpekar, S. A., Raju, I. S., and O'Brien, T. K., 1988, ''Strain Energy Release Rate Analysis of the End Notch Flexure Specimen Using the Finite Element Method,'' J. Compos. Technol. Res., **10**(4), pp. 133–139.

[25] Sela, N., Ishai, O., and Banks-Sills, L., 1989, ''The Effect of Adhesive Thickness on Interlaminar Fracture Toughness of Interleaved CFRP Specimens,'' Composites, **20**(3), pp. 257–264.

[26] Gillespie, Jr., J. W., Carlsson, L. A., and Pipes, R. B., 1986, ''Finite Element Analysis of the End Notch Flexure Specimen for Measuring Mode II Fracture Toughness,'' Compos. Sci. Technol., **27**(3), pp. 177–197.

Fiber-Reinforced Membrane Models of McKibben Actuators

W. Liu
Research Assistant
e-mail: llliuwg@yahoo.com

C. R. Rahn
Professor
e-mail: cdr10@psu.edu

Department of Mechanical and Nuclear Engineering,
The Pennsylvania State University,
University Park, PA 16802

A McKibben actuator consists of an internally pressurized elastic cylindrical tube covered by a shell braided with two families of inextensible fibers woven at equal and opposite angles to the longitudinal axis. Increasing internal pressure causes the actuator to expand radially and, due to the fiber constraint, contract longitudinally. This contraction provides a large force that can be used for robotic actuation. Based on large deformation membrane theory, the actuator is modeled as a fiber-reinforced cylinder with applied inner pressure and axial load. Given the initial shape, material parameters, axial load, and pressure, the analytical model predicts the deformed actuator shape, fiber angle, and fiber and membrane stresses. The analytical results show that for a long and thin actuator the deformed fiber angle approaches 54°44′ at infinite pressure. The actuator elongates and contracts for actuators with initial angles above and below 54°44′ degrees, respectively. For short and thick actuators with initial angles relatively close to 0 deg or 90 deg, however, a fiber angle boundary layer extends to the middle of the actuator, limiting possible extension or contraction. The calculated longitudinal strain and radius change match experimental results to within 5%. [DOI: 10.1115/1.1630812]

1 Introduction

A McKibben actuator consists of a cylindrical flexible tube surrounded by a braided shell. Pressurization of the tube causes the shell to expand radially and contract longitudinally. Large force capacity (approximately 30 N for a 12.7 mm muscle at 60 PSI) and high percent strain (approximately 20–30%) make these attractive actuators for many applications, [1], including robotics, [2], and mobility enhancement, [3,4]. In addition, McKibben actuators are simple to manufacture, compact, and have a high power-to-weight ratio, [5].

Biologists have found crossed fiber arrays in animals as diverse as squids, [6], and worms, [7]. They observe that if the fiber angle (relative to the longitudinal axis) is small, the structures contract when pressurized (e.g., lizard tongues), [8]. At an angle of $\cos(1/\sqrt{3}) = 54°44'$, the hoop and longitudinal stresses balance and increasing volume tensions the fibers without causing either contraction or elongation. This angle also provides the maximum enclosed volume for a given fiber length and produces the strongest structure. Hence, 54°44′ is often used for fiber-reinforced pressure vessels and hosepipes, [9]. For wind angles above 54°44′ (e.g., starfish tube feet, [10]), the structure elongates under pressure.

A number of researchers have developed simple and/or empirical models of McKibben actuators. Chou and Hannaford [11] use energy conservation to find the tension as a function of pressure and actuator length without considering the detailed geometric structure. Based on virtual work theory, Tondu and Lopez [2] extend the static modeling of [11] to dynamic contraction including friction between the fibers.

Using a continuum mechanics approach, one may model the actuator as a thin elastic membrane with continuously distributed inextensible fiber reinforcement undergoing finite deformation. Adkins and Rivlin [12] and Green and Adkins [13] formulate finite deformation theory for thin membranes and solve some axially symmetric problems. McDonald [14] provides a more recent treatment of the finite deformation of elastic membranes. Kydoniefs and Spencer [15] obtain an exact solution for initially cylindrical elastic membranes with axisymmetric deformation when the elastic material has a Mooney strain-energy function. Yang and Feng [16] provide numerical solutions to inflation of a flat membrane, longitudinal stretching of a tube, and flattening of a hemispherical cap. Matsikoudi-Iliopoulou and Lianis [17] found analytical solutions for axisymmetric deformation of membranes including torsion.

Kydoniefs [18] investigates axisymmetric deformations of an initially cylindrical membrane reinforced by two families of inextensible fibers with fixed fiber angles. In [19], Kydoniefs extends his previous work to include fiber angles that vary with deformation. Matsikoudi-Iliopoulou [20] combines fiber [21] and membrane [17] solutions to obtain the solution of a pressurized cylindrical membrane reinforced with one family of inextensible fibers.

This paper combines the theory of Kydoniefs [18] and Matsikoudi-Iliopoulou [20] to generate and solve the static equations for initially cylindrical elastic membranes with two family fiber reinforcement under inner pressure and axial load. The actuator shape and fiber and membrane stresses are calculated and compared with experimental results.

2 Governing Equations

2.1 Coordinate System. Figure 1 shows a McKibben actuator modeled by two families of inextensible fibers reinforcing an elastic, isotropic, and incompressible membrane with uniform undeformed thickness $2h_0$. The fibers form constant angles $\pm\alpha$ with the generators of the undeformed cylinder. Under the applied inner pressure P and axial force F, the polar coordinates (R, Θ, η) of the undeformed configuration (C_0) become (r, θ, z) in the deformed configuration (C). The meridional arc length of C is ξ and the angle between the tangent to C and the z-axis is σ (see Fig. 2). The structure is axisymmetric, so

$$r = r(\xi), \tag{1}$$

$$z = z(\xi), \tag{2}$$

$$\theta = \Theta. \tag{3}$$

Contributed by the Applied Mechanics Division of THE AMERICAN SOCIETY OF MECHANICAL ENGINEERS for publication in the ASME JOURNAL OF APPLIED MECHANICS. Manuscript received by the ASME Applied Mechanics Division, August 20, 2002; final revision, April 28, 2003. Associate Editor: M.-J. Pindera. Discussion on the paper should be addressed to the Editor, Prof. Robert M. McMeeking, Department of Mechanical and Environmental Engineering, University of California–Santa Barbara, Santa Barbara, CA 93106-5070, and will be accepted until four months after final publication of the paper itself in the ASME JOURNAL OF APPLIED MECHANICS.

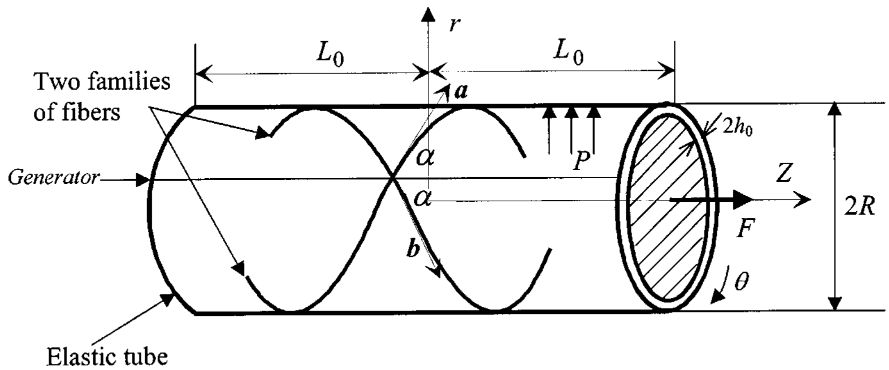

Fig. 1 McKibben actuator model

2.2 Inextensible Fiber Constraint. Let ds_0 and ds be the elements of length in the undeformed and deformed state, respectively, and a be the angle formed by ds_0 with a generator in the undeformed state. From geometry,

$$\left(\frac{ds}{ds_0}\right)^2 = \lambda_1^2 \cos^2 a + \lambda_2^2 \sin^2 a, \tag{4}$$

where

$$\lambda_1 = \frac{d\xi}{d\eta}, \tag{5}$$

$$\lambda_2 = \frac{r}{R}. \tag{6}$$

The strain invariants are

$$I_1 = \lambda_1^2 + \lambda_2^2 + \lambda_3^2, \tag{7}$$

$$I_2 = \frac{1}{\lambda_1^2} + \frac{1}{\lambda_2^2} + \frac{1}{\lambda_3^2}, \tag{8}$$

where the stretch ratio $\lambda_3 = 1/\lambda_1\lambda_2$ due to the incompressibility assumption [13]. In the fiber directions, $a = \alpha$ and, due to the inextensibility assumption, $ds = ds_0$. Substituting into Eq. (4) results in

$$1 = \lambda_1^2 \cos^2 \alpha + \lambda_2^2 \sin^2 \alpha. \tag{9}$$

To determine the deformed fiber angle β, we use geometry and inextensibility to obtain

$$ds = \frac{d\xi}{\cos\beta} = ds_0 = \frac{d\eta}{\cos\alpha}, \tag{10}$$

so

$$\cos\beta = \lambda_1 \cos\alpha. \tag{11}$$

2.3 Stress Tensor. Kydoniefs [21] and Matsikoudi-Iliopoulou and Lianis [17] found the stress tensor solutions for the inextensible fibers and the axisymmetric membrane deformation, respectively. The stress tensor solution for McKibben actuators is the sum of the fiber and membrane stresses. We assume the membrane has a Mooney strain-energy function $W(I_1, I_2) = C[(I_1 - 3) + \Gamma(I_2 - 3)]$, where C and Γ are material parameters. We assume that the fibers are embedded in the cylinder, forming an orthotropic material where λ_1 and λ_2 are the stretches of embedded meridional and azimuthal material curves, respectively. The components of the Cauchy normal stress resultant are

$$n_1 = \frac{2\tau\lambda_2 \sin^2\alpha}{\lambda_1} + \frac{\lambda_2}{\lambda_1}\left(1 - \frac{1}{\lambda_1^2\lambda_2^4}\right) + \frac{\Gamma\lambda_2}{\lambda_1}\left(\lambda_1^2 - \frac{1}{\lambda_2^4}\right), \tag{12}$$

$$n_2 = \frac{2\tau\lambda_1 \cos^2\alpha}{\lambda_2} + \frac{1}{\lambda_1\lambda_2}\left(\lambda_1^2 - \frac{1}{\lambda_1^2\lambda_2^2}\right) + \frac{\Gamma}{\lambda_1\lambda_2}\left(\lambda_1^2\lambda_2^2 - \frac{1}{\lambda_1^2}\right), \tag{13}$$

$$n_3 = 0, \tag{14}$$

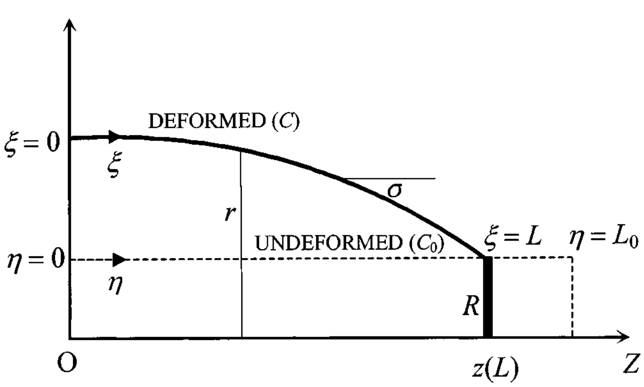

Fig. 2 Coordinate system definition

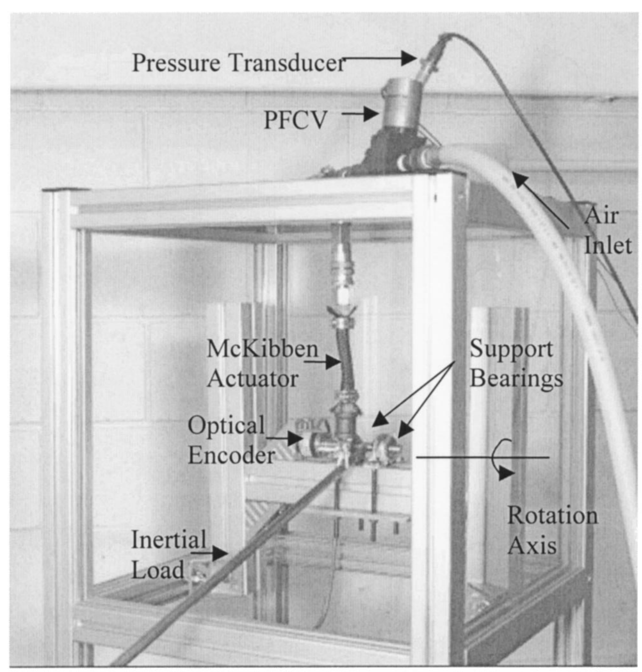

Fig. 3 Experimental setup

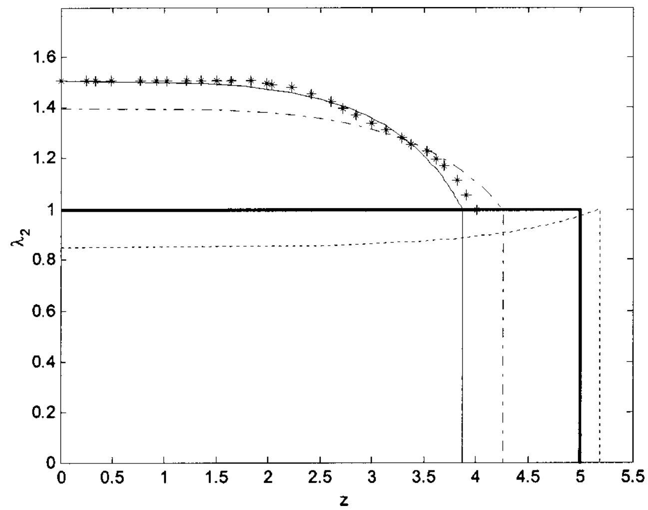

Fig. 4 Actuator shape ($\Gamma=0.0,\alpha=30$ deg, $l_0=5.0$): undeformed (thick solid), $f=0.0$ and $p=3.2$ (thin solid) and experimental (*), $f=5.0$ and $p=6.327054$ (dash-dotted), and $f=5.0$ and $p=0.9538596$ (dotted)

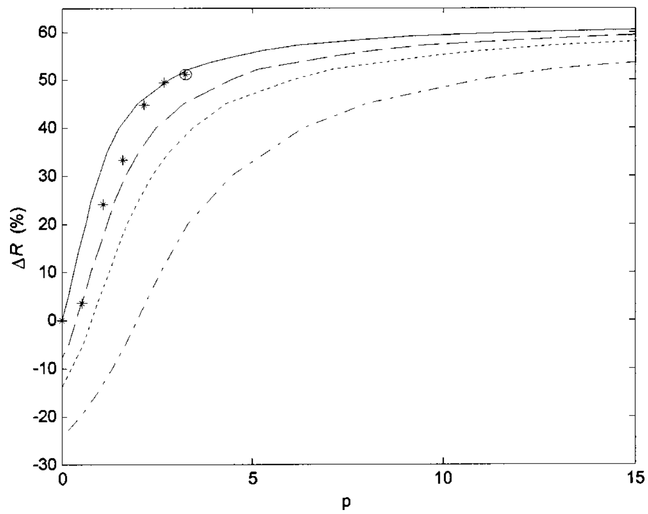

Fig. 6 Midpoint radius enlargement versus pressure ($l_0=5,\Gamma=0.0,\alpha=30$ deg): $f=0.0$ (solid), $f=1.0$ (dashed), $f=2.0$ (dotted), $f=5.0$ (dash-dotted), and experiment with $f=0.54$ (*). Circled point is shown in Fig. 4.

where n_1 and n_2 are the circumferential and axial stresses, respectively, n_3 is the shear stress, and $\tau=T/2C\Delta$ is the nondimensional fiber tension with T and Δ the fiber tension and spacing, respectively. Although the fiber spacing Δ is used to nondimensionalize the fiber tension, the fibers are assumed to be continuously distributed in the membrane.

2.4 Equilibrium Equations. The equilibrium equations for a membrane undergoing large deformation are

$$\frac{d(\lambda_2 n_2)}{d\lambda_2}=n_1, \tag{15}$$

$$\frac{n_1\cos\sigma}{\lambda_2}+n_2\frac{d(\cos\sigma)}{d\lambda_2}=p, \tag{16}$$

where the nondimensional pressure $p=PR/2C$, [20].

Substitution of Eqs. (12)–(14) into Eq. (15) produces

$$A\frac{d\tau}{d\lambda_2}+B\tau+D=0, \tag{17}$$

where

$$A(\lambda_2)=2u^{1/2}\cos\alpha, \tag{18}$$

$$B(\lambda_2)=-\frac{4\lambda_2\cos\alpha\sin^2\alpha}{u^{1/2}}, \tag{19}$$

$$D(\lambda_2)=\frac{\begin{pmatrix} 3u\cos^4\alpha+\Gamma u^3\lambda_2^4-\lambda_2^4u^2-3\lambda_2^2\cos^4\alpha \\ +3\lambda_2^2\cos^6\alpha-\Gamma u^2\lambda_2^6+\Gamma u^2\lambda_2^2\cos^2\alpha \\ -3\Gamma\lambda_2^4\cos^4\alpha+3\Gamma\lambda_2^4\cos^6\alpha+\Gamma u^2\cos^2\alpha \end{pmatrix}}{\lambda_2^3u^{5/2}\cos\alpha}, \tag{20}$$

$$u=1-\lambda_2^2\sin^2\alpha. \tag{21}$$

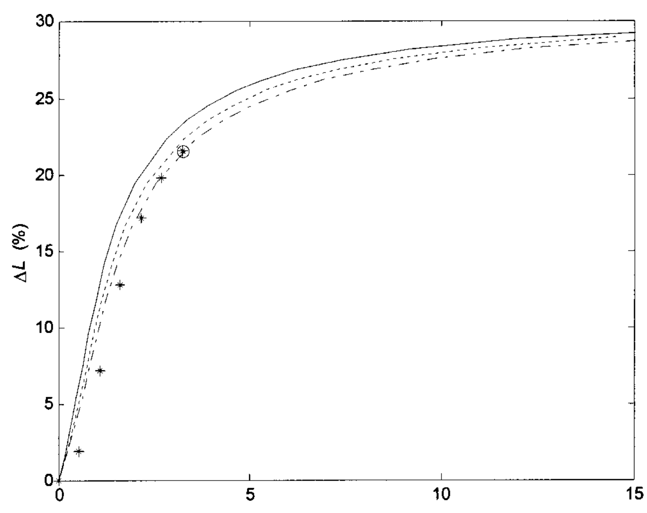

Fig. 5 Strain versus pressure ($\alpha=30$ deg, $f=0.0$, $l_0=5.0$): solid ($\Gamma=0.0$), dashed ($\Gamma=0.20$), dash-dotted ($\Gamma=0.35$), and asterisk (Experiment). Circled point is shown in Fig. 4.

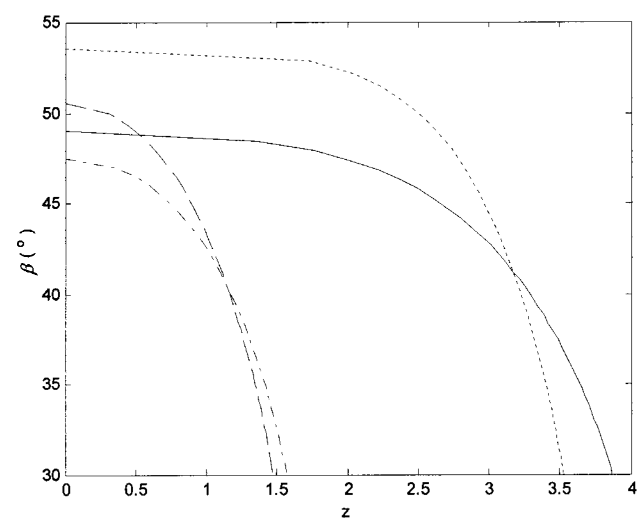

Fig. 7 Fiber angle distribution ($\Gamma=0.0,\alpha=30$ deg, $f=0.0$): solid ($l_0=5.0,p=3.2$), dotted ($l_0=5.0,p=17.7$), dash-dotted ($l_0=2.0,p=3.5$), and dashed ($l_0=2.0,p=18.5$)

Equation (17) is a nonlinear ordinary differential equation with the independent variable λ_2 and dependent variable $\tau(\lambda_2)$. Equation (17) can be solved analytically, but in most cases the expression for $\tau(\lambda_2)$ is very complicated. For the following fiber angles, however, the expressions are relatively simple. At $\alpha = 30$ deg,

$$\tau(\lambda_2) = \frac{\begin{pmatrix} 8\Gamma\lambda_2^6 - \Gamma\lambda_2^8 + 16\lambda_2^4 - 4\lambda_2^6 - 16\Gamma\lambda_2^4 + 27 \\ +24\Gamma\lambda_2^2 + 12\Gamma - 48C_{30}\lambda_2^2 + 12C_{30}\lambda_2^4 \end{pmatrix}}{3\lambda_2^2(\lambda_2^2-4)^2}, \quad (22)$$

at $\alpha = 45$ deg,

$$\tau(\lambda_2) = \frac{24\Gamma\lambda_2^6 - 9\Gamma\lambda_2^8 + 16\lambda_2^4 - 12\lambda_2^6 - 16\Gamma\lambda_2^4 + 3 + 4\Gamma - 16C_{45}\lambda_2^2 + 12C_{45}\lambda_2^4}{\lambda_2^2(3\lambda_2^2-4)^2}, \quad (23)$$

at $\alpha = \cos(1/\sqrt{3}) = 54°44'$,

$$\tau(\lambda_2) = \frac{36\Gamma\lambda_2^6 - 12\Gamma\lambda_2^8 - 27\Gamma\lambda_2^4 + 27\lambda_2^4 - 18\lambda_2^6 + 9\Gamma + 3\Gamma\lambda_2^2 + 9 - 36C_{54}\lambda_2^2 + 24C_{54}\lambda_2^4}{4\lambda_2^2(2\lambda_2^2-3)^2}, \quad (24)$$

and at $\alpha = 60$ deg,

$$\tau(\lambda_2) = \frac{4\Gamma\lambda_2^6 - \Gamma\lambda_2^8 + 4\lambda_2^4 - 2\lambda_2^6 - 4\Gamma\lambda_2^4 + 3 + 2\Gamma + 2\Gamma\lambda_2^2 - 8C_{60}\lambda_2^2 + 4C_{60}\lambda_2^4}{2\lambda_2^2(\lambda_2^2-2)^2}, \quad (25)$$

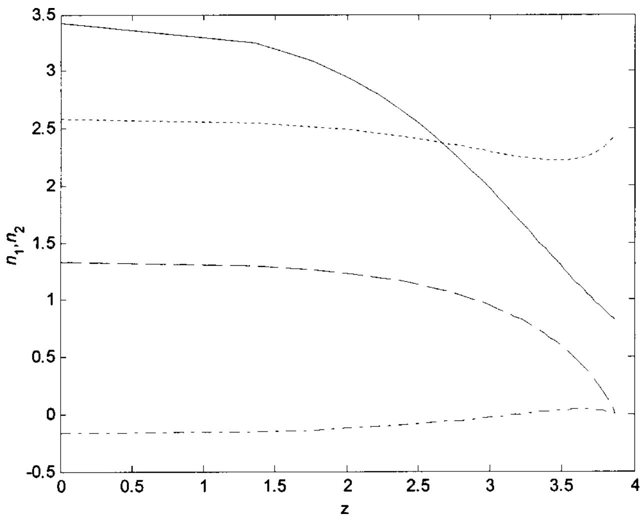

Fig. 8 Fiber n_1 (solid), membrane n_1 (dashed), fiber n_2 (dotted), and membrane n_2 (dash-dotted) stress distributions ($\Gamma = 0.0, \alpha = 30$ deg, $f = 0.0, l_0 = 5.0, p = 3.2$)

where C_{30}, C_{45}, C_{54}, and C_{60} are integration constants. Substitution of $\lambda_2(0)$ into Eqs. (22)–(25) relates integration constants to $\tau(\lambda_2(0))$.

2.5 Boundary Conditions. Using symmetry and force balance conditions, the boundary conditions at $\xi = L$ and $\xi = 0$ are

$$\lambda_2(L) = 1, \quad (26)$$

$$n_2(0) = \frac{p\lambda_2(0)}{2} + \frac{f}{\lambda_2(0)}, \quad (27)$$

$$\sigma(0) = 0, \quad (28)$$

where $f = F/4\pi CR$. Equation (26) establishes the integration limit $\lambda_2(L)$. From Eq. (16), we have

$$\frac{d(\lambda_2 n_2 \cos\sigma)}{d\lambda_2} = p\lambda_2. \quad (29)$$

Integrating the above equation and using Eq. (27) to determine the integration constant,

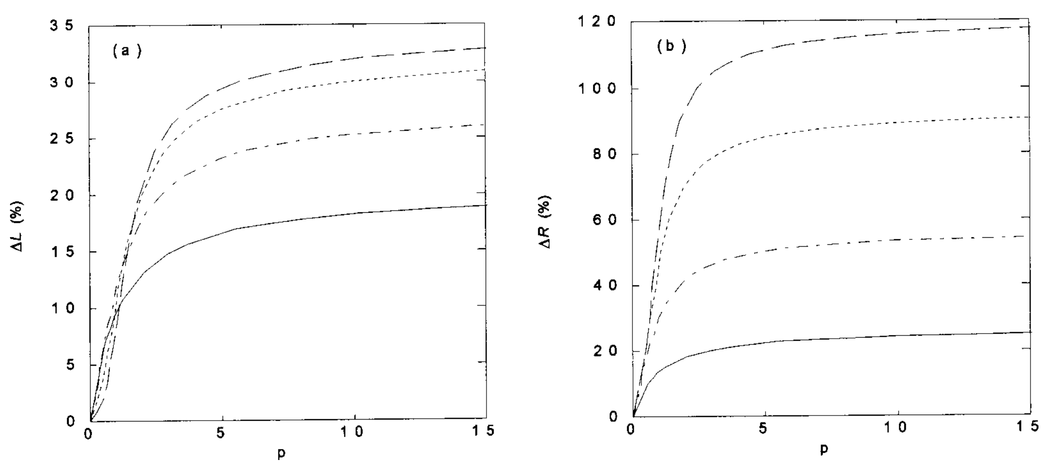

Fig. 9 (*a*) Strain versus pressure, (*b*) midpoint radius enlargement versus pressure ($l_0 = 2.0, \Gamma = 0.0, f = 0.0$): $\alpha = 10.0°$ (dashed), $\alpha = 20.0$ deg (dotted), $\alpha = 30.0$ deg (dash-dotted), and $\alpha = 40.0$ deg (solid)

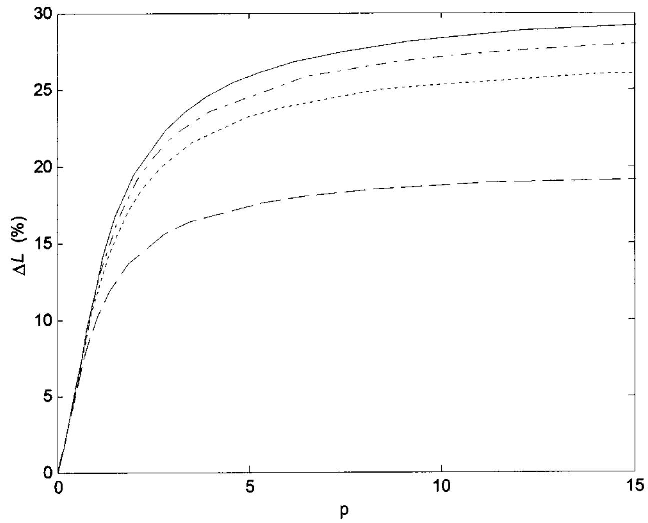

Fig. 10 Strain versus pressure ($\Gamma=0.0, \alpha=30$ deg, $f=0.0$): $l_0=1.0$ (dashed), $l_0=2.0$ (dotted), $l_0=3.0$ (dash-dotted), and $l_0=5.0$ (solid)

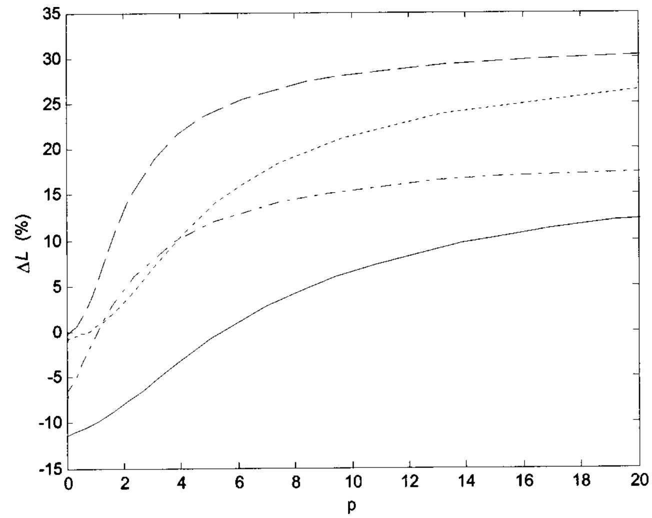

Fig. 12 Strain versus pressure ($l_0=2.0, \Gamma=0.0$): dashed ($\alpha=20.0$ deg, $f=1.0$), dotted ($\alpha=20.0$ deg, $f=5.0$), dash-dotted ($\alpha=40.0$ deg, $f=1.0$), and solid ($\alpha=40.0$ deg, $f=5.0$)

$$\cos\sigma=\frac{p\lambda_2}{2n_2}+\frac{f}{\lambda_2 n_2}. \tag{30}$$

Using Eq. (28),

$$p=\frac{2n_2(0)}{\lambda_2(0)}-\frac{2f}{\lambda_2^2(0)}. \tag{31}$$

From the geometrical shape of the cylindrical membrane, we know

$$l_0=\frac{L_0}{R}=-\int_{\lambda_2(0)}^{1}\frac{d\lambda_2}{\lambda_1\sin\sigma}, \tag{32}$$

$$z(\lambda_2)=\frac{Z(\lambda_2)}{R}=-\int_{\lambda_2(0)}^{\lambda_2}\cot\sigma d\lambda_2. \tag{33}$$

Unfortunately, the integrands in Eqs. (32) and (33) are singular at $\lambda_2=\lambda_2(0)$ ($\sigma=0.0$). The Fortran IMSL library function QDAGS is used to integrate the singular functions.

2.6 Numerical Method. The solution procedure starts with a given deformed midpoint radius $\lambda_2(0)$ and a trial value of $\tau(\lambda_2(0))$. Equation (17) is integrated to obtain $\tau(\lambda_2)$. Stress n_2 is calculated from Eq. (13) and λ_1 from the constraint Eq. (9). The corresponding pressure p is determined from Eq. (31) and substituted into Eq. (30) to solve for σ. Finally, the initial length l_0 is integrated from Eq. (32). The trial $\tau(\lambda_2(0))$ is adjusted according to the difference between the desired and calculated l_0.

3 Numerical and Experimental Results

3.1 Experimental Setup. Figure 3 shows the experimental setup used to validate the theoretical model. The McKibben actuator is mounted between a pivoting rod load and the top support plate. Proportional flow control valves (PFCVs) inlet/exhaust air to/from the actuator. Pressurization of the actuator causes it to shorten and rotate the rod. A 4000 counts per revolution encoder senses the rod rotation angle. A digital camera photographs the deformed shape of the actuator. The experimental parameters are

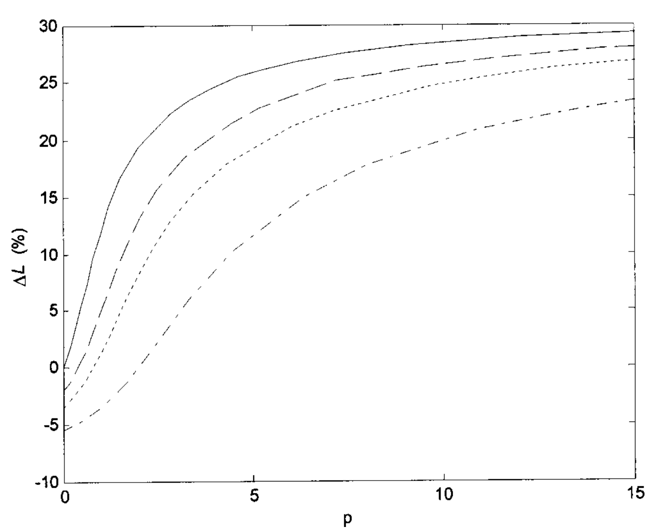

Fig. 11 Strain versus pressure ($l_0=5, \Gamma=0.0, \alpha=30$ deg): $f=0.0$ (solid), $f=1.0$ (dashed), $f=2.0$ (dotted), and $f=5.0$ (dash-dotted)

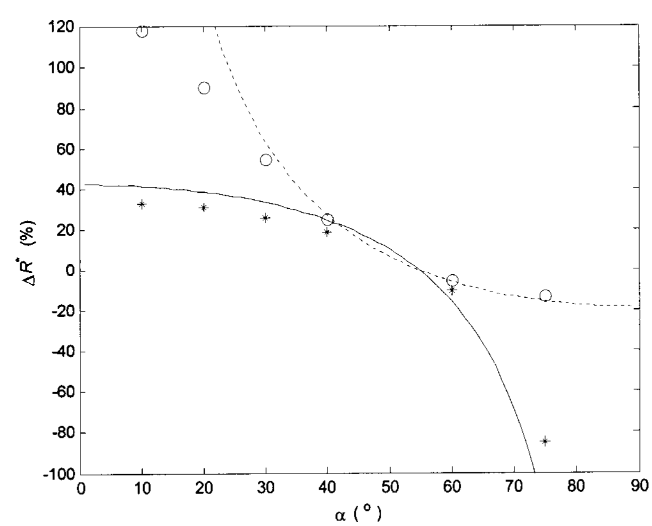

Fig. 13 Locked ($\beta=54°44'$) strain ΔL^* (solid) and midpoint radius enlargement ΔR^* (dotted) versus initial fiber angle α. Numerical results for large p: ΔL (*) and ΔR (○).

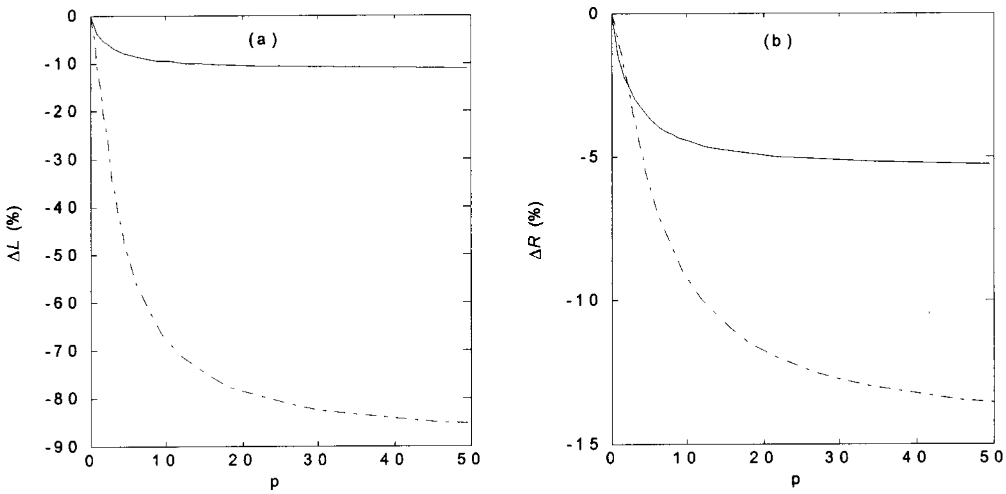

Fig. 14 (*a*) Strain versus pressure; (*b*) midpoint radius enlargement versus pressure ($\Gamma=0.0, f=0.0$): $\alpha=60$ deg, $l_0=1.0$ (solid), and $\alpha=75$ deg, $l_0=0.5$ (dash-dotted)

$$L_0=0.0397\ \text{m},\quad R=0.0079\ \text{m},\quad C=509.33\ \text{N/m}^2,$$
$$P=10-60\ \text{psi},$$
$$l_0=5.0,\quad p=0.5-3.2,\quad \alpha=30\ \text{deg},\quad \Gamma=0.0,\quad f=0. \tag{34}$$

3.2 Experimental Validation of Theoretical Model. Figure 4 compares the theoretical (solid) and experimental (*) actuator shape for $p=3.2$. The theoretically predicted change in length ($z(L)=3.87$) and maximum radius ($r(0)=1.51$) agree within 3% and 2% to the experiment, respectively. Figure 5 shows seven experimental data points of $\Delta L=l_0-z/l_0$ versus p compared with theoretical data for $\Gamma=0$, 0.2, and 0.35. The experimental data best matches the $\Gamma=0.35$ curve with a maximum error of 5%. However, if we assume $\Gamma=0$ the error increases by 10%. Figure 6 compares the experimentally measured $\Delta R=\lambda_2(0)-1$ with theoretical data for different axial loads. The experimental data agrees to within 10% with the theoretical curve for $f=0.0$. Thus, within the limits of experimental accuracy, the proposed theory accurately predicts the experimental performance of a McKibben actuator. The remaining figures explore the interesting physics behind McKibben actuators and predict the effects of parameters and inputs on the actuator response.

3.3 Mechanics of Pressurization. Figure 5 shows the McKibben actuator contracting with increasing internal pressurization. For $\alpha=30$ deg, the maximum ΔL approaches 30%. Similarly, the maximum radius change in Fig. 6 approaches 60%. This saturation effect can be explained by Fig. 7 showing the deformed fiber angle distribution $\beta(z)$. At relatively low pressurization ($p=3.2$) there is a broad boundary layer where the fiber angle increases from the boundary condition $\alpha=30$ deg to $\beta=49$ deg at $z=0$. At high pressurization ($p=17.7$), the boundary layer shrinks and β saturates below the lock angle of $54°44'$. Thus, ΔR and ΔL saturate as boundary layer shrinkage requires higher pressurization to obtain smaller incremental dimension changes.

Figure 8 shows the circumferential (n_1) and axial (n_2) stress distributions for the fibers and membrane. The circumferential and axial fiber stresses are at least 2.5 and 10.0 times larger than the corresponding membrane stresses, respectively. This shows that the membrane primarily acts to apply the pressure loading to the fiber network. The response to pressurization is primarily governed by the fiber equilibrium conditions. This also explains why the membrane properties (e.g., Γ) have little effect on the pressurization response. The fibers and membrane are constrained to move together (i.e., no relative motion) and this causes the axial membrane stress to be slightly negative over much of the length. In practice, the fibers can slide on the membrane, potentially relieving these compressive stresses.

3.4 Parameter and Loading Effects. Figure 9 shows the effect of initial fiber angle (α) on the pressurization response. The maximum ΔL and ΔR increase with decreasing fiber angle. At low pressurization ($p<0.9$), however, the $\alpha=30$ deg case outperforms the $\alpha=10$ deg and $\alpha=20$ deg cases. Thus, the selection of initial fiber angle depends on the maximum pressure available or possible due to stress constraints.

Figure 10 shows that the initial length of the actuator greatly affects the achievable strain. An $l_0=1$ actuator has only one half of the ΔL of an $l_0=5$ actuator. This can be explained using Fig. 7. The boundary layer thickness does not scale proportional to actuator length. Thus the maximum deformed fiber angle is smaller for the same applied pressure and the resulting ΔL is smaller.

Figure 11 shows that applied loads increase the actuator length (decrease ΔL). The actuator shape changes with applied loading. In Fig. 4 the applied load reduces the diameter and eventually necks down the actuator for sufficiently large f relative to the applied pressure. Figure 12 shows that actuators with small initial fiber angles can support higher loads. In both loading cases shown ($f=1.0$ and $f=5.0$) the $\alpha=20$ deg ΔL is much greater than the $\alpha=40$ deg ΔL.

3.5 Locked Solutions. If we neglect boundary and membrane effects and assume the fibers are locked at $\sigma=0$, we obtain the locked solution $\beta=54°44'$. From Eqs. (30) and (16) with $\sigma=0$ and the locking condition $d(\cos\sigma)/d\lambda_2=0$, we obtain

$$n_2^*=\frac{p\lambda_2^*}{2}=\frac{n_1^*}{2}, \tag{35}$$

where $()^*$ indicates a locked solution. Substitution of Eqs. (12), (13), and (11) into Eq. (35) yields

$$2\cos^2\beta^*=1-\cos^2\beta^*, \tag{36}$$

or $\beta^*=\cos^{-1}(1/\sqrt{3})=54°44'$. From Eq. (11), we obtain

$$\lambda_1^*=\frac{\cos\beta^*}{\cos\alpha}. \tag{37}$$

Substitution of Eq. (37) into the inextensibility Eq. (4) produces

$$\lambda_2^* = \sqrt{\frac{1-\cos^2\beta^*}{\sin^2\alpha}} = \frac{\sin\beta^*}{\sin\alpha}. \quad (38)$$

Figure 13 shows the locked strain $\Delta L^* = 1 - \lambda_1^*$ and radius $\Delta R^* = \lambda_2^* - 1$ versus α, respectively. The locked solutions agree fairly well with the numerical solutions for large p. The agreement improves for long actuators with fiber angles near $54°44'$. The differences observed for short actuators and/or large or small fiber angles are due to boundary effects. The fiber angle distribution (See Fig. 7) does not converge to a uniform distribution with sharp changes in σ at the boundaries. Instead, the equilibrium shape converges to a smooth boundary layer with increasing pressure. Thus, the locking angle is only obtained (if at all) in the middle of the actuator. For short actuators or small/large fiber angles, the boundary layer occupies a large percentage of the actuator length, reducing the maximum strain and radius.

3.6 Extending Actuator Solutions. McKibben actuators with initial fiber angles greater than $54°44'$ extend when pressurized. Although these are typically not used due to buckling problems, the theory predicts the strain and maximum radius versus pressure in Fig. 14. Larger initial fiber angle results in larger extension. The radius contracts as the actuator extends.

4 Conclusions

A large deformation membrane model with two families of inextensible fibers accurately predicts the static response of McKibben actuators. The results show that the fiber stresses dominate the membrane stresses. Hence, the initial fiber angle is the most important parameter governing the actuator response. For small and large initial fiber angles the actuator contacts and extends, respectively. At $\alpha = 54°44'$, the actuator maintains its initial shape under pressurization. The maximum contraction/extension can be estimated from the locked solution Eq. (37) for long actuators with α near $54°44'$. For short actuators with large/small α, however, the boundary layer includes a significant percentage of the actuator length and the maximum strain and radius decrease.

Acknowledgments

This research was supported by NASA.

References

[1] Klute, G., Czerniecki, J., and Hannaford, B., 1999, ''McKibben Artificial Muscles: Pneumatic Actuators With Biomechanical Intelligence,'' *IEEE International Conference on Advanced Intelligent Mechatronics*, Sept. 19–22, Atlanta, GA, IEEE, Piscataway, NJ, pp. 1–5.

[2] Tondu, B., and Lopez, P., 2000, ''Modeling and Control of McKibben Artificial Muscle Robot Actuators,'' IEEE Control Syst. Mag., **Apr.**, pp. 15–38.

[3] Repperger, D., Phillips, C., Johnson, D., Harmon, R., and Johnson, K., 1997, ''A Study of Pneumatic Muscle Technology for Possible Assistance in Mobility,'' *IEEE 19th International Conference*, Oct. 30–Nov. 2, Chicago, IL, IEEE, Piscataway, NJ, pp. 1884–1887.

[4] Reppberger, D., and Phillips, C., 2000, ''Developing Intelligent Control From a Biological Perspective to Examine Paradigms for Activation Utilizing Pneumatic Muscle Actuators,'' *IEEE International Symposium on Intelligent Control*, July 17–19, Pio, Patras, Greece, IEEE, Piscataway, NJ, pp. 205–209.

[5] Caldwell, D., Medrano-Cerda, G., and Goodwin, M., 1995, ''Control of Pneumatic Muscle Actuators,'' IEEE Control Syst. Mag., **Feb.**, pp. 40–48.

[6] Van Leeuwan, J. L., and Kier, W. M., 1997, ''Functional Design of Tentacles in Squid: Linking Sarcomere Ultrastructure to Gross Morphological Dynamics,'' Philos. Trans. R. Soc. London, Ser. B, **264**, pp. 1–21.

[7] Clark, R. B., and Cowey, J. B., 1958, ''Factors Controlling the Change of Shape of Some Worms,'' J. Exp. Biol., **35**, pp. 731–748.

[8] Kier, W. M., and Smith, K. K., 1985, ''Tongues, Tentacles and Trunks: The Biomechanics of Movement in Muscular-Hydrostats,'' Zool. J. Linnean Soc., **83**, pp. 307–324.

[9] Spencer, A. J. M., 1972, *Deformation of Fibre-Reinforced Materials*, Clarendon Press, Oxford, UK.

[10] McCurley, R. S., and Kier, W. M., 1995, ''The Functional Morphology of Starfish Tube Feet: The Role of a Crossed-Fiber Helical Array in Movement,'' Biol. Bull., **188**, Apr., pp. 197–209.

[11] Chou, Ching-Ping, and Hannaford, B., 1996, ''Measurement and Modeling of McKibben Pneumatic Artificial muscles,'' IEEE Trans. Rob. Autom., **12**(1), pp. 90–102.

[12] Adkins, J. E., and Rivlin, R. S., 1952, ''Large Elastic Deformations of Isotropic Materials IX,'' Philos. Trans. R. Soc. London, Ser. A, **244**, p. 505.

[13] Green, A. E., and Adkins, J. E., 1960, *Large Elastic Deformations*, The Clarendon Press, Oxford, UK.

[14] McDonald, P. H., 1995, *Continuum Mechanics*, PWS Publishing, Boston, MA.

[15] Kydoniefs, A. D., and Spencer, A. J. M., 1969, ''Finite Axisymmetric Deformations of an Initially Cylindrical Elastic Membrane,'' Q. J. Mech. Appl. Math., **22**, pp. 87–95.

[16] Yang, W. H., and Feng, W. W., 1970, ''On Axisymmetrical Deformation of Non-linear Membranes,'' ASME J. Appl. Mech., **37**, pp. 1002–1011.

[17] Matsikoudi-Iliopoulou, M., and Lianis, G., 1982, ''Non Linear Elastic Axisymmetric Deformation of Membranes With Torsion,'' Acta Mech., **42**, pp. 153–170.

[18] Kydoniefs, A. D., 1970, ''Finite Axisymmetric Deformations of an Initially Cylindrical Membrane Reinforced With Inextensible Cords,'' Q. J. Mech. Appl. Math., **23**, pp. 481–488.

[19] Kydoniefs, A. D., 1970, ''Finite Axisymmetric Deformations of Initially Cylindrical Reinforced Membranes,'' Rubber Chem. Technol., **43**, pp. 1677–1683.

[20] Matsikoudi-Iliopoulou, M., 1987, ''Finite Axisymmetric Deformations With Torsion of an Initially Cylindrical Membrane Reinforced With One Family Inextensible Cords,'' Int. J. Eng. Sci., **25**(6), pp. 673–680.

[21] Kydoniefs, A. D., 1977, ''Deformations of Corded Membranes With Applications to Tire Mechanics,'' Lett. Appl. Eng. Sci., **5**(1), pp. 63–83.

K. M. Liew[1]
e-mail: mkmliew@ntu.edu.sg
Fellow, ASME

J. Z. Zhang

Center for Advanced Numerical Engineering Simulations,
Nanyang Technological University,
Nanyang Avenue,
Singapore 639798

T. Y. Ng
School of Mechanical and Production Engineering,
Nanyang Technological University,
Nanyang Avenue,
Singapore 639798
Mem. ASME

J. N. Reddy
Advanced Computational Mechanics Laboratory,
Department of Mechanical Engineering,
Texas A&M University,
College Station, TX 77843-3123
Fellow, ASME

Dynamic Characteristics of Elastic Bonding in Composite Laminates: A Free Vibration Study

In conventional analyses of composite laminates, the assumption of perfect bonding of adjoining layers is well accepted, although this is an oversimplification of the reality. It is possible that the bond strength may be less than that of the laminae. Thus, the study of weak bonding is an interesting focus area. In this study, an elastic bonding model based on three-dimensional theory of elasticity in a layerwise framework is used to study composite laminates. The differential quadrature (DQ) discretization is used to analyze the layerwise model. The present model enables the simulation of actual bonding stress states in laminated structures. The interfacial characteristics of transverse stress continuity as well as the kinematic continuity conditions are satisfied through the inclusion of the elastic bonding layer. The present model is employed to investigate the free vibration of thick rectangular cross-ply laminates of different boundary conditions and lamination schemes. [DOI: 10.1115/1.1604838]

1 Introduction

1.1 Background. Composite materials in the form of laminates have been utilized in a broad range of engineering structures, including space, underwater, and aircraft structures, electronic and medical components, and high-end sporting equipment, to name a few. In laminated composite structures, layers of different materials (or orientation) are bonded together to form a laminate, and the resulting laminate is, in general, anisotropic. The anisotropic nature of composite laminates is responsible for complex and coupled modes of mechanical response. This in turn leads to difficulties in the analysis of laminated structures, especially when interlaminar stresses have to be determined accurately.

Laminated composite plate and shell structures are often analyzed using two-dimensional plate and shell theories. The classical plate theory (CPT) is based on the assumption of infinite transverse rigidity in the transverse direction, and therefore it overpredicts the buckling loads and vibration frequencies and underpredicts the deflections, see Reddy [1]. The first-order and third-order plate theories, which include the effect of transverse shear deformation, provide a crude remedy to this situation. All two-dimensional plate theories are based on the assumption of perfect bonding between layers, and the laminate is treated as if it is an equivalent single-layer plate. These equivalent single-layer theories (ESLT) directly evolved from plate theories used for single-layer theories, and they still leave a lot to be desired in terms of refining the accuracy of solution for the distribution of stress components at the ply level. Noting the restrictions of the traditional plate and shell theories, Reddy [1–3] proposed and advanced a layerwise theory that is based on independent displacement fields for each material layer; the theory allows a possibility for accommodating the interlaminar kinematic characteristics (i.e., continuity and discontinuity of proper stresses and strains) of the laminate. The layerwise theory is a special form of three-dimensional theory in which the variation of the field variables in the transverse (or thickness) direction is approximated using a desired degree of polynomials. This has also been further investigated by Soldatos and Watson [4,5], Soldatos and Liu [6], and Messina and Soldatos [7]. Srinivas and Rao [8] adopted the three-dimensional theory of elasticity in the study of vibration of laminated rectangular plates and results were presented only for simply-supported square sandwich laminates, and these are widely cited as benchmark solutions. Three-dimensional solutions were also obtained for other boundary conditions, see Savoia and Reddy [9], and Teo and Liew [10]. A full three-dimensional theory is computationally too expensive to be efficient for most practical structures.

As stated earlier, in the two-dimensional analysis (using equivalent single-layer plate and shell theories) of laminated composite structures, the interface between layers is always assumed to be perfectly bonded, i.e., the displacements on the interface are single valued. Since the ply interface is mainly dominated by the low shear modulus matrix material, with possible additional defective bonding occurring during manufacturing or its service life, the interface may not be perfect. It has been recognized, see Lu and Liu [11], that low shear moduli of polymer matrix materials have significant effects on the transverse shear deformation, and consequently the interfacial stress and deformation can strongly affect the service behavior of laminates. In order to accurately predict the performance of composite laminates, it is necessary to account for the bonding layer in an appropriate way, i.e., the transverse shear effect and the continuity requirements of both displacements and interlaminar stresses on the interface. One of the

[1]To whom correspondence should be addressed.

Contributed by the Applied Mechanics Division of THE AMERICAN SOCIETY OF MECHANICAL ENGINEERS for publication in the ASME JOURNAL OF APPLIED MECHANICS. Manuscript received by the ASME Applied Mechanics Division, July 4, 2002; final revision, Feb. 5, 2003. Associate Editor: D. A. Siginer. Discussion on the paper should be addressed to the Editor, Prof. Robert M. McMeeking, Department of Mechanical and Environmental Engineering, University of California–Santa Barbara, Santa Barbara, CA 93106-5070, and will be accepted until four months after final publication of the paper itself in the ASME JOURNAL OF APPLIED MECHANICS.

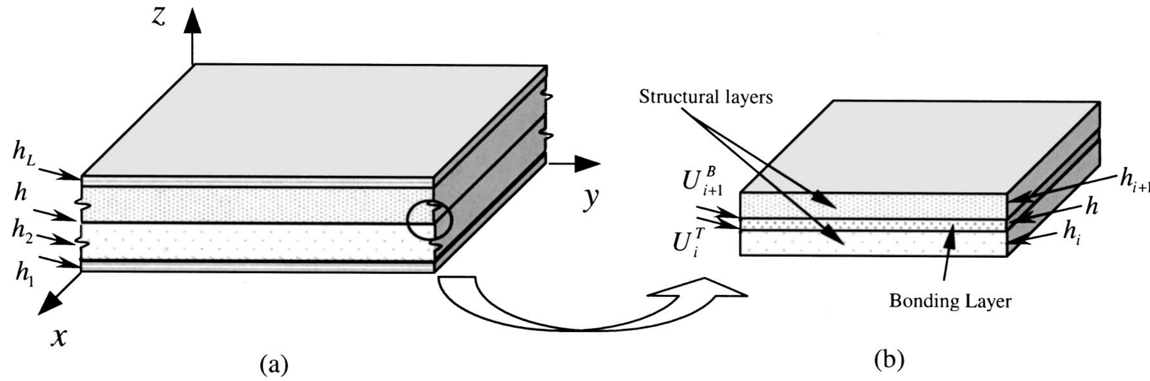

Fig. 1 Laminated plate structure with an elastic adhesive bonding layer

pioneering works in the study of imperfectly bonded interfaces in composite structures was by Newmark et al. [12], who developed a linear shear slip in the layer interface by means of the Euler-Bernoulli beam theory. Toledano and Murakami [13] developed a laminate theory that accounts for both transverse shear effect and interlaminar shear stress continuity to study interlaminar effects. Elasticity studies of sandwich beams with imperfect bonding were also presented by Rao and Ghosh [14] and Fazio et al. [15].

There are three types of weak bond models: a shear model with slip between layers; normal separation model with an opening between layers; and general weak bond that combines both of these models. The main feature of weakly bonded layers is the inclusion of a certain displacement jump, see Lu and Liu [11], Liu et al. [16], and Soldatos and Shu [17], at an interface, and connecting it with the interlaminar stress through an appropriate constitutive relation. Due to the high interlaminar stresses and weak bonding between composite layers, delamination can occur at the ply interface, which in turn reduces the integrity of structure, causing severe structural degradation. Recent works, such as those of Willians and Addessio [18], Willians [19], and Shu and Soldatos [20], extended the concept of shear slip in weakly bonded laminates towards modeling general delamination.

1.2 Rigid, Weak, and Elastic Bonding. Two laminae may be bonded together in two different ways: glue bonding and warm-pressed bonding. In both, a new layer is formed between the original layers. The rigid bonding model prohibits transverse strain while imposing the continuity of transverse stresses, whereas the weak bonding model, and also the present elastic bonding model, tolerates shear slip and transverse opening along the lamina interface. Although usually extremely thin, the existence of a bonding layer causes the rigid bonding model to yield incorrect stress distributions along the lamina interface and through the thickness as well. The weak bonding model is a simplified model that relaxes the rigidity in the rigid bonding model. The rigid bonding models is obtained when the stiffness of the weak bonding model tends to infinity. However, the weak bonding model excludes the effect of in-plane deformation of the bonding layer on the global behavior as well as the stress distribution through thickness.

In this paper, the authors present an elastic bonding model, analogous to that developed in Liew et al. [21] for the bending problem. In this model, an elastic material layer acts as the physical bonding entity between two laminae. This model will amend some of the drawbacks of existing weak and rigid models. In the present work, details of this model, which is based on a layerwise framework and utilizes differential quadrature discretization, will be presented for free-vibration analysis of thick laminated cross-ply composite plates.

1.3 Differential Quadrature (DQ) Method. Circumventing the difficulties of often very complex mathematical derivation in analytical approaches, numerical methods, supported by dramatic advances in computational speed and storage capability, provide almost the only effective tools for the solution of complicated engineering problems. The finite element method (FEM) is a very popular numerical method for the analysis of a variety of engineering problems. Without the simplifications of a ESLT, a laminate can still be modeled with three-dimensional elements through standard FEM, but an excessively refined in-plane mesh would be required because the thickness of an individual lamina, to a large extent, dictates the aspect ratio of the elements, thus resulting in adversely high computational requirements. To take advantage of the full potential of composite materials, accurate tools of analysis and design methodologies of general applicability are crucial. There is therefore a real incentive to develop more powerful modeling tools for composite materials in engineering applications. The differential quadrature (DQ) method is one such prospective numerical alternative originated by Bellman [22] to solve linear and nonlinear differential equations. The basic idea of the DQ method is that the partial derivative of a function with respect to a variable at a given discrete point can be approximated as a weighted linear sum of the function values at all discrete points in the domain of that variable. Details of the interpolations and the various grid point distribution schemes can be found in Liew et al. [23] and will not be repeated here.

Since its introduction, the DQ method has been widely applied to various mechanics problems such as bending, vibration and buckling of beams, columns, and plates. The successful implementation of this method have been widely reported in a number of publications; see Bert et al. [24], Jang et al. [25], Farsa et al. [26], Han and Liew [27], and Liu and Liew [28]. For a review of the developments and applications of the DQ method in computational mechanics one may consult the article by Bert and Malik [29].

2 Interface Modeling of Elastic Bonding

2.1 Physical Model of Elastic Bonding. Consider a rectangular laminate composed of N_L layers, h_i being the thickness of the ith lamina, as depicted in Fig. 1. For two adjacent laminae bonded together, the material entity in the interfacial region of the laminae is considered independently as an isotropic or anisotropic layer of finite thickness. It will be termed as the natural layer. Since such a layer will consist of the matrix material with randomly mixed fibers, this layer may be reasonably regarded as isotropic.

With its bonding characteristics, the natural layer is assumed to be rigidly bonded to the neighboring laminae, and the continuity conditions of transverse stresses are enforced along the interfaces between the natural layer and the neighboring laminae. It must be emphasized, however, that the existence of a distinct thin material region connecting two adjacent laminae presents new challenges.

Both the rigid and existing weak bonding models are oversimplified to that of a three-dimensional linear spring linking two material points initially on opposite sides of the interface via constitutive relations describing the displacement jumps and corresponding stresses. The present elastic bonding model fully incorporates the natural layer, integrating it into the governing equations, thus sharply distinguishing from previously existing models, not only in concept, but also in physical meaning. Furthermore, the concept of elastic bonding allows detailed analysis of the bonding effect through examining the mechanical parameters E, ν, ρ, and h of the bonding layer.

2.2 Theory of Elastic Bonding Model. To establish a theoretical basis for elastic bonding, three-dimensional theory of elasticity is integrated within the framework of the layerwise theory. We first define the displacements in the x, y and z-directions, U_i, V_i and W_i, of the ith layer as

$$U_i=u_i(x,y,z), \quad V_i=v_i(x,y,z), \quad W_i=w_i(x,y,z) \qquad i=1,2,3,\ldots N_L. \tag{1}$$

The strains in the ith layer are

$$\varepsilon_x^{(i)}=\frac{\partial U_i}{\partial x}, \quad \varepsilon_y^{(i)}=\frac{\partial V_i}{\partial y}, \quad \varepsilon_z^{(i)}=\frac{\partial W_i}{\partial z}$$
$$\gamma_{xy}^{(i)}=\frac{\partial U_i}{\partial y}+\frac{\partial V_i}{\partial x}, \quad \gamma_{yz}^{(i)}=\frac{\partial V_i}{\partial z}+\frac{\partial W_i}{\partial y}, \quad \gamma_{zx}^{(i)}=\frac{\partial W_i}{\partial x}+\frac{\partial U_i}{\partial z}. \tag{2}$$

The constitutive relations are

$$\{\sigma_x,\sigma_y,\sigma_z,\tau_{yz},\tau_{zx},\tau_{xy}\}^T=[C_{ij}]\cdot\{\varepsilon_x,\varepsilon_y,\varepsilon_z,\gamma_{yz},\gamma_{zx},\gamma_{xy}\}^T \tag{3}$$

where σ_x, σ_y, σ_z are normal stresses, τ_{yz}, τ_{zx}, τ_{xy} are shear stresses, and C_{ij} $(i,j=1,2,\ldots,6)$ denote the stiffness coefficients. The equations of motion for each lamina and bonding layer are

$$\frac{\partial\sigma_x}{\partial x}+\frac{\partial\tau_{xv}}{\partial y}+\frac{\partial\tau_{xz}}{\partial z}=\rho\frac{\partial^2 u}{\partial t^2}, \quad \frac{\partial\sigma_y}{\partial y}+\frac{\partial\tau_{xy}}{\partial x}+\frac{\partial\tau_{yz}}{\partial z}=\rho\frac{\partial^2 v}{\partial t^2},$$
$$\frac{\partial\sigma_z}{\partial z}+\frac{\partial\tau_{xz}}{\partial x}+\frac{\partial\tau_{yz}}{\partial y}=\rho\frac{\partial^2 w}{\partial t^2}. \tag{4}$$

Here ρ denotes the mass density of the layer. Equation (4) can be written in terms of the lamina displacement field.

It is important to note that the bonding layer is so thin that it is deemed unnecessary to establish the true displacements, strains or stress distributions within it. However, to reflect the dynamic effect of bonding layer on the overall response of the laminated structure, three sets of grid points within the bonding layer, two surface sets and one set in the middle of the layer thickness are used. At the two surface sets, continuity conditions of transverse stresses are enforced, and equations of dynamic equilibrium, Eq. (4), are satisfied at the midpoint set.

For simply-supported laminate the boundary conditions are given by

$$w=\sigma_x=\tau_{xy}=0, \quad \text{at the edges of } x=\text{constant}$$
$$w=\sigma_y=\tau_{xy}=0, \quad \text{at the edges of } y=\text{constant} \tag{5}$$

and clamped edge conditions are

$$u=v=w=0, \quad \text{at the edges of } x,y=\text{constant} \tag{6}$$

with the surface conditions written as

$$\sigma_z=\tau_{xz}=\tau_{yz}=0, \quad \text{at bottom and top of laminate.} \tag{7}$$

Obviously, the interfacial characteristics of rigid bonding, i.e., continuity and discontinuity of displacements, strains and stresses, are no longer valid, and the corresponding constraints are transferred through the material bonding layer based on the elastic bonding model (see Fig. 1(b)). At the interface between the lower lamina and the bonding layer, the continuity conditions are

$$\begin{Bmatrix}\sigma_z^{(i)}\\ \tau_{zx}^{(i)}\\ \tau_{zy}^{(i)}\end{Bmatrix}_{\text{top}}=\begin{Bmatrix}\sigma_z^{(BL)}\\ \tau_{zx}^{(BL)}\\ \tau_{zy}^{(BL)}\end{Bmatrix}_{\text{bottom}} \qquad i=1,2,\ldots,N_L-1 \tag{8}$$

and at the interface between the bonding layer and the upper lamina, the conditions are

$$\begin{Bmatrix}\sigma_z^{(BL)}\\ \tau_{zx}^{(BL)}\\ \tau_{zy}^{(BL)}\end{Bmatrix}_{\text{top}}=\begin{Bmatrix}\sigma_z^{(i+1)}\\ \tau_{zx}^{(i+1)}\\ \tau_{zy}^{(i+1)}\end{Bmatrix}_{\text{bottom}} \qquad i=2,\ldots,N_L-1,N_L \tag{9}$$

where the superscripts, i or $i+1$, indicate the layer numbers, and BL refers to the bonding layer.

All the governing equations can be expressed by the derivatives of displacements through the DQ methodology, and satisfied numerically. It should be noted that the kinematic equations, Eq. (2), constitutive relations, Eq. (3), equations of motion, Eq. (4), and interlaminar continuity conditions, Eqs. (8) and (9), are all three-dimensional in nature. These equations are based on the theory of elasticity, and not on plate theories. Thus the numerical results obtained from this model are numerical analogs of exact three-dimensional solutions. The DQ method is a (element-free) numerical method that provides the flexibility of arranging the grid points (not elements) in the domain of interest.

Substituting Eq. (2) into Eq. (3), and assuming orthotropic material behavior, we obtain

$$\sigma_x=C_{11}\frac{\partial u}{\partial x}+C_{12}\frac{\partial v}{\partial y}+C_{13}\frac{\partial w}{\partial z},$$
$$\sigma_y=C_{21}\frac{\partial u}{\partial x}+C_{22}\frac{\partial v}{\partial y}+C_{23}\frac{\partial w}{\partial z}$$
$$\sigma_z=C_{31}\frac{\partial u}{\partial x}+C_{32}\frac{\partial v}{\partial y}+C_{33}\frac{\partial w}{\partial z} \tag{10}$$
$$\tau_{yz}=C_{44}\left(\frac{\partial v}{\partial z}+\frac{\partial w}{\partial y}\right), \quad \tau_{zx}=C_{55}\left(\frac{\partial w}{\partial x}+\frac{\partial u}{\partial z}\right),$$
$$\tau_{xy}=C_{66}\left(\frac{\partial u}{\partial y}+\frac{\partial v}{\partial x}\right).$$

The following nondimensionalization is used:

$$X=\frac{x}{a} \quad Y=\frac{y}{b} \quad Z_i=\frac{z}{h_i}$$
$$\overline{U}=\frac{u}{a} \quad \overline{V}=\frac{v}{b} \quad \overline{W}=\frac{w}{H} \tag{11}$$

where Z_i is the thickness coordinate of the ith layer and a and b are the length and width of the laminate, respectively. Further, let

$$H=\sum h_i+(N_L-1)\cdot h$$
$$\frac{b}{a}=B_p, \quad \frac{h_i}{a}=D_i, \quad \frac{H}{h_i}=H_i. \tag{12}$$

The three normalized equilibrium equations for the ith lamina $(i=1,2,\ldots,N_L)$ interior have been given in Liew et al. [23] except that the right-hand sides of the current dynamic equations are now, respectively,

$$\rho\cdot b^2\frac{\partial^2\overline{U}}{\partial t^2}, \quad \rho\cdot a^2\frac{\partial^2\overline{V}}{\partial t^2} \quad \text{and} \quad \rho\cdot a^2\cdot H_i\frac{\partial^2\overline{W}}{\partial t^2}. \tag{13}$$

The support conditions in Eqs. (5) and (6) can also be normalized. For simply-supported edge conditions, we have

$$\overline{W}=0,\quad C_{11}\frac{\partial\overline{U}}{\partial X}+C_{12}\frac{\partial\overline{V}}{\partial Y}+C_{13}\frac{\partial\overline{W}}{\partial Z_i}=0,$$

$$C_{66}\left(\frac{1}{B_p}\frac{\partial\overline{U}}{\partial Y}+B_p\frac{\partial\overline{V}}{\partial X}\right)=0\quad\text{at the edge }x=\text{constant}\tag{14a}$$

$$\overline{W}=0,\quad C_{21}\frac{\partial\overline{U}}{\partial X}+C_{22}\frac{\partial\overline{V}}{\partial Y}+C_{23}\frac{\partial\overline{W}}{\partial Z_i}=0,$$

$$C_{66}\left(\frac{1}{B_p}\frac{\partial\overline{U}}{\partial Y}+B_p\frac{\partial\overline{V}}{\partial X}\right)=0\quad\text{at the edge }y=\text{constant}$$

and for clamped edge conditions, we have

$$\overline{U}=\overline{V}=\overline{W}=0\quad\text{at the edges }x,y=\text{constant}.\tag{14b}$$

The normalized DQ equilibrium equations at a lamina interior grid point or bonding layer middle point have been given in Liew et al. [23] except that the right-hand sides of the current dynamic equations are now, respectively,

$$\rho\cdot b^2\overline{U}^{(i)}_{,tt}(X_k,Y_m,Z_r,t),\quad \rho\cdot a^2\overline{V}^{(i)}_{,tt}(X_k,Y_m,Z_r,t),$$
$$\text{and}\quad \rho\cdot a^2\cdot H_i\overline{W}^{(i)}_{,tt}(X_k,Y_m,Z_r,t).\tag{15}$$

Similarly, the normalized simply-supported edge conditions are given by

$$\overline{W}^{(i)}(X_1\text{ or }X_{N_x},Y_g,Z_f)=0\quad i=1,2,\ldots,N_L;$$
$$g=1,2,\ldots,N_y;\quad f=1,2,\ldots,N_{zi},$$

$$C_{11}^{\{i\}}\sum_{j=1}^{N_x}A_{X1j}^{[1]}\overline{U}^{(i)}(X_j,Y_g,Z_f)+C_{12}^{\{i\}}\sum_{m=1}^{N_y}A_{Ygm}^{[1]}\overline{V}^{(i)}(X_1,Y_m,Z_f)$$
$$+C_{13}^{\{i\}}H_i\sum_{q=1}^{N_{zi}}A_{Zfq}^{[1]}\overline{W}^{(i)}(X_1,Y_g,Z_q)=0$$

or

$$C_{11}^{\{i\}}\sum_{j=1}^{N_x}A_{XN_xj}^{[1]}\overline{U}^{(i)}(X_j,Y_g,Z_f)+C_{12}^{\{i\}}\sum_{m=1}^{N_y}A_{Ygm}^{[1]}\overline{V}^{(i)}(X_K,Y_m,Z_f)$$
$$+C_{13}^{\{i\}}H_i\sum_{q=1}^{N_{zi}}A_{Zfq}^{[1]}\overline{W}^{(i)}(X_K,Y_g,Z_q)=0,$$

$$C_{66}^{\{i\}}\left[B_p\sum_{j=1}^{N_x}A_{X1j}^{[1]}\overline{V}^{(i)}(X_j,Y_g,Z_f)+\frac{1}{B_p}\sum_{m=1}^{N_y}A_{Ygm}^{[1]}\overline{U}^{(i)}(X_1,Y_m,Z_f)\right]=0$$

or

$$C_{66}^{\{i\}}\left[B_p\sum_{j=1}^{N_x}A_{XN_xj}^{[1]}\overline{V}^{(i)}(X_j,Y_g,Z_f)+\frac{1}{B_p}\sum_{m=1}^{N_y}A_{Ygm}^{[1]}\overline{U}^{(i)}(X_K,Y_m,Z_f)\right]=0$$

$$\text{at the edges of }x=\text{constant}$$

$$\overline{W}^{(i)}(X_j,Y_1\text{ or }Y_{N_y},Z_f)=0\quad i=1,2,\ldots,N_L;$$
$$j=1,2,\ldots,N_x;\quad f=1,2,\ldots,N_{zi},$$

$$C_{21}^{\{i\}}\sum_{k=1}^{N_x}A_{Xjk}^{[1]}\overline{U}^{(i)}(X_k,Y_1,Z_f)+C_{22}^{\{i\}}\sum_{m=1}^{N_y}A_{Y1m}^{[1]}\overline{V}^{(i)}(X_j,Y_m,Z_f)$$
$$+C_{23}^{\{i\}}H_i\sum_{q=1}^{N_{zi}}A_{Zfq}^{[1]}\overline{W}^{(i)}(X_j,Y_1,Z_q)=0$$

or

$$C_{21}^{\{i\}}\sum_{k=1}^{N_x}A_{Xjk}^{[1]}\overline{U}^{(i)}(X_k,Y_M,Z_f)+C_{22}^{\{i\}}\sum_{m=1}^{N_y}A_{YN_ym}^{[1]}\overline{V}^{(i)}(X_j,Y_m,Z_f)$$
$$+C_{23}^{\{i\}}H_i\sum_{q=1}^{N_{zi}}A_{Zfq}^{[1]}\overline{W}^{(i)}(X_j,Y_M,Z_q)=0,$$

$$C_{66}^{\{i\}}\left[B_p\sum_{k=1}^{N_x}A_{Xjk}^{[1]}\overline{V}^{(i)}(X_k,Y_1,Z_f)+\frac{1}{B_p}\sum_{m=1}^{N_y}A_{Y1m}^{[1]}\overline{U}^{(i)}(X_j,Y_m,Z_f)\right]=0$$

or

$$C_{66}^{\{i\}}\left[B_p\sum_{k=1}^{N_x}A_{Xjk}^{[1]}\overline{V}^{(i)}(X_k,Y_M,Z_f)+\frac{1}{B_p}\sum_{m=1}^{N_y}A_{YN_ym}^{[1]}\overline{U}^{(i)}(X_j,Y_m,Z_f)\right]=0$$

$$\text{at the edges of }y=\text{constant}.\tag{16a}$$

The normalized clamped edge conditions take the form

$$\overline{U}^{(i)}(X_1\text{ or }X_{N_x},Y_g,Z_f)=\overline{V}^{(i)}(X_1\text{ or }X_{N_x},Y_g,Z_f)=\overline{W}^{(i)}(X_1\text{ or }X_{N_x},Y_g,Z_f)=0$$
$$i=1,2,\ldots,N_L;\quad g=1,2,\ldots,N_y,$$
$$f=1,2,\ldots,N_{zi}\quad\text{at the edges of constant }x\tag{16b}$$

$$\overline{U}^{(i)}(X_j,Y_1\text{ or }Y_{N_y},Z_f)=\overline{V}^{(i)}(X_j,Y_1\text{ or }Y_{N_y},Z_f)=\overline{W}^{(i)}(X_j,Y_1\text{ or }Y_{N_y},Z_f)=0$$
$$i=1,2,\ldots,N_L;\quad g=1,2,\ldots,N_y,$$
$$f=1,2,\ldots,N_{zi}\quad\text{at the edges of constant }y.$$

The normalized surface conditions at interior grid points $(X_k,Y_m,0)$ and (X_k,Y_m,H) for the bottom of the bottom layer and the top of the top layer, have been given in Liew et al. [23] and will not be repeated here.

The normalized interlaminar continuity conditions at interior grid point (X_k,Y_m,H_i^T), where H_i^T is the thickness coordinate at the interface between the lower lamina and bonding layer, are

$$C_{31}^{\{i\}}\sum_{j=1}^{N_x}A_{Xkj}^{[1]}\overline{U}^{(i)}(X_j,Y_m,H_i^T)+C_{32}^{\{i\}}\sum_{g=1}^{N_y}A_{Ymg}^{[1]}\overline{V}^{(i)}(X_k,Y_g,H_i^T)$$
$$+C_{33}^{\{i\}}H_i\sum_{f=1}^{N_{zi}}A_{ZN_{zi}f}^{[1]}\overline{W}^{(i)}(X_k,Y_m,Z_f)$$
$$=\frac{E}{(1+\nu)\cdot(1-2\nu)}\left\{(1-\nu)\frac{H}{h}\sum_{f=1}^{3}A_{Z1f}^{[1]}\overline{W}(X_k,Y_m,Z_f)+\nu\cdot\left[\sum_{j=1}^{N_x}A_{Xkj}^{[1]}\overline{U}^{(i)}(X_j,Y_m,H_i^T)+\sum_{g=1}^{N_y}A_{Ymg}^{[1]}\overline{V}^{(i)}(X_k,Y_g,H_i^T)\right]\right\}$$

$$C_{55}^{\{i\}}\left[H_iD_i\sum_{j=2}^{N_x-1}A_{Xkj}^{[1]}\overline{W}^{(i)}(X_j,Y_m,H_i^T)+\frac{1}{D_i}\sum_{f=1}^{N_{zi}}A_{ZN_{zi}f}^{[1]}\overline{U}^{(i)}(X_k,Y_m,Z_f)\right]=G\cdot\left[H_iD_i\sum_{j=2}^{N_y-1}A_{Xkj}^{[1]}\overline{W}^{(i)}(X_j,Y_m,H_i^T)+\frac{a}{h}\sum_{f=1}^{3}A_{Z1f}^{[1]}\overline{U}(X_k,Y_m,Z_f)\right] \quad (17)$$

$$C_{44}^{\{i\}}\left[H_i\frac{D_i}{B_p}\sum_{g=2}^{N_y-1}A_{Ymg}^{[1]}\overline{W}^{(i)}(X_k,Y_g,H_i^T)+\frac{B_p}{D_i}\sum_{f=1}^{N_{zi}}A_{ZN_{zi}f}^{[1]}\overline{V}^{(i)}(X_k,Y_m,Z_f)\right]=G\cdot\left[H_i\frac{D_i}{B_p}\sum_{g=2}^{N_y-1}A_{Ymg}^{[1]}\overline{W}^{(i)}(X_k,Y_g,H_i^T)+\frac{b}{h}\sum_{f=1}^{3}A_{Z1f}^{[1]}\overline{V}(X_k,Y_m,Z_f)\right]$$

and at (X_k,Y_m,H_{i+1}^B) where H_{i+1}^B is the thickness coordinate at the interface between bonding layer and the upper lamina

$$\frac{E}{(1+\nu)\cdot(1-2\nu)}\left\{(1-\nu)\frac{H}{h}\sum_{f=1}^{3}A_{Z3f}^{[1]}\overline{W}(X_k,Y_m,Z_f)+\nu\cdot\left[\sum_{j=1}^{N_x}A_{Xkj}^{[1]}\overline{U}^{(i+1)}(X_j,Y_m,H_{i+1}^B)+\sum_{g=1}^{N_y}A_{Ymg}^{[1]}\overline{V}^{(i+1)}(X_k,Y_g,H_{i+1}^B)\right]\right\}=C_{31}^{(i+1)}\sum_{j=1}^{N_x}A_{Xkj}^{[1]}\overline{U}^{(i+1)}(X_j,Y_m,H_{i+1}^B)+C_{32}^{\{i+1\}}\sum_{g=1}^{N_y}A_{Ymg}^{[1]}\overline{V}^{(i+1)}(X_k,Y_g,H_{i+1}^B)+C_{33}^{\{i+1\}}H_{i+1}\sum_{f=1}^{N_{zi+1}}A_{Z1f}^{[1]}\overline{W}^{(i+1)}(X_k,Y_m,Z_f) \quad (18)$$

$$G\cdot\left[H_{i+1}D_{i+1}\sum_{j=2}^{N_x-1}A_{Xkj}^{[1]}\overline{W}^{(i+1)}(X_j,Y_m,H_{i+1}^B)+\frac{a}{h}\sum_{f=1}^{3}A_{Z3f}^{[1]}\overline{U}(X_k,Y_m,Z_f)\right]=C_{55}^{\{i+1\}}\left[H_{i+1}D_{i+1}\sum_{j=2}^{N_x-1}A_{Xkj}^{[1]}\overline{W}^{(i+1)}(X_j,Y_m,H_{i+1}^B)+\frac{1}{D_{i+1}}\sum_{f=1}^{N_{zi+1}}A_{Z1f}^{[1]}\overline{U}^{(i+1)}(X_k,Y_m,Z_f)\right]$$

Table 1 Material properties used in the examples

Example 1		
$E_y/E_x=0.543103$		$E_z/E_x=0.530172$
$E_{xy}/E_x=0.23319$	$E_{xz}/E_x=0.010776$	$E_{yz}/E_x=0.098276$
$G_{xy}/E_x=0.262931$	$G_{xz}/E_x=0.159914$	$G_{yz}/E_x=0.26681$
Example 2		
$E_x=55.8979$	$E_y=13.7293$	$E_z=13.7293$
$\nu_{xy}=0.277$	$\nu_{zx}=0.068$	$\nu_{yz}=0.400$
$G_{xy}=5.5898$	$G_{xz}=5.5898$	$G_{yz}=4.9033$
Examples 3 and 4		
$E_1/E_2=20, 40$		$E_2=E_3$
$G_{12}=G_{13}=0.6\,E_2$		$G_{23}=0.5\,E_2$
$\nu_{12}=\nu_{13}=0.25$		$\nu_{23}=0.49$

$$G\cdot\left[H_{i+1}\frac{D_{i+1}}{B_p}\sum_{g=2}^{N_y-1}A_{Ymg}^{[1]}\overline{W}^{(i+1)}(X_k,Y_g,H_{i+1}^B)+\frac{b}{h}\sum_{f=1}^{3}A_{Z3f}^{[1]}\overline{V}(X_k,Y_m,Z_f)\right]=C_{44}^{(i+1)}\left[H_{i+1}\frac{D_{i+1}}{B_p}\sum_{g=2}^{N_y-1}A_{Ymg}^{[1]}\overline{W}^{(i+1)}(X_k,Y_g,H_{i+1}^B)+\frac{B_p}{D_{i+1}}\sum_{f=1}^{N_{zi+1}}A_{Z1f}^{[1]}\overline{V}^{(i+1)}(X_k,Y_m,Z_f)\right].$$

Here G denotes the shear modulus of bonding layer.

In the next section, several examples of the free vibration of thick laminates with different edge conditions are presented to demonstrate the accuracy and efficiency of the present model and computational methodology.

3 Results and Discussion

In the first example, we consider the vibration three-ply (0°/90°/0°) simply-supported square sandwich plates, see Srinivas and Rao [8]. The moduli, and the properties of the surface layers are listed in Table 1. The thickness of the top and bottom plies is taken to be one tenth of the total thickness of the laminate; and the side-to-thickness ratio is taken to be 10. The through-thickness mesh consists of three grid points that describe the transverse field in the top and bottom plies, and five grid points are correspondingly used for the core layer. A convergence study is carried out with respect to the in-plane grid point distribution. From the results shown in Table 2, it is observed that the convergence is rapid and stable. The converged results were obtained with a 9×9 grid point distribution. Further, in Table 2, comparison is made between the frequency results obtained from the present three-dimensional elastic bonding model and the rigid bonding model of Srinivas and Rao [8], where analytical solutions were presented. Note that "DQR" refers to results based on the rigid bonding model (without in-plane flexibilities), but using the present layer-wise theory with DQ implementation. The results in Table 2 are noticeably different from those of Srinivas and Rao [8], stemming from the modeling of elastic bonding layers. It appears that Young modulus E of bonding layer has the dominant effect on the frequencies. Further, the thickness h of the bonding layer has slightly more significant influence as compared to the Poisson's ratio ν, especially when E is relatively larger. An important observation here is that stable results can be obtained within a rather flexible and broad combination of values of the material parameters.

In the second example, the free vibration of two-ply (0°/90°) and three-ply (0°/90°/0°) square laminates with various thickness ratios is considered, see Bhimaraddi and Stevens [30]. The material properties are listed in Table 1. The fundamental frequencies

Table 2 Comparison of fundamental frequency (normalized by $\sqrt{\rho H^2/E_{2x}}$) of simply-supported square sandwich laminates, [0°/90°/0°] (material properties are given in Table 1; E_{1x} is the modulus of surface layers and E_{2x} is the modulus of the second layer)

E_{1x}/E_{2x}	E	h	ν	5×5 (grid)	7×7 (grid)	9×9 (grid)	11×11 (grid)
1	0.1	10^{-3}	0.03	0.043421	0.045008	0.045294	0.045366
			0.3	0.043437	0.045018	0.045301	0.045371
		5×10^{-4}	0.03	0.043363	0.044952	0.045240	0.045312
			0.3	0.043371	0.044957	0.045243	0.045315
	1	10^{-3}	0.03	0.044268	0.045913	0.046208	0.046281
			0.3	0.044485	0.046090	0.046373	0.046443
		5×10^{-4}	0.03	0.043789	0.045407	0.045700	0.045773
			0.3	0.043899	0.045496	0.045764	0.045855
		Srinivas and Rao [8]			0.047419		
		{DQR}			0.047338		
5	0.1	10^{-3}	0.03	0.071175	0.073025	0.073193	0.073209
			0.3	0.071214	0.073077	0.073218	0.073233
		5×10^{-4}	0.03	0.070782	0.072597	0.072802	0.072815
			0.3	0.070802	0.072667	0.072811	0.072827
	1	10^{-3}	0.03	0.073166	0.075164	0.075209	0.075221
			0.3	0.073702	0.075543	0.075663	0.075675
		5×10^{-4}	0.03	0.071796	0.073683	0.073827	0.073842
			0.3	0.072072	0.073927	0.074060	0.074074
		Srinivas and Rao [8]			0.077148		
		{DQR}			0.076936		

Table 3 Comparison of nondimensionalized fundamental frequency (normalized by $\sqrt{\rho H^2/E_{2x}}$) of simply-supported two-ply square laminates [0°/90°] (material properties are given in Table 1; E_{2x} is the modulus of the second layer, and h_1 and h_2 are the thicknesses of the first and second layers, respectively)

h_2/h_1	H/a	E	h	ν	7×7 (grid)	9×9 (grid)	11×11 (grid)	13×13 (grid)
1	0.1	10	10^{-2}	0.05	0.063518	0.063837	0.063938	0.063954
				0.4	0.063456	0.063814	0.063915	0.063930
			5×10^{-3}	0.05	0.063213	0.063573	0.063675	0.063692
				0.4	0.063202	0.063562	0.063664	0.063680
		50	10^{-2}	0.05	0.063620	0.063984	0.064087	0.064104
				0.4	0.063583	0.063947	0.064050	0.064066
			5×10^{-3}	0.05	0.063283	0.063647	0.063750	0.063766
				0.4	0.063265	0.063628	0.063731	0.063748
			Bhimaraddi and Stevens [30]			0.06572		
			{DQR}			0.065447		
	0.3	10	10^{-2}	0.05	0.440447	0.440411	0.440342	0.440310
				0.4	0.440308	0.440270	0.440200	0.440168
			5×10^{-3}	0.05	0.440095	0.440060	0.439991	0.439959
				0.4	0.440027	0.439990	0.439920	0.439888
		50	10^{-2}	0.05	0.440938	0.440931	0.440868	0.440838
				0.4	0.440852	0.440837	0.440773	0.440743
			5×10^{-3}	0.05	0.440319	0.440315	0.440253	0.440223
				0.4	0.440283	0.440269	0.440206	0.440175
			Bhimaraddi and Stevens [30]			0.47275		
			{DQR}			0.46312		
5	0.1	10	10^{-2}	0.05	0.068507	0.068824	0.068913	0.068925
				0.4	0.068538	0.068851	0.068939	0.068951
			5×10^{-3}	0.05	0.068377	0.068693	0.068782	0.068795
				0.4	0.068393	0.068707	0.068795	0.068808
		50	10^{-2}	0.05	0.069078	0.069399	0.069487	0.069498
				0.4	0.069243	0.069549	0.069633	0.069643
			5×10^{-3}	0.05	0.068668	0.068986	0.069074	0.069086
				0.4	0.068752	0.069062	0.069149	0.069160
			Bhimaraddi and Stevens [30]			0.07061		
			{DQR}			0.070604		
	0.3	10	10^{-2}	0.05	0.464416	0.464359	0.464300	0.464283
				0.4	0.464439	0.464380	0.464320	0.464303
			5×10^{-3}	0.05	0.464251	0.464194	0.464135	0.464117
				0.4	0.464262	0.464204	0.464145	0.464127
		50	10^{-2}	0.05	0.465295	0.465219	0.465156	0.465137
				0.4	0.465577	0.465499	0.465436	0.465417
			5×10^{-3}	0.05	0.464705	0.464630	0.464566	0.464547
				0.4	0.464844	0.464771	0.464707	0.464689
			Bhimaraddi and Stevens [30]			0.48536		
			{DQR}			0.48418		

Table 4 **Comparison of nondimensionalized fundamental frequency (normalized by $\sqrt{\rho H^2/E_{2x}}$) of simply-supported square sandwich laminates [0°/90°/0°] (material properties are given in Table 1; E_{2x} is the modulus of the second layer, and h_1, h_2, and h_3 are the thicknesses of the first, second, and third layers, and $h_r = h_2/h_1 = h_2/h_3$)**

h_r	H/a	E	h	ν	7×7 (grid)	9×9 (grid)	11×11 (grid)	13×13 (grid)
1	0.1	10	10^{-2}	0.05	0.068544	0.068837	0.068919	0.068932
				0.4	0.068529	0.068817	0.068897	0.068909
			5×10^{-3}	0.05	0.067942	0.068235	0.068319	0.068332
				0.4	0.067935	0.068225	0.068308	0.068321
		50	10^{-2}	0.05	0.068955	0.069265	0.069351	0.069365
				0.4	0.069078	0.069376	0.069459	0.069472
			5×10^{-3}	0.05	0.068139	0.068445	0.068532	0.068546
				0.4	0.068202	0.068502	0.068586	0.068600
		Bhimaraddi and Stevens [30]				0.07304		
			{DQR}			0.073006		
	0.3	10	10^{-2}	0.05	0.447945	0.447932	0.447916	0.447926
				0.4	0.447624	0.447604	0.447585	0.447594
			5×10^{-3}	0.05	0.447134	0.447123	0.447106	0.447116
				0.4	0.446977	0.446960	0.446941	0.446950
		50	10^{-2}	0.05	0.449196	0.449250	0.449254	0.449275
				0.4	0.449376	0.449407	0.449405	0.449422
			5×10^{-3}	0.05	0.447696	0.447755	0.447759	0.447779
				0.4	0.447807	0.447842	0.447840	0.447857
		Bhimaraddi and Stevens [30]				0.49119		
			{DQR}			0.48923		
5	0.1	10	10^{-2}	0.05	0.060645	0.060966	0.061083	0.061115
				0.4	0.060769	0.061076	0.061188	0.061218
			5×10^{-3}	0.05	0.060141	0.060457	0.060574	0.060606
				0.4	0.060204	0.060512	0.060627	0.060658
		50	10^{-2}	0.05	0.062401	0.062772	0.062897	0.062929
				0.4	0.063062	0.063373	0.063480	0.063506
			5×10^{-3}	0.05	0.061019	0.061373	0.061497	0.061531
				0.4	0.061362	0.061681	0.061795	0.061825
		Bhimaraddi and Stevens [30]				0.07424		
			{DQR}			0.073300		
	0.3	10	10^{-2}	0.05	0.426236	0.426503	0.426570	0.426609
				0.4	0.426393	0.426637	0.426697	0.426733
			5×10^{-3}	0.05	0.425453	0.425722	0.425788	0.425828
				0.4	0.425540	0.425793	0.425855	0.425892
		50	10^{-2}	0.05	0.429361	0.429781	0.429897	0.429958
				0.4	0.430821	0.431149	0.431238	0.431286
			5×10^{-3}	0.05	0.426897	0.427324	0.427438	0.427498
				0.4	0.427681	0.428035	0.428128	0.428179
		Bhimaraddi and Stevens [30]				0.53438		
			{DQR}			0.49934		

of two-ply laminates are presented in Table 3, while those of the three-ply laminates in Table 4. Converged results were obtained with a 11×11 in-plane grid point distribution. Similar to the first example, the results in Tables 3 and 4 reveal that the present elastic bonding model is quite different from that of rigid bonding model, as the structural rigidity of the laminate is reduced. From these numerical results, we note that when the thickness is $H/a = 0.1$ (in which a is the in-plane dimension of the laminate, and H is the total thickness of the laminate), the present results are quite close to the results of Bhimaraddi and Stevens [30], who used a two-dimensional but higher-order plate theory. However, when the thickness is increased to $H/a = 0.3$, a larger difference between the two sets of results is observed. From the results of Bhimaraddi and Stevens [30], it is noted that the stiffness of the two and three-layered laminates consisting of equally thick plies is generally softer than that of laminates with unequal lamina thickness. However, for the present elastic bonding cases, the observations are different. For two-ply laminates, the stiffness of the laminates consisting of equally thick plies, is softer than that of the laminates with unequal lamina thickness; however, for the three-ply laminates, the converse is true, where the stiffness of the laminates consisting of equally thick plies, is stiffer than that of the laminates with unequal lamina thickness. Since the present analysis is based on a three-dimensional model, the difference may be attributed to certain limitations of higher-order plate theory in modeling thick laminates of the present configuration.

In the third example, the vibration of two-ply (0°/90°) and three-ply (0°/90°/0°) rectangular laminates with simply-supported edges along opposite edges (x = constant), and clamped along the other opposite edges (y = constant), is considered. The material properties of the layers are listed in Table 1, and this example has been considered previously by Khdeir [31], Reddy and Khdeir [32], and Khdeir [33]. Both square and rectangular laminates are analyzed. Results for the two-ply laminates are presented in Tables 5(a) and 5(b), and those of the three-ply laminates are presented in Tables 6(a) and 6(b). Converged solution is obtained again with a 11×11 in-plane grid point distribution. Present results show reasonable agreement with the results of Khdeir [31,33], and Reddy and Khdeir [32], who used the third-order plate theory of Reddy [1,34]. From the results in Tables 5(a), 5(b), 6(a), and 6(b), it can be observed that the rigid bonding model is slightly stiffer than the elastic bonding model when using an isotropic elastic bonding layer with modulus equivalent to the matrix material of the composite.

In the fourth and final example, the vibration of fully clamped two-ply (0°/90°) and three-ply (0°/90°/0°) rectangular laminates of various aspect and thickness ratios is studied. The material properties of these laminates are the same as that of the previous example. This problem has no known analytical solution. Results for the two-ply laminates are shown in Table 7, while those for the three-ply laminates are presented in Table 8. Again, converged solution is obtained with a 11×11 in-plane grid point distribution. It is interesting to observe here that, unlike the simply-supported cases of Example 1, the influence of bonding parameters for the fully clamped plates is less obvious.

Table 5 (a) Comparison of nondimensionalized fundamental frequency (normalized by $\sqrt{\rho a^4/H^2E_2}$) of two-ply square laminates [0°/90°] with SCSC edge conditions (material properties are given in Table 1)

H/a	E_1/E_2	E	h	ν	7×7 (grid)	9×9 (grid)	11×11 (grid)	13×13 (grid)
0.1	20	1	10^{-3}	0.1	12.7302	12.7192	12.7135	12.7102
				0.4	12.7280	12.7169	12.7112	12.7079
			5×10^{-4}	0.1	12.7566	12.7457	12.7400	12.7366
				0.4	12.7555	12.7445	12.7388	12.7355
		20	10^{-3}	0.1	12.8599	12.8454	12.8385	12.8349
				0.4	12.8668	12.8495	12.8413	12.8370
			5×10^{-4}	0.1	12.8214	12.8086	12.8023	12.7988
				0.4	12.8250	12.8107	12.8038	12.8000
			Khdeir [31]			12.990		
			{DQR}			12.7672		
	40	1	10^{-3}	0.1	14.4896	14.4769	14.4700	14.4665
				0.4	14.4877	14.4750	14.4680	14.4646
			5×10^{-4}	0.1	14.5301	14.5175	14.5105	14.5071
				0.4	14.5291	14.5165	14.5096	14.5061
		40	10^{-3}	0.1	14.6836	14.6611	14.6506	14.6459
				0.4	14.6919	14.6655	14.6533	14.6478
			5×10^{-4}	0.1	14.6281	14.6096	14.6007	14.5966
				0.4	14.6323	14.6120	14.6022	14.5977
			Khdeir [31]			15.218		
			{DQR}			14.5471		
0.2	20	1	10^{-3}	0.1	9.6745	9.6670	9.6631	9.6598
				0.4	9.6720	9.6645	9.6606	9.6573
			5×10^{-4}	0.1	9.6813	9.6737	9.6698	9.6666
				0.4	9.6800	9.6725	9.6686	9.6653
		20	10^{-3}	0.1	9.7158	9.7055	9.7009	9.6974
				0.4	9.7157	9.7055	9.7008	9.6971
			5×10^{-4}	0.1	9.7021	9.6929	9.6887	9.6853
				0.4	9.7020	9.6930	9.6887	9.6852
			{DQR}			9.6733		
	40	1	10^{-3}	0.1	10.3278	10.3191	10.3157	10.3132
				0.4	10.3257	10.3170	10.3136	10.3110
			5×10^{-4}	0.1	10.3358	10.3271	10.3237	10.3211
				0.4	10.3347	10.3260	10.3226	10.3200
		40	10^{-3}	0.1	10.3842	10.3694	10.3643	10.3610
				0.4	10.3837	10.3692	10.3641	10.3607
			5×10^{-4}	0.1	10.3647	10.3524	10.3481	10.3451
				0.4	10.3642	10.3523	10.3480	10.3445
			Reddy & Khdeir [32]			11.890		
			{DQR}			10.3294		

Table 5 (b) Comparison of nondimensionalized fundamental frequency (normalized by $\sqrt{\rho a^4/H^2E_2}$) of two-ply rectangular laminates ($a/b=2$, $a/H=10$) [0°/90°] with SCSC edge conditions (material properties are given in Table 1)

E_1/E_2	E	h	ν	5×7 (grid)	5×9 (grid)	7×11 (grid)	7×13 (grid)
20	1	10^{-3}	0.1	33.5409	33.0988	33.0278	32.9968
			0.4	33.5219	33.0811	33.0104	32.9792
		5×10^{-4}	0.1	33.5720	33.1352	33.0642	33.0332
			0.4	33.5625	33.1264	33.0555	33.0244
	20	10^{-3}	0.1	33.8307	33.3637	33.2728	33.2369
			0.4	33.8854	33.3774	33.2871	33.2502
		5×10^{-4}	0.1	33.7188	33.2681	33.1864	33.1528
			0.4	33.7464	33.2748	33.1937	33.1597
		{DQR}			33.0712		
40	1	10^{-3}	0.1	35.0134	34.7512	34.6763	34.6451
			0.4	34.9958	34.7349	34.6603	34.6288
		5×10^{-4}	0.1	35.0487	34.7923	34.7173	34.6861
			0.4	35.0399	34.7841	34.7093	34.6779
	40	10^{-3}	0.1	35.4280	35.1029	34.9845	34.9411
			0.4	35.4835	35.1127	34.9965	34.9523
		5×10^{-4}	0.1	35.2667	34.9731	34.8733	34.8351
			0.4	35.2930	34.9769	34.8793	34.8408
		Reddy & Khdeir [32]			40.925		
		{DQR}			34.7269		

Table 6 (a) Comparison of nondimensionalized fundamental frequency (normalized by $\sqrt{\rho a^4/H^2 E_2}$) of square sandwich laminates [0°/90°/0°] with SCSC edge conditions (material properties are given in Table 1)

H/a	E_1/E_2	E	h	ν	First Mode	Second Mode	Third Mode
0.1	20	1	5×10^{-4}	0.2	13.7852	23.1748	23.2471
				0.4	13.7817	23.1718	23.2357
			5×10^{-5}	0.2	13.8124	23.2372	23.2818
				0.4	13.8120	23.2369	23.2807
		20	5×10^{-4}	0.2	13.9016	23.4361	24.6940
				0.4	13.9179	23.4759	24.4845
			5×10^{-5}	0.2	13.8223	23.2589	23.4295
				0.4	13.8242	23.2636	23.4075
			Khdeir [33]		18.124	⋯	⋯
			{DQR}		13.8124	23.2337	23.3057
	40	1	5×10^{-4}	0.2	16.4612	23.4604	25.7236
				0.4	16.4536	23.4485	25.7178
			5×10^{-5}	0.2	16.5040	23.4952	25.8069
				0.4	16.5032	23.4940	25.8063
		40	5×10^{-4}	0.2	16.6274	26.0682	26.3859
				0.4	16.6477	25.9813	26.1169
			5×10^{-5}	0.2	16.5174	23.8012	25.8336
				0.4	16.5200	23.7568	25.8399
			Khdeir [33]		20.315	⋯	⋯
			{DQR}		16.5051	23.5289	25.8047
0.2	20	1	5×10^{-4}	0.2	10.5456	11.5640	16.8450
				0.4	10.5423	11.5611	16.8410
			5×10^{-5}	0.2	10.5557	11.5731	16.8602
				0.4	10.5554	11.5728	16.8598
		20	5×10^{-4}	0.2	10.5860	11.9295	16.9119
				0.4	10.5895	11.8761	16.9180
			5×10^{-5}	0.2	10.5587	11.6068	16.8646
				0.4	10.5592	11.6018	16.8656
			{DQR}		10.5568	11.5839	16.8552
	40	1	5×10^{-4}	0.2	11.5028	11.6498	17.5349
				0.4	11.4984	11.6467	17.5304
			5×10^{-5}	0.2	11.5146	11.6590	17.5517
				0.4	11.5141	11.6587	17.5512
		40	5×10^{-4}	0.2	11.5528	12.3992	17.6153
				0.4	11.5564	12.2934	17.6217
			5×10^{-5}	0.2	11.5179	11.7306	17.5564
				0.4	11.5185	11.7202	17.5576
			Khdeir [33]		12.333	⋯	⋯
			{DQR}	11.5159	11.6739	17.5473	

Table 6 (b) Comparison of nondimensionalized fundamental frequency (normalized by $\sqrt{\rho a^4/H^2 E_2}$) of rectangular sandwich laminates ($a/b=2$, $a/H=10$) [0°/90°/0°] with SCSC edge conditions (material properties are given in Table 1)

E	h	ν	First Mode	Second Mode	Third Mode
		$E_1/E_2=20$			
1	5×10^{-4}	0.2	41.2896	43.6831	47.7328
		0.4	41.2424	43.6390	47.7092
	5×10^{-5}	0.2	41.3565	43.7639	47.8023
		0.4	41.3517	43.7594	47.8000
20	5×10^{-4}	0.2	41.6812	44.1331	50.7335
		0.4	41.6654	44.1241	50.2981
	5×10^{-5}	0.2	41.3966	43.8119	48.1046
		0.4	41.3947	43.8104	48.0596
	{DQR}		41.3640	43.7730	47.8102
		$E_1/E_2=40$			
1	5×10^{-4}	0.2	43.0619	45.7661	47.8671
		0.4	43.0135	45.7213	47.8431
	5×10^{-5}	0.2	43.1323	45.8599	47.9366
		0.4	43.1274	45.8553	47.9343
40	5×10^{-4}	0.2	43.5908	46.3842	53.8664
		0.4	43.5656	46.3688	53.0386
	5×10^{-5}	0.2	43.1903	45.9297	48.5636
		0.4	43.1864	45.9264	48.4726
	Khdeir [33]		46.693	⋯	⋯
	{DQR}		43.1399	45.8701	47.9445

Table 7 Comparison of nondimensionalized fundamental frequency (normalized by $\sqrt{\rho a^4/H^2E_2}$) of two-ply laminates ($a/H=10$, $E_1/E_2=40$) [0°/90°] with CCCC edge conditions (material properties are given in Table 1)

a/b	E	h	ν	7×7 (grid)	9×9 (grid)	11×11 (grid)	13×13 (grid)
1	1	10^{-3}	0.1	17.8728	17.8296	17.8087	17.8000
			0.4	17.8705	17.8274	17.8068	17.7979
		5×10^{-4}	0.1	17.9173	17.8744	17.8537	17.8449
			0.4	17.9161	17.8733	17.8527	17.8438
	40	10^{-3}	0.1	18.0997	18.0419	18.0155	18.0047
			0.4	18.1288	18.0653	18.0363	18.0241
		5×10^{-4}	0.1	18.0321	17.9809	17.9569	17.9469
			0.4	18.0469	17.9930	17.9678	17.9571
		{DQR}			17.8893		
a/b	E	h	ν	5×7 (grid)	5×9 (grid)	7×11 (grid)	7×13 (grid)
2	1	10^{-3}	0.1	36.5263	36.5154	36.2467	36.2444
			0.4	36.5091	36.4982	36.2307	36.2284
		5×10^{-4}	0.1	36.5657	36.5548	36.2916	36.2893
			0.4	36.5571	36.5462	36.2836	36.2813
	40	10^{-3}	0.1	36.9478	36.9327	36.6027	36.5998
			0.4	37.0144	36.9980	36.6253	36.6221
		5×10^{-4}	0.1	36.7865	36.7733	36.4741	36.4715
			0.4	36.8189	36.8051	36.4848	36.4820
		{DQR}			36.3340		

Table 8 Comparison of nondimensionalized fundamental frequency (normalized by $\sqrt{\rho a^4/H^2E_2}$) of sandwich laminates [0°/90°/0°] with CCCC edge conditions (material properties are given in Table 1; $E_1/E_2=40$)

a/b	E	h	ν	First Mode	Second Mode	Third Mode
1	1	5×10^{-4}	0.2	21.1403	28.7202	40.2980
			0.4	21.1209	28.7056	40.2549
		5×10^{-5}	0.2	21.1894	28.8065	40.3695
			0.4	21.1874	28.8050	40.3651
	40	5×10^{-4}	0.2	21.3637	29.0887	40.7008
			0.4	21.3721	29.1220	40.6959
		5×10^{-5}	0.2	21.2123	28.8438	40.4118
			0.4	21.2131	28.8472	40.4108
		{DQR}		21.1943	28.8157	40.3771
2	1	5×10^{-4}	0.2	43.7278	47.9239	56.5948
			0.4	43.6801	47.8806	56.5567
		5×10^{-5}	0.2	43.8035	48.0225	56.7226
			0.4	43.7987	48.0181	56.7187
	40	5×10^{-4}	0.2	44.2697	48.5453	57.3141
			0.4	44.2488	48.5377	57.3273
		5×10^{-5}	0.2	43.8629	48.0894	56.7988
			0.4	43.8594	48.0875	56.7992
		{DQR}		43.8117	48.0332	56.7366

4 Conclusions

In this paper, three-dimensional elasticity theory within a layerwise framework is used to model a laminate and an elastic bonding model, which embodies a physical material layer at the interface of two adjacent layers, is presented. The interfacial characteristics of continuity and discontinuity are satisfied in a kinematic sense through the elastic bonding layer. Furthermore, the differential quadrature method (DQM) is employed to analyze the equations of motion for vibration response. All three-dimensional equations are satisfied and vibration results for a number of laminates are presented. The present model is validated through comparisons with existing three-dimensional results from the open literature. Examples are also included to show that even higher-order plate theories do not predict accurate solutions for thick laminates. The results indicate that the three-dimensional layerwise theory coupled with the elastic bonding model and the DQ methodology is computationally efficient and accurate. This can be attributed to the correct representation of the kinematics of the laminate and proper exploitation of DQ method for numerical modeling. Unlike existing rigid bonding model or weak bonding model, the present elastic bonding model provides a flexible approach that is adaptable to the actual physical characteristics of the variety of bonding mechanisms that may be present in a laminate.

References

[1] Reddy, J. N., 1997, *Mechanics of Laminated Composite Plates: Theory and Analysis*, CRC Press, Boca Raton, FL.
[2] Reddy, J. N., 1987, "A Generalization of Two-Dimensional Theories of Laminated Composite Plates," Commun. Appl. Numer. Methods, **3**, pp. 173–180.
[3] Reddy, J. N., 1989, "On the Generalization of Displacement-Based Laminate Theories," Appl. Mech. Rev., **42**, pp. 213–222.
[4] Soldatos, K. P., and Watson, P., 1997, "Accurate Stress Analysis of Laminated Plates Combining a Two-Dimensional Theory With the Exact Three-Dimensional Solution for Simply Supported Edges," Math. Mech. Solids, **2**, pp. 459–489.
[5] Soldatos, K. P., and Watson, P., 1997, "A General Four-Edges-of-Freedom Theory Suitable for the Acourate Stress Analysis of Homogeneous and Laminated Composites Beam," Int. J. Solids Struct., **34**, pp. 2857–2885.
[6] Soldatos, K. P., and Liu, S. L., 2001, "On the Generalized Plane Strain Deformations of Thick Anisotropic Composite Laminated Plates," Int. J. Solids Struct., **38**, pp. 479–482.
[7] Messina, A., and Soldatos, K. P., 2002, "A General Vibration Model of Angle-Ply Laminated Plates That Accounts for the Continuity of Interlaminar Stresses," Int. J. Solids Struct., **39**, pp. 617–635.
[8] Srinivas, S., and Rao, A. K., 1970, "Bending, Vibration and Buckling of Simply Supported Thick Orthotropic Rectangular Plates and Laminates," Int. J. Solids Struct., **6**, pp. 1463–1481.
[9] Savoia, M., and Reddy, J. N., 1992, "A Variational Approach to Three-Dimensional Elasticity Solutions of Laminated Composite Plates," ASME J. Appl. Mech., **59**, Part 2, pp. S166–S175.
[10] Teo, T. M., and Liew, K. M., 2001, "Three-Dimensional Elasticity Solutions to Some Orthotropic Plate Problems," Int. J. Solids Struct., **36**, pp. 5301–5326.
[11] Lu, X., and Liu, D., 1992, "Interlayer Shear Slip Theory for Cross-Ply Laminates With Nonrigid Interfaces," AIAA J., **30**, pp. 1063–1073.
[12] Newmark, N. M., Seiss, C. P., and Viest, I. M., 1951, "Tests and Analysis of Composite Beams With Incomplete Interaction," *Proceedings of Society for Experimental Stress Analysis*, Brookfield Center, Brookfield, CT, Vol. 9, pp. 73–79.
[13] Toledano, A., and Murakami, H., 1988, "Shear-Deformable Two-Layer Plate Theory With Interlayer Slip," J. Eng. Mech., **114**, pp. 605–623.
[14] Rao, K. M., and Ghosh, B. G., 1980, "Imperfectly Bonded Unsymmetric Laminated Beam," J. Eng. Mech., **106**, pp. 685–697.
[15] Fazio, P., Hussein, R., and Ha, K. H., 1982, "Beam-Columns With Interlayer Slips," J. Eng. Mech., **108**, pp. 354–366.
[16] Liu, D., Xu, L., and Lu, X., 1994, "Stress Analysis of Imperfect Composite Laminates With an Interlaminar Bonding Theory," Int. J. Numer. Methods Eng., **37**, pp. 2819–2839.
[17] Soldatos, K. P., and Shu, X. P., 2001, "Modelling of Perfectly and Weakly Bonded Laminated Plates and Shallow Shells," Comp. Sci. Tech., **61**, pp. 247–260.
[18] Willians, T. O., and Addessio, F. L., 1997, "A General Theory for Laminated Plates With Delaminations," Int. J. Solids Struct., **34**, pp. 2003–2024.
[19] Williams, T. O., 1999, "A Generalized Multilength Scale Nonlinear Composite

Plate Theory With Delamination,'' Int. J. Solids Struct., **36**, pp. 3015–3050.
[20] Shu, X. P., and Soldatos, K. P., 2001, ''An Accurate Delamination Model for Weakly Bonded Laminates Subjected to Different Sets of Edge Boundary Conditions,'' Int. J. Mech. Sci., **43**, pp. 935–959.
[21] Liew, K. M., Zhang, J. Z., Ng, T. Y., and Meguid, S. A., 2003, ''Three-Dimensional Modelling of Elastic Bonding in Composite Laminates Using Layerwise Differential Quadrature,'' Int. J. Solids Struct., **40**, pp. 1745–1764.
[22] Bellman, R. E., 1973, *Methods of Nonlinear Analysis*, Academic Press, San Diego, CA.
[23] Liew, K. M., Ng, T. Y., and Zhang, J. Z., 2002, ''Differential Quadrature-Layerwise Modeling Technique for Three-Dimensional Analysis of Cross-Ply Laminated Plates of Various Edge Supports,'' Comput. Methods Appl. Mech. Eng., **191**, pp. 3811–3832.
[24] Bert, C. W., Jang, S. K., and Striz, A. G., 1988, ''Two New Approximate Methods for Analyzing Free Vibration of Structural Components,'' AIAA J., **26**, pp. 612–618.
[25] Jang, S. K., Bert, C. W., and Striz, A. G., 1989, ''Application of Differential Quadrature to Static Analysis of Structural Components,'' Int. J. Numer. Methods Eng., **28**, pp. 561–577.
[26] Farsa, J., Kukreti, A. R., and Bert, C. W., 1993, ''Fundamental Frequency Analysis of Laminated Rectangular Plates by the Differential Quadrature Method,'' Int. J. Numer. Methods Eng., **36**, pp. 2341–2356.
[27] Han, J. B., and Liew, K. M., 1995, ''Numerical Differential Quadrature Method for Reissner/Mindlin Plates on Two-Parameter Foundations,'' Int. J. Mech. Sci., **39**, pp. 977–990.
[28] Liu, F.-L., and Liew, K. M., 1997, ''Static Analysis of Mindlin Plates by Differential Quadrature Element Method,'' ASME J. Appl. Mech., **65**, pp. 705–710.
[29] Bert, C. W., and Malik, M., 1996, ''Differential Quadrature Method in Computational Mechanics: A Review,'' Appl. Mech. Rev., **49**, pp. 1–28.
[30] Bhimaraddi, A., and Stevens, L. K., 1984, ''A Higher Order Theory for Free Vibration of Orthotropic, Homogeneous, and Laminated Rectangular Plates,'' ASME J. Appl. Mech., **51**, pp. 195–198.
[31] Khdeir, A. A., 1989, ''Free Vibration and Buckling of Unsymmetric Cross-Ply Laminated Plates Using a Refined Theory,'' J. Sound Vib., **128**, pp. 377–395.
[32] Reddy, J. N., and Khdeir, A. A., 1989, ''Buckling and Vibration of Laminated Composite Plates Using Various Plate Theories,'' AIAA J., **27**, pp. 1808–1817.
[33] Khdeir, A. A., 1988, ''Free Vibration and Buckling of Symmetric Cross-Ply Laminated Plates by an Exact Method,'' J. Sound Vib., **126**, pp. 447–461.
[34] Reddy, J. N., 1984, ''A Simple Higher-Order Theory for Laminated Plates,'' ASME J. Fluids Eng., **51**, pp. 745–752.

Nonstick and Stick-Slip Motion of a Coulomb-Damped Belt Drive System Subjected to Multifrequency Excitations

G. Cheng

J. W. Zu[1]
Associate Professor
e-mail: zu@mie.utoronto.ca

Department of Mechanical & Industrial Engineering,
University of Toronto,
5 King's College Road,
Toronto, ON M5S 3G8, Canada

In this paper, the rotational vibration of a belt drive system with a dry friction tensioner subjected to multiple harmonic excitations is studied. The work is focused on the impact of the dry friction torque combined with the multiexcitation frequencies on dynamic characteristics of the system. An analytical solution procedure is developed for the first time to predict two kinds of periodic responses of the system, i.e., nonstop and one-stop motion characterized by the nonstick and stick-slip vibration of the tensioner arm in the system, respectively. Utilizing this method, parametric studies are carried out to obtain the frequency response of a prototypical belt drive system subjected to harmonic excitations from both the driving and driven pulleys. It is found that the tensioner Coulomb friction torque has a significant impact on the amplitude response of the system—it reduces the vibration amplitude of the tensioner arm, but for other components in the belt system it can either decrease or increase the amplitudes under different situations. Furthermore, if the excitation frequency from the driving pulley is larger than or equal to that from the driven pulley, the system vibration amplitudes are much larger than those under the opposite condition. [DOI: 10.1115/1.1629754]

1 Introduction

Belt drive systems have long been employed in engine applications to power accessories such as alternator, air conditioner, power steering, and pumps. A typical automotive belt drive consists of a crankshaft, accessories and a ''serpentine'' belt tensioned by a dynamic tensioner. Such systems can exhibit complex dynamic behavior including rotational vibrations, which can be induced by crankshaft excitation, applied moments on driven accessories, pulley eccentricities, etc.

The rotational vibration of a belt drive system has been studied in recent research. In 1991, Hawker [1] investigated natural frequencies of damped belt drive systems with a dynamic tensioner. Barker et al. [2] utilized a Runge-Kutta method to solve the transient rotational response of a front end accessory drive system due to engine accelerations using experimentally measured torque characteristics of the tensioner. Later, Hwang et al. [3] determined rotational mode natural frequencies and mode shapes for the free response of a linearized system of equations for a serpentine belt drive system and applied the results to predict the onset of belt slip. Beikmann et al. [4] used the prototypical model of two pulleys with a tensioner to examine the coupling between the rotational and transverse motions, which led to new conclusions regarding linear free vibrations. The natural frequencies and mode shapes of an operating serpentine belt drive system were determined with analytical and experimental methods. In the paper [5] of Kraver et al., a complex modal procedure was developed to analyze the frequency response characteristics of a flat belt pulley system assuming viscous belt and tensioner damping. Iwatsubo et al. [6] proposed a method for analyzing the dynamic characteristics of belt drive systems consisting of multiple belts and pulleys. An algorithm that derives the linear equations of motion for arbitrary multicoupled belt systems was given.

All of the above studies assumed no dry friction at the tensioner hub or used approximate linear viscous damping models. In reality, however, dry friction at the tensioner hub represents a strong nonlinearity that may produce rich dynamic responses that can not be captured with linear viscous damping models. The subject of dry friction has been extensively studied in recent years. Shaw [7] determined the stability of periodic orbits of a system with dry friction. In the paper of Popp et al. [8], stick-slip vibrations induced by dry friction were investigated both numerically and experimentally. Later, Feeny et al. [9] studied the chaotic dynamics of a harmonically forced dry friction oscillator. More recently, Natsiavas [10] presented a stability analysis for periodic motions of a class of harmonically excited piecewise linear oscillators with viscous and dry friction damping.

To accurately model the dry friction at the tensioner hub, Leamy et al. [11] developed a nonlinear model that is capable of capturing the nonlinear effects of dry friction at the tensioner arm. The tensioner dry friction is assumed to be governed by the classical Coulomb law. The derived equations were solved by an adaptive time-step Runge-Kutta explicit integration method. Furthermore, Leamy et al. [12] solved the system by the incremental harmonic balance method (IHB), which was proposed by Pierre et al. [13]. This numerical method can efficiently compute the primary and secondary resonances in a FEAD system. The solution clearly captures the stick-slip motions of the tensioner arm.

In the aforementioned work, only a single excitation from the crankshaft was considered. However, the excitation on the belt drive system is of multifrequency in nature since the vibration of the system can be excited by multiple sources such as applied moments from the driving pulley or driven accessories, pulley eccentricities, irregular pulley radii and belt properties, or motion of pulley support. As a classic problem in the theory of nonlinear oscillations, multifrequency oscillation has been studied for one and two degrees-of-freedom systems with weakly nonlinearity, [14–16]. Most of the research effort in the above work has gone

[1]To whom correspondence should be addressed.

Contributed by the Applied Mechanics Division of THE AMERICAN SOCIETY OF MECHANICAL ENGINEERS for publication in the ASME JOURNAL OF APPLIED MECHANICS. Manuscript received by the ASME Applied Mechanics Division, Octer 15, 2002; final revision, June 4, 2003. Associate Editor: J. R. Barber. Discussion on the paper should be addressed to the Editor, Prof. Robert M. McMeeking, Department of Mechanical and Environmental Engineering, University of California—Santa Barbara, Santa Barbara, CA 93106-5070, and will be accepted until four months after final publication of the paper itself in the ASME JOURNAL OF APPLIED MECHANICS.

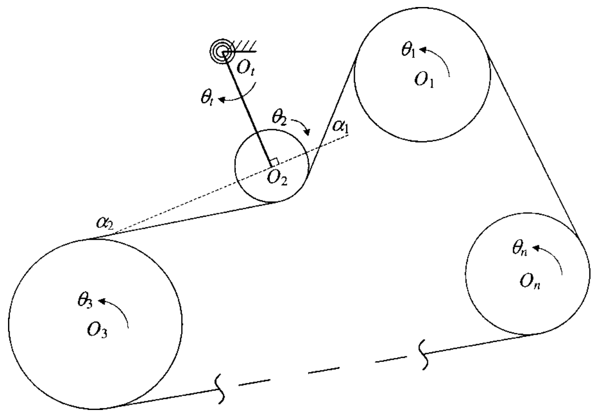

Fig. 1 A belt drive system

into studying the special relationship between the natural frequencies and the multiple excitation frequencies of a system, nonlinear modal interactions and the resultant rich nonlinear phenomena, such as combination resonances. The recent research in this area is reported in the following. Eneremadu et al. [17] discussed the vibration stability of a cylindrical shell subjected to two-frequency excitations using Floquet's theory. Subsequently, Wang [18] studied the multifrequency resonances of flexible linkages. Fung [19] considered a weakly nonlinear beam system subjected simultaneously to parametric and harmonic excitations by use of the averaging method. Steady-state responses are shown for the various cases of resonances. In Maccari's paper, [20], the transient and steady-state response of a general nonlinear oscillator to a finite number of harmonic forcing terms was analyzed by the asymptotic perturbation method. Three cases of the frequency relationship were considered. Most recently, chaotic phenomena were demonstrated in the response of a two-frequency excited mechanical oscillator by Nichols et al. [21].

In summary, the prior research on the rotational vibration of belt drive systems with dry friction tensioners only deals with single-frequency excitation using numerical solutions. To address the lack of research in this area, it is the objective of this paper to study a belt drive system with a dry friction tensioner subjected to multifrequency excitations using an analytical approach. Based on the analytical method presented by Den Hartog [22], periodic solutions are developed and derived for two kinds of steady-state responses, i.e., the nonstop (nonstick) and one-stop (stick-slip) motions, for the belt drive system. Attention is focused on studying the effect of the tensioner dry friction and the multiple excitation frequencies on dynamic behavior of the system. New and interesting results are obtained from parametric studies in numerical simulations.

2 System Model

Consider a belt drive system, which consists of a belt, a driving pulley and $n-1$ ($n \geqslant 3$) driven pulleys including a tensioner pulley supported by its tensioner arm, as shown schematically in Fig. 1. The assumptions made in the model are as follows:

1. The belt does not slip on the pulleys.
2. The belt stretches in a quasi-static manner, and the belt spans are modeled as massless axial linear springs and viscous dampers.
3. Pulleys other than the tensioner have fixed axes.
4. The pulley rotational damping is assumed to be linear, and the tensioner arm is subjected to both linear viscous damping and Coulomb dry friction at the pivot.
5. The tensioner spring is linear.
6. The motion of the driving pulley and any torque input from the driven pulleys are prescribed.
7. The geometric nonlinearities of the system are negligible.

Under the above assumptions, the equations of motion for the belt drive system can be derived as (cf. [23]),

$$\mathbf{M}\ddot{\boldsymbol{\theta}}+\mathbf{C}\dot{\boldsymbol{\theta}}+\mathbf{K}\boldsymbol{\theta}=\mathbf{T}=\mathbf{T}_{e1}+\mathbf{T}_{e2}+\mathbf{T}_f \tag{1}$$

where $\mathbf{M}$, $\mathbf{C}$, and $\mathbf{K}$ are $n\times n$ mass, damping, and stiffness matrices, respectively, and in particular, $\mathbf{M}$ is diagonal:

$$\mathbf{M}=\mathrm{diag}\{I_2,I_3,\cdots,I_n,I_t\}. \tag{2}$$

In Eq. (1), $\boldsymbol{\theta}$ is the rotational displacement vector taking the form of

$$\boldsymbol{\theta}=[\theta_2,\theta_3,\cdots,\theta_n,\theta_t]^T \tag{3}$$

with the subscripts $2,3,\ldots,n$ denoting the driven pulleys and t denoting the tensioner arm. The vector $\mathbf{T}$ represents the external excitation and contains three parts, namely, $\mathbf{T}_{e1}$, $\mathbf{T}_{e2}$, and $\mathbf{T}_f$. They are induced by the driving pulley motion, dynamic torques of the driven pulleys and the tensioner dry friction torque, respectively:

$$\mathbf{T}_{e1}=\begin{bmatrix} T_{11}\cos(\omega_1 t+\varphi_{11}) \\ T_{12}\cos(\omega_1 t+\varphi_{12}) \\ \vdots \\ T_{1(n-1)}\cos(\omega_1 t+\varphi_{1(n-1)}) \\ T_{1n}\cos(\omega_1 t+\varphi_{1n}) \end{bmatrix},$$

$$\mathbf{T}_{e2}=\begin{bmatrix} T_2\cos(\omega_2 t+\varphi_2) \\ T_3\cos(\omega_3 t+\varphi_3) \\ \vdots \\ T_n\cos(\omega_n t+\varphi_n) \\ 0 \end{bmatrix}, \quad \mathbf{T}_f=\begin{bmatrix} 0 \\ 0 \\ \vdots \\ 0 \\ T_f \end{bmatrix} \tag{4}$$

where ω_j ($j=1,2,\ldots,n$) are the excitation frequencies, T_{1j} ($j=1,2,\ldots,n$) and T_j ($j=2,3,\ldots,n$) the excitation amplitudes, φ_{1j} ($j=1,2,\ldots,n$) and φ_j ($j=2,3,\ldots,n$) the initial phase angles, respectively. T_f is the tensioner dry friction torque and is governed by the classical Coulomb law:

$$\begin{aligned} T_f&=-T_{fm} \quad \text{if } \dot{\theta}_t>0 \\ -T_{fm}\leqslant T_f&\leqslant T_{fm} \quad \text{if } \dot{\theta}_t=0 \\ T_f&=T_{fm} \quad \text{if } \dot{\theta}_t<0 \end{aligned} \tag{5}$$

in which T_{fm} is the magnitude of the friction torque when the tensioner arm is moving. It should be mentioned that the n components in $\mathbf{T}_{e1}$ are determined uniquely by the driving pulley motion:

$$\theta_1=\Theta\cos(\omega_1 t+\varphi_1) \tag{6}$$

where Θ is the amplitude and φ_1 is the initial phase angle.

In this paper, two types of steady-state vibrations are studied: nonstop motion and one-stop motion. In the nonstop motion, the tensioner arm never comes to a dead stop, while in the one-stop motion, the tensioner arm moves during $0<t<t_0$ and is at a standstill during $t_0<t<T/2$, where T is the period of the motion. It is assumed that the periodic response is symmetric in such a way that the following relationship is satisfied:

$$\mathbf{x}(t)=-\mathbf{x}(t+T/2) \tag{7}$$

where $\mathbf{x}$ is a state vector defined as

$$\mathbf{x}=[\theta_2,\theta_3,\ldots,\theta_n,\theta_t,\dot{\theta}_2,\dot{\theta}_3,\ldots,\dot{\theta}_n,\dot{\theta}_t]^T. \tag{8}$$

It is noted that the physical meaning of Eq. (7) is that for each half-cycle, the motion of the system follows the same law.

Suppose that there exists a symmetric periodic solution to Eq. (1), whose circular frequency is ω. From Eqs. (1) and (7), it is clear that

$$\mathbf{T}(t+\pi/\omega)=-\mathbf{T}(t). \tag{9}$$

Substituting Eq. (4) into the above equation, it can be derived that the following relationship between the excitation frequencies and the frequency of the motion must be satisfied, so that Eq. (9) holds true at any time t.

$$\omega_j = (2k_j + 1)\omega \quad (j = 1,2, \ldots, n; k_j = 0,1,2, \ldots) \tag{10}$$

Obviously, Eq. (10) is a necessary condition for the existence of symmetric periodic solutions.

3 Nonstop Vibration

The equation of motion (1) can be rewritten in the first order form using the state vector $\mathbf{x}$:

$$\dot{\mathbf{x}} = \mathbf{A}\mathbf{x} + \mathbf{b} \tag{11}$$

where

$$\mathbf{A} = \begin{bmatrix} \mathbf{0} & \mathbf{I} \\ -\mathbf{M}^{-1}\mathbf{K} & -\mathbf{M}^{-1}\mathbf{C} \end{bmatrix} \tag{12}$$

in which $\mathbf{I}$ is the identity matrix. $\mathbf{b}$ in Eq. (11) is defined as

$$\mathbf{b} = \begin{bmatrix} \mathbf{0} \\ \mathbf{M}^{-1}\mathbf{T} \end{bmatrix}. \tag{13}$$

Without loss of generality, assume that $\mathbf{A}$ has $2n$ different complex eigenvalues λ_j, $j = 1,2, \ldots, 2n$, which correspond to $2n$ linearly independent complex eigenvectors $\tilde{\mathbf{x}}_j$, $j = 1,2, \ldots, 2n$. The general solution of the homogeneous form of Eq. (11) can be expressed in terms of the eigenvalues and eigenvectors:

$$\mathbf{x}(t) = \mathbf{X}e^{\Lambda t}\mathbf{c} \tag{14}$$

where

$$\mathbf{X} = [\tilde{\mathbf{x}}_1 \ \ \tilde{\mathbf{x}}_2 \cdots \tilde{\mathbf{x}}_{2n}] \tag{15}$$

$$e^{\Lambda t} = \mathrm{diag}\{e^{\lambda_1 t}, e^{\lambda_2 t}, \cdots, e^{\lambda_{2n} t}\} \tag{16}$$

and $\mathbf{c}$ is the vector of complex integral constants defined as

$$\mathbf{c} = [c_1, c_2, \cdots, c_{2n}]^T. \tag{17}$$

Since it is assumed that the system motion follows the same law for each half-cycle, only the motion in the first half-period, i.e., $0 \leq t < \pi/\omega$, will be considered from now on. To tackle the discontinuity of the dry friction toque on the tensioner arm, we make the initial phase angle φ_1 of the driving pulley motion as an unknown while keeping the velocity of the tensioner arm fixed in the following manner:

$$\dot{\theta}_t = 0, \quad t = 0 \tag{18a}$$

$$\dot{\theta}_t < 0, \quad 0 < t < \pi/\omega \tag{18b}$$

Correspondingly, during the first half-period, the tensioner dry friction torque keeps the same sign:

$$T_f = T_{fm}. \tag{19}$$

Substituting Eqs. (2) and (4) into Eq. (13) gives

$$\mathbf{b} = \sum_{j=1}^{n} (\mathbf{q}_j e^{i\omega_j t} + \overline{\mathbf{q}}_j e^{-i\omega_j t}) + \mathbf{b}_0 \tag{20}$$

where

$$\mathbf{b}_0 = [0, \cdots, 0, T_{fm}/I_t]^T \tag{21}$$

$$\mathbf{q}_j = \frac{1}{2}(\mathbf{q}_{j1} - i\mathbf{q}_{j2}), \quad j = 1,2, \cdots, n \tag{22}$$

in which $\mathbf{q}_{j1}$ and $\mathbf{q}_{j2}$ can be transformed into the following submatrix form:

$$\mathbf{q}_{j1} = \begin{bmatrix} \mathbf{0} \\ \mathbf{q}_{j1}^* \end{bmatrix}, \quad \mathbf{q}_{j2} = \begin{bmatrix} \mathbf{0} \\ \mathbf{q}_{j2}^* \end{bmatrix}, \quad j = 1,2, \cdots, n \tag{23}$$

where

$$\mathbf{q}_{11}^* = \begin{bmatrix} T_{11}\cos\varphi_{11}/I_2 \\ T_{12}\cos\varphi_{12}/I_3 \\ \vdots \\ T_{1n}\cos\varphi_{1n}/I_t \end{bmatrix}, \quad \mathbf{q}_{12}^* = \begin{bmatrix} -T_{11}\sin\varphi_{11}/I_2 \\ -T_{12}\sin\varphi_{12}/I_3 \\ \vdots \\ -T_{1n}\sin\varphi_{1n}/I_t \end{bmatrix},$$

$$\mathbf{q}_{21}^* = \begin{bmatrix} T_2\cos\varphi_2/I_2 \\ 0 \\ \vdots \\ 0 \end{bmatrix}, \quad \mathbf{q}_{22}^* = \begin{bmatrix} -T_2\sin\varphi_2/I_2 \\ 0 \\ \vdots \\ 0 \end{bmatrix},$$

$$\mathbf{q}_{31}^* = \begin{bmatrix} 0 \\ T_3\cos\varphi_3/I_3 \\ 0 \\ \vdots \\ 0 \end{bmatrix}, \quad \mathbf{q}_{32}^* = \begin{bmatrix} 0 \\ -T_3\sin\varphi_3/I_3 \\ 0 \\ \vdots \\ 0 \end{bmatrix}, \ldots, \tag{24}$$

$$\mathbf{q}_{n1}^* = \begin{bmatrix} 0 \\ \vdots \\ 0 \\ T_n\cos\varphi_n/I_n \\ 0 \end{bmatrix}, \quad \mathbf{q}_{n2}^* = \begin{bmatrix} 0 \\ \vdots \\ 0 \\ -T_n\sin\varphi_n/I_n \\ 0 \end{bmatrix}.$$

It should be pointed out that throughout this paper, the symbols "i" and "$\overline{\ \ }$", as in Eq. (20), denote the imaginary unit and the complex conjugate, respectively.

The particular solution to Eq. (11) is derived as

$$\mathbf{x}^*(t) = \sum_{j=1}^{n} (\boldsymbol{\kappa}_j e^{i\omega_j t} + \overline{\boldsymbol{\kappa}}_j e^{-i\omega_j t}) - \mathbf{A}^{-1}\mathbf{b}_0 \tag{25}$$

where

$$\boldsymbol{\kappa}_j = [i\omega_j\mathbf{I} - \mathbf{A}]^{-1}\mathbf{q}_j \quad (j = 1,2, \cdots, n). \tag{26}$$

The sum of Eq. (14) and Eq. (25) yields the general solution to the nonhomogeneous differential Eq. (11):

$$\mathbf{x}(t) = \mathbf{X}e^{\Lambda t}\mathbf{c} + \sum_{j=1}^{n} (\boldsymbol{\kappa}_j e^{i\omega_j t} + \overline{\boldsymbol{\kappa}}_j e^{-i\omega_j t}) - \mathbf{A}^{-1}\mathbf{b}_0. \tag{27}$$

Applying Eq. (10), it follows from Eq. (27) that

$$\mathbf{x}(0) = \mathbf{X}\mathbf{c} + \sum_{j=1}^{n} (\boldsymbol{\kappa}_j + \overline{\boldsymbol{\kappa}}_j) - \mathbf{A}^{-1}\mathbf{b}_0 \tag{28}$$

$$\mathbf{x}(\pi/\omega) = \mathbf{X}e^{\Lambda\pi/\omega}\mathbf{c} - \sum_{j=1}^{n} (\boldsymbol{\kappa}_j + \overline{\boldsymbol{\kappa}}_j) - \mathbf{A}^{-1}\mathbf{b}_0. \tag{29}$$

Replacing t by 0 in Eq. (7) gives

$$\mathbf{x}(\pi/\omega) = -\mathbf{x}(0) \tag{30}$$

which, together with Eqs. (28) and (29), determines the complex integral constants

$$\mathbf{c} = 2[\mathbf{I} + e^{\Lambda\pi/\omega}]^{-1}\mathbf{X}^{-1}\mathbf{A}^{-1}\mathbf{b}_0. \tag{31}$$

So far the solution (27) still contains implicitly an unknown, namely, φ_1. By employing Eq. (18a), φ_1 can be solved numerically from the algebraic equation below:

$$\mathbf{U}\cdot\mathbf{x}(0) = 0 \tag{32}$$

where $\mathbf{U}$ is a $1 \times 2n$ matrix

$$\mathbf{U} = [0, \cdots, 0, 1]. \tag{33}$$

Finally, the validity of the solution should be checked, since it has been derived under the assumption, Eq. (18b). Consequently, the solution is valid only if the following inequality holds:

$$\mathbf{U}\cdot\mathbf{x}(t) < 0 \quad (0 < t < \pi/\omega). \tag{34}$$

Table 1 System parameters

PULLEYS				
Pulley No. j	Radius r_j (m)	Moment of Inertia I_j (kg·m^2)	Damping Constant C_{jp} (N·m·s/rad)	Excitation
1	1.1	N/A	N/A	$\theta_1=\theta_0\cos(\omega_1 t+\varphi_1)$, $\theta_0=0.1$ rad
2	1.0	5.0	0.0003	N/A
3	1.2	10.0	0.05	$T_3\cos(\omega_3 t+\varphi_3)$, $T_3=0.4$ N·m, $\varphi_3=0.5$ rad

BELT		
Belt Span No. j	Damping Constant C_{jb} (N·s/m)	Spring Stiffness K_j (N/m)
1, between pulleys No. 1 and No. 2	0.10	0.4
2, between pulleys No. 2 and No. 3	0.12	0.5
3, between pulleys No. 3 and No. 1	0.20	0.4
$\cos\alpha_1=-0.89$		$\cos\alpha_2=0.05$

TENSIONER ARM				
Length r_t (m)	Moment of Inertia of Arm/Pulley I_t (kg·m^2)	Damping Constant C_t (N·m·s/rad)	Spring Stiffness K_t (N·m/rad)	θ_{t0} (deg)
1.0	6.0	0.23	0.60	90

4 One-Stop Vibration

One-stop motion may take place under larger tensioner dry friction torque and certain excitation frequencies. It is assumed that the tensioner arm is in motion during the time interval $0<t<t_0$, and is at rest during $t_0<t<\pi/\omega$. Consequently, the equation of motion for the one-stop vibration remains the same as Eq. (11) while the assumption on the velocity of the tensioner arm changes to

$$\begin{cases} \dot{\theta}_t=0, & t=0 \\ \dot{\theta}_t<0, & 0<t<t_0 \\ \dot{\theta}_t=0, & t_0\leqslant t<\pi/\omega \end{cases}. \tag{35}$$

Clearly, the form of the general solution for the nonstop motion given in Eq. (27) still holds true for the one-stop motion during the interval $0\leqslant t<t_0$, although t_0 is a new unknown variable.

Introducing a new system state vector

$$\mathbf{y}=[\theta_2,\cdots,\theta_n,\dot{\theta}_2,\cdots,\dot{\theta}_n,\theta_t,\dot{\theta}_t]^T=\mathbf{S}\mathbf{x} \tag{36}$$

where

$$\mathbf{S}=\begin{bmatrix} \mathbf{I}_{(n-1)\times(n-1)} & \mathbf{0}_{(n-1)\times 1} & \mathbf{0}_{(n-1)\times(n-1)} & \mathbf{0}_{(n-1)\times 1} \\ \mathbf{0}_{(n-1)\times(n-1)} & \mathbf{0}_{(n-1)\times 1} & \mathbf{I}_{(n-1)\times(n-1)} & \mathbf{0}_{(n-1)\times 1} \\ \mathbf{0}_{1\times(n-1)} & 1 & \mathbf{0}_{1\times(n-1)} & 0 \\ \mathbf{0}_{1\times(n-1)} & 0 & \mathbf{0}_{1\times(n-1)} & 1 \end{bmatrix}, \tag{37}$$

the equation of motion (11) can be transformed to

$$\dot{\mathbf{y}}=\tilde{\mathbf{A}}\mathbf{y}+\tilde{\mathbf{b}} \tag{38}$$

in which

$$\tilde{\mathbf{A}}=\mathbf{SAS}^{-1}=\begin{bmatrix} (\tilde{\mathbf{A}}_{11})_{(2n-2)\times(2n-2)} & (\tilde{\mathbf{A}}_{12})_{(2n-2)\times 2} \\ (\tilde{\mathbf{A}}_{21})_{2\times(2n-2)} & (\tilde{\mathbf{A}}_{22})_{2\times 2} \end{bmatrix} \tag{39}$$

$$\tilde{\mathbf{b}}=\mathbf{Sb}=\begin{bmatrix} (\tilde{\mathbf{b}}_1)_{2n-2} \\ (\tilde{\mathbf{b}}_2)_2 \end{bmatrix}. \tag{40}$$

During $t_0<t<\pi/\omega$, the displacement and velocity of the tensioner arm are constant, and therefore it is convenient to define a new vector describing the state of the pulleys only:

$$\mathbf{u}=[\theta_2,\theta_3,\cdots,\theta_n,\dot{\theta}_2,\dot{\theta}_3,\cdots,\dot{\theta}_n]^T. \tag{41}$$

Separating the above vector from Eq. (38) results in the following equation of motion:

$$\dot{\mathbf{u}}=\tilde{\mathbf{A}}_{11}\mathbf{u}+\tilde{\mathbf{A}}_{12}\mathbf{v}+\tilde{\mathbf{b}}_1, \quad t_0<t<\pi/\omega \tag{42}$$

where $\mathbf{v}$ is the state vector for the tensioner arm during the interval $t_0<t<\pi/\omega$

$$\mathbf{v}=[\theta_t(t_0),0]^T. \tag{43}$$

The general solution to Eq. (42) can be obtained as

$$\mathbf{u}(t)=\tilde{\mathbf{X}}e^{\tilde{\Lambda}t}\tilde{\mathbf{c}}+\sum_{j=1}^{n}(\boldsymbol{\kappa}_j^* e^{i\omega_j t}+\overline{\boldsymbol{\kappa}}_j^* e^{-i\omega_j t})-\tilde{\mathbf{A}}_{11}^{-1}\tilde{\mathbf{A}}_{12}\mathbf{v} \tag{44}$$

where $\tilde{\mathbf{X}}$ is a $(2n-2)\times(2n-2)$ modal matrix whose columns contain the complex eigenvectors of $\tilde{\mathbf{A}}_{11}$, and $e^{\tilde{\Lambda}t}$ and $\tilde{\mathbf{c}}$ are as follows:

$$e^{\tilde{\Lambda}t}=\mathrm{diag}\{e^{\tilde{\lambda}_1 t},e^{\tilde{\lambda}_2 t},\cdots,e^{\tilde{\lambda}_{2n-2}t}\} \tag{45}$$

$$\tilde{\mathbf{c}}=[\tilde{c}_1,\tilde{c}_2,\cdots,\tilde{c}_{2n-2}]^T \tag{46}$$

in which $\tilde{\lambda}_j$ and $\tilde{c}_j$ $(j=1,2,\ldots,2n-2)$ are the complex eigenvalues of $\tilde{\mathbf{A}}_{11}$ and complex integral constants, respectively. $\boldsymbol{\kappa}_j^*$ in Eq. (44) is defined as

$$\boldsymbol{\kappa}_j^*=[i\omega_j\mathbf{I}-\tilde{\mathbf{A}}_{11}]^{-1}\mathbf{q}_j^* \quad (j=1,2,\cdots,n) \tag{47}$$

where

$$\mathbf{q}_j^*=\mathbf{RSq}_j \quad (j=1,2,\cdots,n) \tag{48}$$

in which

$$\mathbf{R}=[\mathbf{I}_{(2n-2)\times(2n-2)}\ \ \mathbf{0}_{(2n-2)\times 2}]. \tag{49}$$

Table 2 Natural frequencies

$\omega_{n1}=0.522\omega_0$, $\omega_{n2}=0.881\omega_0$, $\omega_{n3}=1.229\omega_0$,
$\omega_0=\sqrt{\mathbf{K}[0][0]/\mathbf{M}[0][0]}=0.424$ rad/s

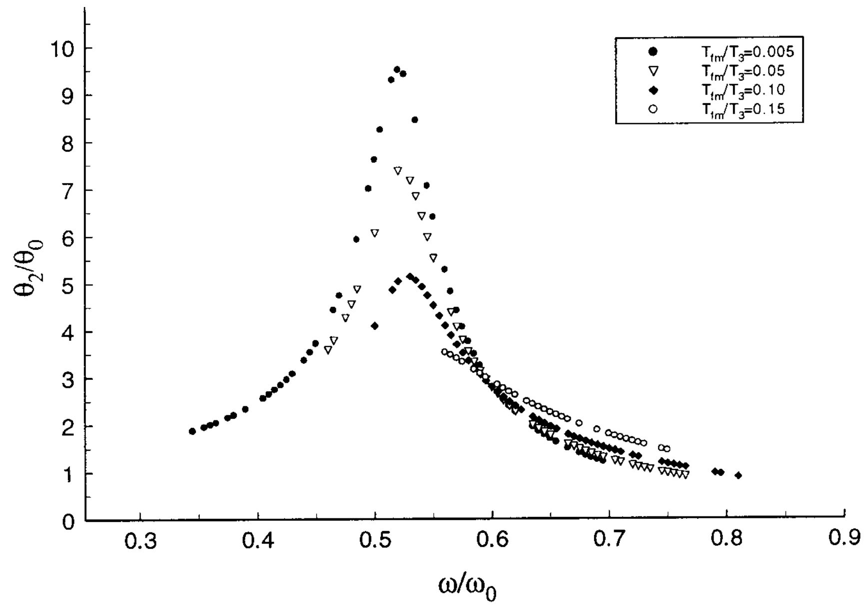

(a) Tensioner pulley

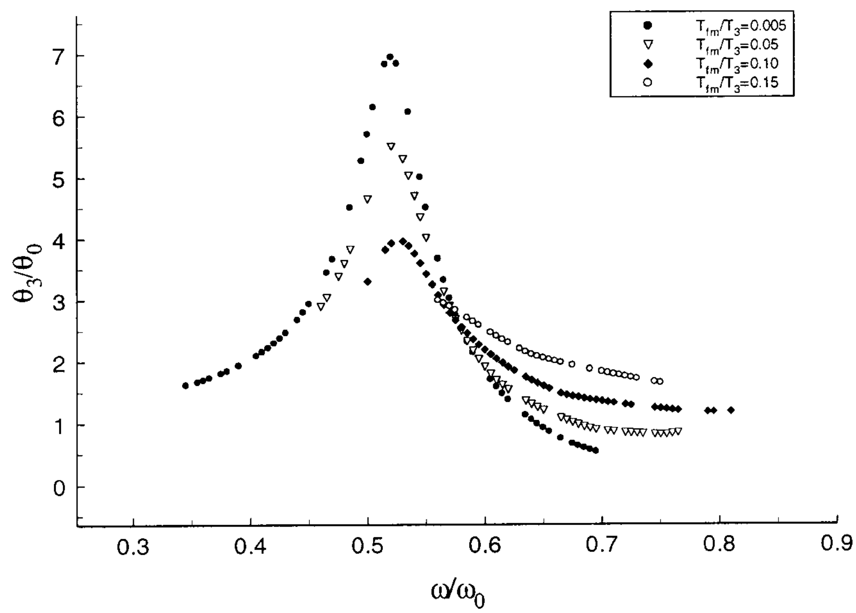

(b) Driven pulley

Fig. 2 Amplitude responses with dry friction as parameter in nonstop vibration

The solutions for the one-stop vibration during the intervals $0 < t < t_0$ and $t_0 < t < \pi/\omega$ have been derived as in Eqs. (27) and (44), respectively, nevertheless, there are still $4n$ unknown quantities, namely, $\mathbf{c}$, $\tilde{\mathbf{c}}$, t_0, and φ_1, to be determined. The following boundary conditions are used to solve these $4n$ unknowns.

$$\dot{\theta}_t(0) = 0 \tag{50.1}$$

$$\dot{\theta}_t(t_0) = 0 \tag{50.2}$$

$$\ddot{\theta}_t(0) = 0 \tag{50.3}$$

$$\theta_t(0) = -\theta_t(t_0) \tag{50.4}$$

$$\mathbf{RSx}(t_0) = \mathbf{u}(t_0) \tag{50.5}$$

$$\mathbf{RSx}(0) = -\mathbf{u}(\pi/\omega) \tag{50.6}$$

Setting $t=0$ in Eq. (38), using the conditions (50.1) and (50.3), and redividing the matrices lead to

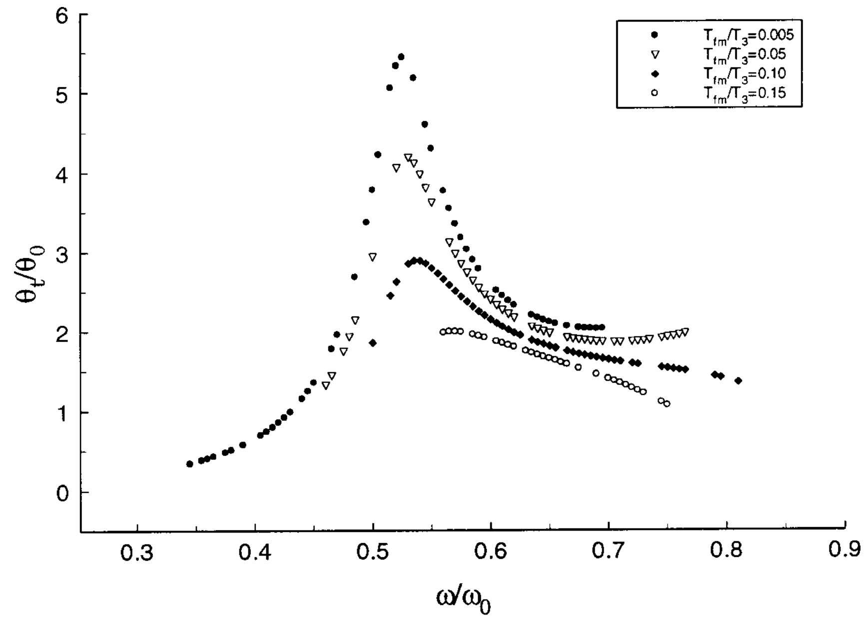

(*c*) Tensioner arm

Fig. 2 (***continued***)

$$\begin{bmatrix} \dot{\mathbf{u}}(0) \\ 0 \\ 0 \end{bmatrix} = \begin{bmatrix} (\tilde{\mathbf{A}}^*_{11})_{(2n-2)\times(2n-2)} & (\tilde{\mathbf{A}}^*_{12})_{(2n-2)\times 1} & (\tilde{\mathbf{A}}^*_{13})_{(2n-2)\times 1} \\ (\tilde{\mathbf{A}}^*_{21})_{1\times(2n-2)} & \tilde{A}^*_{22} & \tilde{A}^*_{23} \\ (\tilde{\mathbf{A}}^*_{31})_{1\times(2n-2)} & \tilde{A}^*_{32} & \tilde{A}^*_{33} \end{bmatrix} \times \begin{bmatrix} \mathbf{u}(0) \\ \theta_t(0) \\ 0 \end{bmatrix} + \begin{bmatrix} \tilde{\mathbf{b}}^*_1(0) \\ \tilde{b}^*_2(0) \\ \tilde{b}^*_3(0) \end{bmatrix} \quad (51)$$

from which $\theta_t(0)$ is derived as

$$\theta_t(0) = \mathbf{W}\mathbf{u}(0) + d \quad (52)$$

where

$$\mathbf{W} = -\tilde{A}^{*-1}_{22}\tilde{\mathbf{A}}^*_{21}, \quad d = -\tilde{A}^{*-1}_{22}\tilde{b}^*_2(0) \quad \text{if } \tilde{A}^*_{22} \neq 0 \quad (53)$$

or

$$\mathbf{W} = -\tilde{A}^{*-1}_{32}\tilde{\mathbf{A}}^*_{31}, \quad d = -\tilde{A}^{*-1}_{32}\tilde{b}^*_3(0) \quad \text{if } \tilde{A}^*_{32} \neq 0. \quad (54)$$

Letting $t=0$ and substituting Eq. (28) into Eq. (36), we have

$$\mathbf{y}(0) = \mathbf{S}\mathbf{x}(0) = \mathbf{S}\mathbf{X}\mathbf{c} + \mathbf{S}\left[\sum_{j=1}^{n} (\boldsymbol{\kappa}_j + \overline{\boldsymbol{\kappa}}_j) - \mathbf{A}^{-1}\mathbf{b}_0\right] \quad (55)$$

which gives $\mathbf{c}$ as a function of $\mathbf{u}(0)$ and the implicit φ_1

$$\mathbf{c} = \mathbf{X}^{-1}\mathbf{S}^{-1}\begin{bmatrix} \mathbf{u}(0) \\ \mathbf{W}\mathbf{u}(0)+d \\ 0 \end{bmatrix} - \mathbf{X}^{-1}\left[\sum_{j=1}^{n} (\boldsymbol{\kappa}_j + \overline{\boldsymbol{\kappa}}_j) - \mathbf{A}^{-1}\mathbf{b}_0\right]. \quad (56)$$

From Eq. (50.6), $\tilde{\mathbf{c}}$ can also be expressed in terms of $\mathbf{u}(0)$ and φ_1

$$\tilde{\mathbf{c}} = [\tilde{\mathbf{X}}e^{\tilde{\Lambda}\pi/\omega}]^{-1}\left\{ -\mathbf{u}(0) - \tilde{\mathbf{A}}^{-1}_{11}\tilde{\mathbf{A}}_{12}\begin{bmatrix} \mathbf{W}\mathbf{u}(0)+d \\ 0 \end{bmatrix} + \sum_{j=1}^{n} (\boldsymbol{\kappa}^*_j + \overline{\boldsymbol{\kappa}}^*_j) \right\}. \quad (57)$$

With $\mathbf{c}$ and $\tilde{\mathbf{c}}$ solved as functions of $\mathbf{u}(0)$ and φ_1, Eqs. (50.2), (50.4), and (50.5) can be turned into a set of nonlinear algebraic equations in $\mathbf{u}(0)$, φ_1, and t_0. Since these equations are transcendental and an explicit solution is impossible, a numerical procedure such as quasi-Newton method is needed to solve for $\mathbf{u}(0)$, φ_1 and t_0. Once they are obtained via a numerical method, $\theta_t(0)$, $\mathbf{c}$ and $\tilde{\mathbf{c}}$ can be derived from Eqs. (52), (56), and (57), respectively. Finally, the solutions for the one-stop motion during $0<t<t_0$ and $t_0<t<\pi/\omega$ are determined using Eqs. (27) and (44).

Remember that the above solution is derived under the assumption, Eq. (35). Therefore, it is necessary to examine whether the solution satisfies the assumption. Since a half-cycle in the one-stop motion is made up of two distinct time intervals, a condition to check the validity of the solution for each interval should be provided. During the period $0<t<t_0$ when the motion of the tensioner arm is continuous, the condition is

$$\dot{\theta}_t < 0, \quad 0<t<t_0. \quad (58)$$

During the period $t_0<t<\pi/\omega$ when the tensioner arm is at rest, the condition is that the absolute value of all external torques acting on the tensioner arm must be smaller than or equal to the dry friction torque, i.e.,

$$|\mathbf{W}_1\mathbf{Z}_1 + \mathbf{W}_2\mathbf{Z}_2 + K_{nn}\theta_t(t_0) - T_{1n}\cos(\omega_1 t + \varphi_{1n})| \leq T_{fm}, \quad t_0<t<\pi/\omega \quad (59)$$

where K_{nn} is the rightmost element at the bottom row of $\mathbf{K}$ in Eq. (1) and

$$\mathbf{W}_1 = [C_{n1}, C_{n2}, \cdots, C_{n(n-1)}] \quad (60)$$

$$\mathbf{Z}_1 = [\dot{\theta}_2, \dot{\theta}_3, \cdots, \dot{\theta}_n]^T \quad (61)$$

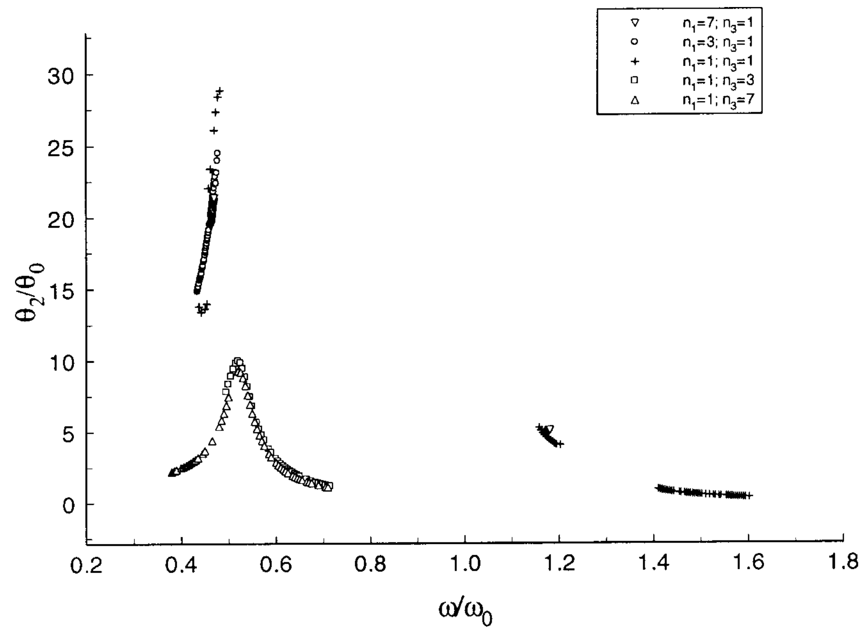

(a) Tensioner pulley

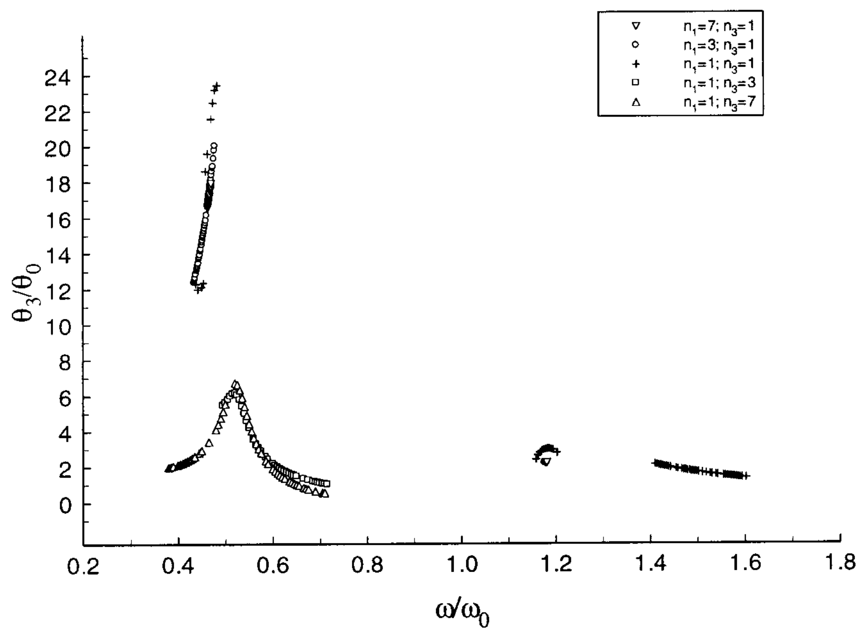

(b) Driven pulley

Fig. 3 Amplitude responses with excitation frequencies as parameter in nonstop vibration

$$\mathbf{W}_2=[K_{n1},K_{n2},\cdots,K_{n(n-1)}] \tag{62}$$

$$\mathbf{Z}_2=[\theta_2,\theta_3,\cdots,\theta_n]^T \tag{63}$$

in which C_{nj} and K_{nj}, $j=1,2,\ldots,n-1$ are elements of matrices **C** and **K** in Eq. (1).

5 Numerical Example

In this section, an example belt drive system is introduced and evaluated to illustrate the capability of the above solution method. Consider a prototypical system consisting of a driving pulley, a driven pulley and a dynamic tensioner, which is a special case $(n=3)$ of the general model shown in Fig. 1. The system is sub-

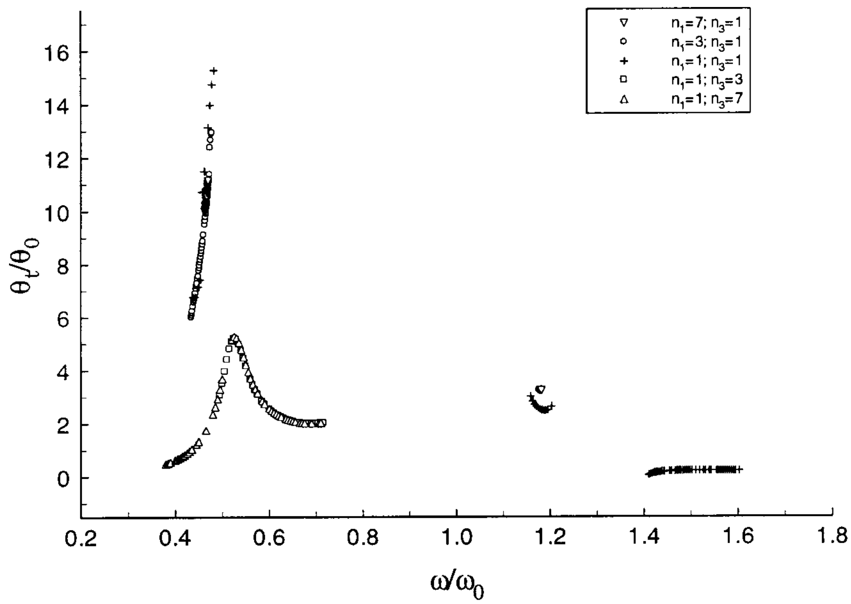

(*c*) Tensioner arm

Fig. 3 (***continued***)

jected to excitations from the driving pulley motion and the dynamic torque on the driven pulley. The equations of motion for the system can be obtained as

$$\mathbf{M}\ddot{\boldsymbol{\theta}}+\mathbf{C}\dot{\boldsymbol{\theta}}+\mathbf{K}\boldsymbol{\theta}=\mathbf{T} \tag{64}$$

where

$$\boldsymbol{\theta}=[\theta_2,\theta_3,\theta_t]^T \tag{65}$$

$$\mathbf{M}=\begin{bmatrix} I_2 & 0 & 0 \\ 0 & I_3 & 0 \\ 0 & 0 & I_t \end{bmatrix} \tag{66}$$

$$\mathbf{C}=\begin{bmatrix} r_2^2(C_{1b}+C_{2b})+C_{2p} & -C_{2b}r_2r_3 & r_2r_t(C_{1b}\cos\alpha_1-C_{2b}\cos\alpha_2) \\ -C_{2b}r_2r_3 & r_3^2(C_{2b}+C_{3b})+C_{3p} & C_{2b}r_3r_t\cos\alpha_2 \\ r_2r_t(C_{1b}\cos\alpha_1-C_{2b}\cos\alpha_2) & C_{2b}r_3r_t\cos\alpha_2 & r_t^2(C_{1b}\cos^2\alpha_1+C_{2b}\cos^2\alpha_2)+C_t \end{bmatrix} \tag{67}$$

$$\mathbf{K}=\begin{bmatrix} r_2^2(K_1+K_2) & -K_2r_2r_3 & r_2r_t(K_1\cos\alpha_1-K_2\cos\alpha_2) \\ -K_2r_2r_3 & r_3^2(K_2+K_3) & K_2r_3r_t\cos\alpha_2 \\ r_2r_t(K_1\cos\alpha_1-K_2\cos\alpha_2) & K_2r_3r_t\cos\alpha_2 & r_t^2(K_1\cos^2\alpha_1+K_2\cos^2\alpha_2)+K_t+Q_0 \end{bmatrix} \tag{68}$$

$$\mathbf{T}=\begin{bmatrix} T_{11}\cos(\omega_1t+\varphi_{11}) \\ T_{12}\cos(\omega_1t+\varphi_{12}) \\ T_{13}\cos(\omega_1t+\varphi_{13}) \end{bmatrix}+\begin{bmatrix} 0 \\ T_3\cos(\omega_3t+\varphi_3) \\ 0 \end{bmatrix}+\begin{bmatrix} 0 \\ 0 \\ T_f \end{bmatrix}. \tag{69}$$

Q_0 in Eq. (68) is defined as

$$Q_0=m_{\text{eff}}\,gL_{\text{eff}}\cos\theta_{t0} \tag{70}$$

in which m_{eff} represents the total mass of the tensioner pulley and arm, L_{eff} represents the distance between the mass center of the tensioner pulley/arm and the arm pivot, and θ_{t0} denotes the initial inclination angle of the tensioner arm with respect to the direction of gravity. In Eq. (69), T_f is the same as defined in Eq. (5) and

$$T_{11}=r_1r_2\theta_0\sqrt{K_1^2+\omega_1^2C_{1b}^2} \tag{71}$$

$$T_{12}=r_1r_3\theta_0\sqrt{K_3^2+\omega_1^2C_{3b}^2} \tag{72}$$

$$T_{13}=r_1r_t\theta_0\cos\alpha_1\sqrt{K_1^2+\omega_1^2C_{1b}^2} \tag{73}$$

$$\varphi_{11}=\varphi_1+\tan^{-1}(C_{1b}\omega_1/K_1) \tag{74}$$

$$\varphi_{12}=\varphi_1+\tan^{-1}(C_{3b}\omega_1/K_3) \tag{75}$$

$$\varphi_{13}=\varphi_1+\tan^{-1}(C_{1b}\omega_1/K_1). \tag{76}$$

The basic system parameters used are listed in Table 1, and the natural frequencies of the system are given in Table 2.

The periodic response for both nonstop and one-stop vibrations is computed, with emphasis laid on studying the influence of the tensioner dry friction and the excitation frequencies on the response. Two parameters are used in the computation: the ratio between the Coulomb friction torque and the amplitude of the external torque, i.e., T_{fm}/T_3, and the ratio between the excitation frequencies and the frequency of the motion, namely, n_1 (ω_1/ω) and n_3 (ω_3/ω). The following plots show the frequency responses of the amplitude ratio for both nonstop and one-stop vibrations as well as the frequency response of $2t_0/T$ (T denotes the period) for the one-stop vibration, under different values of the parameters.

The plots for the nonstop motion are shown in Figs. 2 and 3, where the default parameter values are as follows (since only one parameter is changed at a time, the other parameter takes the default value):

$$T_{fm}/T_3 = 0.01 \qquad (77)$$
$$n_1 = 1, \quad n_3 = 11.$$

Figures 2(a)–2(c) show the influence of the tensioner dry friction on the amplitude responses of the tensioner pulley, the driven pulley and the tensioner arm, respectively, with the parameter T_{fm}/T_3 ranging from 0.005 to 0.15. Apparently, resonance occurs at the first natural frequency of the system. In addition, it is observed that there exists a frequency value at which the tensioner dry friction exerts no influence on the vibration amplitude, for the tensioner pulley and the driven pulley, respectively. Furthermore, the amplitude decreases as the dry friction torque increases before that critical frequency, while the effect of the dry friction torque is

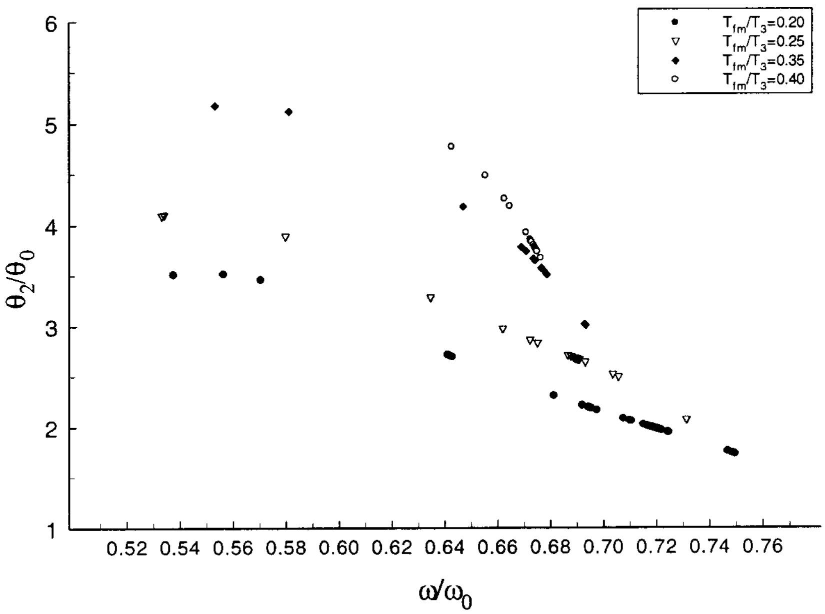

(a) Tensioner pulley

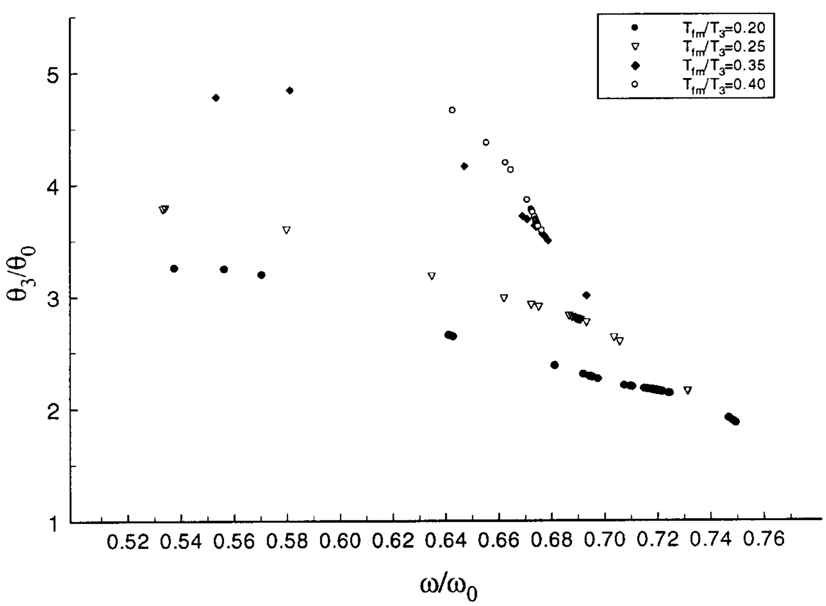

(b) Driven pulley

Fig. 4 Amplitude responses with dry friction as parameter in one-stop vibration

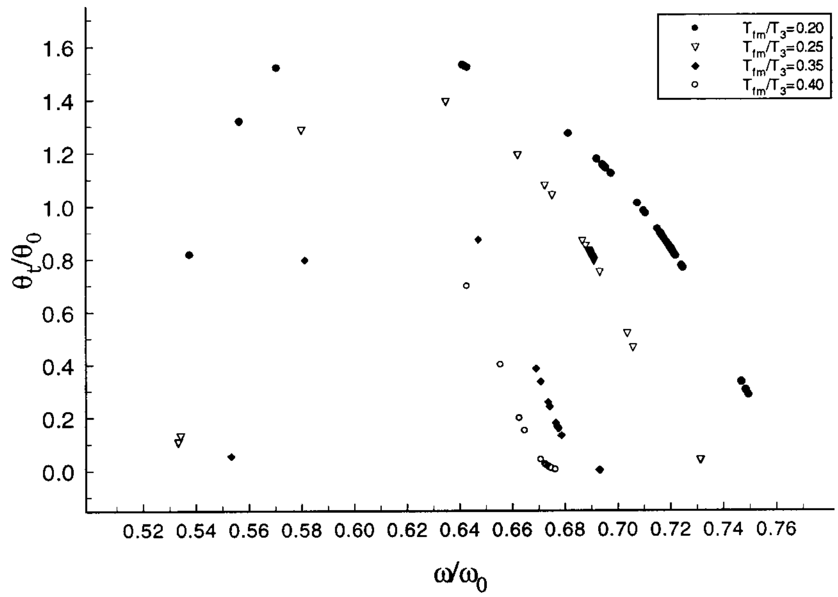

(*c*) Tensioner arm

Fig. 4 (*continued*)

just the opposite after that frequency. In comparison, for the tensioner arm, no such critical frequency exists and the vibration amplitude decreases along with the increase of the tensioner dry friction for all frequency values. It is also found that occurrence of such periodic motion is discontinuous in the frequency domain, which implies the existence of other types of steady motions for the system.

In Figs. 3(*a*)–3(*c*), the effect of different excitation frequencies on the amplitude response is demonstrated. The parameters n_1 and n_3 vary from 1 to 7. From these figures, one can distinguish two types of behavior and thereby categorize the excitation frequencies into two groups. One group corresponds to the case of $n_1 \geqslant n_3$, where the excitation frequency ω_1 is greater than or equal to ω_3, while the other group corresponds to the opposite case, i.e., $n_1 < n_3$. It is clearly seen that the vibration amplitudes for the case of $n_1 \geqslant n_3$ are much larger than those for the case of $n_1 < n_3$. Within each group, however, the amplitude difference between different cases of n_1 and n_3 is very small in comparison with the group difference. Besides, it is displayed that the frequency range where the periodic motion can happen for the group of $n_1 \geqslant n_3$ is noticeably wider than that for the other group.

Similar to the plots for the nonstop motion, Figs. 4–7 show the responses for the one-stop motion, but with a different default parameter value for the dry friction torque

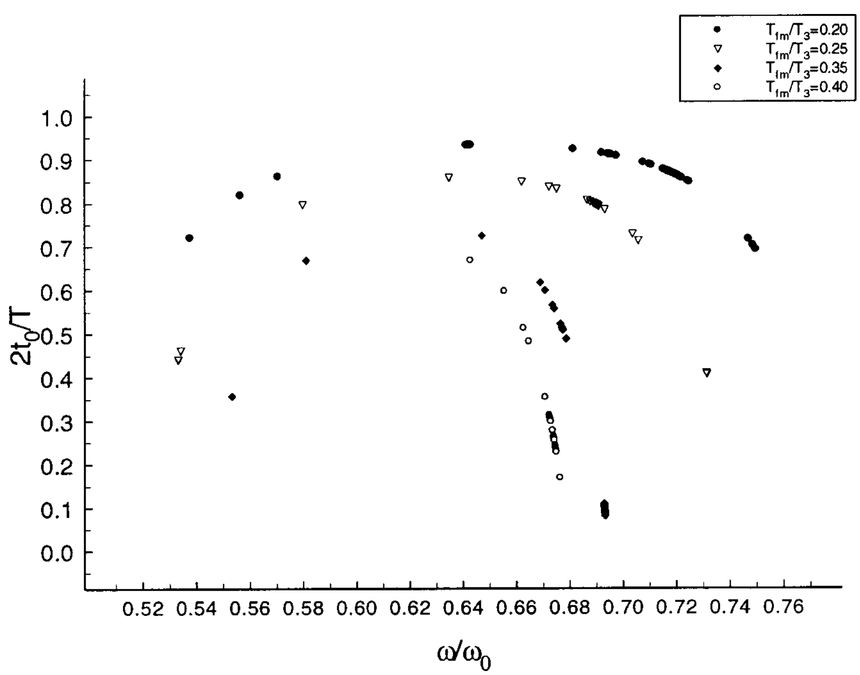

Fig. 5 t_0 responses with dry friction as parameter in one-stop vibration

$$T_{fm}/T_3 = 0.20. \quad (78)$$

Figures 4(a)–4(c) illustrate amplitude responses with T_{fm}/T_3 as parameter, whose values fall into the scope [0.20,0.40]. It is shown that the response pattern for the tensioner arm is quite different from those for the tensioner pulley and the driven pulley. Obviously, the response amplitude of the tensioner arm is much smaller than those of the tensioner pulley and the driven pulley. More interestingly, the influence of the dry friction torque on the response amplitude of the tensioner arm is opposite to that on the amplitudes of the tensioner pulley and the driven pulley. For the tensioner arm the dry friction torque reduces the response amplitude, while for the tensioner pulley and the driven pulley it increases the amplitude. Compared with the nonstop case, the dry friction effect is the same for the tensioner arm. For the tensioner pulley and the driven pulley, however, it is opposite before the critical frequency and the same after the critical frequency, respectively. Another phenomenon worth mention is that the dots in Figs. 4(a)–4(c) are sparsely distributed over the frequency do-

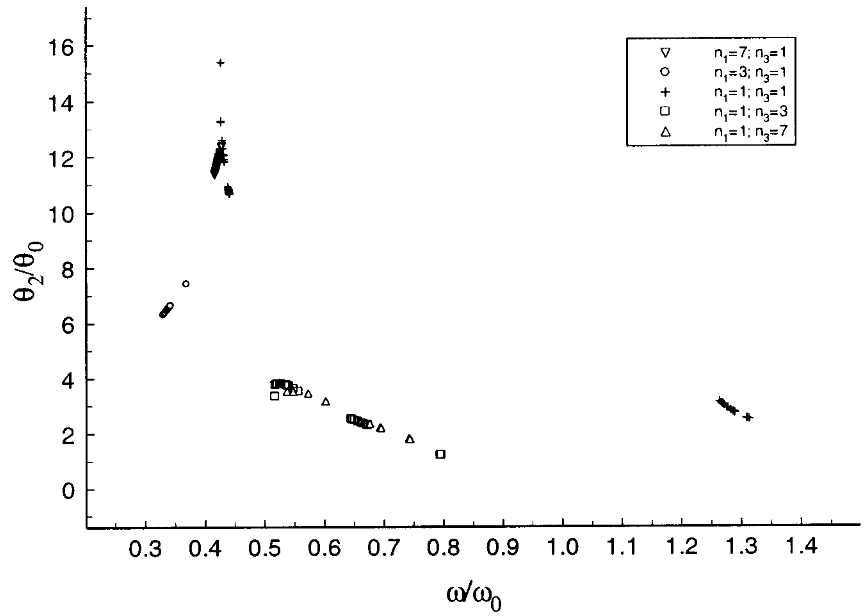

(a) Tensioner pulley

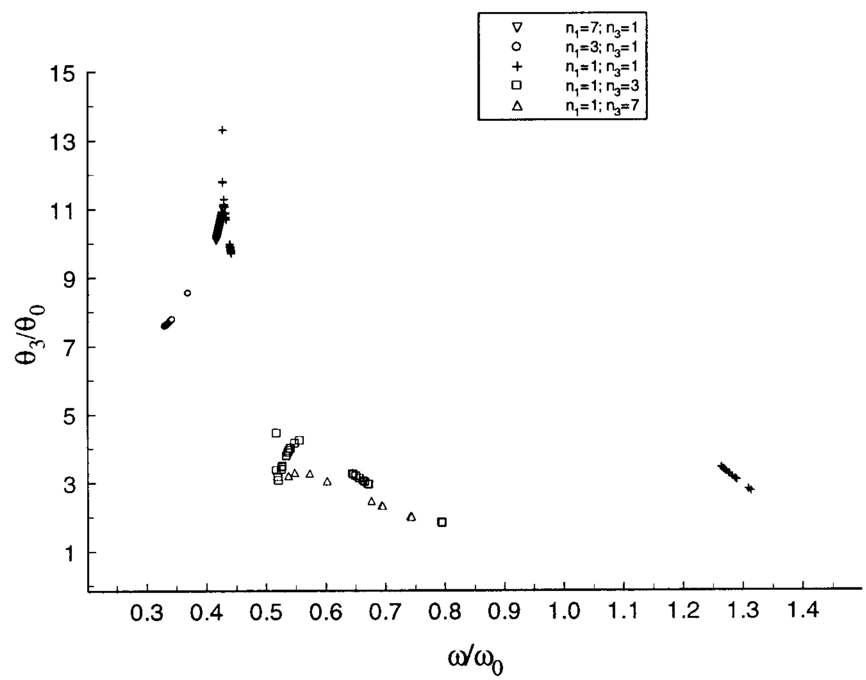

(b) Driven pulley

Fig. 6 Amplitude responses with excitation frequencies as parameter in one-stop vibration

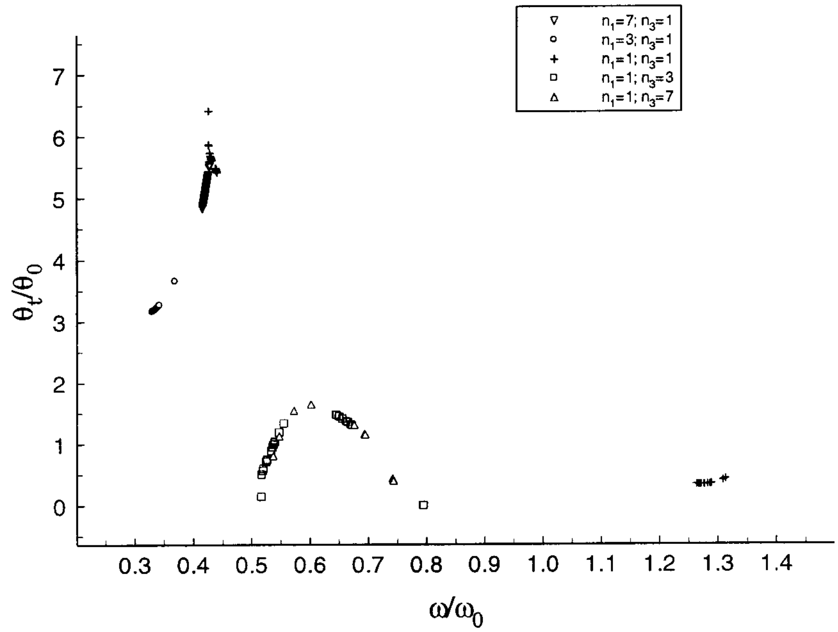

(*c*) Tensioner arm

Fig. 6 (***continued***)

main, which indicates the relatively low possibility of occurrence of such one-stop motion with respect to other possible types of motions for the system.

Figure 5 shows $2t_0/T$ versus ω/ω_0 with the same parameter values as in Fig. 4. Physically, $2t_0/T$ means the percentage of the slip mode of the tensioner arm in the one-stop vibration. Clearly, one can see that the larger the tension dry friction, the lower percentage the slip mode of the tensioner arm. A change tendency of $2t_0/T$ with frequency is also noticed—as the frequency gets larger, $2t_0/T$ increases first and then decreases.

Finally, illustrated in Figs. 6–7 is the effect of different excitation frequencies on the response in the one-stop motion, with n_1 and n_3 taking the same values as in Fig. 3. Similar to the analysis of Fig. 3, the excitation frequencies can be divided into the group of $n_1 \geqslant n_3$ and the group of $n_1 < n_3$. The amplitude responses in Figs. 6(*a*)–6(*c*) take on trends agreeing with those in the nonstop motion. It is shown that the vibration amplitudes for the case of $n_1 \geqslant n_3$ are much larger than those for the case of $n_1 < n_3$. Within each group, however, the amplitude difference is very small. Figure 7 displays $2t_0/T$ as a function of ω/ω_0. It exhibits some

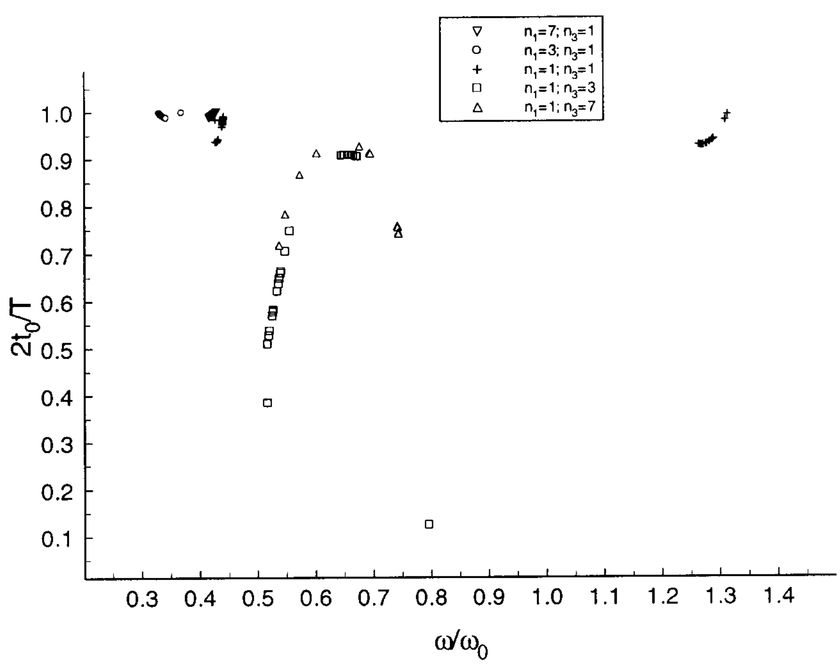

Fig. 7 t_0 **responses with excitation frequencies as parameter in one-stop vibration**

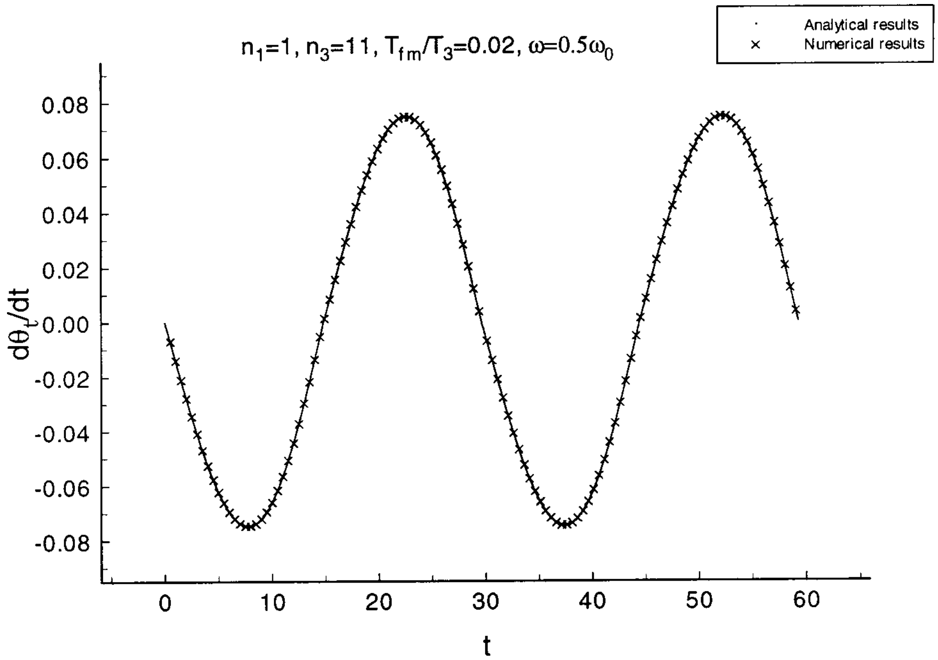

(a) Non-stop vibration

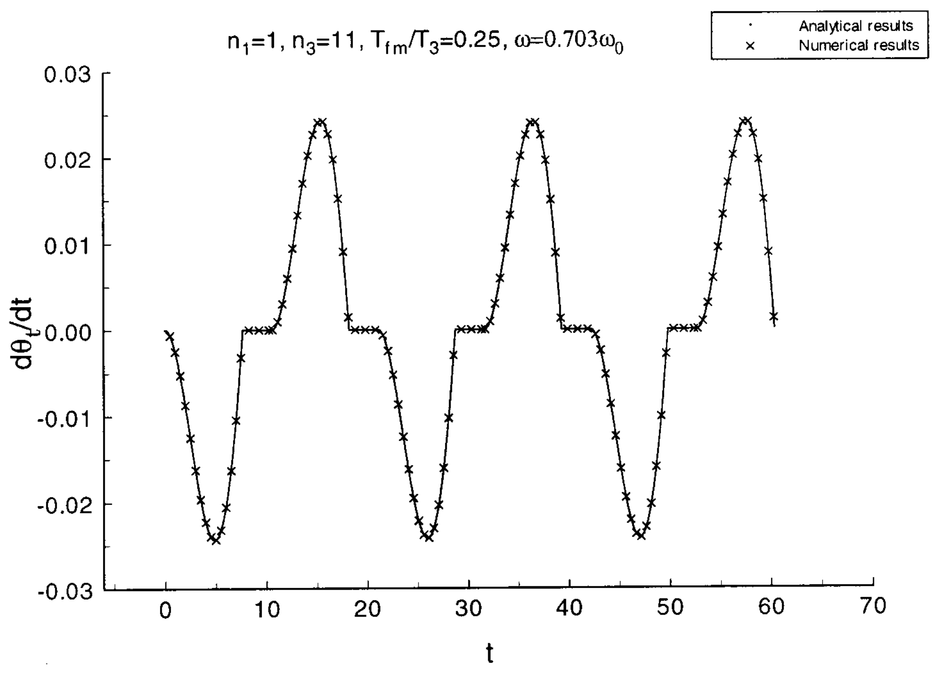

(b) One-stop vibration

Fig. 8 Time history of angular velocity of tensioner arm

unique characteristics: For the case of $n_1 \geqslant n_3$ the values of $2t_0/T$ are close to 1, signifying that the tensioner arm is in the slip state most of the period; for the case of $n_1 < n_3$, $2t_0/T$ increases first and then decreases as the frequency increases.

The above results are verified by comparing them with those obtained via directly integrating Eq. (64). Very good agreement has been reached. As an example, Figs. 8(a) and 8(b) show both the analytical and numerical results for the time history of the angular velocity of the tensioner arm in the nonstop and one-stop motion, respectively.

6 Conclusions

A belt drive system with a Coulomb friction damped tensioner and subjected to multifrequency excitations is studied in this paper. Two kinds of steady-state vibrations of the system—nonstop and one-stop motions are discussed. Applying an analytical method, the periodic responses of the system for both the nonstop and one-stop motions are derived. Furthermore, parametric studies are carried out to analyze the influence of the tensioner dry friction and the excitation frequencies on the dynamic behavior of the system. The following conclusions can be drawn from the study:

1. The existence of both nonstop and one-stop motions is discontinuous in frequency domain.

2. The tensioner dry friction has a significant impact on the amplitude response of the system. For the tensioner arm, the vibration amplitude decreases as the Coulomb friction torque increases in both nonstop and one-top motions. For the tensioner pulley and the driven pulley in the nonstop motion, there exists a critical frequency before which the dry friction torque reduces the vibration amplitude but after which it enlarges the amplitude. In the one-stop motion, the dry friction torque increases the amplitude of the tensioner pulley and the driven pulley.

3. In the one-stop motion, the larger the dry friction torque is, the higher percentage of the period the tensioner arm stays in the stick mode.

4. For both nonstop and one-stop motions, if the excitation frequency from the driving pulley is larger than or equal to that from the driven pulley, the system vibration amplitudes are much larger than those under the opposite condition.

5. In the one-stop motion, the tensioner arm stays in the slip state for the most of the period when the excitation frequency from the driving pulley is larger than or equal to that from the driven pulley.

Nomenclature

$\mathbf{M}$ = mass matrix $(n\times n)$
$\mathbf{C}$ = damping matrix $(n\times n)$
$\mathbf{K}$ = stiffness matrix $(n\times n)$
$\boldsymbol{\theta}$ = rotational displacement vector (n)
$\mathbf{T}$ = external excitation vector (n)
$\mathbf{x}$ = state vector $(2n)$
$\mathbf{A}$ = system matrix $(2n\times 2n)$
$\mathbf{b}$ = transformed excitation vector $(2n)$
$\mathbf{y}$ = transformed state vector $(2n)$
$\mathbf{u}$ = state vector for driven pulleys $(2n-2)$
$I_j\ (j=2,3,\ldots,n)$ = driven pulley's moment of inertia about pivot
I_t = moment of inertia of tensioner pulley/arm about pivot
$\theta_j\ (j=1,2,\ldots,n)$ = angular coordinate
θ_t = tensioner arm angle
$\omega_j\ (j=1,2,\ldots,n)$ = excitation frequency
$\varphi_j\ (j=1,2,\ldots,n)$ = initial phase angle
θ_0 = excitation amplitude from driving pulley
$T_j\ (j=2,3,\ldots,n)$ = amplitude of external torque
T_f = tensioner dry friction torque
T_{fm} = magnitude of tensioner dry friction torque
T = period of motion
ω = circular frequency of motion
t_0 = critical time in one-stop motion
$n_j\ (j=1,2,\ldots,n)$ = ratio between frequencies of excitation and of motion
m_{eff} = total mass of tension pulley/arm
L_{eff} = distance between pivot and mass center of tensioner pulley/arm
θ_{t0} = installed position of tensioner arm
$r_j\ (j=1,2,\ldots,n)$ = pulley radius
$C_{jp}\ (j=2,3,\ldots,n)$ = damping constant of driven pulley
$C_{jb}\ (j=1,2,\ldots,n)$ = damping constant of belt span
$K_j\ (j=1,2,\ldots,n)$ = elastic constant of belt span
C_t = damping constant of tensioner arm
K_t = tensioner arm stiffness
r_t = length of tensioner arm
$\omega_{nj}\ (j=1,2,\ldots,n)$ = natural frequency
ω_0 = reference frequency

References

[1] Hawker, L. E., 1991, ''A Vibration Analysis of Automotive Serpentine Accessory Drive System,'' Ph.D. dissertation, University of Windsor, Ontario, Canada.
[2] Barker, C. R., Oliver, L. R., and Brieg, W. F., 1991, ''Dynamic Analysis of Belt Drive Tension Forces During Rapid Engine Acceleration,'' SAE Paper No. 910687.
[3] Hwang, S.-J., Perkins, N. C., Ulsoy, A. G., and Meckstroth, R. J., 1994, ''Rotational Response and Slip Prediction of Serpentine Belt Drive Systems,'' ASME J. Vibr. Acoust., **116**, pp. 71–78.
[4] Beikmann, R. S., Perkins, N. C., and Ulsoy, A. G., 1996, ''Free Vibration of Serpentine Belt Drive Systems,'' ASME J. Vibr. Acoust., **118**, pp. 406–413.
[5] Kraver, T. C., Fan, G. W., and Shah, J. J., 1996, ''Complex Modal Analysis of a Flat Belt Pulley System With Belt Damping and Coulomb-Damped Tensioner,'' ASME J. Mech. Des., **118**, pp. 306–311.
[6] Iwatsubo, T., and Hasegawa, K., 1997, ''The Formulation and Dynamic Analysis of a Multiple Belt System,'' J. Sound Vib., **205**, pp. 293–307.
[7] Shaw, S. W., 1986, ''On the Dynamic Response of a System With Dry Friction,'' J. Sound Vib., **108**, pp. 305–325.
[8] Popp, K., and Stelter, P., 1990, ''Stick-Slip Vibrations and Chaos,'' Philos. Trans. R. Soc. London, Ser. A, **332**, pp. 89–105.
[9] Feeny, B. F., and Moon, F. C., 1994, ''Chaos in a Forced Oscillator With Dry Friction: Experiments and Numerical Modeling,'' J. Sound Vib., **170**, pp. 303–323.
[10] Natsiavas, S., 1998, ''Stability of Piecewise Linear Oscillators With Viscous and Dry Friction Damping,'' J. Sound Vib., **217**(3), pp. 507–522.
[11] Leamy, M. J., Perkins, N. C., Barber, J. R., and Meckstroth, R. J., 1997, ''Influence of Tensioner Friction on Accessory Drive Dynamics,'' SAE Paper No. 971962.
[12] Leamy, M. J., and Perkins, N. C., 1998, ''Nonlinear Periodic Response of Engine Accessory Drives With Dry Friction Tensioners,'' ASME J. Vibr. Acoust., **120**, pp. 909–916.
[13] Pierre, C., Ferri, A. A., and Dowell, E. H., 1985, ''Multi-Harmonic Analysis of Dry Friction Damped Systems Using an Incremental Harmonic Balance Method,'' ASME J. Appl. Mech., **52**, pp. 958–964.
[14] Mook, D. T., Plaut, R. H., and Haquang, N., 1986, ''The Influence of an Internal Resonance on Nonlinear Structural Vibration Under Combination Resonance Conditions,'' J. Sound Vib., **104**, pp. 229–241.
[15] Nayfeh, A. H., 1984, ''Combination Tones in the Response of Single Degree-of-Freedom Systems With Quadratic and Cubic Nonlinearities,'' J. Sound Vib., **92**, pp. 379–386.
[16] Van Dooren, R., 1971, ''Combination Tones of Summed Type in a Nonlinear Damped Vibratory System With Two Degrees of Freedom,'' Int. J. Non-Linear Mech., **6**, pp. 237–254.
[17] Eneremadu, K. O., and Zu, J. W., 1997, ''Stability of Nonlinear Two-Frequency Oscillation of Cylindrical Shells,'' J. Eng. Mech. Div., **123**, pp. 1034–1040.
[18] Wang, Y. X., 1998, ''Multifrequency Resonances of Flexible Linkages,'' Mech. Mach. Theory, **33**, pp. 255–271.
[19] Fung, R. F., 1997, ''The Effect of Non-Linear Inertia on the Steady State Response of a Beam System Subjected to Combined Excitations,'' J. Sound Vib., **203**, pp. 373–387.
[20] Maccari, A., 1999, ''Non-Linear Oscillation with Multiple Resonant or Non-Resonant Forcing Terms,'' Int. J. Non-Linear Mech., **34**, pp. 27–34.
[21] Nichols, J. M., and Virgin, L. N., 2001, ''Practical Evaluation of Invariant Measures for the Chaotic Response of a Two-Frequency Excited Mechanical Oscillator,'' Nonlinear Dyn., **26**, pp. 67–86.
[22] Den Hartog, J. P., 1931, ''Forced Vibrations With Combined Coulomb and Viscous Friction,'' Trans. ASME, **53**, pp. 107–115.
[23] Iwatsubo, T., and Hasegawa, K., 1997, ''The Formulation and Dynamic Analysis of a Multiple Belt System,'' J. Sound Vib., **205**, pp. 293–307.

Analysis of Asymmetric Nonviscously Damped Linear Dynamic Systems

S. Adhikari[1]
Department of Aerospace Engineering,
University of Bristol
Queen's Building, University Walk,
Bristol BS8, 1TR, UK

N. Wagner
Institut A für Mechanik,
University of Stuttgart

Multiple-degree-of-freedom linear asymmetric nonviscously damped systems are considered. It is assumed that the nonviscous damping forces depend on the past history of velocities via convolution integrals over exponentially decaying kernel functions. An extended state-space approach involving a single asymmetric matrix is proposed. The nature of the eigensolutions in the extended state space has been explored. Some useful results relating the modal matrix in the extended state space and the modal matrix in the original space has been derived. Numerical examples are provided to illustrate the results.
[DOI: 10.1115/1.1601251]

1 Introduction

Viscous damping is the most common model for the modeling of vibration damping. This model assumes that the instantaneous generalized velocities are the only relevant variables that determine damping. Viscous damping models are used widely for their simplicity and mathematical convenience even though the true damping behavior is expected to be nonviscous. Damping models in which the dissipative forces depend on any quantity other than the instantaneous generalized velocities will be called nonviscous damping models. Of many nonviscous damping models, the convolution integral model ([1–3]) is possibly the most general model within the scope of linear analysis. In this paper we consider that the damping model consists of viscous and nonviscous damping. The equations of motion of a N-degree-of-freedom linear system with such damping can be expressed by

$$\mathbf{M}\ddot{\mathbf{u}}(t)+\mathbf{D}\dot{\mathbf{u}}(t)+\int_0^t \boldsymbol{\mathcal{G}}(t-\tau)\dot{\mathbf{u}}(\tau)d\tau+\mathbf{K}\mathbf{u}(t)=\mathbf{f}(t), \qquad (1)$$

where $\mathbf{u}(t)\in\mathbb{R}^N$ is the vector of generalized coordinates, $\mathbf{M}\in\mathbb{R}^{N\times N}$ is the mass matrix, $\mathbf{K}\in\mathbb{R}^{N\times N}$ is the stiffness matrix, $\mathbf{D}\in\mathbb{R}^{N\times N}$ is the viscous damping matrix, and $\mathbf{f}(t)\in\mathbb{R}^N$ is the forcing vector. The matrix of the damping functions, $\boldsymbol{\mathcal{G}}(t-\tau)$, can have various mathematical forms. For example, when $\boldsymbol{\mathcal{G}}(t-\tau)=\mathbf{D}\delta(t-\tau)$, where $\delta(t)$ is the Dirac delta function, the kernel function reduces to the case of viscous damping. Among many other mathematically possible damping functions, the exponential damping model is physically most meaningful ([4]). For this damping model the kernel function matrix has the special form

$$\boldsymbol{\mathcal{G}}(t-\tau)=\sum_{k=1}^{n}\mu_k e^{-\mu_k(t-\tau)}\mathbf{C}_k, \qquad (2)$$

where $\mu_k\in\mathbb{R}^+$ are known as the relaxation parameters, $\mathbf{C}_k\in\mathbb{R}^{N\times N}$ are the damping coefficient matrices, and n denotes the number relaxation parameters used to describe the damping behavior.

A brief review of literature on dynamics of nonviscously damped systems may be found in Ref. [3]. Muravyouv [5,6] and Muravyov and Hutton [7,8] have considered this kind of system where the exponential kernel function is associated with the stiffness matrix. Recently Wagner and Adhikari [9] have proposed an exact state-space method for the analysis of linear systems with exponential damping. Their approach was based on representing Eq. (1) in terms of two *symmetric* matrices in an augmented state space. In this paper an alternative approach based on only one asymmetric matrix is suggested and the relationships between the eigenvectors in the state space and the eigenvectors in the original space have been derived.

It is assumed that $\mathbf{M}^{-1}$ exists, that is, systems with a singular mass matrix is not considered in the present work. For the sake of generality the usual symmetry and non-negative definiteness properties of the system matrices are not assumed. Further, it is also considered that in general the system is neither symmetrizable ([10,11]), nor simultaneously diagonalizable by any linear transformations ([12]). In Sec. 2, the eigenvalue problem associated with Eq. (1) is briefly reviewed. The state-space approach based on internal variables is formulated in Sec. 3. The eigenvalue problem in the state space and some properties of the eigensolutions are discussed in Sec. 4. In Sec. 5, the proposed results are illustrated by a numerical example.

2 Background: The Eigenvalue Problem

Free vibration characteristics of the system is governed by the eigenvalue problem associated with the equations of motion (1). Assuming the initial conditions

$$\mathbf{u}(t=0)=\boldsymbol{u}_0\in\mathbb{R}^N \quad \text{and} \quad \dot{\mathbf{u}}(t=0)=\dot{\boldsymbol{u}}_0\in\mathbb{R}^N \qquad (3)$$

and taking the Laplace transform of Eq. (1) one obtains

$$s^2\mathbf{M}\overline{\mathbf{u}}(s)-s\mathbf{M}\boldsymbol{u}_0-\mathbf{M}\dot{\boldsymbol{u}}_0+s[\mathbf{D}+\mathbf{G}(s)]\overline{\mathbf{u}}(s)$$
$$-[\mathbf{D}+\mathbf{G}(s)]\boldsymbol{u}_0+\mathbf{K}\overline{\boldsymbol{u}}(s)=\overline{\mathbf{f}}(s) \qquad (4)$$

$$\text{or}\quad s^2\mathbf{M}\overline{\mathbf{u}}(s)+s[\mathbf{D}+\mathbf{G}(s)]\overline{\boldsymbol{u}}(s)+\mathbf{K}\overline{\boldsymbol{u}}(s)=\overline{\mathbf{p}}(s). \qquad (5)$$

Here

$$\overline{\mathbf{p}}(s)=\overline{\mathbf{f}}(s)+\mathbf{M}\dot{\boldsymbol{u}}_0+[s\mathbf{M}+\mathbf{D}+\mathbf{G}(s)]\boldsymbol{u}_0 \qquad (6)$$

is the equivalent forcing function in the Laplace domain. In the above equations $\overline{\boldsymbol{u}}(s)=\mathcal{L}[\mathbf{u}(t)]\in\mathbb{C}^N$, $\overline{\mathbf{f}}(s)=\mathcal{L}[\mathbf{f}(t)]\in\mathbb{C}^N$ and $\mathcal{L}[\bullet]$ denotes the Laplace transform. The matrix $\mathbf{G}(s)\in\mathbb{C}^{N\times N}$ is the Laplace transform of $\boldsymbol{\mathcal{G}}(t)$ and can be obtained from Eq. (2) as

[1]To whom correspondence should be addressed. E-mail: S.Adhikari@bristol.ac.uk.

Contributed by the Applied Mechanics Division of THE AMERICAN SOCIETY OF MECHANICAL ENGINEERS for publication in the ASME JOURNAL OF APPLIED MECHANICS. Manuscript received by the ASME Applied Mechanics Division, November 20, 2001; final revision, February 20, 2003. Associate Editor: A. A. Ferri. Discussion on the paper should be addressed to the Editor, Prof. Robert M. McMeeking, Department of Mechanical and Environmental Engineering, University of California—Santa Barbara, Santa Barbara, CA 93106-5070, and will be accepted until four months after final publication of the paper itself in the ASME JOURNAL OF APPLIED MECHANICS.

$$\mathbf{G}(s)=\sum_{k=1}^{n}\frac{\mu_k}{s+\mu_k}\mathbf{C}_k. \tag{7}$$

In the context of structural dynamics, the Laplace parameter $s=i\omega$, where $i=\sqrt{-1}$ and $\omega\in\mathbb{R}^+$ denotes the frequency. Considering the free vibration from Eq. (5) the right-eigenvalue problem can be represented by

$$\left[\lambda_j^2\mathbf{M}+\lambda_j\mathbf{D}+\lambda_j\sum_{k=1}^{n}\frac{\mu_k}{\lambda_j+\mu_k}\mathbf{C}_k+\mathbf{K}\right]\boldsymbol{u}_j=\mathbf{0}. \tag{8}$$

Similarly the left-eigenvalue problem can be expressed as

$$\boldsymbol{v}_j^T\left[\lambda_j^2\mathbf{M}+\lambda_j\mathbf{D}+\lambda_j\sum_{k=1}^{n}\frac{\mu_k}{\lambda_j+\mu_k}\mathbf{C}_k+\mathbf{K}\right]=\mathbf{0}^T. \tag{9}$$

Here $\lambda_j\in\mathbb{C}$ is the jth eigenvalue and $\boldsymbol{u}_j\in\mathbb{C}^N$ is the jth eigenvector. Suppose the number of eigenvalues is m. The methods for solving this kind of problem follow mainly two routes, (a) the extended state-space method [13–16,7,6,9], and (b) the methods in the configuration space or "N" space ([2,3]). In the next section an extended state-space method based on a set of internal variables is proposed.

For lightly damped systems, among the m eigenvalues $2N$ appear in complex conjugate pairs and the rest are purely real and negative ([3,17]). We emphasize that these results are simply observations and a detailed mathematical proof of the conditions under which such results are valid are not yet available. A physical explanation, however, can be given. The N pairs of complex conjugate eigenvalues can be related to the N (complex) modes of structural vibration. These modes are therefore called *elastic modes* ([3]). The other $(m-2N)$ purely dissipative modes appear due to nonviscous nature of the damping model and therefore called *nonviscous modes* ([3]). Nonviscous modes, or similar to these, are known by different names in the literature of different subjects, for example, "wet modes" in the context of ship dynamics ([18]) and "damping modes" in the context of viscoelastic structures ([15]). For convenience we construct and partition the following matrices:

$$\boldsymbol{\Lambda}=\mathrm{diag}[\lambda_1,\lambda_2,\ldots,\lambda_m]\in\mathbb{C}^{m\times m}=\mathrm{diag}[\boldsymbol{\Lambda}_e,\boldsymbol{\Lambda}_e^*\boldsymbol{\Lambda}_{nv}], \tag{10}$$

$$\mathbf{U}=[\boldsymbol{u}_1,\boldsymbol{u}_2,\ldots,\boldsymbol{u}_m]\in\mathbb{C}^{n\times m}=[\mathbf{U}_e,\mathbf{U}_e^*,\mathbf{U}_{nv}], \tag{11}$$

$$\text{and}\quad \mathbf{V}=[\boldsymbol{v}_1,\boldsymbol{v}_2,\ldots,\boldsymbol{v}_m]\in\mathbb{C}^{n\times m}=[\mathbf{V}_e,\mathbf{V}_e^*,\mathbf{V}_{nv}]. \tag{12}$$

Here $(\bullet)^*$ denotes complex conjugation, the subscript $(\bullet)_e$ corresponds to elastic modes, and the subscript $(\bullet)_{nv}$ corresponds to nonviscous modes.

3 State-Space Formulation

For viscously damped systems, the state-space method based on one asymmetric system matrix has been used extensively in literature (see Newland [19,20]). Here this approach will be extended to system (1) by using a set of internal variables. In what follows next, two physically realistic cases, namely, (a) when all $\mathbf{C}_k$ matrices are of full rank and, (b) all $\mathbf{C}_k$ matrices are rank deficient, have been considered in details. A third possible case, when only some $\mathbf{C}_k$ matrices are rank deficient, can be easily derived from the two preceding cases.

3.1 Case A: All $\mathbf{C}_k$ Matrices are of Full Rank.

Here it is assumed that

$$\mathrm{rank}\ (\mathbf{C}_k)=N,\quad \forall k=1,\ldots,n. \tag{13}$$

We introduce a set of internal variables $\mathbf{y}_k(t)\in\mathbb{R}^N$, $\forall k=1,\ldots,n$ by

$$\mathbf{y}_k(t)=\int_0^t\mu_k e^{-\mu_k(t-\tau)}\dot{\mathbf{u}}(\tau)d\tau. \tag{14}$$

Applying Leibniz's rule for differentiation of an integral to Eq. (14) one obtains

$$\dot{\mathbf{y}}_k(t)=\int_0^t-\mu_k^2e^{-\mu_k(t-\tau)}\dot{\mathbf{u}}(\tau)d\tau+\mu_k\dot{\mathbf{u}}(t). \tag{15}$$

Multiplying Eq. (14) by the relaxation parameter μ_k, then adding it to Eq. (15) results in

$$\dot{\mathbf{y}}_k(t)+\mu_k\mathbf{y}_k(t)=\mu_k\dot{\mathbf{u}}(t). \tag{16}$$

Now, taking account of the kernel function matrix (2), Eq. (1) can be rewritten as

$$\mathbf{M}\ddot{\mathbf{u}}(t)+\mathbf{D}\dot{\mathbf{u}}(t)+\sum_{k=1}^{n}\mathbf{C}_k\left\{\int_0^t\mu_k e^{-\mu_k(t-\tau)}\dot{\mathbf{u}}(\tau)d\tau\right\}+\mathbf{K}\mathbf{u}(t)=\mathbf{f}(t). \tag{17}$$

Substituting Eq. (14) into Eq. (17) leads to

$$\mathbf{M}\ddot{\mathbf{u}}(t)+\mathbf{D}\dot{\mathbf{u}}(t)+\sum_{k=1}^{n}\mathbf{C}_k\mathbf{y}_k(t)+\mathbf{K}\mathbf{u}(t)=\mathbf{f}(t). \tag{18}$$

Using additional state variables

$$\mathbf{v}(t)=\dot{\mathbf{u}}(t) \tag{19}$$

and assuming that $\mathbf{M}^{-1}$ exists, Eq. (17) can be rewritten as

$$\dot{\mathbf{v}}(t)+\mathbf{M}^{-1}\mathbf{D}\dot{\mathbf{u}}(t)+\sum_{k=1}^{n}\mathbf{M}^{-1}\mathbf{C}_k\mathbf{y}_k(t)+\mathbf{M}^{-1}\mathbf{K}\mathbf{u}(t)=\mathbf{M}^{-1}\mathbf{f}(t). \tag{20}$$

Rearranging Eqs. (16), (19), and (20) one obtains

$$\dot{\mathbf{u}}(t)=\mathbf{v}(t), \tag{21}$$

$$\dot{\mathbf{v}}(t)=-\mathbf{M}^{-1}\mathbf{D}\mathbf{v}(t)-\sum_{k=1}^{n}\mathbf{M}^{-1}\mathbf{C}_k\mathbf{y}_k(t)-\mathbf{M}^{-1}\mathbf{K}\mathbf{u}(t)+\mathbf{M}^{-1}\mathbf{f}(t), \tag{22}$$

$$\dot{\mathbf{y}}_k(t)=\mu_k\mathbf{I}\mathbf{v}(t)-\mu_k\mathbf{I}\mathbf{y}_k(t),\quad \forall k=1,\ldots,n \tag{23}$$

or in the matrix form

$$\dot{\mathbf{z}}(t)=\mathbf{A}\mathbf{z}(t)+\mathbf{r}(t), \tag{24}$$

where

$$\mathbf{A}=\begin{bmatrix}\mathbf{O} & \mathbf{I} & \mathbf{O} & \mathbf{O} & \cdots & \mathbf{O}\\ -\mathbf{M}^{-1}\mathbf{K} & -\mathbf{M}^{-1}\mathbf{D} & -\mathbf{M}^{-1}\mathbf{C}_1 & -\mathbf{M}^{-1}\mathbf{C}_2 & \cdots & -\mathbf{M}^{-1}\mathbf{C}_n\\ \mathbf{O} & \mu_1\mathbf{I} & -\mu_1\mathbf{I} & \mathbf{O} & \cdots & \mathbf{O}\\ \mathbf{O} & \mu_2\mathbf{I} & \mathbf{O} & -\mu_2\mathbf{I} & \cdots & \mathbf{O}\\ \vdots & \vdots & \vdots & \vdots & \ddots & \vdots\\ \mathbf{O} & \mu_n\mathbf{I} & \mathbf{O} & \mathbf{O} & \mathbf{O} & -\mu_n\mathbf{I}\end{bmatrix}\in\mathbb{R}^{m\times m}, \tag{25}$$

$$\mathbf{r}(t)=\begin{Bmatrix}\mathbf{O}\\ \mathbf{M}^{-1}\mathbf{f}(t)\\ \mathbf{O}\\ \mathbf{O}\\ \vdots\\ \mathbf{O}\end{Bmatrix}\in\mathbb{R}^m, \tag{26}$$

$$\text{and}\quad \mathbf{z}(t)=\begin{Bmatrix}\mathbf{u}(t)\\ \mathbf{v}(t)\\ \mathbf{y}_1(t)\\ \mathbf{y}_2(t)\\ \vdots\\ \mathbf{y}_n(t)\end{Bmatrix}\in\mathbb{R}^m. \tag{27}$$

In the above equations $\mathbf{z}(t)$ is the extended state vector, $\mathbf{A}$ is the system matrix in the extended state space, $\mathbf{r}(t)$ is the force vector in the extended state space, $\mathbf{O}\in\mathbb{R}^{N\times N}$ is a null matrix, and $\mathbf{I}\in\mathbb{R}^{N\times N}$ is an identity matrix. It is clear that the order of the system m is

$$m=2N+nN. \tag{28}$$

In the viscous damping limit, *all* the internal variables can be disregarded, that is, all $n\times N$ equations after the first $2N$ rows in Eq. (24) can be deleted from the formulation. Under these conditions it is easy to see that the equations of motion (24) reduce to the standard form ([19,20]) for viscously damped systems with

$$\mathbf{A}=\begin{bmatrix}\mathbf{O} & \mathbf{I}\\ -\mathbf{M}^{-1}\mathbf{K} & -\mathbf{M}^{-1}\mathbf{D}\end{bmatrix},\quad \mathbf{r}(t)=\begin{Bmatrix}\mathbf{O}\\ \mathbf{M}^{-1}\mathbf{f}(t)\end{Bmatrix},$$

and

$$\mathbf{z}(t)=\begin{Bmatrix}\mathbf{u}(t)\\ \mathbf{v}(t)\end{Bmatrix}. \tag{29}$$

This shows that the representation of the equations of motion by Eq. (24) is a natural generalization of the standard state-space formulation for viscously damped systems.

3.2 Case B: All $\mathbf{C}_k$ Matrices are Rank Deficient. In a large engineering structure it is possible to have different damping in different parts of a structure. For example, different members of a space frame may have different damping properties, each associated with its relaxation parameter μ_k. In this case the associated coefficient matrix $\mathbf{C}_k$ will be rank deficient because it will have nonzero blocks corresponding to the associated elements only. In this section we assume that in general

$$r_k=\text{rank}\ (\mathbf{C}_k)\leqslant N,\quad \forall k=1,\ldots,n. \tag{30}$$

This implies that the number of nonzero eigenvalues of $\mathbf{C}_k$ is r_k. Therefore there exist two matrices $\tilde{\mathbf{U}}_k\in\mathbb{R}^{N\times N}$ and $\tilde{\mathbf{V}}_k\in\mathbb{R}^{N\times N}$ such that

$$\tilde{\mathbf{V}}_k^T\mathbf{C}_k\tilde{\mathbf{U}}_k=\begin{bmatrix}\mathbf{d}_k & \mathbf{O}_{1k}\\ \mathbf{O}_{1k}^T & \mathbf{O}_{2k}\end{bmatrix}. \tag{31}$$

In the above equation $\mathbf{d}_k\in\mathbb{R}^{r_k\times r_k}$ is a diagonal matrix consisting of only the nonzero eigenvalues of $\mathbf{C}_k$, $\mathbf{O}_{1k}$ and $\mathbf{O}_{2k}$ are null matrices of orders $r_k\times(N-r_k)$ and $(N-r_k)\times(N-r_k)$, respectively. For convenience partition $\tilde{\mathbf{U}}_k$ and $\tilde{\mathbf{V}}_k$ as

$$\tilde{\mathbf{U}}_k=[\tilde{\mathbf{U}}_{1k}|\tilde{\mathbf{U}}_{2k}] \tag{32}$$

$$\text{and}\quad \tilde{\mathbf{V}}_k=[\tilde{\mathbf{V}}_{1k}|\tilde{\mathbf{V}}_{2k}]. \tag{33}$$

The columns of matrices $\tilde{\mathbf{U}}_{1k}\in\mathbb{R}^{N\times r_k}$ and $\tilde{\mathbf{V}}_{1k}\in\mathbb{R}^{N\times r_k}$ are the eigenvectors of $\mathbf{C}_k$ and $\mathbf{C}_k^T$ corresponding to the nonzero block $\mathbf{d}_k$ and the columns of matrices $\tilde{\mathbf{U}}_{2k}\in\mathbb{R}^{N\times(N-r_k)}$ and $\tilde{\mathbf{V}}_{2k}\in\mathbb{R}^{N\times(N-r_k)}$ are the eigenvectors of $\mathbf{C}_k$ and $\mathbf{C}_k^T$ corresponding to the other $(N-r_k)$ numbers of zero eigenvalues. Now defining the rectangular transformation matrices

$$\mathbf{R}_k=\tilde{\mathbf{U}}_{1k}\in\mathbb{R}^{N\times r_k} \tag{34}$$

$$\text{and}\quad \mathbf{L}_k=\tilde{\mathbf{V}}_{1k}\in\mathbb{R}^{N\times r_k} \tag{35}$$

it is easy to show that

$$\mathbf{L}_k^T\mathbf{C}_k\mathbf{R}_k=\mathbf{d}_k. \tag{36}$$

Thus the matrices $\mathbf{R}_k$ and $\mathbf{L}_k$ in Eqs. (34) and (35) transform the originally rank deficient matrix $\mathbf{C}_k$ to a full-rank matrix with rank r_k.

Now we define a set of internal variables of reduced dimension $\tilde{\mathbf{y}}_k(t)\in\mathbb{R}^{r_k}$ using the rectangular transformation matrix $\mathbf{R}_k$ as

$$\mathbf{y}_k(t)=\mathbf{R}_k\tilde{\mathbf{y}}_k(t). \tag{37}$$

From this equation it immediately follows that

$$\dot{\mathbf{y}}_k(t)=\mathbf{R}_k\dot{\tilde{\mathbf{y}}}_k(t), \tag{38}$$

where $\mathbf{y}_k(t)$ is defined in Eq. (14). Using these relationships, Eqs. (22) and (23) can be expressed as

$$\dot{\mathbf{v}}(t)=-\mathbf{M}^{-1}\mathbf{D}\mathbf{v}(t)-\sum_{k=1}^{n}\mathbf{M}^{-1}\mathbf{C}_k\mathbf{R}_k\tilde{\mathbf{y}}_k(t)-\mathbf{M}^{-1}\mathbf{K}\mathbf{u}(t)+\mathbf{M}^{-1}\mathbf{f}(t) \tag{39}$$

$$\text{and}\quad \mathbf{R}_k\dot{\tilde{\mathbf{y}}}_k(t)=\mu_k\mathbf{v}(t)-\mu_k\mathbf{R}_k\tilde{\mathbf{y}}_k(t). \tag{40}$$

Because Eq. (40) still represents a set of N equations, we premultiply this by $\mathbf{L}_k^T$ to obtain a reduced set of r_k equations:

$$[\mathbf{L}_k^T\mathbf{R}_k]\dot{\tilde{\mathbf{y}}}_k(t)=\mu_k\mathbf{L}_k^T\mathbf{v}(t)-\mu_k[\mathbf{L}_k^T\mathbf{R}_k]\tilde{\mathbf{y}}_k(t). \tag{41}$$

Taking the inverse of $[\mathbf{L}_k^T\mathbf{R}_k]$, the preceding equation may be rewritten as

$$\dot{\tilde{\mathbf{y}}}_k(t)=\mu_k\mathbf{T}_k\mathbf{v}(t)-\mu_k\mathbf{I}_{r_k}\tilde{\mathbf{y}}_k(t), \tag{42}$$

$$\text{where}\quad \mathbf{T}_k=[\mathbf{L}_k^T\mathbf{R}_k]^{-1}\mathbf{L}_k^T\in\mathbb{R}^{r_k\times N},\quad \forall k=1,\ldots,n. \tag{43}$$

Now Eqs. (21), (39), and (42) can be combined into the first-order form as

$$\dot{\tilde{\mathbf{z}}}(t)=\tilde{\mathbf{A}}\tilde{\mathbf{z}}(t)+\tilde{\mathbf{r}}(t), \tag{44}$$

where

$$\tilde{\mathbf{A}}=\begin{bmatrix} \mathbf{O} & \mathbf{I}_N & \mathbf{O}_{N,r_1} & \mathbf{O}_{N,r_2} & \cdots & \mathbf{O}_{N,r_n} \\ -\mathbf{M}^{-1}\mathbf{K} & -\mathbf{M}^{-1}\mathbf{D} & -\mathbf{M}^{-1}\mathbf{C}_1\mathbf{R}_1 & -\mathbf{M}^{-1}\mathbf{C}_2\mathbf{R}_2 & \cdots & -\mathbf{M}^{-1}\mathbf{C}_n\mathbf{R}_n \\ \mathbf{O}_{r_1,N} & \mu_1\mathbf{T}_1 & -\mu_1\mathbf{I}_{r_1} & \mathbf{O}_{r_1,r_2} & \cdots & \mathbf{O}_{r_1,r_n} \\ \mathbf{O}_{r_2,N} & \mu_2\mathbf{T}_2 & \mathbf{O}_{r_2,r_1} & -\mu_2\mathbf{I}_{r_2} & \cdots & \mathbf{O}_{r_2,r_n} \\ \vdots & \vdots & \vdots & \vdots & \ddots & \vdots \\ \mathbf{O}_{r_n,N} & \mu_n\mathbf{T}_n & \mathbf{O}_{r_n,r_1} & \mathbf{O}_{r_n,r_2} & \cdots & -\mu_n\mathbf{I}_{r_n} \end{bmatrix} \in \mathbb{R}^{m\times m}, \tag{45}$$

$$\tilde{\mathbf{r}}(t)=\begin{Bmatrix} \mathbf{0}_N \\ \mathbf{M}^{-1}\mathbf{f}(t) \\ \mathbf{0}_{r_1} \\ \mathbf{0}_{r_2} \\ \vdots \\ \mathbf{0}_{r_n} \end{Bmatrix} \in \mathbb{R}^m, \tag{46}$$

$$\text{and }\ \tilde{\mathbf{z}}(t)=\begin{Bmatrix} \mathbf{u}(t) \\ \mathbf{v}(t) \\ \tilde{\mathbf{y}}_1(t) \\ \tilde{\mathbf{y}}_2(t) \\ \vdots \\ \tilde{\mathbf{y}}_n(t) \end{Bmatrix} \in \mathbb{R}^m. \tag{47}$$

In the above equations

$$m=2N+\sum_{k=1}^{n} r_k \tag{48}$$

is the order of the system, $\mathbf{O}_{ij}$ are $i\times j$ null matrices, $\mathbf{I}_j$ are $j\times j$ identity matrices, and $\mathbf{0}_j$ are vectors of j zeros. The terms $(\tilde{\cdot})$ are corresponding to terms $(\cdot)$ defined in Eq. (24). When all $\mathbf{C}_k$ matrices are of full rank, that is, when $r_k=N, \forall k$, then one can choose all $\mathbf{R}_k$ and $\mathbf{L}_k$ matrices as the identity matrices and Eq. (44) reduces to Eq. (24).

4 The Eigenvalue Problem

4.1 Case A: All $\mathbf{C}_k$ Matrices are of Full Rank. The right and the left eigenvalue problems associated with Eq. (24) can be expressed as

$$\mathbf{A}\boldsymbol{\phi}_j=\lambda_j\boldsymbol{\phi}_j \tag{49}$$

$$\text{and }\ \boldsymbol{\psi}_j^T\mathbf{A}=\lambda_j\boldsymbol{\psi}_j^T \quad j=1,2,\dots,(2+n)N, \tag{50}$$

where $\lambda_j\in\mathbb{C}$ is the jth eigenvalue, $\boldsymbol{\phi}_j\in\mathbb{C}^{(2+n)N}$ and $\boldsymbol{\psi}_j\in\mathbb{C}^{(2+n)N}$ are respectively the jth right and left eigenvectors. Because $\mathbf{A}$ is a real matrix the eigenvalues can only be real or, if complex, then must appear in complex conjugate pairs. Construct the "modal matrices:"

$$\boldsymbol{\Phi}=[\phi_1,\phi_2,\dots,\phi_{(2+n)N}]\in\mathbb{C}^{(2+n)N\times(2+n)N} \tag{51}$$

$$\text{and }\ \boldsymbol{\Psi}=[\psi_1,\psi_2,\dots,\psi_{(2+n)N}]\in\mathbb{C}^{(2+n)N\times(2+n)N}. \tag{52}$$

It can be easily shown that the right eigenvectors and the left eigenvectors satisfy a biorthogonality relationship, i.e., $\boldsymbol{\psi}_k^T\mathbf{A}\boldsymbol{\phi}_j=0$, $\forall k\neq j$. We also normalize the eigenvectors such that

$$\boldsymbol{\Psi}^T\boldsymbol{\Phi}=\mathbf{I}_{(2+n)N} \tag{53}$$

$$\text{and }\ \boldsymbol{\Psi}^T\mathbf{A}\boldsymbol{\Phi}=\boldsymbol{\Lambda}. \tag{54}$$

However, it should be noted that the above normalization is not sufficient to define $\boldsymbol{\Phi}$ and $\boldsymbol{\Psi}$ uniquely.

4.1.1 The Structure of the Modal Matrices. From the definition of $\mathbf{z}(t)$ in Eq. (27), the right eigenvectors in the extended state space can be related to the right eigenvectors in the original space (8) by

$$\boldsymbol{\phi}_j=\begin{Bmatrix} \boldsymbol{u}_j \\ \lambda_j\boldsymbol{u}_j \\ \boldsymbol{y}_{1j} \\ \boldsymbol{y}_{2j} \\ \vdots \\ \boldsymbol{y}_{nj} \end{Bmatrix}, \tag{55}$$

where $\boldsymbol{y}_{1j},\boldsymbol{y}_{2j},\dots,\boldsymbol{y}_{nj}$ are components of the jth eigenvector corresponding to the internal variables $\mathbf{y}_1(t),\mathbf{y}_2(t),\dots,\mathbf{y}_n(t)$. The vectors $\boldsymbol{y}_{kj}\in\mathbb{C}^N$, $\forall k=1,2,\dots,n$ can be related to $\boldsymbol{u}_j$ using Eq. (16). Taking the Laplace transform of Eq. (16) results in

$$s\overline{\mathbf{y}}_k+\mu_k\overline{\mathbf{y}}_k=s\mu_k\overline{\mathbf{u}}, \tag{56}$$

where $\overline{\mathbf{y}}_\mathbf{k}$ is the Laplace transform of $\mathbf{y}_k(t)$. For the jth eigenvalue one obtains

$$\lambda_j\boldsymbol{y}_{kj}+\mu_k\boldsymbol{y}_{kj}=\lambda_j\mu_k\boldsymbol{u}_j \quad\text{or}\quad (\lambda_j+\mu_k)\boldsymbol{y}_{kj}=\lambda_j\mu_k\boldsymbol{u}_j. \tag{57}$$

Provided $\lambda_j\neq-\mu_k$, from the preceding equation,

$$\boldsymbol{y}_{kj}=\frac{\lambda_j\mu_k}{\lambda_j+\mu_k}\boldsymbol{u}_j, \quad \forall k=1,2,\dots,n;\ \ \forall j=1,2,\dots,(2+n)N. \tag{58}$$

Using Eqs. (55) and (58) the right eigenvectors in the state space $\boldsymbol{\phi}_j$ can be related to the right eigenvectors in the original space $\boldsymbol{u}_j$. It is useful to represent this relationship in a matrix form. Define a matrix

$$\boldsymbol{Y}_k=[\boldsymbol{y}_{k1},\boldsymbol{y}_{k_2},\dots,\boldsymbol{y}_{k_{(2+n)N}}]\in\mathbb{C}^{N\times(2+n)N}. \tag{59}$$

For $j=1,2,\dots,(2+n)N$, Eq. (57) can be written in a matrix form as

$$\boldsymbol{Y}_k\boldsymbol{\Lambda}+\mu_k\boldsymbol{Y}_k=\mu_k\mathbf{U}\boldsymbol{\Lambda}. \tag{60}$$

Dividing this equation by μ_k one obtains

$$\boldsymbol{Y}_k=\mathbf{U}\boldsymbol{\Lambda}[\boldsymbol{\Lambda}/\mu_k+\mathbf{I}_{(2+n)N}]^{-1}. \tag{61}$$

Using this expression the matrix of right eigenvectors in the state space, given by Eq. (51), can be expressed as

$$\boldsymbol{\Phi}=\begin{bmatrix} \mathbf{U} \\ \mathbf{U}\boldsymbol{\Lambda} \\ \mathbf{U}\boldsymbol{\Lambda}[\boldsymbol{\Lambda}/\mu_1+\mathbf{I}_{(2+n)N}]^{-1} \\ \mathbf{U}\boldsymbol{\Lambda}[\boldsymbol{\Lambda}/\mu_2+\mathbf{I}_{(2+n)N}]^{-1} \\ \vdots \\ \mathbf{U}\boldsymbol{\Lambda}[\boldsymbol{\Lambda}/\mu_n+\mathbf{I}_{(2+n)N}]^{-1} \end{bmatrix}. \tag{62}$$

In view of the partitions shown in Eqs. (10) and (11), the preceding equation can be conveniently partitioned as

$$\mathbf{\Phi}=\begin{bmatrix} \mathbf{U}_e & \mathbf{U}_e^* & \mathbf{U}_{nv} \\ \mathbf{U}_e\mathbf{\Lambda}_e & \mathbf{U}_e^*\mathbf{\Lambda}_e^* & \mathbf{U}_{nv}\mathbf{\Lambda}_{nv} \\ \mathbf{U}_e\mathbf{\Lambda}_e[\mathbf{\Lambda}_e/\mu_1+\mathbf{I}_N]^{-1} & \mathbf{U}_e^*\mathbf{\Lambda}_e^*[\mathbf{\Lambda}_e^*/\mu_1+\mathbf{I}_N]^{-1} & \mathbf{U}_{nv}\mathbf{\Lambda}_{nv}[\mathbf{\Lambda}_{nv}/\mu_1+\mathbf{I}_{nN}]^{-1} \\ \mathbf{U}_e\mathbf{\Lambda}_e[\mathbf{\Lambda}_e/\mu_2+\mathbf{I}_N]^{-1} & \mathbf{U}_e^*\mathbf{\Lambda}_e^*[\mathbf{\Lambda}_e^*/\mu_2+\mathbf{I}_N]^{-1} & \mathbf{U}_{nv}\mathbf{\Lambda}_{nv}[\mathbf{\Lambda}_{nv}/\mu_2+\mathbf{I}_{nN}]^{-1} \\ \vdots & \vdots & \vdots \\ \mathbf{U}_e\mathbf{\Lambda}_e[\mathbf{\Lambda}_e/\mu_n+\mathbf{I}_N]^{-1} & \mathbf{U}_e^*\mathbf{\Lambda}_e^*[\mathbf{\Lambda}_e^*/\mu_n+\mathbf{I}_N]^{-1} & \mathbf{U}_{nv}\mathbf{\Lambda}_{nv}[\mathbf{\Lambda}_{nv}/\mu_n+\mathbf{I}_{nN}]^{-1} \end{bmatrix}. \tag{63}$$

This equation completely defines the structure of the right-modal matrix in the state space. Note that the right-modal matrix of a viscously damped system consists of only a $2N\times 2N$ block in the top left corner of this expression.

Now consider the left eigenvectors. Suppose

$$\psi_j=\begin{Bmatrix} \boldsymbol{p}_{1j} \\ \boldsymbol{p}_{2j} \\ \boldsymbol{x}_{1j} \\ \boldsymbol{x}_{2j} \\ \vdots \\ \boldsymbol{x}_{nj} \end{Bmatrix}. \tag{64}$$

Expanding Eq. (50) we get the following equations:

$$-\boldsymbol{p}_{2j}^T\mathbf{M}^{-1}\mathbf{K}=\lambda_j\boldsymbol{p}_{1j}^T, \tag{65}$$

$$\boldsymbol{p}_{1j}^T-\boldsymbol{p}_{2j}^T\mathbf{M}^{-1}\mathbf{D}+\sum_{k=1}^{n}\mu_k\boldsymbol{x}_{kj}^T=\lambda_j\boldsymbol{p}_{2j}^T, \tag{66}$$

$$\text{and}\quad -\boldsymbol{p}_{2j}^T\mathbf{M}^{-1}\mathbf{C}_k-\mu_k\boldsymbol{x}_{kj}^T=\lambda_j\boldsymbol{x}_{kj}^T,\quad \forall k=1,\ldots,n. \tag{67}$$

Multiplying Eq. (66) by λ_j and using Eq. (65) results in

$$-\boldsymbol{p}_{2j}^T\mathbf{M}^{-1}\mathbf{K}-\lambda_j\boldsymbol{p}_{2j}^T\mathbf{M}^{-1}\mathbf{D}+\lambda_j\sum_{k=1}^{n}\mu_k\boldsymbol{x}_{kj}^T=\lambda_j^2\boldsymbol{p}_{2j}^T. \tag{68}$$

Provided $\lambda_j\neq-\mu_k$, from Eq. (67) we further obtain

$$\boldsymbol{x}_{kj}^T=-\frac{1}{\mu_k+\lambda_j}\boldsymbol{p}_{2j}^T\mathbf{M}^{-1}\mathbf{C}_k. \tag{69}$$

Substituting $\boldsymbol{x}_{kj}^T$ from Eq. (69), Eq. (68) results in

$$\boldsymbol{p}_{2j}^T\mathbf{M}^{-1}\mathbf{K}+\lambda_j\boldsymbol{p}_{2j}^T\mathbf{M}^{-1}\mathbf{D}+\lambda_j\sum_{k=1}^{n}\frac{\mu_k}{\mu_k+\lambda_j}\boldsymbol{p}_{2j}^T\mathbf{M}^{-1}\mathbf{C}_k+\lambda_j^2\boldsymbol{p}_{2j}^T=\mathbf{0}^T \tag{70}$$

$$\text{or}\quad \boldsymbol{p}_{2j}^T\mathbf{M}^{-1}\left[\lambda_j^2\mathbf{M}+\lambda_j\mathbf{D}+\lambda_j\sum_{k=1}^{n}\frac{\mu_k}{\lambda_j+\mu_k}\mathbf{C}_k+\mathbf{K}\right]=\mathbf{0}^T. \tag{71}$$

Comparing Eq. (71) with Eq. (9) immediately results in

$$\boldsymbol{p}_{2j}^T\mathbf{M}^{-1}=\boldsymbol{v}_j^T \tag{72}$$

$$\text{or}\quad \boldsymbol{p}_{2j}=\ =\mathbf{M}^T\boldsymbol{v}_j. \tag{73}$$

Using Eqs. (72) and (65) one obtains

$$\boldsymbol{p}_{1j}=-\mathbf{K}^T\boldsymbol{v}_j/\lambda_j. \tag{74}$$

Similarly, using Eqs. (72) and (69) results in

$$\boldsymbol{x}_{kj}=-\frac{1}{\mu_k+\lambda_j}\mathbf{C}_k^T\boldsymbol{v}_j. \tag{75}$$

From Eqs. (73)–(75), the left eigenvectors in the state space given by Eq. (64) can be expressed as

$$\psi_j=\begin{Bmatrix} -\mathbf{K}^T v_j/\lambda_j \\ \mathbf{M}^T\boldsymbol{v}_j \\ -\mathbf{C}_1^T\boldsymbol{v}_j/(\mu_1+\lambda_j) \\ -\mathbf{C}_2^T\boldsymbol{v}_j/(\mu_2+\lambda_j) \\ \vdots \\ -\mathbf{C}_n^T\boldsymbol{v}_j/(\mu_n+\lambda_j) \end{Bmatrix}. \tag{76}$$

Recalling the partitions in Eqs. (10) and (12), for $j=1,2,\ldots,(2+n)N$, the matrix of left eigenvectors can be expressed as

$$\mathbf{\Psi}=\begin{bmatrix} -\mathbf{K}^T\mathbf{V}_e\mathbf{\Lambda}_e^{-1} & -\mathbf{K}^T\mathbf{V}_e^*\mathbf{\Lambda}_e^{*-1} & -\mathbf{K}^T\mathbf{V}_{nv}\mathbf{\Lambda}_{nv}^{-1} \\ \mathbf{M}^T\mathbf{V}_e & \mathbf{M}^T\mathbf{V}_e^* & \mathbf{M}^T\mathbf{V}_{nv} \\ -\mathbf{C}_1^T\mathbf{V}_e[\mathbf{\Lambda}_e+\mu_1\mathbf{I}_N]^{-1} & -\mathbf{C}_1^T\mathbf{V}_e^*[\mathbf{\Lambda}_e^*+\mu_1\mathbf{I}_N]^{-1} & -\mathbf{C}_1^T\mathbf{V}_{nv}[\mathbf{\Lambda}_{nv}+\mu_1\mathbf{I}_{nN}]^{-1} \\ -\mathbf{C}_2^T\mathbf{V}_e[\mathbf{\Lambda}_e+\mu_2\mathbf{I}_N]^{-1} & -\mathbf{C}_2^T\mathbf{V}_e^*[\mathbf{\Lambda}_e^*+\mu_2\mathbf{I}_N]^{-1} & -\mathbf{C}_2^T\mathbf{V}_{nv}[\mathbf{\Lambda}_{nv}+\mu_2\mathbf{I}_{nN}]^{-1} \\ \vdots & \vdots & \vdots \\ -\mathbf{C}_n^T\mathbf{V}_e[\mathbf{\Lambda}_e+\mu_n\mathbf{I}_N]^{-1} & -\mathbf{C}_n^T\mathbf{V}_e^*[\mathbf{\Lambda}_e^*+\mu_n\mathbf{I}_N]^{-1} & -\mathbf{C}_n^T\mathbf{V}_{nv}[\mathbf{\Lambda}_{nv}+\mu_n\mathbf{I}_{nN}]^{-1} \end{bmatrix}. \tag{77}$$

This equation completely defines the structure of the left-modal matrix in the extended state space. For viscously damped systems, the left-modal matrix consists of only $2N\times 2N$ block in the top left corner of this expression.

4.2 Case B: All $\mathbf{C}_k$ Matrices are Rank Deficient. The right and the left eigenvalue problems associated with Eq. (44) can be expressed as

$$\tilde{\mathbf{A}}\tilde{\phi}_j=\lambda_j\tilde{\phi}_j \tag{78}$$

$$\text{and}\quad \tilde{\psi}_j^T\tilde{\mathbf{A}}=\lambda_j\tilde{\psi}_j^T\quad j=1,2,\ldots,m, \tag{79}$$

where $\tilde{\boldsymbol{\phi}}_j\in\mathbb{C}^m$ and $\tilde{\boldsymbol{\psi}}_j\in\mathbb{C}^m$ are respectively the jth right and left eigenvectors and the order of the system m is defined in Eq. (48). Again we construct the modal matrices

$$\tilde{\mathbf{\Phi}}=[\tilde{\phi}_1,\tilde{\phi}_2,\ldots,\tilde{\phi}_m]\in\mathbb{C}^{m\times m} \tag{80}$$

$$\text{and}\quad \tilde{\mathbf{\Psi}}=[\tilde{\psi}_1,\tilde{\psi}_2,\ldots,\tilde{\psi}_m]\in\mathbb{C}^{m\times m}. \tag{81}$$

These modal matrices also satisfy the biorthogonality property defined in Eqs. (53) and (54).

4.2.1 The Structure of the Modal Matrices. From the definition of $\mathbf{z}(t)$ in Eq. (47), the right eigenvectors in the extended state space can be related to the right eigenvectors in the original space (9) by

$$\phi_j=\begin{Bmatrix} \boldsymbol{u}_j \\ \lambda_j \boldsymbol{u}_j \\ \tilde{\boldsymbol{y}}_{1_j} \\ \tilde{\boldsymbol{y}}_{2_j} \\ \vdots \\ \tilde{\boldsymbol{y}}_{n_j} \end{Bmatrix}, \tag{82}$$

where $\tilde{\boldsymbol{y}}_{1_j}\in\mathbb{C}^{r_1}$, $\tilde{\boldsymbol{y}}_{2_j}\in\mathbb{C}^{r_2},\ldots,\tilde{\boldsymbol{y}}_{n_j}\in\mathbb{C}^{r_n}$ are components of the jth eigenvector corresponding to the internal variables $\tilde{\mathbf{y}}_1(t),\tilde{\mathbf{y}}_2(t),\ldots,\tilde{\mathbf{y}}_n(t)$. From Eq. (37) we may obtain

$$\boldsymbol{y}_{k_j}=\boldsymbol{R}_k\tilde{\boldsymbol{y}}_{k_j}. \tag{83}$$

Premultiplying by $\mathbf{L}_k^T$ yields

$$\tilde{\boldsymbol{y}}_{k_j}=\mathbf{T}_k\boldsymbol{y}_{k_j}, \tag{84}$$

where $\mathbf{T}_k$ is defined in Eq. (43) and $\boldsymbol{y}_{k_j}$ is defined in Eq. (58). Substituting $\tilde{\boldsymbol{y}}_{k_j}$ in Eq. (82) for $j=1,2,\ldots,m$, the matrix of right eigenvectors in the extended state space can be obtained as

$$\tilde{\boldsymbol{\Phi}}=\begin{bmatrix} \mathbf{U}_e & \mathbf{U}_e^* & \mathbf{U}_{nv} \\ \mathbf{U}_e\boldsymbol{\Lambda}_e & \mathbf{U}_e^*\boldsymbol{\Lambda}_e^* & \mathbf{U}_{nv}\boldsymbol{\Lambda}_{nv} \\ \mathbf{T}_1\mathbf{U}_e\boldsymbol{\Lambda}_e[\boldsymbol{\Lambda}_e/\mu_1+\mathbf{I}_N]^{-1} & \mathbf{T}_1\mathbf{U}_e^*\boldsymbol{\Lambda}_e^*[\boldsymbol{\Lambda}_e^*/\mu_1+\mathbf{I}_N]^{-1} & \mathbf{T}_1\mathbf{U}_{nv}\boldsymbol{\Lambda}_{nv}[\boldsymbol{\Lambda}_{nv}/\mu_1+\mathbf{I}_{nN}]^{-1} \\ \mathbf{T}_2\mathbf{U}_e\boldsymbol{\Lambda}_e[\boldsymbol{\Lambda}_e/\mu_2+\mathbf{I}_N]^{-1} & \mathbf{T}_2\mathbf{U}_e^*\boldsymbol{\Lambda}_e^*[\boldsymbol{\Lambda}_e^*/\mu_2+\mathbf{I}_N]^{-1} & \mathbf{T}_2\mathbf{U}_{nv}\boldsymbol{\Lambda}_{nv}[\boldsymbol{\Lambda}_{nv}/\mu_2+\mathbf{I}_{nN}]^{-1} \\ \vdots & \vdots & \vdots \\ \mathbf{T}_n\mathbf{U}_e\boldsymbol{\Lambda}_e[\boldsymbol{\Lambda}_e/\mu_n+\mathbf{I}_N]^{-1} & \mathbf{T}_n\mathbf{U}_e^*\boldsymbol{\Lambda}_e^*[\boldsymbol{\Lambda}_e^*/\mu_n+\mathbf{I}_N]^{-1} & \mathbf{T}_n\mathbf{U}_{nv}\boldsymbol{\Lambda}_{nv}[\boldsymbol{\Lambda}_{nv}/\mu_n+\mathbf{I}_{nN}]^{-1} \end{bmatrix}. \tag{85}$$

Now consider the left eigenvectors. Suppose

$$\psi_j=\begin{Bmatrix} \mathbf{p}_{1_j} \\ \mathbf{p}_{2_j} \\ \tilde{\mathbf{x}}_{1_j} \\ \tilde{\mathbf{x}}_{2_j} \\ \vdots \\ \tilde{\mathbf{x}}_{n_j} \end{Bmatrix}. \tag{86}$$

Following the procedure outlined in the previous section, it can be shown that $\boldsymbol{p}_{2_j}$ and $\boldsymbol{p}_{1_j}$ are again given by Eqs. (73) and (74) while $\tilde{\boldsymbol{x}}_{k_j}$ is given by

$$\tilde{\mathbf{x}}_{k_j}=-\frac{1}{\mu_k+\lambda_j}\mathbf{R}_k^T\mathbf{C}_k^T\mathbf{v}_j\,. \tag{87}$$

Substituting $\tilde{\boldsymbol{x}}_{k_j}$ in Eq. (86) for $j=1,2,\ldots,m$, the matrix of left eigenvectors in the extended state space can be expressed as

$$\tilde{\boldsymbol{\Psi}}=\begin{bmatrix} -\mathbf{K}^T\mathbf{V}_e\boldsymbol{\Lambda}_e^{-1} & -\mathbf{K}^T\mathbf{V}_e^*\boldsymbol{\Lambda}_e^{*^{-1}} & -\mathbf{K}^T\mathbf{V}_{nv}\boldsymbol{\Lambda}_{nv}^{-1} \\ \mathbf{M}^T\mathbf{V}_e & \mathbf{M}^T\mathbf{V}_e^* & \mathbf{M}^T\mathbf{V}_{nv} \\ -\mathbf{R}_1^T\mathbf{C}_1^T\mathbf{V}_e[\boldsymbol{\Lambda}_e+\mu_1\mathbf{I}_N]^{-1} & -\mathbf{R}_1^T\mathbf{C}_1^T\mathbf{V}_e^*[\boldsymbol{\Lambda}_e^*+\mu_1\mathbf{I}_N]^{-1} & -\mathbf{R}_1^T\mathbf{C}_1^T\mathbf{V}_{nv}[\boldsymbol{\Lambda}_{nv}+\mu_1\mathbf{I}_{nN}]^{-1} \\ -\mathbf{R}_2^T\mathbf{C}_2^T\mathbf{V}_e[\boldsymbol{\Lambda}_e+\mu_2\mathbf{I}_N]^{-1} & -\mathbf{R}_2^T\mathbf{C}_2^T\mathbf{V}_e^*[\boldsymbol{\Lambda}_e^*+\mu_2\mathbf{I}_N]^{-1} & -\mathbf{R}_2^T\mathbf{C}_2^T\mathbf{V}_{nv}[\boldsymbol{\Lambda}_{nv}+\mu_2\mathbf{I}_{nN}]^{-1} \\ \vdots & \vdots & \vdots \\ -\mathbf{R}_n^T\mathbf{C}_n^T\mathbf{V}_e[\boldsymbol{\Lambda}_e+\mu_n\mathbf{I}_N]^{-1} & -\mathbf{R}_n^T\mathbf{C}_n^T\mathbf{V}_e^*[\boldsymbol{\Lambda}_e^*+\mu_n\mathbf{I}_N]^{-1} & -\mathbf{R}_n^T\mathbf{C}_n^T\mathbf{V}_{nv}[\boldsymbol{\Lambda}_{nv}+\mu_n\mathbf{I}_{nN}]^{-1} \end{bmatrix}. \tag{88}$$

The analysis presented here clarifies the structure of the modal matrices in the extended state space. The response to the system subjected to dynamic forces and initial conditions can be easily obtained by utilizing the biorthogonality of the left and the right eigenvectors (see the Appendix). In the next section the results derived here are illustrated by a numerical example.

5 Numerical Example

We consider a three-degree-of-freedom system with asymmetric coefficient matrices. The purpose of this example is to verify some of the mathematical expressions derived in this paper. The damping of the system is expressed as a sum of two exponential kernels. For this special case the equations of motion (1) reads

$$\mathbf{M}\ddot{\mathbf{u}}(t)+\int_0^t[\mu_1 e^{-\mu_1(t-\tau)}\mathbf{C}_1+\mu_2 e^{-\mu_2(t-\tau)}\mathbf{C}_2]\dot{\mathbf{u}}(\tau)\mathrm{d}\tau+\mathbf{K}\mathbf{u}(t)$$
$$=\mathbf{f}(t). \tag{89}$$

The mass and the stiffness matrices of the system are defined by

$$\mathbf{M}=\begin{bmatrix} 0.5740 & 1.3858 & 1.3858 \\ 0.7070 & 0.7070 & -0.7070 \\ 0.4620 & -0.1914 & -0.1914 \end{bmatrix} \tag{90}$$

and

$$\mathbf{K}=\begin{bmatrix} 1.3748 & 10.9440 & 25.2975 \\ 1.2625 & 2.8770 & -17.4195 \\ 0.7455 & -4.1244 & 0.8625 \end{bmatrix}. \tag{91}$$

Numerical values for the entries of **M** and **K** matrices are taken from Adhikari [21]. Note that these matrices are asymmetric and not positive definite. The damping coefficient matrices are given by

$$\mathbf{C}_1=\begin{bmatrix} 0.3588 & -1.3747 & -1.1471 \\ -0.3574 & 2.6618 & -2.1707 \\ 0.0210 & -1.4199 & 3.3674 \end{bmatrix} \tag{92}$$

and

$$\mathbf{C}_2=\begin{bmatrix} 1.1198 & 1.1915 & 1.1495 \\ 1.7641 & 1.8770 & 1.8109 \\ 0.6881 & 0.7321 & 0.7063 \end{bmatrix}. \tag{93}$$

Numerical values for the relaxation parameters are assumed to be

$$\mu_1=1.5 \quad \text{and} \quad \mu_2=0.1. \tag{94}$$

Both of the damping coefficient matrices have rank deficiencies because one can easily verify that

$$\tau_1=\operatorname{rank}(\mathbf{C}_1)=2\leqslant 3 \tag{95}$$

$$\text{and} \quad \tau_2=\operatorname{rank}(\mathbf{C}_2)=1\leqslant 3. \tag{96}$$

The order of the system matrix in the extended state space can be obtained from Eq. (48) as $m=2\times 3+(2+1)=9$ and the matrix itself can be obtained using the procedure described in Sec. 3.2. The transformation matrices $\mathbf{R}_k$ and $\mathbf{L}_k$ for $k=1,2$ given by Eqs. (34) and (35) are obtained as

$$\mathbf{R}_1=\begin{bmatrix} 0.0397 & -0.8274 \\ -0.7128 & 0.4356 \\ 0.7002 & 0.3545 \end{bmatrix}, \quad \mathbf{L}_1=\begin{bmatrix} 0.0497 & -0.1887 \\ -0.5719 & 0.6828 \\ 0.8188 & 0.7058 \end{bmatrix} \tag{97}$$

$$\text{and} \quad \mathbf{R}_2=\begin{bmatrix} 0.5091 \\ 0.8019 \\ 0.3128 \end{bmatrix}, \quad \mathbf{L}_2=\begin{bmatrix} 0.5603 \\ 0.5961 \\ 0.5751 \end{bmatrix}. \tag{98}$$

Using these, the system matrix in the extended state space in Eq. (45) is given by

$$\tilde{\mathbf{A}}=\begin{bmatrix} 0 & 0 & 0 & 1.0000 & 0 & 0 & 0 & 0 & 0 \\ 0 & 0 & 0 & 0 & 1.0000 & 0 & 0 & 0 & 0 \\ 0 & 0 & 0 & 0 & 0 & 1.0000 & 0 & 0 & 0 \\ -1.7281 & 4.8272 & -8.0485 & 0 & 0 & 0 & -6.2763 & -0.6986 & -2.6209 \\ -0.1670 & -9.3966 & 8.8830 & 0 & 0 & 0 & 6.7959 & 0.4790 & -0.9270 \\ -0.1093 & -0.5001 & -23.8041 & 0 & 0 & 0 & -4.3340 & 0.7501 & 0.6523 \\ 0 & 0 & 0 & 0.0759 & -0.8728 & 1.2494 & -1.5000 & 0 & 0 \\ 0 & 0 & 0 & -0.4021 & 1.4554 & 1.5044 & 0 & -1.5000 & 0 \\ 0 & 0 & 0 & 0.0594 & 0.0632 & 0.0610 & 0 & 0 & -0.1000 \end{bmatrix} \tag{99}$$

The nine eigenvalues of the system are arranged according to Eq. (10). The diagonal matrices containing the eigenvalues are given by

$$\begin{aligned} \mathbf{\Lambda}_e=\operatorname{diag}[&0.0217+1.4060i, \quad 0.0371+3.1929i, \\ &-0.2359+5.6940i] \end{aligned} \tag{100}$$

$$\text{and} \quad \mathbf{\Lambda}_{nv}=\operatorname{diag}[-0.0905, \quad -0.8755, \quad -1.7798]. \tag{101}$$

Note that the eigenvalues corresponding to the nonviscous modes are purely real and negative. The right and the left eigenvector matrices corresponding to these eigenvalues are obtained as

$$\tilde{\mathbf{\Phi}}=\begin{bmatrix} 0.0088-0.5690i & 0.0070+0.1364i & 0.0020-0.0866i & 0.0088+0.5690i & 0.0070-0.1364i & 0.0020+0.0866i & 0.8662 & 0.3905 & -0.1046 \\ -0.0029+0.0147i & 0.0026-0.2245i & -0.0017+0.1015i & -0.0029-0.0147i & 0.0026+0.2245i & -0.0017-0.1015i & 0.0171 & -0.2630 & 0.0428 \\ -0.0082+0.0102i & 0.0209-0.0531i & -0.0043-0.1030i & -0.0082-0.0102i & 0.0209+0.0531i & -0.0043+0.1030i & -0.0168 & 0.1207 & 0.0320 \\ 0.8002+0.0000i & -0.4353+0.0275i & 0.4925+0.0317i & 0.8002-0.0000i & -0.4353-0.0275i & 0.4925-0.0317i & -0.0784 & -0.3419 & 0.1861 \\ -0.0207-0.0037i & 0.7169+0.0000i & -0.5774-0.0338i & -0.0207+0.0037i & 0.7169-0.0000i & -0.5774+0.0338i & -0.0015 & 0.2302 & -0.0762 \\ -0.0146-0.0114i & 0.1702+0.0646i & 0.5872+0.0000i & -0.0146+0.0114i & 0.1702-0.0646i & 0.5872-0.0000i & 0.0015 & -0.1057 & -0.0570 \\ 0.0179-0.0238i & -0.0335+0.1236i & 0.0527-0.2122i & 0.0179+0.0238i & -0.0335-0.1236i & 0.0527+0.2122i & -0.0019 & -0.5748 & -0.0338 \\ -0.1399+0.1145i & 0.2024-0.3644i & -0.0161+0.0236i & -0.1399-0.1145i & 0.2024+0.3644i & -0.0161-0.0236i & 0.0224 & 0.5021 & 0.9702 \\ 0.0021-0.0321i & 0.0021-0.0093i & -0.0002-0.0050i & 0.0021+0.0321i & 0.0021+0.0093i & -0.0002+0.0050i & -0.4923 & 0.0157 & -0.0016 \end{bmatrix} \tag{102}$$

and

$$\tilde{\boldsymbol{\Psi}}=\begin{bmatrix} 0.0001+0.8070i & -0.0033+0.0672i & 0.0020+0.0129i & 0.0001-0.8070i & -0.0033-0.0672i & 0.0020-0.0129i & 0.1088 & 0.0407 & 0.1185 \\ 0.0193+0.5788i & 0.1252+1.7383i & 0.0302-0.2378i & 0.0193-0.5788i & 0.1252-1.7383i & 0.0302+0.2378i & 0.1130 & -0.8364 & -0.7962 \\ 0.4716-0.7060i & -0.1955+2.4606i & 0.3681+3.1361i & 0.4716+0.7060i & -0.1955-2.4606i & 0.3681-3.1361i & 0.1211 & 1.4596 & -2.3903 \\ 0.6231-0.0078i & 0.0344+0.0088i & 0.0159+0.0013i & 0.6231+0.0078i & 0.0344-0.0088i & 0.0159-0.0013i & 0.0053 & 0.0257 & 0.1441 \\ 0.4119-0.0068i & 0.5793-0.0450i & -0.1716-0.0202i & 0.4119+0.0068i & 0.5793+0.0450i & -0.1716+0.0202i & 0.0038 & -0.0658 & -0.0634 \\ -0.0991-0.0271i & 0.5349+0.0026i & 0.6844-0.0649i & -0.0991+0.0271i & 0.5349-0.0026i & 0.6844+0.0649i & 0.0001 & 0.0204 & -0.2511 \\ -0.2023+0.2660i & 0.0770-0.4024i & -0.1344+0.7134i & -0.2023-02660i & 0.0770+0.4024i & -0.1344-0.7134i & -0.0056 & -1.1162 & 0.8826 \\ -0.1167+0.0959i & 0.0736-0.1696i & 0.0057-0.0725i & -0.1167-0.0959i & 0.0736+0.1696i & 0.0057+0.0725i & -0.0013 & -0.0547 & 1.1414 \\ -0.1207+1.4685i & 0.0026+0.0872i & -0.0071-0.0988i & -0.1207-1.4685i & 0.0026-0.0872i & -0.0071+0.0988i & -1.8409 & -0.0090 & 0.2873 \end{bmatrix}. \tag{103}$$

The eigenvectors are normalized so that $\tilde{\boldsymbol{\Psi}}^T\tilde{\boldsymbol{\Phi}}$ is an identity matrix. However, it should be noted that this normalization does not make the eigenvectors unique.

In view of Eq. (85), the right-eigenvector matrix corresponding to the elastic modes in the space of the original variables, $\mathbf{U}_e$, can be obtained directly by taking a 3×3 block in the top left corner of Eq. (102):

$$\mathbf{U}_e=\begin{bmatrix} 0.0088-0.5690i & 0.0070+0.1364i & 0.0020-0.0866i \\ -0.0029+0.0147i & 0.0026-0.2245i & -0.0017+0.1015i \\ -0.0082+0.0102i & 0.0209-0.0531i & -0.0043-0.1030i \end{bmatrix}. \tag{104}$$

Similarly $\mathbf{U}_{nv}$ can be obtained by taking first three rows and last three columns of Eq. (102):

$$\mathbf{U}_{nv}=\begin{bmatrix} 0.8662 & 0.3905 & -0.1046 \\ 0.0171 & -0.2630 & 0.0428 \\ -0.0168 & 0.1207 & 0.0320 \end{bmatrix}. \tag{105}$$

Now consider the left eigenvectors. Because it is assumed that $\mathbf{M}^{-1}$ exists, from the blocks (2,1) and (2,3) of Eq. (88), $\mathbf{V}_e$ and $\mathbf{V}_{nv}$ can be obtained. So, from the corresponding blocks in Eq. (103) we obtain

$$\mathbf{V}_e=\begin{bmatrix} 0.1901-0.0150i & 0.3462-0.0047i & 0.2712-0.0316i \\ 0.3614+0.0144i & 0.0314-0.0337i & -0.6054+0.0317i \\ 0.5594-0.0202i & -0.4039+0.0765i & 0.6239-0.0065i \end{bmatrix} \tag{106}$$

$$\text{and}\quad \mathbf{V}_{nv}=\begin{bmatrix} 0.0021 & 0.0036 & -0.0840 \\ 0.0026 & -0.0610 & 0.1327 \\ 0.0049 & 0.1445 & 0.2131 \end{bmatrix}. \tag{107}$$

As mentioned before, $\mathbf{U}_{nv}$ and $\mathbf{V}_{nv}$ turned out to be real matrices. This is expected because the eigenvalues corresponding to these modes (the nonviscous modes) are purely real.

Using these numerical values one can easily verify Eqs. (85) and (88). A typical case for block (3,2) in Eq. (88) is considered here. Using the numerical values given by Eqs. (92), (94), (97), (100), and (106) one obtains

$$-\mathbf{R}_1^T\mathbf{C}_1^T\mathbf{V}_e^*[\boldsymbol{\Lambda}_e^*+\mu_1\mathbf{I}_3]^{-1}=\begin{bmatrix} -0.2023-0.2660i & 0.0770+0.4024i & -0.1344-0.7134i \\ -0.1167-0.0959i & 0.0736+0.1696i & 0.0057+0.0725i \end{bmatrix}. \tag{108}$$

These values can be exactly identified in $\tilde{\boldsymbol{\Psi}}_{ij}$ given by Eq. (103) for $i=7,8$ and $j=4,5,6$, which corresponds to block (3,2) in Eq. (88). This illustrates the relationship between the modal matrices in the extended state space and the modal matrices in the original N space.

6 Conclusions

Linear vibration of multiple-degree-of-freedom damped systems with combined viscous damping and exponentially fading damping memory kernels has been considered. It has been assumed that in general, the mass, the stiffness and the damping coefficient matrices are neither symmetric nor positive definite. An extended state-space method based on a set of internal variables has been proposed. Two physically realistic cases, namely (a) when all the damping coefficient matrices are of full rank, and (b) when the damping coefficient matrices are rank deficient, have been presented. It was shown that for both the cases the equation of motion in the extended state space can be represented in terms of a single asymmetric matrix of higher dimension. The dimension of this matrix depends on the rank of the damping coefficient matrices. The eigenvalues and the corresponding eigenvectors of the system were obtained by solving the standard eigenvalue problem in the state space.

Closed-form exact relationships relating the modal matrices in the extended state space and the modal matrices in the original space have been derived. All the entries of the modal matrices in the extended state space can be represented in terms of the eigenvalues, the systems matrices, and the modal matrices in the original space. It is expected that these results will be useful to understand the nature of the eigensolutions of nonviscously damped systems.

Appendix A: Dynamic Response of Asymmetric Nonviscously Damped Systems

In this section the dynamic response of the system will be obtained by using the mode superposition method, commonly employed for undamped or proportionally damped systems. We begin by assuming that all the initial conditions are zero. Taking the Laplace transform of Eqs. (24) or (44) one obtains

$$s\overline{\mathbf{z}}(s)=\boldsymbol{\mathcal{A}}\overline{\mathbf{z}}(s)+\overline{\mathbf{r}}(s), \tag{109}$$

where the system matrix $\boldsymbol{\mathcal{A}}$ is given by Eqs. (25) or (45), depending on the ranks of the $\mathbf{C}_k$ matrices. Similarly $\overline{\mathbf{z}}(s)$ and $\overline{\mathbf{r}}(s)$ are the Laplace transforms of $\mathbf{z}(t)$ and $\mathbf{r}(t)$ or $\tilde{\mathbf{z}}(t)$ and $\tilde{\mathbf{r}}(t)$, respectively. Using the modal transformation

$$\overline{\mathbf{z}}(s)=\mathbf{\Phi}\overline{\mathbf{q}}(s) \tag{110}$$

and the orthogonality relationships (53) and (54), we obtain

$$(s\mathbf{I}-\mathbf{\Lambda})\overline{\mathbf{q}}(s)=\mathbf{\Psi}^T\overline{\mathbf{r}}(s) \quad \text{or} \quad \overline{\mathbf{q}}(s)=(s\mathbf{I}-\mathbf{\Lambda})^{-1}\mathbf{\Psi}^T\overline{\mathbf{r}}(s). \tag{111}$$

Substitution of $\overline{\mathbf{q}}(s)$ from the preceding equation in Eq. (110) results in

$$\overline{\mathbf{z}}(s)=\mathbf{\Phi}(s\mathbf{I}-\mathbf{\Lambda})^{-1}\mathbf{\Psi}^T\overline{\mathbf{r}}(s)=\sum_{j=1}^{m}\frac{\phi_j\psi_j^T}{s-\lambda_j}\overline{\mathbf{r}}(s). \tag{112}$$

Using the expression of $\boldsymbol{\psi}_j$ in Eq. (64) and recalling that only $N+1$ to $2N$ rows of $\overline{\mathbf{r}}(s)$ is nonzero, one has

$$\boldsymbol{\psi}_j^T\overline{\mathbf{r}}(s)=\boldsymbol{p}_{2j}^T\mathbf{M}^{-1}\overline{\mathbf{f}}(s). \tag{113}$$

Substituting p_{2j} from Eq. (73), Eq. (112) can be rewritten as

$$\overline{\mathbf{z}}(s)=\sum_{j=1}^{m}\frac{\boldsymbol{v}_j^T\overline{\mathbf{f}}(s)}{s-\lambda_j}\boldsymbol{\phi}_j. \tag{114}$$

Taking only the first N rows of Eq. (114) and using Eq. (55) one obtains the displacement response

$$\overline{\mathbf{u}}(s)=\sum_{j=1}^{m}\frac{\boldsymbol{v}_j^T\overline{\mathbf{f}}(s)}{s-\lambda_j}\boldsymbol{u}_j. \tag{115}$$

In view of the partitions (10)–(12), the preceding expression can be conveniently expressed as

$$\overline{\mathbf{u}}(s)=\sum_{j=1}^{N}\left[\frac{\boldsymbol{v}_j^T\overline{\mathbf{f}}(s)}{s-\lambda_j}\boldsymbol{u}_j+\frac{\boldsymbol{v}_j^{*T}\overline{\mathbf{f}}(s)}{s-\lambda_j^*}\boldsymbol{u}_j^*\right]+\sum_{j=2N+1}^{m}\frac{\boldsymbol{v}_{nv_j}^T\overline{\mathbf{f}}(s)}{s-\lambda_{nv_j}}\boldsymbol{u}_{nv_j}. \tag{116}$$

This expression of the dynamic response is in terms of the left and the right eigenvectors of the system in N space. The second part of Eq. (116) is the contribution of the nonviscous modes to the global dynamic response. This part is not present for viscously damped systems and consequently the response of a viscously damped system can be obtained only form the first part of the right-hand side of Eq. (116). In the presence of nonzero initial conditions the vector $\overline{\mathbf{f}}(s)$ needs to be replaced by $\overline{\mathbf{p}}(s)$ defined in Eq. (6). Therefore the dynamic response with nonzero initial conditions can be expressed as

$$\overline{\mathbf{u}}(s)=\sum_{j=1}^{m}\frac{1}{s-\lambda_j}\left(\boldsymbol{v}_j^T\overline{\mathbf{f}}(s)+\boldsymbol{v}_j^T\mathbf{M}\dot{\mathbf{u}}_0+\boldsymbol{v}_j^T\mathbf{D}\mathbf{u}_0+s\boldsymbol{v}_j^T\mathbf{M}\mathbf{u}_0+\sum_{k=1}^{n}\mu_k\frac{\boldsymbol{v}_j^T\mathbf{C}_k\mathbf{u}_0}{s+\mu_k}\right)\boldsymbol{u}_j. \tag{117}$$

In the time domain the response can be obtained by taking the inverse Laplace transform of Eq. (117):

$$\begin{aligned}\mathbf{u}(t)&=\mathcal{L}^{-1}[\overline{\mathbf{u}}(s)]\\&=\mathcal{L}^{-1}\left[\sum_{j=1}^{m}\frac{1}{s-\lambda_j}\left(\boldsymbol{v}_j^T\overline{\mathbf{f}}(s)+\sum_{k=1}^{n}\frac{1}{s+\mu_k}\mu_k(\boldsymbol{v}_j^T\mathbf{C}_k\mathbf{u}_0)\right)+\frac{\boldsymbol{v}_j^T\mathbf{M}\dot{\mathbf{u}}_0+\boldsymbol{v}_j^T\mathbf{D}\mathbf{u}_0}{s-\lambda_j}+\left(\frac{s}{s-\lambda_j}\right)\boldsymbol{v}_j^T\mathbf{M}\mathbf{u}_0\right]\boldsymbol{u}_j\\&=\sum_{j=1}^{m}\left(\int_0^t e^{\lambda_j(t-\tau)}\boldsymbol{v}_j^T\mathbf{f}(\tau)d\tau+\sum_{k=1}^{n}\int_0^t\mu_k e^{\lambda_j t-(\lambda_j+\mu_k)\tau}\boldsymbol{v}_j^T\mathbf{C}_k\mathbf{u}_0 d\tau\right)\boldsymbol{u}_j+e^{\lambda_j t}(\boldsymbol{v}_j^T\mathbf{M}\dot{\mathbf{u}}_0\\&\quad+\boldsymbol{v}_j^T\mathbf{D}\mathbf{u}_0)\boldsymbol{u}_j+\{\lambda_j e^{\lambda_j t}+\delta(t)\}(\boldsymbol{v}_j^T\mathbf{M}\mathbf{u}_0)\boldsymbol{u}_j.\end{aligned} \tag{118}$$

For $t>0$ the preceding equation may be rewritten as

$$\mathbf{u}(t)=\sum_{j=1}^{m}\left\{\int_0^t e^{\lambda_j(t-\tau)}\boldsymbol{v}_j^T\mathbf{f}(\tau)d\tau+a_j(t)\right\}\boldsymbol{u}_j, \tag{119}$$

$$\text{where}\quad a_j(t)=e^{\lambda_j t}(\boldsymbol{v}_j^T\mathbf{M}\dot{\mathbf{u}}_0+\boldsymbol{v}_j^T\mathbf{D}\mathbf{u}_0)+\lambda_j e^{\lambda_j t}(\boldsymbol{v}_j^T\mathbf{M}\mathbf{u}_0)+\sum_{k=1}^{n}\mu_k\frac{(e^{\lambda_j t}-e^{-\mu_k t})}{\lambda_j+\mu_k}\boldsymbol{v}_j^T\mathbf{C}_k\mathbf{u}_0. \tag{120}$$

It is interesting to note that the expression of $a_j(t)$ is independent of the ranks of the $\mathbf{C}_k$ matrices. The ranks of the $\mathbf{C}_k$ matrices only effect the number of terms (m) to be added in Eq. (119) to obtain $\mathbf{u}(t)$.

References

[1] Biot, M. A., 1958, "Linear Thermodynamics and the Mechanics of Solids," *Proceedings of the Third U.S. National Congress on Applied Mechanics*, ASME, New York.
[2] Woodhouse, J., 1998, "Linear Damping Models for Structural Vibration," J. Sound Vib., **215**, pp. 547–569.
[3] Adhikari, S., 2002, "Dynamics of Non-Viscously Damped Linear Systems," J. Eng. Mech., **128**, pp. 328–339.
[4] Cremer, L., and Heckl, M., 1973, *Structure-Borne Sound*, second edition, Springer-Verlag, Berlin, Germany, translated by E. E. Ungar.
[5] Muravyov, A., 1997, "Analytical Solutions in the Time Domain for Vibration Problems of Discrete Viscoelastic Systems," J. Sound Vib., **199**, pp. 337–348.
[6] Muravyov, A., 1998, "Forced Vibration Responses of a Viscoelastic Structure," J. Sound Vib., **218**, pp. 892–907.
[7] Muravyov, A., and Hutton, S. G., 1997, "Closed-Form Solutions and the Eigenvalue Problem for Vibration of Discrete Viscoelastic Systems," ASME J. Appl. Mech., **64**, pp. 684–691.
[8] Muravyov, A., and Hutton, S. G., 1998, "Free Vibration Response Characteristics of a Simple Elasto-Hereditary System," ASME J. Vibr. Acoust., **120**, pp. 628–632.
[9] Wagner, N., and Adhikari, S., 2003, "Symmetric State-Space Formulation for a Class of Non-Viscously Damped Systems" Vol. 41, No. 5, pp. 951–956.
[10] Inman, D. J., 1983, "Dynamics of Asymmetric Non-Conservative Systems," ASME J. Appl. Mech., **50**, pp. 199–203.
[11] Adhikari, S., 2000, "On Symmetrizable Systems of Second Kind," ASME J. Appl. Mech., **67**, pp. 797–802.
[12] Adhikari, S., 2001, "Classical Normal Modes in Non-Viscously Damped Linear Systems," AIAA J., **39**, pp. 978–980.
[13] Bagley, R. L., and Torvik, P. J., 1983, "Fractional Calculus—A Different Approach to the Analysis of Viscoelastically Damped Structures," AIAA J., **21**, pp. 741–748.
[14] Golla, D. F., and Hughes, P. C., 1985, "Dynamics of Viscoelastic Structures—A Time Domain Finite Element Formulation," ASME J. Appl. Mech., **52**, pp. 897–906.
[15] McTavish, D. J., and Hughes, P. C., 1993, "Modeling of Linear Viscoelastic Space Structures," ASME J. Vibr. Acoust., **115**, pp. 103–110.
[16] Wagner, N., 2001, "Ein Direktes Verfahren zur Numerischen Lösung von Schwingungssystemen mit Nachlassendem Gedächtnis," Z. Angew. Math. Mech., **81**, pp. S 327–328.
[17] Adhikari, S., 2001, "Eigenrelations for Non-Viscously Damped Systems," AIAA J., **39**, pp. 1624–1630.
[18] Bishop, R. E. D., and Price, W. G., 1979, "An Investigation into the Linear Theory of Ship Response to Waves," J. Sound Vib., **62(3)**, pp. 353–363.
[19] Newland, D. E., 1987, "On the Modal Analysis of Nonconservative Linear Systems," J. Sound Vib., **112**, pp. 69–96.
[20] Newland, D. E., 1989, *Mechanical Vibration Analysis and Computation*, Longman, Harlow and John Wiley, New York.
[21] Adhikari, S., 1999, "Modal analysis of linear asymmetric non-conservative systems," J. Eng. Mech., **125**(12), pp. 1372–1379.

Transient Growth Before Coupled-Mode Flutter

P. J. Schmid[1]

E. de Langre

Laboratoire d'Hydrodynamique (LadHyX),
Ecole Polytechnique,
F-91128 Palaiseau, France

Transient growth of energy is known to occur even in stable dynamical systems due to the non-normality of the underlying linear operator. This has been the object of growing attention in the field of hydrodynamic stability, where linearly stable flows may be found to be strongly nonlinearly unstable as a consequence of transient growth. We apply these concepts to the generic case of coupled-mode flutter, which is a mechanism with important applications in the field of fluid-structure interactions. Using numerical and analytical approaches on a simple system with two degrees-of-freedom and antisymmetric coupling we show that the energy of such a system may grow by a factor of more than 10, before the threshold of coupled-mode flutter is crossed. This growth is a simple consequence of the nonorthogonality of modes arising from the nonconservative forces. These general results are then applied to three cases in the field of flow-induced vibrations: (a) panel flutter (two-degrees-of-freedom model, as used by Dowell) (b) follower force (two-degrees-of-freedom model, as used by Bamberger) and (c) fluid-conveying pipes (two-degree-of-freedom model, as used by Benjamin and Païdoussis) for different mass ratios. For these three cases we show that the magnitude of transient growth of mechanical energy before the onset of coupled-mode flutter is substantial enough to cause a significant discrepancy between the apparent threshold of instability and the one predicted by linear stability theory. [DOI: 10.1115/1.1631591]

1 Introduction

Flow-induced vibration phenomena are a ubiquitous feature in numerous engineering applications ranging from buffeting of airfoils to deformation of building structures and bridges under wind loads. In most cases, these vibrations are undesirable, causing material fatigue at best and catastrophic failure at worst. It is thus not surprising that a substantial body of literature is devoted to the analysis and control of flow-induced instabilities. Low-dimensional models are often used to approximate prohibitively complex systems, and the critical parameters for the onset of flutter are computed for a moderate number of degrees-of-freedom. The analysis follows a typical modal approach where the temporal motion of the structure is assumed to behave exponentially in time. In the very common mechanism of coupled-mode flutter two (or more) purely oscillatory states merge and produce exponentially growing (and decaying) motion. For parameter values below this critical one, it is believed that stable motion prevails.

A similar argument has been used for the onset of transition to turbulence: As exponentially growing solutions of the linearized fluids equations are encountered, the transition to turbulent fluid motion is expected. In recent years, however, it has been discovered that short-term instabilities are present even at subcritical parameter values, and that these type of instabilities are a consequence of the nature of the underlying stability equations (see, e.g., [1–4]).

The equations governing many cases of fluid-structure interactions are also of this type, and it therefore appears likely that the governing equations support transiently growing solutions for parameter values below the critical one for the onset of coupled-mode flutter. If this transient growth is sufficiently large, finite-amplitude effects can be triggered even though infinitesimal motion is asymptotically stable.

It is the goal of this study to explore the potential of short-term energy growth at subcritical conditions for simple two-degrees-of-freedom approximations to technologically relevant configurations.

The organization of the paper is as follows. We will first consider a simple undamped two-degrees-of-freedom model of coupled-mode flutter and establish the mathematical framework for stability calculations. Modal and nonmodal stability will be considered, and asymptotic scalings as well as upper bounds on disturbance growth will be presented. Effects of damping on the stability characteristics will be treated as well. Three classical applications then follow, namely, panel flutter, [5], follower-force, [6], and fluid-conveying pipes, [7], which will further exemplify the techniques of the previous sections. Summarizing comments conclude this paper.

2 Theoretical Framework

2.1 General Undamped Two-Degrees-of-Freedom System

Many problems involving fluid-structure interactions can be modeled by a coupled system of oscillators of the form

$$\ddot{x}+x=ay \tag{1a}$$

$$\ddot{y}+\Omega^2 y=-ax \tag{1b}$$

describing the temporal evolution of the two degrees-of-freedom x and y. The left-hand side describes harmonic oscillators of frequencies 1 and Ω, while the right-hand side accounts for the coupling of the two oscillators with a as the coupling coefficient. Systems of this form often arise when equations governing the continuous deformation of flexible structures are approximated by a model capturing the two modes of deflection. This typically applies to problems such as flutter of flexible airfoils, fluidelastic instability of tube arrays in cross flow or unstable whirl of rotating shafts in confined fluids (see, for instance, [5,8,9]).

Traditional stability analysis of the above system is straightforward and leads to a critical coupling coefficient a_c of

[1]Permanent address: Department of Applied Mathematics, University of Washington, Box 352420, Seattle, WA 98195-2420.

Contributed by the Applied Mechanics Division of THE AMERICAN SOCIETY OF MECHANICAL ENGINEERS for publication in the ASME JOURNAL OF APPLIED MECHANICS. Manuscript received by the ASME Applied Mechanics Division, August 13, 2002; final revision, June 12, 2003. Associate Editor: A. A. Ferri. Discussion on the paper should be addressed to the Editor, Prof. Robert M. McMeeking, Department of Mechanical and Environmental Engineering, University of California–Santa Barbara, Santa Barbara, CA 93106-5070, and will be accepted until four months after final publication of the paper itself in the ASME JOURNAL OF APPLIED MECHANICS.

$$a_c = \frac{\Omega^2 - 1}{2}. \tag{2}$$

For two oscillators with a supercritical coupling coefficient exponentially growing solutions are encountered. For coupling coefficients below the critical one, we observe purely oscillatory behavior. The above critical coupling coefficient is a widely used and accepted tool for determining the onset of unstable motion. It is commonly believed that for coupling coefficients below the critical one no amplification of infinitesimal disturbances is possible.

2.2 Transient Amplification of Disturbance Energy. The goal of this manuscript is to explore the potential for short-term linear instabilities in the absence of exponentially growing solutions. To this end we treat the above system of equations as a general initial value problem of the form

$$\frac{d}{dt}\begin{pmatrix} x \\ \dot{x} \\ y \\ \dot{y} \end{pmatrix} = \begin{pmatrix} 0 & 1 & 0 & 0 \\ -1 & 0 & a & 0 \\ 0 & 0 & 0 & 1 \\ -a & 0 & -\Omega^2 & 0 \end{pmatrix} \begin{pmatrix} x \\ \dot{x} \\ y \\ \dot{y} \end{pmatrix} \quad \text{or} \quad \frac{d}{dt}\mathbf{q} = \mathbf{A}\mathbf{q}. \tag{3}$$

The formal solution of this initial value problem can be written in terms of the matrix exponential of $\mathbf{A}$. We obtain

$$\mathbf{q}(t) = \exp(t\mathbf{A})\mathbf{q}_0 \tag{4}$$

with $\mathbf{q}_0$ as the vector of initial conditions x_0, $\dot{x}_0$, y_0, and $\dot{y}_0$. Using this formulation, we wish to compute the amplification of disturbances by determining the ratio of the disturbance energy at a given time t to the initial energy of a general perturbation. Maximizing this ratio over all possible initial conditions results in the largest possible amplification of initial perturbations over a time span $[0\ t]$. Mathematically, we define the largest possible energy amplification $G(t)$ as

$$G(t) = \max_{\mathbf{q}_0} \frac{E(t)}{E(0)} = \max_{\mathbf{q}_0} \frac{\|\mathbf{q}(t)\|^2}{\|\mathbf{q}_0\|^2} = \max_{\mathbf{q}_0} \frac{\|\exp(t\mathbf{A})\mathbf{q}_0\|^2}{\|\mathbf{q}_0\|^2} = \|\exp(t\mathbf{A})\|^2 \tag{5}$$

where we have assumed that taking the norm of the state vector $\mathbf{q}$ is equivalent to computing the energy of the state vector. We therefore define

$$\|\mathbf{q}\|^2 = x^2 + \dot{x}^2 + \Omega^2 y^2 + \dot{y}^2 \tag{6}$$

which is easily related to the standard L_2-norm $\|\cdot\|_2$ by introducing weight matrices $\mathbf{F}$ according to

$$\|\mathbf{q}\|^2 = \|\mathbf{F}\mathbf{q}\|_2^2 \quad \mathbf{F} = \begin{pmatrix} 1 & 0 & 0 & 0 \\ 0 & 1 & 0 & 0 \\ 0 & 0 & \Omega & 0 \\ 0 & 0 & 0 & 1 \end{pmatrix}. \tag{7}$$

Reformulating the energy amplification $G(t)$ in terms of the L_2-norm results in

$$G(t) = \|\mathbf{F}\exp(t\mathbf{A})\mathbf{F}^{-1}\|_2^2. \tag{8}$$

It is often desirable to bound the maximum amplification of energy. Using the definition of the energy amplification it is straightforward to derive lower and upper bounds as follows:

$$\exp(2\lambda t) \leqslant G(t) = \|\mathbf{S}\exp(\Lambda t)\mathbf{S}^{-1}\|^2 \leqslant \kappa^2(\mathbf{S})\exp(2\lambda t) \tag{9}$$

where λ is the real part of the least stable eigenvalue of $\mathbf{A}$, and $\mathbf{S}$ denotes the 4×4 matrix of normalized eigenvectors of $\mathbf{A}$. The symbol

$$\kappa(\mathbf{S}) \equiv \|\mathbf{S}\|\|\mathbf{S}^{-1}\| \tag{10}$$

stands for the condition number of $\mathbf{S}$, and Λ is a diagonal 4×4 matrix containing the eigenvalues of $\mathbf{A}$.

We notice the following relation. For systems with $\kappa(\mathbf{S}) = 1$ the upper and lower bound coincide, and the temporal evolution of G is entirely governed by the real part of the least stable eigenvalue. Systems with $\kappa(\mathbf{S}) = 1$ are known as *normal* systems. On the other hand, if $\kappa(\mathbf{S})$ is larger than 1, the discrepancy between lower and upper bound allows for short-term effects before the exponential behavior governed by λ prevails as $t\to\infty$. Systems with $\kappa(\mathbf{S}) > 1$ are categorized as *non-normal* systems. Non-normal systems have a set of nonorthogonal eigenvectors and the source of short-term energy growth lies in this nonorthogonality of the system's eigenvectors. Even under subcritical conditions, i.e., for coupling coefficients below the critical one, a nonorthogonal superposition of exponentially decaying eigensolutions can lead to substantial disturbance growth.

2.3 Asymptotic Scalings. To further probe the solution behavior as we approach the critical coupling coefficient a_c we Laplace transform the governing equations to obtain

$$(p^2+1)X - aY = px_0 + \dot{x}_0 \tag{11a}$$

$$(p^2+\Omega^2)Y - aX = py_0 + \dot{y}_0 \tag{11b}$$

with $X(p)$ and $Y(p)$ as the Laplace transform of the dependent variables $x(t)$ and $y(t)$, respectively. Solving for $X(p)$ we obtain the expression

$$X(p) = \frac{1}{(p^2+1)(p^2+\Omega^2)+a^2}[A + pB + p^2C + p^3D] \tag{12}$$

with A, B, C, and D determined from the initial conditions. An analogous expression can be derived for $Y(p)$. After inversion of the Laplace transform we get the following expression for the variable $x(t)$:

$$x(t) = \frac{1}{2a_c\sqrt{1-(a/a_c)^2}}[A'\cos\alpha t + B'\sin\alpha t + C'\cos\beta t + D'\sin\beta t] \tag{13}$$

where

$$\alpha^2, \beta^2 = \frac{1}{2}(1 + \Omega^2 \pm \sqrt{(\Omega^2-1)^2 - 4a^2}) \tag{14}$$

and A', B', C', and D' depend on initial conditions. This last expression yields the behavior of $x(t)$ as the critical coupling coefficient is approached. We obtain

$$x(t) \sim \frac{1}{\sqrt{1-(a/a_c)^2}}. \tag{15}$$

The same holds true for $\dot{x}(t)$, $y(t)$, and $\dot{y}(t)$. Consequently, the energy E of the coupled oscillators is expected to behave as

$$E \sim \frac{1}{1-(a/a_c)^2} \tag{16}$$

as the stability boundary is approached, when time is fixed.

2.4 Numerical Results. The quantity $G(t)$, computed from Eq. (8), represents the maximum possible energy amplification, which for each instant in time is optimized over all possible initial conditions of unit energy, as is apparent from Eq. (5). The specific initial condition that achieves an amplification of $G(t)$ may be different for different times, and $G(t)$ should be thought of as the envelope of the energy evolution of individual initial conditions of unit energy. The energy amplification $G(t)$ for the undamped general system with $\Omega^2 = 1.1$ and $a/a_c = 0.9$ is shown in Fig. 1(*a*) together with the energy evolution of four randomly chosen initial conditions of unit energy. We notice an amplification of energy of nearly twenty times the initial energy after approximately 150

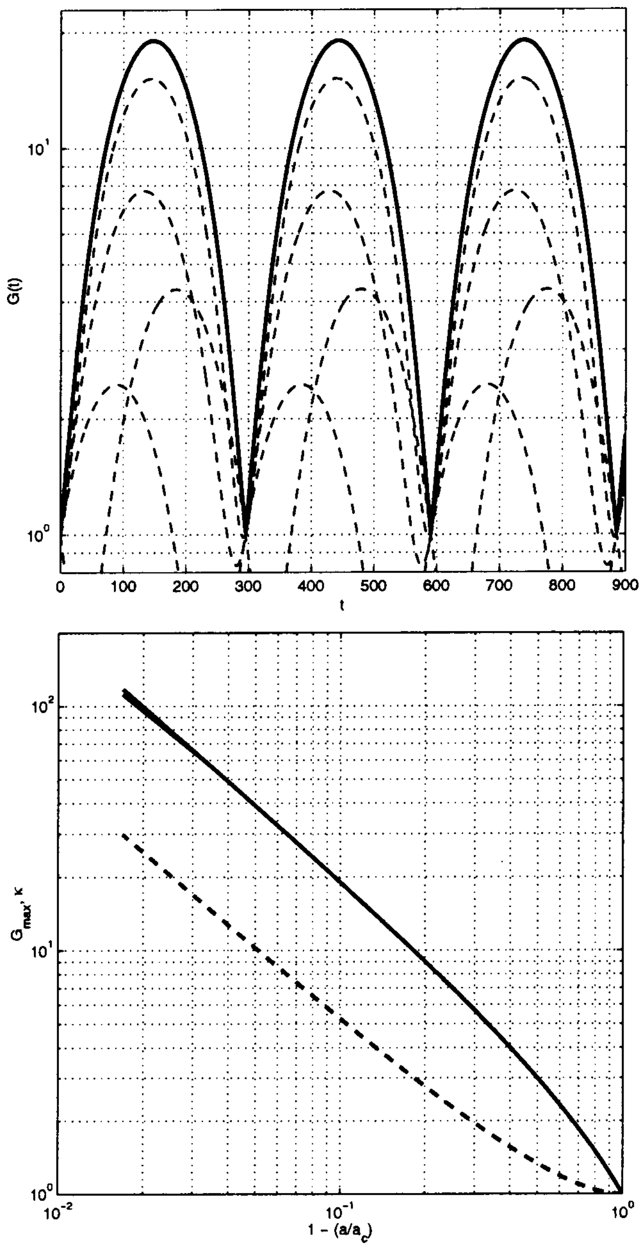

Fig. 1 General undamped system with $\Omega^2=1.1$ and $a/a_c=0.9$. Optimal energy amplification versus time (top, solid line) and energy amplification for four random initial conditions of unit energy (top, dashed lines). Maximum energy amplification versus the coupling coefficient (bottom). The dashed curve (bottom) represents the function $1/(1-(a/a_c)^2)$. The continuous curve (bottom) represents both the maximum of $G(t)$ over time and the upper bound given in Eq. (9).

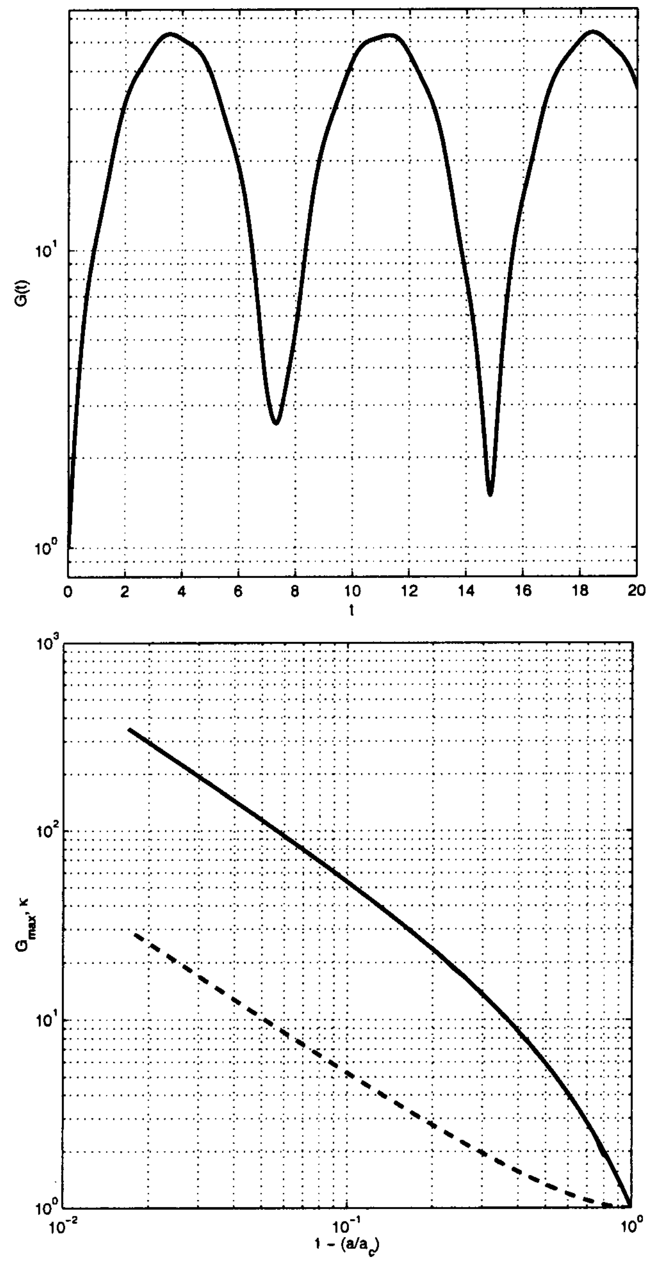

Fig. 2 General undamped system with $\Omega^2=10$ and $a/a_c=0.9$. Energy amplification versus time (top) and maximum energy amplification versus the coupling coefficient (bottom). The dashed curve represents the function $1/(1-(a/a_c)^2)$. The continuous curve represents both the maximum of $G(t)$ over time and the upper bound given in Eq. (9).

time units. We like to emphasize that this amplification occurs at a value of the coupling coefficient that is below the critical one for the onset of couple-mode flutter. As the critical coupling coefficient for this particular frequency ratio Ω is approached we obtain an even larger transient amplification of initial energy, as depicted in Fig. 1(*b*). The asymptotic behavior given by (16) is included as the dashed curve. As the critical coupling coefficient is approached, the maximum transient amplification of energy $G_{\max} \equiv \max_t G(t)$ follows the correct asymptotic behavior.

The transient amplification of disturbance energy prevails also for a significantly larger frequency ratio. Figure 2(*a*) shows the temporal evolution of G for a frequency ratio of $\Omega^2=10$. Again, we observe a short-term amplification of initial energy of up to fifty times. The behavior of $G_{\max}$ as the critical coupling coefficient is approached is displayed in Fig. 2(*b*) together with the asymptotic behavior (16).

2.5 Effects of Damping. Damping is a naturally occuring effect in many fluid-structure systems that has to be accounted for or modeled when analyzing the onset of coupled-mode flutter. In this paper, we are mainly interested how additional damping terms modify the observations we made in the previous section. We again start by analyzing a simple two-degrees-of-freedom model, but add a damping term proportional to the velocity. We get

$$\ddot{x}+b\dot{x}+x=ay \tag{17a}$$

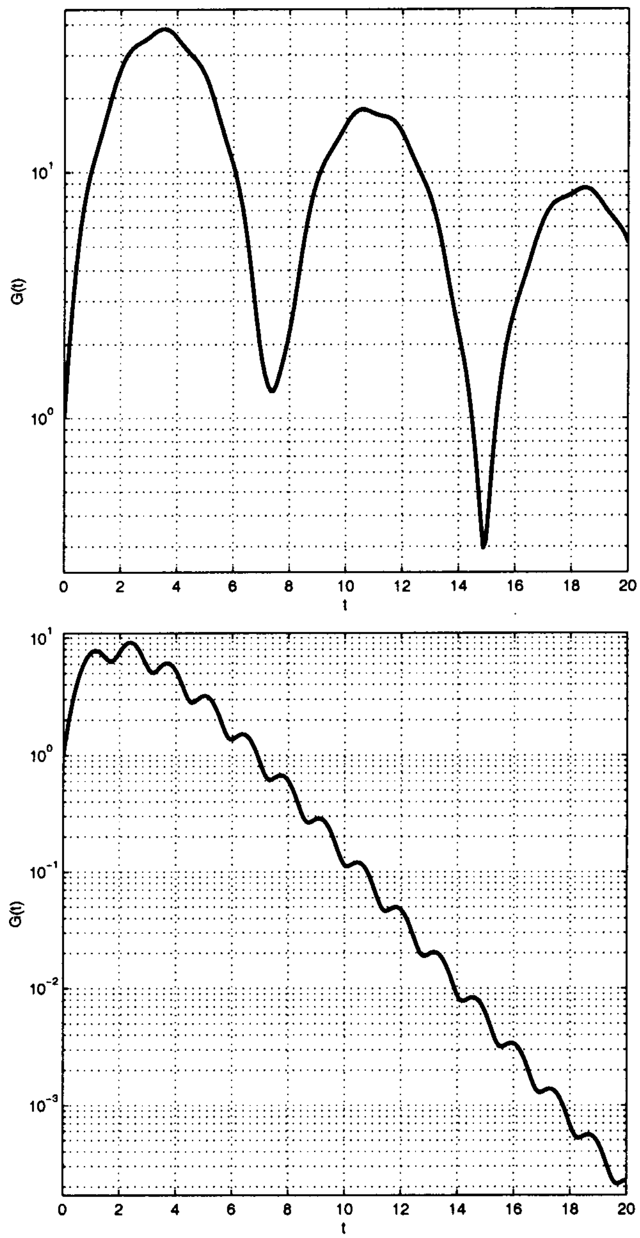

Fig. 3 General damped system with $\Omega^2=10$ and $a/a_c=0.9$. For damping a coefficient of $b=0.1$, (top) and a damping coefficient of $b=1$ (bottom).

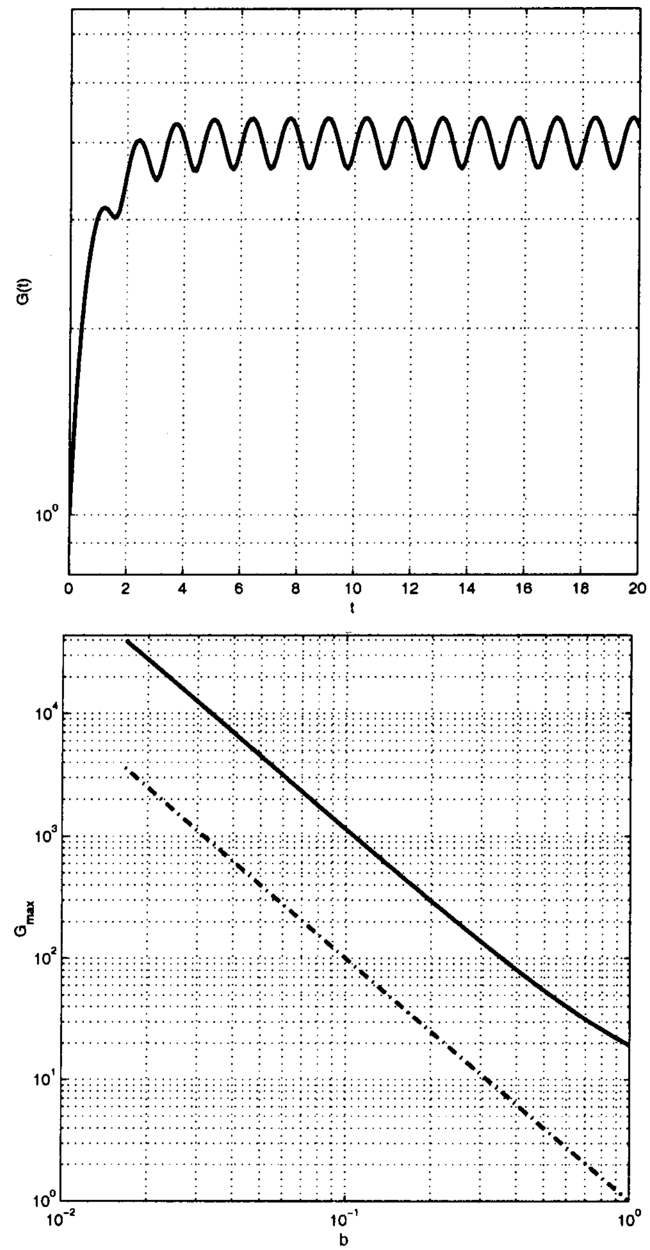

Fig. 4 General damped system with $\Omega^2=10$ at criticality. Energy amplification versus time for $b=1$ (top), and maximum energy amplification versus damping coefficient (bottom). The dashed curve represents the asymptotic behavior $\sim 1/b^2$.

$$\ddot{y}+b\dot{y}+\Omega^2 y=-ax \tag{17b}$$

with b as the damping coefficient. Traditional stability analysis of this problem follows along the same lines as for the undamped case. Applying a Laplace transform to the initial value problem results in the relation

$$\det\begin{vmatrix} p^2+bp+1 & -a \\ a & p^2+bp+\Omega^2 \end{vmatrix}=0 \tag{18}$$

from which—via Routh's criterion—we obtain a value for the critical coupling coefficient for the onset of flutter motion:

$$a_c=a_c^0\sqrt{1-2b^2\frac{\Omega^2+1}{(\Omega^2-1)^2}}. \tag{19}$$

The above formula describes the modification of the critical coupling coefficient when a velocity-dependent damping term is introduced into the governing equations.

We are of course also interested in the effects of damping on the potential for transient amplification at subcritical values of the coupling constant. Modifying the system matrix **A** to account for the additional damping terms, we compute the amplification of disturbance energy $G(t)$ as in the previous section.

The results in Fig. 3 demonstrate that the additional damping terms exert a rather substantial—but not surprising—influence on the long-term behavior. The short-term amplification of energy, on the other hand, is only mildly influenced by damping. We still observe an energy amplification of approximately forty times the initial energy for a damping coefficient of $b=0.1$, and even for an excessively large damping of $b=1$ we obtain an increase in energy of nearly one order of magnitude before strong decay sets in

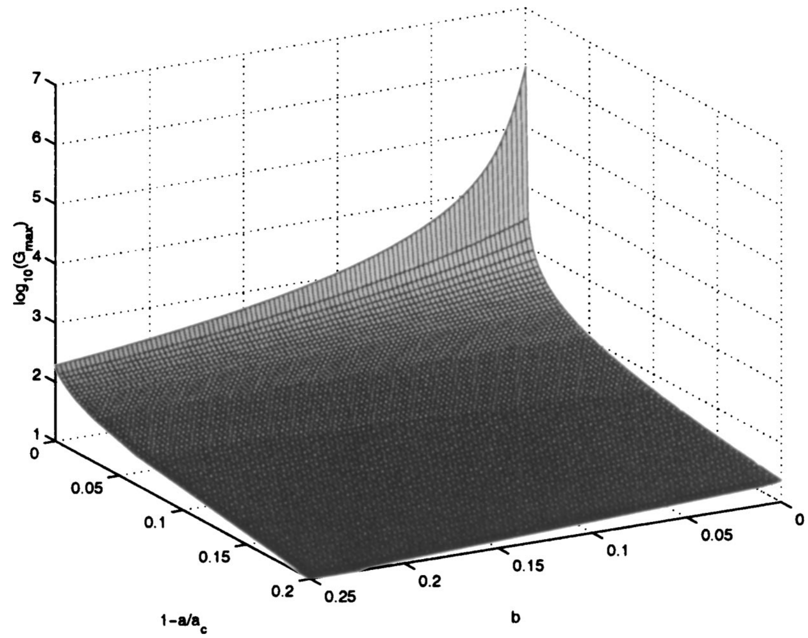

Fig. 5 Maximum energy amplification as a function of coupling and damping coefficient for the general damped system at $\Omega^2=10$

(see Fig. 3). As the critical coupling parameter (19) is approached, an oscillatory state is reached for $G(t)$ with a maximum amplification of more than forty times the initial energy (see Fig. 4(*a*)).

A simple analysis shows that at the onset of instability, i.e., for $a=a_c$, the solution to the damped system behaves like

$$x \sim e^{-bt}(\cos \alpha t + t \cos \alpha t + \cdots) \tag{20}$$

and similarly for the y-component. For this solution behavior, the maximum of the energy amplification is found to occur at $t \approx 1/b$ and the maximum transient growth scales like $G_{\max} \sim 1/b^2$. This scaling is verified by numerical computations with the results shown in Fig. 4(*b*). The asymptotic scaling is displayed as the dashed curve.

A two-dimensional parameter study of the maximum amplification of initial disturbance energy is depicted in Fig. 5. We observe a substantial amount of maximum transient growth as the stability boundary is approached.

The above analysis describes external damping that acts with equal magnitude on the two degrees-of-freedom. It is a well-known fact (see [10,11]) that a discrepancy between the damping in the equations for x and y can have a stabilizing or destabilizing effect and thus change the critical coupling constant. Following Bolotin [10] and introducing a damping coefficient of b and ηb into the x and y-equation, respectively, the critical coupling coefficient can be derived as

$$a_c = a_c^0 \left(\frac{2\sqrt{\eta}}{1+\eta} \right) \sqrt{1 + b^2 \frac{(1+\eta)\Omega^2 + \eta + \eta^2}{(\Omega^2 - 1)^2}} \tag{21}$$

which represents the generalization of Eq. (19) which is recovered for $\eta=1$. Numerical experiments have revealed that the transient effects observed for $\eta=1$ prevail qualitatively for the more general case once the critical coupling coefficient has been redefined according to Eq. (21).

3 Applications

The strong short-term amplification of initial energy for parameters below the critical ones for the onset of coupled-mode flutter can have significant consequences for the design of systems that exhibit aeroelastic deformations or other fluid-structure phenomena. The above analysis of a simple two-degrees-of-freedom system provides the mathematical tools as well as the motivation to investigate more realistic models of fluid-structure interactions for their potential to amplify energy in the subcritical parameter regime. To this end, we concentrate on three classical and well-studied examples of two-degrees-of-freedom systems: (a) panel flutter, (b) follower-force, and (c) fluid-conveying pipes (see Fig. 6 for a sketch of the geometry). For each system we will compute and present the amplification of energy $G(t)$ over a range of governing parameters.

3.1 Panel Flutter. As high-speed flow passes a flat plate with clamped edges, the induced elastic bending in the direction normal to the flow can lead to vibrational instabilities. This type of instabilities is prototypical and very important for many con-

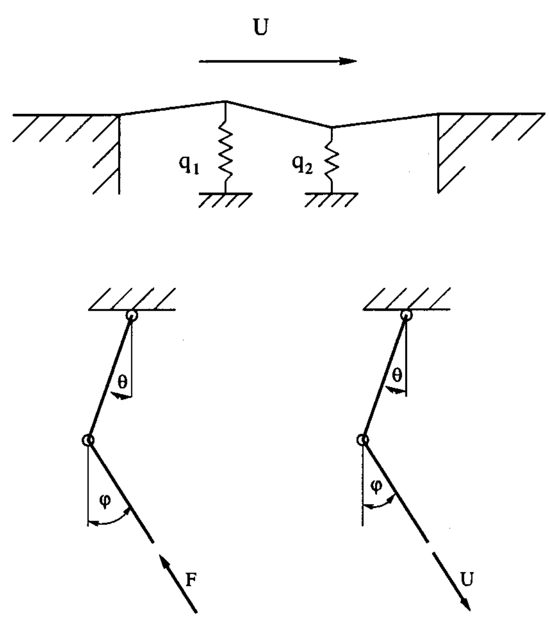

Fig. 6 Geometry sketch for panel flutter (top), follower force (bottom left), and fluid-conveying pipe (bottom right)

figurations in aerospace applications (supersonic flow past an airfoil) and has thus been studied extensively. In this paper we will focus on a highly simplified, yet physically relevant, model which will capture some of the main features of panel flutter instabililies. The model under investigation is taken from Dowell [5]. Three plates of length l and mass m are linked together and supported at each end (see Fig. 6(a)) introducing two degrees-of-freedom for the motion of the system. With q_1 and q_2 as the vertical displacement of the interior nodes, Dowell [5] derives the following set of equations

$$\frac{2}{3}ml\ddot{q}_1+\frac{ml}{6}\ddot{q}_2+kq_1+\frac{\rho_\infty U_\infty^2}{2M_\infty}q_2=0 \qquad (22a)$$

$$\frac{ml}{6}\ddot{q}_1+\frac{2}{3}ml\ddot{q}_2+kq_2-\frac{\rho_\infty U_\infty^2}{2M_\infty}q_1=0 \qquad (22b)$$

where k denotes the spring constant, and ρ_∞, U_∞, and M_∞ stand for the freestream density, velocity, and Mach number, respectively. Nondimensionalizing the above equations using $\lambda=\rho_\infty U_\infty^2/2M_\infty k$ and $\sqrt{ml/k}$ as a characteristic time scale, we obtain

$$\frac{2}{3}\ddot{q}_1+\frac{1}{6}\ddot{q}_2+q_1=-\lambda q_2, \qquad (23a)$$

$$\frac{1}{6}\ddot{q}_1+\frac{2}{3}\ddot{q}_2+q_2=\lambda q_1. \qquad (23b)$$

We can further simplify the system by introducing new dependent variables defined as $x=\sqrt{5/3}(q_1+q_2)$ and $y=q_1-q_2$ which yields

$$\ddot{x}+x=ay \qquad (24a)$$

$$\ddot{y}+\Omega^2 y=-ax \qquad (24b)$$

with $\Omega^2=5/3$ and $a=\sqrt{5/3}\lambda$.

In this form, the reduced system resembles the undamped two-degrees-of-freedom system of the previous section, and we should expect the existence of transient amplification of energy for subcritical coupling coefficients λ. The critical coupling coefficient is $a_c=1/3$, equivalent to $\lambda_c=1/\sqrt{15}$ in [5]. Figure 7(a) shows the maximum energy amplification $G(t)$ as a function of time for $a/a_c=0.9$ or, equivalently, $(U_\infty/U_c)^2=0.9$ where U_c is the critical flow velocity. For this choice of parameter we observe an amplification of 20 times the initial energy. As the critical coupling coefficient is approached, we again recover the proper asymptotic scaling (dashed curved) as displayed in Fig. 7(b). These results clearly demonstrate that large disturbance growth is possible even before the coalescence of natural frequencies and, thus, the onset of panel flutter.

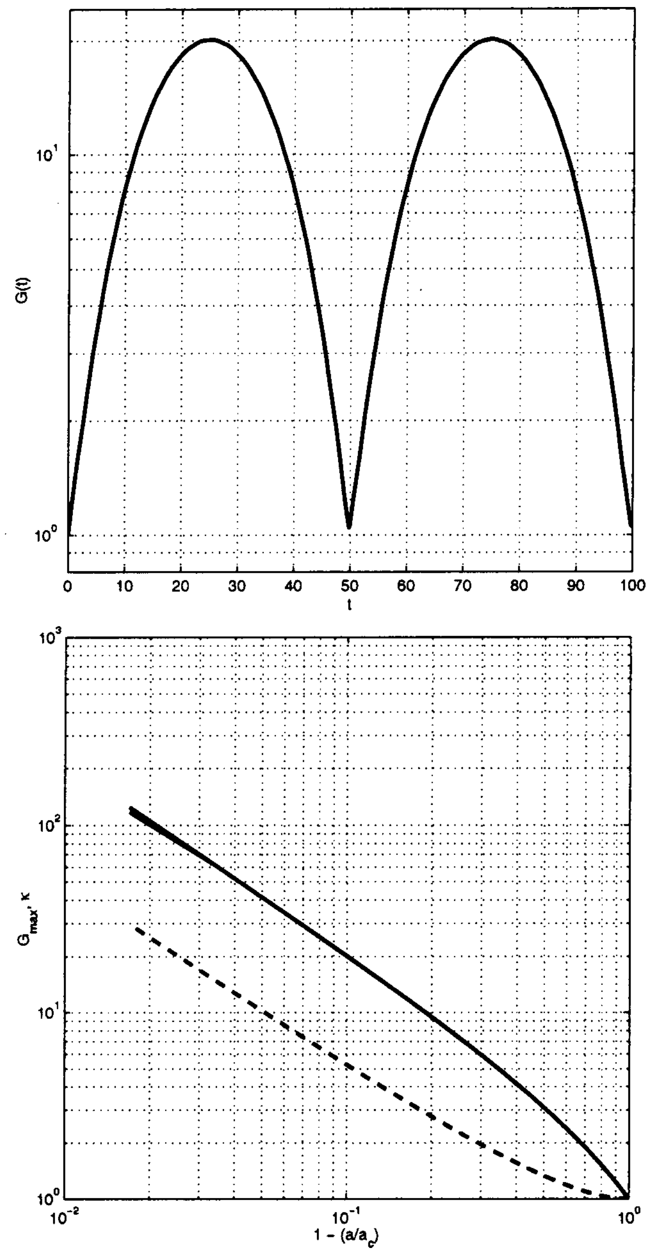

Fig. 7 Energy amplification for undamped panel flutter with $a/a_c=0.9$ versus time (top), maximum energy amplification versus coupling coefficient (bottom). The dashed curve represents the asymptotic behavior $1/(1-(a/a_c)^2)$. The continuous curve represents both the maximum of $G(t)$ over time and the upper bound given in Eq. (9).

3.2 Follower Force.

A slightly more complex two-degrees-of-freedom model is sketched in Fig. 6(b) where two hinged rods of length l are subject to a force F acting on the bottom and in the direction of the lower rod. The motion of the two rods is affected by a torsional spring acting at the hinge. The configuration of the rods is described by the angles θ and ϕ measured with respect to the vertical axis. We will follow Bamberger [6] in deriving the system of equations governing the above configuration. Benjamin [7] has studied models of this type and the specific case illustrated in Fig. 6(b) emerges as a particular case of a fluid-conveying pipe for zero mass ratio β and infinite fluid velocity U, but constant $\sqrt{\beta}U$ (see Païdoussis [12]).

According to Bamberger [6], but using the dimensionless parameters of Benjamin [7] for the sake of clarity, the governing equations are given as

$$\begin{bmatrix}4 & 3/2\\ 3/2 & 1\end{bmatrix}\begin{bmatrix}\ddot{\theta}\\ \ddot{\phi}\end{bmatrix}+\begin{bmatrix}2 & -1\\ -1 & 1\end{bmatrix}\begin{bmatrix}\theta\\ \phi\end{bmatrix}=a\begin{bmatrix}1 & -1\\ 0 & 0\end{bmatrix}\begin{bmatrix}\theta\\ \phi\end{bmatrix} \qquad (25)$$

with $a=F/kl$ as the coupling coefficient.

At a value of $a=0.1$, we determine the two natural frequencies of the system as $\omega_1=0.337$ and $\omega_2=2.243$ which results in the square of the frequency ratio $\Omega^2=44.4$. Increasing the parameter a beyond this critical point, which Bamberger [6] determined as $a_c=2.54$, exponentially growing solutions are encountered. Again, we wish to probe the possibility and amount of short-term energy growth for parameter values a below the critical one.

In order to use the formalism introduced in this paper, we define the system matrix $\mathbf{A}$ in (3) as

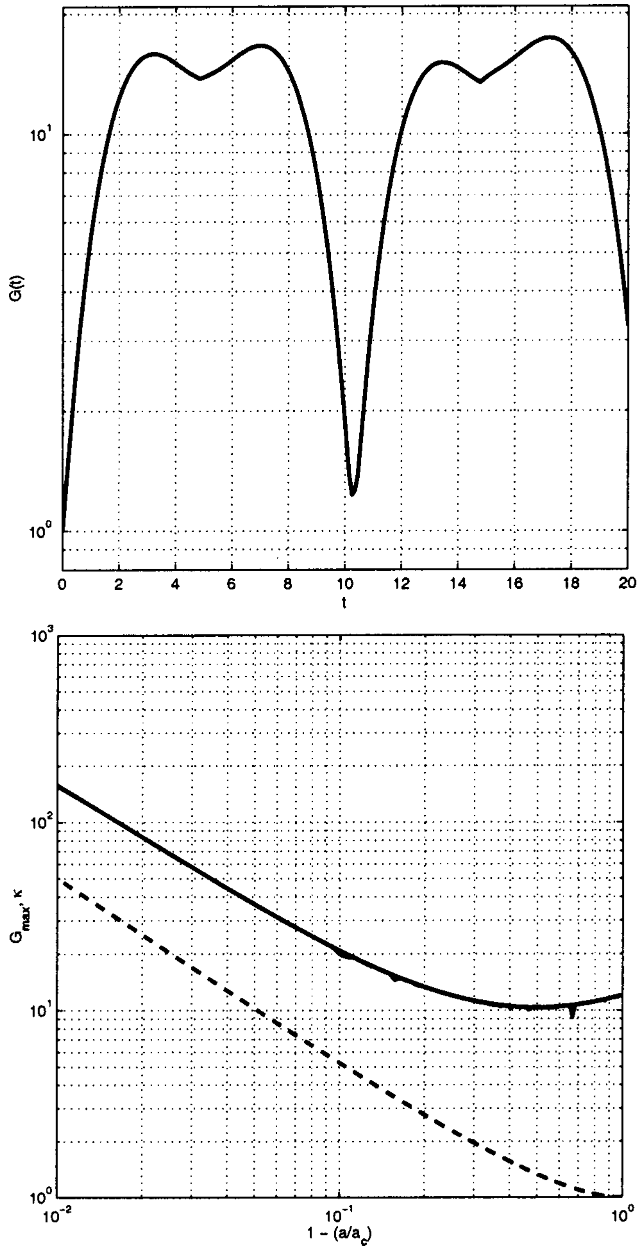

Fig. 8 Energy amplification for undamped follower force problem with $a/a_c = 0.9$ versus time (top), maximum energy amplification versus coupling coefficient (bottom). The dashed curve represents the asymptotic behavior $1/(1-(a/a_c)^2)$. The continuous curve represents both the maximum of $G(t)$ over time and the upper bound given in Eq. (9).

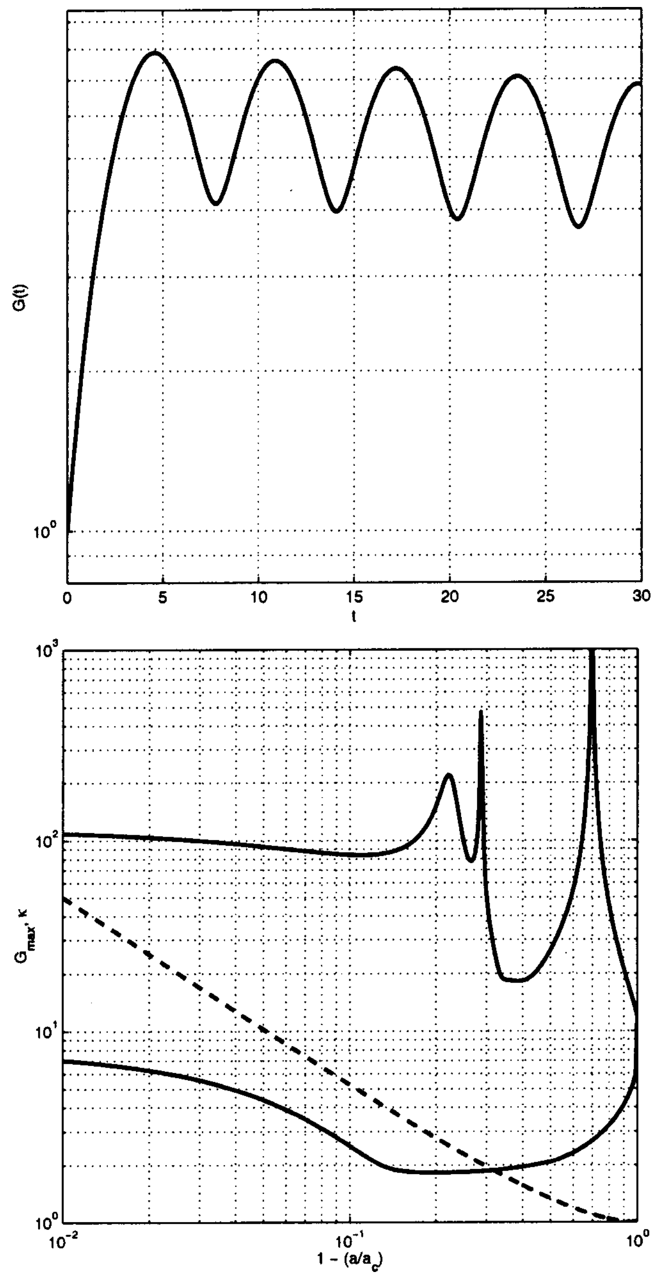

Fig. 9 Energy amplification for the fluid-conveying pipe problem with $a/a_c = 0.999$ versus time (top), maximum energy amplification versus coupling coefficient (bottom). The dashed curve represents the asymptotic behavior $1/(1-(a/a_c)^2)$. The top curve represents the square of the condition number of the eigenvector matrix and acts as an upper bound on the maximum energy amplification.

$$\mathbf{A} = \begin{pmatrix} 1 & 0 & 0 & 0 \\ 0 & 4 & 0 & 3/2 \\ 0 & 0 & 1 & 0 \\ 0 & 3/2 & 0 & 1 \end{pmatrix}^{-1} \begin{pmatrix} 0 & 1 & 0 & 0 \\ (a-2) & 0 & (1-a) & 0 \\ 0 & 0 & 0 & 1 \\ 1 & 0 & -1 & 0 \end{pmatrix}. \tag{26}$$

Alternatively, using different dependent variables the governing equations can be rewritten in the form

$$\ddot{x} + x = \alpha(y - \xi x) \tag{27a}$$

$$\ddot{y} + \Omega^2 y = -\alpha(x + \zeta y) \tag{27b}$$

with $\Omega^2 = 44.4$ and α proportional to a. Strictly speaking, due to the different coupling term, the above system does not resemble the general undamped system introduced previously. Nevertheless, the results of our analysis are similar to the ones found for Eq. (3).

Indeed, computing the maximum energy amplification reveals transient growth of more than one order of magnitude even though the coupling coefficient is only 90 percent of the critical one (see Fig. 8(*a*)). The asymptotic scaling as criticality is approached is once again confirmed numerically (Fig. 8(*b*)).

3.3 Fluid-Conveying Pipe. As our last example we consider the instability of an articulated fluid-conveying pipe (see Fig.

6(c)). Benjamin [7] and Païdoussis [12] have studied the stability and dynamics of this configuration in great depth. We will closely follow their derivation, nondimensionalization and choice of governing parameters resulting in the following set of governing equations:

$$\begin{bmatrix} 4 & 3/2 \\ 3/2 & 1 \end{bmatrix}\begin{bmatrix} \ddot{\theta} \\ \ddot{\phi} \end{bmatrix}+\begin{bmatrix} 2 & -1 \\ -1 & 1 \end{bmatrix}\begin{bmatrix} \theta \\ \phi \end{bmatrix}$$
$$=-3\sqrt{\beta}v\begin{bmatrix} 1 & 2 \\ 0 & 1 \end{bmatrix}\begin{bmatrix} \dot{\theta} \\ \dot{\phi} \end{bmatrix}-3v^2\begin{bmatrix} -1 & 1 \\ 0 & 0 \end{bmatrix}\begin{bmatrix} \theta \\ \phi \end{bmatrix} \quad (28)$$

with $\beta=m_{fluid}/(m_{pipe}+m_{fluid})$ as the mass ratio and v as the nondimensional fluid velocity. We recover the follower-force problem discussed in the previous section for the case $\beta=0$.

We again define the system matrix $\mathbf{A}$ in (3) as

$$\mathbf{A}=\begin{pmatrix} 1 & 0 & 0 & 0 \\ 0 & 4 & 0 & 3/2 \\ 0 & 0 & 1 & 0 \\ 0 & 3/2 & 0 & 1 \end{pmatrix}^{-1}\begin{pmatrix} 0 & 1 & 0 & 0 \\ (a-2) & -b & (1-a) & -2b \\ 0 & 0 & 0 & 1 \\ 1 & 0 & -1 & -b \end{pmatrix} \quad (29)$$

where $a=3v^2$ and $b=3\sqrt{\beta}v$.

Evaluating the maximum energy growth versus time we notice that the amplification is somewhat smaller than in the previous cases with energy growth of only about eight times the initial energy (Fig. 9(a)) for a coupling coefficient $a=0.999a_c$. In addition, flow-induced damping effects are clearly present acting mainly on the second mode. Owing to this damping the maximum amplification of initial energy does not follow the asymptotic behavior (16) as the critical coupling coefficient is approached (see Fig. 9(b)). However, in the limit of $\beta\rightarrow 0$ we recover the correct asymptotic behavior of $G_{\max}$ as $a\rightarrow a_c$.

Included in Fig. 9(b) is the upper bound based on the condition number $\kappa(\mathbf{S})$ as introduced in (9). Although the condition number provides a simple estimate, the actual maximum energy growth is one order of magnitude smaller. In all previous cases, the estimate of maximum energy growth (9) based on the condition number was within plotting accuracy of the computed $G_{\max}$.

4 Conclusions

We studied simple two-degrees-of-freedom systems arising in a variety of applications and investigated the potential for short-term amplification of initial energy under subcritical conditions. This amplification is due to the nonorthogonal superposition of modal solutions which in turn is a consequence of the non-normal nature of the underlying system matrix. The maximum achievable growth can be significant and scales like $\sim 1/(1-(a/a_c)^2)$ as the critical coupling coefficient a_c is approached in the absence of damping. For damped systems, the maximum growth scales inversely to the square of the damping constant.

Since the nonorthogonality of the leading eigenfunctions is preserved as more modes are included in an attempt to model the continuous system, we expect transient amplification of energy in discrete models of high degrees-of-freedom as well as in continuous models. In fact, the inclusion of more nonorthogonal modes may give rise to an increase in transient energy growth. Nevertheless, we believe that the simple two-degrees-of-freedom models presented in this article capture the essential characteristics of this phenomenon.

Three classical applications have been considered, and it has been demonstrated that significant amplification of energy before the onset of coupled-mode flutter can occur. Whereas panel-flutter and follower-force computations showed substantial short-term energy growth, the transient amplification of initial perturbation was less marked in the case of a fluid-conveying pipe which can be attributed to the flow-induced damping present in the dynamics of the pipe.

As initial perturbations are amplified, nonlinear effects will come into play, and a marked deviation from linear behavior should be expected. Despite this effect, the underlying linear amplification process constitutes an important component in describing the onset of flutter instabilities. For extensions of dynamical systems that exhibit transient growth into the nonlinear regime the interested reader is referred to [13] and references therein.

The transient amplification of initial energy cannot be captured by analyzing the eigenvalues of the system matrix. Instead, both eigenvalues and eigenvectors are needed to account for short-term instabilities. Since these type of instabilities are present before the onset of flutter and show amplification rates of one to two orders of magnitude, nonlinear finite-amplitude effects may be triggered long before the system exhibits vibrational instabilities. When designing fluid-structure systems, an analysis of the type introduced in this paper is recommended.

Acknowledgments

PS wishes to thank Patrick Huerre and the gentle people at LadHyX for making his sabbatical visit so enjoyable.

References

[1] Butler, K. M., and Farrell, B. F., 1992, ''Three-Dimensional Optimal Perturbations in Viscous Shear Flow,'' Phys. Fluids A, **4**, pp. 1637–1650.
[2] Reddy, S. C., and Henningson, D. S., 1993, ''Energy Growth in Viscous Channel Flows,'' J. Fluid Mech., **252**, pp. 209–238.
[3] Trefethen, L. N., Trefethen, A. E., Reddy, S. C., and Driscoll, T. A., 1993, ''Hydrodynamic Stability Without Eigenvalues,'' Science, **261**, pp. 578–584.
[4] Schmid, P. J., and Henningson, D. S., 2001, *Stability and Transition in Shear Flows*, Springer-Verlag, New York.
[5] Dowell, E. H., 1995, *A Modern Course in Aeroelasticity* 3rd Ed., Kluwer, Dordrecht, The Netherlands.
[6] Bamberger, Y., 1981, *Mechanique de l'Ingenieur. Vol. I. Systémes de Corps Rigides*, Hermann, Paris.
[7] Benjamin, B. T., 1961, ''Dynamics of a System of Articulated Pipes Conveying Fluids I. Theory,'' Proc. R. Soc. London, Ser. A, **261**, pp. 457–486.
[8] Blevins, R. D., 1991, *Flow-Induced Vibration*, 2nd Ed., Van Nostrand Reinhold, New York.
[9] Naudascher, E., and Rockwell, D., 1994, *Flow-Induced Vibrations: An Engineering Guide*, A. A. Balkema, Rotterdam.
[10] Bolotin, V. V., 1963, *Nonconservative Problems of the Theory of Elastic Stability*, Pergamon Press, New York.
[11] Semler, C., Alighabari, H., and Païdoussis, M. P., 1998, ''A Physical Explanation of the Destabilizing Effect of Damping,'' ASME J. Appl. Mech., **65**, pp. 642–648.
[12] Païdoussis, M. P., 1998, *Fluid Structure Interactions. Slender Structures and Axial Flow*, Vol. I, Academic Press, San Diego, CA.
[13] Gebhardt, T., and Grossmann, S., 1994, ''Chaos Transition Despite Linear Stability,'' Phys. Rev. E, **50**, pp. 3705–3711.

Modeling Air Entrainment and Temperature Effects in Winding

H. Lei
e-mail: herong.lei@Kodak.com

K. A. Cole

S. J. Weinstein

Eastman Kodak Company,
Rochester, NY 14652

Rolls of films and paper are routinely stored under varying conditions before being unwound into downstream operations. During storage, interlayer pressures can change relative to the pressures generated during winding. These changes can lead to problems such as film/paper blocking (increased interlayer pressure) and roll shifting/cinching (decreased interlayer pressure). To study the storage effect, a nonlinear wound roll stress model including air entrainment is first developed and applied to predict the in-roll stresses during film/paper winding. Thereafter, a thermal stress model is used to study the temperature effect on wound roll stresses. Key inputs to the models are the stack modulus, contact clearance, and air film reference clearance. A method is developed to measure these key model inputs. Results of a parametric study show that among the processing conditions, storage temperature and thermal expansion coefficients of the core and the film/paper are key factors that affect in-roll stresses during storage. Limitations of the models will also be discussed along with recommendations for future modeling development. [DOI: 10.1115/1.1629758]

1 Introduction

Wound roll quality is primarily a function of the level and distribution of stresses developed within a roll both during and after winding. Because of this relationship, developing an improved understanding of wound roll stresses has historically been the main driver in the development of wound roll models. It is well known that wound roll stresses are influenced by many factors including process parameters, product parameters, and environmental conditions. Owing to the increasing desire to streamline process and product design, the complexity of wound roll models has increased over the last few years. In particular, researchers have sought to include more of the factors influencing wound roll stresses into the models. The wound roll model presented in this paper seeks to combine physical effects that have been studied in the past. In addition, a discussion is presented noting the limitations of the model along with recommendations for future modeling.

There is a rich history of literature devoted to the wound roll problem. We will cite only a few selected papers here. One of the earliest works was that of Altmann [1] who idealized the winding process as the addition of a sequence of stretched hoops shrink fit onto the roll. This idealization has been employed ever since. He further assumed that the roll could be modeled as a linear orthotropic material enabling an analytic solution to the winding problem. Connolly and Winarski [2] built on Altmann's work by adding temperature and humidity effects. They formulated the problem in terms of radial displacements and obtained solutions numerically. Hakiel [3] extended the earlier works by treating the roll as a nonlinear orthotropic material, specifically noting that the radial compressive modulus is a nonlinear function of pressure. Solutions were obtained numerically using a quasilinearization procedure. Qualls [4] extended the work of Hakiel [3] by including the thermoelastic effect into the winding model. The problem was formulated in terms of radial stress and verification experiments were presented. Results indicated that the thermoelastic behavior could have a significant impact on wound roll stress level.

Contributed by the Applied Mechanics Division of THE AMERICAN SOCIETY OF MECHANICAL ENGINEERS for publication in the ASME JOURNAL OF APPLIED MECHANICS. Manuscript received by the ASME Applied Mechanics Division, October 15, 2002; final revision, June 4, 2003. Associate Editor: R. C. Benson. Discussion on the paper should be addressed to the Editor, Prof. Robert M. McMeeking, Department of Mechanical and Environmental Engineering University of California–Santa Barbara, Santa Barbara, CA 93106-5070, and will be accepted until four months after final publication of the paper itself in the ASME JOURNAL OF APPLIED MECHANICS.

Good et al. [5] further extended Hakiel's formulation to include the effect of an idling pressure roll (Fig. 1). Pressure rolling is used to minimize air entrainment and Good showed that, at low winding speeds, a simple modification to the outer lap pressure boundary condition is required to model the effect. Good and Holmberg [6] were the first to add air entrainment to the centerwinding model. Foil bearing theory was used to estimate the amount of entrained air while the in-roll problem was treated by modifying the Hakiel formulation to include an additional component of radial compressive modulus because of isothermal compression of air. Side leakage was not considered in their formulation. Good and Covell [7] examined air entrainment in the presence of an idling pressure roll. A simple hydrodynamic model without compressibility was used to estimate the magnitude of entrained air. The in-roll problem was treated as in Good and Holmberg [6]. A more detailed theoretical study of air entrainment in the presence of a nip roller was performed by Chang et al. [8] This work showed that air compressibility has a significant impact on the amount of air that passes through the nip. An experimental study was performed by Taylor and Good [9] which showed that Chang's work accurately predicts the magnitude of entrained air.

Forrest [10,11] formulated a more complete air entrainment centerwinding model by considering roughness and air pressure coupling under the idling pressure roll. The in-roll problem was solved using a plane-strain formulation. A buckling analysis was also presented enabling prediction of machine and cross direction buckles. Bouquerel and Bourgin [12] presented a similar model, but like Good and Covell [7], they used an air entrainment nip model that neglected contact between the pressure roll and the winding roll. One extension that was considered in the model was an empirical treatment of side leakage during and after winding. Later papers, i.e., Bourgin [13] and Forrest [14], surveyed the state of art in winding models and included in their discussions air entrainment, side leakage, and wound roll defect prediction. It was noted that the time scale of side leakage was highly dependent on factors such as initial lap-to-lap clearance and web width. Finally, several papers, Pfeiffer [15,16] and Forrest [17], provided discussions and work directed toward the measurement of the radial compressive modulus. It is clear from these references that the measurement of this property requires care. Details such as sample preparation, test equipment, test procedures, and data analysis can all have a major impact on experimental results.

The main objective of the present study is to present a model that combines the effects of air entrainment during pressure roll centerwinding with the thermoelastic effect after winding. Meth-

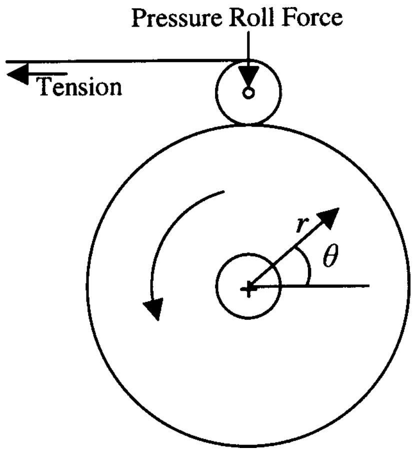

Fig. 1 Center winding with an idling pressure roll. Center of the winding roll is driven by a motor.

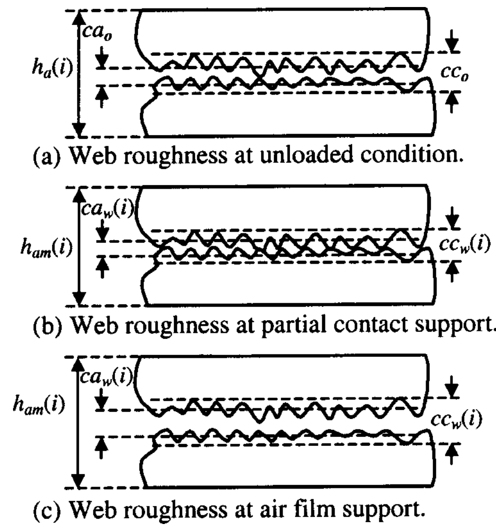

Fig. 2 Web roughness model

ods to measure the inputs to the model are discussed. Experimental results validating the winding model are also presented. A parametric study is presented that indicates the mitigating effect of air entrainment on the impact of thermoelastic expansion on wound roll stresses. It is finally noted that side leakage is not considered in the model. A detailed analysis is presented justifying this approach. This analysis provides quantitative guidance as to when side leakage must be considered and further provides insight into future model extensions.

2 Air Entrainment Winding Model

In this section, the air entrainment winding model is developed. First, a model for web roughness is presented. This model, along with the theoretical results from Chang et al. [8] is then used to analyze the amount of air entrained into the wound roll as the web passes between the pressure roll and the winding roll. Finally, the in-roll model is derived and includes the combined effects of roughness contact and air pressure.

2.1 Web Roughness Model. In order to determine the amount of air entrainment during winding, a simple model for web roughness is first presented. The roughness parameters used in the air entrainment model are defined in Fig. 2. Part (*a*) of the figure shows a cross section of two webs at incipient contact in vacuum conditions. As compressive loading is applied to the webs, displacements will occur in the roughness interface and within the support. The contact reference clearance, cc_o, is defined as the combined height of the roughness over which interfacial displacements occur. The air film reference clearance, ca_o, is the average of void space (gap) between two webs at the incipient contact condition. Contact and air film reference clearances are determined from Wyko® surface roughness measurements of both the front and backside of the web. Two of the key parameters from the Wyko® measurements are the peak-to-valley surface roughness R_z and mean-peak-roughness, R_{pm}. In the model, the root-mean-square of the front and backside R_z are used as the contact reference clearance, cc_o. The root-mean-square of the engagement heights of the front and back surfaces, [18], is used as an approximation to the air film reference clearance, ca_o.

Part (*b*) and (*c*) in Fig. 2 show the geometry for two cases that are possible once air entrainment occurs. Part (*b*) shows the corresponding contact clearance, $cc_w(i)$, and air film clearance, $ca_w(i)$, under the outer lap away from the web/pressure roller nip for winding conditions where roughness contact occurs. The variable i indicates the lap number. Note that the clearance, $cc_w(i)$, between two webs is reduced relative to the contact reference clearance, cc_o. This will occur under low speed winding where the air entrainment effect is minimal. On the other hand, for high-speed winding when the pressure roller load is not sufficiently large, the air film clearance will be increased from the reference clearance as the outer lap winds onto the roll because of air entrainment (Part (*c*)). In this case all the belt wrap loading will be air supported.

In addition to the clearance definitions under the outer lap, the contact clearance, $cc(i)$, and the air film clearance, $ca(i)$, within the wound roll are also defined. These additional variables are needed to enable the model to track clearance and interlayer pressure as the roll winds.

2.2 Pressure Roller Nip Analysis. From the above discussion, it is clear that for a nonzero winding speed under nonvacuum conditions, air will always contribute to the interlayer pressure. In order to determine the magnitude of this contribution during pressure roller winding, the air entrained in the outer lap must first be determined.

Consider a winding roll with widthwise invariant web and core properties. Under the pressure roller, the nip force per web width, $f_p(i)$, is comprised of an air force, $f_a(i)$, and/or a contact force, $f_c(i)$:

$$f_p(i)=f_a(i)+f_c(i). \tag{1}$$

The air force arises because of entraining of air and the contact force arises if the web wrapping the pressure roller is in physical contact to the roll through its rough surface. From Chang et al. [8], the air film clearance beneath the pressure roller nip, $ca_n(i)$, can be expressed as a function of the developed air force $f_a(i)$:

$$\frac{ca_n(i)}{R(i)}=\begin{cases} 6.5\left(\dfrac{\mu V}{p_aR(i)}\right)^{0.65}\left(\dfrac{f_a(i)}{p_aR(i)}\right)^{-0.28}\left(\dfrac{E(i)}{p_a}\right)^{-0.44} & \text{for } 0.69\leqslant E\leqslant 4.84 \text{ MPa} \\ 8.7\left(\dfrac{\mu V}{p_aR(i)}\right)^{0.72}\left(\dfrac{f_a(i)}{p_aR(i)}\right)^{-0.49}\left(\dfrac{E(i)}{p_a}\right)^{-0.48} & \text{for } 4.84\leqslant E\leqslant 34.5 \text{ MPa} \end{cases} \tag{2}$$

where V is the winding speed, p_a is atmospheric pressure, and $R(i)$ and $E(i)$ are the equivalent radius and equivalent modulus of the pressure roller/winding roll.

The air film clearance is related to the contact clearance if it is assumed that under loading, the reduction in contact clearance is equivalent to the reduction in air clearance:

$$cc_n(i) - cc_o = ca_n(i) - ca_o. \tag{3}$$

This assumption is not rigorously justified; however for typical loads and for webs dominated by very fine roughness with a random distribution of sparse high roughness, this would seem to be a reasonable assumption since the interfacial displacements would occur mainly in these high roughness areas.

From the Hertzian contact theory, [19], the contact force, $f_c(i)$, in terms of the contact clearance, $cc_n(i)$, is found to be

$$f_c(i) = \frac{\pi R(i)}{E(i)} P_n^2(cc_n(i)), \tag{4}$$

where $P_n(cc_n)$ is the contact pressure under the nip and is related to the contact clearance via a look up table generated from the stack modulus measurement:

$$P_n(cc_n(i)) = f(cc_n(i)) = \begin{cases} f^*(cc_n(i)) & \text{for } cc_n \leqslant cc_o \\ 0 & \text{for } cc_n > cc_o \end{cases}. \tag{5}$$

The above equations are well posed to solve for the unknowns under the nip, $cc_n(i)$, $ca_n(i)$, $f_c(i)$, and $f_a(i)$.

2.3 Internal Outer Lap Analysis. The analysis of this section uses the results of the pressure roller nip analysis to determine the air film clearance, air pressure, and contact condition under the outer lap away from the nip.

Empirical studies, [7], have shown that the effective winding tension (wound-in-tension) in pressure roller winding, $t_a(i)$, can be expressed as

$$t_a(i) = t(i) + \mu_w w f_c(i), \tag{6}$$

where μ_w is the front-to-back friction coefficient of the web, w is the width of the web and $t(i)$ is the upstream winding tension. This expression indicates that an additional component, known as the nip-induced tension, arises during winding when a pressure roller is added.

The winding tension stress under the outer lap away from the nip is related to the effective winding tension by

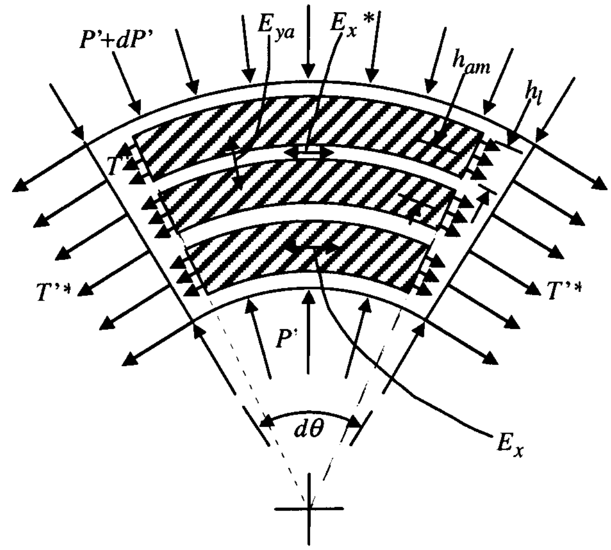

Fig. 3 Continuum differential force element in the wound roll

$$\sigma_\theta(i) = \frac{t_a(i)}{w h_l}, \tag{7}$$

where h_l is the load sharing web thickness (Fig. 3). The belt wrap pressure under the outer lap away from the nip is supported by air pressure and possibly contact pressure:

$$P'(i) = \frac{h_l \sigma_\theta(i)}{r_d(i)} = \frac{t_a(i)}{w r_d(i)} = P'_g(i) + P'_c(i). \tag{8}$$

The contact pressure is related to the contact clearance in the same fashion as Eq. (5). The air pressure under the outer lap away from the nip, $P'_g(i)$, is related to the air film clearance by a sequence of two equations. The first, according to Chang et al. [8], relates the clearance adjusted to atmospheric pressure to the pressure roller air load, $f_a(i)$,

$$\frac{ca_a(i)}{R(i)} = \begin{cases} 7.4\left(\frac{\mu V}{p_a R(i)}\right)^{0.66}\left(\frac{f_a(i)}{p_a R(i)}\right)^{-0.21}\left(\frac{E(i)}{p_a}\right)^{-0.33} & \text{for } 0.69 \leqslant E \leqslant 4.84 \text{ MPa} \\ 12.5\left(\frac{\mu V}{p_a R(i)}\right)^{0.71}\left(\frac{f_a(i)}{p_a R(i)}\right)^{-0.20}\left(\frac{E(i)}{p_a}\right)^{-0.23} & \text{for } 4.84 \leqslant E \leqslant 34.5 \text{ MPa} \end{cases}, \tag{9}$$

where $ca_a(i)$ is the air film clearance under the outer lap away from the nip adjusted to atmospheric pressure. The second relates the air pressure to the air film clearance using the perfect gas law:

$$p_a ca_a(i) = (p_a + P'_g(i)) ca_w(i). \tag{10}$$

By using the relation between $ca_w(i)$ and $cc_w(i)$ (the same fashion as in Eq. (3)), the above becomes

$$P'_g(i) = \frac{p_a ca_a(i)}{cc_w(i) - cc_o + ca_o} - p_a. \tag{11}$$

Once the pressure roller air load is determined, the above equations can be solved for contact clearance and air pressure under the outer lap away from the nip.

2.4 In-Roll Analysis. Prior to the addition of the next lap, say the ith, the roll will have a radius, $r_d(i)$. Assume that the next lap under wound-in-tension, $t_a(i)$, is added to the roll. The roll profile after the addition of the ith lap, $r_d(i+1)$ is

$$r_d(i+1) = r_d(i) + U'(i) + h_{am}(i), \tag{12}$$

where $U'(i)$ is the radial displacement of the roll due to the force exerted by the ith lap and $h_{am}(i)$ is the reference web thickness added to the roll profile accounting for air entrainment and contact if present

$$h_{am}(i) = h_a + cc_w(i) - cc_o. \tag{13}$$

The derivation of in-roll analysis begins by considering the forces that act on a differential element located in the wound roll at a nominal wound roll radius. Figure 3 shows such an element that can be thought of as a continuum equivalent of the actual situation where the load sharing web thickness, h_l, will be less than the reference web thickness, $h_{am}(i)$.

To accommodate this difference, two in-roll tension stress parameters are defined. The first, T'^*, is the continuum approximation to the actual incremental in-roll stress, T', which is distributed over the load sharing thickness. The apostrophe is added to denote that the stresses are incremental due to the addition of a single lap. In addition, anisotropic constitutive properties are defined for the continuum approximation (E_x^*, $\nu_{r\theta}^*$, and $\nu_{\theta r}^*$).

To simplify the development of the remaining equations in this section, explicit reference to lap number will be excluded from the model variables. It is understood that the stresses are evaluated at each lap.

Consider first the continuum approximation. A fundamental relationship between the continuum in-roll tension stress, T'^*, and the interlayer pressure stress, P', can be obtained by force equilibrium:

$$P' + T'^* + r\frac{dP'}{dr} = 0. \tag{14}$$

The continuum in-roll tension stress is related to the actual in-roll tension stress by considering a balance of total tension within the circumferential load carrying thickness and total web thickness:

$$T'^* h_{am} = h_l T', \tag{15}$$

which reflects the fact that the actual in-roll tension stress acts over a proportionally smaller radial differential than the continuum in-roll tension stress.

The strain-displacement and constitutive relationships for the continuum approximation are given by

$$\varepsilon'_\theta = \frac{U'}{r} = \frac{T'^*}{E_x^*} + \frac{\nu_{\theta r}^* P'}{E_{ya}} = \varepsilon'_{\theta\theta} + \varepsilon'_{\theta r},$$

$$\varepsilon'_r = \frac{dU'}{dr} = -\frac{P'}{E_{ya}} - \frac{\nu_{r\theta}^* T'^*}{E_x^*} = \varepsilon'_{rr} + \varepsilon'_{r\theta}, \tag{16}$$

where $\nu_{\theta r}^*$ and $\nu_{r\theta}^*$ are the two components of Poisson's ratio relating strain in one direction to strain in the other. In Eq. (16), it has been assumed that the strains from the continuum model represent the actual strains when $h_l \neq h_{am}$. This will be true when these strains equal the following alternate expressions:

$$\varepsilon'_{\theta\theta} = \frac{T'}{E_x}, \quad \varepsilon'_{\theta r} = \frac{\nu_{\theta r} P'}{E_{ya}}, \quad \varepsilon'_{rr} = \frac{-P'}{E_{ya}}, \quad \varepsilon'_{r\theta} = \frac{-h_l \nu_{r\theta} T'}{h_{am} E_x}. \tag{17}$$

From Eqs. (15)–(17), the continuum constitutive properties are related to the physical properties of the web (E_x, $\nu_{r\theta}$, and $\nu_{\theta r}$) by

$$E_x^* = \frac{h_l}{h_{am}} E_x, \quad \nu_{\theta r}^* = \nu_{\theta r}, \quad \nu_{r\theta}^* = \frac{h_l}{h_{am}} \nu_{r\theta}. \tag{18}$$

Strain energy consideration, [3], gives the following relationship between the constitutive properties:

$$\frac{\nu_{\theta r}^*}{E_{ya}} = \frac{\nu_{r\theta}^*}{E_x^*}. \tag{19}$$

Combining Eqs. (14) to (19) yields the following differential equation for the incremental interlayer pressure:

$$r^2\frac{d^2P'}{dr^2} + 3r\frac{dP'}{dr} + \left(1 - \frac{h_l E_x}{h_{am} E_{ya}}\right)P' = 0. \tag{20}$$

This is a second-order ordinary differential equation and its solution requires that two boundary conditions be specified. At the periphery of the winding roll, a single winding lap exerts a pressure on the roll that is given by the wound in tension as

$$P'(i) = \frac{t_a(i)}{wr(i)} \quad \text{at the periphery.} \tag{21}$$

At the periphery of the core, since the radial displacement of the core must equal that of the roll, a boundary condition can be written

$$\frac{dP'}{dr} = \frac{2}{c}\left(\frac{E_x h_l}{E_c h_{am}} - 1 + \frac{h_l}{h_{am}}\nu\right)P' \quad \text{at the core/roll interface.} \tag{22}$$

The total pressure in-roll is the sum of total air pressure and total contact pressure if the neighboring layers are in contact:

$$P = P_c + P_g. \tag{23}$$

As the total pressure increases, when more laps are wound, the air pressure, contact pressure, and thus the contact clearance will change as well. Within the roll, the contact pressure and contact clearance cc are related by Eq. (5). On the other hand, the air pressure in roll is related, by the ideal gas law, to the amount of air entrained while the local lap was being wound:

$$(P_g + p_a)(cc - cc_0 + ca_0) = (P'_g + p_a)ca_w. \tag{24}$$

When winding more laps, the contact clearance between laps in the existing roll can then be updated according to Eqs. (23) and (24).

3 Thermal Stress After Winding

Roll winding usually takes place in a temperature-controlled environment where the temperature variation is minimal. After being wound, the rolls are often stored in facilities where the temperature can be significantly different from the winding temperature. In the following we model the effect of temperature changes after winding to in-roll stresses.

After winding, the force equilibrium Eq. (14) still governs the stress distribution in roll. The constitutive relations, including the effect of temperature, are

$$\varepsilon'_\theta = \frac{U'}{r} = \frac{1}{E_x^*}T'^* + \frac{\nu_{\theta r}^*}{E_{ya}}P' + \alpha_t F',$$

$$\varepsilon'_r = \frac{dU'}{dr} = -\frac{1}{E_{ya}}P' - \frac{\nu_{r\theta}^*}{E_x^*}T'^* + \alpha_r F', \tag{25}$$

where P' and T'^* are the increments of in-roll pressure and tension stress due to the temperature change $F'(r)$.

For simplicity, the material properties such as web moduli excluding air and Poisson's ratio are assumed independent of temperature. From Eqs. (18) and (25)

$$\frac{d\varepsilon'_\theta}{dr} = \frac{h_{am}}{h_l E_x}\frac{dT'^*}{dr} + \frac{\nu_{r\theta}}{E_x}\frac{dP'}{dr} + \alpha_t\frac{dF'}{dr}. \tag{26}$$

To arrive the above equation, we have assumed the load sharing thickness, web circumferential modulus, coefficient of thermal expansion, and Poissons ratio are invariant with the radius. The variation of h_{am} with radius is typically very small, and therefore is neglected here. Combining Eqs. (14), (25), and (26) gives the differential equation for the increment in interlayer pressure due to a temperature change

$$r^2\frac{d^2P'}{dr^2}+3r\frac{dP'}{dr}+\left(1-\frac{h_lE_x}{h_{am}E_{ya}}\right)P'+\frac{h_l}{h_{am}}E_x(\alpha_r-\alpha_t)F' - \frac{h_l}{h_{am}}\alpha_tE_xr\frac{dF'}{dr}=0. \quad (27)$$

The boundary conditions for the second order ordinary differential Eq. (27) are the following. At the periphery of the wound roll, there is no pressure increment

$$P'=0 \quad \text{at the periphery.} \quad (28)$$

At the surface of the core ($r=c/2$) the radial displacement continuity due to the local pressure and core temperature change (P_1',F_1') yields

$$U_c'(c/2)=-\frac{P_1'c}{2E_c}+\frac{\alpha_c cF_1'}{2}, \quad (29)$$

where α_c is an equivalent thermal expansion coefficient of the core, and E_c is the core modulus evaluated at initial temperature and assumed not varying with temperature.

Equation (29) is based on the assumption that the temperature increase within the core is uniform. This is a valid assumption only if heat transfer in the core is much faster than that in the wound roll so that the core reaches thermal equilibrium much faster than the roll.

When Eq. (29) is combined with Eq. (25), it yields the second boundary condition

$$\left.\frac{dP'}{dr}\right|_{r=c/2}=\frac{2}{c}\left[\frac{E_xh_l}{E_ch_{am}}-1+\frac{h_l}{h_{am}}\nu\right]P_1'+\frac{2h_l}{ch_{am}}E_x(\alpha_t^r-\alpha_c)F_1'. \quad (30)$$

Temperature variations after winding change the in-roll pressure, and thus the air pressure, contact pressure, and contact clearance change as well. These in-roll variables can be updated by the same routine as that in the in-roll analysis, except when the temperature effect on air pressure is included, Eq. (24) becomes

$$\frac{(P_g'+p_a)ca_w}{F_s}=\frac{(P_g+p_a)(cc-cc_0+ca_0)}{F}, \quad (31)$$

where F_s is the roll temperature at the start of the thermal analysis. Temperatures F and F_s are absolute in reference to $-273°$C ($-460°$F).

4 Modified Stack Modulus to Include Air and Temperature Effects

In Eq. (19) the stack modulus with the air effect, E_{ya}, is a modified version of the stack modulus E_y without air entrainment. The purpose of this section is to develop an expression for E_{ya} in terms of E_y and the thickness variables of the model. The analysis first establishes basic definitions where air entrainment is neglected. This is followed by a derivation for the stack modulus where air entrainment between the laps is considered. Finally, a derivation is presented for the stack modulus which additionally includes the temperature effect.

4.1 Stack Modulus Excluding Air Entrainment. Consider part (*a*) of Fig. 2, which shows incipient contact of two webs in a vacuum. In this figure, the reference web thickness is the total web thickness h_a, and the contact reference clearance is cc_o. The total web thickness, h_a, can be broken into two layers, one of which is the support with reference thickness h_l and bulk modulus E_s, and the other is the layer consisting of surface roughness with reference thickness cc_o and modulus E_r. When air is excluded, these two layers are modeled as elastic springs linearly connected in series (Fig. 4(*a*)). The stack modulus of the total web excluding air is

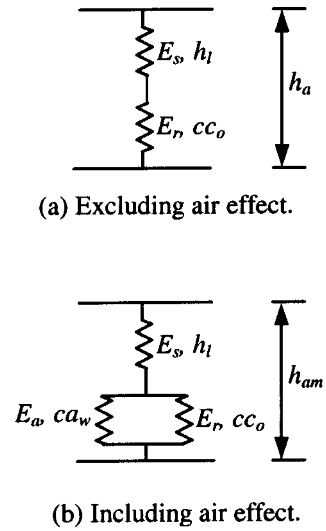

Fig. 4 Stack modulus

$$E_y=\frac{h_aE_rE_s}{cc_oE_s+h_lE_r}. \quad (32)$$

The above equation can be solved for the roughness modulus E_r if the stack modulus E_y, bulk modulus E_s, and reference thickness of each layer are available.

4.2 Stack Modulus Including Air Entrainment. Next, consider parts (*b*) and (*c*) of Fig. 2 that shows the relative position of the outermost two laps after the outer lap has passed onto the wound roll. In this figure, the reference web thickness, h_{am}, is now the total web thickness including the effect of air entrainment and the effect of roughness if contact occurs under the outer lap such as shown in Part (*b*) of Fig. 2. The contact reference clearance is now cc_w and air film reference is ca_w. These quantities are computed in the outer lap analysis.

The air trapped in the roughness area between two laps will affect the compressibility of the roll. When air is included, the roughness area is modeled as two springs in parallel (Fig. 4(*b*); one represents the roughness surface with reference thickness cc_o and modulus E_r, and the other represents the air film reference thickness ca_w and modulus E_a. The total web is modeled as this roughness layer and the support layer (reference thickness h_l and bulk modulus E_s) connected in series. The air film modulus is from the compressibility of the air. When air leakage through the sidewall is excluded and the air follows the ideal gas law, the air film modulus is, [6],

$$E_a=\frac{(P_g+p_a)^2}{(P_g'+p_a)}. \quad (33)$$

The stack modulus of the total web is then

$$E_{ya}=\begin{cases}\dfrac{h_{am}}{\dfrac{h_l}{E_s}+\dfrac{ca_w}{E_a}} & \text{when the laps are not in contact}\\[2ex] \dfrac{h_{am}}{\dfrac{h_l}{E_s}+\dfrac{1}{\dfrac{E_a}{ca_w}+\dfrac{E_r}{cc_o}}} & \text{when the laps are in contact}\end{cases}. \quad (34)$$

In the in-roll stress analysis, before the *i*th lap is added, the stack modulus is computed along the radius in the winding roll. This is done at each radial location as follows. First, the roughness interface modulus is computed using Eq. (32). Then Eq. (34) is

Table 1 Winding conditions and results from experiments and model predictions

Test #	Speed, m/s	Start tension per width, N/m	Finish tension per width, N/m	Nip force per width, N/m	Accel at cinching, m/s^2	Torque per width at core, N	Contact pressure at core, kPa	Contact pressure at core from model, kPa
1	4.3	622	263	263	0.76	572	73	97
2	4.3	727	306	263	>1.02	>762	>97	104
3	4.3	832	350	263	>1.02	>762	>97	108
4	5.1	727	306	263	1.02	762	97	102
5	5.1	766	766	263	1.02	762	97	103
6	5.1	832	350	263	>1.02	>762	>97	106

used to evaluate the stack modulus with the air entrainment effect included. Once the stack modulus is known, the incremental in-roll solution for the *i*th lap can be found. Finally, the cumulative in-roll solution is determined.

4.3 Stack Modulus Including Air Entrainment and Thermal Effect. We assumed the support and roughness moduli do not vary with temperature in the temperature range of interest. With this assumption, the effect of temperature on stack modulus depends solely on E_a, the modulus of the air film. Using the ideal gas law under isothermal expansion, the air film modulus is

$$E_a=\frac{(P_g+p_a)^2F_s}{(P_g'+p_a)F}. \tag{35}$$

Then the stack modulus, including air entrainment and temperature effect, is available by substituting the above equation into Eq. (34).

4.4 Stack Modulus Measurement and Data Reduction. In order to perform numerical simulations using the winding model, several material properties and geometric parameters must be measured empirically. Some of these are measured conventionally (e.g., Young's modulus of the web); however, several new variables have been introduced and so some discussion on how to measure them is now provided.

The new material properties required of the model include the underlying support modulus and the roughness modulus as defined in Eq. (32). To obtain these parameters, the circumferential load carrying thickness and the total web thickness must be known as well. The total web thickness is the sum of the load sharing thickness and the contact reference clearance. It is determined from experimental stack modulus measurements as follows. First, three stacks of support are constructed from individual plies having an area of 1.27 cm by 5.08 cm. The number of plies within each stack is chosen such that the height is 0.51 cm. Each of the three stacks is sequentially placed between two parallel plates and compressed to a small preload of 103 Kpa. The load is then reduced to 13.8 KPa and the height of each stack noted via the average output from three LVDT's located at 120° increments around the perimeter of the upper and lower platens. The total stack height is divided by the number of individual plies and the resulting thickness is averaged from the three separate measurements to yield the total web thickness.

Following this measurement, each stack is then compressed at a constant strain rate of 0.51 mm/min up to a final stress of 12.4 MPa. Displacements are measured as the average output of the three LVDTs and stress is measured using a load cell. From this data, the radial compressive modulus excluding air is computed since the stack area is sufficiently small enough to mitigate the air effect during compression. The bulk modulus is determined by computing the tangent modulus from the stress-strain data near the upper end of the stress range. Presumably, at the higher stresses, the roughness interface has been significantly compressed and the stress-strain behavior is predominately governed by the bulk modulus.

Finally, the roughness modulus is computed by inverting Eq. (32) once the contact reference clearance is known. As previously mentioned, the contact reference clearance is determined from the root-mean-square of the front and backside R_z (measured via the Wyko®).

5 Numerical Solution

The solution of the above model was obtained numerically. The numerical algorithm "winds" one lap after another onto the "core" until the last lap is wound. During winding of each individual lap, the algorithm is as follows:

1. *Pressure roller nip analysis*: Given the nip load, winding speed, web reference clearances, and roll/pressure roller geometry, the equivalent radius and equivalent modulus of the roll/pressure roller are evaluated. Then Eqs. (1) to (5) are solved by Newton's iterative method for the contact force $f_c(i)$, air force $f_a(i)$, contact clearance $cc_n(i)$, and air film clearance $ca_n(i)$ under the nip.
2. *Internal outer lap analysis*: The contact force from the step 1 is used to obtain the nip induced tension and wound-in-tension. Then Eq. (9) is used to evaluate $ca_a(i)$, the air film clearance under the outer lap away from the nip adjusted to the atmospheric pressure. Equations (8), (10), and (11) are solved afterwards to obtain the contact clearance $cc_w(i)$, the contact pressure $P_c'(i)$, and air pressure $P_g'(i)$ under the outer lap away from the nip.
3. *In-roll analysis*: The stack moduli including the air effect are first evaluated using the in-roll conditions. Central finite difference method is then applied to solve the ordinary differential Eq. (20) with the boundary conditions (21) and (22).
4. *Roll profile and stress update*: Results from step 3 are used to update the roll profile and in-roll stress distribution.
5. *Repeat*: Steps 1 to 4 are repeated until all laps are wound onto the roll.
6. *Thermal stress analysis after winding*: The nonlinear boundary value problem of the thermal stress analysis (Eq. (27)) is solved by Newton's iterative method.

6 Experimental Verification and Parametric Study

6.1 Experiments. Experiments are conducted in the Kodak conveyance and winding laboratory. The experiments consisted of winding a sequence of polymer-coated paper (224 μm thick and 7925 m long, roll OD 1.5 m) onto 0.127 m (5 inch) outer diameter cardboard cores. Test rolls are wound with a pressure roller force of 263 N/m (1.5 pli) contact force under two levels of speed, 4.3 and 5.1 m/s (850 and 1000 fpm), and five levels of tension profile, as detailed in Table 1. The tension profiles, with the exception of test 5, which is at constant tension, are linearly tapered with the length of the web wound onto the roll.

After winding, the rolls are tested to evaluate the torque transmission capability. Before testing, straight lines are drawn on both sides of every test roll. Then the rolls are repeatedly accelerated up to 5.1 m/s (1000 fpm) using incremental acceleration rates and then stopped. The acceleration rate starts at 0.25 m/s^2 (50 fpm/

Table 2 Material properties used in modeling

c (m)	0.127	E_x (MPa)	5720	ν	0.02	E_s (MPa)	179
ca_o (μm)	8.387	h_a (μm)	235	E_p (MPa)	2	density, kg/m^3	1107
cc_o (μm)	10.64	h_l (μm)	224	r_p (m)	0.0762	roll OD, m	1.5
E_c (MPa)	410	μ_w	0.31	v_p	0.495	lap number	3089

sec), and then increases up to 1.02 m/s^2 (200 fpm/sec) in 0.25 m/s^2 increments. The rolls are then decelerated at a much gentle deceleration rate of 0.05 m/s^2 (10 fpm/sec). After rolls are stopped, they are checked for cinches (circumferential breaks of the straight lines on both ends). Results are shown in Table 1, from which half of the six rolls do not cinch at 1.02 m/s^2, the maximum acceleration capability of the lab equipment. Among the three rolls that cinched, one cinched at 0.76 m/s^2 (150 fpm/sec), and two cinched at 1.02 m/s^2. For all of these three rolls, cin ching takes place near the core. The acceleration rate when cinching starts can be used to estimate the contact pressure at the core. In this calculation, it is assumed that it is the contact pressure that provides the roll with torque transmission capability. The contact pressures at the core from the cinch tests are shown in Table 1.

6.2 Model Predictions. The computer program described above is used to predict the in-roll stress distribution of rolls wound at the winding conditions listed in Table 1. Key inputs to the model are summarized in Table 2, and the relationship among contact clearance, contact pressure, and roughness modulus from testing of the same polymer coated paper is listed in Table 3. From the model prediction, the contact pressures at the core at different winding conditions are listed in Table 1, and they agree fairly well with the respective contact pressures from the torque transmission tests.

When using the winding conditions of test 1 in Table 1, the total interlayer pressure, contact pressure, and air gage pressure distribution after winding are shown in Fig. 5. For comparison purposes, the interlayer pressure from a nonair entrainment model is also included. With the air entrainment effect, the total pressure is the sum of contact pressure and air pressure, the former of which is supported by roughness contact of two neighboring laps and the later from air gage pressure. The result indicates the existence of a core zone where the total pressure and gage pressure start at low values and then rapidly increase to peak pressures. Further out in the roll, the total pressure and gage pressure fall and become close to zero at the finished roll surface. The presence of the core zone is mostly due to the soft cardboard core, which results in a low core modulus, thus resulting in a sharp drop in the pressures at the core. In winding and in downstream unwinding, the torque from the core is transmitted from the inner laps to the outer laps by a friction force induced by direct contact pressure. The contact pressure at the core therefore determines the local torque transmission capability. The interlayer pressure from the non-air entrainment model is higher than the contact pressure but lower than the total interlayer pressure from the air entrainment model.

Figure 6 shows the interlayer tension, wound-in-tension, and machine tension stress distributions. Again, the interlayer tension from the non-air entrainment model is included for comparison purposes. Because of the low core modulus when the air effect is included, the interlayer tension stress near the core is highly negative, which could potentially cause local buckling. The wound-in-tension (tension in the outer lap downstream of the pressure roller) is higher than the machine tension (tension upstream of the pressure roller) due to the friction force induced by the pressure load underneath the pressure roller nip. The interlayer tension stress from the nonair entrainment model is different than that from the air entrainment model, and in this example does not show a region of sharp change near the core.

The contact clearances under the pressure roller, under the outer lap away from the nip, and after winding are shown in Fig. 7. All clearances are lower than the reference contact clearance cc_o and air film reference clearance ca_o. This indicates that throughout

Table 3 Roughness modulus of the polymer coated paper excluding air effect

Contact Clearance, μm	Contact Pressure, MPa	Stack Modulus, MPa
10.640	0.000	0.021
4.933	0.014	0.083
3.896	0.028	0.227
3.416	0.041	0.396
2.210	0.138	1.609
1.380	0.345	4.326
0.798	0.689	8.887
0.282	1.379	20.057
0.016	2.413	69.154

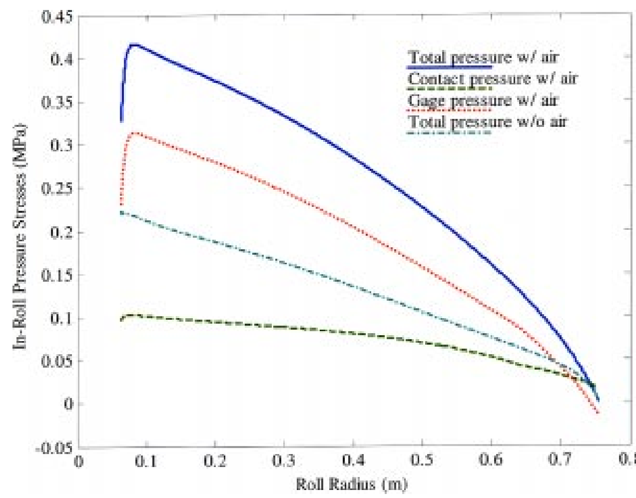

Fig. 5 In-roll pressure stresses right after winding from both air entrainment model and nonair entrainment model. The gage pressure is the air pressure above the ambient pressure.

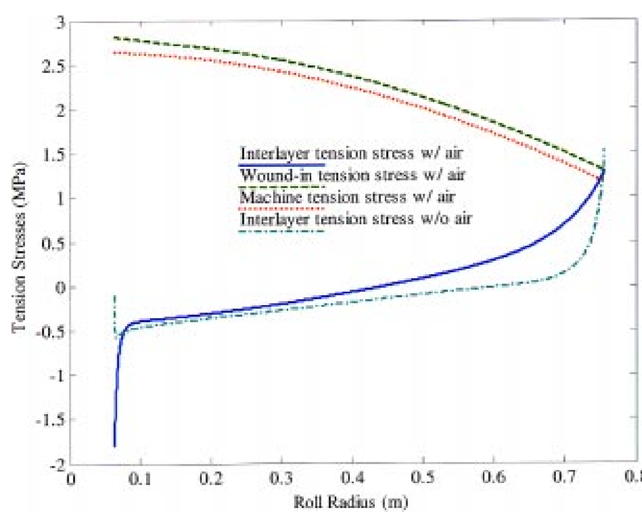

Fig. 6 In-roll tension stresses right after winding from both air entrainment model and nonair entrainment model

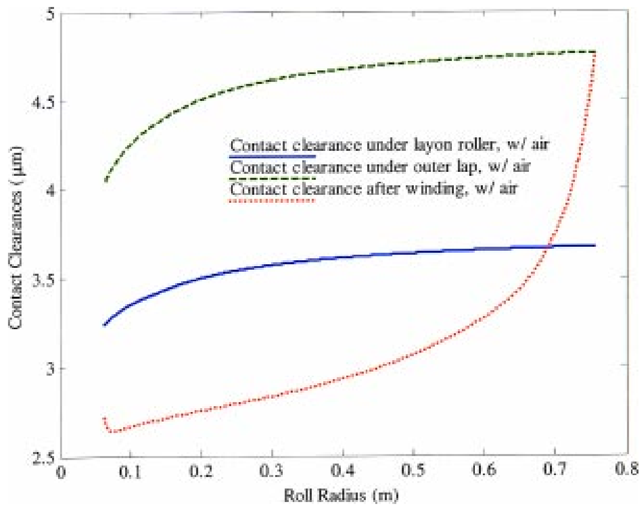

Fig. 7 Contact clearances under the pressure roller, under the outer lap away from the nip, and after winding

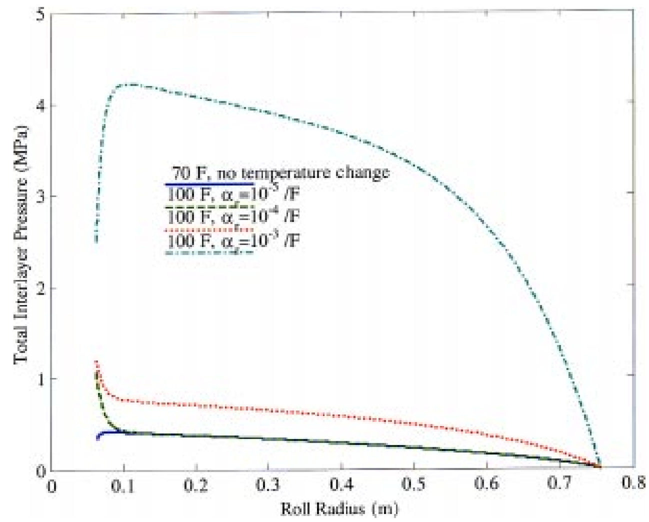

Fig. 8 The effect of roll radial CTE on total interlayer pressure right after winding at 70°F and after heated to 100°F. Results are from the air entrainment model. The radial CTE of the roll is indicated in the figure. Other CTEs are $\alpha_\theta=10^{-5}$/°F and $\alpha_c=10^{-4}$/°F.

the winding process, no laps are floating or are purely supported by air pressure. The contact clearance under the outer lap is below the contact reference clearance due to the existence of the pressure roller, which squeezes out most of the air under the nip and only lets a small amount of entrapped air into the roll. Contact clearance under the outer lap away from the nip is higher than that under the pressure roller, which suggests that right after being compressed by the pressure roller nip, the air under the outer lap expands. Depending on how much air passes through the nip and the wound-in-tension, the gage pressure could be negative under the outer lap away from the pressure roller nip, resulting in subambient air pressure locally.

6.3 Thermoelastic Effect. After winding, the rolls are usually put into storage before unwinding. The typical storage time varies from hours to years. Often, rolls are stored in nontemperature controlled warehouses where the roll temperature varies with the season. In some manufacturing processes, rolls are intentionally stored at elevated temperatures for a specific time to control certain web properties (such as core set curl). In-roll stress changes with roll temperature mostly because the coefficient of thermal expansion (CTE) of the web is anisotropic, and the core CTE is different than that of the web. The interlayer pressure increases at elevated temperature when the CTE along the radial direction is higher than that of the circumferential direction because the roll expands more along the radial direction than the hoop direction.

In the following, the temperature effect on wound roll stress is studied by assuming the roll is wound using test 1 (Table 1) winding conditions at an ambient temperature of 70°F, and after winding there is a step change in roll temperature from 70°F to 100°F. After the temperature change, the total interlayer pressure and contact pressure from the air entrainment model are shown in Figs. 8 and 9 at three levels of radial coefficient of thermal expansion, $\alpha_r=10^{-5}$, 10^{-4}, and 10^{-3} (1/°F). Other coefficients of thermal expansion are fixed at $\alpha_\theta=10^{-5}$ 1/°F tangentially for the web, and $\alpha_c=10^{-4}$ 1/°F for the core. As shown in Figs. 8 and 9, the total interlayer pressure is much more sensitive to the radial CTE than the contact pressure. This indicates that the increase in total interlayer pressure is mostly from the increase in gage pressure (the difference between the total interlayer pressure and contact pressure), which is due to both a higher temperature and a lower air gap.

When using the non-air entrainment model, the temperature effect to interlayer pressure is given in Fig. 10, which shows the effect of temperature change on interlayer pressure is similar to the total interlayer pressure when the air effect is included.

Besides the thermal expansion coefficients of the web, the wound roll stress is also affected by the thermal expansion coefficient of the core. At a temperature change from 70°F to 100°F, Figs. 11 and 12 give the model predictions of the total interlayer pressure and contact pressure at three levels of core coefficient of thermal expansion, $\alpha_c=10^{-5}$, 10^{-4}, and 10^{-3} (1/°F). Web coefficients of thermal expansion are fixed at $\alpha_r=10^{-4}$ 1/°F radially and $\alpha_\theta=10^{-5}$ 1/°F tangentially. When using the nonair entrainment model, the results are shown in Fig. 13. From the predictions, the core effect is only localized to the laps close to the core. A higher core thermal expansion coefficient than the web would enhance the thermal stress effect, and make the local in-roll pressure even higher when heated, and even lower when cooled.

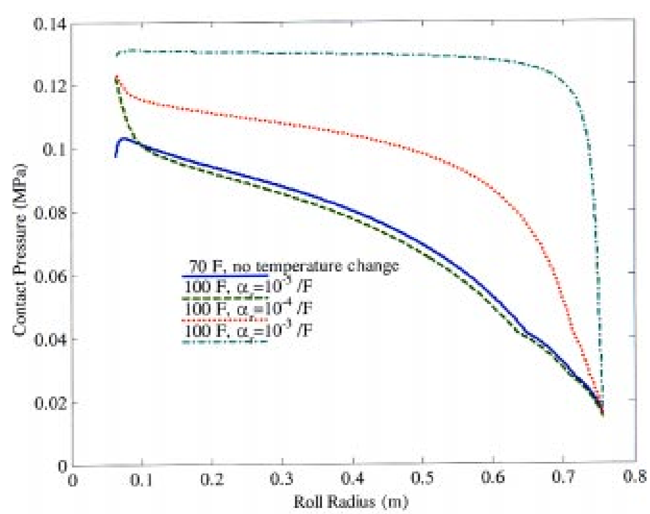

Fig. 9 The effect of roll radial CTE on contact pressure right after winding at 70°F and after heated to 100°F. Results are from the air entrainment model. The radial CTE of the roll is indicated in the figure. Other CTEs are $\alpha_\theta=10^{-5}$/°F and $\alpha_c=10^{-4}$/°F.

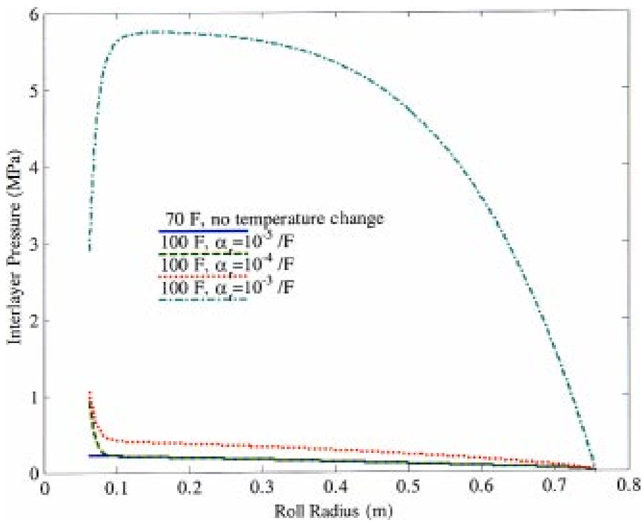

Fig. 10 The effect of roll radial CTE on interlayer pressure right after winding at 70°F and after heated to 100°F. Results are from the nonair entrainment model. The radial CTE of the roll is indicated in the figure. Other CTEs are $\alpha_\theta = 10^{-5}/°F$ and $\alpha_c = 10^{-4}/°F$.

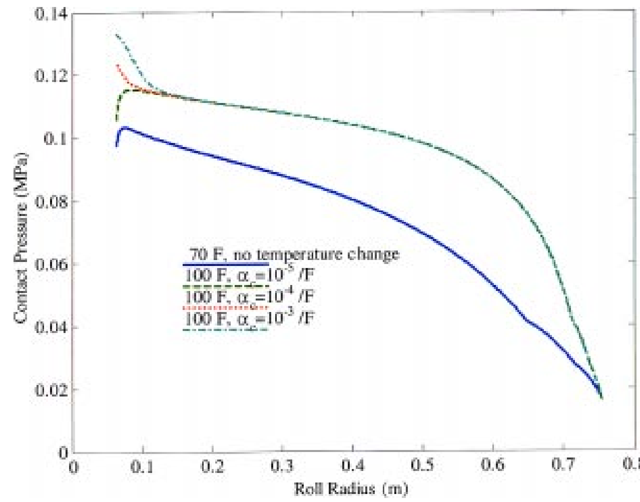

Fig. 12 The effect of roll core CTE on contact pressure right after winding at 70°F and after heated to 100°F. Results are from the air entrainment model. The core CTE of the roll is indicated in the figure. Other CTEs are $\alpha_r = 10^{-4}/°F$ and $\alpha_\theta = 10^{-5}/°F$.

7 Model Limitations

The model presented in this paper neglects the effect of side leakage both during and after winding. As the experimental results indicate, reasonable agreement is obtained for a specific test case. However, as process conditions are changed, it is expected that this assumption will no longer be valid. For example, as web width is decreased, the air under the outer lap will be more significantly affected by the atmospheric boundary conditions at either end of the roll. To further investigate the quantitative impact of this limitation, a simple theory was developed to establish time scales for air leakage from a wound roll and is presented in the Appendix.

Results from the analysis are presented in Figs. 14 and 15. These figures give a plot of the percentage of original air mass lost from the first lap of the roll (nearest the core) as a function of the initial clearance and the web width. The results are computed at the completion of winding and indicate that wider webs with smaller initial clearances have smaller air leakage and that less air leakage occurs at higher winding speeds. For example, as indicated in the Appendix, the initial clearance under the lap nearest the core after the 4th lap of the roll is added is equal 1.464 μm. This corresponds to results from test 1 from Table 1. Using these values and the web width in test 1, the percentage of air mass lost under the lap nearest the core at the completion of winding is between 25 and 40%. While this magnitude of air loss is significant, it is cumulative over the winding duration and therefore probably does not invalidate the winding model since the impact of added laps to interlayer pressure is localized to laps in the vicinity of the radial location of interest.

However, since even more air will leak out of the roll after winding, the subsequent assumption of no side leakage during the thermoelastic portion of the analysis is probably invalid. This sug-

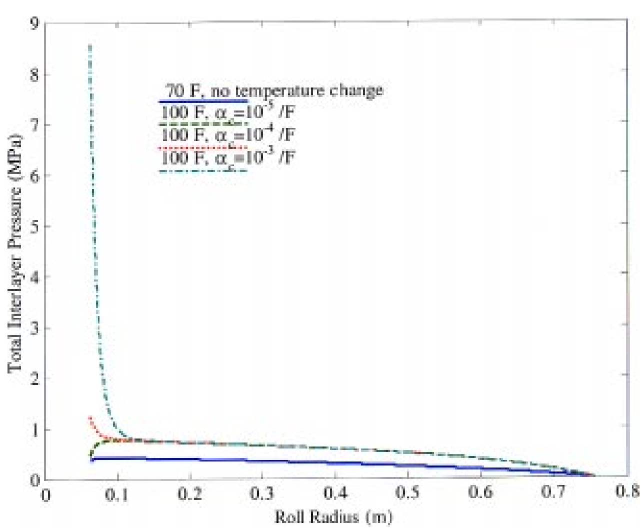

Fig. 11 The effect of roll core CTE on total interlayer pressure right after winding at 70°F and after heated to 100°F. Results are from the air entrainment model. The core CTE of the roll is indicated in the figure. Other CTEs are $\alpha_r = 10^{-4}/°F$ and $\alpha_\theta = 10^{-5}/°F$.

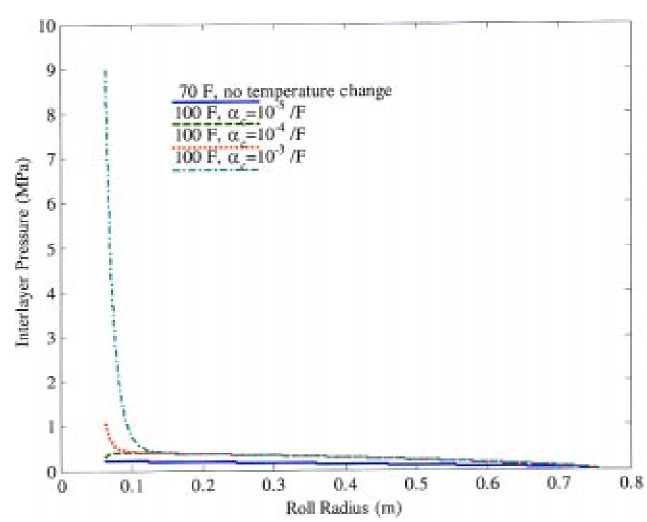

Fig. 13 The effect of roll core CTE on interlayer pressure right after winding at 70°F and after heated to 100°F. Results are from the nonair entrainment model. The core CTE of the roll is indicated in the figure. Other CTEs are $\alpha_r = 10^{-4}/°F$ and $\alpha_\theta = 10^{-5}/°F$.

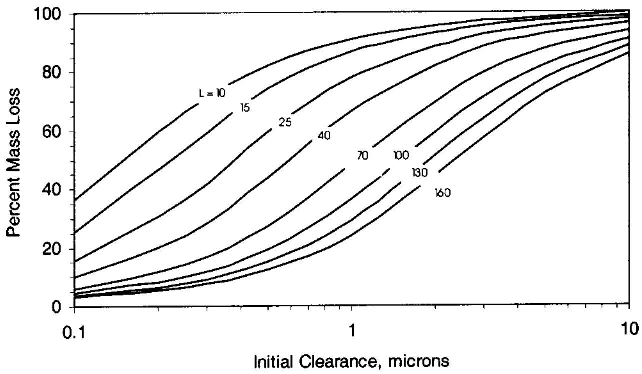

Fig. 14 Total mass of air lost from the first lap of a roll after winding 3089 laps at 2.54 m/s (500 ft/min), expressed as a percentage of the original mass in the lap. The half-width of the roller in centimeters, *L*, is indicated on the figure. Data are presented here for a core having outer diameter of 0.127 m (5 inches), and for a web thickness of 224 μm.

gests that for the range of speeds and for the web width considered in this study that the no side leakage assumption is not reasonable. However, as the web width is increased, the assumption is better met and in the limit for a very wide web, our thermoelastic results will be accurate. Therefore, for many practical web winding simulations, side leakage needs to be incorporated into the winding model. However, this will introduce much more complexity into the model and will be expected to be numerically intensive.

8 Conclusions

An air entrainment model was developed. The model includes a web roughness model, a pressure roller nip analysis, an outer lap analysis, and an in-roll analysis. In addition, the effect of temperature on thermoelastic stresses after winding is included. The winding model gives reasonable predictions compared with winding experiments on polymer coated paper. The parametric study showing the effect of CTEs on in-roll stress is also presented. Comparison to previous models excluding air entrainment indicates a very significant reduction in contact interlayer pressure caused by the trapped air. The model does not include side leakage during and after winding. An analysis was developed indicating the range over which this assumption is valid. Future modeling will be extended to include the effect of side leakage.

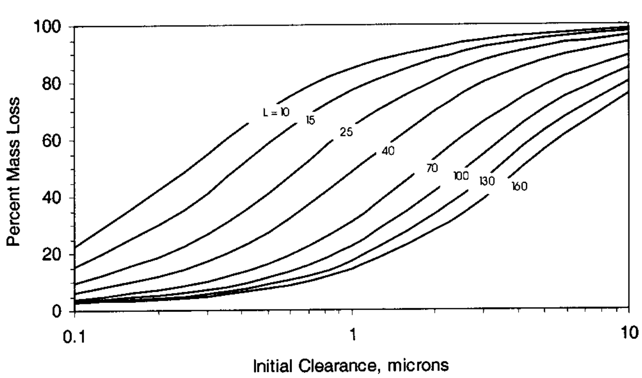

Fig. 15 Total mass of air lost from the first lap of a roll after winding 3089 laps at 7.62 m/s (1500 ft/min), expressed as a percentage of the original mass in the lap. The half-width of the roller in centimeters, *L*, is indicated on the figure. Data are presented here for a core having outer diameter of 0.127 m (5 inches), and for a web thickness of 224 μm.

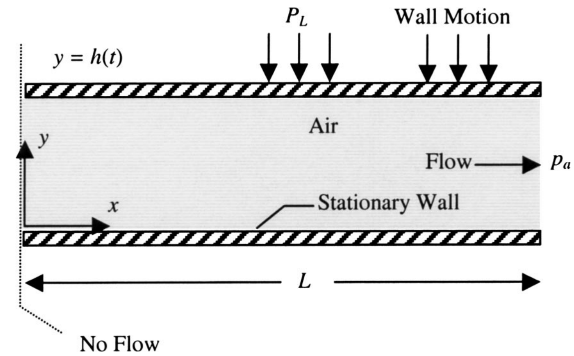

Fig. 16 Geometry for lubrication analysis of squeezing flow

Appendix

Air Leakage in Winding. The purpose of this appendix is to set forth a simple theory that establishes time scales for air leakage from a wound roll under a tensile load. The results of this theory may be used to demonstrate the validity of various assumptions used in winding models, which often involve issues regarding air leakage out of the widthwise edges of a roll while winding is occurring. The incorporation of air leakage into a winding model introduces much complexity and is numerically intensive; as such, the subsequent analysis can justify when the added complexity is necessary, and when a simpler nonleakage model is adequate.

Theory of Air Loss. We first consider a simple one-dimensional lubrication model for the "squeezing" of air out of a gap as it closes under a constant external load. This is to model the approximate air loss occurring on any single lap of the roll. We then provide some limiting cases of the lubrication model. Lastly, we show how the model is used to approximate the cumulative air loss in a given lap as more laps are added to a roll.

Consider the configuration shown in Fig. 16 in which walls bound a region containing air. The x-y coordinate system is as indicated, and the z-direction extends out of the figure. The domain has length L; we assume that the flow is invariant in the z-direction. At the location $x=0$, we assume that there can be no flow, and at $x=L$, we assume that the air pressure is atmospheric, p_a. We assume that the top wall of the domain is entirely flat and is set in motion due to a pressure difference between an external pressure load P_L, and an initial air pressure in the gap, P_H. We parameterize the moving top wall location as $y=h(t)$, while the bottom wall at $y=0$ remains stationary. As a result, the internal air generates a pressure field $P(x,t)$ that opposes this load, and there is a resulting air flow exiting from the domain at $x=L$. We assume that the air obeys a polytropic relation between the local density ρ and pressure, i.e.,

$$\rho = cP^{1/\gamma}, \tag{A1}$$

where c and γ are constants. For isothermal compression, $\gamma=1$, while for adiabatic compression, $\gamma=C_p/C_v$, where C_p and C_v are the respective heat capacities at constant pressure and volume ($\gamma\sim1.4$ for air); the flow is incompressible in the limit as γ approaches infinity. We further assume that inertial effects are negligible, and that the assumptions of lubrication theory are valid. These two assumptions are satisfied, provided

$$\frac{h_0}{L} \ll 1, \quad \left(\frac{\rho_0 Q_s}{\mu}\right)\left(\frac{h_0}{L}\right) \ll 1, \tag{A2}$$

where h_0 and ρ_0 are characteristic scales for the gap clearance and density, respectively; we choose these quantities as $h(t=0)=h_0$ and $\rho(t=0)=\rho_0$. Q_s is a volumetric flow per width scale given in ($A3g$). Our goal is to determine the pressure field in the small gap, the location of the top surface $h(t)$, and the mass of air exiting the domain to atmosphere as a function of time.

With the above stated assumptions, the dimensionless system governing the location of the moving wall and internal pressure is given by

$$\frac{\partial}{\partial \bar{t}}(\overline{hP^{1/\gamma}})+\frac{\partial}{\partial \bar{x}}(\overline{P}^{1/\gamma}\overline{Q})=0, \tag{A3a}$$

$$\overline{Q}=-\bar{h}^3\frac{\partial \overline{P}}{\partial \bar{x}}, \tag{A3b}$$

$$\int_0^1 \overline{P}d\bar{x}=1, \tag{A3c}$$

$$\overline{P}=\overline{P}_H, \quad \bar{h}=1, \quad \text{at } \bar{t}=0, \tag{A3d}$$

$$\frac{\partial \overline{P}}{\partial \bar{x}}=0 \quad \text{at } \bar{x}=0, \tag{A3e}$$

$$\overline{P}=\overline{P}_A \quad \text{at } \bar{x}=1, \tag{A3f}$$

where

$$\overline{P}=\frac{P}{P_L}, \quad \overline{P}_H=\frac{P_H}{P_L}, \quad \overline{P}_A=\frac{p_a}{P_L}, \quad \bar{x}=\frac{x}{L}, \quad \bar{t}=\frac{t}{t_s},$$

$$\overline{Q}=\frac{Q}{Q_s}, \quad t_s=\frac{12\mu L^2}{h_0^2 P_L}, \quad Q_s=\frac{h_0^3 P_L}{12\mu L}. \tag{A3g}$$

As indicated in (A3), our convention is that overbars denote dimensionless variables. In (A3), $\overline{Q}$ is the dimensionless volumetric flow rate per unit width. The above system (A3) is standard, except for the integral constraint (A3c) that balances forces on the moving wall. Note that in keeping with the constraints of lubrication theory, we have also neglected inertial effects in (A3c). The system (A3) is well posed to solve for the pressure and web location.

Of particular interest is the mass exiting the domain to atmosphere at $\bar{x}=1$. We determine this quantity as follows. First, the Eq. (A3a) is integrated in $\bar{x}$ between the limits 0 and 1 using the pressure boundary conditions in (A3e) and (A3f) to obtain

$$\overline{Q}|_{\bar{x}=1}=-\frac{1}{\overline{P}_A^{1/\gamma}}\frac{\partial}{\partial \bar{t}}\left(\bar{h}\int_0^1 \overline{P}^{1/\gamma}d\bar{x}\right). \tag{A4a}$$

The expression (A4a) yields the volumetric flow rate existing the domain. Since the flow is compressible, the mass flow rate, Q_m, is the useful quantity. Using the density given by (A1), the relation between the dimensionless mass and volumetric flow rate can be expressed as

$$\overline{Q}_m=\overline{P}_A^{1/\gamma}\overline{Q}, \quad \overline{Q}_m=\frac{Q_m}{cP_L^{1/\gamma}Q_s}, \tag{A4b}$$

and thus

$$\overline{Q}_m|_{\bar{x}=1}=-\frac{\partial}{\partial \bar{t}}\left(\bar{h}\int_0^1 \overline{P}^{1/\gamma}d\bar{x}\right). \tag{A4c}$$

The result (A4c) is integrated over time to yield the total mass per unit width that has left the domain at any time t, $M(t)$. Using the initial condition (A3d), we thus obtain

$$\overline{M}(\bar{t})=\overline{P}_H^{1/\gamma}-\bar{h}(\bar{t})\int_0^1 \overline{P}(\bar{x},\bar{t})^{1/\gamma}d\bar{x}, \quad \overline{M}(\bar{t})=\frac{M}{M_s},$$

$$M_s=cP_L^{1/\gamma}h_0L. \tag{A4d}$$

The original mass in the domain per unit width, M_0, can be expressed in dimensionless form using the density (A1), initial condition (A3d), and the dimensionless scaling for mass M_s given in (A4d) as

$$\overline{M}_0=\overline{P}_H^{1/\gamma}. \tag{A4e}$$

Finally, combining (A4d) and (A4e), we obtain the desired expression for the fraction of the original mass lost at any time as

$$\frac{M(t)}{M_0}=\frac{\overline{M}(\bar{t})}{\overline{M}_0}=1-\frac{\bar{h}(\bar{t})}{\overline{P}_H^{1/\gamma}}\int_0^1 \overline{P}(\bar{x},\bar{t})^{1/\gamma}d\bar{x}. \tag{A4f}$$

This concludes our derivation of the squeezing flow problem.

A numerical solution of (A3) is required except in certain limiting cases. To proceed, a new variable $U=\overline{hP^{1/\gamma}}$ is introduced into (A3). The resulting system is then solved using finite differences with a Crank-Nicholson implicit scheme, and a full Newton iteration at each time step.

An analytic solution to (A3) can be obtained for the limiting case of an incompressible fluid, for which $\gamma \sim \infty$ in (A1). Under such circumstances the $\overline{P}^{1/\gamma}$ terms in (A3a) are lost. Then, since $\overline{P}=\overline{P}(\bar{x},\bar{t})$ and $\bar{h}=\bar{h}(\bar{t})$, Eqs. (A3a) with (A3b) are separable and can be integrated; after subsequent application of the boundary conditions in (A3) we obtain

$$\bar{h}=[1+6(1-\overline{P}_A)\bar{t}]^{-1/2}, \tag{A5a}$$

$$\overline{P}=\frac{3}{2}(1-\overline{P}_A)(1-\bar{x}^2)+\overline{P}_A. \tag{A5b}$$

We note here that (A5b) does not satisfy the initial pressure condition in (A3d); an incompressible fluid instantaneously yields the pressure field (A5b) underneath the closing gap for all times. There is no finite transient in pressure as can be obtained in the case of a compressible fluid. For an incompressible fluid, the expression (A4f) for the fraction of the original mass lost from the domain becomes

$$\frac{M(t)}{M_0}=1-\bar{h}(\bar{t}), \tag{A5c}$$

which is identical to the fraction of the volume lost as expected.

On the other hand, for cases of negligible flow, $\overline{Q}\rightarrow 0$ in (A3a), and the system (A3) yields the simple result that

$$\overline{hP^{1/\gamma}}=K, \tag{A6}$$

where K is a constant. This case corresponds to the situation where there is no air leakage from the domain, and the pressure field is constant everywhere.

We now consider how the preceding model may be used to approximate the air leakage in a winding roll. To proceed, we assume that the air flow variations in the direction of the web motion are small compared with those across the width of the web. Thus, we focus attention solely on the air flow occurring in the widthwise direction towards the edges of the web. The no flux condition located at $x=0$ in Fig. 16 is interpreted as a symmetry condition for the roll width; thus, the computational length of the domain, L, is taken to be half of the roll width. We fix our view on a given lap in the roll, and track the mass of air lost in that particular lap as additional laps are added. Since the first lap (i.e., at the core) has the longest time available for air leakage and generally experiences the highest pressure loading, the cumulative amount of air leakage is the largest of all laps. For this reason, we examine the first lap in this appendix. We assume that when the first lap is an outer lap of the roll, it experiences a constant load (due to the roll tension) until one revolution of the roll occurs, at which time a second lap begins to be wound. At this point, there is an instantaneous pressure load increase on the original lap, which

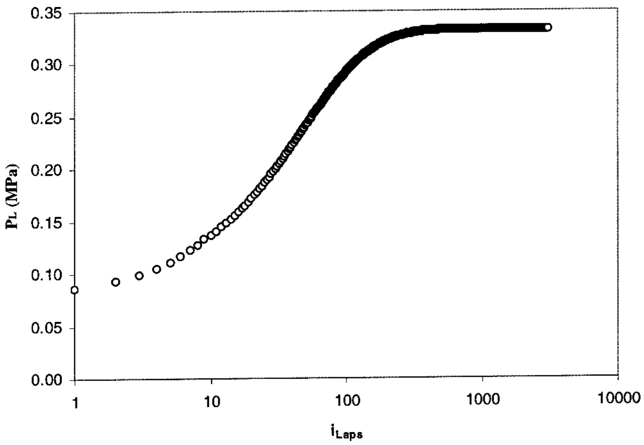

Fig. 17 Calculated absolute air pressures under the first lap (circles) from full winding model. These air pressures are used to model the air loss under the first lap.

again remains constant for the whole lap. This procedure is continued as more laps are added. For a web moving at speed V, the time to complete a revolution, t_R, is given by

$$t_R=\frac{2\pi(r+(i-1)h_a)}{V}. \tag{A7}$$

Thus, in (A7), any given pressure load is applied for the length of time t_R.

A relation between the load pressure, P_L, and the number of laps being wound onto the roll, i, is required so that (A3) may be solved on each lap. One such relationship may be obtained via a simple membrane theory between pressure and tension in which there is no contact between laps as additional laps are added. A more realistic pressure load model incorporates the effect of web-to-web contact, which tends to reduce the pressure load on the air. To obtain such an expression, the full winding model detailed in this report was utilized; as in the case of our air leakage model, the full winding model assumes that the pressure load remains constant until a new lap is added. Although this relationship generally changes as winding conditions are altered, we simplified our calculations by obtaining a single relationship between P_L and i for one set of intermediate winding parameters, and then used this relationship for all data generated from the simple model. As the pressure relationship from the full winding model assumes no air leakage, we can assume that the results of our simple model are self-consistent when the mass loss due to air flow is small. In cases where the mass loss is large, the full winding model is invalid for those specific conditions.

The numerical procedure is thus as follows. For the outer lap, the system (A3) is solved as written. When the next lap is added, the pressure load increases. The system (A3) is then solved again, where the initial condition (A3d) is replaced by the pressure field and height of the web at the end of the previous lap. This procedure is repeated as more laps are added to the roll.

Air Loss Results. We begin by obtaining the relationship between pressure loading, P_L, and the lap number, i, from the winding model; this relationship is used in the generation of all subsequent data from the simple air-leakage model. The winding model with air entrainment (no side leakage) was run to give the pressure loading and the lap number under the first lap (Fig. 17) using the winding conditions in test I of Table 1. We next proceeded to generate data from the simple air flow model following the algorithm in the preceding section. Note that as the full winding model is assumed to be isothermal, all subsequent calculations are for isothermal conditions, i.e., $\gamma=1$ in (A3) and (A4). Comparisons between results for cases where the compressibility is assumed to be adiabatic versus isothermal show some relatively small quantitative differences, but the qualitative trends are the same. Figure 14 gives a plot of the percentage of the original air mass lost from the first lap of the roll as a function of the initial clearance between the web and the roll, for various web widths. Data is provided after winding 3089 laps for a winding speed of 2.54 m/s (500 ft/min); the air exits the web at the ambient atmospheric pressure. It is assumed that the initial pressure in the gap at time $t=0$ is equal to the imposed load pressure (i.e., $\bar{P}_H=1$ in (A3) and (A4) in the first lap at the start of the calculation). Figure 15 provides data for the same conditions as Fig. 14, except at 7.62 m/s (1500 ft/min). Note that in generating these figures, we started our calculation when the 4th lap of the roll was added ($P_H=0.105$ MPa and $ca=h_0=1.464\,\mu$m), as this is the first lap for which the pressure in the clearance (i.e., between the web and the roller) is larger than atmospheric pressure. In the simple model, if the pressure in the clearance is subatmospheric, then air moves into the gap and initially increases the clearance. Furthermore, the simple model predicts a relatively large increase in clearance; calculations show it takes hundreds of laps to again squeeze this increased mass out of the domain as the pressure loading increases. It is our opinion that this behavior is not physical, as the neglected local deformation of the web would presumably reduce this large increase in air mass. Figures 14 and 15 indicate that, as expected, wider webs with smaller initial clearances have smaller air leakage, where less air leakage occurs at faster winding speeds.

References

[1] Altmann, H. C., 1968, "Formulas for Computing the Stresses in Center Wound Rolls," Tappi J., **51**, pp. 176–179.
[2] Connolly, D., and Winarski, D. J., 1984, "Stress Analysis of Wound Magnetic Tape," ASLE Special Publication SP-16, pp. 148–157.
[3] Hakiel, Z., 1987, "Nonlinear Model for Wound Roll Stresses," Tappi J., **70**, pp. 113–117.
[4] Qualls, W. R., 1995, "Hygrothermomechanical Characterization of Viscoelastic Centerwound Rolls," Ph.D. thesis, Oklahoma State University.
[5] Good, J. K., Wu, Z., and Fikes, M. W. R., 1994, "The Internal Stresses in Wound Rolls With the Presence of a Nip Roller," ASME J. Appl. Mech., **61**, pp. 182–185.
[6] Good, J. K., and Holmberg, M. W., 1993, "The Effect of Air Entrainment in Centerwound Rolls," *Proceedings of the Second International Conference on Web Handling*, James K. Good, ed., Web Handling Research Center, Oklahoma State University, Stillwater, OK.
[7] Good, J. K., and Covell, S. M., 1995, "Air Entrapment and Residual Stresses in Rolls Wound With a Rider Roll," *Proceedings of the Third International Conference on Web Handling*, James K. Good, ed., Web Handling Research Center, Oklahoma State University, Stillwater, OK.
[8] Chang, Y. B., Chambers, F. W., and Shelton, J. J., 1996, "Elastohydrodynamic Lubrication of Air-Lubricated Rollers," ASME J. Tribol., **118**, pp. 623–628.
[9] Taylor, R. M., and Good, J. K., 1997, "Entrained Air Films in Center Wound Rolls—With and Without the Nip," *Proceedings of the Fourth International Conference on Web Handling*, James K. Good, ed., Web Handling Research Center, Oklahoma State University, Stillwater, OK.
[10] Forrest, A. W., 1995, "Air Entrainment During Film Winding With Layon Rolls," *Proceedings of the Third International Conference on Web Handling*, James K. Good, ed., Web Handling Research Center, Oklahoma State University, Stillwater, OK.
[11] Forrest, A. W., 1995, "Wound Roll Stress Analysis Including Air Entrainment and the Formation of Roll Defects," *Proceedings of the Third International Conference on Web Handling*, James K. Good, ed., Web Handling Research Center, Oklahoma State University, Stillwater, OK.
[12] Bouquerel, F., and Bourgin, P., 1993, "Irreversible Reduction of Foil Tension Due to Aerodynamical Effects," *Proceedings of the Second International Conference on Web Handling*, James K. Good, ed., Web Handling Research Center, Oklahoma State University, Stillwater, OK.
[13] Bourgin, P., 1997, "Air Entrainment in Web Handling: To be Avoided or Mastered?" *Proceedings of the Fourth International Conference on Web Handling*, James K. Good, ed., Web Handling Research Center, Oklahoma State University, James K. Good, ed., Web Handling Research Center, Oklahoma State University, Stillwater, OK.
[14] Forrest, A. W., 1999, "Optimization of Equipment and Process Conditions for Film Winding," *Proceedings of the Fifth International Conference on Web Handling*, James K. Good, ed., Web Handling Research Center, Oklahoma State University, Stillwater, OK.

[15] Pfeiffer, J. D., 1981, ''Measurement of K2 Factor for Paper,'' Tappi J., **64**, pp. 105–106.
[16] Pfeiffer, J. D., 1999, ''Compressive Modulus Measurement Techniques,'' *Proceedings of the Fifth International Conference on Web Handling*, James K. Good, ed., Web Handling Research Center, Oklahoma State University, Stillwater, OK.
[17] Forrest, A. W., 1993, ''A Mathematical and Experimental Investigation of the Stack Compression of Films,'' *Proceedings of the Second International Conference on Web Handling*, James K. Good, ed., Web Handling Research Center, Oklahoma State University, Stillwater, OK.
[18] Rice, B. S., Cole, K. A., and Müftü, S., 1999, ''An Experimental and Theoretical Study of Web Traction Over a Nonvented Roller,'' *Proceedings of the Fifth International Conference on Web Handling*, James K. Good, ed., Web Handling Research Center, Oklahoma State University, Stillwater, OK.
[19] Timoshenko, S., 1970, *Theory of Elasticity*, McGraw-Hill, New York, p. 418.

Weakly Nonlinear Stability Analysis of Condensate/ Evaporating Power-Law Liquid Film Down an Inclined Plane

R. Usha

B. Uma

Department of Mathematics,
Indian Institute of Technology, Madras,
Chennai 600 036, India

Weakly nonlinear stability analysis of thin power-law liquid film flowing down an inclined plane including the phase change effects at the interface has been investigated. A normal mode approach and the method of multiple scales are employed to carry out the linear stability solution and the nonlinear stability solution for the film flow system. The results show that both the supercritical stability and subcritical instability are possible for condensate, evaporating and isothermal power-law liquid film down an inclined plane. The stability characteristics of the power-law liquid film show that isothermal and evaporating films are unstable for any value of power-law index 'n' while there exists a critical value of power-law index 'n' for the case of condensate film above which condensate film flow system is always stable. Thus, the results of the present analysis show that the mass transfer effects play a significant role in modifying the stability characteristics of the non-Newtonian power-law fluid flow system. The condensate (evaporating) power-law fluid film is more stable (unstable) than the isothermal power-law fluid film flowing down an inclined plane. [DOI: 10.1115/1.1631592]

1 Introduction

The stability of fluid flowing down a vertical or inclined wall has been the subject of considerable research due to its importance in many industrial applications such as film coating and interface heat and mass transfer processes in chemical technology and energetics. The problem of linear stability of thin liquid layers draining down an inclined plane surface has been considered by Yih [1] for isothermal films. The elegant explanation by Landau [2] for the transition mechanism from laminar to turbulent flow has provided a motivation for later developments on nonlinear film stability. Benjamin [3] and Yih [4] have formulated the disturbed wave equation of free film surface and studied the flow and stability characteristics of an isothermal film on an inclined plane.

Although the theory of laminar film condensation flow due to gravity has been analyzed by Nusselt [5], the stability of condensate film has not been studied until the 1970s. The stability analysis of a condensate film down a vertical or an inclined plane has been performed by Bankoff [6], Marshall and Lee [7], and Lin [8] and their investigations have revealed that the critical Reynolds number is small for all practical condensation problems so that the liquid film can be regarded as unstable. They have also pointed out that condensation would stabilize the film flow whereas evaporation would destabilize the flow. Ünsal and Thomas [9] have considered the effects of mass transfer at the interface and have presented the linear stability analysis of condensate film flow. It is known that the effects of heat transfer appear mainly in thermocapillary and vapor recoil effects. Since surface tension generally decreases with temperature, very thin layers of a non-volatile liquid on a heated surface tend to destabilize the film. On the other hand, vapor recoil effects are destabilizing for a volatile liquid, [10,11].

Contributed by the Applied Mechanics Division of THE AMERICAN SOCIETY OF MECHANICAL ENGINEERS for publication in the ASME JOURNAL OF APPLIED MECHANICS. Manuscript received by the ASME Applied Mechanics Division, Mar. 3, 2002; final revision, Apr. 23, 2003. Associate Editor: D. A. Siginer. Discussion on the paper should be addressed to the Editor, Prof. Robert M. McMeeking, Department of Mechanical and Environmental Engineering University of California–Santa Barbara, Santa Barbara, CA 93106-5070, and will be accepted until four months after final publication of the paper itself in the ASME JOURNAL OF APPLIED MECHANICS.

Using perturbation methods, Ünsal and Thomas [12] have investigated the nonlinear stability of vertical condensate film flow. Hwang and Weng [13] have examined the finite-amplitude stability analysis of liquid film down a vertical plane with and without interfacial phase change and have shown that both supercritical stability and subcritical instability are possible for condensate film flow system.

In contrast to the vast majority of investigations on Newtonian film flows (isothermal, condensate, evaporating), relatively few papers have been published on the dynamics of non-Newtonian film flows. The dynamics of non-Newtonian fluids are important in the understanding of the rheological behavior of fluids during the manufacturing process, movement of biological fluids, application of paints and performance of lubricants. Apart from investigation on flow characteristics and linear stability analysis of non-Newtonian fluid films along a vertical or an inclined plane, [14–17], investigations on films of inelastic non-Newtonian fluids have considered either the boundary layer development in the entrance region or linear instability analysis of the primary flow, [18,19].

Motivated by the scarcity of nonlinear theories for large Reynolds number flows of non-Newtonian fluids, Lee [20] has focussed his attention on the investigation of stability characteristics of an inelastic fluid of shear-thinning type down an incline using dynamical systems approach. He has employed a new rheological model with three parameters, called the modified power-law which exhibits the shear thinning behavior away from the zero shearing rate.

The investigations on the stability characteristics of Newtonian fluid film down an inclined/a vertical plane show that in the linear theory, the film flow system is unstable for any Reynolds number. However, the finite-amplitude stability analysis of liquid films down a vertical wall by Hwang and Weng [13] with interfacial phase change reveal that the isothermal and evaporating Newtonian films are unstable for any Reynolds number while there exists a finite critical Reynolds number for the case of condensate film below which condensate Newtonian film flow system is always stable. This shows that the effect of mass transfer at the interface of a Newtonian fluid film strongly modifies the stability characteristics of the film flow when the phase change is considered. In

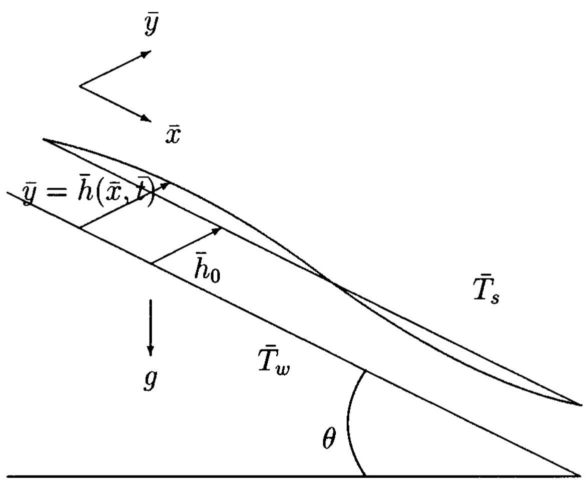

Fig. 1 Schematic representation of a thin film flow down an inclined plane

view of this, it becomes important to include the effects of phase change at the interface in the study of stability characteristics of a fluid film down an inclined or a vertical wall. Such an investigation has not been considered so far, for non-Newtonian inelastic fluids.

In this paper, the weakly nonlinear instability of condensate/evaporating power-law liquid film flowing down an inclined plane is investigated. The finite-amplitude stability of the power-law film is examined and the study extends the investigation by Lin and Hwang [21] by including the effects of phase change at the interface. The method of multiple scales is employed to solve the nonlinear generalized kinematic equation order by order. This leads to a secular equation of Ginzburg-Landau type. The analysis shows that supercritical stability and subcritical instability are both possible for the film flow system. Applications of the results to isothermal, condensate, and evaporating power-law film flow indicate that mass transfer into (away from) the liquid phase stabilizes (destabilizes) the film flow and that the power-law index 'n' strongly influences the stability characteristics of the non-Newtonian inelastic fluids.

2 Mathematical Formulation

A thin power-law liquid film flow with phase change at the interface $\bar{y}=\bar{h}(\bar{x},\bar{t})$ flowing down an inclined plane $\bar{y}=0$ (Fig. 1) is considered.

The governing equations, [13,21], are the two-dimensional mass, momentum, and energy balance equations for the power-law model given by

$$\frac{\partial \bar{u}}{\partial \bar{x}}+\frac{\partial \bar{v}}{\partial \bar{y}}=0 \tag{1}$$

$$\rho\left(\frac{\partial \bar{u}}{\partial t}+\bar{u}\frac{\partial \bar{u}}{\partial \bar{x}}+\bar{v}\frac{\partial \bar{u}}{\partial \bar{y}}\right)=-\frac{\partial \bar{p}}{\partial \bar{x}}+\rho g\sin\theta(1-\gamma)+\frac{\partial \bar{\tau}_{xx}}{\partial \bar{x}}+\frac{\partial \bar{\tau}_{xy}}{\partial \bar{y}} \tag{2}$$

$$\rho\left(\frac{\partial \bar{v}}{\partial t}+\bar{u}\frac{\partial \bar{v}}{\partial \bar{x}}+\bar{v}\frac{\partial \bar{v}}{\partial \bar{y}}\right)=-\frac{\partial \bar{p}}{\partial \bar{y}}-\rho g\cos\theta(1-\gamma)+\frac{\partial \bar{\tau}_{yx}}{\partial \bar{x}}+\frac{\partial \bar{\tau}_{yy}}{\partial \bar{y}} \tag{3}$$

$$\left(\frac{\partial \bar{T}}{\partial t}+\bar{u}\frac{\partial \bar{T}}{\partial \bar{x}}+\bar{v}\frac{\partial \bar{T}}{\partial \bar{y}}\right)=\frac{K}{\rho c_p}\left(\frac{\partial^2 \bar{T}}{\partial \bar{x}^2}+\frac{\partial^2 \bar{T}}{\partial \bar{y}^2}\right) \tag{4}$$

where K is the thermal conductivity, ρ is the density, c_p is the liquid specific heat, g is the gravity, γ is the ratio of vapor density to liquid density and $\bar{T}$ is the temperature.

The boundary conditions at the wall are the no slip condition of velocity and a constant wall temperature ($\bar{T}_w$) given by

$$\bar{u}=0,\quad \bar{v}=0,\quad \bar{T}=\bar{T}_w \quad \text{on } \bar{y}=0. \tag{5}$$

The boundary conditions at the liquid-vapor interface, [12,13], are the balance of normal and tangential stresses, the relation of interfacial energy balances and the equality of liquid and saturated vapor temperatures ($\bar{T}_s$) and are given by

$$\begin{aligned}\bar{p}&+\left(2\frac{\partial \bar{h}}{\partial \bar{x}}\bar{\tau}_{xy}-\left(\frac{\partial \bar{h}}{\partial \bar{x}}\right)^2\bar{\tau}_{xx}-\bar{\tau}_{yy}\right)\left(1+\left(\frac{\partial \bar{h}}{\partial \bar{x}}\right)^2\right)^{-1}\\&+K^2 h_{fg}^{-2}\frac{(\gamma-1)}{\rho\gamma}\left(\frac{\partial \bar{T}}{\partial \bar{y}}-\frac{\partial \bar{h}}{\partial \bar{x}}\frac{\partial \bar{T}}{\partial \bar{x}}\right)^2\left(1+\left(\frac{\partial \bar{h}}{\partial \bar{x}}\right)^2\right)^{-1}\\&+\sigma\frac{\partial^2 \bar{h}}{\partial \bar{x}^2}\left[1+\left(\frac{\partial \bar{h}}{\partial \bar{x}}\right)^2\right]^{-3/2}=\bar{p}_a \quad \text{on } \bar{y}=\bar{h}\end{aligned} \tag{6}$$

$$\frac{\partial \bar{h}}{\partial \bar{x}}(\bar{\tau}_{yy}-\bar{\tau}_{xx})+\left(1-\left(\frac{\partial \bar{h}}{\partial \bar{x}}\right)^2\right)^{-1}\bar{\tau}_{xy}=0 \quad \text{on } \bar{y}=\bar{h} \tag{7}$$

$$K\left(\frac{\partial \bar{T}}{\partial \bar{y}}-\frac{\partial \bar{h}}{\partial \bar{x}}\frac{\partial \bar{T}}{\partial \bar{x}}\right)-\rho h_{fg}\left(\frac{\partial \bar{h}}{\partial \bar{t}}+\bar{u}\frac{\partial \bar{h}}{\partial \bar{x}}-\bar{v}\right)=0 \quad \text{on } \bar{y}=\bar{h} \tag{8}$$

$$\bar{T}=\bar{T}_s \quad \text{on } \bar{y}=\bar{h} \tag{9}$$

where

$$\bar{\tau}_{xx}=2\mu_n\frac{\partial \bar{u}}{\partial \bar{x}}\left(\frac{\partial \bar{u}}{\partial \bar{y}}\right)^{n-1} \tag{10}$$

$$\bar{\tau}_{xy}=\bar{\tau}_{yx}=\mu_n\left(\frac{\partial \bar{u}}{\partial \bar{y}}\right)^{n} \tag{11}$$

$$\bar{\tau}_{yy}=-2\mu_n\frac{\partial \bar{u}}{\partial \bar{x}}\left(\frac{\partial \bar{u}}{\partial \bar{y}}\right)^{n-1} \tag{12}$$

and μ_n is the consistency coefficient, n is the flow index. When the power-law exponent n is equal to 1, then the model describes the Newtonian fluid; If $n<1$, the fluid is said to be pseudoplastic or shear thinning and if $n>1$, the fluid is called dilatant or shear thickening. It is important to note that the zero shear assumption in Eq. (7) is a reasonable approximation for external gravity dominated flows ($\theta>0$ deg) only and not for shear dominated horizontal or near horizontal flows. Using the dimensionless quantities defined by

$$u=\frac{\bar{u}}{\bar{u}_0},\quad v=\frac{\bar{v}}{\alpha\bar{u}_0},$$

(velocities in the $\bar{x}$ and $\bar{y}$ directions, respectively)

$$x=\frac{\alpha\bar{x}}{h_0},\quad y=\frac{\bar{y}}{h_0},$$

$$t=\frac{\alpha\bar{u}_0\bar{t}}{h_0}\ \text{(time)},\quad H=\frac{\bar{h}}{h_0},\quad \text{(film thickness)},$$

$$\text{Fr}=\frac{\bar{u}_0^2}{g(1-\gamma)h_0},\quad \text{(Froude number)},$$

$$\bar{u}_0=\frac{n}{n+1}\left(\frac{\rho g(1-\gamma)\sin\theta}{\mu_n}\right)^{1/n}\bar{h}_0^{(n+1)/n}\ \text{(reference velocity)},$$

$$\alpha=\frac{2\pi\overline{h}_0}{\lambda}\ \text{(wave number)},$$

$$p=\frac{\overline{p}-\overline{p}_a}{\rho\overline{u}_0^2}\ \text{(pressure)},$$

$$\Theta=\frac{\overline{T}-\overline{T}_w}{T_s-T_w}\ \text{(temperature)},$$

$$\mathrm{Re}_n=\frac{\rho\overline{u}_0^{2-n}\overline{h}_0^n}{\mu_n}\ \text{(Reynolds number)},\qquad(13)$$

$$\mathrm{Pr}_n=\frac{\mu_n\overline{u}_0^{n-1}\overline{h}_0^{1-n}c_p}{K}\ \text{(Prandtl number)},$$

$$Pe_n=\mathrm{Pr}_n\cdot\mathrm{Re}_n\ \text{(Peclet number)},$$

$$\xi=\frac{c_p\Delta T}{h_{fg}}(h_fg-\text{latent heat}),$$

$$Fi_n=\frac{\sigma}{\rho\overline{u}_0^2\overline{h}_0}=\mathrm{We}_n\,\mathrm{Re}_n^{-(3n+2)/(n+2)}\times\left(\frac{1}{\sin\theta}\right)^{(3n-2)/(n+2)},$$

$$Nd=\frac{\xi^2}{\gamma Pr_n^2},$$

$$\mathrm{We}_n=\sigma\rho^{-1}\left[\left(\frac{n+1}{n}\right)^{n(3n-2)}\times[(1-\gamma)g]^{-(3n-2)}\nu^{-4}\right]^{1/(n+2)}$$

(Weber number)

the nondimensional governing equations and the boundary conditions are obtained as

$$\frac{\partial u}{\partial x}+\frac{\partial v}{\partial y}=0\qquad(14)$$

$$\alpha\left(\frac{\partial u}{\partial t}+u\frac{\partial u}{\partial x}+v\frac{\partial u}{\partial y}+\frac{\partial p}{\partial x}\right)=\frac{\sin\theta}{Fr}+\frac{\alpha^2}{\mathrm{Re}_n}\frac{\partial r_{xx}}{\partial x}+\frac{1}{\mathrm{Re}_n}\frac{\partial\tau_{xy}}{\partial y}\qquad(15)$$

$$\alpha^2\left(\frac{\partial v}{\partial t}+u\frac{\partial v}{\partial x}+v\frac{\partial v}{\partial y}\right)=-\frac{\partial p}{\partial y}-\frac{\cos\theta}{\mathrm{Fr}}+\frac{\alpha}{\mathrm{Re}_n}\left(\frac{\partial\tau_{yx}}{\partial x}+\frac{\partial\tau_{yy}}{\partial y}\right)\qquad(16)$$

$$\frac{\partial^2\Theta}{\partial y^2}=\alpha Pe_n\left(\frac{\partial\Theta}{\partial t}+u\frac{\partial\Theta}{\partial x}+v\frac{\partial\Theta}{\partial y}\right)-\alpha^2\frac{\partial^2\Theta}{\partial x^2}\qquad(17)$$

$$u=0,\quad v=0,\quad\Theta=0\quad\text{on }y=0\qquad(18)$$

$$p+\frac{1}{\mathrm{Re}_n}\left[2\alpha\frac{\partial H}{\partial x}\tau_{xy}-\alpha\tau_{yy}-\alpha^3\left(\frac{\partial H}{\partial x}\right)^2\tau_{xx}\right]\left(1+\alpha^2\left(\frac{\partial H}{\partial x}\right)^2\right)^{-1}+\alpha^2Fi_n\frac{\partial^2H}{\partial x^2}\left(1+\alpha^2\left(\frac{\partial H}{\partial x}\right)^2\right)^{-3/2}+Nd\,\mathrm{Re}_n^{-2}(\gamma-1)\left(\frac{\partial\Theta}{\partial y}-\alpha^2\frac{\partial H}{\partial x}\frac{\partial\Theta}{\partial x}\right)^2\left(1+\alpha^2\left(\frac{\partial H}{\partial x}\right)^2\right)^{-1}=0\quad\text{on }y=H\qquad(19)$$

$$\alpha^2\frac{\partial H}{\partial x}(\tau_{yy}-\tau_{xx})+\left(1-\alpha^2\left(\frac{\partial H}{\partial x}\right)^2\right)^{-1}\tau_{xy}\quad\text{on }y=H\qquad(20)$$

$$\xi\left(\frac{\partial\Theta}{\partial y}-\alpha^2\frac{\partial H}{\partial x}\frac{\partial\Theta}{\partial x}\right)-\alpha Pe_n\left(\frac{\partial H}{\partial t}+u\frac{\partial H}{\partial x}-v\right)=0\quad\text{on }y=H\qquad(21)$$

$$\Theta=1\quad\text{on }y=H.\qquad(22)$$

In (21), $\xi>0$ corresponds to condensate film flow, $\xi<0$ to evaporating film flow and $\xi=0$ corresponds to isothermal film.

It is to be noted that when $n=1$, $\theta=90$ deg, the above equations and boundary conditions reduce to evaporating or condensating Newtonian flow down a vertical wall investigated by Hwang and Weng [13] and for $\xi=0$ (with no phase change at the interface), they reduce to the equations obtained for isothermal power-law fluid film flow investigated by Lin and Hwang [21]. When $n=1$, $\xi=0$ and $\theta=90$ deg, the equations agree with the equations governing the Newtonian film flow down a vertical wall investigated by Hung et al. [22] (for a fluid with no micropolar effect). Since the long wavelength modes are the most unstable ones for the film flow, the physical quantities u, v, p, and Θ are expanded in powers of small wave number α. Substituting these in (14)–(22) and collecting the coefficients of like powers of α, the zeroth and the first-order equations are obtained. Noting that We_n is large in practical applications, $\alpha^2\mathrm{We}_n$ is taken to be of order one. Also, since the effect of Nd has been found to be negligible on stability, [9], $Nd\,\mathrm{Re}_n^{-2}$ is taken to be of order α^2. Further, in the analysis, $\mathrm{Re}_n\simeq O(1)$ and $\mathrm{Pe}_n\simeq O(1)$. The solutions are given by

$$u_0=\left(\frac{\mathrm{Re}_n\sin\theta}{\mathrm{Fr}}\right)^{1/n}\left(\frac{n}{n+1}\right)[H^{(n+1)/n}-(H-y)^{(n+1)/n}],$$

$$v_0=-\left(\frac{\mathrm{Re}_n\sin\theta}{\mathrm{Fr}}\right)^{1/n}\times H_x\left[H^{1/n}y+\frac{n}{n+1}(H-y)^{(n+1)/n}-\frac{n}{n+1}H^{(n+1)/n}\right],$$

$$p_0=\frac{\cos\theta}{\mathrm{Fr}}(H-y)-\alpha^2\mathrm{Fi}_nH_{xx}\qquad(23)$$

$$\Theta_0=\frac{y}{H}$$

$$
\begin{aligned}
u_1 = &-\frac{\mathrm{Re}_n\,\xi}{(n+1)\alpha\mathrm{Pe}_n}\left(\frac{\mathrm{Re}_n\sin\theta}{\mathrm{Fr}}\right)^{(2-n)/n}\frac{1}{H}\left[H^{1/n}(H^{(n+1)/n}-(H-y)^{(n+1)/n})-\frac{n}{n+2}(H^{(n+2)/n}-(H-y)^{(n+2)/n})\right]\\
&+\frac{\mathrm{Re}_n}{(n+1)^2}\left(\frac{\mathrm{Re}_n\sin\theta}{\mathrm{Fr}}\right)^{(3-n)/n}H_xH^{1/n}\left[H^{(n+1)/n}(H^{(n+1)/n}-(H-y)^{(n+1)/n})-\frac{n}{2(2n+1)}(H^{2(n+1)/n}-(H-y)^{2(n+1)/n})\right]\\
&-\frac{\mathrm{Re}_n}{(n+1)}\frac{\cos\theta}{\mathrm{Fr}}\left(\frac{\mathrm{Re}_n\sin\theta}{\mathrm{Fr}}\right)^{(1-n)/n}H_x[H^{(n+1)/n}-(H-y)^{(n+1)/n}]\\
&+\frac{\mathrm{Re}_n}{(n+1)}\left(\frac{\mathrm{Re}_n\sin\theta}{\mathrm{Fr}}\right)^{(1-n)/n}\alpha^2Fi_nH_{xxx}[H^{(n+1)/n}-(H-y)^{(n+1)/n}],\\
v_1 = &-\frac{\mathrm{Re}_n\,\xi}{(n+1)\alpha\mathrm{Pe}_n}\left(\frac{\mathrm{Re}_n\sin\theta}{\mathrm{Fr}}\right)^{(2-n)/n}\frac{H_x}{H^2}\left[H^{1/n}\left(H^{(n+1)/n}y+\frac{n}{2n+1}(H-y)^{(2n+1)/n}-\frac{n}{2n+1}H^{(2n+1)/n}\right)\right.\\
&\left.-\frac{n}{n+2}\left(H^{(n+2)/n}y+\frac{n}{2(n+1)}(H-y)^{2(n+1)/n}-\frac{n}{2(n+1)}H^{2(n+1)/n}\right)\right]\\
&+\frac{\mathrm{Re}_n\,\xi}{(n+1)\alpha\mathrm{Pe}_n}\left(\frac{\mathrm{Re}_n\sin\theta}{\mathrm{Fr}}\right)^{(2-n)/n}\frac{H_x}{H}\left[\frac{H^{(1-n)/n}}{n}\left(H^{(n+1)/n}y+\frac{n}{2n+1}(H-y)^{(2n+1)/n}-\frac{n}{2n+1}H^{(2n+1)/n}\right)\right.\\
&\left.+\frac{n+1}{n}H^{1/n}\left(H^{1/n}y+\frac{n}{n+1}(H-y)^{(n+1)/n}-\frac{n}{(n+1)}H^{(n+1)/n}\right)-\left(H^{2/n}y+\frac{n}{n+2}(H-y)^{(n+2)/n}-\frac{n}{(n+2)}H^{(n+2)/n}\right)\right]\\
&-\frac{\mathrm{Re}_n}{(n+1)^2}\left(\frac{\mathrm{Re}_n\sin\theta}{\mathrm{Fr}}\right)^{(3-n)/n}H_{xx}H^{1/n}\left[H^{(n+1)/n}\left(H^{(n+1)/n}y+\frac{n}{2n+1}(H-y)^{(2n+1)/n}-\frac{n}{2n+1}H^{(2n+1)/n}\right)\right.\\
&\left.-\frac{n}{2(2n+1)}\left(H^{2(n+1)/n}y+\frac{n}{(3n+2)}(H-y)^{(3n+2)/n}-\frac{n}{(3n+2)}H^{(3n+2)/n}\right)\right]\\
&-\frac{\mathrm{Re}_n}{(n+1)^2}\left(\frac{\mathrm{Re}_n\sin\theta}{\mathrm{Fr}}\right)^{(3-n)/n}\frac{H_x^2}{n}H^{(1-n)/n}\left[H^{(n+1)/n}\left(H^{(n+1)/n}y+\frac{n}{2n+1}(H-y)^{(2n+1)/n}-\frac{n}{2n+1}H^{(2n+1)/n}\right)\right.\\
&\left.-\frac{n}{2(2n+1)}\left(H^{2(n+1)/n}y+\frac{n}{(3n+2)}(H-y)^{(3n+2)/n}-\frac{n}{(3n+2)}H^{(3n+2)/n}\right)\right]\\
&-\frac{\mathrm{Re}_n}{(n+1)^2}\left(\frac{\mathrm{Re}_n\sin\theta}{\mathrm{Fr}}\right)^{(3-n)/n}H_x^2H^{1/n}\left[\frac{n+1}{n}H^{1/n}\left(H^{(n+1)/n}y+\frac{n}{2n+1}(H-y)^{(2n+1)/n}-\frac{n}{2n+1}H^{(2n+1)/n}\right)\right.\\
&+\frac{n+1}{n}H^{(n+1)/n}\left(H^{1/n}y+\frac{n}{n+1}(H-y)^{(n+1)/n}-\frac{n}{(n+1)}H^{(n+1)/n}\right)\\
&\left.-\frac{(n+1)}{2n+1}\left(H^{(n+2)/n}y+\frac{n}{2(n+1)}(H-y)^{2(n+1)/n}-\frac{n}{2(n+1)}H^{2(n+1)/n}\right)\right]\\
&+\frac{\mathrm{Re}_n}{(n+1)}\frac{\cos\theta}{\mathrm{Fr}}\left(\frac{\mathrm{Re}_n\sin\theta}{\mathrm{Fr}}\right)^{(1-n)/n}H_{xx}\left[H^{(n+1)/n}y+\frac{n}{2n+1}(H-y)^{(2n+1)/n}-\frac{n}{2n+1}H^{(2n+1)/n}\right]\\
&+\frac{\mathrm{Re}_n}{(n+1)}\frac{\cos\theta}{\mathrm{Fr}}\left(\frac{\mathrm{Re}_n\sin\theta}{\mathrm{Fr}}\right)^{(1-n)/n}H_x^2\frac{n+1}{n}\left[H^{1/n}y+\frac{n}{n+1}(H-y)^{(n+1)/n}-\frac{n}{n+1}H^{(n+1)/n}\right]\\
&-\frac{\mathrm{Re}_n}{(n+1)}\left(\frac{\mathrm{Re}_n\sin\theta}{\mathrm{Fr}}\right)^{(1-n)/n}\alpha^2Fi_nH_{xxxx}\left[H^{(n+1)/n}y+\frac{n}{2n+1}(H-y)^{(2n+1)/n}-\frac{n}{2n+1}H^{(2n+1)/n}\right]\\
&-\frac{\mathrm{Re}_n}{(n+1)}\left(\frac{\mathrm{Re}_n\sin\theta}{\mathrm{Fr}}\right)^{(1-n)/n}\alpha^2Fi_nH_xH_{xxx}\frac{n+1}{n}\left[H^{1/n}y+\frac{n}{n+1}(H-y)^{(n+1)/n}-\frac{n}{n+1}H^{(n+1)/n}\right],\\
\Theta_1 = &\,\mathrm{Pe}_n\left[\frac{\xi}{6\alpha\mathrm{Pe}_nH^3}(H^3-y^3)-\frac{\xi}{6\alpha\mathrm{Pe}_nH}(H-y)+\left(\frac{\mathrm{Re}_n\sin\theta}{\mathrm{Fr}}\right)^{1/n}\frac{n}{n+1}\frac{1}{H^2}H_x\left\{H^{(n+1)/n}\left[\frac{(H-y)^3}{6}-\frac{H^2(H-y)}{6}\right]\right.\right.\\
&\left.\left.-\frac{n^2}{(3n+1)(4n+1)}[(H-y)^{(4n+1)/n}-H^{(3n+1)/n}(H-y)]\right\}\right].
\end{aligned}
\tag{24}
$$

The generalized kinematic equation is obtained from (21) using (23) and (24) as

$$H_t+X(H)+A(H)H_x+B(H)H_{xx}+C(H)H_{xxxx}+D(H)H_x^2+E(H)H_xH_{xxx}+O(\alpha^2)=0$$

where

$$\begin{aligned}
X(H)&=-\frac{\xi}{\alpha \mathrm{Pe}_n}\left(1-\frac{\xi}{3}\right)\frac{1}{H},\\
A(H)&=\left(\frac{\mathrm{Re}_n \sin\theta}{\mathrm{Fr}}\right)^{1/n}H^{(n+1)/n}\\
&\quad-\xi\left\{\left(\frac{\mathrm{Re}_n \sin\theta}{\mathrm{Fr}}\right)^{1/n}\frac{n(6n+1)}{6(3n+1)(4n+1)}H^{(n+1)/n}\right\}\\
&\quad-\frac{\xi}{\mathrm{Pr}_n}\left\{\left(\frac{\mathrm{Re}_n \sin\theta}{\mathrm{Fr}}\right)^{(2-n)/n}\frac{(3n+2)(n+2)}{2n(n+1)^2(2n+1)}H^{2/n}\right\},\\
B(H)&=\frac{2\alpha\,\mathrm{Re}_n}{(2n+1)(3n+2)}\left(\frac{\mathrm{Re}_n \sin\theta}{\mathrm{Fr}}\right)^{(3-n)/n}H^{(3n+3)/n}\\
&\quad-\frac{\alpha\,\mathrm{Re}_n}{(2n+1)}\frac{\cos\theta}{\mathrm{Fr}}\left(\frac{\mathrm{Re}_n \sin\theta}{\mathrm{Fr}}\right)^{(1-n)/n}H^{(2n+1)/n},\\
C(H)&=\frac{\alpha^3\,\mathrm{Re}_n}{(2n+1)}\left(\frac{\mathrm{Re}_n \sin\theta}{\mathrm{Fr}}\right)^{(1-n)/n}Fi_nH^{(2n+1)/n},\\
D(H)&=\frac{2\alpha\,\mathrm{Re}_n(3n+3)}{n(2n+1)(3n+2)}\left(\frac{\mathrm{Re}_n \sin\theta}{\mathrm{Fr}}\right)^{(3-n)/n}H^{(2n+3)/n}\\
&\quad-\frac{\alpha\,\mathrm{Re}_n}{n}\frac{\cos\theta}{\mathrm{Fr}}\left(\frac{\mathrm{Re}_n \sin\theta}{\mathrm{Fr}}\right)^{(1-n)/n}H^{(n+1)/n}\\
&\quad-\frac{\xi\alpha}{Pe_n}\left(1-\frac{\xi}{3}\right)\frac{1}{H},\\
E(H)&=\frac{\alpha^3\,\mathrm{Re}_n}{n}\left(\frac{\mathrm{Re}_n \sin\theta}{\mathrm{Fr}}\right)^{(1-n)/n}Fi_nH^{(n+1)/n}
\end{aligned}\tag{25}$$

3 Stability Analysis

As the variation of the film thickness of the base flow is found to be very small for $|\alpha H_x|\ll 1$ using an analysis based on Nusselt assumption, the dimensionless film thickness is expressed as

$$H=1+\eta(x,t)$$

where $\eta(x,t)$ is the perturbation of the stationary film thickness. The approximation $|\alpha H_x|\ll 1$ gives qualitative results for the constant film thickness assumption at the zeroth order. It is important to note that this constant film thickness approximation with long wave perturbations are reasonable approximations only for certain segments of weakly condensing and evaporating flows. Substituting for $H(x,t)$ in (25) and retaining terms up to the order of η^3, the evolution equation for η is obtained as

$$\begin{aligned}
&\eta_t+X'\eta+A\eta_x+B\eta_{xx}+C\eta_{xxxx}\\
&\quad=-\left[\frac{X''\eta^2}{2}+\frac{X'''\eta^3}{6}+\left(A'\eta+A''\frac{\eta^2}{2}\right)\eta_x\right.\\
&\qquad+\left(B'\eta+B''\frac{\eta^2}{2}\right)\eta_{xx}+\left(C'\eta+C''\frac{\eta^2}{2}\right)\eta_{xxxx}\\
&\qquad\left.+(D+D'\eta)\eta_x^2+(E+E'\eta)\eta_x\eta_{xxx}\right]+O(\eta^4)
\end{aligned}\tag{26}$$

where the values of X, A, B, C, D, E and their derivatives are evaluated at the dimensionless height of the film $H=1$.

3.1 Linear Stability Analysis.

For the linear stability analysis, the nonlinear terms of Eq. (26) are neglected and the linearized equation

$$\eta_t+X'\eta+A\eta_x+B\eta_{xx}+C\eta_{xxxx}=0\tag{27}$$

is obtained. Assuming the normal mode solution as

$$\eta=ae^{i(x-dt)}+\bar{a}e^{-i(x-dt)},\tag{28}$$

the complex wave celerity corresponding to linear stability problem is given by

$$d=d_r+id_i=A+i(B-C-X')\tag{29}$$

where d_r is the linear wave speed, and d_i is the linear growth rate of the amplitudes. The flow is in a linearly unstable supercritical condition for $d_i>0$ and in a linearly stable subcritical condition for $d_i<0$. For $d_i=0$, the flow is neutrally stable.

3.2 Nonlinear Stability Analysis.

The nonlinear stability analysis of Eq. (26) by the method of multiple scales, [23], yields

$$(L_0+\epsilon L_1+\epsilon^2L_2)(\epsilon\eta_1+\epsilon^2\eta_2+\epsilon^3\eta_3)=-\epsilon^2N_2-\epsilon^3N_3\tag{30}$$

where

$$\begin{gathered}
\eta(\epsilon,x,x_1,t,t_1,t_2)=\epsilon\eta_1+\epsilon^2\eta_2+\epsilon^3\eta_3;\\
t_1=\epsilon t,\quad t_2=\epsilon^2t,\quad x_1=\epsilon x\\
\frac{\partial}{\partial t}\to\frac{\partial}{\partial t}+\epsilon\frac{\partial}{\partial t_1}+\epsilon^2\frac{\partial}{\partial t_2};\quad \frac{\partial}{\partial x}\to\frac{\partial}{\partial x}+\epsilon\frac{\partial}{\partial x_1}\\
L_0=\frac{\partial}{\partial t}+X'+A\frac{\partial}{\partial x}+B\frac{\partial^2}{\partial x^2}+C\frac{\partial^4}{\partial x^4}\\
L_1=\frac{\partial}{\partial t_1}+A\frac{\partial}{\partial x_1}+2B\frac{\partial^2}{\partial x\partial x_1}+4C\frac{\partial^4}{\partial x^3\partial x_1}\\
L_2=\frac{\partial}{\partial t_2}+B\frac{\partial^2}{\partial x_1^2}+6C\frac{\partial^4}{\partial x^2\partial x_1^2}
\end{gathered}\tag{31}$$

$$\begin{aligned}
N_2&=\frac{X''}{2}\eta_1^2+A'\eta_1\eta_{1x}+B'\eta_1\eta_{1xx}+C'\eta_1\eta_{1xxxx}+D\eta_{1x}^2\\
&\quad+E\eta_{1x}\eta_{1xxx}\\
N_3&=X''\eta_1\eta_2+\frac{X'''}{6}\eta_1^3+A'(\eta_1\eta_{2x}+\eta_{1x}\eta_2+\eta_1\eta_{1x_1})\\
&\quad+B'(\eta_1\eta_{2xx}+2\eta_1\eta_{1xx_1}+\eta_{1xx}\eta_2)+C'(\eta_1\eta_{2xxxx}\\
&\quad+4\eta_1\eta_{1xxxx_1}+\eta_{1xxxx}\eta_2)+D(2\eta_{1x}\eta_{2x}+2\eta_{1x}\eta_{1x_1})\\
&\quad+E(\eta_{1x}\eta_{2xxx}+3\eta_{1x}\eta_{1xxx_1}+\eta_{1xxx}\eta_{2x}+\eta_{1xxx}\eta_{1x_1})\\
&\quad+\frac{A''}{2}\eta_1^2\eta_{1x}+\frac{B''}{2}\eta_1^2\eta_{1xx}+\frac{C''}{2}\eta_1^2\eta_{1xxxx}+D'\eta_1\eta_{1x}^2\\
&\quad+E'\eta_1\eta_{1x}\eta_{1xxx}.
\end{aligned}$$

The solution of Eq. (30) at the order $O(\epsilon)$ is obtained by solving $L_0\eta_1=0$ and is in the form

$$\eta_1=ae^{i(x-d_rt)}+\bar{a}e^{-i(x-d_rt)}\tag{32}$$

where $a(x_1,t_1,t_2)$ is the nonlinear amplitude function and $\bar{a}(x_1,t_1,t_2)$ is its complex conjugate. The solution of the equation $L_0\eta_2+L_1\eta_1=-N_2$ at the $O(\epsilon^2)$ is in the form

$$\eta_2=ea^2e^{2i(x-d_rt)}+\overline{ea}^2e^{-2i(x-d_rt)}.\tag{33}$$

Using the solutions for η_1 and η_2 in the $O(\epsilon^3)$ equation given by $L_0\eta_3+L_1\eta_2+L_2\eta_1=-N_3$, the equation for the perturbation amplitude $a(x_1,t_1,t_2)$ is obtained as

$$\frac{\partial a}{\partial t_2}+D_1\frac{\partial^2 a}{\partial x_1^2}-\epsilon^{-2}d_i a+(E_1+iF_1)a^2\bar{a}=0$$

from the secular condition for $O(\epsilon^3)$, where

$$D_1=B-6C,$$

$$F_1=(X''-5B'+17C'+4D-10E)e_i+A'e_r+\frac{A''}{2}$$

$$E_1=(X''-5B'+17C'+4D-10E)e_r$$

$$-A'e_i+\left(\frac{X'''}{2}-\frac{3}{2}B''+\frac{3}{2}C''+D'-E'\right) \tag{34}$$

$$e_r+ie_i=\frac{\left(-\frac{X''}{2}+B'-C'+D-E\right)-iA'}{(16C-4B+X')}.$$

The weakly nonlinear behavior of the fluid film can be investigated using Eq. (34). It is important to note that such an expansion is only valid for wave numbers close to neutral and not near-critical when α approaches zero. The solution of (34) for a filtered wave in which spatial modulation does not exist and the diffusion terms in (34) vanishes is obtained by taking $a=a_0e^{-ib(t_2)t_2}$. This leads to the Ginzburg-Landau equation given by

$$\frac{\partial a_0}{\partial t_2}=(\epsilon^{-2}d_i-E_1a_0^2)a_0 \tag{35}$$

$$\frac{\partial(b(t_2)t_2)}{\partial t_2}=F_1a_0^2. \tag{36}$$

The second term in Eq. (35) induced by the effect of nonlinearity can either accelerate or decelerate the exponential growth of the linear disturbance depending upon the signs of d_i and E_1. The perturbed wave speed caused by the infinitesimal disturbances appearing in the nonlinear system can be modified using Eq. (36). The threshold amplitude ϵa_0 is given by

$$\epsilon a_0=\sqrt{\frac{d_i}{E_1}} \tag{37}$$

and the nonlinear wave speed is given as

$$Nc_r=\epsilon^2 b=d_r+d_i\frac{F_1}{E_1}. \tag{38}$$

It is observed from (37) that in the linearly unstable region ($d_i>0$), the condition for existence of a supercritical stable region is $E_1>0$ and ϵa_0 is the threshold amplitude. In the linearly stable region ($d_i<0$), if $E_1<0$, then the flow has the behavior of subcritical instability and ϵa_0 is the threshold amplitude. The condition for the existence of a subcritical stable region is $E_1>0$ and $E_1=0$ gives the condition of existence of a neutral stability curve.

4 Numerical Results and Discussion

In order to understand the flow characteristics and the associated time dependent properties of power-law fluid film down an inclined plane, the conditions obtained for linear and nonlinear stability of the flow system are numerically evaluated for Reynolds number Re_n, Weber number We_n, and Prandtl number Pr_n, which are defined in terms of power-law index n. The values of dimensional quantities are taken as, [21], $\rho=998$ Kg/m^3, $\mu_n=1.002\times10^{-3}$ m Pas^n, $h_0=10^{-4}$ m, $\sigma=0.0727$ N/m, $\gamma=0.000611$, and $\theta=60$ deg. The temperature at the interface is taken as $\bar{T}_s=373$ K and the temperature difference between the wall and the interface as $\bar{T}_s-\bar{T}_w=\pm47$ K. Under such temperature conditions, the phase change parameter ξ takes values $|\xi|=0.0872$ (with phase change) and $|\xi|=0$ (without phase change). In what follows, attention is focussed on the investigation of the influence of the phase change at the interface on the stability of the flow of the power-law fluid film down an incline.

4.1 Linear Stability Solutions. The linear stability analysis yields the neutral stability curve, which separates the α-n plane into two regions depending on the value of phase change parameter ξ. Figure 2 shows the neutral stability curve for isothermal ($\xi=0$), condensate ($\xi>0$) and evaporating ($\xi<0$) power-law films.

It is observed that linearly unstable region becomes smaller as the phase change parameter increases and the linearly stable region is more for dilatant fluids than pseudoplastic fluids. The neutral stability curve for condensate film shows that, there exists a critical value for n, above which condensate power-law fluid film is always stable. It is also observed that condensate power-law fluid film is more stable than the corresponding isothermal and evaporating power-law fluid film.

Figure 3 shows the temporal growth rate of power-law fluid given by Eq. (29). It is observed that the temporal growth rate is less for a condensate power-law fluid film than for an isothermal power-law fluid film. On the other hand, for an evaporating power-law film, the temporal growth rate is more than for isothermal power-law film. Further, temporal growth rate decreases with increase in power-law index n. The results of the linear stability analysis are in agreement with those of Hwang and Weng [13] (Newtonian condensate/evaporating film) and Lin and Hwang [21] (isothermal power-law liquid films).

4.2 Nonlinear Stability Solutions. As the perturbed wave grows to a finite amplitude, linear stability theory cannot be used to predict the flow behavior accurately. Therefore, in order to examine whether the finite-amplitude disturbance in the linearly stable region causes instability (subcritical instability) and to investigate whether the subsequent nonlinear evolution of disturbances in the linearly unstable region develops into a new equilibrium state with a finite-amplitude (subcritical stability) or grows to be unstable, the nonlinear stability analysis is employed. It is observed from the nonlinear amplitude Eq. (35) that a negative value of E_1 can make the system unstable. Such a type of instability in the linearly stable region is called subcritical instability. In this case, the amplitude of disturbance is larger than the threshold amplitude and causes the system to reach an explosive state.

The neutral stability curves are obtained from Eqs. (29) and (34) by equating to zero, the linear amplification rate d_i and the nonlinear amplification rate E_1. Figure 4 shows regions of subcritical instability ($d_i<0,E_1<0$) in the linearly stable region and supercritical explosive state ($d_i>0,E_1<0$) in the linearly unstable region. It is clear from Fig. 4 that both these states of the film flow system are possible for isothermal as well as condensate or evaporating films. However, for the condensate film, supercritical explosive state exists only for pseudoplastic fluids. The condensate film, exhibits two distinct disjoint regions of subcritical instability near lower and upper branches of neutral stability curve. This is in contrast to the isothermal and evaporating films, which exhibit only one such region. The regions of supercritical stability ($d_i>0,E_1>0$) in the linearly unstable region and subcritical stability ($d_i<0,E_1>0$) in the linearly stable region are shown in Fig. 4. Further, from Fig. 4 it is observed that subcritical stable region increases, while supercritical stable region decreases as the phase-change parameter ξ increases. Also, for the condensate film, supercritical stable region exists only for pseudoplastic fluids. For condensate (evaporating) film, the region of stability is more (less) than that for isothermal film.

An infinitesimal disturbance in the linearly unstable region ($d_i>0$) will attain a finite equilibrium amplitude, when the nonlinear amplification rate E_1 in the region is positive. Figure 5

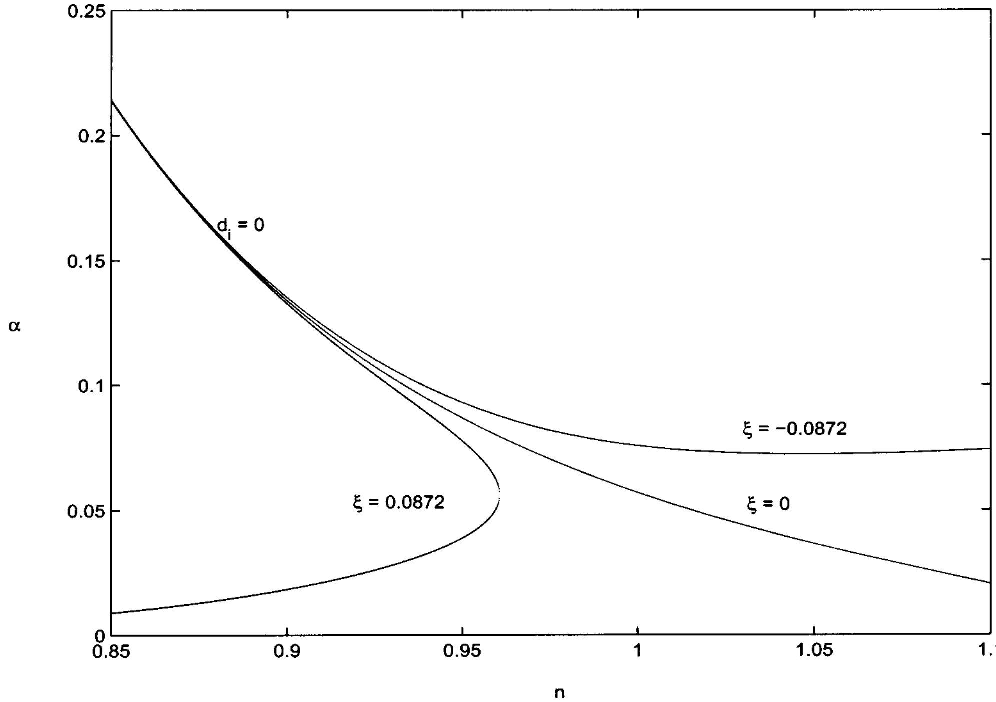

Fig. 2 Neutral stability curves for isothermal, condensate, and evaporating films

shows the threshold amplitude and the nonlinear wave speed in the supercritical stable region for various values of wave number α. It is noted that the threshold amplitude and the nonlinear wave speed are less for the condensate pseudoplastic fluid film. In the supercritical stable region, the nonlinear wave speed of the pseudoplastic fluid is more than the linear wave speed.

Figure 6 shows the threshold amplitude and the nonlinear wave speed in the subcritical unstable region for various values of wave number α. It is observed that the threshold amplitude and the nonlinear wave speed increase with the increase in phase change parameter ξ and it is more for dilatant fluids.

5 Conclusion

Weakly nonlinear stability of a condensate or evaporating power-law liquid film flowing down an inclined plane is investi-

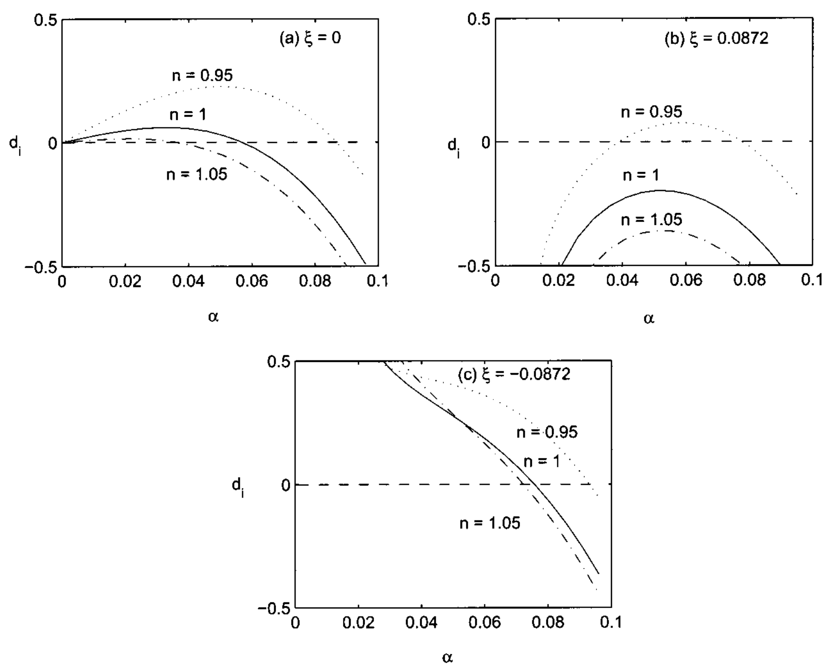

Fig. 3 Growth rate for different values of phase change parameter, (*a*) isothermal film flow, (*b*) condensate film flow, (*c*) evaporating film flow

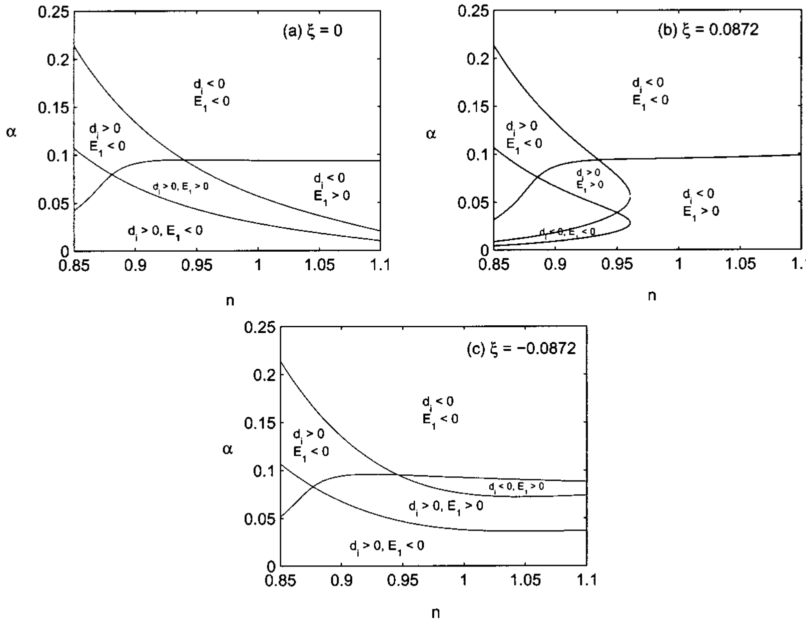

Fig. 4 Neutral stability curve in the α-n plane: (*a*) isothermal film flow, (*b*) condensate film flow, (*c*) evaporating film flow

gated by the method of long-wave perturbation. The interfacial boundary conditions include the effects of phase change across the interface. The generalized nonlinear kinematic equation of the free surface is obtained for the condensate or evaporating film and the stability of the film flow system is investigated. As the power-law exponent 'n' decreases, the effective viscosity decreases and hence 'n' influences the Reynolds number Re_n and Weber number We_n. The effect of increasing the phase change parameter ξ is to stabilize the film flow system. Further, the dimensional quantities used to discuss the stability characteristics of the power-law model in terms of the power-law exponent 'n' show that there exists a critical value of 'n' for the condensate film, above which the film flow system is always stable (Fig. 2), while isothermal and evaporating power-law fluid films are unstable for any value of power-law index 'n'.

The nonlinear stability analysis of the power-law film flow system using long-wave theory and the results obtained in the previous sections are based on rather restrictive assumptions. These results are even more qualitative than the linearised stability results and they reveal that

(i) both subcritical instability ($d_i<0, E_1<0$) and supercritical stability ($d_i>0, E_1>0$) are possible for isothermal and evaporating power-law fluid films.

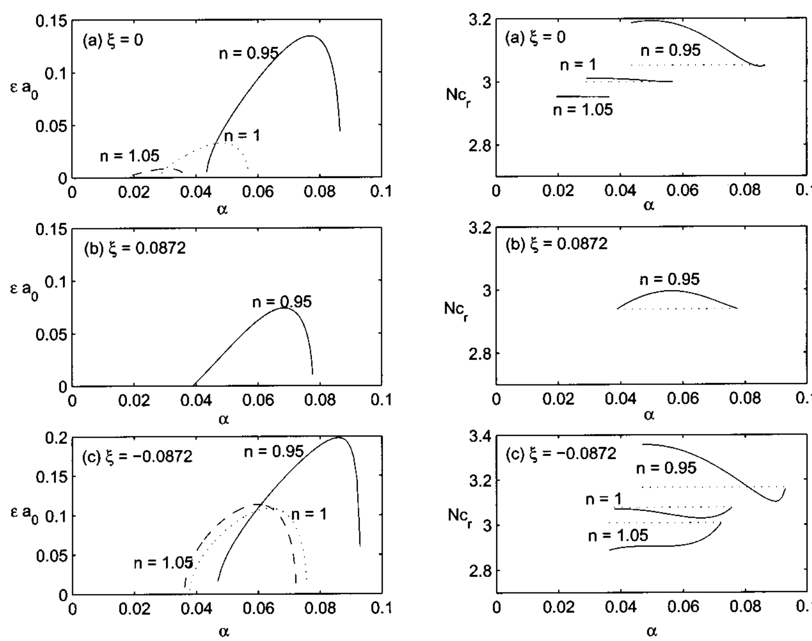

Fig. 5 Amplitude and nonlinear wave speed of supercritical wave for different values of n, (*a*) isothermal film flow, (*b*) condensate film flow, (*c*) evaporating film flow

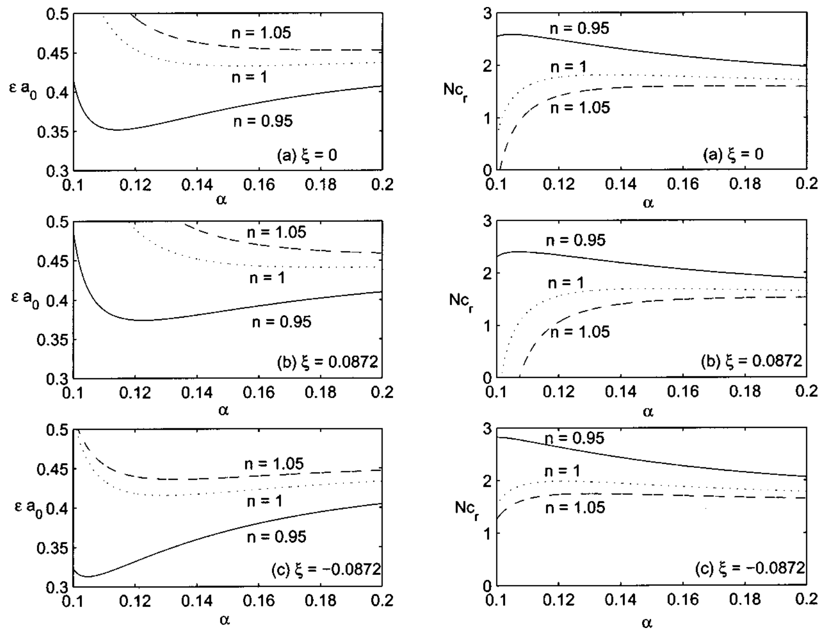

Fig. 6 Amplitude and nonlinear wave speed of subcritical wave for different values of *n*; (*a*) isothermal film flow, (*b*) condensate film flow, (*c*) evaporating film flow

(ii) power-law evaporating (condensate) fluid films are more unstable (stable) than the power-law isothermal films.

(iii) pseudoplastic evaporating films are the most unstable (Figs. 4 and 5) and the dilatant condensate films are the most stable films (Figs. 4 and 5).

(iv) supercritical stabiliy ($d_i>0, E_1>0$) and supercritical explosive state ($d_i>0, E_1<0$) are not possible for condensate dilatant fluid films (Fig. 4).

The investigations on the stability characteristics of the power-law fluid film down an inclined plane by Lin and Hwang [21] show that the isothermal film flow system is unstable for any power-law index '*n*'. The present results show that isothermal and evaporating films are unstable for any value of power-law index '*n*' while there exists a critical value of power-law index '*n*' for the case of condensate film above which condensate film flow system is always stable. Thus, the results of the present analysis show that the mass transfer effects play a significant role in modifying the stability characteristics of the non-Newtonian power-law fluid flow systems.

Acknowledgment

The authors sincerely thank the referees and Prof. Dennis A. Signier, Associate Editor, JAM, for their very useful comments and suggestions which have helped in improving the quality, content and style of the manuscript.

References

[1] Yih, C. S., 1954, "Stability of Parallel Laminar Flow With a Free Surface," Proc. 2nd U.S. Congr. Appl. Mech., pp. 623–628.
[2] Landau, L. D., 1944, "On the Problem of Turbulence," C. R. (Dokl.) Acad. Sci. URSS, **44**, pp. 311–314.
[3] Benjamin, T. B., 1957, "Wave Formation in Laminar Flow Down an Inclined Plane," J. Fluid Mech., **2**, pp. 554–574.
[4] Yih, C. S., 1963, "Stability of Liquid Flow Down an Inclined Plane," Phys. Fluids, **6**, pp. 321–334.
[5] Nusselt, W., 1916, "Die Oberflachen Kondensation des Wasserdamfes," Z. VDI, **50**, pp. 541–546.
[6] Bankoff, S. G., 1971, "Wave Formation in Laminar Flow Down an Inclined Plane," J. Fluid Mech., **14**, pp. 377–385.
[7] Marshall, E., and Lee, C. Y., 1973, "Stability of Condensate Flow Down a Vertical Wall," Int. J. Heat Mass Transfer, **16**, pp. 41–48.
[8] Lin, S. P., 1975, "Stability of a Liquid Down a Heat Incline Plane," Lett. Heat Mass Transfer, **2**, pp. 361–370.
[9] Ünsal, M., and Thomas, W. C., 1978, "Linear Stability Analysis of Film Condensation," ASME J. Heat Transfer, **100**, pp. 629–634.
[10] Burelbach, J. P., Bankoff, S. G., and Davis, S. H., 1988, "Nonlinear Stability of Evaporating/Condensing Liquid Films," J. Fluid Mech., **195**, pp. 463–494.
[11] Joo, S. W., Davis, S. H., and Bankoff, S. G., 1991, "Long-Wave Instabilities of Heated Falling Films: Two-Dimensional Theory of Uniform Layers," J. Fluid Mech., **230**, pp. 117–146.
[12] Ünsal, M., and Thomas, W. C., 1980, "Nonlinear Stability of Film Condensation," ASME J. Heat Transfer, **102**, pp. 483–488.
[13] Hwang, C. C., and Weng, C. I., 1987, "Finite-Amplitude Stability Analysis of Liquid Films Down a Vertical Wall With and Without Interfacial Phase Change," Int. J. Multiphase Flow, **13**, pp. 803–814.
[14] Gupta, A. S., 1967, "Stability of a Visco-Elastic Liquid Film Flowing Down an Inclined Plane," J. Fluid Mech., **28**, pp. 17–28.
[15] Dandapat, B. S., and Gupta, A. S., 1997, "Solitary Waves on the Surface of a Viscoelastic Fluid Running Down an Inclined Plane," Rheol. Acta, **36**, pp. 135–143.
[16] Shaqfeh, E. S. G., Larson, R. G., and Fredrickson, G.H., 1989, "The Stability of Gravity Driven Viscoelastic Film Flow at Low to Moderate Reynolds Number," J. Non-Newtonian Fluid Mech., **31**, pp. 87–113.
[17] Joo, S. W., 1994, "The Stability and Nonlinear Flow Developments of a Viscoelastic Draining Film With Shear Thinning," J. Non-Newtonian Fluid Mech., **51**, pp. 125–140.
[18] Andersson, H. I., and Irgens, F., 1988, "Gravity-Driven Laminar Film Flow of Power-Law Fluids Along Vertical Walls," J. Non-Newtonian Fluid Mech., **27**, pp. 153–172.
[19] Hwang, C. C., Chen, J. L., Wang, J. S., and Lin, J. S., 1994, "Linear Stability of Power-Law Liquid Film Flows Down an Inclined Plane," J. Phys. D **27**, pp. 2297–2301.
[20] Lee, J. J., 1996, "Nonlinear Dynamics of a Rapidly Flowing Viscous Fluid Layer Down an Incline," Ph.D. Thesis, Massachusetts Institute of Technology, Cambridge, MA.
[21] Lin, J. S., and Hwang, C. C., 2000, "Finite Amplitude Long-Wave Instability of Power-Law Liquid Films," Int. J. Non-Linear Mech., **35**, pp. 769–777.
[22] Hung, C. I., Tsai, J. S., and Chen, C. K., 1996, "Nonlinear Stability of the Thin Micropolar Liquid Film Flowing Down on a Vertical Plane," ASME Trans. J. Fluids Eng., **118**, pp. 498–505.
[23] Nayfeh, A. H., and Mook, D. T., 1979, *Nonlinear Oscillations*, John Wiley and Sons, New York.

Journal of Applied Mechanics

Brief Notes

A Brief Note is a short paper that presents a specific solution of technical interest in mechanics but which does not necessarily contain new general methods or results. A Brief Note should not exceed 2500 words *or equivalent* (a typical one-column figure or table is equivalent to 250 words; a one line equation to 30 words). Brief Notes will be subject to the usual review procedures prior to publication. After approval such Notes will be published as soon as possible. The Notes should be submitted to the Editor of the JOURNAL OF APPLIED MECHANICS. Discussions on the Brief Notes should be addressed to the Editorial Department, ASME International, Three Park Avenue, New York, NY 10016-5990, or to the Editor of the JOURNAL OF APPLIED MECHANICS. Discussions on Brief Notes appearing in this issue will be accepted until two months after publication. Readers who need more time to prepare a Discussion should request an extension of the deadline from the Editorial Department.

Constant Flux Diffusion Across a Corner

C. Y. Wang
Department of Mathematics, Michigan State University, East Lansing, MI 48824 Mem. ASME

The temperature distribution of a curved barrier heated by constant flux on one side is studied. Both the right-angled corner and the rounded corner are solved by the method of domain decomposition and matching. It is found that hot spot temperatures may reach 2.5 times that of a flat barrier but may be tempered with appropriate rounding at the corner. [DOI: 10.1115/1.1629105]

Introduction

The diffusion of mass or heat across a barrier is important in many engineering and biological processes. We shall use the terminology of heat transfer, although the results may apply to mass transfer as well. Previous work on diffusion across a corner considered constant temperature boundary conditions. For a right-angled corner, it is possible to solve the Dirichlet problem by conformal mapping (see e.g., Wang [1] and Ivanov and Trubetskov [2]). For a rounded corner numerical methods or domain decomposition and matching, [3], are needed.

The present paper considers the case where one surface of the corner is heated by constant flux. This situation occurs when the heating is produced by an exothermic chemical reaction or by electric heating elements. In most cases, the boundary condition is somewhere between constant temperature and constant flux conditions. Both the right-angled corner and the rounded corner will be studied.

The Right-Angled Corner

Figure 1(a) shows the right-angled corner with lengths normalized by the thickness H. Two subcases are considered. The interior surface (DEF) heated by constant flux and the exterior surface (ABC) cooled by constant temperature or vice-versa, with the exterior surface heated by constant flux. Note that for constant flux heating, conformal mapping is impractical. We shall use the domain decomposition method.

The corner is partitioned into a square (Region 1) and a strip (Region 2) with their own axes as shown. The other leg is a reflection of Region 2. Let q be the constant flux on one surface and T_0 be the fixed temperature on the other surface. Construct a normalized temperature $T=(T'-T_0)\kappa/qH$ where T' is the dimensional temperature and κ is the thermal conductivity. If the interior is heated by constant flux, the boundary conditions are

$$T_1(x,0)=0 \tag{1}$$

$$T_2(x,0)=0 \tag{2}$$

$$\frac{\partial T_2}{\partial y}(x,0)=1. \tag{3}$$

Also due to symmetry along $\overline{BE}$

$$T_1(x,y)=T_1(y,x) \tag{4}$$

and continuity along the partition

$$T_1(1,y)=T_2(0,y) \tag{5}$$

$$\frac{\partial T_1}{\partial x}(1,y)=\frac{\partial T_2}{\partial x}(0,y). \tag{6}$$

Equations (2)–(8) are to be solved. The general solution of T_1 satisfying Eqs. (1), (4) and the Laplace equation is

$$T_1=\sum_{n=1}^{\infty} B_n[\sin(\lambda_n y)(e^{\lambda_n(x-1)}-e^{-\lambda_n(x+1)}) + \sin(\lambda_n x)(e^{\lambda_n(y-1)}-e^{-\lambda_n(y+1)})] \tag{7}$$

where $\lambda_n=(n-\frac{1}{2})\pi$ and B_n are constant coefficients. The general solution to Eqs. (2), (3) is

$$T_2=y+\sum_{n=1}^{\infty} A_n \sin(\lambda_n y)e^{-\lambda_n x}. \tag{8}$$

The series are truncated to N terms and the matching conditions Eqs. (5), (6) are applied. Multiplying with $\sin(\lambda_m y)$ and integrating from 0 to 1 give a set of linear algebraic equations which can be easily inverted.

The accuracy can be improved by increasing N. In general three significant digits are obtained for $N=40$. There is a "cold spot" on the inside heated surface is $T_1(1,1)=0.649$. Linear temperature is established far from the corner at $y\rightarrow\infty$.

Contributed by the Applied Mechanics Division of THE AMERICAN SOCIETY OF MECHANICAL ENGINEERS for publication in the ASME JOURNAL OF APPLIED MECHANICS. Manuscript received by the ASME Applied Mechanics Division, Feb. 1999, final revision, Aug. 2000. Associate Editor: L. T. Wheeler.

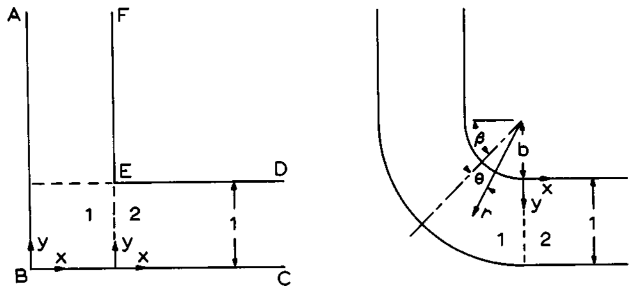

Fig. 1 (*a*) the right-angled corner, (*b*) the rounded corner

Next we look at the subcase where the constant flux heating is on the outside. Equations (1)–(3) are supplanted by

$$\frac{\partial T_1}{\partial y}(x,0) = -1 \tag{9}$$

$$T_2(x,1) = 0, \quad \frac{\partial T_2}{\partial y}(x,0) = -1. \tag{10}$$

The appropriate expansions are

$$T_1 = 2 - x - y + \sum_{n=1}^{\infty} B_n[\cos(\lambda_n y)(e^{\lambda_n(x-1)} + e^{-\lambda_n(x+1)}) + \cos(\lambda_n x)(e^{\lambda_n(y-1)} + e^{-\lambda_n(y+1)})] \tag{11}$$

$$T_2 = 1 - y + \sum_{n=1}^{\infty} A_n \cos(\lambda_n y) e^{-\lambda_n x}. \tag{12}$$

Using the matching conditions and similarly integrating, one obtains the coefficients.

We find there exists a "hot spot" $T_1(0,0) = 2.542$ at the outer corner. Since the maximum temperature of a flat plate is 1 under the same circumstances, such a right-angled corner heated from the outside elicits a local temperature more than 2.5 times higher; which is unlikely to be acceptable.

The Rounded Corner

We investigate whether the rounded corner would alleviate the local temperature rise due to constant flux heating. Let the rounded section have inner radius b, outer radius $1+b$ and opening angle 2β. Figure 1(b) shows polar coordinates (r,θ) for the rounded section (Region 1) and Cartesian coordinates for the straight section.

First consider constant flux heating on the inside. The expansion for T_1 satisfying the cylindrical Laplace equation and the boundary conditions on curved surfaces is

$$T_1(r,\theta) = b \ln\left(\frac{1+b}{r}\right) + \sum_{n=1}^{\infty} B_n \cos\left[\alpha_n \ln\left(\frac{r}{b}\right)\right](e^{\alpha_n(\theta-\beta)} + e^{-\alpha_n(\theta+\beta)}). \tag{13}$$

The eigenvalues are uncommon,

$$\alpha_n = \frac{\left(n - \frac{1}{2}\right)\pi}{\ln(1+1/b)}. \tag{14}$$

The expansion for T_2 is

$$T_2(x,y) = 1 - y + \sum_{n=1}^{\infty} A_n \cos(\lambda_n y) e^{-\lambda_n x} \tag{15}$$

where $\lambda_n = (n - \frac{1}{2})\pi$. The matching conditions are then similarly applied,

$$T_1(y+b,\beta) = T_2(0,y) \tag{16}$$

$$\frac{1}{(y+b)} \frac{\partial T_1}{\partial \theta}(y+b,\beta) = \frac{\partial T_2}{\partial x}(0,y). \tag{17}$$

Except for very low values of b, convergence is fairly fast. Usually five terms in the series would ensure a three-digit accuracy.

In the case the rounded corner is heated from the outside, the proper expansions are

$$T_1(r,\theta) = (1+b)\ln\left(\frac{r}{b}\right) + \Sigma B_n \sin\left[\alpha_n \ln\left(\frac{r}{b}\right)\right](e^{\alpha_n(\theta-\beta)} + e^{-\alpha_n(\theta+\beta)}) \tag{18}$$

$$T_2(x,y) = y + \Sigma A_n \sin(\lambda_m y) e^{-\lambda_n x}. \tag{19}$$

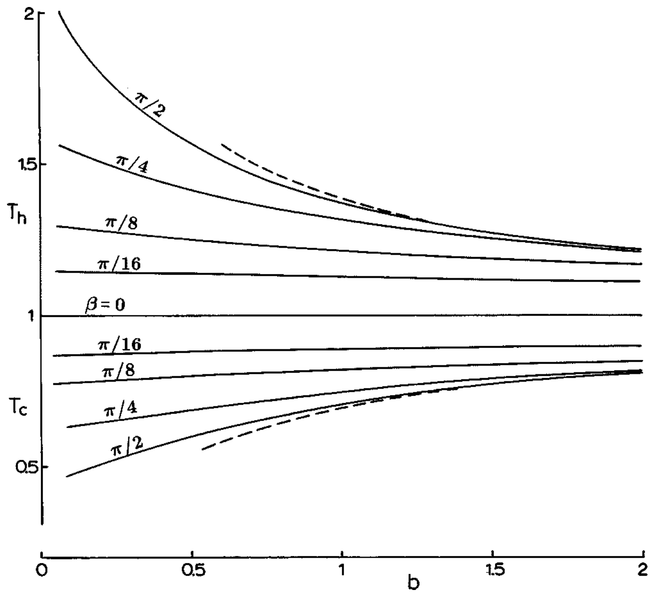

Fig. 2 Hotspot temperature T_h for exterior constant flux heating and coldspot temperature T_c for interior constant flux heating of a rounded corner. Dashed lines show exact annular formulas.

Figure 2 shows the predicted hot spot and cold spot temperatures on the constant flux heated surface. The barrier becomes flat for either $b \to \infty$ or $\beta = 0$, where the temperature on the heated surface would be 1. The dashed lines correspond to the case of annular cylinder, either heated inside by constant flux or outside by constant flux. The exact formulas are

$$T_c = b \ln\left(1 + \frac{1}{b}\right) \tag{20}$$

$$T_h = (1+b)\ln\left(1 + \frac{1}{b}\right). \tag{21}$$

These curves serve as bounds for the temperature extremums. Note that $\beta = \pi/4$ is the right-angled rounded corner and

$\beta = \pi/2$ represents a cylinder head with a U-shaped cross section. Due to poor convergence for small b, results for $b < 0.05$ are not presented, although extrapolation to $b = 0$ is possible.

Conclusion and Discussion

The constant flux heating of a corner is studied in detail. In contrast to constant temperature heating, there exist hot spots and cold spots on the heated surface. The worst case is the right-angled corner heated from the outside. The local temperature at the apex reaches 2.5 times higher than a flat plate of same thickness. If the corner is rounded, the highest temperature is at most 1.6 times higher (when $b = 0$).

We have used the domain decomposition and matching method which is quite efficient. Numerical finite differences can also be used, but the infinite geometry and the sharp corners need to be compromised.

References

[1] Wang, C. Y., 1995, ''Diffusion Across a Corrugated Saw-Tooth Plate,'' Mech. Res. Commun., **22**, pp. 589–597.
[2] Ivanov, V. I., and Trubetskov, M. K., 1995, *Handbook of Conformal Mapping With Computer-Aided Visualization*, CRC Press, Boca Raton, FL.
[3] Wang, C. Y., 1993, ''Steady-State Heat Conduction Across a Bent Sheet,'' Mech. Res. Commun., **20**, pp. 237–242.

Application of a Hybrid Method to the Solution of the Nonlinear Burgers' Equation

Bor-Lih Kuo
Department of Mechanical Engineering, Chengshiu Institute of Technology, Kaohsiung, Taiwan 833, Republic of China
e-mail: borlih@cc.csit.edu.tw

Chao-Kuang Chen
Department of Mechanical Engineering, National Cheng Kung University, Tainan, Taiwan 710, R.O.C.

This paper presents the use of a hybrid method which combines differential transformation and finite difference approximation techniques in the solution of the nonlinear Burgers' equation for various values of Reynolds number including high values. In order to demonstrate the accuracy and validity of the proposed method, it is used to solve several examples of Burgers' equation, with each example having different initial conditions and boundary conditions. It is found that the results obtained are in good agreement with the analytical solutions, and that the results are more accurate than those provided by other approximate numerical methods. [DOI: 10.1115/1.1629107]

Introduction

Burgers' equation is used as a model for governing equations of many mechanics problems. Therefore, it is important to develop analytical methods or numerical approaches which may be used in its solution. Cole [1] studied the general properties of Burgers' equation and its use in the solution of related fluid mechanics problems. In his study, he also provided some exact solutions for mathematical models of turbulence. Caldwell and Smith [2] solved Burgers' equation for two different initial conditions by using a finite element method and a finite difference method. The numerical results provided by the two methods for various Reynolds numbers were discussed and were found to be in good agreement with those generated by analytical solutions. More recently, the differential transformation method has been applied to many nonlinear problems. For example, in 1996 Chen and Ho [3] introduced the concept of a differential transformation method for the solution of eigenvalue problems. A few years later, Yu and Chen [4] adopted a hybrid method combining the Taylor transformation and the finite difference approximation to solve the nonlinear transient conduction-convection-radiation heat transfer annular fin equation.

The purpose of this paper is to present the use of a hybrid method, which combines differential transformation and finite difference approximation, in the analysis of Burgers' equation with specified initial conditions and boundary conditions. The study begins by applying differential transformation and finite difference approximation methods to the complete nonlinear Burgers' equation and to its initial and boundary conditions. The study then considers two different cases of initial condition and boundary conditions and uses the proposed method to solve Burgers' equation in the form of a finite power series. Finally, the results which are derived using this method are compared carefully with those given by analytical solutions, particularly in the case of high Re numbers. The validity of the proposed method is demonstrated by comparing the steady-state solutions of Burgers' equation derived by the proposed hybrid method with those obtained from the analytical approach.

Problem—Burgers' Equation

The complete nonlinear Burgers' equation is expressed as follows:

$$\frac{\partial u}{\partial t} + u\frac{\partial u}{\partial x} = \frac{1}{\mathrm{Re}}\frac{\partial^2 u}{\partial x^2} \tag{1}$$

where $u = u(x,t)$ in some domain and Re is the Reynolds number which characterizes the flow. The equation is a parabolic partial differential equation, which is composed of an unsteady term, a nonlinear convective term and a viscous term.

The initial condition is given by

$$u(x,0) = f(x) \quad a \leqslant x \leqslant b. \tag{2}$$

The boundary conditions are expressed as

$$\begin{aligned} u(a,t) &= g(t) \\ u(b,t) &= w(t) \quad t > 0. \end{aligned} \tag{3}$$

Differential Transformation

The basic principles of the differential transformation method may be explained as follows.

Differential transformation of function $y(t)$ is defined as

$$Y(k) = \frac{H^k}{k!}\left[\frac{\partial^k y(t)}{\partial t^k}\right]_{t=0}. \tag{4}$$

In this equation, $Y(k)$ is the transformed function in the transformation domain, $y(t)$ is the original function in the time domain, k is the transformation parameter, and H is the time interval.

The differential inverse transformation of $Y(k)$ is expressed as

$$y(t) = \sum_{k=0}^{\infty}\left(\frac{t}{H}\right)^k Y(k). \tag{5}$$

Substituting Eq. (4) into Eq. (5) yields

Contributed by the Applied Mechanics Division of THE AMERICAN SOCIETY OF MECHANICAL ENGINEERS for publication in the ASME JOURNAL OF APPLIED MECHANICS. Manuscript received by the ASME Applied Mechanics Division, July 19, 2002; final revision, Apr. 12, 2003. Associate Editor: D. A. Siginer.

$$y(t)=\sum_{k=0}^{\infty}\frac{t^k}{k!}\left[\frac{d^k y(t)}{dt^k}\right]_{t=0}. \tag{6}$$

Equation (6) implies that the concept of differential transformation is derived from the Taylor series expansion. Therefore, the basic operation properties of the differential transform are given by

$$\text{Linearity:}\quad T\{y(t)+z(t)\}=Y(k)+Z(k) \tag{7}$$

$$\text{Convolution:}\quad T\{y(t)\cdot z(t)\}=Y(k)*Z(k)=\sum_{k=0}^{\infty}Y(l)Z(k-l) \tag{8}$$

$$\text{Derivative:}\quad T\left\{\frac{d^n y(t)}{dt^n}\right\}=\frac{(k+1)(k+2)\cdots(k+n)}{H^n}Y(k+n) \tag{9}$$

where T denotes differential transformation and "$*$" denotes the convolution operation in the transformation domain.

If the method of differential transformation is applied with respect to the time domain, t, then Eqs. (1)–(3) may be rewritten in the following form:

$$\frac{k+1}{H}U(x,k+1)+\sum_{l=0}^{k}\frac{dU(x,l)}{dx}U(x,k-l)=\frac{1}{\mathrm{Re}}\frac{d^2U(x,k)}{dx^2} \tag{10}$$

$$U(x,0)=F(x) \tag{11}$$

$$\begin{aligned}U(a,k)&=G(k)\\ U(b,k)&=W(k)\end{aligned} \tag{12}$$

where $U(x,k)$, $F(x)$, $G(k)$, and $W(k)$ are the spectrum of $u(x,t)$, $f(x)$, $g(t)$, and $w(t)$, respectively, k and l are transformation parameters and H is the time interval.

The finite difference approximation method may be applied with respect to x in Equations (10)–(12). The region $a\leqslant x\leqslant b$ is divided into several equal intervals. Each interval, Δ, is given by $\Delta=(b-a)/\mathrm{m}$, where m is the total number of intervals. By using the second-order accurate central difference formula for the first and second derivatives, it is possible to express Eq. (10) at any position, i, within the flow as

$$\frac{k+1}{H}U_i(k+1)+\sum_{l=0}^{k}\frac{U_{i+1}(l)-U_{i-1}(l)}{2\Delta}U_i(k-l)=\frac{1}{\mathrm{Re}}\frac{U_{i-1}(k)-2U_i(k)+U_{i+1}(k)}{\Delta^2} \tag{13}$$

where i indicates the position number in the flow direction.

To demonstrate the use of the hybrid method in the solution of Burgers' equation, the present study considers two different cases of initial condition and boundary conditions. These are as follows:

$$\text{Case 1:}\quad u(x,0)=\sin\pi x\quad 0\leqslant x\leqslant 1 \tag{14}$$

$$u(0,t)=u(1,t)=0\quad t>0 \tag{15}$$

$$\text{Case 2:}\quad u(x,0)=0\quad 0\leqslant x\leqslant 1 \tag{16}$$

$$\begin{aligned}u(0,t)&=1\\ u(1,t)&=0\quad t>0.\end{aligned} \tag{17}$$

Applying the method of differential transformation to these initial and boundary conditions gives

$$\text{Case 1:}\quad U_i(0)=\sin\pi x \tag{18}$$

$$U_0(k)=U_j(k)=0 \tag{19}$$

$$\text{Case 2:}\quad U_i(0)=0 \tag{20}$$

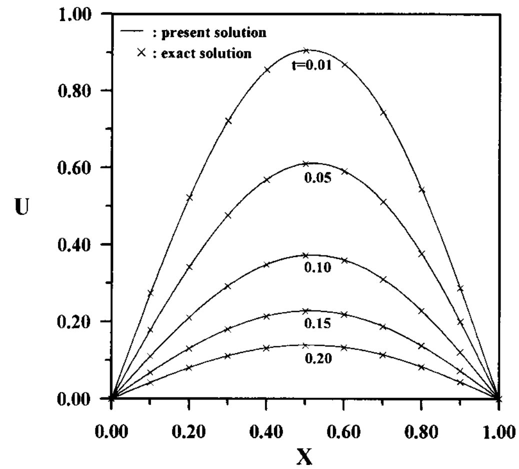

Fig. 1 Comparison of present results with exact solutions for Re=1

$$\begin{aligned}U_0(k)&=\delta(k)\\ U_j(k)&=0\quad t>0\end{aligned} \tag{21}$$

where j represents the number of the final position in the flow direction, and

$$\delta(k)=\begin{cases}1 & \text{for}\quad k=0\\ 0 & \text{otherwise}\end{cases}.$$

When the various values of $U_i(k)$ are obtained by using Eq. (13), together with the transformed initial condition and boundary conditions, the solution of Burger's equation is given by

$$u(x,t)=\sum_{k=0}^{\infty}\left(\frac{t}{H}\right)^k U_i(k). \tag{22}$$

For the present study, the function $u(x,t)$ is expressed by the following finite series:

$$u(x,t)=\sum_{k=0}^{6}\left(\frac{t}{H}\right)^k U_i(k)$$

where k represents the number of terms within the series, and depends on the convergence of the solutions. In the cases considered with the current study, a value of $k=6$ was adopted.

Numerical Results and Discussion

In order to illustrate the proposed hybrid method, a series of numerical calculations were carried out at various values of Reynolds Number. Figures 1 and 2 compare the numerical results with the exact solutions of Burgers' equation under case 1 conditions for values of Re=1 and 100, respectively. It is seen that the numerical results obtained from the proposed hybrid method are in good agreement with the exact solutions. Tables 1 and 2 provide a detailed comparison of the obtained numerical results with the exact solutions for Re=1 and 100. Observation of these tables confirms that the present results agree very closely with the exact solutions. It is to be noted that the analytical results of the equation (i.e., the exact solutions referred to above) are obtained from the closed-form solution derived by Cole [1], which is presented as an Appendix in this paper. Using the present method, it is necessary to determine the number of intervals of x to be used for the nonlinear convergence problems. In this study, the number of intervals was chosen to be 20 and 100 for the cases of Re=1 and 100, respectively. When the value of Reynolds number is high, it is very difficult to determine the exact solution of the Burgers' equations or to obtain numerical approximations using existing

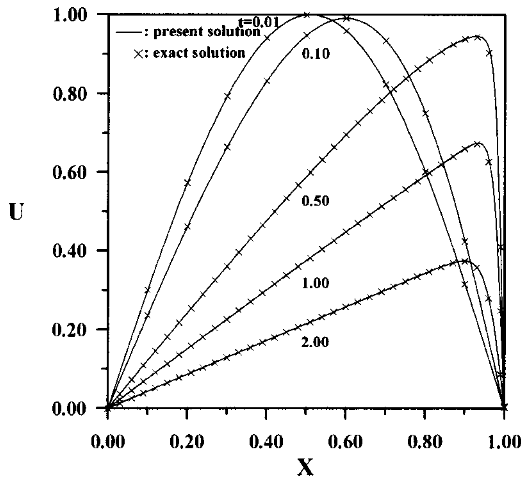

Fig. 2 Comparison of present results with exact solutions for Re=100

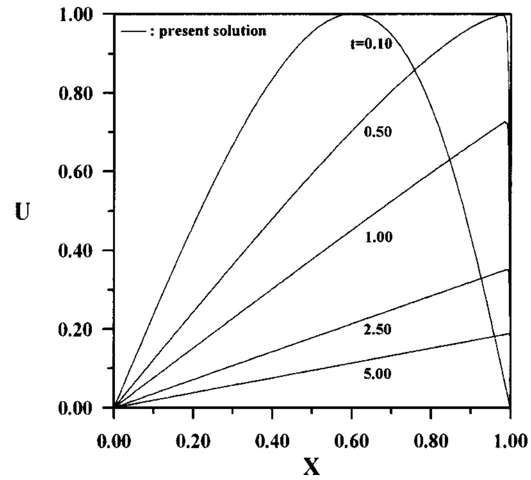

Fig. 3 Numerical results obtained by the present method for Re=10,000

techniques. In this study, the proposed hybrid method was used to solve the equation for value of Re=10,000. The numerical results are shown in Fig. 3. These results show the appearance of increasing disturbance for higher values of Reynolds number. The disturbance is manifested in the form of a ripple effect which becomes more exaggerated, and which decays more slowly, as the Reynolds number rises to 10,000 (as discussed also by Caldwell and Smith [2]). The proposed method was used to obtain the steady-state solutions of Burgers' equation for values of Reynolds number from 1 to 10,000, and with initial and boundary conditions of $u(x,0)=0$; $u(0,t)=1$, $u(1,t)=0$. From Fig. 4 it can be seen that the numerical results are once again in good agreement with the analytical solutions. Figures 5 and 6 show that the time history of

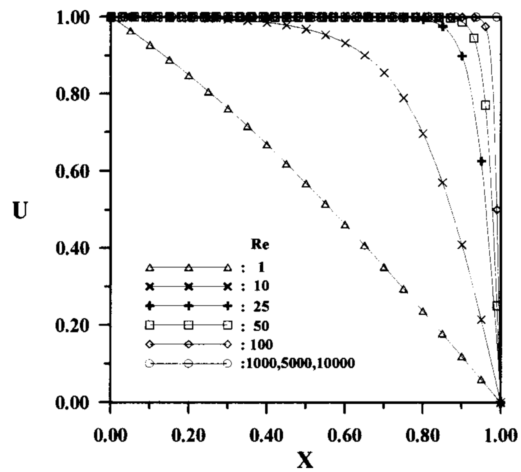

Fig. 4 Steady-state solutions of Burgers' equation for Re =1∼10,000

Table 1 Solutions of Burgers' equation for Re=1

	$t=0.01$		$t=0.10$		$t=0.20$	
x	Exact	Present	Exact	Present	Exact	Present
.00	.000000	.000000	.000000	.000000	.000000	.000000
.10	.273239	.273310	.109538	.109727	.041929	.042090
.20	.521564	.521697	.209792	.210164	.079994	.080306
.30	.721852	.722028	.291896	.292437	.110622	.111060
.40	.854590	.854784	.347924	.348604	.130822	.131351
.50	.905713	.905901	.371577	.372348	.138473	.139045
.60	.868333	.868496	.359045	.359836	.132582	.133141
.70	.744098	.744222	.309905	.310624	.113469	.113957
.80	.543820	.543902	.227817	.228369	.082841	.083203
.90	.286998	.287039	.120687	.120987	.043689	.043881
1.00	.000000	.000000	.000000	.000000	.000000	.000000

Table 2 Solutions of Burgers' equation for Re=100

	$t=0.10$		$t=1.00$		$t=2.00$	
x	Exact	Present	Exact	Present	Exact	Present
.00	.000000	.000000	.000000	.000000	.000000	.000000
.10	.235941	.235947	.075382	.075383	.042964	.042964
.20	.461225	.461237	.150645	.150648	.085915	.085915
.30	.664325	.664343	.225666	.225670	.128840	.128841
.40	.831864	.831887	.300309	.300315	.171726	.171728
.50	.947414	.947440	.374420	.374429	.214558	.214560
.60	.990156	.990179	.447816	.447828	.257322	.257325
.70	.934119	.934140	.520268	.520285	.299998	.300002
.80	.750783	.751328	.591476	.591499	.342409	.342435
.90	.423599	.427744	.660019	.660351	.373278	.374070
1.00	.000000	.000000	.000000	.000000	.000000	.000000

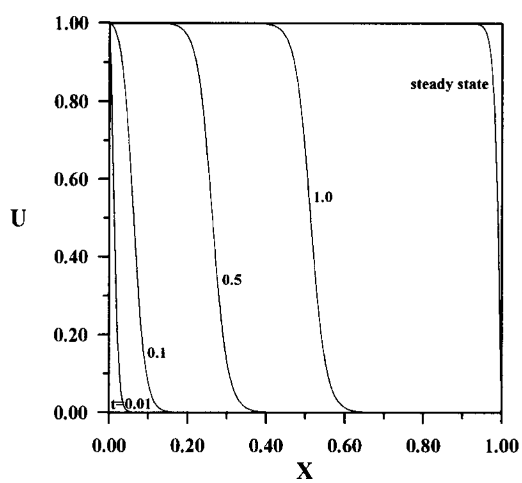

Fig. 5 Time history of propagating wave fronts for Re=100

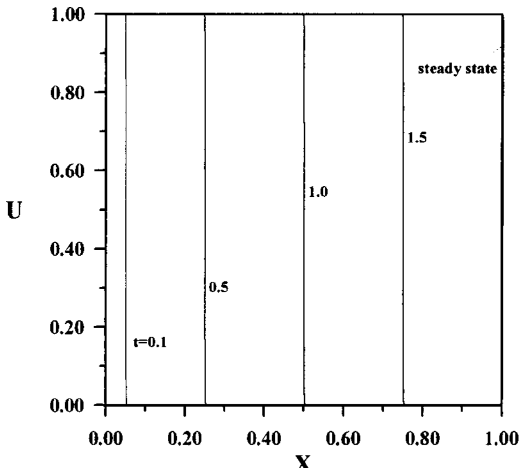

Fig. 6 Time history of propagating wave fronts for Re=10,000

the propagating wave fronts for various values of Re. It is seen that as Re increases the propagating wave fronts become more steep particularly for Re tend to 10,000.

Conclusions

In the present study, a powerful numerical analysis, which is referred to as a hybrid method since it combines the methods of differential transformation and finite difference approximation, has been employed to analyze Burgers' equation for various values of Reynolds numbers (including high values of Re). Two examples of Burgers' equation have been investigated using the proposed method, i.e., with two different sets of initial condition and boundary conditions. It has been demonstrated that the obtained numerical results are in good agreement with the analytical solutions. The numerical results indicate that the proposed hybrid method is simple, fast, and accurate. For large values of Re, it is difficult to determine the solutions of Burgers' equation using analytical methods or other numerical approximations such as the Fourier series approach, spline collocation method, boundary element method, etc. However, it is the current authors' belief that the method presented in this paper overcomes these problems and provides a powerful technique for the solution of the nonlinear Burgers' equation with initial and boundary conditions, particularly for cases where the value of Reynolds number is high.

References

[1] Cole, J. D., 1951, "On a Quasi-Linear Parabolic Equation Occurring in Aerodynamics," Q. Appl. Math., **9**(3), pp. 225–236.

[2] Caldwell, J., and Smith, P., 1982, "Solution of Burgers' Equation With a Large Reynolds Number," Appl. Math. Model., **6**, pp. 381–385.

[3] Chen, C. K., and Ho, S. H., 1996, "Application of Differential Transformation to Eigenvalue Problems," Appl. Math. Comput., **79**, pp. 173–188.

[4] Yu, L. T., and Chen, C. K., 1999, "Application of the Hybrid Method to the Transient Thermal Stresses Response in Isotropic Annular Fins," ASME J. Appl. Mech., **66**, pp. 340–346.

Journal of Applied Mechanics

Discussion

Discussion: "On Global Energy Release Rate of a Permeable Crack in Piezoelectric Ceramic" (Li, S., 2003 ASME J. Appl. Mech., 70, pp. 246–252)

X.-F. Li
College of Mathematics and Computer Science,
Hunan Normal University, Changsha 410081,
People's Republic of China.
e-mail: xfli@post.com

K. Y. Lee
School of Mechanical Engineering, Yonsei University,
Seoul 120-749, South Korea.
e-mail: KYL2813@yahoo.co.kr

In studying crack problems in a piezoelectric material, many crack models have been proposed and some fracture criteria have been established. The author of [1] presented a new permeable crack model. That is, a permeable crack is modeled as a rectangular hole having height h_0. The first-order perturbation solution in terms of small parameter h_0 is derived, and asymptotic electroelastic field, together with field intensity factors, local and global energy release rates are further determined. The obtained theoretical prediction agrees basically with experimental observation. Here, we would like to make some discussions on [1].

In deriving the results in [1], Eq. (45) is crucial. However, based on (44), (45) does not hold unless $\tilde{E}_X(X,Y)$ and $\tilde{E}_X^a(X,Y)$ are linear functions with respect to variable Y and independent of variable X. The reason is that, if denoting

$$f(X,\pm h(X))=\tilde{E}_X(X,\pm h(X))-\tilde{E}_X^a(X,\pm h(X)), \tag{1}$$

the Fourier cosine transform of $f(X,\pm h(X))$ is

$$\int_0^\infty f(X,\pm h(X))\cos(\zeta X)dX=\int_0^a f(X,\pm h_0)\cos(\zeta X)dX + \int_a^\infty f(X,0)\cos(\zeta X)dX, \tag{2}$$

rather than

$$f^*\left(\zeta,\pm h_0\frac{\sin(a\zeta)}{\zeta}\right), \tag{3}$$

where

$$f^*(\zeta,Y)=\int_0^\infty f(X,Y)\cos(\zeta X)dX. \tag{4}$$

Consequently, (45), i.e.,

$$f^*\left(\zeta,\pm h_0\frac{\sin(a\zeta)}{\zeta}\right)=0,\quad 0<\zeta<\infty, \tag{5}$$

cannot follow from (44), i.e.,

$$f(X,\pm h(X))=0,\quad -\infty<X<\infty, \tag{6}$$

where $h(x)$ is given by (12) in [1].

In addition it is seen from (81)–(83) that the height of a rectangular crack has been taken into account. However, for such a rectangular crack, (or strictly speaking a rectangular hole), $\sigma_{YZ}(X,0)$, $\epsilon_{YZ}(X,0)$, $D_Y(X,0)$, and $E_Y(X,0)$ should have no singularity near the points $(\pm a,0)$ since the points $(\pm a,0)$ are not the crack tips $(h_0>0)$. Instead, the electromechanical field near the apexes of the rectangle $(\pm a,\pm h_0)$ exhibits a singularity. Moreover, the singularity is no longer an inverse square-root singularity. The classical definition of field intensity factors is therefore employed directly except for the case of $h_0=0$.

Reference

[1] Li, S., 2003, "On Global Energy Release Rate of a Permeable Crack in a Piezoelectric Ceramic," Transactions of the ASME, J. Appl. Mech., **70**, pp. 246–252.

Closure to "On Global Energy Release Rate of a Permeable Crack in Piezoelectric Ceramic" (2003, ASME J. Appl. Mech., 70, p. 930)

S. Li
Department of Civil and Environmental Engineering,
University of California, Berkeley, CA 94720

(1) For a finite height $h_0>C$, $C>0$, we define real functions

$$h(X):=\begin{cases} h_0, & |X|<a \\ 0, & |X|>a \end{cases}, \tag{1}$$

and

$$F(X,h(X)):=\tilde{E}_X(X,h(X))-\tilde{E}_X^a(X,h(X)). \tag{2}$$

It is true that in general the Fourier transform of $F(X,h(X))$,

$$F^*(\zeta):=\int_0^\infty F(X,h(X))\cos(\zeta X)dX\neq f^*(\zeta,h^*(\zeta)), \tag{3}$$

where

$$f^*(\zeta,Y):=\int_0^\infty F(X,Y)\cos(\zeta X)dX, \tag{4}$$

$$h^*(\zeta) := \int_0^\infty h(X)\cos(\zeta X)\,dX. \tag{5}$$

However, when $h_0 \to 0$,

$$\int_0^\infty F(X,0)\cos(\zeta X)\,dX = f^*(\zeta,0). \tag{6}$$

In other words, we expect

$$\lim_{h_0\to 0} F^*(\zeta) \to f^*(\zeta,0). \tag{7}$$

During this limiting process, the four corners of the slit will merge and become the two crack tips at $(X=\pm a,0)$. One of the main technical difficulties of fracture mechanics of piezoelectric materials is how to correctly describe this limiting process.

Ref. [1] suggests that in the Fourier transform domain the limiting process may be approximated as

$$\lim_{h_0\to 0} F^*(\zeta) \to \lim_{h_0\to 0} f^*(\zeta, h^*(\zeta)) = f^*\left(\zeta, h_0\frac{\sin(a\zeta)}{\zeta}\right) \to f^*(\zeta,0) \tag{8}$$

which, the author believed, is plausible in an asymptotic sense.

Moreover, the approximation (8) becomes exact when $F(X,Y)$ is a linear function with respect variable Y, which is the difference of $\tilde{E}_X(X,Y)$ and $\tilde{E}_X^a(X,Y)$. To require the same restriction on $\tilde{E}_X(X,Y)$ and $\tilde{E}_X^a(X,Y)$ may be too strong.

(2) From the perspective of classical fracture mechanics, it is also true that for a finite rectangular slit, there is no singularity for the electrical/mechanical fields at $X=\pm a$ an $Y=0$. The singularities will appear at the four corners of the rectangular slit, $(\pm a, \pm h_0)$, with a singularity power index different from $-1/2$.

Nonetheless, it has become a consensus now that the fracture process of a piezo-electric ceramic is in fact a coupled multiscale phenomenon. This can be argued based on both its physical nature and its mathematical structure.

Ref. [1] tried to explore the asymptotic multiscale structure of the problem. Intuitively, the crack-tip field was viewed as the outer problem, and it was assumed that it has the form of the classical solution with respect to the ''slow'' coordinate variables (therefore there is basically no slit there). On the other hand, the electrostatic problem inside the crack was viewed as an inner problem that is controlled by the slit height, h_0, which is the length scale of the problem and it is associated with the ''fast'' coordinate variable.

The essential idea of this approach is using Eq. (8) to match the outer (macro) solution with the inner (micro) solution. Of course, the asymptotic multiscale analysis could be done differently.

Reference

[1] Li, S., 2003, ''On Global Energy Release Rate of a Permeable Crack in a Piezoelectric Ceramic,'' ASME Journal of Applied Mechanics, **70**, pp. 246–252.